Dynamique de systèmes physiques aux transitions de phase et interfaces libres

Vadim Nikolayev

Université Pierre et Marie Curie Paris VI

Habilitation à Diriger des Recherches

Présentée par

Vadim Nikolayev

Service des Basses Températures, DSM/DRFMC/CEA-Grenoble
et Laboratoire de Physique et Mécanique des Milieux Hétérogènes,
École Supérieure de Physique et de Chimie Industrielles de la Ville de Paris

Spécialité : Physique
Option : Physique des liquides

Dynamique de systèmes physiques aux transitions de phase et interfaces libres

Soutenue le 15 décembre 2005 devant la commission d'examen :

Mme	**Anne-Marie CAZABAT**	Rapporteur
MM.	**Daniel BEYSENS**	
.	**Yves POMEAU**	Président
.	**Lounès TADRIST**	Rapporteur
.	**José Eduardo WESFREID**	
.	**Stéphane ZALESKI**	Rapporteur

A mes parents et grands-parents qui m'ont élevé dans le respect de la Science

Résumé : Cette thèse décrit les études théoriques de deux catégories de phénomènes physiques : les transitions de phase et l'hydrodynamique physique. Dans la première catégorie se rangent plusieurs phénomènes ayant lieu dans des solides et dans des fluides. Les solides considérés sont des cristaux non-stœchiométriques supraconducteurs à haute température critique qui présentent des structures périodiques à période longue. Pour les fluides, on s'intéresse surtout à la cinétique des transitions de phase : il s'agit de la séparation de phase dans des mélanges binaires liquides, de l'ébullition et enfin de la condensation naturelle (rosée ou buée). La deuxième catégorie inclut la modélisation du mouvement de la ligne triple de contact liquide-gaz-solide le long d'un substrat hétérogène ainsi que l'analyse de l'instabilité d'une couche liquide placée dans le champ électrique.

Cette thèse peut être téléchargée à l'adresse suivante :
http://www.pmmh.espci.fr/~vnikol

Table des matières

1 Mon parcours professionnel

1.1 CV

1980–1985

J'ai débuté ma carrière de chercheur pendant ma troisième année d'études à l'Université de Kiev (en Ukraine, URSS à l'époque), faculté de Radio-Physique, http://www.rpd.univ.kiev.ua. La recherche menée dans cette faculté, axée sur la physique appliquée. Elle concerne surtout les aspects de la physique des ondes et du signal, leurs émission, transformation et enregistrement. Je faisais partie du laboratoire d'enregistrement d'images optiques dirigé par les professeurs M. G. Nakhodkin et M. K. Novoselets. Le laboratoire s'occupait de l'optimisation des paramètres du système thermoplastique, un système pour l'enregistrement des images holographiques utilisé à l'époque surtout à bord des stations spatiales soviétiques en raison de sa réversibilité et de sa grande résistance aux rayonnements. Son principe de fonctionnement (voir le chapitre 2.2 ci-dessous) est purement physique. Sa description théorique implique la résolution de problèmes d'hydrodynamique, d'électrostatique, de physique statistique et, bien sûr, d'optique. Mon premier article [34], basé sur ma thèse de diplôme de physicien-ingénieur, était consacré à l'analyse de l'instabilité électro-capillaire dans une couche de fluide newtonien. J'ai obtenu en 1985 le diplôme de physicien-ingénieur en radio-physique de l'Université d'Etat de Kiev avec la mention excellent.

1985–1988

J'ai effectué ma thèse de doctorat "Analyse statistique d'un milieu déformable pour l'enregistrement de l'information optique" au sein du même laboratoire. Ma recherche était concentrée sur les études du bruit dans le système thermoplastique par des méthodes de la physique statistique. Les origines du bruit et son impact sur les paramètres informatiques (rapport signal-bruit, fidélité de reproduction de l'image,...) ont été analysés. Le travail a été publié en russe dans les revues [31-34], les actes de congrès [59-65], et des rapports classés à cause des applications spatiales. L'aperçu de ce travail est donné dans le chapitre 2. Pendant mes études doctorales, j'ai encadré pendant deux ans des travaux dirigés sur le sujet "Principes des transformations et de l'enregistrement d'images optiques" pour des étudiants de troisième année. Ma thèse s'est terminée en 1988 et fut soutenue en 1989 à l'Université de Kiev.

1988–1993

Après avoir terminé mes études doctorales en 1988, j'ai été embauché à l'institut Bogoliubov de Physique Théorique de l'Académie Nationale des Sciences d'Ukraine, cf. http://www.bitp.kiev.ua. J'ai travaillé dans le département de Physique Non-linéaire de la Matière Condensée dirigé par l'académicien A. S. Davydov, puis par ses élèves professeurs Yu. B. Gaididei et V. M. Loktev. L'objet de ma recherche était les supraconducteurs à haute température critique qui venaient d'être découverts. J'ai étudié surtout la structure complexe de ces alliages céramiques. Mon travail a été publié dans des revues [26-30] et en tant que chapitre d'un livre [58]. Le compte-rendu de cette recherche est présenté dans le chapitre 3. Pendant deux ans j'ai donné le cours "L'ordinateur personnel comme outil du physicien-théoricien" pour les étudiants

et doctorants de la faculté de physique de l'Université de Kiev.

En 1993, j'ai co-organisé une expédition à Féodisia (Crimée, Ukraine) avec D. Beysens et I. Mylymuk. Notre équipe franco-ukrainienne comprenait des physiciens, hydrologues et archéologues. L'objectif était d'étudier les restes des premiers condenseurs de l'histoire humaine servant à récupérer l'eau atmosphérique. Les résultats de nos recherches ont été publiés dans "La Recherche" [25] ainsi que dans une revue spécialisée [24] (cf. chapitre 7).

1994–1995

Avec une bourse du gouvernement français, je suis resté un an et demi en 1994–1995 dans le Service de Physique de l'Etat Condensé du CEA-Saclay où j'ai travaillé sur la cinétique de séparation de phase [22, 23] (voir le chapitre 4) et sur l'optique de la buée. Ces dernières études ont donné lieu à des articles [21, 55] et à un brevet [38] (cf. chapitre 7.6). J'ai co-encadré un étudiant DEA (P. Sibille) sur ce sujet. Un projet [68] dont je suis le co-signataire a été rédigé. Il a été sélectionné par la suite par la NASA. Grâce à ce projet, un séjour aux USA (voir ci-dessous) est devenu possible.

En **1996–1997**, j'ai travaillé pendant un an au DRFMC, CEA-Grenoble en tant que collaborateur temporaire étranger sur la physique de l'ébullition. En interaction avec des ingénieurs d'EDF-Chatou, j'ai étudié la crise d'ébullition par caléfaction [20, 56] (voir aussi le chapitre 5). Des études sur la condensation naturelle ont été également poursuivies [52].

En **1997–1999**, j'ai effectué un séjour en tant que *Visiting Assistant Professor* au Département de Physique de l'Université de la Nouvelle-Orléans en Louisiane, USA. Dans le cadre du projet de la NASA [68], l'évaporation des fluides au voisinage de leur point critique ("ébullition critique") a été explorée [19, 53, 54].

1999–présent

Après avoir quitté définitivement l'institut Bogoliubov à Kiev, j'ai été embauché fin 1999 au CEA-Grenoble au laboratoire ESEME (Equipe du Supercritique pour l'Environnement, les Matériaux et l'Espace), nouvellement créé au sein du Service des Basses Températures (SBT). Les études de l'ébullition ont été poursuivies [7, 11,49-51...]. Le banc de lévitation magnétique de l'hydrogène développé au SBT a permis d'étudier des phénomènes en microgravité [13] sans nécessairement utiliser des ressources spatiales très chères. A Grenoble, j'ai encadré un étudiant (C. Lenormand de l'Université Joseph Fourier) pendant son stage de maîtrise en 2000. L'ESEME, dirigée par Daniel Beysens, est devenu en 2000 équipe mixte CEA-CNRS et a déménagé dans les locaux de l'Institut de Chimie de la Matière Condensée de Bordeaux (ICMCB). Ce déménagement a permis une collaboration très étroite avec le groupe de Y. Garrabos surtout en ce qui concerne d'une part l'interprétation et l'explication [15, 17, 18] des résultats obtenus à l'aide du dispositif ALICE franco-russe qui fonctionnait à bord de la station spatiale Mir et d'autre part la préparation du programme des nouvelles expériences dans le dispositif DECLIC (CNES-NASA-ESA) qui volera à bord de la Station Spatiale Internationale en 2008. Je coordonne maintenant des projets évalués comme excellents par l'ESA [66] et le CNES [69] sur l'ébullition critique. Il s'agit de coordonner les activités expérimentales de DECLIC et du banc de lévitation magnétique au SBT, avec des volets théorique et de simulations en collaboration avec plusieurs équipes françaises et une équipe ukrainienne. Cette dernière a récemment rejoint le projet d'ébullition et travaille dans le cadre d'un projet franco-ukrainien [67] en cours.

Les études sur la condensation atmosphérique (cf. chapitre 7) ont été poursuivies en collaboration avec l'université de Corse (UMR CNRS 6134) à Ajaccio [5, 10, 47, 48]. Je co-encadre un étudiant en thèse (O. Clus) qui développe ce sujet.

Les observations de la coalescence des gouttes sessiles [6, 16] ont stimulé la recherche de l'impact des hétérogénéités du substrat sur la dynamique de mouillage [8, 14], voir chapitre 6.

En **2004**, ESEME s'est intégré au laboratoire PMMH (Physique et Mécanique des Milieux Hétérogènes, UMR 7636) de l'ESPCI (École Supérieure de Physique et de Chimie Industrielles de la ville de Paris) et j'ai déménagé sur la région parisienne suite à ma mise à disposition de l'ESPCI. Je travaille à l'ESPCI-PMMH depuis.

1.2 Liste de publications

a) Articles dans des revues avec comité de lecture :

1. Narhe R., Beysens D., **Nikolayev V.** Dynamics of drop coalescence on a surface : the role of initial conditions and surface properties, *Int. J. Thermophysics*, **26**(6), 1743 – 1757 (2005).
2. Hegseth J., Oprisan A., Garrabos Y., **Nikolayev V. S.**, Lecoutre-Chabot C. & Beysens D. Wetting film dynamics during evaporation under weightlessness in a near-critical fluid, *Phys. Rev. E*, **72**, 031602 (2005).
3. Iliev S., Pesheva N., **Nikolayev V. S.**, Quasi-static relaxation of arbitrarily shaped sessile drops, *Phys. Rev. E*, **72**, 011606 (2005) ; voir page 266 de cette thèse.
4. **Nikolayev V. S.**, Dynamics and depinning of the triple contact line in the presence of periodic surface defects, *J. Phys. Cond. Matt.* **17**(13), 2111 – 2119 (2005) ; voir page 257 de cette thèse.
5. Beysens D., Muselli M., **Nikolayev V.**, Narhe R. and Milimouk I., Measurement and modelling of dew in island, coastal and alpine areas, *Atmospheric Research* **73**(1-2), 1 – 22 (2005).
6. Narhe R., Beysens D., **Nikolayev V.** Contact Line Dynamics in Drop Coalescence and Spreading, *Langmuir* **20**, 1213 – 1221 (2004) ; voir page 248 de cette thèse.
7. **Nikolayev V. S.**, Beysens D., Garrabos Y., Crise d'ébullition : inhibition du détachement de la bulle de vapeur par la force de recul, *Mécanique & Industries* **5**(5), 553 – 558 (2004) ; voir page 242 de cette thèse.
8. **Nikolayev V. S.**, Beysens D., Equation of motion of the triple contact line along an inhomogeneous surface, *Europhysics Letters* **64**(6), 763 – 768 (2003) ; voir page 225 de cette thèse.
9. **Nikolayev V. S.**, Dejoan A., Garrabos Y. & Beysens D. Fast heat transfer calculations in supercritical fluids versus hydrodynamic approach, *Phys. Rev. E* **67**, 061202-1 – 11 (2003) ; voir page 231 de cette thèse.
10. Beysens D., Milimouk I., **Nikolayev V.**, Muselli M., Marcillat J. Using radiative cooling to condense atmospheric vapor : a study to improve water yield, *Journal of Hydrology* **276**, 1 – 11 (2003).
11. Beysens D., **Nikolayev V. S.**, Garrabos Y., Vapor spreading and the boiling crisis, *J. Phys. : Condensed Matter* **15**, S435 – S442 (2003).
12. Beysens D., Garrabos Y., **Nikolayev V. S.**, Lecoutre C., Delville J.-P., and Hegseth J., Liquid-vapor phase separation in a thermocapillary force field, *Europhysics Letters* **59**(2), 245 – 251 (2002) ; voir page 183 de cette thèse.
13. Chatain D., **Nikolayev V. S.**, Using magnetic levitation to produce cryogenic targets for inertial fusion energy : experiment and theory, *Cryogenics* **42**, 253 – 261 (2002).

14. **Nikolayev V. S.**, Beysens D.A., Relaxation of non-spherical sessile drops towards equilibrium, *Phys. Rev. E*, **65**, 046135 (2002) ; voir page 217 de cette thèse.
15. Hegseth J., Garrabos Y., **Nikolayev V. S.**, Lecoutre-Chabot C., Wunenburger R., Beysens D., Gas "wets" a solid wall in orbit, *International Journal of Thermophysics* **23**, 89 – 101 (2002).
16. Andrieu C., Beysens D., **Nikolayev V. S.**, Pomeau Y. Coalescence of sessile drops, *J. Fluid. Mech.* **453**, 427 – 438 (2002) ; voir page 205 de cette thèse.
17. Garrabos Y., Dejoan A., Lecoutre C., Beysens D., **Nikolayev V.**, Wunenburger R., Piston effect in a supercritical fluid sample cell : a phenomenological approach of the mechanisms, *Journal de Physique IV (France)* **11**, Pr 6-23 – 34 (2001).
18. Garrabos Y., Lecoutre-Chabot C., Hegseth J., **Nikolayev V. S.**, Beysens D. & Delville J.-P. Gas spreading on a heated wall wetted by liquid, *Phys. Rev. E* **64**(5), 051602-1 – 10 (2001) ; voir page 173 de cette thèse.
19. **Nikolayev V. S.**, Beysens D.A., Lagier G.-L., Hegseth J. Growth of a dry spot under a vapor bubble at high heat flux and high pressure, *International Journal of Heat and Mass Transfer* **44**, 3499 – 3511 (2001) ; voir page 160 de cette thèse.
20. **Nikolayev V. S.**, Beysens D.A. Boiling crisis and non-equilibrium drying transition, *EuroPhysics Letters* **47**(3), 345 – 351 (1999) ; voir page 153 de cette thèse.
21. **Nikolayev V. S.**, Sibille P., Beysens D. Coherent light transmission by a dew pattern, *Optics Communications* **150**, 263 – 269 (1998) ; voir page 146 de cette thèse.
22. **Nikolayev V. S.**, Beysens D.A. Coalescence limited by hydrodynamics, *Physics of Fluids* **9** (11), 3227 – 3234, (1997) ; voir page 138 de cette thèse.
23. **Nikolayev V. S.**, Beysens D., Guenoun P. New hydrodynamic mechanism for droplet coarsening, *Phys. Rev. Lett.* **76**(17), 3144 – 3147, (1996) ; voir page 134 de cette thèse.
24. **Nikolayev V. S.**, Beysens D., Gioda A., Milimouk I., Katiushin E., Morel J.-P. Water recovery from dew, *Journal of Hydrology* **182**, 19 – 35, (1996) ; voir page 117 de cette thèse.
25. Beysens D., Gioda A., Katiushin E., Milimouk I., Morel J.-P., **Nikolayev V. S.** Les Puits Aériens, *La Recherche*, Mai(287), 30 – 33 (1996) ; trad. espagnole : Los pozos de rocío, un sueño reflotado, *Mundo Cientifico* Julio/Agosto(170), 620 – 623 (1996).
26. **Nikolayev V. S.** Twin Spacing and the structural phase transitions in $RBa_2Cu_3O_{7-\delta}$ high-T_c superconductors, *Phys. Rev. B* **50**(6), 4163 – 4167 (1994) ; voir page 112 de cette thèse.
27. Gorbar E.V., Loktev V.M., **Nikolayev V. S.** About the structure of the superconducting order parameter of 2D Fermi system with an arbitrary carrier density, *Sverkhprovodimost' : Fizika, Khimia, Tekhnika* **7** (1), 1 – 11 (1994), en Russe, trad. angl. : *Soviet Superconductivity : Physics, Chemistry, Technics.*
28. **Nikolayev V. S.** Twin spacing versus size of a monocrystal for the nonstoichiometric 1 :2 :3 superconductors, *Phys. Lett. A* **180**, 157 – 163 (1993).
29. **Nikolayev V. S.** About the Ferroelastic Properties of the Twin Structure of 1-2-3-type High- T_c Superconductors, *Ukrainskij Fizicheskij Zhurnal* **36**(7), 1111 – 1115 (1991), en Russe, trad. angl. : *Ukr. J. of Phys.*.

30. Gaididei Yu.B., Loktev V.M., **Nikolayev V. S.** On the Theory of Formation of a Twin (Ferroelastic) Structure in High-Temperature Superconductors with Oxygen Nonstoichiometry, *Solid State Commun.* **75**(6), 503 – 506 (1990).
31. Nakhodkin M.G., **Nikolayev V. S.**, Novoselets M.K. Fluctuations and Formation of the Chaotic Relief on the Surface of Viscous Liquid Layer in the Electric Field. Part 2. Linear Theory for the Layers with Conducting Surface, *Ukrainskij Fizicheskij Zhurnal (Ukr. J. of Phys.)*, **34**(1), 80 – 84 (1989), en Russe.
32. Novoselets M.K., **Nikolayev V. S.** Anisotropic Spinodal Decomposition of Binary Polymer Blend in the Electric Field, *Himicheskaya Fizika (Chem. Phys. Moscow)* **7**, 1291 – 1292 (1988), en Russe ; voir page 110 de cette thèse.
33. Nakhodkin M.G., **Nikolayev V. S.**, Novoselets M.K. Fluctuations and Formation of the Chaotic Relief on the Surface of Viscous Liquid Layer in the Electric Field. Part 1. Linear Theory for the Layers with Non-Conducting Surface, *Ukrainskij Fizicheskij Zhurnal (Ukr. J. of Phys.)*, **33**(8), 1185 – 1192 (1988), en Russe.
34. Novoselets M.K., **Nikolayev V. S.** Electric Instability of Capillary Waves for Newton Liquid of Finite Depth, *Ukrainskij Fizicheskij Zhurnal (Ukr. J. of Phys.)* **32**(5), 713 – 718 (1987), en Russe ; voir page 103 de cette thèse.

b) Thèse :

35. **Nikolayev V. S.** *Analyse statistique d'un milieu déformable pour l'enregistrement de l'information optique*. Thèse de Candidat es sciences (doctorat) en physique et mathématique, Université d'Etat de Kiev, 1989. Approuvée par la Haute Commission d'Attestation à Moscou.

c) Articles en cours de publication :

36. Beysens D., Milimouk I., **Nikolayev V.**, Berkowicz S., Muselli M., Heusinkveld B., & Jacobs A. F. G. Comment on "The moisture from the air as water resource in arid regions : hopes, doubt and facts" by Kogan & Trahtman, *J. Arid Environments*, soumis (2005).
37. **Nikolayev V. S.**, Gavrilyuk S. L. & Gouin H., Influence of the fluid inertia on the moving deformed triple contact line, soumis.

d) Brevet :

38. Beysens D., Marcos-Martin M., **Nikolayev V.**, Sibille P. Procédé et dispositif de caractérisation d'une modification au cours du temps de l'état de condensation de gouttelettes sur une cible. Brevet français #96 11310 du 17/09/1996 au nom du CEA (Réf. DD 1511).

e) Actes de congrès, chapitres dans des livres, etc. :

39. **Nikolayev V. S.**, Beysens D., La crise d'ébullition vue comme l'étalement des bulles sur la paroi chauffante, 17ème Congrès Français de Mécanique, Troyes, 29/8-2/09 2005, publié sur un CD-ROM, AFM (2005) ; résumé accessible sur : http://www-cfm2005.utt.fr/programmedetailleparsession.php?theme=C11
40. **Nikolayev V. S.**,Motion of the triple contact line, 17ème Congrès Français de Mécanique, Troyes, 29/8-2/09 2005, publié sur un CD-ROM, AFM (2005) ; résumé accessible sur : http://www-cfm2005.utt.fr/programmedetailleparsession.php?theme=S8
41. **Nikolayev V.**, Beysens D. Boiling crisis : theory, simulation, and experiments in microgravity, "Theory and simulations", Bulletin DRFMC No. 4 (Novembre), 44 – 45 CEA, Grenoble (2004) téléchargeable sur http://www-drfmc.cea.fr/Phocea/file.php?file=Bulletin/Bulletin_N4.pdf&class=std.
42. **Nikolayev V. S.**, Beysens D., Garrabos Y., Crise d'ébullition : inhibition du détachement de la bulle de vapeur par la force de recul, 16ème Congrès Français de Mécanique, Nice, 1 - 5/09 2003, publié sur un CD-ROM, AFM (2003).
43. Narhe R., Beysens D., **Nikolayev V.** Dynamics of Drop Coalescence on a Surface : The Role of Initial Conditions and Surface Properties, 15th Symposium on Thermophysical Properties, Boulder, CO (USA) 22-27/6/2003, publié sur un CD-ROM, accessible sur http://symp15.nist.gov/pdf/p81.pdf.
44. Beysens D., Chatain D., **Nikolayev V. S.**, Garrabos Y., Magnetic facility gives heat transfer data in H_2 at various acceleration levels, paper #148, 4th Int. Conf. on Launcher Technology "Space Launcher Liquid Propulsion", 3-6/12/2002, Liege, Belgium, publié sur un CD-ROM, (CNES, Toulouse, 2002) ; résumé accessible sur : http://cnes.cborg.net/propulsion/program/propellant_management_in_tanks_2/0148-0212prop.PDF.
45. **Nikolayev V. S.**, Beysens D.A. 2D BEM modeling of a singular thermal diffusion free boundary problem with phase change, Boundary elements XXIV (Incorporating meshless solutions), Eds. C.A. Brebbia, A. Tadeu & V. Popov, *Int. Series on Advances in Boundary Elements* **13** WIT Press (Southhampton, Boston) 501–525 (2002) ; voir page 190 de cette thèse.
46. **Nikolayev V. S.**, Beysens D.A., Garrabos Y., Hegseth J. CHF as a Non- Equilibrium Drying Transition, *Proceedings of the 4th International Conference on Multiphase Flow (ICMF), New Orleans, LA (USA), May 27-June 1, 2001,* Ed. E. E. Michaelides, published on a CD-ROM , paper 937, Tulane University (2001).
47. Beysens D., **Nikolayev V. S.**, Milimouk I. and Muselli M. A study of Dew and frost precipitation at Grenoble, France, *Proceedings of the 2nd International Conference on Fog and Fog Collection*, St John's (Canada), July 16-20, 2001, Eds. R. S. Schemenauer and H. Puxbaum, IDRC, 329 – 331 (2001).
48. **Nikolayev V. S.**, Beysens D. and Muselli M. A Computer Model for Assessing Dew/Frost Surface Deposition. *Proceedings of the 2nd International Conference on Fog and Fog Collection*, St John's (Canada), July 16-20, 2001, Eds. R. S. Schemenauer and H. Puxbaum, IDRC, 333 – 336 (2001).
49. Garrabos Y., Wunenburger R., Lecoutre C., **Nikolayev V.**, Beysens D., Hegseth J. Heat and Mass Transfer Phenomena in Two-phase Near-critical Fluid Observed in Microgravity,

Presented at 1^{st} International Symposium on Microgravity Research & Applications in Physical Sciences and Biotecnology, Sorrento (Italy), Sept. 10-15, 2000, Published in ESA-SP **454**,157 – 166 (2001).

50. Hegseth J., Garrabos Y., **Nikolayev V. S.**, Lecoutre-Chabot C., Wunenburger R., Beysens D., Gas "wets" a solid wall in orbit, 14^{th} Symposium on Thermophysical Properties, Boulder, CO (USA) 25-30/6/2000, publié sur un CD-ROM, accessible sur http://symp14.nist.gov/PDF/WET05HEG.PDF.
51. **Nikolayev V. S.**, Beysens D.A., Hegseth J., Boiling Crisis as a Non- Equilibrium Drying Transition, 14^{th} Symposium on Thermophysical properties, Boulder, CO (USA) 25-30/6/2000, publié sur un CD-ROM, accessible sur http://symp14.nist.gov/PDF/WET10NIK.PDF.
52. Beysens D.A., Milimouk I., **Nikolayev V.** Old Dreams and Actual Results, First International Conference on Fog and Fog Collection, Vancouver, Canada, July 19-24, 1998, 269 – 272.
53. Hegseth J., **Nikolayev V.**, Beysens D., Garrabos Y. et Chabot C. Growth and Morphology of Phase Separating Supercritical Fluids (GMSF), Boiling in Subcritical Fluids, and Critical Fluctuations, Proc. Fourth Microgravity Fluids Physics and Transport Phenomena Conf., Aug. 12- 14, 1998, Cleveland, Ohio (USA), 184 – 189 ; Published as a CD-ROM, see http://ncmr04610.cwru.edu/events/fluids1998/papers/433.pdf.
54. Hegseth J., Beysens D., **Nikolayev V.**, Garrabos Y. et Chabot C. Phase Separation and Boiling Near the Critical Point in Pure Fluids – Proceedings of the 1997 NASA/JPL Microgravity Fundamental Physics Workshop, NASA Document D-15677, 127 – 137 (1998).
55. **Nikolayev V. S.**, Beysens D. Coherent light transmission by a drop pattern, in : Diffractive Optics, European Optical Society, Topical Meetings Digests Series : **12**, Savonlinna, Finland, 154 – 155 (1997).
56. Hegseth J., Beysens D., Perrot F., **Nikolayev V.**, et Garrabos Y. Growth and Morphology of Phase Separating Supercritical Fluids – Third Microgravity Fluid Physics Conference, NASA Conf. Publ. 3338, 35 – 40 (1996).
57. Matviychuk S.G., **Nikolayev V. S.**, Vakhnenko O.O. Dynamics of the two-component soliton in the discrete molecular chain, Preprint of the Institute for Theoretical Physics (Academy of Sciences of Ukraine), Kiev, no. ITP-93-56E, 1–9 (1993).
58. **Nikolayev V. S.** About the Influence of Uniaxial Pressure on the Twin Structure in the 1-2-3 System, in : Electron-Electron Correlation Effects in Low-Dimensional Conductors and Superconductors, A.A.Ovchinnikov, I.I.Ukrainskii (Eds.), Springer-Verlag, 54 – 59 (1991).
59. Novoselets M.K., **Nikolayev V. S.** Sources of Noise of Photothermoplastic Media and Top Information Characteristics, 5th All-Union Conference on Unsilver and Unusual Photographic Processes, Suzdal, USSR (1988) (en Russe).
60. Novoselets M.K., **Nikolayev V. S.** Statistical Description of the Noise of the Photothermoplastic Media, 5th All-Union Conference on Silverless and Unusual Photographic Processes, Suzdal, USSR (1988) (en Russe).
61. Novoselets M.K., **Nikolayev V. S.** Spinodal Decomposition and Formation of the Chaotic Relief in the Photothermoplastic Media, 5th All-Union Conference on Unsilver and Unusual Photographic Processes, Suzdal, USSR (1988) (en Russe).
62. Novoselets M.K., **Nikolayev V. S.** Spinodal Decomposition in the Photothermoplastic Recording Media, Conference on Holography, Correlation Analysis and Recording Media. Chernovtsy, USSR (1988) (en Russe).

63. Novoselets M.K., **Nikolayev V. S.**, Kurnosikov O.V. Statistical Parameters of Noise in the Photothermoplastic Media, Conference on Holography, Correlation Analysis and Recording Media. Chernovtsy, USSR, (1988) (en Russe).
64. **Nikolayev V. S.** Spinodal Decomposition in the Optical Media that Contains a Polymer Blend, 3-d All-Union Conference of Young Scientists on Theoretical and Applied Optics, Leningrad, USSR, 458–459 (1988) (en Russe).
65. Nakhodkin M.G., **Nikolayev V. S.**, Novoselets M.K. Maximum Level of Noise of the Photothermoplastic Media, 2-nd All-Union Conference on Formation of an Optical Image and Methods of Image Processing, Kishinev, USSR (1985) (en Russe).

f) Subventions obtenues :

66. **Nikolayev V. S.**, Beysens D., Chatain D., Evesque P., Hegseth J., Garrabos Y. & Lecoutre C., Boiling crisis and near-critical fluids, LifePhys ESA AO (2005).
67. **Nikolayev V. S.**, Beysens D., Garrabos Y., Fermigier M., Chatain D., Feuillebois F., Polyakov M., Kochubey O., Prykhodko O., Yevdokymov, D., Brazaluk Yu., Bevza E., Grishay M., Modélisation physique et mathématique de la crise d'ébullition, PAI France-Ukraine "Dnipro", EGIDE (2005–2007).
68. Hegseth J., **Nikolayev V.**, Beysens D. & Perrot F. Growth and Morphology of Phase Separating Supercritical Fluids, NASA Grant NAG-1906 (1997–1999).
69. **Nikolayev V. S.**, Beysens D., Chatain D., Bennacer R., El Ganaoui M., Prud'homme R., Garrabos Y. & Lecoutre C., Etude de l'ébullition à l'échelle mesoscopique : théorie et expérimentation en microgravité, Proposition de recherche scientifique spatiale, CNES (2005).
70. **Nikolayev V. S.** Deux Subventions de International Science (Soros) Foundation (1993-1994).

g) Conférences invitées :

71. **Nikolayev V. S.** Singularités hydrodynamique et thermique de la ligne de contact gaz-liquide- solide en mouvement, séminaire ESPCI/PMMH, le 27 février 2004, résumé accessible sur http://www.pmmh.espci.fr/resumes/nikolayev.html
72. **Nikolayev V. S.** Dynamique de la ligne triple de contact en présence de défauts sur la surface solide, séminaire ENS/LPS 15/12/2004, résumé accessible sur http://www.lps.ens.fr/seminaire_lps/resumes/nikolayev.html
73. **Nikolayev V. S.**, Beysens D. Une méthode efficace pour calculer le transfert de chaleur en microgravité dans des fluides proches de leur point critique, Séminaire CEA-GAMNI "La mécanique des fluides numérique", Institut Henri Poincaré, 26-27/1/2004 ; résumé accessible sur http://www.cmap.polytechnique.fr/~allaire/gamni/resumes/nikolaev.html.
74. **Nikolayev V. S.**, Beysens D. Out of equilibrium drying transition, Workshop "Wetting : From microscopic origins to industrial applications", Hyères, 6-12/5/2000.

75. **Nikolayev V. S.** Spinodal decomposition and wetting in near-critical fluids, 79th Statistical Mechanics Conference, Rutgers University (USA), May, 1998.

2 Amplification de fluctuations dans le système thermoplastique

2.1 Motivation

Le système thermoplastique qui a été étudié dans ma thèse [8] a été inventé dans les années 1960 [5, 4] pour pouvoir enregistrer une image holographique quasiment instantanément, sans traitement onéreux de film. Pendant les trois décennies suivantes, des systèmes de ce type ont été produits par de nombreuses sociétés (HC-300 de Newport Research Corp., caméra holographique FH2AR de Fujinon, TPC 200 de Steinbichler Optotechnik Gmbh. . .). Les études du laboratoire du Traitement des Images Optiques de l'Université de Kiev où j'ai fait ma thèse ont été surtout motivées par des applications spatiales. Parmi les avantages de ce système on peut citer le temps de traitement très réduit (1 s par cycle d'enregistrement), une bonne résolution spatiale (2000-3000 lignes par mm), une bonne sensibilité (1-5 erg/cm^2) dans la plage 400-800 nm de longueur d'onde. Pour les applications spatiales, sa réversibilité (jusqu'à 1500 cycles d'enregistrement sur le même support pour les meilleurs systèmes) et son insensibilité aux rayonnements extérieurs, très gênants pour les films photographiques traditionnels, sont ses attraits principaux. Cependant, ce système a ses inconvénients, notamment un haut niveau de bruit. Le but de mes études doctorales était donc d'étudier les fluctuations et leur amplification, due à plusieurs instabilités que l'on trouve dans ce système et qui sont à l'origine du bruit optique.

2.2 Principe de fonctionnement du système thermoplastique

Le système thermoplastique est une couche de polymère déposée sur un support métallisé (Figs. 2.1). La couche possède en même temps les propriétés d'un thermoplastique (i.e. devient liquide sous chauffage) et d'un photoconducteur (i.e. tout en restant isolant dans l'obscurité, elle devient conductrice une fois illuminée). L'ensemble est transparent.

Pour préparer ce système à l'enregistrement, une charge électrostatique est déposée sur sa surface (Fig. 2.1a) dans l'obscurité. Pendant la durée de la phase d'exposition (Fig. 2.1b) à la lumière, une partie de la charge quitte la surface en raison des propriétés photoconductives de la couche et l'image se trouve donc enregistrée comme une variation spatiale de charge superficielle. Le développement de l'image (Fig. 2.1c) se produit dans l'obscurité quand le système est chauffé (éventuellement par une impulsion de courant électrique à travers la métallisation). La couche devient alors liquide et sa surface se déforme sous l'action des forces électrostatiques. La rugosité superficielle correspondant à l'image enregistrée peut être lue (Fig. 2.1d) grâce à la diffraction d'une lumière cohérente. Le reste de la charge s'en va au travers de la couche en même temps. Le cycle d'enregistrement peut être répété après avoir effacé la rugosité en chauffant le milieu (par effet de la tension superficielle).

Le bruit dans ce système prend sa source dans les fluctuations spatiales de la charge électrique déposée pendant la phase de préparation. Deux autres sources (les fluctuations hydrodynamiques

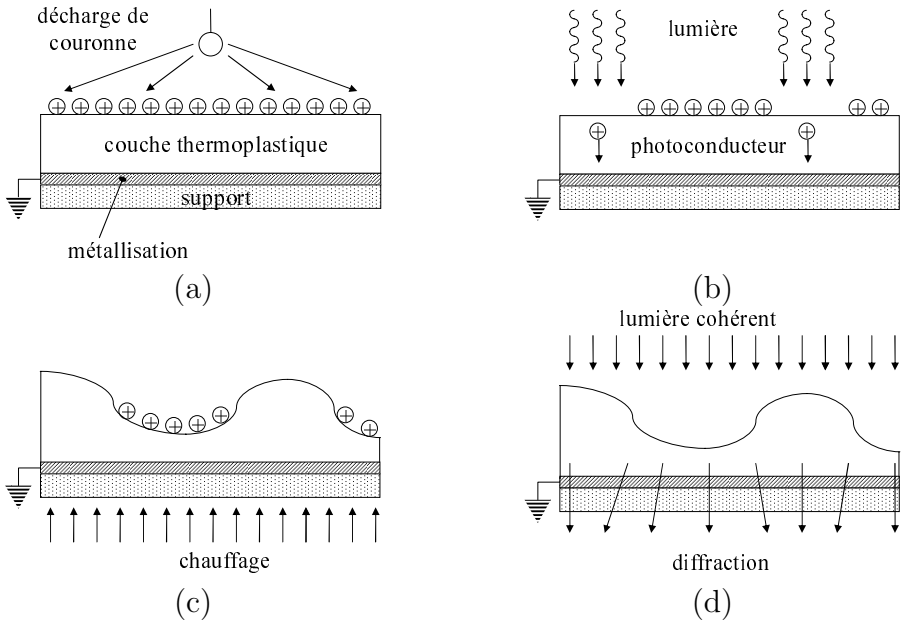

FIGURE 2.1: Le cycle d'enregistrement du système thermoplastique : (a) préparation ; (b) enregistrement ; (c) développement ; (d) lecture

et celles du courant électrique) se rajoutent pendant la phase de développement.

Il est connu qu'une couche de fluide sous champ électrique homogène peut devenir instable. Une déformation de surface se développe. Cette instabilité a été étudiée d'une part pour un métal liquide dans un champ externe [13, 3] d'autre part pour un fluide non-visqueux [12]. On appelle cette instabilité "électrocapillaire" car son critère est défini par le bilan des forces électriques et capillaires.

Un autre phénomène peut apparaître dans ce système en raison de la composition de la couche thermoplastique, qui est le plus souvent un mélange de plusieurs types de polymères. Quand la température change, une séparation de phase peut se produire. Dans un champ électrique très fort, la courbe de co-existence est modifiée et la transition de phase se produit pour une température différente [11]. A cause du changement rapide de température, la séparation de phase peut être du type "décomposition spinodale" [2] dont le critère dépend aussi du champ [6].

D'un côté, ces instabilités peuvent servir à amplifier la rugosité utile de la surface, c.-à-d. le signal même. Mais d'un autre côté, elles augmentent aussi la rugosité chaotique, c.-à-d. le bruit. L'étude détaillée de ces deux instabilités s'avérait donc indispensable. Dans le chapitre suivant, nous allons discuter de ces deux instabilités dont l'analyse nous semble la partie la plus intéressante des travaux de ma thèse [8].

2.3 Instabilités d'une couche liquide dans un champ électrique

2.3.1 Instabilité électrocapillaire

Dans le travail [9] nous avons obtenu une relation de dispersion pour les ondes de surface d'une couche d'épaisseur d et de tension superficielle γ. Le fluide est newtonien incompressible de den-

sité ρ et viscosité dynamique μ. Le fluide est diélectrique, ε et ε' étant les constantes diélectriques respectives du fluide et du gaz au-dessus. Deux modes de création du champ électrostatique ont été prévus : par une électrode externe éloignée (champ E_0 constant quand $x_3 \to \infty$, cf. Fig. 1 sur la page 714 de l'article [9] pour la géométrie du problème, p. 103 de cette thèse) et par des charges distribuées sur la surface supérieure de la couche avec une densité superficielle σ (de valeur moyenne σ_0). La surface inférieure est supposée équipotentielle. Les charges peuvent migrer le long de l'interface en raison de la conductivité superficielle $\varkappa_s$.

Les équations ont été linéarisées et ce problème bidimensionnel a été résolu par les transformations de Fourier sur la coordonnée horizontale x et de Laplace sur le temps t, ce qui est équivalent à la recherche d'une solution sous la forme

$$h = \tilde{h}(k, s) \exp(ikx + st). \tag{2.1}$$

La relation de dispersion $s(k)$ prend alors la forme encombrante (10) de l'article [9] où $\xi = kd$ et les coefficients A_n et A_τ sont définies dans (8) (voir p. 715 de l' article [9] (p. 103 de cette thèse). L'influence du champ y est introduite par des composants $\varphi_1 = E_0 d\varepsilon'/\varepsilon$ et $\varphi_2 = \sigma_0 d/(\varepsilon/\varepsilon_0)$ du potentiel de la surface non-perturbée de la couche dû au champ extérieur et à la charge de surface respectivement, ε_0 étant la constante diélectrique du vide.

En analysant cette relation de dispersion avec la méthode de Vychegradsky-Nyquist, nous avons montré qu'une perturbation de la surface n'est jamais convectée. En gardant la même position, soit elle décroît, soit elle s'amplifie dans le temps.

On trouve que la surface conductrice ($\varkappa_s \neq 0$) est instable quand

$$(\varphi_1 - \varphi_2)^2 \coth \xi + \frac{\varepsilon}{\varepsilon'} \varphi_1^2 > \varphi_0 \xi, \tag{2.2}$$

où $\varphi_0 = \sqrt{\gamma d/(\varepsilon\varepsilon_0)}$. Pour des métaux liquides ($\varepsilon \to \infty$), la condition (2.2) se réduit à la condition [3]

$$\varepsilon' \varepsilon_0 E_0^2 > \gamma k \tag{2.3}$$

qui ne dépend pas de l'épaisseur de la couche. On note que pour le cas d'une surface conductrice, la couche est instable dans un champ électrique, même très petit. Le critère d'instabilité pour la surface non-conductrice ($\varkappa_s = 0$) est différent :

$$\frac{\varepsilon}{\varepsilon'} \left[\varphi_1 \left(1 - \frac{\varepsilon'}{\varepsilon} \right) + \frac{\varepsilon'}{\varepsilon} \varphi_2 \right]^2 + \xi \left[\varphi_1 \varphi_2 (1 + \tanh \xi) - \varphi_2^2 \right] / \left(\frac{\sinh 2\xi}{2} - \xi \right) > \xi \left(1 + \frac{\varepsilon'}{\varepsilon} \tanh \xi \right) \varphi_0^2. \tag{2.4}$$

On s'aperçoit que la surface n'est instable qu'à partir d'une valeur critique de charge superficielle, c.-à-d. pour $\varphi_2 > \varphi_{2cr}$. De plus, contrairement au cas $\varkappa_s \neq 0$, les ondes de grande longueur (de petit k) sont stables.

Bien que les critères (2.2,2.4) ne dépendent pas de la viscosité, son influence de celle-ci est très marquante sur l'incrément de l'instabilité s (cf. eq. 2.1), la courbe $s(\mu)$ passant par un maximum. Quand $\varphi_1, \varphi_2 \gg \varphi_0$, l'incrément atteint une saturation. Pour $\xi = kd \gg 1$ la valeur saturée s'exprime :

$$s = \frac{4\varepsilon\varepsilon'}{(\varepsilon - \varepsilon')^2} \frac{\mu k^2}{\rho}. \tag{2.5}$$

Conclusion

Le résultat le plus marquant de cette analyse est la détermination des critères d'instabilité d'une couche liquide dans un champ électrique qui ne dépendent pas de la viscosité du liquide. En contrepartie, la dynamique de la croissance instable d'une déformation de surface dépend de la viscosité, et la vitesse de croissance maximum est atteinte pour une viscosité bien définie. Nous avons montré qu'une déformation de surface qui apparaît et grossit à cause de l'instabilité, n'est jamais convectée le long de la surface.

2.3.2 Décomposition spinodale anisotrope

Puisque ce sujet n'a été abordé que très brièvement dans la publication [10] et comme ce problème n'a jamais été traité dans la littérature francophone ni anglophone, nous donnons ici un aperçu plus détaillé.

Rappel de la théorie de Cahn-Hilliard

La théorie standard de la décomposition spinodale [1] consiste à écrire une expression pour l'énergie libre d'un mélange de deux composants, la concentration $c = c(\vec{r}, t)$ d'un des composants étant variable d'un point $\vec{r}$ à l'autre :

$$F = \int \left[f(c) + \frac{K}{2} (\nabla c)^2 \right] \mathrm{d}\vec{r}, \tag{2.6}$$

où le coefficient $K > 0$ est constant et $f(c)$ est l'énergie du mélange homogène :

$$f(c) = f(\bar{c}) + \left.\frac{\mathrm{d}f}{\mathrm{d}c}\right|_{c=\bar{c}} \hat{c} + \frac{1}{2} \left.\frac{\mathrm{d}^2 f}{\mathrm{d}c^2}\right|_{c=\bar{c}} \hat{c}^2. \tag{2.7}$$

Ici la barre signifie une valeur moyennée sur le volume du mélange et le chapeau signifie une déviation à cette valeur : $\hat{c}(\vec{r}) = c(\vec{r}) - \bar{c}$. La cinétique de c est définie par l'équation de continuité

$$\frac{\partial c}{\partial t} = -\mathrm{div}\vec{j}, \tag{2.8}$$

où le flux diffusif $\vec{j}$

$$\vec{j} = -M \nabla \mu \tag{2.9}$$

s'exprime à travers du gradient du potentiel chimique μ qui à son tour est une dérivée fonctionnelle de F :

$$\mu = \frac{\delta F}{\delta c(\vec{r})}. \tag{2.10}$$

Quand l'énergie est décrite par la fonctionnelle (2.6), on trouve

$$\mu = \frac{\mathrm{d}f}{\mathrm{d}c} - K \Delta c. \tag{2.11}$$

La substitution des éqs. (2.10, 2.7) dans les éqs. (2.8, 2.9) et la transformée de Fourier sur $\vec{r}$ résulte en l'équation

$$\frac{\mathrm{d}\tilde{c}}{\mathrm{d}t} = R(\vec{k})\tilde{c}, \tag{2.12}$$

écrite pour l'image $\tilde{c}(\vec{k})$ de $\hat{c}(\vec{r})$. L'incrément $R(\vec{k}) = -Mk^2(A + Kk^2)$ est isotrope, c.-à-d. ne dépend que de $k = |\vec{k}|$. Evidemment, quand

$$A = \left.\frac{\mathrm{d}^2 f}{\mathrm{d}c^2}\right|_{c=\bar{c}} < 0, \tag{2.13}$$

$R(k) > 0$ pour le nombre d'onde

$$k < \sqrt{|A|/K}, \tag{2.14}$$

et le mélange est instable par rapport à une perturbation harmonique de c qui alors augmente dans le temps et mène à la séparation de phase. Ce régime de séparation s'appelle la décomposition spinodale. Le critère de celle-ci est donné par l'éq. 2.13.

Puisque R ne dépend pas de la direction du vecteur $\vec{k}$, la croissance conduira à une structure quasi-périodique isotrope de la phase minoritaire incrustée dans la matrice de la phase majoritaire.

Cas du champ électrique externe

Le champ électrique apporte de l'énergie supplémentaire dans le système. La variation de cette énergie correspondant à la variation de la constante diélectrique $\delta\varepsilon$ s'écrit [7]

$$\delta F_e = -\int \delta\varepsilon \frac{\varepsilon_0 E^2}{2}\,\mathrm{d}\vec{r}, \tag{2.15}$$

et donc

$$\frac{\delta F_e}{\delta\varepsilon} = -\frac{\varepsilon_0 E^2}{2}. \tag{2.16}$$

On cherche ensuite ε du mélange homogène des deux composants avec les constantes ε_1 et ε_2 telles que $\alpha = \varepsilon_1 - \varepsilon_2 \ll \varepsilon_1, \varepsilon_2$. Une constante diélectrique ε^* satisfaisant l'égalité

$$\langle\vec{D}\rangle = \varepsilon^*\varepsilon_0\langle\vec{E}\rangle, \tag{2.17}$$

où les crochets signifient le moyennage sur des configurations spatiales aléatoires et $\vec{E}, \vec{D}$ sont respectivement le champ et l'induction électrique, s'écrit [7]

$$\varepsilon^* = \varepsilon' - \frac{\alpha^2}{3\varepsilon'}c(1-c), \quad \varepsilon' = c\varepsilon_1 + (1-c)\varepsilon_2. \tag{2.18}$$

Cependant il nous faut trouver une constante diélectrique moyenne $\varepsilon(c)$ qui est définie par une équation différente de (2.17),

$$\langle F_e\rangle = \frac{1}{2}\varepsilon(c)\varepsilon_0\langle\vec{E}\rangle^2, \tag{2.19}$$

Nous avons démontré [8] qu'en fait ε^* de (2.17) et $\varepsilon(c)$ coïncident avec la précision α^2. Alors il est facile de déduire de (2.18) que

$$\frac{\mathrm{d}\varepsilon}{\mathrm{d}c} = a + \frac{2\alpha^2}{3\bar{\varepsilon}}\,\hat{c} + o(\hat{c}), \tag{2.20}$$

où $a = \alpha + O(\alpha^2)$ est un terme indépendant de $\hat{c}$. Combinée avec (2.16), l'éq. (2.20) résulte en l'équation linéarisée

$$\frac{\delta F_e}{\delta c} = -\frac{1}{2}\varepsilon_0 a\hat{E}^2 - \frac{1}{3\bar{\varepsilon}}\varepsilon_0\bar{E}\alpha^2\hat{c}, \tag{2.21}$$

où $\bar{E}$ est le module du champ moyen.

Incrément R en présence du champ électrostatique

On part des équations de l'électrostatique

$$\mathrm{div}(\varepsilon\vec{E}) = 0, \tag{2.22}$$

$$\vec{E} = -\nabla\varphi, \tag{2.23}$$

où φ est le potentiel. En linéarisant ces équations et en choisissant l'axe z parallèlement au champ imposé $\bar{\vec{E}}$, on obtient l'équation

$$\bar{\varepsilon}\Delta\hat{\varphi} = \frac{\partial\hat{\varepsilon}}{\partial z}\bar{E}. \tag{2.24}$$

En appliquant la transformée de Fourier et en tenant compte de l'éq. (2.20), on obtient la solution dans l'approximation linéaire

$$\tilde{\varphi} = -ik_z\frac{a\bar{E}}{\bar{\varepsilon}k^2}\tilde{c} = -i\frac{a(\vec{k}\cdot\bar{\vec{E}})}{\bar{\varepsilon}k^2}\tilde{c}, \tag{2.25}$$

où k_z est la composante z du vecteur $\vec{k}$.

Dans l'approximation linéaire $\tilde{E}^2 = 2\bar{E}\tilde{E}_z$. $\tilde{E}_z$ peut être obtenue en utilisant les éqs. (2.23, 2.25). A l'aide de l'éq. (2.21), on obtient alors à la place de (2.12) une expression [10] valable avec la précision α^2 :

$$R(\vec{k}) = -Mk^2\left\{A + Kk^2 + \frac{\alpha^2\varepsilon_0}{\bar{\varepsilon}}\left[\frac{(\vec{k}\cdot\bar{\vec{E}})^2}{k^2} - \frac{\bar{E}^2}{3}\right]\right\}, \tag{2.26}$$

Conclusion

Puisque l'incrément de l'instabilité (2.26) dépend de la direction du vecteur $\vec{k}$, les domaines croissants de la phase minoritaire seront anisotropes. Notamment, l'incrément dans la direction perpendiculaire au champ est plus grand que dans la direction parallèle. Cela veut dire que les domaines seront allongés perpendiculairement au champ. On note aussi qu'un champ électrique rend le mélange plus instable [11], donc que la décomposition spinodale est initiée plus facilement sous champ.

Un autre résultat important concerne le couplage entre la croissance de l'hétérogénéité en volume et la rugosité superficielle de la couche. Cette corrélation apparaît grâce au couplage de

ces deux phénomènes avec la variation spatiale du champ, voir l'éq. (2.25). Hormis ce couplage qui augmente l'instabilité de la surface du système thermoplastique, l'effet de la décomposition spinodale se voit directement sur l'image optique car les hétérogénéités de volume diffusent la lumière, elles aussi.

2.4 Bibliographie

[1] Cahn, J. W., & Hilliard, J. E. Free energy of a nonuniform system : III. Nucleation in a two-component incompressible fluid. *J. Chem. Phys.* **31**(3) 688 – 699 (1959).

[2] de Gennes, P.-G. *Scaling concepts in polymer physics*, 2nd ed. Cornell University Press, Ithaca, 1985.

[3] Frenkel, Y. I. About the Tonks' theory of liquid surface rupture by a uniform electric field in vacuum. *Zh.Eksp.Teor.Fiz.* **6**(4) 347 – 350 (1936). (Presented as a problem at the end of chapter I in the book [7]).

[4] Gaynor, J., & Aftergut, S. Photoplastic recording. *Phot. Sci. Eng.* **7** 209 – 213 (1963).

[5] Glenn, W. E. Thermoplastic recording system. U.S. Pat. 2896507, cl.788 - 861.

[6] Hopper, R. W., & Uhlmann, D. R. Effects of electric fields on spinodal decomposition. *Phys. and Chem. of Glasses* **14**(2) 37 – 44 (1973).

[7] Landau, L. D., & Lifschitz, E. M. *Electrodynamics of continuous media*. Pergamon, Oxford, New York, 1960.

[8] Nikolayev, V. S. *Analyse statistique d'un milieu déformable pour l'enregistrement de l'information optique*. Thèse de Candidat es sciences (doctorat) en physique et mathématique, Université d'Etat de Kiev, 1989. Approuvée par la Haute Commission d'Attestation à Moscou.

[9] Novoselets, M. K., & Nikolayev, V. S. Electric instability of capillary waves for newton liquid of finite depth. *Ukrainskij Fizicheskij Zhurnal (Ukr. J. of Phys.)* **32**(5) 713 – 718 (1987). (voir page 103 de cette thèse).

[10] Novoselets, M. K., & Nikolayev, V. S. Anisotropic spinodal decomposition of binary polymer blend in the electric field. *Himicheskaya Fizika (Chem. Phys. Moscow)* **7** 1291 – 1292 (1988). (voir page 110 de cette thèse).

[11] Reich, S., & Gordon, J. M. Electric field dependence of lower critical phase separation behavior in polymer-polymer mixtures. *J. of Polymer Sci. : Polymer Phys. Ed.* **17**(3) 371 – 378 (1979).

[12] Shikin, V. B., & Leiderer, P. Oscillations and stability of a charged helium surface. *Sov.Phys.JETP* **54** 92–101 (1981).

[13] Tonks, L. Theory of liquid surface rupture by a uniform electric field. *Phys. Rev.* **48**(1) 562 – 570 (1935).

3 Structures des domaines à 90° dans des supraconducteurs à haute température critique

3.1 Cadre général de l'étude

Les supraconducteurs à haute température critique possèdent une structure cristalline très complexe. La non-stœchiométrie est l'une de leurs caractéristiques principales. Prenons l'exemple du composé dont la formule générique est $RBa_2Cu_3O_{7-\delta}$ (dit du type 1-2-3) où R signifie la terre rare, yttrium (Y) pour la plupart des applications. La structure cristalline stratiforme du composé 1-2-3 est présentée sur la fig. 3.1 pour le cas $\delta = 0$. Nous allons nous intéresser aux plans cristallins [001] (marqués par des flèches) constitués par les atomes de cuivre et d'oxygène. On appelle ces plans plans de base ou plans $CuO_{1-\delta}$. Quand ils sont complètement remplis comme sur la fig. 3.1, (ce qui correspond à la composition stœchiométrique avec $\delta = 0$) les atomes forment des chaînes parallèles Cu-O-Cu-O-... Cependant la symétrie cristalline nous suggère qu'il existe deux directions équivalentes pour ces chaînes : (010) (comme sur la fig. 3.1) et (100). Deux types de domaines avec des directions de chaînes perpendiculaires sont donc possibles. Ils s'appellent des jumeaux structurels ("twin domains" en anglais) ou encore domaines à 90°. Il est bien connu [1, 11] que des jumeaux forment des domaines périodiques dans les cristaux ferroélastiques où la direction des domaines est définie non pas par les chaînes d'atomes mais uniquement par la déformation ϵ de la cellule cristalline dont le module élastique est désigné

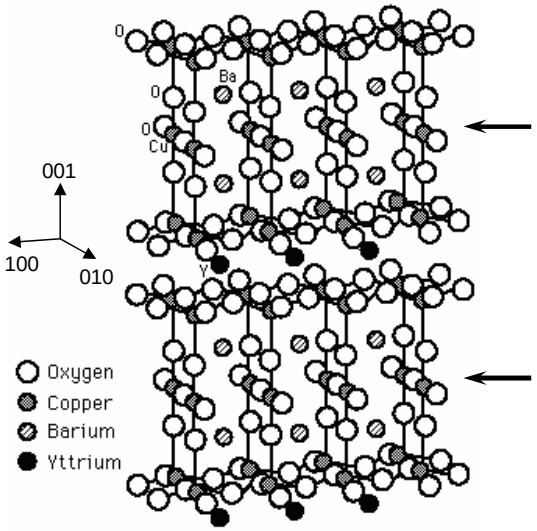

FIGURE 3.1: Structure cristalline du composé 1-2-3. Les directions cristallines ainsi que les plans de base sont indiqués par des flèches.

par Q. On retrouve cette structure par exemple dans $BaTiO_3$ [2]. On note ici que la cellule cristalline du composé 1-2-3 avec $\delta = 0$ est aussi légèrement déformée dans la direction des chaînes et appartient alors à la symétrie orthogonale.

La structure des jumeaux ressemble alors à un tissu de *tweed* (fig. 3.2).

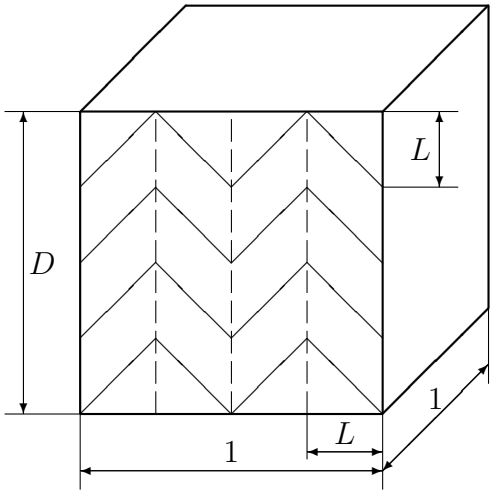

FIGURE 3.2: Structure périodique des jumeaux dans un monocristal. Les lignes inclinées montrent les directions (100) ou (010) de la déformation dans chaque domaine. Les lignes en pointillés indiquent les positions des joints des domaines. Les joints sont parallèles aux directions (110) ou $(\bar{1}10)$.

Les domaines ferroélastiques sont semblables aux domaines ferromagnétiques. Ils sont très bien décrits par la théorie classique [4] suivant laquelle on découpe l'énergie du cristal (voir la fig. 3.2 pour les mesures) en deux parties,

$$\mathcal{W} = LQ\epsilon^2/2 + ED. \tag{3.1}$$

Le premier terme est une énergie des contraintes élastiques qui existent près de la surface du cristal dans une couche dont l'épaisseur est proportionnelle à la période de la structure L. Le deuxième terme est une énergie de volume égale à la somme des énergies des joints des domaines. E désigne l'énergie par unité de volume, $E = \sigma/L$, où la tension de l'interface σ entre les domaines est multipliée par le nombre de joints par unité de volume $1/L$.

En minimisant $\mathcal{W}$ par rapport à L on obtient

$$L \sim \sqrt{D}. \tag{3.2}$$

Lors de la dérivation de cette formule, on suppose que les joints sont très étroits par rapport à L et donc que l'on peut négliger leurs interactions.

En pratique, le composé 1-2-3 est toujours non-stœchiométrique, ce qui signifie que des atomes d'oxygène manquent dans le plan de base, $(0 < \delta \leq 1)$. Les atomes restants sont donc moins ordonnés. La distribution spatiale de ces atomes est corrélée avec la déformation. Notre travail consistait alors à trouver cette corrélation et étudier l'effet de la non-stœchiométrie sur les propriétés des cristaux et sur la périodicité. Les propriétés des joints des domaines suscitent aussi de l'intérêt car ils représentent des lignes d'accrochage pour des vortex d'Abrikosov ou encore des "liens faibles" qui peuvent servir de jonctions de Josephson à l'intérieur d'un supraconducteur.

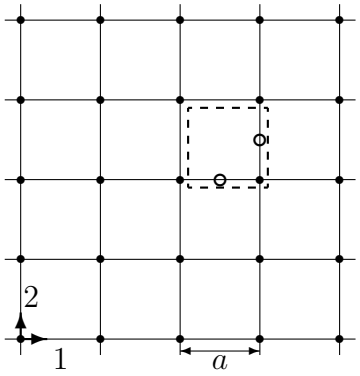

FIGURE 3.3: Structure d'un plan de base d'un composé 1-2-3. Les emplacements des atomes Cu sont indiqués par des ronds pleins. Les lacunes d'oxygène sont au milieu des côtés de chaque cellule. Le carré en pointillé montre la maille élémentaire et les ronds vides précisent les emplacements des lacunes en oxygène à l'intérieur. La direction de l'axe x (ou 1) coïncide avec la direction cristallographique (100). La direction de l'axe y (ou 2) coïncide avec la direction cristallographique (010).

3.2 Modélisation de la structure périodique

Pour expliquer certains résultats expérimentaux, nous avons proposé dans nos travaux de prendre en compte l'interaction à longue portée entre les frontières qui apparaît en raison de l'interaction entre l'élasticité du réseau cristallin et l'arrangement des atomes d'oxygène dans le plan de base. Deux modèles *bidimensionnels* (qui ne considèrent que le plan de base) ont été proposés. Le premier a été inspiré par l'analogie entre des structures non-stœchiométriques et incommensurables. Pour décrire ces dernières, le modèle de Frenkel-Kontorova [6] est employé avec succès.

3.2.1 Modèle du type Frenkel-Kontorova

Dans ce modèle, discuté dans des références [3, 8, 7], on suppose que les atomes d'oxygène peuvent se déplacer librement dans le plan de base. Alors, ces déplacements couplés avec la déformation du réseau cristallin constitueront les variables principales.

Description du modèle

On découpe l'énergie E en deux parties :

$$E = U + W + E_{el}. \tag{3.3}$$

U est un potentiel moyen pour les atomes d'oxygène, créé par le reste du réseau cristallin. Il possède ses minima dans des lacunes d'oxygène au milieu des atomes de cuivre (fig. 3.3) :

$$W = \sum_i V \left[1 - \cos\left(\frac{2\pi X_i}{a}\right)\right] \left[1 - \cos\left(\frac{2\pi Y_i}{a}\right)\right], \tag{3.4}$$

où on somme sur toutes les lacunes d'oxygène de coordonnées $\vec{R}_i = (X_i, Y_i)$ à l'intérieur d'un carré $L \times L$, a étant la période du réseau des atomes du cuivre.

L'interaction U entre les atomes d'oxygène est supposée harmonique :

$$U = \sum_{i,j} \frac{K}{2} |\vec{r}_i - \vec{R}_i - \vec{r}_j + \vec{R}_j|^2, \tag{3.5}$$

où $\vec{r}_i$ sont les positions des atomes d'oxygène dans le réseau périodique qui existait en l'absence du potentiel W. La période a_O de ce réseau est déterminée par l'égalité des aires occupées par ce réseau imaginaire et le réseau des atomes de cuivre : $a_O = a/\sqrt{1-\delta}$[3]. On ne tient compte que des interactions entre les atomes d'oxygène les plus proches, avec la constante d'interaction K. On suppose maintenant que $\delta \ll 1$ et on peut alors remplacer la somme sur les positions des lacunes par la somme sur les positions des *atomes* d'oxygène. On définit ensuite le vecteur $\vec{u}(\vec{\rho}) = \vec{r}_n - \vec{\rho}$ qui est le déplacement d'un atome d'oxygène de l'emplacement $\vec{\rho} = a\vec{n}$ correspondant à une lacune avec le même numéro n consécutif. Puisque le nombre des atomes d'oxygène est inférieur au nombre des lacunes, il est évident que $\vec{u}(n)$ doit être décrit par une fonction croissante. On obtient alors de l'éq. 3.5 l'expression

$$U = \sum_{n,j} \frac{K}{2} \left| \vec{u}(\vec{n} + \vec{\Delta}_j) - \vec{u}(\vec{n}) - \vec{\Delta}_j \frac{a_O - a}{a} \right|^2, \tag{3.6}$$

où $\vec{\Delta}_j$ est un vecteur qui désigne la position relative d'une des quatre lacunes les plus proches de la lacune $\vec{n}$.

En supposant que les frontières sont parallèles à la direction (110), on cherche à minimiser le Hamiltonien pour trouver $u \equiv u_x = u_y$ en fonction de la distance

$$\phi = (\rho_x + \rho_y)/\sqrt{2}. \tag{3.7}$$

Après passage à une description continue, on obtient

$$U + W = \int \mathrm{d}\phi \left\{ 2K \left[\left(\frac{\mathrm{d}u}{\mathrm{d}\phi} \right)^2 - \frac{a_O - a}{a} \sqrt{2} \frac{\mathrm{d}u}{\mathrm{d}\phi} \right] + V \sin^2 \left(\frac{2\pi u}{a} \right) \right\}. \tag{3.8}$$

Le troisième terme E_{el} dans le Hamiltonien (3.3) est la contribution de l'énergie élastique. On introduit comme paramètre d'ordre la déformation orthorhombique qui se traduit pour le plan de base en déformation rhombique (carré→rectangle)

$$\epsilon = (\epsilon_{11} - \epsilon_{22})/\sqrt{2} \tag{3.9}$$

où ϵ_{ij} et le tenseur des déformations. La contribution E_{el} alors s'écrit

$$E_{el} = \int \mathrm{d}\phi \left[\frac{Q\epsilon^2}{2} - b\epsilon \cos \left(\frac{2\pi u}{a} \right) - P\epsilon \right], \tag{3.10}$$

où P est la différence des composantes de la pression externe : $P = P_1 - P_2$. Le deuxième terme de l'intégrale couple la déformation et le déplacement des atomes d'oxygène. Puisque la constante de couplage b est positive, ce terme atteint son minimum lorsque le réseau est étiré le long des chaînes d'oxygène, conformément à l'expérience.

Minimisation de l'énergie

Comme les termes U et W sont indépendant du paramètre d'ordre ϵ, on peut minimiser uniquement E_{el} par rapport à ϵ, ce qui donne

$$\epsilon = \frac{P}{Q} + \frac{b}{Q}\cos\left(\frac{2\pi u}{a}\right). \tag{3.11}$$

En re-injectant (3.11) dans (3.10) on obtient

$$E_{el} = \int \mathrm{d}\phi \left[\frac{b^2}{2Q}\sin^2\left(\frac{2\pi u}{a}\right) - \frac{bP}{Q}\cos\left(\frac{2\pi u}{a}\right)\right]. \tag{3.12}$$

On constate qu'en absence de pression extérieure, la contribution de la déformation conduit seulement à une renormalisation de V :

$$V \to V' = V + \frac{b^2}{2Q} \tag{3.13}$$

En introduisant les paramètres adimensionnés

$$\kappa = \sqrt{\frac{V'}{K}}; \quad \Gamma = \frac{2}{\kappa}\frac{a_O - a}{a} \sim \delta; \quad \psi = \frac{\kappa\pi\sqrt{2}}{a}\varphi;$$
$$s = \frac{4\pi u}{a}; \quad \bar{P} = \frac{2b}{QV'}P,$$

on transforme la somme des fonctionnelles (3.8) et (3.12) en

$$E = \int \mathrm{d}\psi \left[\frac{1}{2}\left(\frac{\mathrm{d}s}{\mathrm{d}\psi}\right)^2 - \Gamma\frac{\mathrm{d}s}{\mathrm{d}\psi} + 2\sin^2\frac{s}{2} - \bar{P}\cos\frac{s}{2}\right]. \tag{3.14}$$

En minimisant cette fonctionnelle, on obtient l'équation "double sin-Gordon" stationnaire [8, 7] dont on trouve facilement la première intégrale. Une solution périodique $s(\psi)$ peut être trouvée aussi facilement. En réinjectant cette solution dans (3.14) et en minimisant le résultat relativement à la période

$$L = \int_0^{2\pi} \frac{\mathrm{d}s}{s'(s)}, \tag{3.15}$$

on trouve que le minimum peut être atteint sur une trajectoire pour laquelle [3] $s' > 0$. Le minimum existe si

$$\Gamma > \Gamma_{cr} = \frac{4}{\pi}\left[\sqrt{1+x} + x\log(1+\sqrt{1+x}) - \frac{x}{2}\log x\right], \tag{3.16}$$

où $x = \bar{P}/4$. Cette condition est équivalente au critère $\delta > \delta_{cr}(P) \approx \kappa\Gamma_{cr}(P)$, ce qui détermine la conclusion la plus importante de ce modèle : la structure de domaines-jumeaux ne peut exister que quand δ excède une valeur critique. Une autre conclusion concerne l'influence de la pression sur la structure périodique : la période augmente avec la pression. Mais en même temps, les jumeaux perdent leur symétrie : l'un des domaines devient plus large que l'autre. Ces résultats sont conformes à de nombreux résultats expérimentaux.

3.2.2 Modèle statistique

Bien que le modèle précédent explique correctement beaucoup de résultats expérimentaux, il comporte des insuffisances. Ce sont avant tout la limitation $\delta \ll 1$ et l'hypothèse de déplacement des atomes d'oxygène sur des distances comparables à la maille élémentaire. Un autre défaut essentiel — l'indépendance de la période de la taille du monocristal D, contredit l'expérience. Nous avons donc proposé un modèle plus réaliste dans les articles [9, 10]. Ce modèle s'applique à une plage de δ plus large. Nous discutons ce modèle ci-dessous.

Description du modèle

Il s'agit d'un modèle statistique dont les variables principales sont les probabilités d'occupation des lacunes d'oxygène. On introduit deux variables principales qui sont les probabilités p_1 et p_2 (avec $0 \leq p_i \leq 1$) d'occuper les lacunes d'oxygène dans la maille élémentaire (fig. 3.3) le long des axes 1 et 2 respectivement. En utilisant une approche du type champ moyen, on considère sa variation en échelle de plusieurs constantes a de la maille cristalline. Un ensemble équivalent de variables est introduit : $c = p_1 + p_2$ (la concentration de l'oxygène dans la maille élémentaire)) et $\eta = p_1 - p_2$ (le paramètre d'ordre différent de signe dans les jumeaux voisins).

L'énergie libre par unité de l'aire du plan de base peut être découpée en quatre parties :

$$F = F_o + F_e + F_i - TS. \tag{3.17}$$

La première partie est l'énergie de Coulomb d'interaction des ions d'oxygène

$$F_o = V_1(c^2 - \eta^2) + (V - V_1)c^2 + r(\nabla\eta)^2, \tag{3.18}$$

où V_1 est une interaction avec les proches voisins et $V - V_1$ est l'interaction avec les autres ions d'oxygène.

La deuxième partie de (3.17) est l'énergie élastique du réseau $F_e = c_{ijkl}\epsilon_{ij}\epsilon_{kl}/2$, où c_{ijkl} signifie les composantes du tenseur élastique et ϵ_{ij} celles du tenseur de déformation. Selon la symétrie, seules les composantes du tenseur élastique $c_{1111} = c_{2222}$ et $c_{1122} = c_{2211}$ sont différentes de zéro. Le terme

$$F_i = -c_{ijkl}(A^1_{kl}p_1 + A^2_{kl}p_2)\epsilon_{ij}, \tag{3.19}$$

définit l'interaction entre la position de l'atome O dans la maille élémentaire et sa déformation. Selon la symétrie tétragonale,

$$A^1 = \begin{pmatrix} b_1 & 0 \\ 0 & b_2 \end{pmatrix}, \quad A^2 = \begin{pmatrix} b_2 & 0 \\ 0 & b_1 \end{pmatrix}$$

b_i étant des constantes matérielles.

Le dernier terme introduit la température T dans le modèle, l'entropie étant donné par l'expression conventionnelle

$$S = -[p_i \ln p_i + (1 - p_i)\ln(1 - p_i)]. \tag{3.20}$$

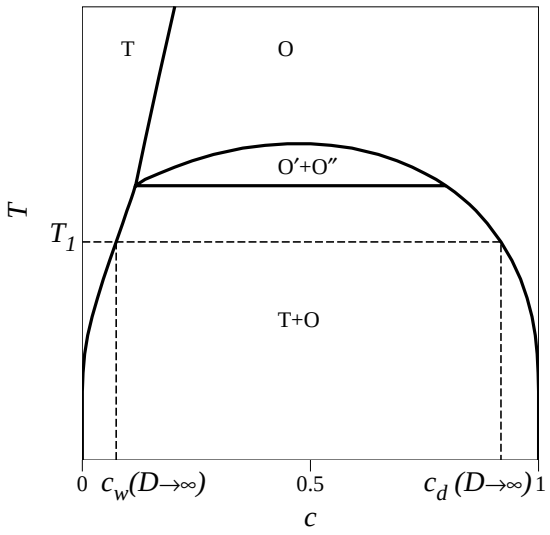

FIGURE 3.4: Le diagramme de phase du composé 1-2-3 obtenu à l'aide de l'approximation du champ moyen strict ($g = 0$). L'abscisse est la valeur moyenne de c dans le plan de base ($= 1 - \delta$). La région $O' + O''$ existe pour $\gamma < 4$.

Minimisation de l'énergie élastique

L'énergie est minimisée de la même façon que pour le modèle précédent. D'abord on cherche la déformation ϵ_{ij} minimisant la contribution élastique. On retrouve la proportionnalité de la déformation rhombique (3.9) et η : $\epsilon = \eta(b_2 - b_1)/\sqrt{2}$. En réinjectant ϵ_{ij} dans F on obtient l'expression

$$F/V = c^2 - \gamma\eta^2 + g^2(d\eta/d\phi)^2 - \tau S, \tag{3.21}$$

où $\tau = T/V$, $g^2 = 2r/V$,

$$\gamma = ((b_1 - b_2)^2 Q/4 + V_1)/V, \quad Q = c_{1111} - c_{1122}. \tag{3.22}$$

Le problème devient unidimensionnel car c et η ne dépendent que de la coordonnée (3.7) mesurée le long de la direction (110). Notons la renormalisation du coefficient d'interaction (3.22) à cause de l'élasticité de réseau de la même façon que dans le modèle précédent (3.13).

Diagramme de phase

Le diagramme de phase correspondant à l'expression (3.21) calculée pour $\nabla\eta = 0$ a été obtenu dans l'article [5]. Il est présenté sur la fig. 3.4 et met en évidence quatre régions de stabilité de phases différentes. Dans la région T, la phase tétragonale est stable. Cela veut dire que $p_1 = p_2$, c.-à-d. que les atomes d'oxygène sont distribués de façon homogène sur le plan de base, dont la déformation est égale à zéro. Les jumeaux ne peuvent donc pas exister. Dans la région orthorhombique (O), les chaînes des atomes d'oxygène apparaissent et la maille cristalline est déformée. Les phases tétragonale et orthorhombique co-existent dans le domaine T+O et deux phases orthorhombiques avec un degré de déformation différent co-existent dans la région $O' + O''$. Notre modèle de formation de jumeaux ne concerne que les domaines T+O et O.

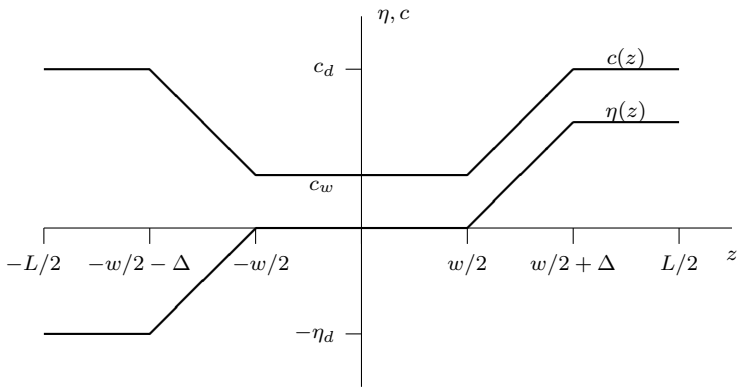

FIGURE 3.5: Approximations linéaires par morceaux de $c(z)$ et $\eta(z)$ utilisées pour la modélisation. c_d (η_d) est la valeur de c (η) à l'intérieur d'un domaine. c_w est la valeur de c à l'intérieur d'un joint de grain où $\eta = 0$.

Propriétés de la structure périodique

Nous voulons étudier comment des phases différentes sont distribuées dans l'espace. Pour cela, nous avons besoin de minimiser la fonctionnelle

$$E = \frac{N}{L} \int_{-L/2}^{L/2} F dz, \tag{3.23}$$

où F est définie par (3.21) et N est le nombre de mailles élémentaires par unité de volume, sous la contrainte de conservation du nombre total d'atomes d'oxygène :

$$1 - \delta = \frac{1}{L} \int_{-L/2}^{L/2} c(z) dz. \tag{3.24}$$

On peut démontrer que ce problème variationnel possède des solutions périodiques. Plutôt que de les chercher rigoureusement, on utilisera une approximation linéaire par morceaux (fig. 3.5).

En injectant ces dépendances dans (3.21) et ensuite dans (3.23), E devient une fonction des paramètres de l'approximation : c_d, η_d, c_w, Δ, w... On minimise ensuite (3.23) par rapport à ces paramètres en trouvant la valeur optimale $E(L)$ qui ne dépend que de la période L et des paramètres T et δ.

Deux types de joints de grain sont possibles en fonction de la valeur optimale du paramètre w. Pour des joints du type "O-O", $w = 0$ et des joints connectent deux domaines de la phase orthorhombique. Si $w > 0$, on parle de joints "O-T-O", ce qui veut dire que la phase tétragonale se trouve à l'intérieur des joints.

La différence principale avec le modèle de type Frenkel-Kontorova, c'est que la fonction $E(L)$ ne possède pas de minimum. Pour $L \to \infty$, $E \sim 1/L$ et on retrouve la théorie classique. La prise en compte de l'énergie de surface du monocristal et la minimisation de l'énergie totale (3.1) sont alors nécessaires.

La dépendance $L(D)$ qui en résulte est présentée sur la fig. 3.6. On retrouve $L \sim D^{1/2}$ quand L est grand. Le point de singularité correspond à la transition entre les régimes où les joints des domaines sont du types O-O et O-T-O . La température de cette transition correspond *grosso modo* à la température définie par la courbe séparant les phases T et O sur la fig. 3.4. Mais la position exacte de cette transition dépend légèrement de D ce qui est est mis en évidence

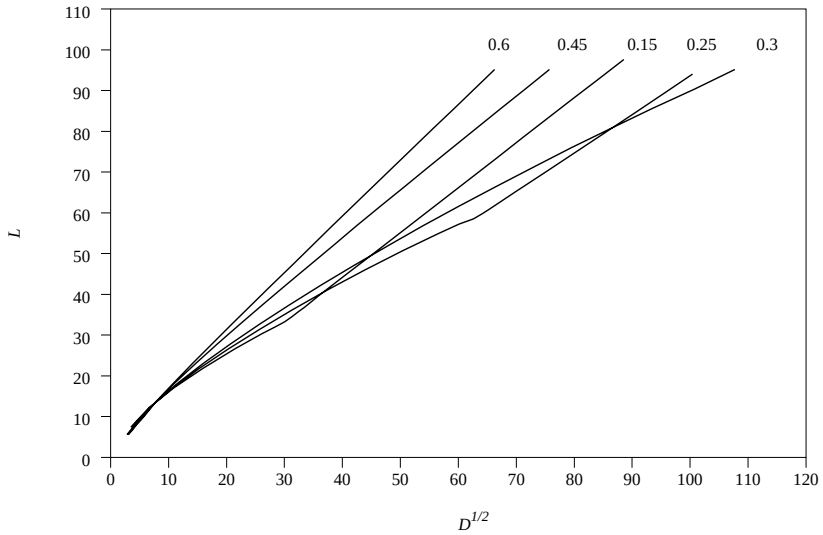

FIGURE 3.6: Période de la structure en fonction de la taille du monocristal calculée pour $\delta = 0.1$. Les deux sont exprimées en unités arbitraires. Le paramètre des courbes est T/V.

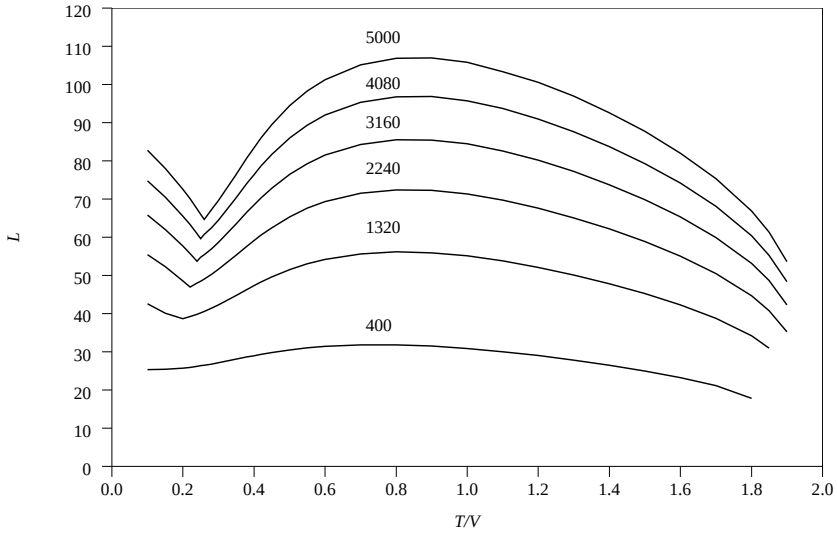

FIGURE 3.7: Période de la structure en fonction de la température pour $\delta = 0.1$. Le paramètre des courbes est D. La taille du monocristal et la période sont exprimées dans les mêmes unités.

par la fig. 3.7. La transition se manifeste par le minimum de la fonction $L(T)$. On voit que sa position se déplace avec D. Quand $D \to \infty$, la position du minimum tend vers la limite donnée par le diagramme de phase de la fig. 3.4 ($\approx 0,37$ pour $\delta = 0,1$). De la même façon, les valeurs des concentrations d'oxygène à l'intérieur des domaines c_d et dans ses joints c_w ne correspondent aux valeurs données par le diagramme de phase de la fig. 3.4 que si $D \to \infty$ (cf. les lignes en pointillés). Indépendamment de la taille du monocristal, la période L s'annule quand la température approche le point de la transition de phase T-O (≈ 1.98 pour $\delta = 0.1$).

Le calcul montre que c_w est inférieur à c_d, c.-à-d. que les joints des domaines contiennent moins d'oxygène que les domaines eux-même.

Le modèle statistique a un champ d'application plus large que le modèle considéré dans le

chapitre 3.2.1. Il reste valide dans l'intervalle $\beta < \delta \lesssim 0.5$ où $\beta > 0$ est déterminé par l'apparition des domaines à 180° (domaines antiphases). La limitation supérieure apparaît à cause du fait qu'on ne considère que 2 atomes d'oxygène par maille élémentaire. On néglige donc la formation de la structure "ortho-II" qui devient plus avantageuse que les domaines à 90° pour $\delta > 0.5$.

Concernant le domaine $O' + O''$ du diagramme de phase (fig. 3.4) où deux phases orthorhombiques avec un paramètre d'ordre différent doivent co-exister, on note que la structure des domaines à 90° peut y être décrite également avec le modèle statistique. Seulement, à la place du profil à deux coudes pour $\eta(z)$ (fig. 3.5), il faudra utiliser un profil plus compliqué à quatre coudes.

3.3 Conclusion

Dans ce chapitre, nous avons étudié la structure périodique des domaines à 90° (les domaines-jumeaux structurels). Les caractéristiques inhabituelles de cette structure apparaissent en raison de la non-stœchiométrie d'oxygène de ce composé supraconducteur. On note que les atomes d'oxygène sont les donneurs d'électrons, ce qui est nécessaire pour les propriétés supraconductrices, d'où l'importance de ces études. La distribution spatiale des atomes d'oxygène est corrélée fortement à la déformation élastique du réseau. Notre modélisation explique un grand nombre de faits expérimentaux liés à la structure périodique. Notamment, on montre que la phase tétragonale peut co-exister avec la phase orthorhombique car elle se situe dans des joints de domaine qui peuvent être assez larges. La concentration d'oxygène est donc moins forte dans les joints et les atomes y sont distribués de façon aléatoire. La dépendance de la période L de différents paramètres (température T, taille du monocristal) est analysée. Nous mettons en évidence le caractère non-monotone de la fonction $L(T)$, avec un minimum correspondant à une transition de phase. Nous avons démontré que cette transition variait faiblement avec la taille du monocristal.

Beaucoup de composés chimiques sont caractérisés par la non-stœchiométrie en oxygène et par une symétrie similaire. La modélisation ci-dessus peut être donc leur être aussi appliquée.

3.4 Bibliographie

[1] Barsch, G. R., & Krumhansl, J. A. Twin boundaries in ferroelastic media without interface dislocations. *Phys. Rev. Lett.* **53**(11) 1069 – 1072 (1984).

[2] Floquet, N., Valot, C. M., Mesnier, M. T., Niepce, J. C., Normand, L., Thorel, A., & Kilaas, R. Ferroelectric domain walls in $BaTiO_3$: Fingerprints in XRPD diagrams and quantitative HRTEM image analysis. *J. Phys. III France* **7** 1105 – 1128 (1997).

[3] Gaididei, Y. B., Loktev, V. M., & Nikolayev, V. S. On the theory of formation of a twin (ferroelastic) structure in high-temperature superconductors with oxygen nonstoichiometry. *Solid State Commun.* **75**(6) 503 – 506 (1990).

[4] Khachaturyan, A. G. *Theory of Structural Transformations in Solids.* Wiley, New York, 1983.

[5] Khachaturyan, A. G., Semenovskaya, S. V., & Morris, Jr., J. W. Phase diagram of the superconducting oxide $YBa_2Cu_3O_{6+\delta}$. *Phys. Rev. B* **37**(4) 2243 – 2246 (1988).

[6] Kontorova, T. A., & Frenkel, Y. I. *Phys. Z. Sowjetunion* **13** 1 (1938).

[7] Nikolayev, V. S. About the ferroelastic properties of the twin structure of 1-2-3-type high-tc superconductors. *Ukrainskij Fizicheskij Zhurnal (Ukr. J. of Phys.)* **36**(7) 1111 – 1115 (1991).

[8] Nikolayev, V. S. About the influence of uniaxial pressure on the twin structure in the 1-2-3 system. In *Electron-Electron Correlation Effects in Low-Dimensional Conductors and Superconductors*, A. A. Ovchinnikov & I. I. Ukrainskii, Eds. Springer, Heidelberg, 1991, pp. 54 – 59.

[9] Nikolayev, V. S. Twin spacing versus size of a monocrystal for the nonstoichiometric 1 :2 :3 superconductors. *Phys. Lett. A* **180**(1,2) 157 – 163 (1993).

[10] Nikolayev, V. S. Twin spacing and the structural phase transitions in $RBa_2Cu_3O_{7-\delta}$ high-T_c superconductors. *Phys. Rev. B* **50**(6) 4163 – 4167 (1994). (voir page 112 de cette thèse).

[11] Yamada, Y. Theory of pseudoelasticity and the shape-memory effect. *Phys. Rev. B* **46**(10) 5906 – 5911 (1992).

4 Cinétique de séparation de phase dans les mélanges binaires

4.1 Introduction

La première étape de la séparation de phase, notamment la décomposition spinodale, a été étudiée dans le chapitre 2.3.2. Bien que ce phénomène s'observe facilement dans des mélanges de polymères où la mobilité diffusive est faible, il se produit très rapidement et est donc plus difficilement observable dans des mélanges se composant de molécules légères. Dans ce chapitre nous nous concentrons sur la cinétique des étapes plus tardives.

Considérons un mélange de composants A et B. Son diagramme de phase est présenté schématiquement sur la fig. 4.1 où la concentration c du composant A est choisie comme paramètre d'ordre. Le diagramme comporte une région monophasique (au-dessus de la courbe de coexistence ou binodale) et une région diphasique au-dessous. Le maximum de la courbe de coexistence est le point critique de coordonnées (c_c, T_c). Choisissons un mélange de concentration $\bar{c}$ de température initiale correspondant à la région monophasique et baissons la température rapidement pour que le mélange atteigne la région diphasique (fig. 4.1). Après cette trempe thermique, le mélange commence à se séparer en deux phases M^+ et M^-. A la fin de la séparation, les concentrations c_- et c_+ dans chacune des phases sont données par la courbe de coexistence. La fraction volumique ϕ de la phase minoritaire (M^+ pour $\bar{c} < c_c$) peut être obtenue à partir de la conservation de la

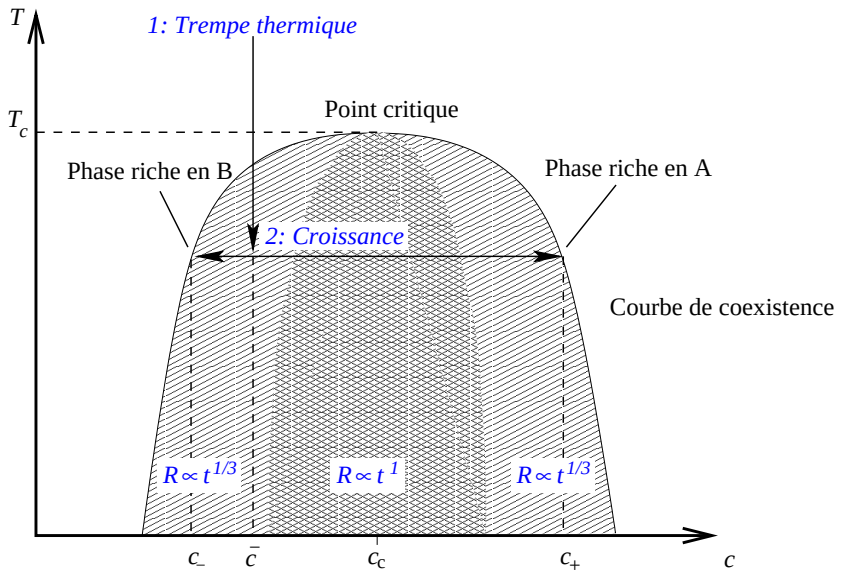

FIGURE 4.1: Diagramme de phase schématique d'un mélange binaire. La courbe séparant les deux régimes de croissance est définie par l'équation $\phi = \phi_s = cst$.

quantité du composant A et est définie par l'expression

$$\phi = 1/2 - |\bar{c} - c_c|/(c_+ - c_-), \tag{4.1}$$

où la symétrie axiale de la courbe de coexistence a été supposée. Cette dernière hypothèse est correcte près du point critique où le ralentissement critique permet à la séparation de phase d'être observée expérimentalement pendant un temps raisonnablement long par rapport au temps de la trempe.

Au cours de la séparation de phase, on observe la croissance de domaines de la phase minoritaire au sein de la phase majoritaire. A cause de la différence de densité des deux phases, la gravité terrestre entraîne la sédimentation et donc perturbe la cinétique de la croissance. Les meilleurs résultats expérimentaux sont donc obtenus là où la sédimentation est neutralisée.

Nous sommes intéressés par les étapes tardives de la croissance quand les frontières entre les phases sont déjà bien développées et les concentrations du composant A dans les phases sont très proches des valeurs d'équilibre c_- et c_+. Alors, les domaines croissent par coalescence (parce que le système tend à réduire l'aire de l'interface entre les phases) et ϕ ne dépend plus du temps.

D'après les résultats expérimentaux [7] obtenus près du point critique d'un mélange binaire choisi de telle façon que les densités des phases sont très proches, deux scenarii alternatifs de croissance sont possibles. Le premier d'entre eux se caractérise par la croissance de domaines sphériques distincts de rayon moyen R croissant selon la loi $R \sim t^{1/3}$ (t est le temps qui s'est écoulé après la trempe). C'est une croissance "lente" qui peut durer des dizaines de minutes, voire une heure. Dans le deuxième régime, les domaines grossissent selon une structure inter-connectée quasi-périodique dont la "période" R est soumise à la loi de croissance $R \sim t^1$. Cette croissance "rapide" prend typiquement quelques minutes. Ces régimes dépendent de ϕ : on obtient le régime $t^{1/3}$ quand $\phi \lesssim 0,3$ et le régime t^1 quand $\phi \gtrsim 0,3$.

L'analyse [14] des résultats expérimentaux montre que la loi $t^{1/3}$ peut être expliquée par la coalescence de domaines qui suivent un mouvement brownien plutôt que par le mécanisme de Lifshitz-Slyozov [8], mécanisme valable seulement pour $\phi \to 0$ et qui pour cette raison ne sera plus discuté ici.

Depuis le travail [15], l'origine hydrodynamique de la loi $R \sim t^1$ a été établie mais le mécanisme de la croissance restait incertain. Dans les articles [10, 11] nous avons proposé un modèle de coalescence en chaîne qui explique cette loi ainsi que plusieurs autre faits expérimentaux jusque là incompris. Avant de décrire ce modèle, discutons le modèle expliquant le régime $t^{1/3}$.

4.1.1 La coalescence brownienne et la loi en $t^{1/3}$

Ce mécanisme est mentionné souvent comme celui de Binder et Stauffer puisque ce sont eux [4] qui l'ont appliqué à la séparation de phase. Selon ce mécanisme, le taux de collisions par volume unitaire dû au mouvement brownien de gouttes sphériques dans le liquide est

$$N_B = 16\pi D R n^2 g, \tag{4.2}$$

où n est un nombre moyen de gouttes par volume, R est le rayon moyen des gouttes. Le coefficient de diffusion des gouttes D est définie par l'expression

$$D = \frac{k_B T}{5\pi\mu R}, \tag{4.3}$$

où l'on suppose que les deux phases ont la même viscosité dynamique μ, ce qui est justifié au voisinage du point critique. Le facteur g représente la correction qui tient compte de l'interaction

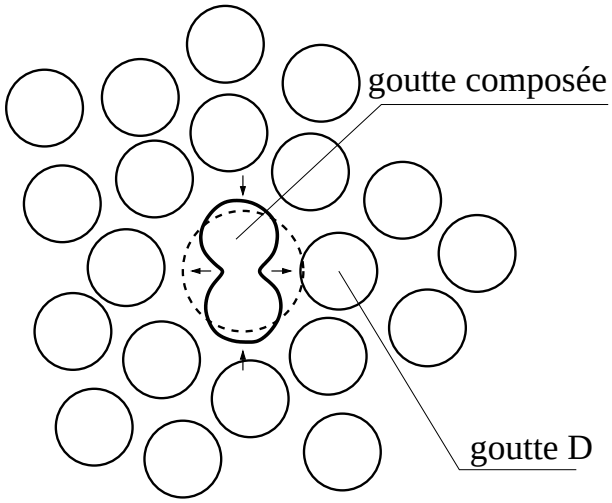

FIGURE 4.2: Croquis des gouttes subissant la coalescence.

hydrodynamique entre les gouttes. Il dépend du rapport des viscosités du fluide à l'intérieur et en dehors des gouttes et de la distance moyenne entre les gouttes, donc de ϕ. Dans la limite diluée ($\phi \to 0$), $g = 0,56$ et change peu avec ϕ. Cette valeur de g sera utilisée par la suite.

On peut négliger le temps de fusion des gouttes par rapport au temps entre les collisions. La coalescence est la seule raison de la diminution du nombre de gouttes,

$$\frac{\mathrm{d}n}{\mathrm{d}t} = -N_B. \tag{4.4}$$

Puisque R et n sont liés par la condition

$$\phi = \frac{4}{3}\pi R^3 n = \mathrm{cst}, \tag{4.5}$$

N_B prends la forme

$$N_B = \frac{9k_BTg(\phi)\phi^2}{5\mu\pi^2R^6}. \tag{4.6}$$

Sa substitution dans l'éq. (4.4) résulte en la loi $R \sim t^{1/3}$.

4.2 Le modèle de coalescence en chaîne et la loi en t^1

Contrairement au modèle précédent de coalescence brownienne, un modèle purement déterministe de coalescence est discuté ici. Notre considération est basée sur l'idée suivante. D'abord imaginons un ensemble des gouttes suspendues dans le vide plutôt qu'à l'intérieur d'un autre liquide, afin de pouvoir négliger toutes les interactions entre elles. Deux gouttes en fusion sont en train de former une goutte "composite". Si la distance moyenne entre les gouttes d_0 est inférieure à une valeur seuil (que l'on appelle "la limite de coalescence"), la goutte composée touchera une goutte voisine, "goutte D" (fig. 4.2). Une deuxième coalescence suit qui induit une autre si les gouttes sont suffisamment près les unes des autres. Les coalescences peuvent ainsi s'enchaîner.

La limite de coalescence dépend seulement de la forme des gouttes et peut être calculée [11] à partir de seuls arguments géométriques, $L_V = d_0/R \approx 0,99$.

En retournant à la séparation de phase, considérons maintenant le début de la croissance où les petites gouttes de la phase M^+ viennent d'être formées. Quand ces gouttes sont incluses dans un autre liquide (la phase M^-), le scénario change en raison des interactions hydrodynamiques. La relaxation de la goutte composée induit un écoulement, dont la direction est montrée par les flèches sur la fig. 4.2. Cet écoulement éloigne la goutte D et gêne la deuxième coalescence. La limite hydrodynamique L_H de coalescence devrait être ainsi inférieure à la limite L_V pour les gouttes suspendues dans le vide.

Les forces de lubrification qui empêchent deux interfaces de s'approcher sont très fortes. C'est pourquoi les interfaces de la goutte composée et de la goutte D ne s'approcheraient jamais en absence des gouttes environnantes. Or, les mêmes forces de lubrification agissent entre la goutte D et les gouttes voisines. Alors la goutte D ne peut pas être poussée infiniment par l'écoulement produit par la goutte composée et les interfaces des deux gouttes se rapprochent finalement. Nous supposons qu'au moment où les surfaces des deux gouttes se rapprochent à une distance ψ que nous appelons la "distance de coalescence", un pont entre elles se forme immédiatement et la coalescence commence. ψ peut être définie par la portée des forces attractives de van der Waals ou bien par l'épaisseur de l'interface.

Nous notons que ce processus est censé être auto-similaire, ce qui veut dire que toutes les gouttes participent à des processus similaires. La taille moyenne des gouttes croît dans le temps de façon continue.

4.2.1 Simulation de la coalescence

Nous voulons examiner numériquement l'écoulement produit par la coalescence de deux gouttes et son influence sur la troisième goutte D voisine. Cependant, il est nécessaire de tenir compte du retardement du mouvement de la goutte D par les gouttes environnantes. Puisque les forces hydrodynamiques s'affaiblissent lentement avec la distance, un nombre très grand de gouttes doit être simulé, ce qui est très difficile, voir impossible. Une manière alternative de démontrer l'effet avec un nombre restreint de gouttes est de les entourer par une coque fermée qui imiterait le champ moyen des vitesses créé par les gouttes environnantes.

La géométrie choisie pour la position initiale des interfaces est présentée sur la fig. 4.3.

La goutte composée est l'agrégat des deux gouttes qui viennent de former un pont. Une autre goutte de rayon R (goutte D) se trouve à la distance d_0 de la goutte composée. Ces deux gouttes sont enveloppées par une coque sphérique ayant la même tension superficielle σ que les gouttes.

L'ensemble de trois gouttes sphériques a un bas degré de symétrie et donc nécessite un temps de calcul assez long. C'est pourquoi nous avons choisi à sa place l'ensemble possédant une symétrie cylindrique par rapport à l'axe z (fig. 4.3). Autrement dit, la goutte composée ressemble plutôt à un "tore sans trou" qu'une haltère. On s'attend à ce qu'une telle configuration maintienne les caractéristiques principales du vrai système physique qui est une structure des interfaces reliées ensemble où les gouttes ne ressemblent pas du tout à des objets sphériques [7]. La discussion étendue sur la validité de l'approximation de la coque peut être trouvée dans l'article [11].

Examinons d'abord le critère géométrique de la deuxième coalescence, avec la goutte D. Le diamètre de coque D_s au moment initial peut être défini selon la fig. 4.3 en fonction de R, ψ et d_0. Le diamètre final de la goutte composée D_c après sa relaxation peut être obtenu à partir de son volume initial car il est conservé pendant l'évolution. Il est évident (cf. la fig. 4.4) que si $D_s \leq D_c + 2R + 3\psi$, la deuxième coalescence devra avoir lieu parce que les deux gouttes

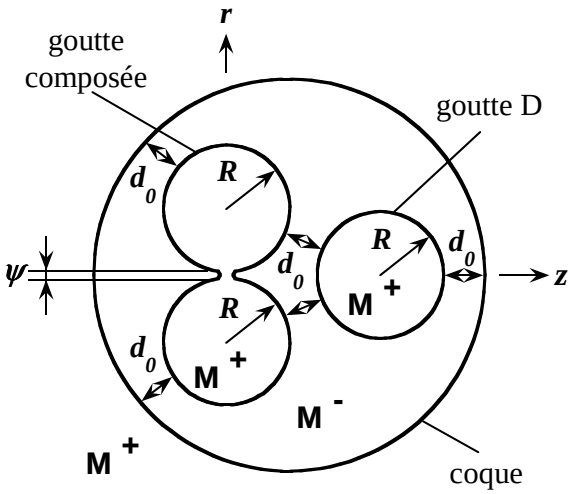

FIGURE 4.3: Les positions des gouttes au début de la simulation. ψ est la distance de coalescence et d_0 est la distance initiale entre les gouttes.

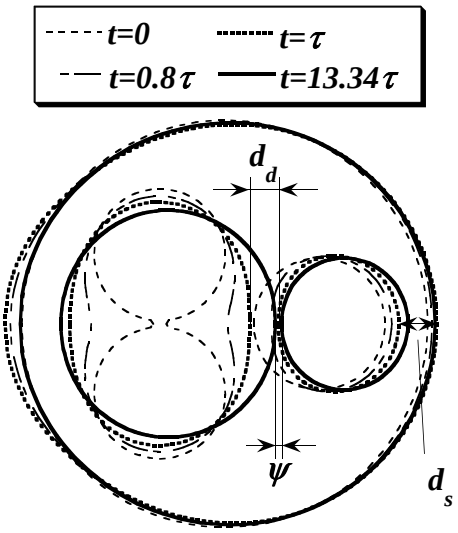

FIGURE 4.4: Evolution temporelle des interfaces pour $d_0/R = 0,65$. La deuxième coalescence a lieu à $t = t_c = 13,34\tau$, $\tau = \mu R/\sigma$. Les distances entre deux gouttes d_d et entre la goutte D et la coque d_s sont indiquées pour $t = \tau$.

se rapprocheront entre elles ou avec la coque à la distance ψ de coalescence. Cette condition nous donne la limite d_0^G géométrique de coalescence L_G qui pour la valeur de $\psi = R/10$ donne $L_G = d_0^G/R \approx 0,484$.

Le problème hydrodynamique est posé dans l'approximation de Stokes car le nombre de Reynolds est très petit [15]. Nous supposons que juste avant que la coalescence ait lieu, le mouvement du fluide est beaucoup plus faible qu'après la coalescence. La vitesse zéro est donc choisie comme condition initiale. L'écoulement dans notre système modèle est créé par la goutte composée qui relaxe sous l'action de sa tension superficielle. Nous nous intéressons au temps t_c avant la deuxième coalescence en fonction de d_0. La méthode de l'intégrale de frontière ("boundary integral method" en anglais) est utilisé [11] pour résoudre ce problème hydrodynamique aux interfaces libres.

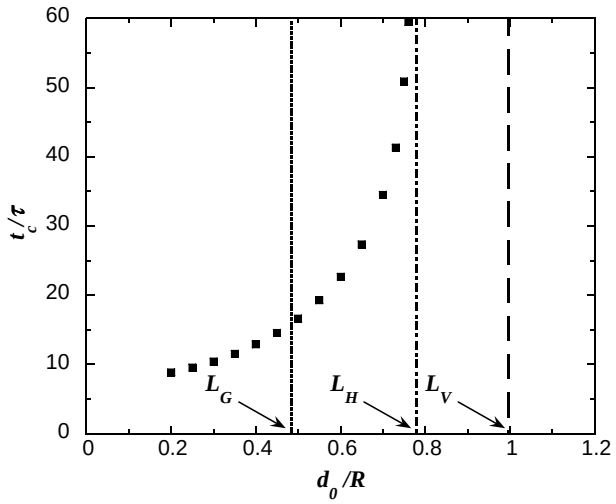

FIGURE 4.5: Temps entre deux coalescences consécutives t_c en fonction de d_0, $\tau = \mu R/\sigma$. Les lignes verticales montrent les limites géométrique L_G et hydrodynamique L_H de coalescence et la limite de coalescence dans le vide L_V.

L'évolution temporelle des interfaces est présentée sur la fig. 4.4. On voit que grâce au ralentissement du recul de la goutte D, la deuxième coalescence peut se produire même quand $d_0/R > L_G$. Examinons le temps t_c entre les coalescences

$$t_c = \alpha \mu R/\sigma, \tag{4.7}$$

où α ne dépend que de d_0/R. Cette dépendance est présentée sur la fig. 4.5. La deuxième coalescence a lieu quand $d_0/R < L_H$ où $L_H \approx 0,769$ est la limite hydrodynamique de coalescence. Elle est définie comme la distance initiale réduite où le temps entre deux coalescences (t_c) devient infini.

Notons que la coalescence se produit entre la goutte composée et la goutte D et non pas entre la goutte D et la coque. Cela signifie que l'interaction de lubrification avec les gouttes environnantes (avec la coque dans notre modèle) crée une attraction effective entre la goutte relaxante et sa voisine. Une nouvelle goutte composée se forme. Remarquez que la forme de cette nouvelle goutte devient plus compliquée que celle de la goutte composée d'origine (puisque la relaxation n'a pas le temps d'aboutir à la forme sphérique entre deux coalescences consécutives). La forme complexe interconnectée des domaines s'explique donc naturellement.

4.2.2 Généralisation du modèle hydrodynamique

Pour exprimer α en termes de la fraction de la phase minoritaire ϕ qui ne dépend que de l'arrangement géométrique des gouttes, relions d_0/R à ϕ :

$$\phi = b[1 + d_0/(2R)]^{-3}. \tag{4.8}$$

La constante b dépend de l'arrangement spatial des gouttes. L'interaction hydrodynamique entre les gouttes est toujours répulsive à cause de la force de lubrification. Ainsi les gouttes tentent-elles d'être aussi loin l'une de l'autre que possible. D'ailleurs, l'expérience montre une corrélation en position des gouttes. Une telle corrélation explique pourquoi les gouttes ne se connectent pas quand la fraction ϕ de volume atteint la limite *aléatoire* de percolation ($\phi \approx 0,15$).

Puisque aucune information quantitative n'est disponible pour déterminer b, nous calculons ses limites supérieure et inférieure. Pour avoir la limite supérieure, nous supposons que les gouttes sont arrangées dans un ordre parfait aussi loin les unes des autres que possible. C'est donc un arrangement de réseau cubique à faces centrées où $b = \pi/3\sqrt{2} \approx 0,74$. Nous pouvons considérer comme limite inférieure l'empilement dense aléatoire ("random tight packing limit" en anglais) pour des sphères de rayon $R + d_0/2$. Ceci correspond à l'absence d'un ordre à courte portée et implique $b \approx 0,64$. Nous voyons que la valeur de b n'est pas très sensible à un arrangement particulier. Par la suite, nous adopterons la valeur médiane $b = 0,69$.

Maintenant, nous pouvons généraliser le mécanisme hydrodynamique ci-dessus pour une forme arbitraire de gouttes. L'auto-similarité de la croissance implique la relation suivante pour les tailles caractéristiques des gouttes entre deux coalescences consécutives i et $(i+1)$: $R^{(i+1)} = \beta R^{(i)}$, où β est un facteur de forme universel, qui ne dépend que de ϕ. Nous pouvons réécrire également l'éq. (4.7) sous la forme $t_c^{(i)} = \alpha(\phi)\mu R^{(i)}/\sigma$, où $\alpha(\phi)$ est la fonction universelle.

Après m coalescences

$$R = \beta^m R^{(0)}, \quad t = \sum_{i=0}^{m-1} t_c^{(i)}$$

et

$$R = R^{(0)} + \frac{\beta - 1}{\alpha} \cdot \frac{\sigma}{\mu} t, \tag{4.9}$$

où $R^{(0)}$ est le rayon initial de la goutte. Notant que $\beta = 2^{1/3}$ pour les sphères et $\beta \gtrsim 1$ pour des longs tubes, nous pouvons prendre $\beta \sim 1,1$ pour l'évaluation. D'après la fig. 4.5 et l'éq. (4.8), $\alpha \sim 10$ pour $\phi = 0,5$. Nous obtenons alors la loi $R \sim 0,01\sigma/\mu\, t$, qui est conforme à l'expérience [6], où le facteur numérique est 0,04.

4.2.3 Compétition entre les deux mécanismes

En utilisant l'éq. (4.8), nous pouvons obtenir à partir de L_H la valeur de ϕ correspondante : $\phi_H \approx 0,26$. Il est clair que le mécanisme hydrodynamique décrit ci-dessus fonctionne seulement quand $\phi > \phi_H$ tandis que la coalescence brownienne a lieu dans la gamme entière de ϕ. Considérons l'intervalle $\phi > \phi_H$ afin de localiser la frontière entre les régimes $t^{1/3}$ et t^1 sur le diagramme de phase.

Ne tenant compte que de la croissance purement hydrodynamique, écrivons

$$\frac{\mathrm{d}n}{\mathrm{d}t} = -N_H, \tag{4.10}$$

au lieu de (4.4), où N_H est le taux de coalescences dues à l'hydrodynamique qui peut être calculé en employant (4.9) et la relation entre n et R. Or la dernière dépend de la forme de la goutte. En supposant qu'au début de l'évolution les gouttes sont sphériques, nous employons l'éq. (4.5) :

$$N_H = -\frac{\mathrm{d}n}{\mathrm{d}t} = \frac{9\phi}{4\pi R^4}\frac{\mathrm{d}R}{\mathrm{d}t} = \frac{9k_BT\phi}{5\mu\pi^2 C\alpha(\phi)R^4\xi^2} \tag{4.11}$$

où

$$C = \frac{4\gamma}{5\pi(\beta - 1)}.$$

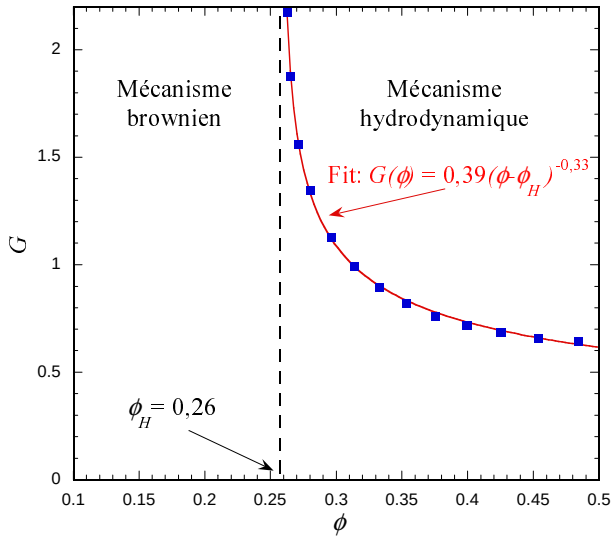

FIGURE 4.6: Fonction $G(\phi)$ définie par l'éq. 4.13. Son fit est aussi indiqué.

Nous avons employé ici l'expression $\sigma = k_B T/\gamma\xi^2$ valable au voisinage du point critique ; ξ est la longueur de corrélation dans la région diphasique, $\gamma \approx 0,39$ est une constante universelle. Le mécanisme brownien domine quand $N_B > N_H$. Alors en utilisant les éqs. (4.6, 4.11) nous réduisons la dernière inégalité à

$$\frac{R^2}{\xi^2} < G(\phi), \tag{4.12}$$

$$\text{où} \quad G(\phi) = C\phi g\alpha(\phi). \tag{4.13}$$

Nous rappelons que toutes nos considérations sont valides seulement quand les interfaces des gouttes se sont déjà formées (les étapes tardives de la croissance), ce qui signifie que le rayon initial d'une goutte ne peut pas être moins grand que l'épaisseur d'interface, c.-à-d. $\approx 4\xi$ [3]. Alors d'après l'inégalité (4.12) le régime $R \sim t^{1/3}$ se réalisera quand

$$G(\phi) > 16. \tag{4.14}$$

La fonction $G(\phi)$ est représentée dans la fig. 4.6. Il est clair que (4.14) est valide quand $0 < \phi - \phi_H \lesssim 10^{-6}$. Dans la pratique, ceci signifie que pour tout $\phi > \phi_H$, le mécanisme hydrodynamique *seulement* déterminera la croissance dès le début de la croissance. Alternativement, pour $\phi < \phi_H$, les gouttes grossissent selon un mécanisme brownien seulement. Ceci explique la transition brusque dans la cinétique ($t^1 \to t^{1/3}$) qui est commandée par la fraction de volume de la phase de minorité comme observé dans [7, 14]. La courbe qui correspond à une valeur seuil un peu plus grande ($\phi = 0,32$) est tracée sur la fig. 4.7. Elle montre un accord raisonnable avec les données expérimentales issues de plusieurs expériences avec des mélanges binaires ainsi qu'avec des fluides simples au voisinage de la frontière entre les deux régimes. Il s'agit d'expériences de séparation de phases liquide-gaz réalisées en microgravité [14, 13], seul moyen de supprimer l'effet de la convection. D'autre part, le mécanisme de coalescence en chaîne suggéré pour expliquer le régime t^1 a été confirmé par des simulations numériques directes de la transition de phase [1].

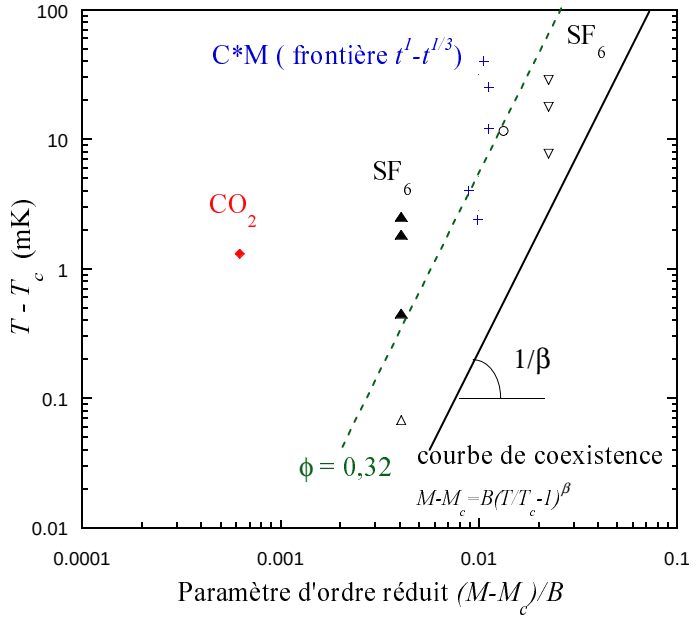

FIGURE 4.7: Données expérimentales obtenues au voisinage de la frontière $t^1 - t^{1/3}$ placées sur une moitié du diagramme de phase dans les coordonnées universelles, où le paramètre d'ordre M signifie c/c_c pour le mélange binaire et ρ/ρ_c pour des fluides simples. Symboles vides : croissance rapide t^1. Symboles pleins : croissance lente $t^{1/3}$. Croix : la frontière $t^1 - t^{1/3}$ d'après l'expérience [7]. La ligne solide correspond à la courbe de coexistence. La ligne en pointillés correspond à $\phi = 0,32$. Les données expérimentales viennent de [14, 13].

4.3 Séparation de phase dans un gradient de température

Dans ce chapitre nous abordons la cinétique de la transition de phase liquide-vapeur dans un fluide simple soumis à un gradient de température [2].

Une expérience de séparation de phase consiste à tremper un fluide pur (ici CO_2), de l'état monophasique initial (ρ, T_i) à un autre état (ρ, T_f) où la séparation de phase se produit (ρ est la densité moyenne de l'échantillon. T_i est la température initiale, et T_f est la température finale, cf. la fig. 4.8). L'évolution du système est définie par le rapport entre la température critique T_c, la température de coexistence T_{cx}, et la profondeur $\delta T = T_{cx} - T_f$ de la trempe. Comme cela a été décrit dans le chapitre précédent, selon la fraction volumique ϕ de la phase minoritaire, la transition de phase peut procéder soit par la croissance des gouttelettes isolées quand $\phi \lesssim 30\%$ (insert (b) dans la fig. 4.9) ou par la croissance de domaines interconnectés quand $\phi \gtrsim 30\%$ (insert (a)).

Les données pour une taille moyenne R de domaines concernant chacun des régimes $R \sim t^1$ et $R \sim t^{1/3}$ peuvent être mis sur des courbes maîtresses [14] dans les coordonnées réduites $Q_m = 2\pi\xi^-/R$ et $\tau = t/t_\xi$, où ξ^- et $t_\xi = 6\pi\mu_o(\xi^-)^3/k_B T_f$ sont, respectivement, la longueur de corrélation des fluctuations de densité dans le domaine diphasique et l'échelle de temps de relaxation associée, μ_o étant la viscosité dynamique.

L'expérience a été conduite à bord de la station spatiale Mir afin d'éviter la convection gravitationnelle du fluide. Un faisceau laser très mince (diamètre $2\omega = 300$ μm) a été utilisé pour chauffer localement le centre de la cellule cylindrique avec des hublots transparents en saphir

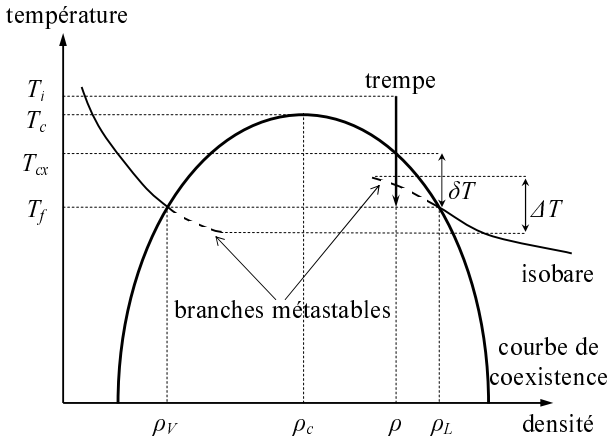

FIGURE 4.8: Diagramme de phase schématique pour les fluides simples dans les coordonnées température-densité. L'isobare qui correspond à l'état final du fluide est montrée avec ses branches métastables.

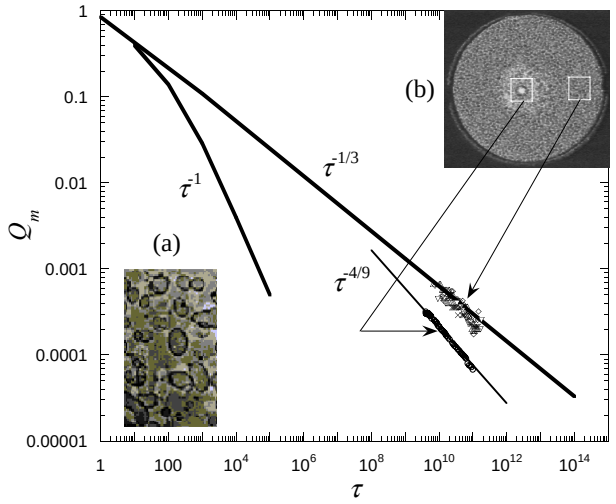

FIGURE 4.9: Courbes maîtresses pour la séparation de phase près du point critique dans les coordonnées réduites (longueur inverse Q_m, temps τ). Les points expérimentaux illustrent la croissance de la bulle solitaire centrale pour $\delta T = 85, 90, 100$ mK et celle des autres bulles (fenêtre (a)) qui suivent la loi conventionnelle brownienne. Le fit avec l'exposant théorique $-4/9$ est montré aussi. La zone appauvrie en petites bulles qui entoure la bulle centrale est visible dans la fenêtre (b).

dont le diamètre était 11,6 mm. Une très petite partie $\gamma \approx 2 \cdot 10^{-6}$ de la puissance du laser $P = 1$ mW est absorbée par le saphir qui chauffe donc le fluide. On observe une croissance plus rapide d'une bulle solitaire au centre de la cellule (fig. 4.9).

Le piégeage d'une grande bulle ainsi que sa croissance plus rapide peuvent être expliqués par un effet de Marangoni provoqué par une variation de la température à l'interface de chacune des petites bulles. En conséquence, une force les pousse vers l'endroit le plus chaud, c.-à-d. vers le centre de la cellule où une grande bulle solitaire se forme par leur coalescence. La question se pose si une telle variation peut exister dans un fluide pur (sa pureté était de l'ordre $2 \cdot 10^{-4}$). Quand l'interface liquide-gaz est au début de l'évolution vers l'équilibre (vers l'état de saturation), il

semble évident [5, 9, 12] que l'interface reste isotherme pendant son évolution à moins qu'une contamination soit présente dans le fluide. Or, dans le travail actuel, le système est déjà initialement (juste après la trempe) hors d'équilibre. Puisque la pression du système est équilibrée rapidement, le système évolue le long des branches métastables de l'isobare (fig. 4.7) pendant la majeure partie de l'évolution. La phase liquide est surchauffée et le gaz est sous-refroidi. Par conséquent, la température d'interface n'est pas nécessairement égale à la température de saturation T_f qui correspond à la pression du système. Elle peut changer ainsi le long de l'interface de la bulle. On peut estimer la limite supérieure pour cette variation comme la différence δT entre les températures maximum et minimum des branches métastables (fig. 4.7).

Pour une petite hétérogénéité de température, la vitesse $\vec{v}$ de migration thermo-capillaire d'une bulle suspendue dans une phase liquide est proportionnelle au gradient de température imposé $\vec{\nabla} T$:

$$\vec{v} = -\frac{2}{2\mu_o + 3\mu_i} \frac{\mathrm{d}\sigma}{\mathrm{d}T} \frac{a}{2 + \lambda_i/\lambda_o} \vec{\nabla} T, \tag{4.15}$$

où μ_o et λ_o (μ_i et λ_i) sont la viscosité dynamique et la conductivité thermique à l'extérieur (resp. à l'intérieur) de la bulle de rayon a. La tension superficielle σ diminue avec la température de sorte que $\mathrm{d}\sigma/\mathrm{d}T < 0$. Selon (4.15), la bulle devrait migrer le long du gradient de température. Puisque, dans notre cas, le chauffage est localisé à l'intérieur du rayon laser, les bulles devraient migrer vers son centre, fusionnant entre elles. La formation d'une bulle unique centrée fournit une démonstration qualitative de la théorie ci-dessus.

Afin de développer une approche quantitative, nous devons déterminer le gradient $\vec{\nabla} T$ induit par le faisceau, avec une distribution radiale gaussienne d'intensité

$$I(r) = \frac{2P}{\pi\omega^2} e^{-2r^2/\omega^2} \tag{4.16}$$

à l'entrée de la cellule. Ici P est la puissance du faisceau et r est la coordonnée mesurée radialement à partir du centre du faisceau.

En raison du petit rapport épaisseur/rayon de la cellule expérimentale, nous supposons que la distribution de température est de symétrie cylindrique avec l'axe le long du faisceau. En d'autres termes, nous faisons l'hypothèse simplificatrice que la puissance est absorbée de façon homogène le long de la partie du faisceau qui croise le fluide, de sorte que la puissance calorifique j développée par volume unitaire du fluide soit $j(r) = 2\gamma I(r)/L$. Le facteur 2 apparaît à cause de deux contacts du fluide avec les hublots (chacun dissipant la puissance γP) le long du chemin optique dans l'épaisseur de la cellule qui est égale à $L = 1,49$ mm.

Pour de longs temps d'observation nous pouvons également raisonnablement supposer que la distribution de la température est donnée par l'équation stationnaire de conduction de la chaleur

$$\lambda_o \nabla^2 T + j = 0, \tag{4.17}$$

qui possède la solution

$$|\vec{\nabla} T| = \frac{\partial T}{\partial r} = -\frac{\gamma P}{\pi r L \lambda_o} \left(1 - e^{-2r^2/\omega^2}\right). \tag{4.18}$$

La vitesse $\vec{v}$ correspondante déterminée via (4.15) s'écrit

$$v = a\beta/r \tag{4.19}$$

et est orientée vers le centre du faisceau. La constante β est définie par

$$\beta = \frac{1}{2\mu_o + 3\mu_i} \left|\frac{\mathrm{d}\sigma}{\mathrm{d}T}\right| \frac{1}{2\lambda_o + \lambda_i} \frac{2\gamma P}{\pi L}. \tag{4.20}$$

Pour la température $T_f = T_c - 139,6$ mK qui correspond à la trempe de $\delta T = 90$ mK, $\beta = 0,173\,\mu$m/s.

On peut maintenant obtenir la loi de croissance pour la bulle centrale. Désignons par $c = c(r)$ le nombre de (petites) bulles de gaz en volume unitaire. Le flux total des bulles

$$\vec{f}(r) = -D\vec{\nabla}c + c\vec{v}, \tag{4.21}$$

a deux contributions. La première correspond à la diffusion des bulles avec la constante de diffusion D, alors que la seconde est responsable de l'advection thermo-capillaire. Dans l'hypothèse d'une distribution presque stationnaire de $c(r)$, $\vec{f}(r)$ satisfait l'équation

$$\mathrm{div}\vec{f} = 0. \tag{4.22}$$

Puisque l'épaisseur de la cellule est beaucoup plus petite que son diamètre, le mouvement des bulles vers le centre du faisceau est presque 2D. Par conséquent, les éqs. (4.21-4.22) devraient être résolues en 2D, c.-à-d. pour une symétrie cylindrique. Cependant, la bulle centrale est sphérique en raison de la tension superficielle et ne peut pas être assumée cylindrique. Pour résoudre cette contradiction, nous imaginons une bulle cylindrique de rayon R_{2D} qui a le même volume V_R que la bulle centrale sphérique,

$$V_R = \frac{4\pi}{3} R^3 = \pi R_{2D}^2\, L. \tag{4.23}$$

En supposant que a est indépendant de r (c.-à-d. que le taux de collisions n'est pas influencé par le gradient faible de c), les éqs. (4.15,4.21,4.22) peuvent être résolues avec deux conditions aux limites $c(R_{2D}) = 0$ (qui correspond à la disparition des petites bulles quand elles touchent la bulle centrale) et $c(\infty) = c_\infty$, la concentration constante à l'infini. Le résultat s'écrit

$$c(r) = c_\infty[1 - (r/R_{2D})^{-a\beta/D}] \tag{4.24}$$

et montre autour de la bulle centrale une zone appauvrie en petites bulles. Cette zone peut être définie par $0 < r \leq L_D/2$ où $c(r) \leq 0.9\, c_\infty$, les conditions qui résultent en

$$L_D \sim R_{2D} \sim t^{2/3}. \tag{4.25}$$

On peut voir cette zone sur la fenêtre (b) de la fig. 4.9. La loi (4.25) est conforme aux données expérimentales de la fig. 4.10.

La bulle hémisphérique centrale croît aux dépens des petites bulles qui sont absorbées par la coalescence,

$$\mathrm{d}V_R/\mathrm{d}t = 2\pi R_{2D} L f(R_{2D}) V_a, \tag{4.26}$$

où $f(R_{2D}) = c_\infty \beta a / R_{2D}$ et V_a est le volume d'une petite bulle. Le produit $c_\infty V_a$ est égale à la fraction volumique de vapeur $\phi = (\rho_L - \rho)/(\rho_L - \rho_V)$, ρ_L and ρ_V sont définies sur la fig. 4.8. L'éq. (4.26) résulte alors en

$$R_{2D}\, \mathrm{d}R_{2D}/\mathrm{d}t = \beta\phi a. \tag{4.27}$$

Comme $a = a_0\, t^{1/3}$, en utilisant (4.23) on obtient la loi de croissance

$$R = (9L\beta\phi a_0/8)^{1/3}\; t^{4/9}. \tag{4.28}$$

Le fit des données expérimentales est présenté sur la fig. 4.9. On constate la bonne correspondance des exposants avec l'expérience.

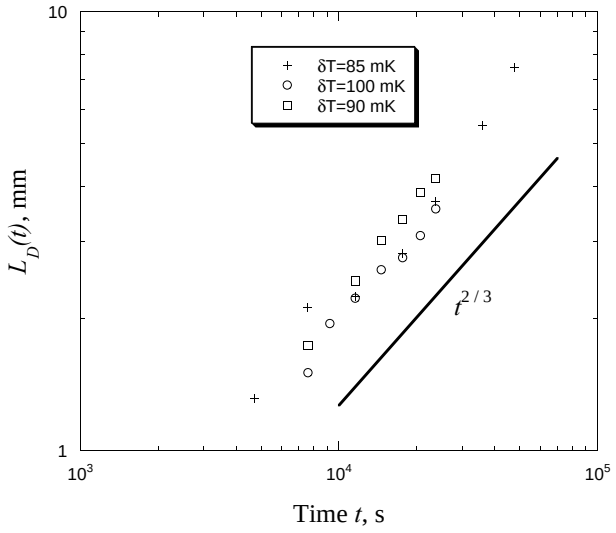

FIGURE 4.10: Croissance du rayon de la zone appauvrie en petites bulles. La ligne solide indique la pente 2/3.

4.4 Conclusion

Nous avons étudié dans ce chapitre la cinétique de séparation de phase. Un nouveau mécanisme, celui de coalescences en chaîne, a été proposé pour expliquer le régime dit "hydrodynamique" de la croissance. Il a déjà permis d'expliquer l'essentiel des résultats de séparation de phase près d'un point critique. Le rôle des coalescences en chaîne se confirme par des études numériques d'autres auteurs. Ce modèle permet de faire progresser les études de la séparation de phase. Nous pensons notamment l'analyser en présence de vibrations.

L'analyse de la séparation de phase dans des fluides simples soumis à un gradient thermique a permis d'aborder une question très importante pour les applications : la variation de la température le long de l'interface gaz-liquide. Cette température donne une condition aux limites pour beaucoup de problèmes de thermique en présence de transition de phase. Il s'agit notamment de l'évaporation qui est traitée dans le chapitre suivant.

4.5 Bibliographie

[1] Bastea, S., & Lebowitz, J. L. Spinodal decomposition in binary gases. *Phys. Rev. Lett.* **78**(18) 3499 – 3502 (1997).

[2] Beysens, D., Garrabos, Y., Nikolayev, V. S., Lecoutre-Chabot, C., Delville, J.-P., & Hegseth, J. Liquid-vapor phase separation in a thermocapillary force field. *Europhysics Lett.* **59**(2) 245–251 (2002). (voir page 183 de cette thèse).

[3] Beysens, D., & Robert, M. Thickness of fluid interfaces near the critical point from oiptical reflectivity measurements. *J. Chem. Phys.* **87**(5) 3056 – 3061 (1987). Erratum : **93**(9), 6911 (1990).

[4] Binder, K., & Stauffer, D. Theory for the slowing down of the relaxation and spinodal decomposition of binary mixtures. *Phys. Rev. Lett.* **33**(17) 1006 – 1009 (1974).

[5] Garrabos, Y., Lecoutre-Chabot, C., Hegseth, J., Nikolayev, V. S., Beysens, D., & Delville, J.-P. Gas spreading on a heated wall wetted by liquid. *Phys. Rev. E* **64**(5) 051602 (2001). (voir page 173 de cette thèse).

[6] Guenoun, P., Gastaud, R., Perrot, F., & Beysens, D. Spinodal decomposition patterns in an isodensity critical binary fluid : Direct-visualization and light-scattering analyses. *Phys. Rev. A* **36**(10) 4876 – 4890 (1987).

[7] Jayalakshmi, Y., Khalil, B., & Beysens, D. Phase separation under a weak concentration gradient. *Phys. Rev. Lett.* **69** 3088 (1992).

[8] Lifshitz, I. M., & Slyozov, V. V. The kinetics of precipitation from supersaturated solid solutions. *J. Phys. Chem. Solids* **19** 35 – 50 (1961).

[9] Marek, R., & Straub, J. The origin of thermocapillary convection in subcooled nucleate pool boiling. *Int. J. Heat Mass Transfer* **44**(3) 619 – 632 (2001).

[10] Nikolayev, V. S., Beysens, D., & Guenoun, P. New hydrodynamic mechanism for drop coarsening. *Phys. Rev. Lett.* **76**(17) 3144 – 3147 (1996). (voir page 134 de cette thèse).

[11] Nikolayev, V. S., & Beysens, D. A. Coalescence limited by hydrodynamics. *Physics of Fluids* **9**(11) 3227 – 3234 (1997). (voir page 138 de cette thèse).

[12] Onuki, A. Dynamic van der Waals theory of two-phase fluids in heat flow. *Phys. Rev. Lett.* **94**(5) 054501 (2005).

[13] Perrot, F., Beysens, D., Garrabos, Y., Fröhlich, T., Guenoun, P., Bonetti, M., & Bravais, P. Morphology transition observed in a phase separating fluid. *Phys. Rev. E* **59**(3) 3079 – 3083 (1999).

[14] Perrot, F., Guenoun, P., Baumberger, T., Beysens, D., Garrabos, Y., & Le Neindre, B. Nucleation and growth of tightly packed droplets in fluids. *Phys. Rev. Lett.* **73**(5) 688 – 691 (1994).

[15] Siggia, E. D. Late stages of spinodal decomposition in binary mixtures. *Phys. Rev. A* **20**(2) 595 – 605 (1979).

5 Crise d'ébullition et recul de la vapeur

5.1 Crise d'ébullition

L'ébullition est en général un moyen très efficace de transfert de chaleur entre une paroi chauffante métallique et un fluide. C'est pour cette raison qu'elle est souvent utilisée dans l'industrie. Plusieurs régimes d'ébullition peuvent être identifiés. Ils sont mis en évidence par la courbe de Nukiyama schématisée sur la fig. 5.1 qui présente le flux thermique de la paroi en fonction de sa température pour une expérience d'ébullition stagnante (en absence du flux de fluide imposé extérieurement). La pente de cette courbe donne le coefficient de transfert de chaleur.

A partir d'un certain seuil de température, des bulles de vapeur commencent à se former sur des défauts superficiels de la paroi chauffante et l'ébullition nucléée se développe. Elle est caractérisée par un échange de chaleur très efficace.

Dans un autre régime d'ébullition, l'ébullition en film, la paroi se couvre d'un film de vapeur continu. L'évaporation se passe à l'interface vapeur-liquide. Ce régime est caractérisé par un transfert de chaleur très lent car la vapeur est un mauvais conducteur de chaleur, comme le montre l'expérience classique de caléfaction.

Regardons maintenant ce qui ce passe quand on conduit des expériences d'ébullition sous un flux thermique imposé constant, de plus en plus grand pour les expériences consécutives. Quand ce flux dépasse une valeur critique (le flux critique, CHF en anglais), la vapeur forme

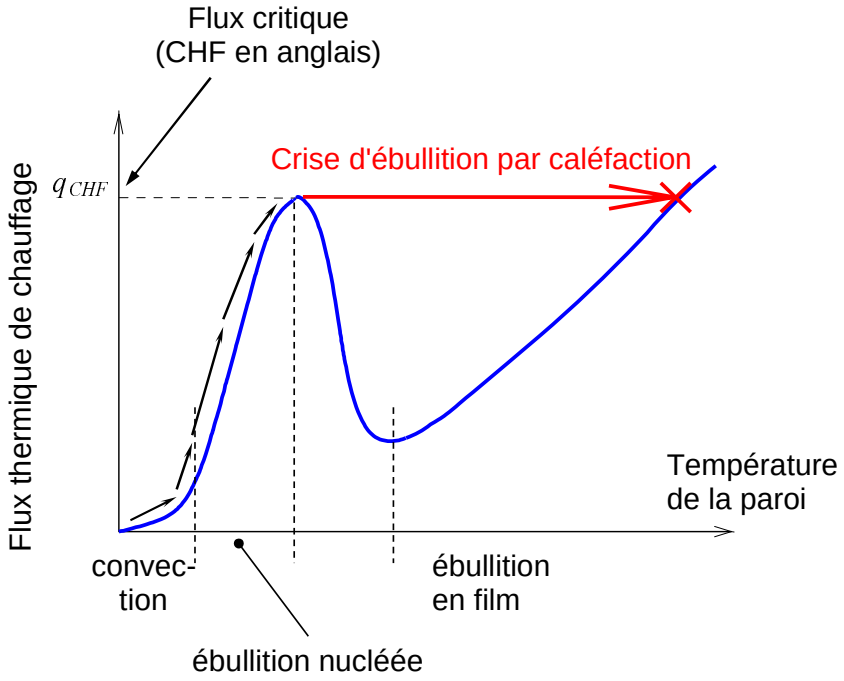

FIGURE 5.1: Schéma de la courbe d'ébullition dite de Nukiyama.

brutalement un film sur la paroi chauffante, qui l'isole thermiquement du liquide. En d'autres termes, la paroi chauffante se dessèche brusquement. Le transfert thermique est inhibé et la température de la paroi croît rapidement (fig. 5.1) ce qui peut conduire à la fusion de la paroi. Ce phénomène s'appelle la crise d'ébullition par caléfaction ("departure from nucleate boiling" ou "CHF phenomenon" ou "boiling crisis" en anglais).

Puisque l'efficacité des échangeurs de chaleur augmente avec la température, les industriels sont intéressés pour connaître sa valeur de crise afin d'augmenter le flux de travail sans atteindre la valeur du CHF. Son évaluation correcte exige une compréhension claire du phénomène physique qui déclenche la crise. De nombreux modèles ont été proposés, cf. [4] pour une revue. Pourtant, chacun d'eux ne s'applique qu'à des régimes et des configurations d'expériences très particuliers. Pour des raisons purement industrielles, les expériences d'ébullition les plus communes sont effectuées sous pesanteur terrestre à des pressions basses par rapport à la pression critique du fluide donné. La valeur du CHF est alors grande. Pour l'observer, il faut recourir à de grandes puissances de chauffage, ce qui rend l'ébullition violente et les observations difficiles. Même les dispositifs les plus avancés [14, 2] ne peuvent aider à valider l'un ou l'autre modèle avec certitude. Cependant, de nombreuses observations montrent que la crise commence par la croissance d'une tache sèche sous les bulles de vapeur attachées à la paroi.

Tous les modèles physiques de croissance de la tache sèche peuvent être classés en deux catégories distinctes. La première suppose que la tache sèche grossit par coalescence des bulles attachées à la paroi. La deuxième considère la croissance de la tache sèche sous des bulles isolées. Bien que nous nous rendons compte de l'importance des coalescences pendant le déroulement de la crise, nous ne pensons pas que les coalescences en soi peuvent initier la crise, et cela pour plusieurs raisons. D'abord, la consommation de la chaleur latente pendant la croissance de chaque bulle crée autour de sa base un anneau froid sur la paroi chauffante. Celle-ci empêche ou ralentit la croissance des bulles dans son voisinage immédiat. Ensuite, la coalescence des bulles est gênée par les forces de lubrification entre les interfaces. Ainsi, une force extérieure apparaît nécessaire pour pousser les bulles les unes contre les autres (cf. le chapitre 4.2 pour la discussion des forces des lubrification). Le troisième argument se trouve dans le travail de thèse [3] qui démontre par simulation numérique que la température de la tache sèche n'augmente que si on suppose la coalescence simultanée et régulière d'au moins trois bulles attachées, ce qui est peu probable.

Récemment, les études de l'ébullition en général et de la crise d'ébullition en particulier ont reçu une nouvelle impulsion liée au développement du nouveau moteur Vinci pour l'étage supérieur de la fusée Ariane 5 qui doit être rallumable sous des conditions de microgravité [1]. Un tel redémarrage nécessite le refroidissement de turbopompes avec des pertes minimales du liquide réfrigérant – en même temps le combustible. Comme l'écoulement massif du liquide sur des pompes chaudes entraînerait immédiatement la crise d'ébullition avec perte d'efficacité du refroidissement, des études approfondies en microgravité sont nécessaires afin de minimiser les pertes en liquide.

Dans ce chapitre nous allons développer un modèle de crise d'ébullition basé sur l'étalement de la tache sèche sous une bulle sous l'action de la force de recul de la vapeur.

5.2 Notion de force de recul de la vapeur

Considérons une portion d'une interface liquide-vapeur d'aire dA (fig. 5.2). Le liquide est chauffé par le flux thermique q_L. Pendant le temps dt, le liquide de masse dm est vaporisé. Cette

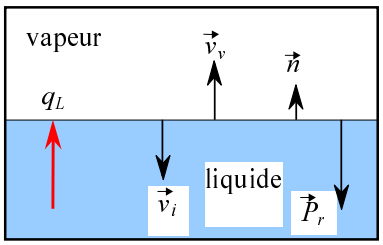

FIGURE 5.2: Calcul de la pression de recul.

masse peut s'exprimer

$$\mathrm{d}m = \rho_V \mathrm{d}V_V = \rho_L \mathrm{d}V_L, \tag{5.1}$$

où $\mathrm{d}V_L$ et ρ_L sont le volume et la densité du liquide évaporé ; $\mathrm{d}V_V$ et ρ_V sont le volume et la densité de la vapeur créée.

Par conséquent, l'interface liquide-vapeur s'est déplacée de $\mathrm{d}\vec{l} = -\vec{n}\mathrm{d}V_L/\mathrm{d}A$, où $\vec{n}$ est le vecteur unitaire normal à l'interface (fig. 5.2).

La conservation du moment pour la portion du fluide représentée sur la fig. 5.2 s'écrit

$$(\vec{v}_v + \vec{v}_i)\mathrm{d}m + \vec{P}_r \mathrm{d}t\mathrm{d}A = 0, \tag{5.2}$$

où $\vec{P}_r$ est la force de recul par unité de surface, $\vec{v}_i = \mathrm{d}l/\mathrm{d}t$ est la vitesse de l'interface et $\vec{v}_v = \vec{n}\mathrm{d}V_V/(\mathrm{d}A\mathrm{d}t)$ est la vitesse de la vapeur *par rapport à l'interface*. En injectant (5.1) et ces expressions, l'éq. (5.2) peut être réécrite sous la forme

$$\vec{P}_r = -\vec{n}\eta^2(\rho_V^{-1} - \rho_L^{-1}), \tag{5.3}$$

où le taux d'évaporation par unité de temps et de surface $\eta = \mathrm{d}m/(\mathrm{d}A\mathrm{d}t)$ est introduit. On note qu'indépendamment du signe de η (condensation ou évaporation), $\vec{P}_r$ est dirigée coté liquide.

L'effet de recul peut paraître insignifiant dans la plupart des situations physiques. Cependant les photos de Hickman (cf. l'article [12]) mettent en évidence la déformation macroscopique de la surface d'un liquide partiellement couverte d'huile. La partie couverte ne s'évapore pas. Une différence de niveau du liquide entre les parties couverte et libre est bien visible. Le recul de la vapeur pousse la surface en évaporation en baissant son niveau par rapport à la surface couverte par l'huile.

En négligeant la conduction thermique dans la vapeur, η peut être relié à q_L par

$$q_L = H\eta, \tag{5.4}$$

où H est la chaleur latente de vaporisation.

Considérons maintenant une bulle de vapeur attachée à la surface de la paroi chauffante (fig. 5.3). Lors de l'ébullition, le liquide est surchauffé dans une couche pariétale d'épaisseur l_r. Cependant, la température de l'interface vapeur-liquide est constante (c'est en fait la température de saturation pour la pression donnée du système). Cela signifie que le flux q_L reste élevé dans une "ceinture" sur la surface au pied de la bulle. De fait, la majeure partie de l'évaporation dans la bulle de vapeur est produite dans cette ceinture, dont l'épaisseur est habituellement beaucoup plus petite que le rayon de la bulle. Le recul de la vapeur près de la ligne de contact est alors beaucoup plus grand que sur l'autre partie de la surface de la bulle. En conséquence, sa surface

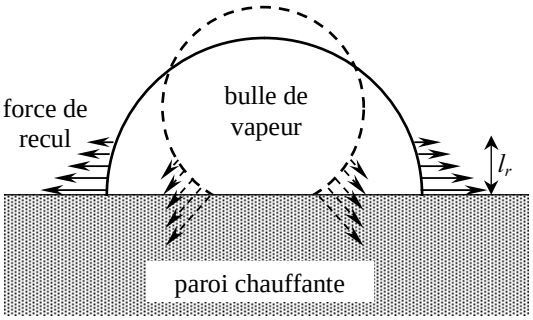

FIGURE 5.3: Etalement d'une bulle de vapeur sous l'action de la force de recul de la vapeur.

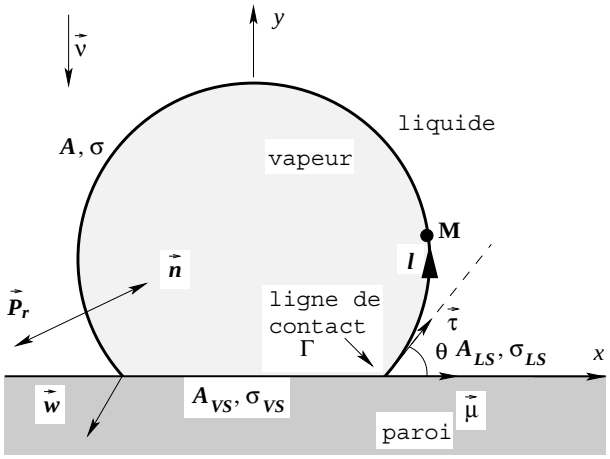

FIGURE 5.4: Bulle de vapeur sur la surface solide entourée par le liquide. Les directions des forces $\vec{P}_r$, $\vec{w}$ et celles des vecteurs unitaires $\vec{\tau}$, $\vec{\mu}$, $\vec{\nu}$ et $\vec{n}$ sont également montrées.

se déforme comme si la ligne triple de contact liquide-vapeur-solide était tirée de coté, comme montré sur la fig. 5.3. Ceci signifie que, sous l'action du recul de la vapeur, la tache sèche sous la bulle de vapeur s'étale et peut couvrir la surface de la paroi chauffante.

Dans notre description de la forme des bulles, nous nous baserons sur l'approche variationnelle de croissance de la bulle dans l'hypothèse d'une croissance lente. Cette hypothèse est justifiée dans le régime des grandes pressions où la forme de la bulle reste quasi-sphérique, sa croissance étant limitée par l'apport de chaleur nécessaire pour la vaporisation ("croissance thermiquement contrôlée").

5.3 Approche variationnelle

Considérons une bulle attachée à la paroi solide et définissons des vecteurs unitaires $\vec{\tau}$, $\vec{\mu}$, $\vec{\nu}$ montrés sur la fig. 5.4. L'angle de contact liquide est désigné par θ. Pour développer une approche générale, on peut introduire la force de réaction du support $\vec{w}$ (par unité de longueur de la ligne triple Γ). La composante $w = \vec{w} \cdot \vec{\mu}$ de $\vec{w}$ tangente à la surface est la force d'accrochage par des défauts de la paroi tandis que sa composante normale $w_\nu = \vec{w} \cdot \vec{\nu}$ est la force d'adhésion de la bulle à la paroi.

L'énergie libre U du système se compose de trois parties. La première partie, l'énergie de

surface, est conventionnelle [5]

$$U_1 = \sigma A + \sigma_{VS} A_{VS} + \sigma_{LS} A_{LS} + \lambda V, \tag{5.5}$$

où σ_{VS} et σ_{LS} sont les tensions superficielles pour les interfaces vapeur-solide et liquide-solide respectivement, A_{VS} et A_{LS} sont les aires correspondantes d'interface, A est l'aire de l'interface vapeur-liquide (fig. 5.4). Le dernier terme assure la conservation du volume de bulle V, λ étant le multiplicateur de Lagrange qui est aussi la différence de pression entre l'intérieur et l'extérieur de la bulle.

On peut démontrer [5] que la variation de U_1 par rapport à un déplacement infinitésimal $\delta\vec{r}$ de l'interface A s'écrit

$$\delta U_1 = \int_{(A)} (-K\sigma + \lambda)\vec{n} \cdot \vec{\delta r} \, \mathrm{d}A - \oint_{(\Gamma)} [\sigma\vec{\tau} + (\sigma_{LS} - \sigma_{VS})\vec{\mu}] \cdot \vec{\delta r} \, \mathrm{d}\Gamma, \tag{5.6}$$

où K est la courbure locale de la bulle. Les vecteurs unitaires $\vec{\tau}$ et $\vec{\mu}$ sont perpendiculaires à Γ, et tangents à A et A_{LS} respectivement (fig. 5.4). L'intégration est effectuée sur l'interface A dans la première intégrale et sur la ligne triple de contact Γ dans la deuxième intégrale.

On s'aperçoit que sur Γ, $\vec{\delta r} = \delta r_\mu \vec{\mu}$ et que $\vec{\tau} \cdot \vec{\mu} = \cos\theta$. La deuxième intégrale de l'éq. (5.6) peut alors être simplifiée :

$$\delta U_1 = \int_{(A)} (-K\sigma + \lambda)\delta r_n \, \mathrm{d}A - \sigma \oint_{(\Gamma)} (\cos\theta - c)\delta r_\mu \, \mathrm{d}\Gamma, \tag{5.7}$$

où $\delta r_n = \vec{n} \cdot \vec{\delta r}$ et

$$c = (\sigma_{VS} - \sigma_{LS})/\sigma \tag{5.8}$$

Notons que si $c \leq 1$, $c \equiv \cos\theta_{eq}$ est en conformité avec la formule d'Young.

La deuxième partie de U est l'énergie gravitationnelle dont la variation est

$$\delta U_2 = \int_{(A)} (\rho_L - \rho_V) g y \delta r_n \, \mathrm{d}A \tag{5.9}$$

si la gravitation est dirigée vers le bas sur la fig. 5.4 et l'axe y dirigé vers le haut.

La troisième partie de U tient compte du travail virtuel des forces externes $\vec{P_r} = -P_r\vec{n}$ et $\vec{w}$. Sa variation est

$$\delta U_3 = \int_{(A)} P_r \delta r_n \, \mathrm{d}A - \oint_{(\Gamma)} w \delta r_\mu \, \mathrm{d}\Gamma. \tag{5.10}$$

Suivant l'hypothèse quasi-statique,

$$\delta U = \delta U_1 + \delta U_2 + \delta U_3 = 0. \tag{5.11}$$

Puisque l'interface A peut être déplacée indépendamment de la ligne triple Γ, chacune des intégrales doit être mise à zéro séparément, ce qui se traduit par deux conditions

$$K\sigma = \lambda + (\rho_L - \rho_V) g y + P_r(l), \tag{5.12}$$

$$\cos\theta = c - w/\sigma. \tag{5.13}$$

Une fois la variation de P_r le long de l'interface A et w données, ces deux conditions sont suffisantes pour déterminer la forme de la bulle et de la ligne de contact. Le paramètre constant λ est à déterminer à partir du volume connu V de la bulle. Nous reviendrons à l'analyse du piégeage de la ligne triple par les défauts de surface solide dans le chapitre suivant. Dans le reste de ce chapitre, nous le négligerons.

5.3.1 Bilan des forces agissant sur une bulle

Pour trouver le bilan des forces agissant sur la bulle, il faut multiplier l'équation représentant les pressions (5.12) sur la composante verticale de la normale $\vec{n}$ et puis l'intégrer sur la surface A de la bulle [7]. La composante verticale est $\vec{n}\cdot\vec{\nu}$, où $\vec{\nu}$ est un vecteur unitaire vertical (fig. 5.4). Utilisons ensuite l'égalité

$$\int\limits_{(A)} \ldots \vec{n}\cdot\vec{\nu}\,\mathrm{d}A = \int\limits_{(A_{VS})} \ldots \mathrm{d}A \tag{5.14}$$

et le théorème intégral de Gauss

$$\int\limits_{(A_{VS})} \mathrm{div}\,\vec{n}\,\mathrm{d}A = -\oint\limits_{(\Gamma)} \vec{n}\cdot\vec{\mu}\,\mathrm{d}\Gamma. \tag{5.15}$$

La partie droite de la dernière intégrale est égale à $-|\Gamma|\sin\theta$, où $|\Gamma|$ est la longueur totale de la ligne triple. En tenant compte de ces formules et de l'expression pour la courbure [5] $K = -\mathrm{div}\,\vec{n}$, on obtient

$$\int\limits_{(A)} K\sigma\ \vec{n}\cdot\vec{\nu}\,\mathrm{d}A = \sigma|\Gamma|\sin\theta. \tag{5.16}$$

Les autres termes de l'éq. (5.12) s'intègrent de la façon évidente et le résultat prend donc la forme suivante,

$$\sigma|\Gamma|\sin\theta = \lambda A_{VS} + \Delta\rho g V + \int\limits_{(A)} P_r^y \mathrm{d}A, \tag{5.17}$$

où $P_r^y = P_r\ \vec{n}\cdot\vec{\nu}$ est la composante verticale de la force du recul.

L'ordre des termes dans l'éq. (5.17) correspond à celui de l'éq. (5.12). Le membre de gauche est la force capillaire d'adhésion. Les premier et deuxième termes de droite sont les forces de pression et d'Archimède qui tendent à retirer la bulle de la paroi.

Le signe du dernier terme n'est pas connu *a priori*. Cependant, on a vu dans la section 5.2 que P_r est beaucoup plus grand près de la ligne de contact que sur la partie restante de A. Dans l'hypothèse $\theta < 90°$ (le cas le plus répandu), l'intégrale de P_r^y est négative et donc crée une adhésion supplémentaire. La force d'adhésion de la bulle qui la retient près de la paroi lors de sa croissance lente s'écrit alors

$$F_{ad} = \sigma|\Gamma|\sin\theta - \int\limits_{(A)} P_r^y \mathrm{d}A. \tag{5.18}$$

Nous reviendrons à cette expression plus tard, dans le chapitre 5.5.4. Etudions maintenant comment l'effet de recul sur la forme de la bulle peut être quantifié.

5.4 Recul de vapeur et angle de contact apparent

L'équation (5.12) est difficile à résoudre analytiquement et le calcul numérique [9, 11] (onéreux au niveau du temps de calcul) s'impose, cf. section suivante. Cependant, une approche simplifiée [8] qui se fonde sur la divergence de P_r discutée dans les sections suivantes permet d'estimer et de mieux comprendre l'effet de la force du recul sur la forme de la bulle. Dans cette section, nous montrons que l'influence du recul de vapeur peut être interprétée en terme de changement d'angle apparent de contact. Nous allons négliger temporairement la force d'Archimède en supposant que la bulle est petite.

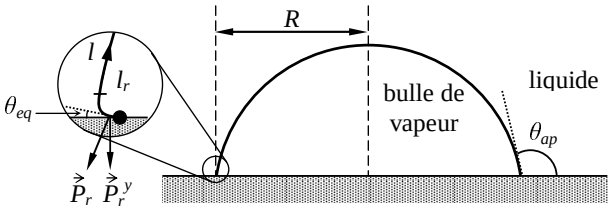

FIGURE 5.5: Angles de contact apparent θ_{ap} et réel θ_{eq}. Le rond noir indique la ligne de contact, c.-à-d. zéro pour la coordonnée curviligne l qui varie le long du contour de la bulle.

Par angle de contact apparent θ_{ap}, nous sous-entendons celui mesuré à la distance l_r (=épaisseur de la couche limite) de la ligne triple comme l'indiquent les figs. 5.3 et 5.5. Cette définition est valable quand $l_r \ll R$, le rayon de la bulle. Dans ce cas-là, la fonction $P_r(l)$ peut être approximée par la fonction δ de Dirac :

$$P_r(l) = 2\sigma_r \delta(l). \tag{5.19}$$

La fonction $\delta(l)$ est définie de telle manière, que $\delta(l) = 0$ si $l \neq 0$, $\delta(0) = \infty$ et $\int_{-\infty}^{\infty} \delta(l)\mathrm{d}l = 1$. D'après (5.12), ceci signifie que le recul de la vapeur est localisé à la ligne de contact, et la tension superficielle donne au reste de la surface de la bulle la forme d'une calotte sphérique. La supposition (5.19) se justifie par un calcul plus rigoureux [9] qui montre que $P_r(l)$ diverge quand $l \to 0$, $\int_0^{\infty} P_r(l)\mathrm{d}l$ restant fini.

En injectant (5.19), l'expression (5.10) se remplace par

$$\delta U_3 = \int\limits_{(A)} P_r \delta r_n \, \mathrm{d}A = \sigma_r \oint\limits_{(\Gamma)} \delta r_n \, \mathrm{d}\Gamma. \tag{5.20}$$

On constate que maintenant P_r contribue plutôt dans l'équation pour l'angle de contact (5.13) qui devient

$$\cos\theta_{ap} = c - N_r \sin\theta_{ap}, \tag{5.21}$$

où θ est remplacé par l'angle de contact apparent θ_{ap} p. Le "nombre de recul" $N_r = \sigma_r/\sigma$ caractérise l'importance de la force de recul relativement à la tension superficielle. On peut le réécrire sous la forme

$$N_r = \frac{1}{\sigma} \int\limits_0^{l_r} P_r(l) \, \mathrm{d}l, \tag{5.22}$$

qui est plus générale et peut s'appliquer à une fonction $P_r(l)$ plus réaliste.

On note que (5.21) peut être obtenue si on s'aperçoit que l'amplitude σ_r a la dimension d'une tension superficielle et doit être incluse dans le bilan de (quasi-) équilibre des tensions agissant sur la ligne de contact montrées sur la fig. 5.6. La ligne de contact est stationnaire quand la

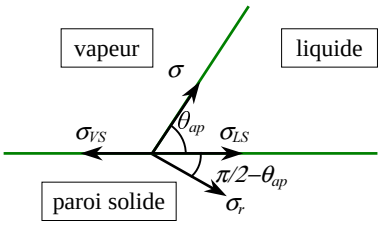

FIGURE 5.6: Equilibre des forces qui agissent sur la ligne triple de contact, où σ_{vs} et σ_{ls} sont les tensions superficielles pour les interfaces respectivement vapeur-solide et liquide-solide.

composante horizontale de la somme des vecteurs de toutes les forces est égale à zéro, ce qui conduit de nouveau à l'éq. (5.21).

Par suite du changement (5.20) de l'expression pour δU, le terme de P_r disparaît de l'éq. (5.12) qui décrit alors, en l'absence de gravité, une bulle sphérique avec l'angle de contact donné par l'éq. (5.21).

La dépendance de θ_{ap} par rapport à N_r, calculée à partir de (5.21), est présentée sur la fig. 5.7. On peut voir que la force de recul augmente l'angle de contact apparent. Lorsque la puissance de

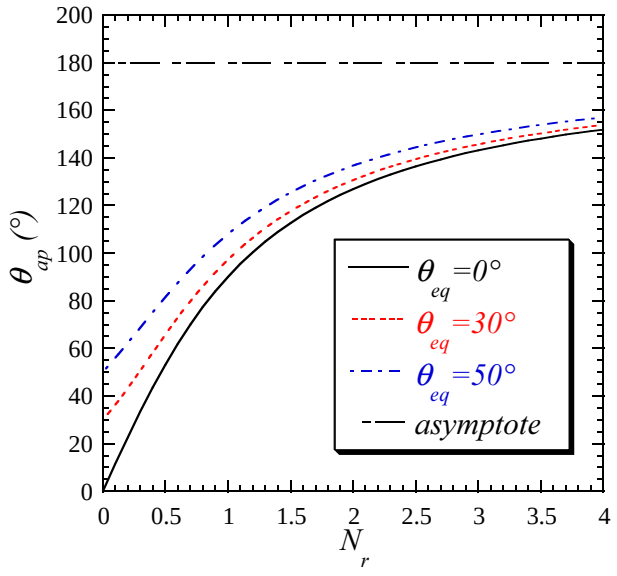

FIGURE 5.7: Angle apparent de contact par rapport au nombre de recul N_r pour différentes valeurs de l'angle de contact d'équilibre.

la paroi chauffante reste constante, le flux de chaleur q_L augmente avec le temps en augmentant N_r. Par conséquent, l'angle de contact apparent croît avec le temps. Comme la bulle reste une calotte sphérique, l'augmentation de l'angle de contact se traduit par l'étalement de la tache sèche, son rayon R_{dry} étant lié au rayon de la bulle R (cf. la fig. 5.5) par l'expression

$$R_{dry} = R \sin \theta_{ap}$$

qui provient de la géométrie de la calotte sphérique.

La force d'adhésion de la bulle à la paroi F_{ad} s'avère très importante pour estimer la valeur du CHF (voir ci-dessous). Elle peut être obtenue à partir de l'éq. 5.18 en tenant compte de l'expression valable sous l'hypothèse (5.19),

$$\int_{(A)} P_r^y \mathrm{d}A = -\sigma_r |\Gamma| \cos\theta_{ap}, \tag{5.23}$$

où la longueur de la ligne triple $|\Gamma| = 2\pi R_{dry}$. On obtient donc finalement que

$$F_{ad} = 2\pi R\sigma(\sin\theta_{ap} + N_r \cos\theta_{ap}) \sin\theta_{ap}. \tag{5.24}$$

Les dépendances de R_{dry} et F_{ad} de N_r sont montrées dans la fig. 5.8. Le comportement pour

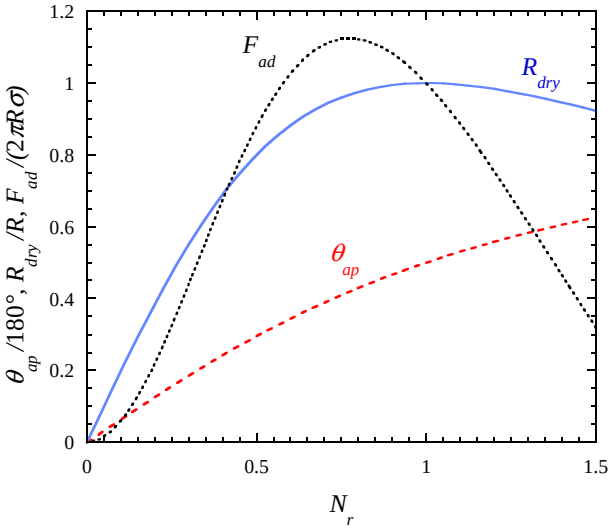

FIGURE 5.8: Rayon R_{dry} de la tache sèche et la force d'adhésion en fonction du nombre du recul N_r pour $\theta_{eq} = 0$. $\theta_{ap}(N_r)$ est rapporté de la fig. 5.7 pour comparaison. La décroissance non-physique qui apparaît pour $\theta_{ap} > 90°$, est due à la déficience de l'approche simplifiée.

de petites valeurs de N_r est correct : toutes les fonctions sont croissantes. Cependant, une décroissance de R_{dry} et de F_{ad} qui apparaît quand θ_{ap} dépasse 90° est paradoxale. La composante verticale P_r^y de $\vec{P}_r$ change alors de signe. Cette incohérence est due au fait que la forme exacte de la bulle dans la proximité de la ligne triple (cf. l'inséré dans fig. 5.5) n'est pas prise en compte. En réalité, la surface est fortement courbée et P_r^y reste négative. Cela montre des limites de l'approche simplifié. Un autre défaut de la théorie simplifiée réside dans l'impossibilité de calculer le temps de départ correctement (puisque avant le départ, la forme de la bulle dévie fortement de celle d'une calotte sphérique). C'est pourquoi il est nécessaire d'abandonner la notion d'angle apparent qui est fondée sur l'expression (5.19) pour la force de recul. Cette dernière doit être obtenue plus rigoureusement pour calculer la forme de la bulle, ce qui sous-entend une approche numérique ou des expériences.

L'approche de l'angle apparent ci-dessus illustre bien l'idée principale de l'étalement sous l'action du recul. Elle permet, en principe, de calculer le champ thermique autour de la bulle en tenant compte de l'effet de recul sans recourir à l'éq. (5.12) pour déterminer la forme de la

bulle. On peut en effet effectuer le calcul thermique pour une calotte sphérique et ajuster son angle de contact en utilisant l'eq. (5.21).

5.4.1 Estimation de l'effet du recul

Le paramètre très important pour la modélisation de la crise d'ébullition est le rayon de la tache sèche R_{dry}. Pour l'estimation, on peut supposer que la crise arrive quand R_{dry} devient comparable à R. D'après la fig. 5.8, cela arrive quand $N_r \sim 1$. Il est intéressant de remonter jusqu'à la valeur de N_r à partir des données expérimentales.

Nous supposons que la chaleur est transférée au fluide seulement par la ceinture de la largeur l_r au pied de la bulle. Le flux thermique arrivant de la paroi chauffante vers le liquide est alors donné par l'estimation

$$q_S \sim 2\pi R l_r n_b q_L, \tag{5.25}$$

où n_b est un nombre de bulles par m^2 de paroi. Au moment de la crise, une grande partie de la paroi est couverte de bulles. Nous supposons la fraction couverte de bulles à 50% pour l'évaluation : $n_b \pi R^2 \sim 0,5$. Alors on obtient de (5.25) que $q_L \sim q_S/a$ où $a = l_r/R$. En injectant les formules (5.3,5.4) dans (5.22), on obtient l'estimation

$$N_r \sim q_L^2 l_r/(H^2 \rho_V \sigma) \sim q_S^2 R/(a H^2 \rho_V \sigma) \tag{5.26}$$

en tenant compte de l'inégalité $\rho_V \ll \rho_L$. L'évaluation de (5.26) donne $N_r \sim 1$ pour $a \sim 0,01$ (habituel pour de grandes bulles) et pour les paramètres caractéristiques de l'eau aux hautes pressions : $R \sim 1$ mm, $q_S \sim q_{CHF} \sim 1$ MW/m^2, $H \sim 1$ MJ/kg, $\rho_v \sim 10$ kg/m^3, et $\sigma \sim 10^{-2}$ N/m.

On constate la cohérence du modèle basé sur le concept du recul qui conduit à la même valeur $N_r \sim 1$ pour identifier la crise.

5.5 Calcul rigoureux de la forme de la bulle

Revenons à l'approche rigoureuse qui se base sur l'éq. 5.12 comportant la force de recul P_r définie par (5.3, 5.4). La résolution du problème thermique est indispensable pour trouver le flux q_L dont dépend P_r.

5.5.1 Problème thermique

En négligeant l'advection de chaleur par le fluide (ce qui est justifié par la petite échelle que l'on considère), on peut écrire l'équation décrivant la variation de la température T_L dans le liquide comme

$$\frac{\partial T_L}{\partial t} = \alpha_L \nabla^2 T_L, \tag{5.27}$$

où α_L est la diffusivité thermique du liquide. Dans notre calcul, qui étudie la cinétique de croissance d'une bulle, la surchauffe nécessaire pour nucléer une bulle n'a pas d'importance. On suppose donc que la bulle d'un petit rayon R_0 et de volume correspondant V_0 est nucléée au moment initial, quand la température est homogène et égale à celle de saturation T_{sat} pour une pression donnée du système :

$$T_L|_{t=0} = T_{sat}. \tag{5.28}$$

Puisqu'il s'agit du raccord des trois milieux sur la ligne triple, le choix des conditions aux limites est très important pour trouver la valeur correcte de P_r.

Conditions aux limites

D'abord, étudions la condition aux limites sur la surface liquide-vapeur $\partial\Omega_i$. Dans le problème considéré il n'y a qu'un seul composant (pas d'impuretés). Cela signifie que la température interfaciale T_i est égale à T_{sat} et la vitesse d'évaporation est contrôlée par l'apport de la chaleur à l'interface. Une diminution locale de T_i causerait une augmentation de l'évaporation ce qui conduirait au dégagement de chaleur latente qui réchaufferait l'interface en maintenant l'égalité $T_i = T_{sat}$. La déviation T_i de T_{sat} (et donc l'effet Marangoni) n'est possible que loin de l'équilibre dynamique (voir chapitre 4.3) ou dans des mélanges où les variations de la concentration le long de l'interface et de T_i peuvent être couplées.

Cependant T_i dépend faiblement du rayon de la bulle. En vertu de l'équation de Clausius-Clapeyron

$$T_{sat} = T_{sat}^{\infty}[1 + \frac{\lambda}{H}(\rho_V^{-1} - \rho_L^{-1})]$$

où T_{sat}^{∞} est la température de saturation pour l'interface plane. Selon (5.12) $\lambda = \sigma/R_s$ où R_s est le rayon de bulle au sommet (où P_r est négligeable), il est donc facile d'estimer que la correction à T_{sat}^{∞} est moins de $10^{-3}\%$, même pour les plus petites tailles de bulle considérées. Nous remarquons que si les forces de van der Waals (qui peuvent être importantes près de la ligne triple dans certains cas) avaient été prises en compte dans (5.12), la conclusion aurait été identique. Par la suite, nous négligerons cet effet en écrivant $T_{sat} \equiv T_{sat}^{\infty}$. Alors, la condition aux limites s'écrit

$$T_L|_{\partial\Omega_i} = T_{sat}. \tag{5.29}$$

La condition aux limites sur la surface de la paroi peut être choisie parmi les trois options suivantes : (i) paroi isotherme ; (ii) flux q_S constant le long de la paroi chauffante ; (iii) flux et température continus à travers l'interface solide-fluide. Cette dernière condition est possible mais plus difficile à traiter puisque le calcul thermique dans le solide devient nécessaire. Considérons d'abord les choix (i) et (ii).

Le choix (i) conduirait à des difficultés importantes car pour maintenir l'évaporation, la température de la paroi doit être supérieure à T_{sat}. L'ambiguïté de la température sur la ligne triple qui en résulte entraîne une singularité non intégrable de $q_L \sim 1/l$ ce qui à son tour entraîne une vitesse infinie de la croissance de la bulle (cf. l'éq. (5.40) ci-dessous) et nous est donc inacceptable.

L'option (ii) ne conduit pas à ces difficultés et peut être utilisée, notamment pour valider le code de calcul. Cependant, il est clair que q_S dans la tache sèche $\partial\Omega_d$ doit être beaucoup plus petit que le flux q_S dans la partie mouillée $\partial\Omega_w$. Nous n'avons donc pas d'autre choix que d'adopter l'option (iii) pour rester cohérent et formuler la condition aux limites comme

$$q_S = -k_S \left.\frac{\partial T_S}{\partial y}\right|_{y=0} = \begin{cases} -k_L \dfrac{\partial T_L}{\partial y} & \text{at} \quad \partial\Omega_w \\ 0 & \text{at} \quad \partial\Omega_d \end{cases}, \tag{5.30}$$

$$T_S|_{\partial\Omega_w} = T_L|_{y=0}, \tag{5.31}$$

où k_S et T_S sont la conductivité thermique et la température à l'intérieur du solide. La paroi chauffante coïncide avec le plan $y = 0$.

Thermique dans le solide

La chaleur est apportée dans le système par un chauffage homogène à l'intérieur du solide avec une puissance volumique $j(t)$, et l'équation de conduction de la chaleur s'écrit

$$\frac{\partial T_S}{\partial t} = \alpha_S \nabla^2 T_S + \frac{\alpha_S}{k_S} j(t), \quad y < 0. \tag{5.32}$$

Le solide est supposé semi-infini. Cette équation doit être résolue avec la condition initiale

$$T_S|_{t=0} = T_{sat}. \tag{5.33}$$

La variation temporelle de la puissance volumique $j(t) = C/\sqrt{t}$ est choisie pour que le flux q_S soit constant et égale à q_0 loin de la bulle,

$$q_0 = C\sqrt{\pi}\alpha_S k_L/(k_S\sqrt{\alpha_L} + k_L\sqrt{\alpha_S})$$

ce qui nous donne le paramètre principal de contrôle.

Le problème thermique (5.27-5.33) ainsi posé, on peut calculer le flux-clé

$$q_L = -k_L(\vec{n}\cdot\nabla)\, T_L|_{\partial\Omega_i}\,. \tag{5.34}$$

5.5.2 Equations décrivant le contour de la bulle

En injectant (5.34) dans (5.3), on peut calculer P_r pour son utilisation dans l'éq. 5.12 qui décrit la forme de la bulle. Une paramétrisation de l'interface est nécessaire pour la résoudre. Nous choisissons comme paramètre la distance l entre la ligne de contact et un point M mesurée le long du contour $\partial\Omega_i$ comme indiqué sur la fig. 5.4. Il est commode d'utiliser aussi une variable ξ adimensionnée par la longueur du demi-contour L de la bulle : $\xi = 1 - l/L$. Les coordonnées du point M(x, y) deviennent des fonctions de ξ. Nous considérerons désormais la bulle en 2D. Utilisons l'expression pour la courbure et introduisons une variable $u = u(\xi)$ qui est l'angle entre la tangente à $\partial\Omega_i$ au point ξ et le vecteur dirigé inversement à l'axe x (fig. 5.4). On arrive à un système d'équations

$$\mathrm{d}x/\mathrm{d}\xi = L\cos u, \tag{5.35}$$
$$\mathrm{d}y/\mathrm{d}\xi = -L\sin u, \tag{5.36}$$
$$\mathrm{d}u/\mathrm{d}\xi = L(\lambda + P_r(\xi))/\sigma \tag{5.37}$$

avec les conditions aux limites issues de la symétrie

$$x(0) = 0, \quad u(0) = 0, \quad y(1) = 0. \tag{5.38}$$

La quatrième condition $u(1) = \pi - \theta$ permet de fixer l'angle de contact θ connu et est nécessaire pour déterminer L. Le cas habituel pour le contact des liquides avec des métaux $\theta = 0$ est considéré par la suite.

La connaissance du volume V de la bulle permet de trouver le paramètre λ grâce à une équation supplémentaire

$$V = -\frac{L}{2}\int_0^L (xn_x + yn_y)\,\mathrm{d}\xi, \tag{5.39}$$

où le vecteur normal $\vec{n} = (n_x, n_y)$ (fig. 5.4) est une fonction de ξ. L'évolution temporelle du volume est contrôlée par le bilan de chaleur latente et la chaleur consommée par la bulle lors de sa croissance :

$$H\rho_V \frac{\mathrm{d}V}{\mathrm{d}t} = \int\limits_{(\partial\Omega_i)} q_L \,\mathrm{d}\,\partial\Omega\,, \quad V|_{t=0} = V_0. \tag{5.40}$$

Le problème (5.35-5.40) permet de déterminer la forme de la bulle. Il est cependant couplé avec le problème thermique (5.27-5.33) en formant un problème aux frontières libres. Le problème peut être résolu avec la méthode des éléments de frontière (Boundary Element Method, BEM en anglais). Les détails techniques peuvent être trouvés dans nos travaux [11, 10].

5.5.3 Résultats de la simulation

Puisque la bulle dans notre simulation reste toujours attachée à la paroi, tôt ou tard la force de recul deviendra importante par rapport à la tension superficielle et la bulle commencera à s'étaler. L'évolution temporelle de la forme de la bulle est montrée sur la fig. 5.9. La bulle grossit. La tache sèche reste petite jusqu'au temps de transition t_c (cf. fig. 5.10) où elle s'agrandit

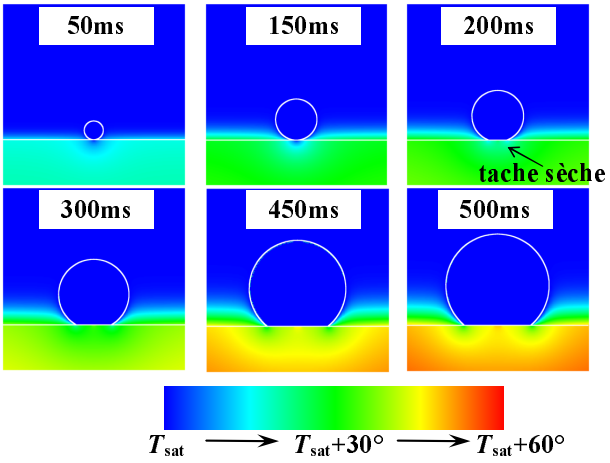

FIGURE 5.9: Evolutions temporelles de la tache sèche au-dessous de la bulle et de la température calculées pour $q_0 = 0.1$ MW/m^2.

brusquement. L'angle de contact apparent augmente, lui aussi. Nous associons cette transition à la crise d'ébullition. La croissance de la tache sèche juste avant la crise est confirmée par nombre de travaux expérimentaux, voir par exemple [14]. Etant très petite jusqu'à l'instant t_c, la force de recul caractérisée par le paramètre N_r devient alors de l'ordre de l'unité (cf. fig. 5.10), ce qui se compare bien avec l'estimation pour le CHF donnée dans l'article [9].

La difficulté de cette simulation réside dans la divergence du flux q_L sur la ligne triple qui correspond au point triple en 2D, cf. fig. 5.11. Pour résoudre cette divergence nous avons été obligés de choisir un maillage hétérogène, très fin (10^{-4} de la longueur totale du contour de la bulle) près du point triple. Pour éviter des problèmes de stabilité numérique apparaissant à cause de ce choix, un traitement très raffiné semi-analytique des coefficients de la matrice de BEM a été effectué [10].

Le flux de la paroi chauffante q_S et la température T_S manifestent des singularités, eux aussi. Tandis que la température reste finie et égale à T_{sat}, cf. (5.29,5.31), les flux q_L et q_S divergent.

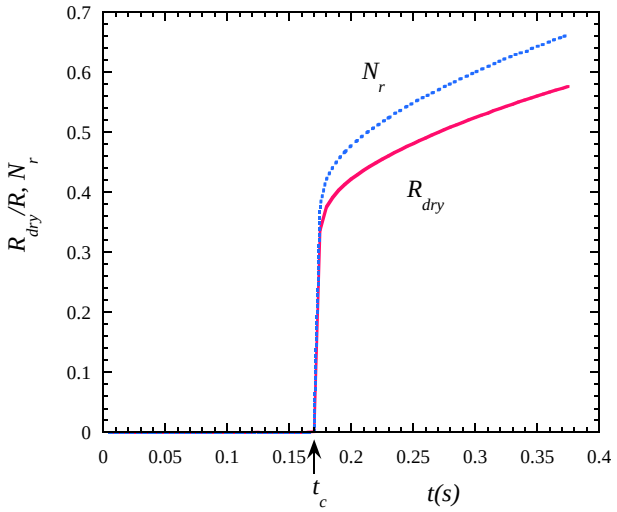

FIGURE 5.10: Evolutions temporelles du rayon R_{dry} de la tache sèche et du coefficient du recul N_r issues du calcul réalisé d'après l'article [11] pour $q_0 = 0.1$ MW/m^2.

Toutefois, les divergences restent intégrables, ce qui permet de garder une vitesse finie de la croissance du volume V de la bulle, cf. (5.40). En approchant le point triple le long de la paroi chauffante du coté liquide (à droite sur la fig. 5.11b) le flux q_S devient égal au flux q_L (fig. 5.11a) mesuré à la même distance curviligne du point triple. Cela veut dire que le flux de chaleur q_S arrivant au fluide près de la ligne triple est consommé par l'évaporation pratiquement sans chauffer le liquide.

Abordons maintenant la question de la valeur du CHF.

5.5.4 Comment estimer le CHF : inhibition du détachement de la bulle par la force de recul

Comme les "forces de départ" (force d'Archimède, poussée du flux hydrodynamique,...) qui tendent à arracher la bulle de la paroi sont absentes de l'eq. (5.12), la bulle reste toujours accrochée sur la paroi dans la simulation de type [11]. Dans la situation réelle, la bulle quitte la paroi au moment t_{dep}. Si t_{dep} est plus petit que le temps t_c issu de la simulation [11], la bulle quitte la paroi avant que la tache sèche puisse s'étaler et la crise d'ébullition ne se produit pas. L'analyse de départ de la bulle s'avère alors cruciale pour trouver la valeur du CHF.

Le temps t_c est une fonction décroissante du flux thermique q_0 de paroi [11]. Cependant, t_{dep} dépends aussi de q_0. Pour trouver la fonction $t_{dep}(q_0)$, on doit calculer la force d'adhésion F_{ad} d'une bulle à la paroi (5.18). Son premier terme est très important surtout au début de la croissance, lorsque la ligne triple est attachée au défaut de la paroi qui a servi de centre de nucléation (et qui donne à θ_{eq} une valeur importante). Elle devient négligeable par la suite et la bulle se détache de la paroi sous l'action de la force de départ. Comme on ne peut pas connaître la valeur locale de θ_{eq}, ce terme est difficile à estimer. On suppose par la suite que $\theta_{eq} = 0$ sur le reste de la paroi où la ligne triple se déplace. La deuxième partie

$$F^r_{ad} = \int P^y_r \mathrm{d}A \tag{5.41}$$

est due à la force de recul dont la composante verticale P^y_r (dirigée vers la paroi) est intégrée sur toute la surface A de la bulle. Bien que le calcul [11] soit bidimensionnel, on peut raisonnablement

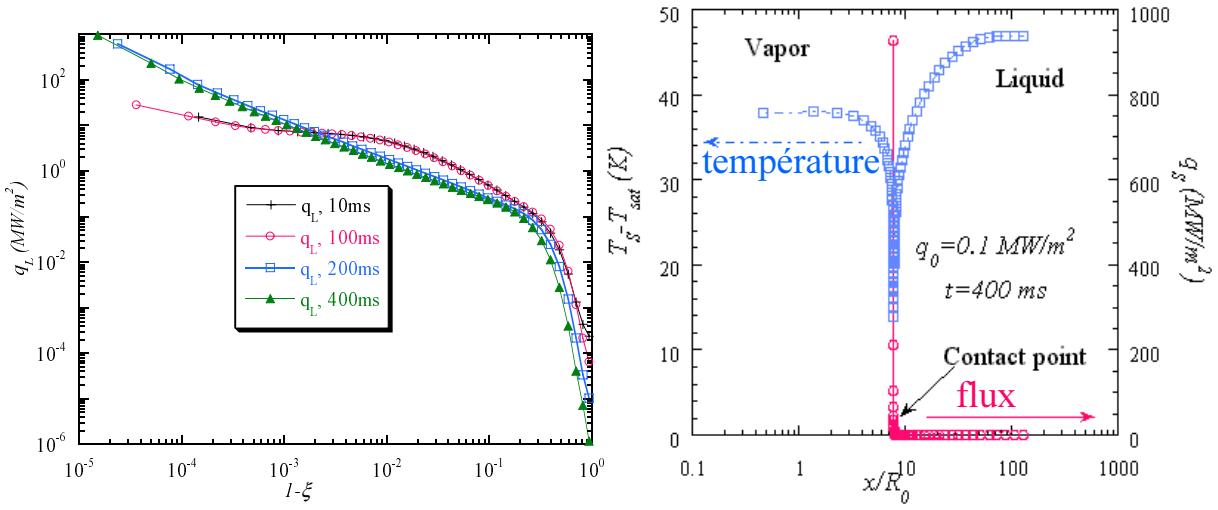

(a) (b)

FIGURE 5.11: Variations spatiales des flux calculées pour $q_0 = 0.1$ MW/m^2 (d'après l'article [11]). (a) Changement du flux q_L d'évaporation le long du contour de la bulle pour des temps de croissance différents. La ligne triple correspond au point $\xi = 1$. (b) Changements du flux chauffant q_S (cercles) et de la température T_S (carrés) le long de la paroi chauffante.

supposer que la valeur de P_r obtenue s'applique aussi pour le cas 3D axi-symétrique (comme si la bulle avait une symétrie axiale en 3D).

Le calcul montre que F^r_{ad} reste très petite au début de l'évolution (ce qui correspond au cas $t_{dep} < t_c$), par rapport aux forces de départ, notamment la force d'Archimède. A partir de l'instant $t = t_c$, la croissance de F^r_{ad} s'accélère brutalement et c'est elle qui domine. Autrement dit, quand la tache sèche commence à croître, la bulle reste attachée à la paroi en coalescant avec les bulles voisines. C'est ainsi que la crise d'ébullition devrait se dérouler. Le crise d'ébullition apparaît ainsi comme la transition entre deux régimes qui ne peuvent pas coexister : le régime de départ et le régime d'étalement de la bulle. A partir d'un calcul tenant compte des forces de départ, la valeur du CHF pourra donc être obtenue comme flux minimum pour lequel la bulle reste attachée à la paroi en s'étalant.

La comparaison des résultats numériques avec ceux du modèle simplifié montre que la force d'adhésion est surestimée par ce dernier d'à-peu-près 50%. Ce fait confirme la nécessité de poursuivre des études numériques qui permettront d'obtenir la valeur du CHF compte tenu des forces de départ.

5.6 Evidence expérimentale de l'étalement d'une bulle

Les expériences [6] confirment que notre modèle d'étalement d'une bulle est valide dans la région critique, c.-à-d. pour des pression p et température T proches de la pression p_c et de la température T_c critiques pour le fluide donné. Le point critique présente beaucoup de propriétés singulières. En particulier, le coefficient de diffusion thermique s'évanouit, ce qui ralentit la croissance des bulles et permet d'observer les détails de la croissance sans une agitation gênante du liquide provoquée par des mouvements rapides. Par exemple, la croissance d'une seule bulle a pu être observée [6] pendant environ quinze minutes.

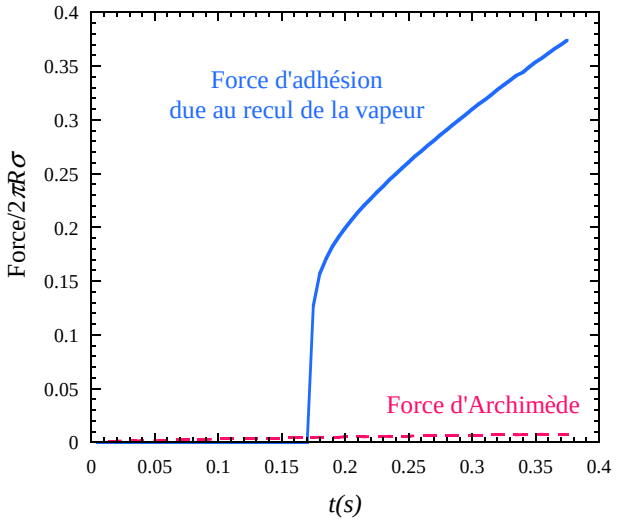

FIGURE 5.12: Evolutions temporelles de la force d'Archimède et de la force d'adhésion F^r_{ad}, issues du calcul réalisé d'après l'article [11] pour un flux $q_0 = 0.1$ MW/m^2. Les forces sont exprimées dans les unités $2\pi R\sigma$ pour pouvoir effectuer une comparaison avec les résultats de l'approche simplifiée (fig. 5.8). F^r_{ad} reste négligeable par rapport à la force d'Archimède pour $t < t_c$.

Cependant, la longueur capillaire $[\sigma/\Delta\rho g]^{1/2}$ (où g est la gravité terrestre) disparaît également au point critique car

$$\Delta\rho \equiv \rho_L - \rho_V \sim (T_c - T)^{\beta}, \tag{5.42}$$

$$\sigma \sim (T_c - T)^{2\nu}, \tag{5.43}$$

où les exposants critiques $\beta \approx 0,325$ et $\nu \approx 0,63$ sont universels. Les bulles sont écrasées contre les parois et l'interface gaz-liquide devient plate. Les bulles de vapeur de forme habituelle convexe ne sont donc pas observables en pesanteur terrestre au voisinage du point critique. Pour cette raison, les expériences doivent être conduites en microgravité.

5.6.1 Comportement du CHF au voisinage du point critique

Puisque la force de recul P_r (5.3) est proportionnelle à $\Delta\rho$, il peut sembler que P_r s'annule quand $T \to T_c$. Pourtant, cet argument ignore le comportement du taux d'évaporation η qui diverge fortement en causant la divergence de P_r. Pour le démontrer, supposons raisonnablement que près du point critique, η obéit à une loi d'échelle

$$\eta(l) = g(l)(T_c - T)^a. \tag{5.44}$$

où T est la température moyenne de l'échantillon et a est un exposant constant. Trouvons cet exposant. La masse m de la bulle de vapeur change dans le temps selon l'expression

$$\mathrm{d}m/\mathrm{d}t = \int_{(A)} \eta \,\mathrm{d}A \sim (T_c - T)^a. \tag{5.45}$$

D'un autre côté,

$$\frac{\mathrm{d}m}{\mathrm{d}t} = \frac{\mathrm{d}}{\mathrm{d}t}(V\phi\rho_V), \tag{5.46}$$

où V est le volume de l'échantillon et ϕ est la fraction volumique de la vapeur. Choisissons $\phi = 0.5$ pour $\rho = \rho_c$, cf. (4.1). V est alors indépendant de T et on obtient le résultat $a = \beta - 1$ à partir des équations $\rho_V = \rho_c - \Delta\rho/2$, (5.42) et (5.45). La force de recul diverge au point critique car $a < 0$. Mais son effet par rapport à la tension superficielle est encore plus marquant :

$$P_r/\sigma \sim (T_c - T)^{3\beta-2-2\nu}, \tag{5.47}$$

où les éqs. (5.42-5.43) ont été utilisées. Selon (5.12), l'expression (5.47) peut être interprétée comme la courbure de la bulle près de la ligne triple. Puisque l'exposant $(3\beta - 2 - 2\nu \approx -2.3)$ est très important, l'effet du recul devrait se manifester même loin du point critique, en accord avec les expériences.

Le coefficient de recul N_r (5.22) contient le même facteur. On rappelle qu'il est proportionnel aussi à q_0^2 selon (5.3) et (5.4) et que la crise d'ébullition ($q_0 = q_{CHF}$) apparaît quand $N_r \sim 1$. On obtient ainsi

$$q_{CHF} \sim (T_c - T)^{1+\nu-3\beta/2} \sim (T_c - T)^{1,1}. \tag{5.48}$$

Le même exposant est également valide pour l'écart de pression lié à l'écart de température par la dérivée $\mathrm{d}p/\mathrm{d}T$ qui reste finie sur la courbe de co-existence,

$$q_{CHF} \sim (p_c - p)^{1,1}. \tag{5.49}$$

L'éq. (5.49) explique la tendance observée expérimentalement : $q_{CHF} \to 0$ quand $p \to p_c$.

5.6.2 Expérience en microgravité

Selon (5.48), le CHF est très petit près du point critique. On s'attend donc à ce qu'un flux de chaleur très faible produise l'étalement de la bulle. De plus, en raison de la lenteur de croissance des bulles mentionnée ci-dessus, la bulle n'est pas déformée par les contraints hydrodynamiques très faibles. Cela justifie l'approximation quasistatique utilisée dans les sections précédentes lors des calculs.

Dans les expériences [6], une cellule expérimentale de forme cylindrique, fabriquée en alliage de cuivre était utilisée. Elle a été remplie par du SF_6 à densité presque critique. Dans une série d'expériences conduites dans l'installation ALICE-2 à bord de la station Mir, nous avons observé [6] l'évolution de la bulle à travers les bases transparentes du cylindre (hublots) en saphir. Le saphir conduit la chaleur moins bien que le cuivre. Le fluide est donc chauffé surtout par la paroi cylindrique. La conception de cette cellule fit que la bulle de vapeur reste coincée près de la paroi, ce qui permet au film de mouillage entre la bulle et la paroi de s'évaporer lors du chauffage. La fig. 5.13 montre comment la bulle, initialement circulaire ($\theta_{eq} = 0$) s'étale sur la paroi chauffante cylindrique. L'angle de contact *apparent* augmente clairement avec le temps. Bien que le volume de la bulle reste constant, la masse de vapeur augmente suite à sa densité qui croît.

5.7 Conclusion

Dans ce chapitre, nous avons proposé une explication physique pour la crise d'ébullition : l'étalement de la tache sèche sous une bulle de vapeur est provoquée par la force de recul de la vapeur. Une fois l'étalement commencé, la bulle reste attachée à la paroi par le même effet

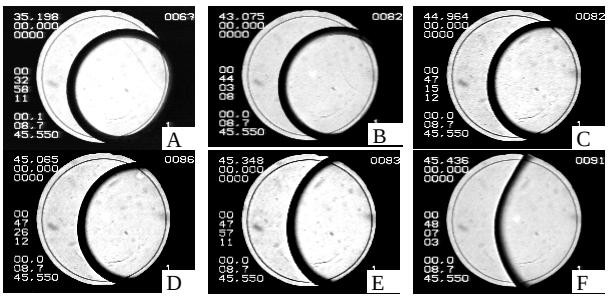

FIGURE 5.13: Evolution d'une bulle de vapeur dans une cellule cylindrique remplie de SF_6 proche de son point critique. Les images ont été obtenues pendant un chauffage continu de la cellule. La dernière image (F) correspond à la température juste en dessous de la température critique. La vapeur se trouve à droite de l'interface.

de recul et l'étalement (accompagné des coalescences possibles avec des bulles voisines) peut se prolonger jusqu'à la formation du film continu de vapeur. L'approche théorique est soutenue par une simulation numérique de croissance de la bulle sous un grand flux de chaleur, ainsi que par des données expérimentales sur la croissance de la bulle dans des conditions proches du point critique. Des simulations numériques basées sur cette approche devraient permettre de déterminer le CHF comme étant le flux thermique de transition entre deux régimes : un régime de départ (la bulle se détache de la paroi) et un régime d'étalement de la bulle.

De nouvelles perspectives sont liées au programme DECLIC du CNES et de la NASA. L'appareil DECLIC qui fonctionnera à bord de la Station Spatiale Internationale nous permettra de quantifier et approfondir les résultats obtenus dans ALICE-2.

Des études préparatoires sont aussi en cours en utilisant le banc de lévitation magnétique au SBT/CEA-Grenoble ainsi que des simulations numériques dans le cadre des projets ESA, CNES et EGIDE.

5.8 Bibliographie

[1] http://www.snecma-moteurs.com/fr/activites/propulsion_spatiale/moteur_vinci/index.htm.

[2] Auracher, H., & Marquardt, W. Heat transfer characteristics and mechanisms along entire boiling curves under steady state and transient conditions. *Int. J. Heat Fluid Flow* **25** 223 – 242 (2004).

[3] Bricard, P., Péturaud, P., & Delhaye, J.-M. Understanding and modeling DNB in forced convective boiling : Modeling of a mechanism based on nucleation site dryout. *Multiphase Sci. Techn.* **9**(4) 329 – 379 (1997).

[4] Buyevich, Y. A. Towards a unified theory of pool boiling – the case of ideally smooth heated wall. *Int. J. Fluid Mech. Res.* **26** 189 – 223 (1999).

[5] Finn, R. *Equilibrium Capillary Surfaces*. Springer, New York, 1986.

[6] Garrabos, Y., Lecoutre-Chabot, C., Hegseth, J., Nikolayev, V. S., Beysens, D., & Delville, J.-P. Gas spreading on a heated wall wetted by liquid. *Phys. Rev. E* **64**(5) 051602 (2001). (voir page 173 de cette thèse).

[7] Nikolayev, V. S., & Beysens, D. Crise d'ébullition comme l'étalement des bulles sur la paroi chauffante. In *17ème Congrès Français de Mécanique, du 29 août - 2 septembre 2005* (Troyes, 2005). publié sur un CD-ROM, AFM (2005) ; résumé accessible sur : http://www-cfm2005.utt.fr/programmedetailleparsession.php?theme=C11.

[8] Nikolayev, V. S., Beysens, D., & Garrabos, Y. Crise d'ébullition : inhibition du détachement de la bulle de vapeur par la force de recul. *Mécanique & Industries* **5**(5) 553 – 558 (2004). (voir page 242 de cette thèse).

[9] Nikolayev, V. S., & Beysens, D. A. Boiling crisis and non-equilibrium drying transition. *Europhysics Lett.* **47**(3) 345 – 351 (1999). (voir page 153 de cette thèse).

[10] Nikolayev, V. S., & Beysens, D. A. 2D BEM modeling of a singular thermal diffusion free boundary problem with phase change. In *Boundary elements XXIV (Incorporating meshless solutions)*, C. A. Brebbia, A. Tadeu, & V. Popov, Eds., vol. 13 of *Int. Series on Advances in Boundary Elements*. WIT Press, Southhampton, 2002, pp. 501 – 525. (voir page 190 de cette thèse).

[11] Nikolayev, V. S., Beysens, D. A., Lagier, G.-L., & Hegseth, J. Growth of a dry spot under a vapor bubble at high heat flux and high pressure. *Int. J. Heat Mass Transfer* **44**(18) 3499 – 3511 (2001). (voir page 160 de cette thèse).

[12] Palmer, H. J. The hydrodynamic stability of rapidly evaporating liquids at reduced pressure. *J. Fluid. Mech.* **75**(part 3) 487 – 511 (1976).

[13] Sefiane, K., Benielli, D., & Steinchen, A. A new model for pool boiling crisis, recoil instability and contact angle influence. *Colloids and Surfaces* **142** 361 – 373 (1998).

[14] Theophanous, T. G., Dinh, T. H., Tu, J. P., & Dinh, A. P. The boiling crisis phenomenon. Part II : Dryout dynamics and burnout. *Exp. Thermal Fluid Sci.* **26** 793 – 810 (2002).

6 Modélisation du mouvement de la ligne triple de contact liquide-solide-gaz le long d'un solide hétérogène

6.1 Problème de la dynamique du mouillage

À l'équilibre, les propriétés de mouillage d'un liquide en contact avec un solide sont bien définies par l'angle statique de contact θ_{eq} [8]. Dans le cas du mouillage complet ($\theta_{eq} = 0$), quand un film mince de prémouillage existe en avant de la majeure partie du liquide, sa dynamique est bien comprise aussi. Pour le mouillage partiel ($\theta_{eq} \neq 0$), la difficulté apparaît quand la ligne triple de contact solide-liquide-gaz se déplace. Depuis le travail [16], il est devenu évident que le mouvement de la ligne de contact ne peut pas être décrit par l'hydrodynamique visqueuse classique en utilisant la condition de non-glissement (vitesse liquide nulle au mur solide). Dans ce cas en effet, la valeur non nulle de la vitesse de la ligne triple de contact conduit à la divergence de la pression hydrodynamique et de la dissipation visqueuse. La seule exception à cette divergence pourrait être le mouvement de roulement [22] qui apparaît dans le cas de non-mouillage ($\theta_{eq} = \pi$). Environ une douzaine de modèles ont été proposés pour résoudre cette singularité, cf. [37] pour une revue. La solution la plus populaire [8] est probablement d'introduire une coupure géométrique à l'échelle atomique où le glissement peut être important. La condition de non-glissement peut être remplacée par la condition de glissement de Navier [15] au voisinage de la ligne de contact ou encore la rhéofluidification peut être supposée [14] (la viscosité tendant vers zéro) sur la ligne triple où les contraintes hydrodynamiques sont grandes. Parmi les modèles les plus populaires où la singularité est résolue en introduisant des effets physiques microscopiques d'origine non-hydrodynamique, on peut énumérer ceux de Blake et Haynes [5], Shikhmurzaev [43] et les modèles à l'interface diffuse [42, 33].

En se basant sur l'analogie qu'il y a avec le cas statique, la plupart des chercheurs caractérisent le comportement dynamique par l'angle dynamique θ de contact lié à la vitesse de ligne de contact v_n mesurée dans la direction normale à celle-ci

$$v_n = \frac{\sigma}{\chi}\mathcal{F}(\theta, \theta_{eq}), \tag{6.1}$$

où σ est la tension de l'interface liquide-gaz, χ est un coefficient propre à chaque modèle, dont la dimension est celle de la viscosité μ de cisaillement, et $\mathcal{F}$ est une fonction de l'ordre de l'unité. Pour la plupart des modèles où θ n'est pas limité à de petites valeurs,

$$v_n = \frac{\sigma}{\chi}(\cos\theta_{eq} - \cos\theta). \tag{6.2}$$

L'angle dynamique de contact semble être une quantité mal définie [37] en raison de difficultés dans sa mesure précise. Dans chaque cas réaliste, l'interface de liquide-gaz est fortement courbée

au voisinage de la ligne de contact. Par conséquent, l'erreur expérimentale de la détermination dynamique de l'angle de contact est importante et la grande dispersion de données expérimentales ne laisse pas confirmer ou réfuter un modèle particulier pour la résolution de la singularité. Au lieu de l'angle de contact, dans notre modélisation, nous choisissons comme variable, la position de ligne de contact, qui peut être mesurée avec une meilleure précision.

Une autre source d'erreur expérimentale, dans le cas du mouillage partiel, est due aux imperfections de la surface du substrat solide inévitables que nous appellerons des "défauts" par la suite. Ces "défauts" peuvent "accrocher" la ligne de contact en la déformant. Peu d'informations sont actuellement disponibles sur l'influence des défauts sur la dynamique de ligne de contact discutée dans ce chapitre.

6.2 Coalescence des gouttes sessiles

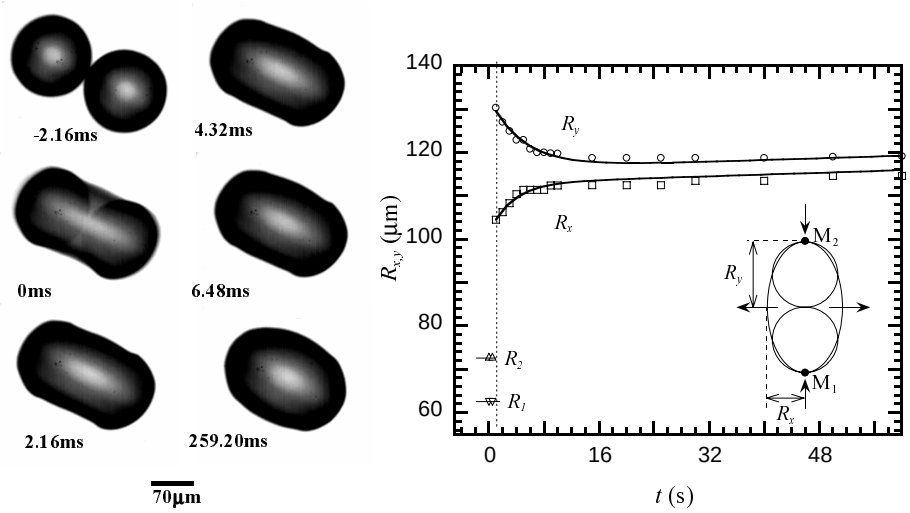

(a) (b)

FIGURE 6.1: (a) Images de la coalescence de deux gouttes obtenues à l'aide d'une caméra rapide. (b) Evolution des grand (R_y) et petit (R_x) rayons de la goutte composée dans une expérience de la chambre de condensation [26]. R_1 et R_2 sont les rayons des deux gouttes avant leur coalescence.

Les expériences [2, 26] sur la relaxation de gouttes sessiles d'eau ont beaucoup motivé nos études sur la dynamique de mouillage. Il s'agit du retour à la forme d'équilibre d'une goutte composée de deux gouttes qui viennent de se toucher et sont donc en train de coalescer (fig. 6.1a). Deux procédés d'initialisation de la coalescence ont été étudiés. D'une part, la coalescence a été observée lors de la condensation très lente sur un substrat froid dans une chambre de condensation. Les gouttes se forment et grossissent avant de se toucher, sans intervention extérieure. D'autre part, la coalescence de deux gouttes situées tout près l'une de l'autre a été initiée par le dépôt sur une des gouttes d'une petite quantité d'eau à l'aide d'une seringue. Dans les deux cas, la relaxation lente suit la formation très rapide d'une goutte composée convexe (fig. 6.1). La dynamique de la ligne triple a été caractérisée en mesurant l'évolution de deux demi-axes $R_x < R_y$ de la goutte composée (fig. 6.1b). Les courbes $R_{x,y}(t)$ concordent très bien avec la loi

exponentielle, ce qui semble naturel car il s'agit de relaxation

$$R_{x,y}(t) = R_0 \exp(-t/t_c) + R + At \tag{6.3}$$

où R est le rayon d'équilibre de la ligne triple de la goutte. Le dernier terme décrit la croissance lente de la goutte composée due à la condensation. Le temps de relaxation est proportionnel au rayon R (fig. 6.2a),

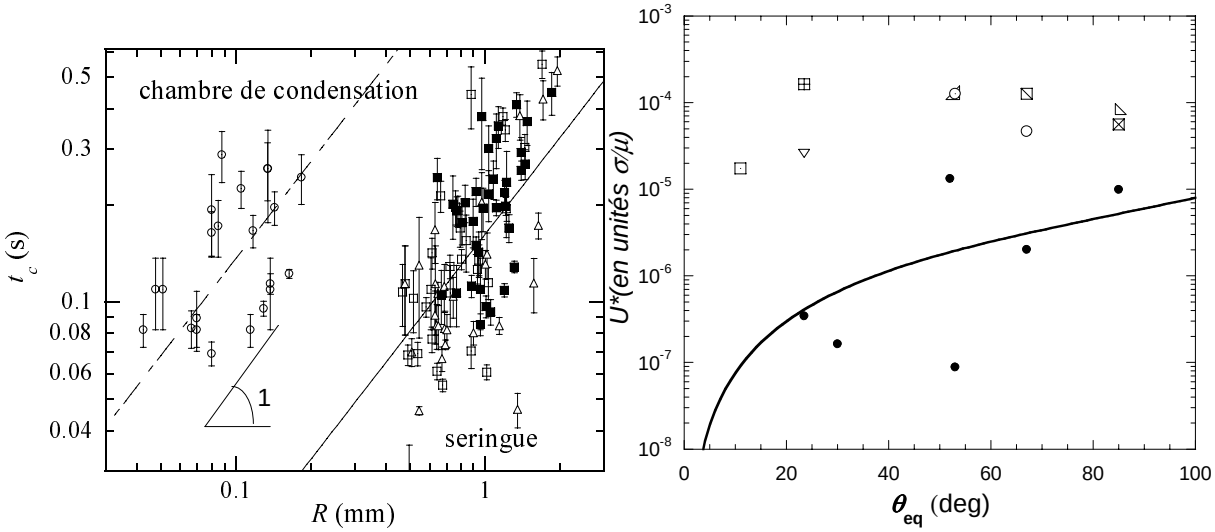

(a) (b)

FIGURE 6.2: (a) Temps de relaxation en fonction de la taille de la goutte pour différentes expériences de condensation sur le même film de polyéthylène. Les données de seringue correspondent à une sursaturation différente en vapeur d'eau (donnée par la température du substrat T_s par rapport à celle de rosée $T_d = 13°C$ pour l'air ambiant). Ronds vides : chambre de condensation ; triangles : seringue, $T_s = T_d + 5°C$; carrés vides : seringue $T_s = T_d$; carrés pleins : seringue $T_s = T_d - 5°C$. (b) U^* pour différents substrats d'après [26]. Ronds pleins : chambre de condensation ; symboles vides : seringue

$$t_c = R/U^* \tag{6.4}$$

où le paramètre U^* caractérise le taux de relaxation de la ligne de contact, que l'on ne confondra pas avec la vitesse de la ligne de contact qui varie durant la relaxation. Les valeurs de U^* obtenues pour plusieurs substrats peuvent être comparées avec l'échelle hydrodynamique de la vitesse de relaxation visqueuse σ/μ (fig. 6.2b). On peut s'apercevoir que

- $U^* \ll \sigma/\mu$ et que
- les valeurs de U^* obtenues dans les expériences de condensation sont de plusieurs ordres de grandeur plus petits que celles obtenues à l'aide d'une seringue.

La lenteur de la relaxation apparaît évidemment du fait de la dissipation anormale au voisinage de la ligne triple. Dans ce travail nous ne discutons pas du mécanisme de mouvement de la ligne triple et donc de l'origine de cette dissipation. A la place, nous introduisons un coefficient phénoménologique $\xi \gg \mu$ qui décrit cette dissipation anormale. Il sera appelé "le coefficient de dissipation" par la suite.

Cependant la dispersion aléatoire des données de quelques ordres de grandeur sur la fig. 6.2b et la comparaison avec d'autres travaux (cf. [9, 24]) suggèrent qu'il peut y avoir d'autres raisons à la lenteur de la relaxation. Notamment on s'intéressera à l'influence des défauts du substrat sur la dynamique et on démontrera dans le chapitre 6.8 ci-dessous que les défauts peuvent ralentir le mouvement de la ligne triple sous certaines conditions.

Discutons maintenant la différence entre deux types d'expériences qui est mise en évidence par les prises de vue avec une caméra rapide dont les images sont présentées sur la fig. 6.3 pour le cas de la déposition par une seringue. Celle-ci entraîne inévitablement une oscillation très

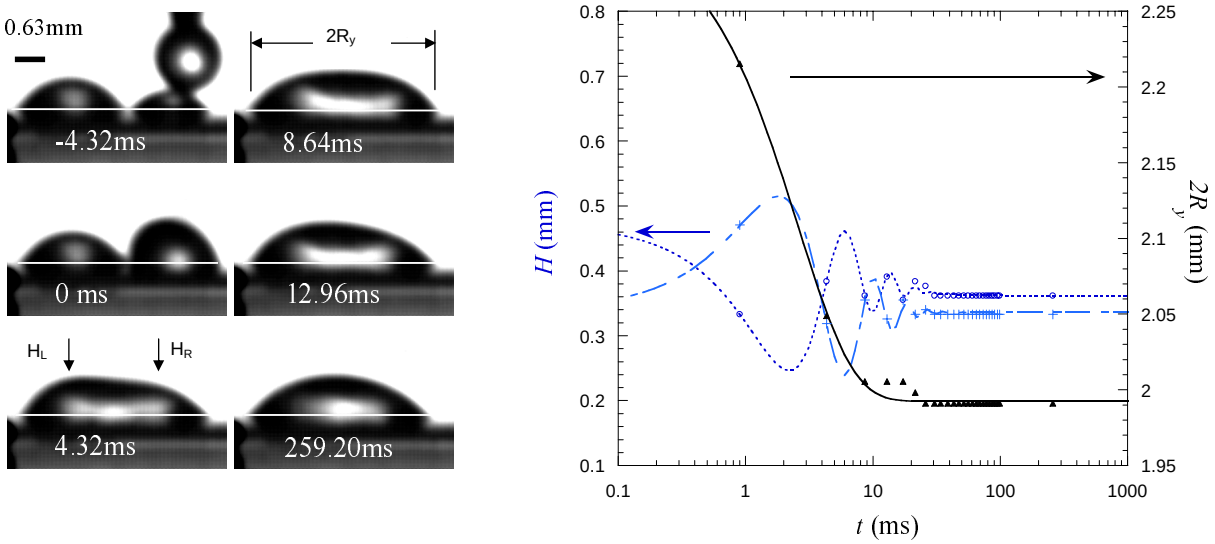

(a) (b)

FIGURE 6.3: (a) Coalescence de deux gouttes d'eau dans une expérience de seringue à une échelle de temps courte [26]. Le trait horizontal blanc indique la surface de substrat. Au-dessous de cette ligne se trouve la réflexion optique. H_L et H_R représentent les hauteurs de la goutte composée mesurées dans des endroits indiqués par les flèches. (b) Evolution de H_L (cercles), H_R (croix) et de la décroissance exponentielle de la largeur totale de la goutte $2R_Y$ (triangles). Les lignes en pointillés correspondent à une oscillation harmonique amortie.

rapide de la goutte composée, la période τ étant de l'ordre

$$\tau \sim (\rho R^3/\sigma)^{1/2} \sim 8\text{ms}. \tag{6.5}$$

Cette échelle de temps caractérise des phénomènes de la capillarité inertielle [36].

Ces résultats montrent le rôle de l'énergie cinétique du fluide qui doit être prise en compte pour décrire les mouvements rapides des gouttes. Le mouvement de la ligne triple se retrouve couplé avec des oscillations de la goutte composée, ce qui accélère sa relaxation en comparant au cas de la condensation dans une chambre où l'approche des gouttes est extrêmement lente et où aucune oscillation de la goutte composée n'a été détectée.

6.3 Approche théorique générale

Dans cette section nous appliquons une autre approche, suggérée dans [9] pour décrire une goutte en forme de calotte sphérique. Cette approche ne suppose ni l'éq. (6.1) ni un mécanisme

particulier de mouvement de ligne. Elle suppose simplement que l'énergie dissipée dans le voisinage de la ligne triple est beaucoup plus grande que dans le reste du fluide en cas du mouillage partiel. Cette hypothèse se fonde sur la grande valeur du rapport ξ/μ. Alors l'énergie dissipée lors du mouvement du fluide possédant la ligne de contact est proportionnelle à la longueur de la ligne et ne dépend pas de la direction du mouvement (avance ou recul). Nous généralisons cette approche pour une forme arbitraire de la surface du fluide.

Pour un mouvement lent de la ligne de contact, la principale contribution à l'énergie dissipée par unité de temps (c.-à-d. la fonction de dissipation) peut être écrite sous la forme

$$T = \int\limits_{(\Gamma)} \frac{\xi\, v_n^2}{2}\, \mathrm{d}\Gamma, \tag{6.6}$$

où l'intégration est effectuée le long de la ligne de contact et ξ est le coefficient constant de dissipation introduit ci-dessus.

Dans une approche Hamiltonienne [21], un système se décrit par l'action

$$a = \int_{t_1}^{t_2} \mathcal{L}\, \mathrm{d}t \tag{6.7}$$

où le lagrangien $\mathcal{L} = W - U$ est une fonction des coordonnées généralisées et de leurs dérivées temporelles, qui sont surmontées par un point. W est l'énergie cinétique du liquide et $U = U(q_j)$ est son énergie potentielle. Cette dernière a déjà été discutée au chapitre 5.3. Dans notre cas, elle est composée de deux termes $U = U_1 + U_2$. Le premier terme est l'énergie de surface

$$U_1 = \sigma A + \sigma_{VS} A_{VS} + \sigma_{LS} A_{LS}, \tag{6.8}$$

le deuxième correspond à l'énergie gravitationnelle. L'équation de Lagrange

$$\frac{d}{dt}\left(\frac{\delta \mathcal{L}}{\delta \dot{h}}\right) - \frac{\delta \mathcal{L}}{\delta h} = -\frac{\delta T}{\delta \dot{h}}, \tag{6.9}$$

où $\delta \ldots / \delta \ldots$ signifie la dérivée fonctionnelle s'écrit en termes de la fonction h qui donne la position de la ligne triple.

Nous pouvons séparer deux cas pour lesquels le mouvement de la ligne triple est lent (le nombre capillaire $Ca = v_n \mu/\sigma \ll 1$) en fonction du nombre de Reynolds Re. Le premier cas correspond au changement très lent de forme de la goutte. Re est alors très petit et l'énergie cinétique W peut donc être négligée. La forme de la surface du liquide sera calculée comme si elle était statique à chaque instant de temps pour la position de la ligne triple donnée. C'est l'approximation quasistatique qui sera considérée dans cette section.

Le deuxième cas correspond par exemple aux oscillations rapides de la goutte couplées avec le mouvement lent de la ligne triple. Dans ce cas, Re peut atteindre 10-100 [26] et W ne peut pas donc être négligée. Ce cas est décrit dans la section 6.9 ci-dessous.

Dans le premier cas, on obtient $\mathcal{L} = -U$ et l'équation de Lagrange (6.9) se réduit à l'expression

$$\frac{\delta U}{\delta h} = -\frac{\delta T}{\delta \dot{h}} \tag{6.10}$$

qui fut proposée initialement pour décrire le mouvement de la ligne triple dans [8]. La variation $\delta U = \delta U_1 + \delta U_2$ à été obtenue au chapitre 5.3. Elle est donné par les expressions (5.7, 5.9).

Puisque la surface est celle de l'équilibre à chaque instant, l'intégrale sur la surface de la goutte A s'annule (car la condition d'équilibre (5.12) est donnée justement par l'annulation de son intégrant) et δU ne contient que l'intégrale sur la ligne triple Γ,

$$\delta U = -\sigma \int_{(\Gamma)} (\cos\theta - c)\delta h \, \mathrm{d}\Gamma, \tag{6.11}$$

où c et le rapport de Young (5.8) qui dans le cas où $c \leq 1$, se réduit à $\cos\theta_{eq}$. En reportant (6.11) et (6.6) dans (6.10), on retrouve (6.2) dans le cas général avec $\chi = \xi$:

$$v_n = \frac{\sigma}{\xi}(\cos\theta_{eq} - \cos\theta). \tag{6.12}$$

Cela signifie que l'hypothèse (6.6) est équivalente à l'hypothèse (6.12) indépendamment de la forme de la ligne triple et de la surface du liquide [17]. En d'autre termes, des modèles (par exemple, [42, 5, 43]) qui aboutissent à l'expression (6.12), sont équivalents à notre hypothèse de la dissipation concentrée sur la ligne triple, la dissipation qui dans ce cas est proportionnelle à la longueur de la ligne triple. Les nombreuses mesures de l'angle de contact dynamique en fonction de la vitesse qui ont servi à justifier l'expression (6.12), justifient également notre approche.

6.4 Modélisation de la relaxation des gouttes sessiles de forme complexe

Puisque la formule (6.12) peut être appliquée à n'importe quelle forme de surface liquide, le mouvement des gouttes de forme complexe peut être étudié. Par exemple, on peut s'interroger sur la relaxation vers l'équilibre des gouttes initialement allongées. Quelle sera le temps de relaxation en fonction de l'angle de contact ? Cette question a été traitée analytiquement [28] et numériquement [17] en se basant sur le modèle de la section précédente.

La goutte a été représentée approximativement par un sphéroïde dont la ligne triple gardait la forme d'une ellipse avec des demi-axes R_x et R_y pendant toute son évolution. La relaxation d'une telle goutte peut être décrite par une exponentielle du deuxième ordre, c.-à-d. avec deux temps de relaxation τ_s et τ_n.

$$\tau_s = \tau_0/[\sin^2\theta_{eq}\,(2 + \cos\theta_{eq})], \tag{6.13}$$

$$\tau_n = 45\,\tau_0\,(1 + \cos\theta_{eq})/[(108 + 41\,\cos\theta_{eq} + 14\,\cos^2\theta_{eq} + 17\,\cos^3\theta_{eq})(1 - \cos\theta_{eq})], \tag{6.14}$$

où $\tau_0 = R\xi/\sigma$. Le temps τ_s correspond à la relaxation de la goutte qui garde la forme d'une calotte sphérique avec $R_x = R_y = R + \Delta R\exp(-t/\tau_s)$. Le temps τ_n correspond à la goutte allongée dont les demi-axes sont représentés par les formules $R_{y,x} = R \pm \Delta R\exp(-t/\tau_n)$, R_y correspondant au signe positif. Evidemment, ce modèle ne s'applique qu'au cas $\Delta R \ll R$. De plus, ce modèle se limite aux petits angles de contact $\theta_{eq} < 90°$.

Ces limitations ont été surmontées dans une approche numérique en 3D [17], qui peut être utilisée pour modéliser la forme arbitraire initiale de la ligne triple (fig. 6.4).

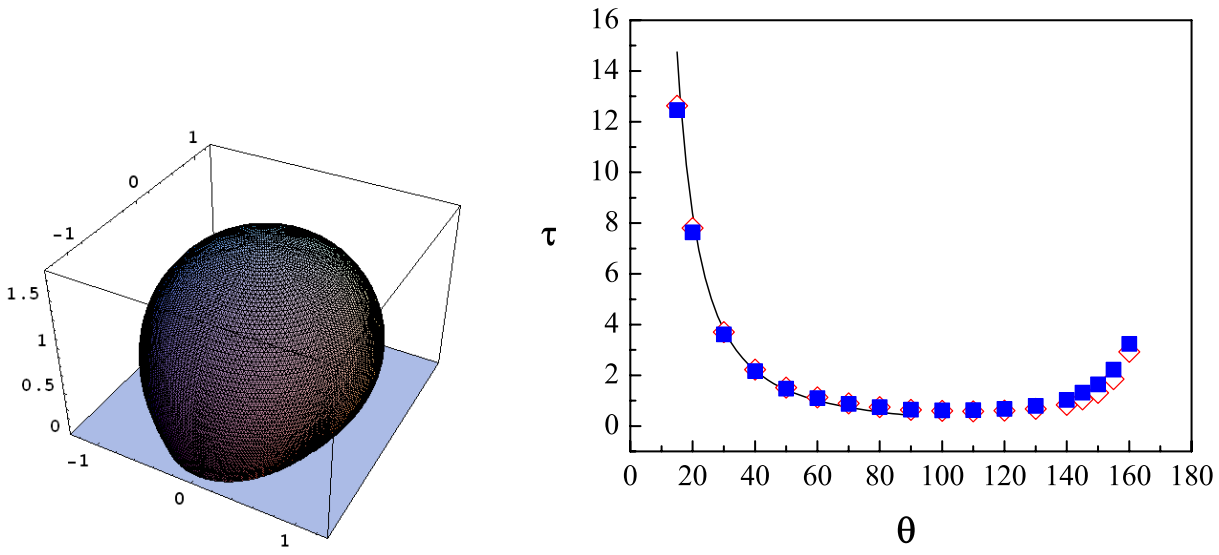

(a) (b)

FIGURE 6.4: Relaxation des gouttes ovales en 3D [17]. (a) Exemple de forme d'une goutte à surface minimale et à ligne de contact elliptique avec $\Delta R = 0,2R$, calculée pour $\theta_{eq} = 120°$ et le volume $V = 5,44R^3$. (b) Temps de relaxation pour une goutte ovale en unités τ_0 en fonction de l'angle de contact d'équilibre θ_{eq} pour $\Delta R = 0,03R$: les carrés et les losanges vides correspondent aux fits exponentiels des résultats numériques obtenus respectivement pour $R_x(t)$ et $R_y(t)$. La ligne solide est τ_n donné par l'éq. (6.14) pour $\theta_{eq} < 90°$.

6.5 Mouvement lent d'un fluide le long d'un mur vertical hétérogène

Dans cette section nous nous concentrons sur la géométrie de la plaque Wilhelmy, fig. 6.5. La plaque verticale hétérogène peut être déplacée avec une vitesse constante u ($u > 0$ pour faire avancer la ligne de contact). La force F exercée à la plaque due à la présence de la ligne mobile de contact peut être mesurée avec précision [24]. On suppose que l'interface liquide-gaz peut être décrite par la fonction $z = f(x, y, t)$ où t est le temps. La position de la ligne de contact est alors donnée par sa hauteur $h = h(y, t)$ tel que $h(y) = f(x = 0, y)$. Dorénavant, nous omettrons l'argument t. Pour que l'énergie du fluide soit finie, nous supposons que f est périodique le long de l'axe y et de période $2L$, période qui pourra au besoin tendre vers l'infini. Suivant [34, 41], les défauts extérieurs sont modélisés par la variation spatiale des tensions de surface σ_{VS} et σ_{LS} le long de la plaque, ce qui est équivalent à poser $c = c(y, z)$. L'énergie de surface U_1 par période est alors décrite par l'expression

$$U_1 = \frac{\sigma}{2L}\int_0^{\infty} \mathrm{d}x \int_{-L}^{L} \left(\sqrt{1+|\nabla f|^2} - 1\right) \mathrm{d}y - \frac{\sigma}{2L}\int_{-L}^{L} \mathrm{d}y \int_0^{h(y,t)} c(y,z)\,\mathrm{d}z, \tag{6.15}$$

tandis que l'énergie gravitationnnelle est donnée par l'expression

$$U_2 = \frac{\rho g}{2L}\int_0^{\infty} \mathrm{d}x \int_{-L}^{L} \mathrm{d}y \int_0^{f} z\,\mathrm{d}z = \frac{\rho g}{4L}\int_0^{\infty} \mathrm{d}x \int_{-L}^{L} f^2 \mathrm{d}y, \tag{6.16}$$

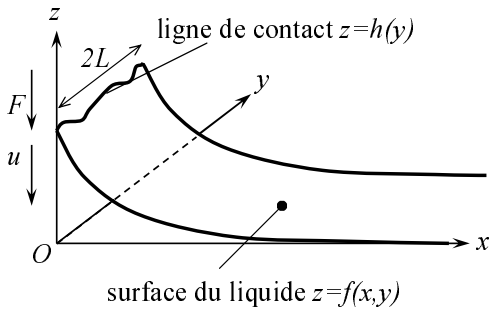

FIGURE 6.5: Schéma de l'expérience avec la plaque de Wilhelmy. La plaque que l'on peut bouger dans la direction verticale avec la vitesse u se situe dans le plan yOz. Les directions positives pour u et pour la force F agissant sur la plaque sont aussi indiquées.

où ρ est la densité du liquide et g est l'accélération de pesanteur. Pour réaliser une approche analytique, on suppose

$$|\nabla f| \ll 1. \tag{6.17}$$

U s'écrit alors

$$U = \frac{\sigma}{4L}\int_0^\infty \mathrm{d}x \int_{-L}^{L} \left(|\nabla f|^2 + f^2/l_c^2\right) \mathrm{d}y - \frac{\sigma}{2L}\int_{-L}^{L} \mathrm{d}y \int_0^{h(y,t)} c(y,z)\,\mathrm{d}z, \tag{6.18}$$

où $l_c = \sqrt{\sigma/\rho g}$ est la longueur capillaire. La minimisation de l'énergie potentielle U du liquide par rapport à f résulte [29] en l'équation suivante :

$$\frac{\partial^2 f}{\partial x^2} + \frac{\partial^2 f}{\partial y^2} = \frac{f}{l_c^2}. \tag{6.19}$$

Elle peut être résolue en séparant les variables, en employant la condition aux limites $f(x \to \infty) = 0$ et en utilisant le fait que la fonction $f(x,y)$ est bornée lorsque $y \to \pm\infty$, ce qui implique

$$f = \frac{1}{2L}\sum_{n=-\infty}^{\infty} \exp\left(-x\sqrt{l_c^{-2} + \pi^2 n^2/L^2}\right) \int_{-L}^{L} \mathrm{d}y' h(y') \cos\frac{\pi n(y-y')}{L}. \tag{6.20}$$

Sous la condition (6.17), l'angle dynamique de contact θ vérifie

$$\cos\theta \simeq -\partial f/\partial x|_{x=0}, \tag{6.21}$$

et

$$v_n = (\dot{h} + u)\left[1 + \left(\frac{\partial h}{\partial y}\right)^2\right]^{-1/2} \simeq \dot{h} + u. \tag{6.22}$$

En reportant les trois dernières équations dans (6.12), on obtient l'équation décrivant le mouvement de la ligne triple

$$\dot{h}(y) + u = \frac{\sigma}{\xi}\left\{c[y, h(y) + ut] - \right.$$
$$\left.\frac{1}{2L}\sum_{n=-\infty}^{\infty} \sqrt{l_c^{-2} + \pi^2 n^2/L^2} \int_{-L}^{L} \mathrm{d}y' h(y') \cos\frac{\pi n(y-y')}{L}\right\}. \tag{6.23}$$

Une forme plus générale (ne se limitant pas aux défauts périodiques) peut être obtenue en prenant sa valeur limite lorsque $L \to \infty$:

$$\dot{h}(y) + u = \frac{\sigma}{\xi}\Bigg\{c(y, h(y) + ut) - \frac{1}{\pi}\int_0^\infty \mathrm{d}p \int_{-\infty}^{\infty} \mathrm{d}y' h(y') \cos[p(y - y')]\sqrt{l_c^{-2} + p^2}\Bigg\}. \tag{6.24}$$

Une équation sous une forme comparable a été déjà été écrite [19]. Cependant, l'ordre d'intégration a été inversé, ce qui a eu pour conséquence une expression mathématiquement insoluble.

On peut facilement obtenir une version plus simple de l'éq. (6.24) en développant $h(y')$ autour de $h(y)$ suivant une série de Taylor :

$$\dot{h} + u = \frac{\sigma}{\xi}\left[c(y, h + ut) - \frac{h}{l_c} + \frac{l_c}{2}\frac{\partial^2 h}{\partial y^2}\right]. \tag{6.25}$$

Nous notons que cette autre simplification est entièrement conforme à l'hypothèse initiale (6.17).

Une version de l'éq. (6.24) dérivée en négligeant la gravité (ce qui correspond au cas où $l_c \to \infty$) a permis de parler d'élasticité effective de la ligne triple et a été discutée à de nombreuses reprises depuis l'article de la revue [8]. L'équation de mouvement sous la forme (6.25) montre clairement pourquoi cette simplification entraîne une erreur du calcul de la déformation de la ligne triple. Quand l'influence de la pesanteur tend vers zéro, le terme décrivant la déformation devient dominant. En d'autres termes, l'influence de la pesanteur sur la déformation de la ligne de contact est importante même dans la limite des grandes longueurs capillaires.

6.6 Force nécessaire au déplacement de la ligne triple

D'une façon générale, pour faire bouger la ligne triple, on ne peut pas appliquer une force directement à la ligne même. La seule exception est probablement le mouvement d'une goutte sessile sur un solide avec un gradient régulier de mouillabilité. Ce cas spécial ne sera pas considéré ici. Dans le cas plus courant de la mouillabilité moyenne homogène, la ligne de contact peut être déplacée en exerçant une force sur l'ensemble du liquide ou en déplaçant le solide dans les expériences de la balance de Wilhelmy, où la force peut être mesurée.

La force additionnelle F (par unité de largeur de la plaque) qui agit sur la plaque de Wilhelmy (fig. 6.5) apparaît grâce à la présence de la ligne de contact. Elle se compose de deux parties [19] : la contribution des tensions d'interface qui agissent dans des directions opposées (cf. fig. 5.6) et la force de "frottement" due à la dissipation d'énergie sur la ligne triple,

$$F = \frac{1}{2L}\int_{-L}^{L} \mathrm{d}y \left\{\sigma_{LS} - \sigma_{VS} + \xi\left[\dot{h}(y) + u\right]\right\}. \tag{6.26}$$

En y utilisant l'éq. (6.12), on obtient finalement l'expression

$$F = -\frac{\sigma}{2L}\int_{-L}^{L} \cos\theta(y)\,\mathrm{d}y, \tag{6.27}$$

l'expression qui signifie que la force en unités σ peut être obtenue en effectuant la moyenne le long de la ligne de contact du cosinus de l'angle dynamique. Cette force peut être mesurée directement en utilisant les techniques expérimentales spéciales qui permettent de la séparer du poids de la plaque [24].

6.7 Un problème simple : celui du défaut linéaire

Divisons h en deux parties. La première

$$h_0 = \frac{1}{2L}\int_{-L}^{L} h(y)\,\mathrm{d}y \tag{6.28}$$

est la hauteur moyenne de l'élévation de la ligne. La deuxième partie, $h_1(y) = h(y) - h_0$ sera appelée par la suite "déformation de la ligne triple". En intégrant l'éq. (6.23) sur la variable y on obtient pour h_0 une équation de la forme

$$\dot{h}_0 + u = -\frac{\sigma}{\xi}(h_0/l_c - c_0), \quad c_0 = \frac{1}{2L}\int_{-L}^{L} c(y, h_1(y) + h_0)\,\mathrm{d}y, \tag{6.29}$$

où c_0 est la moyenne de c le long de la ligne triple. L'équation associée à h_1 s'obtient en soustrayant l'éq. (6.29) de l'éq. (6.24).

$$\dot{h}_1(y) = \frac{\sigma}{\xi}\Bigg\{c_1(y, h_1(y) + h_0) - \frac{1}{\pi}\int_0^{\infty}\mathrm{d}p\int_{-\infty}^{\infty}\mathrm{d}y' h_1(y')\cos[p(y-y')]\sqrt{l_c^{-2}+p^2}\Bigg\}. \tag{6.30}$$

L'équation (6.30) a la même forme que l'éq. (6.24) où c est remplacé par $c_1 = c(y, h_1 + h_0) - c_0$.

La solution de ces équations peut être illustrée sur l'exemple d'une montée capillaire le long d'un mur immobile ($u = 0$) comportant un défaut unique dont la nature ne varie pas en fonction de la hauteur de la l'élévation de la ligne. La fonction c ne dépend pas dans ce cas de z :

$$c(y) = \begin{cases} c_d, & |y| \le w, \\ c_s, & |y| > w, \end{cases} \tag{6.31}$$

où $c_d, c_s \le 1$ et w sont constants. L'équation (6.30) devient donc linéaire et peut être résolue analytiquement notamment par la transformée de Fourier. Nous désignerons les transformées de $h_1(y)$ et $c_1(y)$ par

$$\tilde{h}_1 = \tilde{h}_1(k) = \int_{-\infty}^{\infty} h_1(y)\exp(-iky)\,\mathrm{d}y. \tag{6.32}$$

et $\tilde{c}_1$ respectivement. L'équation associée à h_1 se simplifie dans l'espace de Fourier. En se servant du théorème de convolution [20], on obtient

$$\dot{\tilde{h}}_1 = \frac{\sigma}{\xi}\left(\tilde{c}_1 - \tilde{h}_1\sqrt{l_c^{-2}+k^2}\right). \tag{6.33}$$

Considérons d'abord la solution d'équilibre ($t \to \infty$) obtenue initialement dans [34],

$$\tilde{h}_1^{eq} = \tilde{c}_1/\sqrt{l_c^{-2}+k^2}. \tag{6.34}$$

Il est évident que $c_0 \equiv c_s$ et

$$\tilde{c}_1 = \frac{2\delta c \sin kw}{k}. \tag{6.35}$$

où $\delta c = c_d - c_s$.

En utilisant les tables [4], la transformée de Fourier (6.34) peut être inversée analytiquement,

$$h_1^{eq}(y) = \delta c[A(y+w) - A(y-w)]/\pi, \tag{6.36}$$

La fonction $A(\cdot)$ s'écrit

$$A(y) = \int_0^y K_0(\frac{|y|}{l_c})\,\mathrm{d}y$$

où $K_0(\cdot)$ est la fonction de Bessel modifiée à l'ordre zéro [1]. Ce résultat correspond à la courbe en pointillés sur la fig. 6.6. Loin du défaut ($|y| \gg w$),

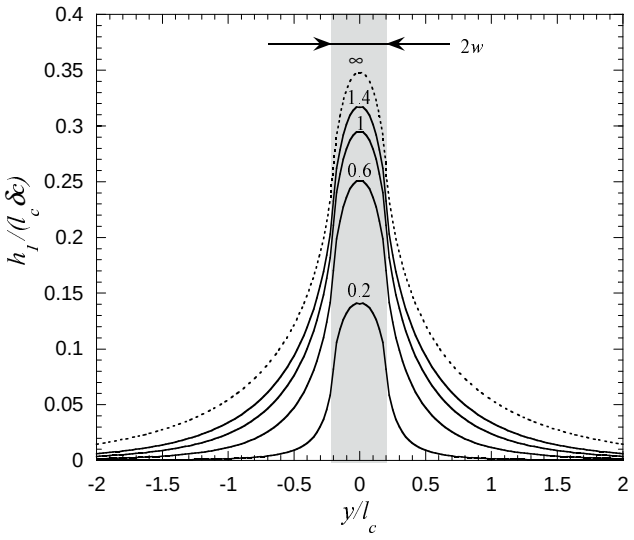

FIGURE 6.6: Evolution de la déformation $h_1(y)$ de la ligne de contact. L'aire de défaut (dont la demi-largeur est $w = 0.2l_c$) est ombrée. Les valeurs respectives des temps dans les unités τ_r sont indiquées au-dessus de chaque courbe.

$$h_1^{eq}(y) \simeq \frac{w\delta c}{\pi} A'(y) = \frac{w\delta c}{\pi} K_0(\frac{|y|}{l_c}). \tag{6.37}$$

On reconnaît le résultat obtenu en [19]. Il conduit à la divergence logarithmique lorsque $y \to 0$,$h_1^{eq} \sim -\log|y|$, résultat propre à la théorie de "l'élasticité de la ligne triple" [8], dans laquelle une coupure pour les petites valeurs de y était nécessaire pour conserver la cohérence physique. Notre analyse montre que l'expression (6.37) n'est pas valable lorsque $y \to 0$. L'expression correcte dans ce cas s'obtient à partir de (6.36) :

$$h_1^{eq}(y) = \frac{\delta c}{\pi}[A(w) + \frac{y^2}{2}A''(w)], \tag{6.38}$$

où pour le défaut ponctuel ($w \ll l_c$), $A(w) = -w\log(w/l_c)$ et $A''(w) = -w^{-1}$. Le comportement de $h_1^{eq}(y)$ est alors physiquement correct.

La solution dynamique peut être obtenue de la même manière en employant la condition initiale $h(t=0)=0$:

$$h_0(t) = c_s l_c[1-\exp(-t/\tau_r)], \tag{6.39}$$

$$h_1(y,t) = \delta c\left[A(w+y)+A(w-y)-D(w+y,t)-D(w-y,t)\right]/\pi, \tag{6.40}$$

où $\tau_r = \xi l_c/\sigma$ et

$$D(y,t) = \int_0^y K_0\left(\sqrt{\frac{y^2}{l_c^2}+\frac{t^2}{\tau_r^2}}\right)\mathrm{d}y$$

L'évolution temporelle de $h_1(y)$ est explicitée sur la fig. 6.6. Ces courbes peuvent être comparées à celles obtenues expérimentalement dans les articles [25, 23, 32]. Le mouvement de la ligne de contact y fut étudié en présence d'un défaut unique. La comparaison montre un bon accord qualitatif. Malheureusement, les résultats ne peuvent pas être comparés quantitativement puisque dans chacun de ces articles plusieurs paramètres intervenant dans l'éq. (6.40) sont manquants.

6.8 Effet collectif de défauts sur la dynamique de la ligne triple

6.8.1 Approche générale

Le mouvement des frontières séparant des phases différentes dans un environnement aléatoire demeure un problème d'intérêt général. Beaucoup d'attention a été prêtée à la "transition de dépiégeage" associée au comportement critique dans des systèmes différents : invasion liquide dans les médias poreux, mouvement des bords de domaines ferromagnétiques, mouvement des vortex de flux dans les supraconducteurs du type II, dynamique des fissures... [3, 13]. La théorie de la transition de dépiégeage est basée sur l'analyse de l'équation suivante donnant la position d'interface h :

$$\frac{\partial h}{\partial t} = F+\zeta(h)+G[h], \tag{6.41}$$

où F est la force imposée de façon extérieure, ζ est le bruit dû au caractère aléatoire des médias et $G[\cdot]$ est un opérateur convenable. Lorsque F est voisin du seuil de dépiégeage F_c (pour lequel l'interface commence à se déplacer), cette approche a généralement pour conséquence une loi de puissance pour la vitesse moyenne d'interface u

$$u \sim (F-F_c)^\beta, \tag{6.42}$$

où l'exposant β est universel. L'origine de cette dépendance se situe dans la dynamique particulière d'interface près du seuil de transition, notamment une succession aléatoire des avalanches d'événements locaux de dépiégeage. Quand $F \gg F_c$, la loi conventionnelle de mobilité

$$u \sim F \tag{6.43}$$

devient valide.

L'approche générale des phénomènes de dépiégeage d'interface est fréquemment appliquée au dépiégeage de la ligne triple [12, 40, 39, 6]. Cependant le désaccord entre la théorie et les

données expérimentales sur le mouvement de ligne de contact est notable. Premièrement, selon les études théoriques $\beta < 1$ (voir le [12, 6]), alors que $\beta \geq 1$ est obtenu expérimentalement [40, 24]. Deuxièmement, le régime linéaire (6.43) n'était jamais obtenu [24]. En suivant l'article [27], dans ce chapitre nous proposons un cadre approprié pour expliquer les résultats.

La force étudiée dans le chapitre 6.6 est la seule qui puisse servir de force externe F intervenant dans l'éq. (6.41). En comparant les équations (6.25) et (6.41), on peut constater la différence entre le dépiégeage de l'interface et celui de la ligne de contact. Pour le dépiégeage de l'interface, la force entre directement dans l'équation de mouvement. La force peut être contrôlée ou imposée. Elle peut prendre une valeur arbitraire. Pour le dépiégeage de la ligne de contact, la force externe n'entre pas directement dans les équations du mouvement (6.24, 6.25). Elle est alors difficilement contrôlable. Cependant, elle peut être mesurée et calculée en utilisant l'éq. (6.27), où la force (par unité de largeur de la plaque) est limitée par la valeur de tension superficielle. Ce fait peut expliquer la non-linéarité $F(u)$ observée dans [24] pour de grandes vitesses. Cependant, le modèle basé sur les éqs. (6.24, 6.25) ne peut pas mettre en évidence cette saturation. En raison des conditions (6.17, 6.21), $|F| \ll \sigma$ a été implicitement supposé lors de l'utilisation des éqs. (6.24, 6.25).

6.8.2 Application aux défauts périodiques

Nous considérons ci-dessous des défauts périodiques dans les directions y et z. Prenons l'exemple des taches rondes de rayon r présentées sur la fig. 6.7a. À l'intérieur des taches, $\theta_{eq} = \theta_d$, pour le reste de la plaque on a $\theta_{eq} = \theta_s$.

En raison de la non-linéarité du terme c, l'éq. (6.23) semble être difficile à résoudre numériquement. Cependant, l'application de l'algorithme numérique FFT (Fast Fourier Transform) [35] facilite beaucoup le calcul.

Nous sommes intéressés par les solutions doublement périodiques relativement à y et à t. La périodicité temporelle est envisagée pour éviter la dépendance de la position initiale de la surface liquide. Les moyennes temporelles sont notées par des crochets, par exemple la force moyenne a pour valeur

$$\langle F \rangle = \frac{1}{P} \int_0^P F(t)\, \mathrm{d}t, \tag{6.44}$$

où $P = 2L/|u|$ est la période temporelle. Ainsi, $\langle v_n \rangle = u$ est la vitesse moyenne de la ligne de contact. Le comportement périodique en temps apparaît après que la ligne de contact ait passé plusieurs premières rangées de défauts.

Un exemple de solution doublement périodique est montré sur la fig. 6.7a. Les positions de la ligne de contact sont présentées pour des intervalles égaux de temps, la vitesse locale peut donc être évaluée à partir de la densité des courbes obtenues. On voit que lorsque la ligne de contact rencontre une ligne des défauts, elle ralentit en laissant la surface liquide accumuler de l'énergie. Durant cette étape, la différence entre les angles dynamique et d'équilibre du contact augmente (étape de l'accrochage, "stick" en anglais). L'étape de glissement ("slip" en anglais) arrive ensuite, et la ligne de contact accélère. La différence entre les vitesses moyennes de ces deux phases peut être très grande près du seuil d'accrochage, voir la courbe solide (fig. 6.7b) associée à $u = 0.01\sigma/\xi$. La partie la plus abrupte correspond au glissement. Cette suite d'accélérations et de décélérations de la ligne de contact est un effet collectif associé au mouvement de ligne de contact en présence des défauts.

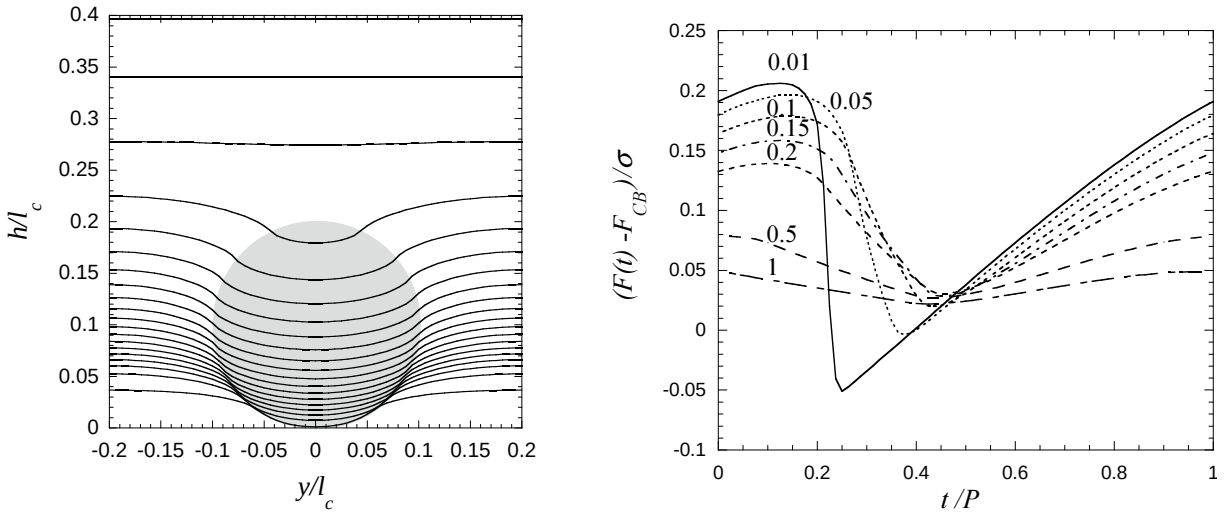

(a) (b)

FIGURE 6.7: Solution périodique spatio-temporelle de l'éq. (6.23) calculée pour $2L/l_c = 0,4$, $r/l_c = 0,1$, $\theta_s = 70°$ et $\theta_d = 110°$. (a) 20 positions de la ligne de contact avec les intervalles de temps égaux à $0,2\xi l_c/\sigma$ sur la maille élémentaire de la structure périodique des défauts (l'aire d'un défaut est ombré) pour $u = 0,1\sigma/\xi$; ce graphe correspond à la période temporelle $P = 4\xi l_c/\sigma$. L'image complète du mouvement de ligne de contact peut être obtenue en prolongeant périodiquement cette figure dans des directions verticale et horizontale. (b) Variations périodiques de la force agissant sur la plaque de Wilhelmy pendant son mouvement de haut en bas. Le paramètre des courbes a pour valeur u dans des unités de σ/ξ.

La force donnée par l'éq. (6.27) peut être calculée en utilisant l'éq. (6.21) pour chacune des courbes $h(y)$ comme celle de la fig. 6.7a. Les courbes $F(t)$ sont présentées sur la fig. 6.7b où F est décomptée à partir du niveau de référence

$$F_{CB} = \xi u - \sigma \cos\theta_{CB}, \tag{6.45}$$

où $\cos\theta_{CB} = \varepsilon^2 \cos\theta_d + (1-\varepsilon^2)\cos\theta_s$ est la valeur moyenne de l'angle statique de contact (dit de Cassie-Baxter), $\varepsilon^2 = \pi(r/2L)^2$ est la densité de défauts. F_{CB} correspond à une force induite par un solide homogène ayant la valeur de l'angle de contact d'équilibre égale à θ_{CB}. La différence $F - F_{CB}$ caractérise donc l'influence de l'accrochage sur les défauts. La dépendance $\langle F\rangle - F_{CB}$ de u (inversée pour la compatibilité avec Fig. 6.8b) est présentée en Fig. 6.8a pour différentes densités de défauts qui correspondent à différentes valeurs de ε^2. Les branches de recul ($u < 0$) et d'avancée ($u > 0$) sont présentées. $\langle F\rangle$ dévie de F_{CB} suivant l'augmentation de la densité croissante des défauts (distance décroissante entre les défauts) qui peut être expliquée par un accrochage de plus en plus important. En rappelant que le cosinus moyen de l'angle de contact est $\langle F\rangle/\sigma$, on constate que l'écart des angles de contact statiques d'avancée et de recul (qui correspondent aux valeurs de $\langle F\rangle/\sigma$ pour $u \to \pm 0$) devient égal à la valeur de Cassie-Baxter avec accrochage croissant.

Lorsque nous étudions l'accrochage pour des défauts périodiques, les exposants propres au comportement aléatoire ne peuvent être trouvés. Il est cependant intéressant d'étudier la dépendance de $\langle F\rangle$ en fonction de u pour la comparer au comportement décrit par les éqs. (6.42, 6.43).

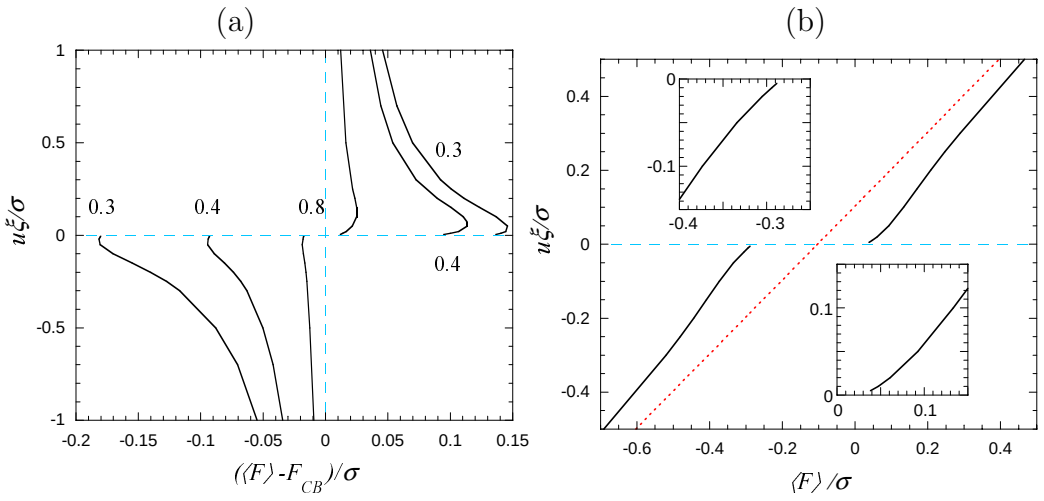

FIGURE 6.8: (a) Ecart $(\langle F\rangle - F_{CB})$ en fonction de u calculé pour différentes distances entre les centres des défauts $2L$ (montrés comme paramètres de courbes dans les unités l_c). (b) Courbe $u(\langle F\rangle)$ pour $2L/l_c = 0.3$. La dépendance $u(F_{CB})$ est présentée par la ligne en pointillés. Les parties des courbes au voisinage du point de $u = 0$ sont agrandis dans des fenêtres. Les paramètres sont les mêmes que pour Fig. 6.7.

Une fonction $u(\langle F\rangle)$ inverse est présentée sur la fig. 6.8b. En absence d'études expérimentales avec des défauts périodiques, cette courbe peut être comparée avec le résultat [24] obtenu pour des défauts aléatoires. Pour $|u|$ petit, le signe de la courbure est le même que celui obtenu expérimentalement et il correspond à $\beta > 1$ dans l'éq. (6.42). Cette comparaison suggère que le comportement de $\beta > 1$ est dû à l'accrochage collectif plutôt qu'au caractère aléatoire. La valeur de F_c est définie par l'angle statique de contact (d'avancée ou de recul selon la direction du mouvement). Cependant, l'augmentation linéaire de $\langle F\rangle(u)$ pour de grandes valeurs de $|u|$ qui ressemble au comportement de l'éq. (6.43) est simplement une conséquence de l'approximation (6.17) discutée ci-dessus. En réalité, $u(\langle F\rangle)$ est fortement non-linéaire pour de grandes valeurs de $|u|$ et devrait avoir des graphes à asymptotes verticales à $\langle F\rangle = \pm\sigma$.

La pente décroissante de la courbe $u(F)$ au voisinage de F_c (qui est due à l'influence des défauts) peut expliquer la relaxation extrêmement lente observée pendant la coalescence des gouttes sessiles (cf. chapitre 6.2 ci-dessus). Dans ce cas une force très petite est imposée par la tension superficielle. Puisque le coefficient effectif de dissipation a été extrait comme l'inverse de la pente de la courbe $u(F)$, il semble être très grand tandis que la valeur réelle de ξ peut être beaucoup plus petite.

6.9 Influence de l'inertie sur la dynamique de la ligne triple

Dans ce chapitre nous montrons comment l'influence de l'inertie du liquide sur le mouvement lent de la ligne triple peut être prise en compte dans le cadre de notre théorie où toute dissipation dans le liquide est supposée être concentrée sur la ligne triple. Nous construisons ce modèle surtout pour pouvoir décrire le couplage du mouvement rapide du fluide (ex : oscillation de sa surface, cf. chapitre 6.2 ci-dessus où $Re \approx 100$) avec un mouvement plus lent de la ligne triple ($Ca \approx 10^{-3}$ dans l'expérience du chapitre 6.2). Les oscillations d'une goutte d'eau couplées au

mouvement de ligne de contact ont été étudiés expérimentalement récemment [31]. Le rapport Re/Ca peut être encore plus grand pour les fluides cryogéniques qui sont industriellement importants [11] (oscillations du carburant de fusée) en raison de la plus faible tension superficielle. Pendant leur étalement, les oscillations des gouttes suivent souvent leur impact avec le solide [38].

En fait, plusieurs tentatives ont été entreprises pour décrire les effets inertiels pendant le mouvement de la ligne de contact [7, 11, 36, 18]. La plupart des modèles supposent le fluide non-visqueux et donc l'absence d'anomalie sur la ligne triple. D'autres modèles sont trop compliqués pour pouvoir décrire la ligne triple déformée initialement ou par des défauts.

La géométrie considérée est celle de la plaque Wilhelmy montrée sur la fig. 6.5. Le repère sera néanmoins différent : le zéro de z est placé au bas du liquide dont la profondeur d sera l'un des paramètres du problème. La surface et la ligne triple sont alors décrites respectivement par les fonctions $z = \hat{f}(x, y) \equiv d + f(x, y)$ et $z = \hat{h}(y) \equiv d + h(y)$.

En suivant l'article [30], nous allons utiliser l'approximation "en eau peu profonde". Bien qu'il soit *a priori* évident que notre modèle néglige la dissipation visqueuse dans le volume liquide, elle peut être importante dans les couches minces. Notre but est d'expliquer comment une telle approche peut être appliquée en utilisant l'avantage d'une telle approximation pour obtenir des solutions analytiques. L'approche peut être facilement généralisée en utilisant la formulation potentielle plus appropriée pour le traitement numérique.

6.9.1 Dérivation des équations de mouvement du liquide

Dans l'approximation en eau peu profonde, l'énergie cinétique du liquide s'écrit

$$W = \frac{1}{2L}\int_0^\infty \mathrm{d}x \int_{-L}^{L} \frac{\rho \hat{f}\,|\vec{v}|^2}{2}\mathrm{d}y, \tag{6.46}$$

où $\vec{v} = (v_x, v_y)$ est le champ de vitesses dans le liquide. En utilisant comme précédemment l'hypothèse (6.17), nous obtenons alors le lagrangien du système $\mathcal{L} = W - U$ où U est défini en (6.18). La variation de l'action (6.7) est soumise à la liaison de la conservation de la masse

$$\frac{\partial \hat{f}}{\partial t} + \nabla \cdot (\hat{f}\vec{v}) = 0 \tag{6.47}$$

et est soumise à la condition aux limites

$$v_x|_{x=0} = 0. \tag{6.48}$$

Puisque la dissipation volumique visqueuse est absente du modèle, la condition aux limites sur la ligne triple est uniquement modifiée par l'introduction de la fonction de dissipation (6.6). Le principe de l'action stationnaire qui peut donc être appliqué dans le volume du fluide permet d'obtenir [30] l'équation donnant la vitesse du liquide :

$$\frac{\partial(\rho\hat{f}\vec{v})}{\partial t} + \vec{v}\,\mathrm{div}(\rho\hat{f}\vec{v}) + \rho\hat{f}(\vec{v}\cdot\nabla)\vec{v} + \rho g\hat{f}\nabla\hat{f} - \sigma\hat{f}\nabla(\Delta\hat{f}) = 0. \tag{6.49}$$

De ce fait, la variation du lagrangien prend la forme

$$\delta\mathcal{L} = \frac{\sigma}{2L}\int_{-L}^{L}\left[\left.\frac{\partial\hat{f}}{\partial x}\right|_{x=0} + \hat{c}(y,\hat{h})\right]\delta\hat{h}\,\mathrm{d}y, \tag{6.50}$$

où $\hat{c}(y,z) \equiv c(y,z-d)$ est la fonction (5.8) définie dans le nouveau repère. En reportant (6.50) dans l'équation de Lagrange (6.9) on obtient la condition aux limites pour l'éq. (6.49)

$$\sigma\left[\left.\frac{\partial \hat{h}}{\partial x}\right|_{x=0} + \hat{c}(y,\hat{h})\right] = \xi\left(\frac{\partial \hat{h}}{\partial t} + u\right). \tag{6.51}$$

6.9.2 Linéarisation partielle

Les conditions sont définies par (6.48, 6.51) et par

$$\hat{f}|_{x\to\infty} = d, \tag{6.52}$$

où d est la profondeur du liquide loin de la plaque supposée constante. Les conditions initiales que nous considérerons sont celles d'un liquide immobile

$$\vec{v}|_{t=0} = 0, \quad \hat{f}|_{t=0} = d. \tag{6.53}$$

Les équations du mouvement (6.47, 6.49) peuvent être linéarisées relativement à la vitesse du liquide $\vec{v}$ supposée petite. En revenant aux variables sans chapeau $f = \hat{f} - d$ et $h = \hat{h} - d$, on obtient

$$\frac{\partial f}{\partial t} + d\nabla\cdot\vec{v} = 0, \quad \rho\frac{\partial \vec{v}}{\partial t} + \rho g\nabla f - \sigma\nabla\Delta f = 0. \tag{6.54}$$

La vitesse $\vec{v}$ s'élimine de ces équations en appliquant la dérivée temporelle à la première d'entre elles, puis en soustrayant la divergence de la seconde. Le résultat s'écrit

$$\rho\frac{\partial^2 f}{\partial t^2} - \rho g d\Delta f + \sigma d\Delta^2 f = 0. \tag{6.55a}$$

Les conditions initiales et les conditions aux limites associées à l'éq. (6.55a) s'obtiennent à partir des éqs. (6.48, 6.52-6.53) et à l'aide de (6.54)

$$f|_{x\to\infty} = 0, \tag{6.55b}$$

$$\left.\frac{\partial}{\partial x}\left(\rho g f - \sigma\Delta f\right)\right|_{x=0} = 0, \tag{6.55c}$$

$$f|_{t=0} = 0, \tag{6.55d}$$

$$\left.\frac{\partial f}{\partial t}\right|_{t=0} = 0. \tag{6.55e}$$

L'équation non-linéaire (6.51) réécrite à l'aide des fonctions f, h devient

$$\frac{\partial h}{\partial t} + u = \frac{\sigma}{\xi}\left[\left.\frac{\partial f}{\partial x}\right|_{x=0} + c(y,h)\right], \tag{6.55f}$$

ce qui clôt la formulation du problème.

On note que (6.55f) coïncide exactement avec l'expression (6.12) obtenue dans l'hypothèse quasistatique.

6.9.3 Solution pour un défaut linéaire

Pour démontrer l'effet de l'inertie sur le mouvement de la ligne triple, considérons le problème du chapitre 6.7 : la montée capillaire le long d'un mur en présence d'un défaut linéaire dont la fonction c associée est définie par l'éq. (6.31). Suivant le même procédé de la résolution, découpons chacune des variables f et h en deux parties,

$$\begin{aligned} f &= f_0(x,t) + f_1(x,y,t), \\ h &= h_0(t) + h_1(y,t). \end{aligned} \tag{6.56}$$

où l'index 0 correspond comme précédemment aux variables moyennées le long de la ligne de contact. Puisque le problème est linéaire dans ce cas simple, les problèmes associés à h_0 et h_1 sont découplés et peuvent être résolus séparément.

En appliquant la transformée de Laplace

$$\bar{h}_0(s) = \int_0^\infty h_0(t)\exp(-st)\,\mathrm{d}t, \tag{6.57}$$

on obtient la solution du problème (6.55) pour $\bar{h}_0$

$$\bar{h}_0(s) = c_s\frac{\sigma}{\xi}\left[s\left(s + \tau_r^{-1}\sqrt{s\sqrt{2\tau_i}+1}\right)\right]^{-1}, \tag{6.58}$$

où $\tau_r = l_c\xi/\sigma$ est une échelle de temps caractéristique pour la relaxation quasistatique et $\tau_i = l_c/\sqrt{gd}$ est le temps caractéristique inertiel. La transformée de Laplace (6.58) peut être inversée

$$\begin{aligned} h_0(t) = c_s l_c\Bigg\{1 - \operatorname{erfc}\left(\sqrt{\frac{t}{2\tau_i}}\right) + \\ \frac{1}{2\sqrt{1+r^2}}\Bigg\{\exp\left[\frac{t}{\tau_r}\left(r+\sqrt{1+r^2}\right)\right]\operatorname{erfc}\left[\sqrt{\frac{t}{2\tau_i}}\left(r+\sqrt{1+r^2}\right)\right] - \\ \exp\left[\frac{t}{\tau_r}\left(r-\sqrt{1+r^2}\right)\right]\operatorname{erfc}\left[\sqrt{\frac{t}{2\tau_i}}\left(r-\sqrt{1+r^2}\right)\right]\Bigg\}\Bigg\}, \end{aligned} \tag{6.59}$$

où $\operatorname{erfc}(\cdot)$ est la fonction d'erreur complémentaire [1], et $r = \tau_i/\tau_r$ est un paramètre caractérisant l'importance relative de l'inertie du liquide ; r est lié au nombre de Weber qui est défini comme le rapport des termes de la tension superficielle et de l'inertie, tous les deux présents dans l'éq. (6.55a), $We = r^2$. Pour le cas limite $r \to 0$, (6.59) se réduit au résultat quasistatique (6.39). La différence entre ces deux dépendances est apparente sur la fig. 6.9a : l'inertie liquide ralentit légèrement le mouvement moyen de la ligne de contact.

La formulation du problème pour f_1 est donnée par le système (6.55) avec une condition additionnelle de disparition de sa valeur moyenne relativement à la variable y. Pour un défaut isolé, cette condition se réduit à $f_1(y \to \pm\infty) = 0$, ce qui permet l'application de la transformée de Fourier (6.32). La transformée de Laplace (6.57) peut ensuite être appliquée à $\tilde{f}_1(x,t)$. L'expression pour $\bar{h}_1$ est complexe et difficile à inverser. De ce fait, on cherche uniquement les solutions pour les petites valeurs du paramètre r, c.-à-d. lorsque la contribution des forces inertielles est faible. Sous cette condition, la solution s'écrit

$$\bar{h}_1 = \tilde{c}_1\left[s\left(\sqrt{k^2 + l_c^{-2}} + l_c^{-1}\tau_r s + B(r\tau_r s)^2\right)\right]^{-1}. \tag{6.60}$$

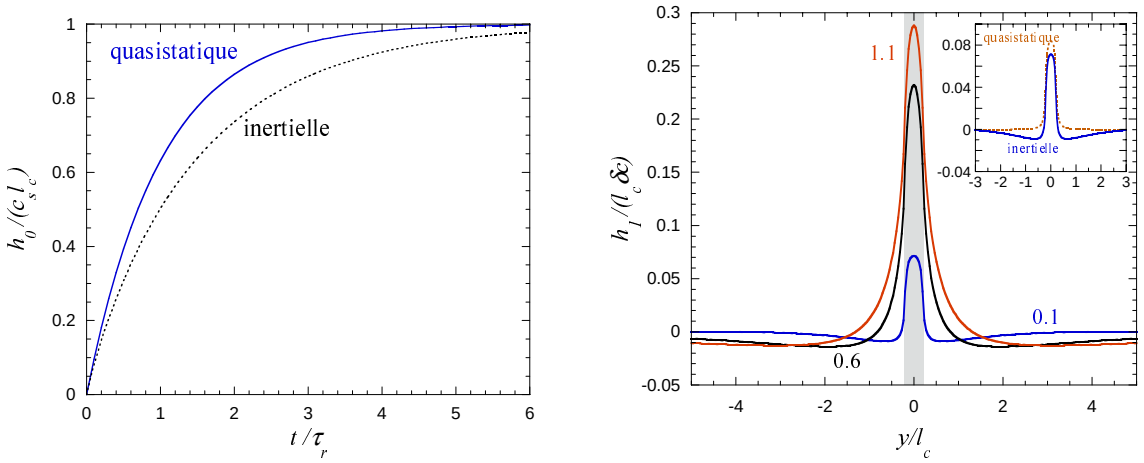

(a) (b)

FIGURE 6.9: Evolution temporelle de la hauteur moyenne h_0 de l'ascension de la ligne de contact (a) et de la déformation de la ligne triple h_1 (b) calculées pour $r = 0.5$. La loi quasistatique exponentielle (6.39) (ligne solide) est comparée au comportement inertiel hydrodynamique (6.59) (ligne en pointillés) sur la fig. (a). Figure (b) : Le paramètre des courbes est le temps t dans les unités de τ_r. L'aire du défaut (dont la demie largeur est égale à $w = 0.2l_c$) est ombrée. Dans la fenêtre, le résultat de la théorie hydrodynamique (courbe pleine) est comparé au résultat quasistatique (courbe en pointillés). Les deux courbes sont calculées pour $t = 0.1\tau_r$.

où le coefficient $B > 0$ est

$$B = \frac{k^2 + l_c^{-2}}{|k|} - \frac{k^2 + 1.5l_c^{-2}}{\sqrt{k^2 + l_c^{-2}}}. \tag{6.61}$$

Cette expression est rationnelle en s et la transformée de Laplace peut alors être inversée avec des méthodes conventionnelles :

$$\tilde{h}_1(t) = \tilde{c}_1 \left\{ \frac{1}{\sqrt{k^2 + l_c^{-2}}} + \frac{1}{B(r\tau_r)^2(s_1 - s_2)} \left[\frac{\exp(s_1 t)}{s_1} - \frac{\exp(s_2 t)}{s_2} \right] \right\}, \tag{6.62}$$

où [(i)]

$$s_{1,2} = \frac{1 \pm \sqrt{1 - 4Bl_c r^2 \sqrt{k^2 l_c^2 + 1}}}{2Bl_c r^2 \tau_r} \tag{6.63}$$

et $\tilde{c}_1$ est donné par (6.35). Pour obtenir la déformation de la ligne triple $h_1(y,t)$, nous avons besoin d'inverser la transformée de Fourier (6.62), ce qui peut être réalisé numériquement en utilisant l'algorithme FFT [35]. Le résultat est présenté sur la fig. 6.9b.

Nous retrouvons le résultat quasistatique (6.40) dans la limite $r \to 0$.

Comme dans le cas de h_0, le ralentissement inertiel se manifeste dans le cas de h_1. La fenêtre de la fig. 6.9b montre que le point le plus élevé de la ligne de contact s'élève plus lentement lorsque

(i). Notons que si $s_{1,2}$ deviennent complexes pour des petites valeurs de k, $\tilde{h}_1$ reste réel.

le mouvement hydrodynamique est pris en considération. Or les effets hydrodynamiques ne sont pas limités à un simple ralentissement. Surtout visible au début de la montée, l'effet commun de l'inertie et de la conservation de masse crée dans le profil de h_1 (fig. 6.9b) deux creux dont le fluide coule et forme une bosse entre eux. Au cours de la montée, ces cavités deviennent de moins en moins profondes et et de plus en plus larges avant disparaître pour la forme d'équilibre de la ligne de contact.

6.10 Conclusion

Ce chapitre est consacré aux études de la dynamique de mouillage. Une théorie quasistatique phénoménologique est développée. Elle est basée sur l'hypothèse que toute la dissipation dans le fluide peut être considérée comme si elle avait lieu uniquement sur la ligne triple. Il est montré que cette hypothèse est équivalente à l'équation (6.12) qui est aussi le résultat de plusieurs autres modèles théoriques et études expérimentales. D'autres résultats préliminaires [10] montrent un bon accord entre l'expérience et notre modèle.

Des expériences sur la coalescence des gouttes sessiles lèvent plusieurs interrogations dont l'une concerne la lenteur de la relaxation de la ligne triple vers sa position finale. Nous expliquons cette lenteur par l'influence des défauts du substrat ; l'influence devient marquante surtout près du seuil de piégeage de la ligne triple. Seulement le cas des défauts périodiques est étudié. Cependant, l'approche est bien adaptée pour considérer les transitions de piégeage ou de dépiégeage en présence de défauts aléatoires, ce qui pourrait être réalisé ultérieurement.

Une autre question relevant de l'influence du mouvement rapide de la surface des gouttes sur la cinétique de la ligne triple découle des expériences. Nous proposons une approche permettant de décrire le couplage des mouvements rapides de la surface d'une goutte avec les mouvements lents dissipatifs de sa ligne de contact. Pour obtenir des solutions analytiques dans la géométrie de la montée capillaire, l'approximation en eau peu profonde a été utilisée. Néanmoins, la méthodologie proposée s'applique également dans le cas plus général. Une approche numérique basée sur l'écoulement potentiel du liquide sera appliquée dans le futur pour décrire les oscillations des gouttes sessiles d'une forme complexe.

6.11 Bibliographie

[1] Abramovitz, M., & Stegun, I. A. *Handbook of Mathematical Functions*. Dover, New York, 1972.

[2] Andrieu, C., Beysens, D. A., Nikolayev, V. S., & Pomeau, Y. Coalescence of sessile drops. *J. Fluid Mech.* **453** 427 – 438 (2002). (voir page 205 de cette thèse).

[3] Barabási, A.-L., & Stanley, H. *Fractal Concepts in Surface Growth*. Cambridge University Press, Cambridge, 1995.

[4] Bateman, H., & Erdélyi, A. *Tables of Integral transforms*, vol. 1. Mc Graw Hill, New York, 1954.

[5] Blake, T. D., & Haynes, J. M. Kinetics of liquid/liquid displacement. *J. Colloid Interface Sci.* **30** 421 – 423 (1969).

[6] Chauve, P., Doussal, P. L., & Wiese, K. Renormalization of pinned elastic systems : How does it work beyond one loop ? *Phys. Rev. Lett.* **86**(9) 1785 – 1788 (2001).

[7] Cox, R. G. Inertial and viscous effects on dynamic contact angles. *J. Fluid Mech.* **357** 249 –278 (1998).

[8] de Gennes, P.-G. Wetting : statics and dynamics. *Rev. Mod. Phys.* **57** 827 – 863 (1985).

[9] de Ruijter, M. J., de Coninck, J., & Oshanin, G. Droplet spreading : partial wetting regime revisited. *Langmuir* **15** 2209 – 2216 (1999).

[10] Delon, G., Fermigier, M., & Nikolayev, V. S. unpublished, 2005.

[11] Dreyer, M., Delgado, A., & Path, H.-J. Capillary rise of liquid between parallel plates under microgravity. *J. Colloid Interface Sci.* **163**(1) 158 – 168 (1994).

[12] Ertaş, D., & Kardar, M. Critical dynamics of contact line depinning. *Phys. Rev. E* **49**(4) R2532 – R2535 (1994).

[13] Fisher, D. S. Collective transport in random media : from superconductors to earthquakes. *Phys. Rep.* **301** 113 – 150 (1998).

[14] Gouin, H. The wetting problem of fluids on solid surfaces. Part 1 : the dynamics of contact lines and Part 2 : the contact angle hysteresis. *Continuum Mechanics and Thermodynamics* **15** 581 – 611 (2003).

[15] Huh, C., & Mason, S. G. The steady movement of a liquid meniscus in a capillary tube. *J. Fluid Mech.* **81** 401– 419 (1977).

[16] Huh, C., & Scriven, L. E. Hydrodynamic model of steady movement of a solid/liquid/fluid contact line. *J. Colloid Interf. Sci.* **35** 85 – 101 (1971).

[17] Iliev, S., Pesheva, N., & Nikolayev, V. S. Quasi-static relaxation of arbitrarily shaped sessile drops. *Phys. Rev. E* **72** 011606 (2005). (voir page 266 de cette thèse).

[18] Joanny, J. F. *Le mouillage : quelques problèmes statiques et dynamiques*. PhD thesis, Université Pierre et Marie Curie Paris VI, 1985.

[19] Joanny, J. F., & Robbins, M. O. Motion of a contact line on a heterogeneous surface. *J. Chem. Phys.* **92** 3206 – 3212 (1990).

[20] Korn, G., & Korn, T. *Mathematical handbook for scientists and engineers*. Dover, New York, 2000.

[21] Landau, L. D., & Lifshitz, E. M. *Mechanics*. Elsevier Science, Burlington, 2003.

[22] Mahadevan, L., & Pomeau, Y. Rolling droplets. *Phys. Fluids* **11** 2449 – 2453 (1999).

[23] Marsh, J. M., & Cazabat, A.-M. Dynamics of contact line depinning from a single defect. *Phys. Rev. Lett.* **71** 2433 – 2436 (1993).

[24] Moulinet, S., Guthmann, C., & Rolley, E. Dissipation in the dynamics of a moving contact line : effect of the substrate disorder. *European Phys. J. B* **37** 127 – 136 (2004).

[25] Nadkarni, G. D., & Garoff, S. An investigation of microscopic aspects of contact angle hysteresis : pinning of the contact line on a single defect. *Europhysics Lett.* **20** 523 – 528 (1992).

[26] Narhe, R., Beysens, D., & Nikolayev, V. Contact line dynamics in drop coalescence and spreading. *Langmuir* **20** 1213 – 1221 (2004). (voir page 248 de cette thèse).

[27] Nikolayev, V. S. Dynamics and depinning of the triple contact line in the presence of periodic surface defects. *J. Phys. Cond. Matt.* **17**(13) 2111 – 2119 (2005). (voir page 257 de cette thèse).

[28] Nikolayev, V. S., & Beysens, D. A. Relaxation of non-spherical sessile drops towards equilibrium. *Phys. Rev. E* **65**(4) 046135 (2002). (voir page 217 de cette thèse).

[29] Nikolayev, V. S., & Beysens, D. A. Equation of motion of the triple contact line along an inhomogeneous surface. *Europhysics Lett.* **64**(6) 763 – 768 (2003). (voir page 225 de cette thèse).

[30] Nikolayev, V. S., Gavrilyuk, S. L., & Gouin, H. Influence of the fluid inertia on the moving deformed triple contact line. Soumis, 2005.

[31] Noblin, X., Buguin, A., & Brochard-Wyart, F. Vibrated sessile drops : transition between pinned and mobile contact line oscillations. *European Phys. J. E* **14** 395 – 404 (2004).

[32] Paterson, A., Fermigier, M., Jenffer, P., & Limat, L. Wetting on heterogeneous surfaces : experiments in an imperfect Hele-Shaw cell. *Phys. Rev. E* **51** 1291– 1298 (1995).

[33] Pomeau, Y. Representation of the moving contact line in the equations of fluid mechanics. *Comptes Rendus Acad. Sci., Serie IIb* **238** 411 – 416 (2000).

[34] Pomeau, Y., & Vannimenus, J. Contact angle on heterogeneous surfaces : weak heterogeneities. *J. Colloid Interf. Sci.* **104**(2) 477 – 488 (1984).

[35] Press, W. H., Teukolsky, S. A., Vetterling, W. T., & Flannery, B. P. *Numerical Recipies in C*, 2nd ed. Cambridge University Press, Cambridge, 1997.

[36] Quéré, D. Inertial capillarity. *Europhysics Lett.* **39**(5) 533 – 538 (1997).

[37] Ramé, E. Moving contact line problem : state of the contact angle boundary condition. In *Encyclopedia of Surface and Colloid Science*, A. T. Hubbard, Ed. Marcel Dekker, New York, 2002.

[38] Roisman, I. V., Rioboo, R., & Tropea, C. Normal impact of a liquid drop on a dry surface : model for spreading and receding. *Proc. R. Soc. London A* **458** 1411 – 1430 (2002).

[39] Rosso, A., & Krauth, W. Origin of the roughness exponent in elastic strings at the depinning threshold. *Phys. Rev. Lett.* **87**(18) 187002 (2001).

[40] Schäffer, E., & Wong, P.-Z. Contact line dynamics near the pinning threshold : a capillary rise and fall experiment. *Phys. Rev. E* **61**(5) 5257 – 5277 (2000).

[41] Schwartz, L. W., & Garoff, S. Contact angle hysteresis on heterogeneous surfaces. *Langmuir* **1** 219 – 230 (1985).

[42] Seppecher, P. Moving contact lines in the Cahn-Hilliard theory. *Int. J. Eng. Sci.* **34** 977 – 992 (1996).

[43] Shikhmurzaev, Y. D. Spreading of droplets on solids in quasi-static regime. *Phys. Fluids* **9** 266 – 275 (1997).

7 Cinétique de la condensation atmosphérique

7.1 Un peu d'histoire

L'eau contenue dans l'atmosphère sous forme de vapeur est une ressource renouvelable qui pourrait s'avérer très intéressante dans les régions arides du monde. Cependant, l'utilisation de procédés qui nécessitent un apport extérieur d'énergie pour refroidir la surface condensante n'est pas économiquement justifiée dans la plupart des cas. En même temps, l'image de la rosée matinale abondante fait penser à des condenseurs dits passifs, c.-à-d. fonctionnant sans apport d'énergie. Pour la première fois dans l'histoire, cette idée fut réalisée par F. Zibold qui a construit un condenseur [13] aux environs de Féodosia en Crimée (Ukraine) en 1912. Zibold suivit le modèle de ce qu'il pensait être les condenseurs des Grecs Anciens qui avaient colonisé la Crimée vers le VI siècle AVJC. Les fouilles archéologiques modernes (y compris celles réalisées dans le cadre de l'expédition de 1994, voir ci-dessous) ont démontré que les tas de pierres que l'on trouve sur les collines environnant la ville ne sont rien d'autre que des kourganes (tombeaux) des Grecs et Scythes qui datent de IV$^{\text{ème}}$-III$^{\text{ème}}$ siècles AVJC, mais le mythe des "condenseurs" Grecs persiste, même dans l'esprit de certains chercheurs [11, 5].

Le condenseur de Zibold était une sorte de soucoupe de béton, de 20 m de diamètre rempli de galets marin formant un cône creux tronqué de 6 m de hauteur. D'après un témoignage oral de l'époque, ce condenseur fournissait jusqu'à 360 l d'eau liquide par jour. Peu après son érection, la soucoupe se mit à fuir et le condenseur fut abandonné. Suivant des informations vagues concernant ce condenseur, plusieurs installations massives furent construites dans le sud de la France dans les années 1930 [10]. En tant que base de la flotte navale Soviétique, Féodosia ne fut accessible qu'après 1992 et donc les bâtisseurs de ces installations n'ont pu avoir accès à l'original. Le condenseur érigé en 1932 par A. Knappen à Trans-en-Provence, a probablement survécu grâce à sa beauté architecturale [3]. Cependant, aucune de ces installations, malgré leur taille imposante, n'ont pu collecter plus que quelques litres d'eau par jour. La raison de ces échecs fut la méconnaissance de la physique de la formation de la rosée.

Avec D. Beysens, j'ai organisé en 1993 une expédition franco-ukrainienne à Féodosia comportant des chercheurs (y compris des archéologues) français et ukrainiens. Avec une autre expédition en 1994 (organisée par I. Mylymuk) cette mission a permis d'un côté de reconstituer l'histoire du condenseur de Zibold jusqu'à là méconnue, et, de l'autre, de réfuter avec certitude le mythe des "condenseurs" grecs. L'aventure de ces deux expéditions est racontée dans l'ouvrage [12].

7.2 Rappel des principes de la condensation naturelle

Pour que le brouillard (gouttes d'eau de 10-30 μm de diamètre suspendues dans l'air) se forme, il faut que la température de l'air baisse au-dessous du point de rosée T_d défini par l'expression

$$p_v = p_{sat}(T_d) \tag{7.1}$$

où p_v est la pression partielle de la vapeur dans l'air et $p_{sat}(T)$ est la pression de saturation à la température T. En connaissant l'humidité relative H de l'air et sa température T_a, p_v s'exprime par :

$$p_v = H\, p_{sat}(T_a). \tag{7.2}$$

Selon la théorie de la nucléation, le seuil de nucléation est plus bas pour des surfaces de meilleure mouillabilité. La condensation sur une surface peut donc démarrer lorsque sa température T_c est inférieure à T_d. Dans notre modèle nous tenons compte de l'angle de contact fini en introduisant un petit décalage $T_0 < 0$ et en supposant que la condensation se produit quand $T_c + T_0 < T_d$.

Pourquoi donc les feuilles des plantes peuvent-elles être plus froides que l'air ? D'après la loi de Stefan-Boltzmann, un corps d'aire S_c et de température T_c exprimée en °C émet le flux de chaleur radiatif

$$R_c = S_i \varepsilon_c \sigma (T_c + 273)^4, \tag{7.3}$$

où σ est la constante de Stefan-Boltzmann, S_i est la superficie externe du condenseur et ε_c est un paramètre de la surface appelé émissivité qui peut varier entre 0 et 1. Pour une géométrie arbitraire du condenseur, nous définissons S_i comme une surface plane d'irradiation effective dont l'irradiation est équivalente à celle du condenseur réel. Si le bilan radiatif de ce corps est négatif, c.-à-d. si le corps reçoit moins d'irradiation qu'il n'en émet, sa température peut baisser. Pour accélérer la condensation, il faut donc éviter l'exposition de la surface condensante aux autres surfaces plus chaudes.

Un mouvement d'air (la convection naturelle et forcée : le vent) qui amène la vapeur d'eau vers la surface est nécessaire pour maintenir un bon taux de condensation. D'autre part, son rôle peut aussi être néfaste [13] car lors de la condensation nocturne l'air est généralement plus chaud que la surface condensante et le vent la réchauffe.

Il est bien connu qu'à partir d'une certaine profondeur (généralement 20 où 30 cm) la température de la terre ne varie pratiquement pas durant le jour. A cause de l'inertie thermique, sa température reste alors plus grande que celle de la surface condensante. Pour augmenter le taux de condensation, le contact thermique avec la terre est donc à éviter.

7.3 Modélisation d'un condenseur

7.3.1 Equations principales

Le modèle mathématique est basé sur les travaux [13, 7]. L'équation d'équilibre thermique pour le condenseur est

$$\frac{\mathrm{d}T_c}{\mathrm{d}t}(Mc_c + mc_w) = R_i + R_{he} + R_{cond}, \tag{7.4}$$

où T_c est la température du condenseur, M et m sont respectivement les masses du condenseur et de l'eau condensée, c_c et c_w sont les chaleurs spécifiques du matériel du condenseur et de l'eau. Ci-après, des unités SI sont supposées pour toutes les valeurs exceptée la température qui est exprimée en degrés celsius. Les variables du coté droit représentent les différents processus physiques impliqués dans l'énergie thermique venant ou partant de la surface de condenseur : R_i est le bilan d'irradiation, R_{he} est l'échange thermique avec l'air environnant, R_{cond} est le gain d'énergie dû à la chaleur latente de condensation H. Ainsi

$$R_{cond} = H\frac{\mathrm{d}m}{\mathrm{d}t}.$$

Le taux d'échange de chaleur par convection peut être exprimé sous la forme habituelle

$$R_{he} = S_c a(T_a - T_c), \tag{7.5}$$

où a est le coefficient de transfert thermique et S_c est la surface de condensation qui peut être différente de S_i si l'air pénètre à l'intérieur du condenseur (c'est le cas du condenseur de Zibold). a se relie à la largeur de la couche limite aérodynamique d'air et dépend ainsi de la vitesse du vent u :

$$a = kf\sqrt{u/D}. \tag{7.6}$$

Dans cette équation, le facteur numérique $f = 4\,\mathrm{WK^{-1}m^{-2}s^{1/2}}$ est empirique [15] pour l'écoulement parallèle à une feuille plate de taille $D = \sqrt{S_c}$. Nous avons introduit ici un coefficient de correction k qui dépend de la position du condenseur par rapport au dispositif mesurant la vitesse du vent et des conditions particulières de circulation d'air.

Le terme d'irradiation de l'éq. (7.4) se compose de plusieurs parties :

$$R_i = R_s + R_l - R_c. \tag{7.7}$$

R_s est l'irradiation solaire que l'on impose $R_s = 0$ dans cette section où uniquement le temps nocturne est considéré. R_c est définie en (7.3) et R_i représente l'irradiation infrarouge reçue du ciel par le condenseur [15],

$$R_l = S_i\varepsilon_c\varepsilon_s\sigma(T_a + 273)^4, \tag{7.8}$$

où ε_s est l'émissivité du ciel qui varie en fonction de T_a et de la fraction N du ciel couvert par les nuages (appelée "nébulosité" ou "couverture nuageuse")

$$\varepsilon_s = \varepsilon_{s0} + N\left(1 - \varepsilon_{s0} - \frac{8}{T_a + 273}\right), \tag{7.9}$$

où $\varepsilon_{s0} = 0,72 + 0,005T_a$ [15]. S_i est la superficie externe du condenseur.

L'équation pour m représente le taux de condensation :

$$\frac{\mathrm{d}m}{\mathrm{d}t} = \begin{cases} S_c b(p_{sat}(T_d) - p_c(T_c)), & \text{si positif,} \\ 0, & \text{sinon.} \end{cases} \tag{7.10}$$

Nous tenons compte des propriétés du mouillage du condenseur en mettant $p_c(T_c) = p_{sat}(T_c + T_0)$. Par la suite nous prendrons $T_0 = -0.35°\mathrm{C}$. L'éq. (7.10) suppose l'absence d'évaporation de

l'eau déjà condensée comme si elle était enlevée aussitôt du condenseur, c.-à-d. versée dans un récipient.

La valeur du coefficient de transfert de masse b est proportionnelle à a (7.6) :

$$b = 0,656ga/(pc_a), \tag{7.11}$$

où p est la pression atmosphérique (supposée constante) et c_a est la chaleur spécifique de l'air. Cette expression ainsi que le facteur numérique sont issus du travail [15]. Nous avons ajouté un coefficient ajustable g pour prendre en compte des conditions particulières de circulation d'air autour du condenseur.

Les éqs. (7.4, 7.10) forment un système d'équations différentielles ordinaires où maintenant tous les termes sont définis.

7.3.2 Simulations de la formation de rosée

Les résultats expérimentaux peuvent être fités à l'aide du modèle proposé dans le chapitre précèdent afin de trouver les paramètres empiriques k et g [6, 7]. Le système d'équations (7.4, 7.10) est intégré pour chaque observation séparément. Le début des calculs est choisi quelque temps après le coucher du soleil, avant que la condensation ne commence, de sorte que la condition initiale $m = 0$ puisse être imposée. Le moment de fin du calcul doit être choisi avant le lever du soleil (avant évaporation). L'acquisition des données est entièrement automatisée et les fichiers de données ont un format uniforme. Un traitement automatique de l'information peut donc être effectué. Plusieurs applications interactives pour PC ont été écrites. Elles sont disponibles sur le site d'OPUR (Organisation Pour Utilisation de la Rosée) http://www.opur.u-bordeaux.fr/angl/progVadim_ang.htm avec son mode d'emploi détaillé. Ces applications permettent d'abord de réunir les données expérimentales dans un seul fichier, puis d'extraire la température expérimentale du condenseur $T_{c,exp}$ correspondant à l'instant de départ de la simulation. Cette température sert de deuxième condition initiale pour le système d'équations (7.4, 7.10) : $T_c(t = 0) = T_{c,exp}$. Le logiciel principal réalise la simulation en rajustant les paramètres k et g pour minimiser l'écart entre les données théoriques et expérimentales. Ensuite les données sont visualisées et enregistrées dans un fichier unique. Les paramètres du condenseur sont montrés dans la Tab. 7.1. Trois condenseurs identiques fonctionnaient à Gre-

Parameter	*Notation*	*Value*
Emissivity	ε_c	0.94
Specific heat	c_c	1674 J/kgK
Thickness	–	5 mm
Density	–	1190 kg/m^3
Surface	$S_c = S_i$	0.16 m^2

TABLE 7.1: Paramètres du condenseur employé pour les expériences. La surface du condenseur était fait de Plexiglas (PMMA).

noble (Isère), à Ajaccio (Corse) et à Bordeaux (Gironde). Les paramètres micro-météorologiques (la vitesse du vent, l'humidité, les températures de l'air et de la surface du condenseur) étaient mesurés. L'acquisition des données expérimentales était faite chaque 15 minutes. La nébulosité était obtenue à partir des données des stations météorologiques des aéroports locaux. Chaque

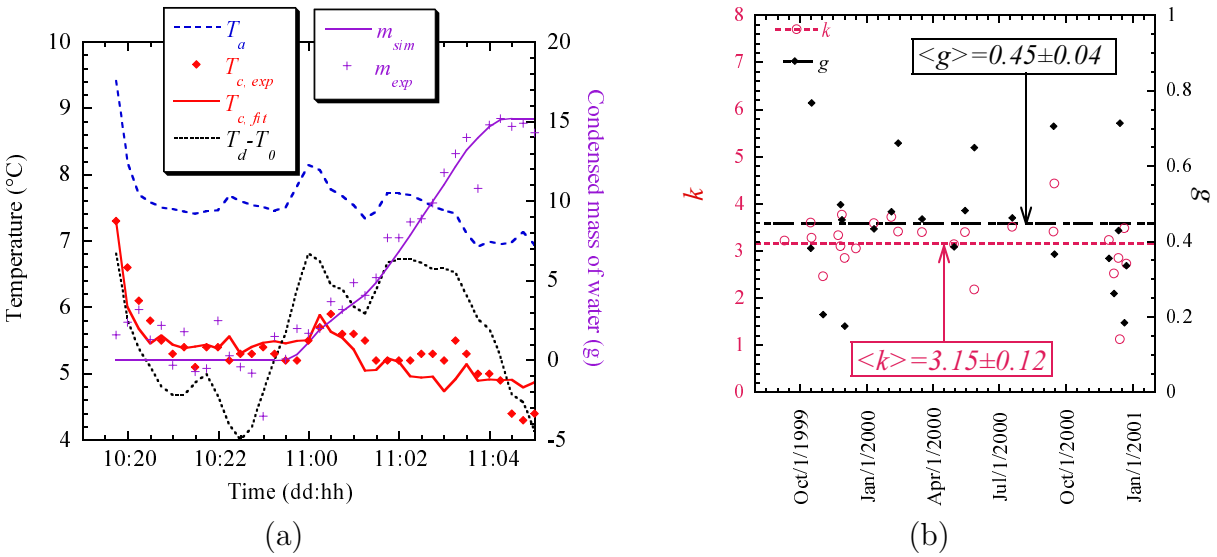

FIGURE 7.1: (a) Données expérimentales typiques (correspondant à la nuit des 10-11 janvier 2000) et le fit de T_c et m (masse de rosée). Le fit est réalisé avec le modèle décrit ci-dessus. Il en résulte $k = 3,59$ et $g = 0,434$. (b) Variation des paramètres k et g obtenus à partir des fits pour chaque observation.

condenseur était monté sur une balance électronique afin de mesurer la masse d'eau condensée. Des résultats typiques obtenus pour le site d'Ajaccio [7] sont montrés sur la fig. 7.1a. La dispersion des points expérimentaux pour la masse d'eau condensée autour de zéro s'explique par les forces aérodynamiques qui apparaissent lors de vent fort. D'un autre côté, quelquefois, le vent chaud ne permet pas à la plaque de se refroidir suffisamment et donc la masse réelle de rosée est égale à zéro. La simulation permet de remonter jusqu'aux paramètres k et g (fig. 7.1b) montrés également pour le site d'Ajaccio.

Malgré les disparités très fortes du climat entre ces trois sites, les paramètres k et g sont presque les mêmes avec la valeurs $k = 2,9 \pm 0,4$ et $g = 0,21 \pm 0,08$.

7.4 Condenseurs "massifs"

L'inertie thermique est la raison principal de l'échec d'un condenseur massif, c.-à-d. un condenseur qui possède une grosse capacité thermique. Comme il garde longtemps la chaleur accumulée pendant le jour, sa superficie et donc l'émission de chaleur nocturne n'est pas assez grande pour atteindre la température de rosée. Pour un critère plus rigoureux, analysons le rendement d'un condenseur ayant $S_c = 2S_i$ comme le condenseur de Zibold [13]. Nous excluons l'influence des conditions initiales sur cette analyse en simulant un jour de 24h et en imposant des conditions aux limites périodiques

$$T_c(0\text{h}) = T_c(24\text{h}),$$
$$m(0\text{h}) = m(24\text{h}),$$

ce qui demande de tenir compte du chauffage du condenseur par le soleil. Pour en tenir compte nous écrivons R_s de l'éq. (7.7) comme $R_s = R_{dir} + R_{dif}$ où R_{dif} est une irradiation diffuse et

R_{dir} est l'irradiation solaire directe. L'irradiation diffuse s'écrit[15] :

$$R_{dif} = S_i R_{sol} \frac{d}{2}(1 - A^q) \sin\alpha. \tag{7.12}$$

Ici $R_{sol} = 1350$ W/m^2 est une constante solaire, $d = 0,5$ est une absorption dans l'infra-rouge proche (“short-wave absorptivity” en anglais) du condenseur, $A = 0,84$ est une constante de transmission atmosphérique, $q = 1/\sin\alpha$, où α est l'angle d'élévation du soleil au-dessus de l'horizon. α peut être estimé par une expression classique [8]

$$\sin\alpha = \sin\phi \sin\delta + \cos\phi \cos\delta \cos[\pi(t - 12)/12], \tag{7.13}$$

où t est l'heure du jour, ϕ est la latitude de l'endroit (pour Féodosia, $\phi = 45°01'45''$) et δ est la déclinaison solaire. Dans cette étude nous fixons la valeur moyenne $\epsilon_s = 0,82$ à la place de (7.9).

L'irradiation directe (“direct beam irradiation” en anglais) s'écrit

$$R_{dir} = S_p R_{sol} d A^q, \tag{7.14}$$

où S_p est l'aire d'une projection géométrique du condenseur sur le plan perpendiculaire au rayons solaires. Pour un condenseur horizontal,

$$S_p = S_i \sin\alpha. \tag{7.15}$$

En prenant une variation journalière typique [13] pour les paramètres micro-météorologiques,

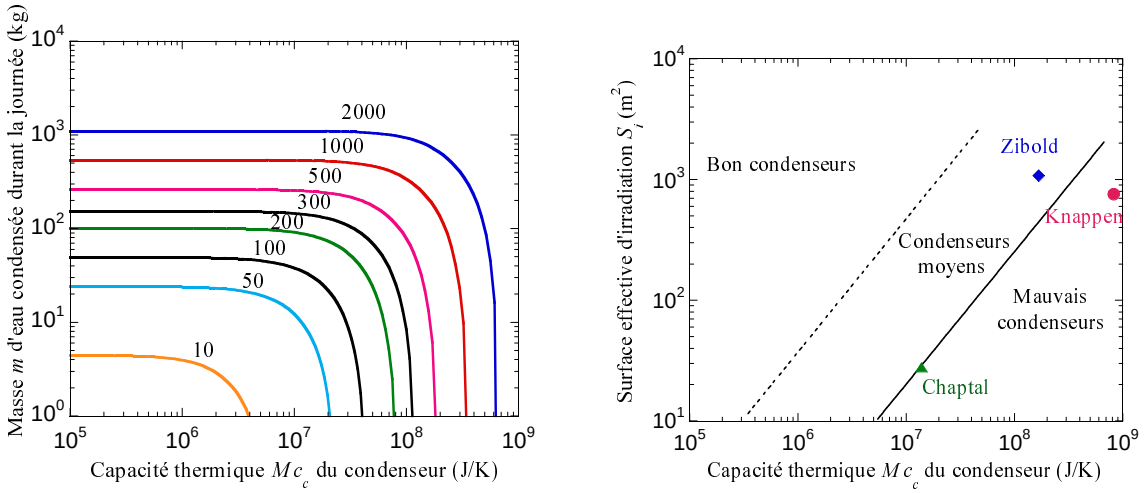

(a) (b)

FIGURE 7.2: (a) Masse d'eau condensée en fonction de la capacité thermique du condenseur. Le paramètre des courbes est la surface effective d'irradiation S_i en m^2. (b) Diagramme des condenseurs massifs. Les symboles pleins correspondent aux condenseurs déjà construits. Les lignes séparent les zones qui classent les condenseurs selon sa qualité.

nous avons obtenu [13] la masse m d'eau condensée par jour en fonction de la capacité thermique Mc_c et la surface S_i d'irradiation du condenseur (fig. 7.2a). Cette figure permet de construire un diagramme (fig. 7.2b) dans l'espace des paramètres $S_i - Mc_c$ permettant de définir les zones où le condenseur serait bon, moyen ou mauvais. En utilisant pour M la masse de la couche supérieure du condenseur où la température change durant le jour, on peut superposer sur ce diagramme les points correspondants aux condenseurs connus. Nous constatons bien que ces condenseurs étaient peu efficaces.

7.5 Vers le condenseur “idéal”

Maintenant on peut formuler les conditions nécessaires pour maximiser la récolte d'eau condensée :

1. Le condenseur doit avoir une faible inertie thermique pour pouvoir se refroidir par rayonnement IR.
2. Il doit se trouver à l'abri des vents forts et sa géométrie doit être optimale pour atténuer la vitesse du vent car le vent réchauffe le condenseur.
3. Le condenseur doit être isolé thermiquement des contacts directs et des irradiations des corps chauds, notamment, de la terre.
4. La géométrie du condenseur doit permettre la collecte de l'eau, par exemple par gravité.
5. L'émissivité de la surface du condenseur doit être grande. Elle doit approcher le plus possible celle du corps noir dans l'infrarouge.
6. La surface doit avoir une bonne mouillabilité par l'eau.

Les critères économique et de longévité se rajoutent à cette liste.

Le critère 1 est quantifié dans le chapitre précédent. Les critères 2–4 concernent la géométrie et l'architecture du condenseur et sont liés l'un à l'autre. Les critères 5–6 concernent le matériau de la surface du condenseur et sont donc liés, eux aussi. Les critères 2–6 font l'objet de la thèse d'Owen Clus que je co-encadre.

En ce qui concerne la géométrie, des études d'aérodynamique et de transfert thermique autour du condenseur sont nécessaires. Pour l'instant, seulement la géométrie d'un plan incliné a été étudiée [6]. Un logiciel commercial de modélisation numérique par la méthode numérique des volumes finis (Phoenics [2]) est utilisé pour modéliser l'aérodynamique et la thermique autour de formes plus compliquées. Une de ces simulations concerne les tests conduits en ce moment

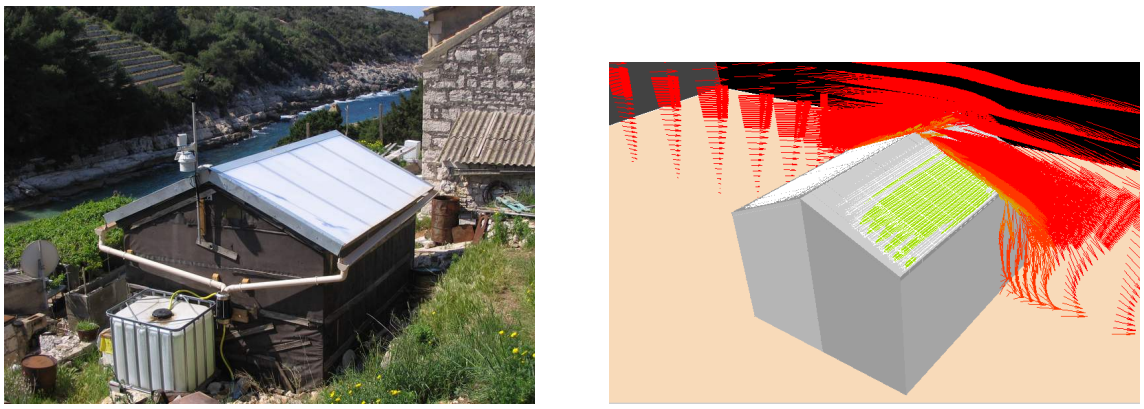

(a) (b)

FIGURE 7.3: (a) La toiture condensante installée sur un abri à l'île de Biševo avec la station météo (sur une tige au-dessus) et le système des mesures de l'eau récoltée. (b) Simulation de l'aérodynamique autour de l'abri (O. Clus).

sur l'île Croate de Biševo dans la mer Adriatique (fig. 7.3b). En l'absence de sources d'eau, seule l'eau de pluie est utilisée. Evidemment, l'eau manque durant la saison sèche. D'où l'intérêt de récupérer l'eau de rosée. Une toiture (fig. 7.3a) de 17 m^2 a été installée sur un abri par O. Clus et moi-même en avril 2005. Cette toiture est isolée par une couche de polystyrène expansé

par dessous pour bloquer l'irradiation du sol. La toiture est faite d'un matériau organique qui possède une haute émissivité. De plus, ce matériau est couvert par une couche "anti-goutte" ce qui le rend très mouillant. Une station météo permet de mesurer tous les paramètres micro-météorologiques ainsi que la quantité d'eau écoulée dans les gouttières chaque 15 minutes. La station météo (visible au-dessus de la toiture sur la fig. 7.3a) est reliée à un ordinateur avec un modem GSM qui sert à récupérer les données depuis la France.

7.6 Caractérisation optique de la buée sur un support transparent

Quand le substrat n'est pas totalement mouillé par l'eau, l'eau se condense en gouttes séparées plutôt qu'en film. Les mesures de la quantité de buée sont difficiles. Dans notre article et un brevet [14, 4] une méthode de caractérisation de la buée a été proposée. J'ai co-encadré un étudiant en DEA (P. Sibille) qui travailla sur le sujet. La cinétique de la formation de la buée a été observée en utilisant la lumière cohérente (fig. 7.4). Nous avons trouvé qu'il était possible d'extraire certaines informations sur la quantité de l'eau condensée à partir de l'intensité de la lumière transmise, c.-à-d. de l'ordre zéro de diffraction I_0. Puisque les gouttes sont arrondies, elles réfractent et

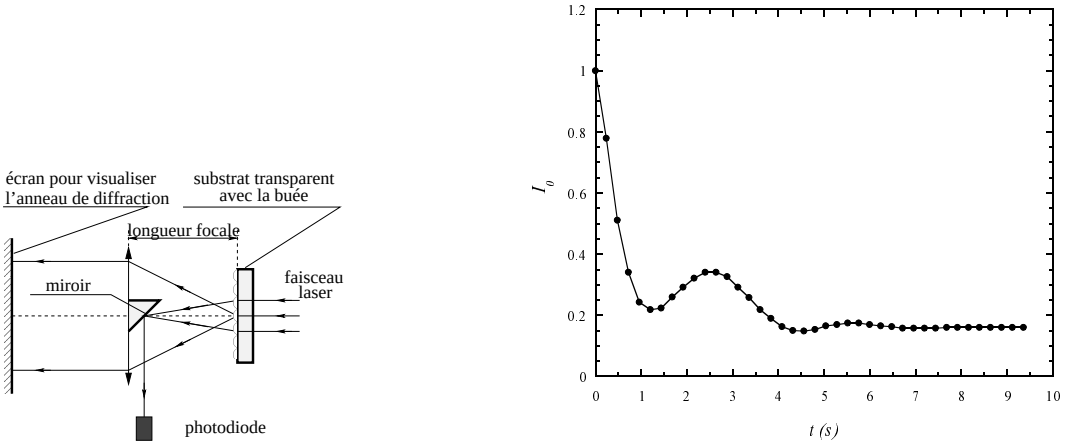

FIGURE 7.4: Expérience de caractérisation optique de la buée sur un support transparent. (a) Schéma expérimental. L'air humide est soufflé sur le substrat et la condensation est permanente. (b) Résultat des mesures de l'intensité de lumière captée par la photodiode durant la croissance des gouttes.

diffusent la lumière et donc en pratique elles peuvent être considérées presque toujours comme des taches noires sur le support en ce qui concerne la lumière transmise. L'amplitude de la lumière transmise est donc proportionnelle à la superficie du support non couvert par les gouttes. Le paramètre principal sera donc la couverture relative du substrat par les gouttes

$$\varepsilon^2 = \pi\langle a^2\rangle/s_1 \tag{7.16}$$

où s_1 est la superficie du substrat illuminé divisée par le nombre total des gouttes. Nous utilisons les crochets pour indiquer une moyenne statistique sur la distribution des tailles des gouttes.

a est le rayon de la projection d'une goutte sur le substrat. L'intensité de la lumière (carré de l'amplitude) dans des unités relatives s'écrit alors

$$I_0^\infty = (1-\varepsilon^2)^2 \tag{7.17}$$

Cependant cette expression n'est valable que si la taille des gouttes excède la longueur d'onde

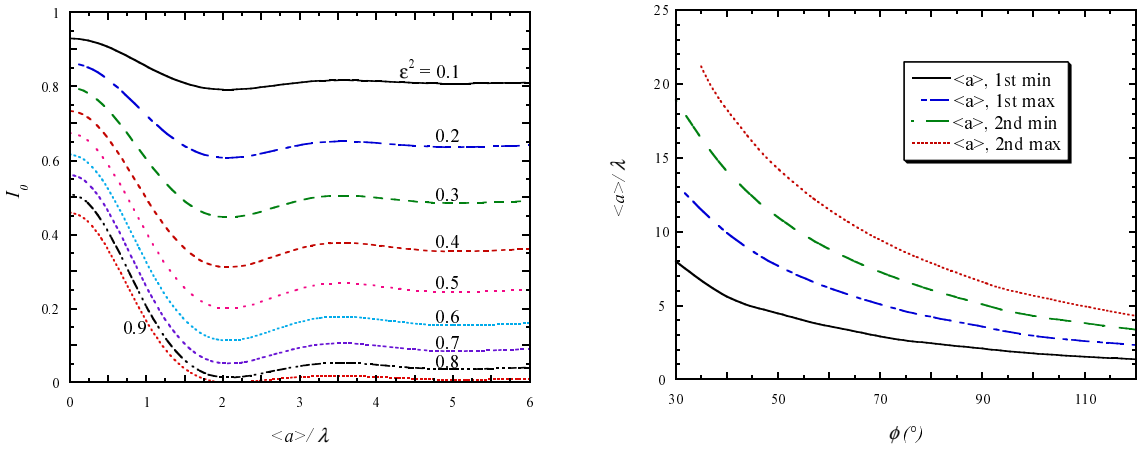

(a) (b)

FIGURE 7.5: (a) Intensité de la lumière transmise I_0 en fonction de la taille moyenne des gouttes d'un angle de contact de 90° pour $g = 0,16$ et différents taux ε^2 de couverture de surface par l'eau. (b) Position des extrêmes des courbes $I_0(\langle a\rangle)$ en fonction de l'angle de contact pour $g = 0,16$ et $\varepsilon^2 = 0,6$.

de la lumière λ, $\langle a\rangle \gg \lambda$. Les comparaisons de (7.17) avec la fig. 7.4b résultent en ε^2 ($\approx 0,6$ pour cette expérience particulière) qui reste constant avec le temps (à partir d'un certain moment) malgré la croissance continue du rayon moyen des gouttes. Ce résultat est universel et a été obtenue précédemment par l'analyse direct des images de la buée [9].

Quand la taille des gouttes est comparable à λ, les rayons diffusés par les gouttes interfèrent et l'intensité est différente de celle donnée par la formule (7.17). Comme approximation de la distribution statistique des tailles des gouttes, nous avons choisi celle de Maxwell

$$H(a) = \frac{B(m)}{a_0}\left(\frac{a}{a_0}\right)^m \mathrm{e}^{-(a/a_0)^2}, \tag{7.18}$$

où $B(m)$ est la constante de normalisation. La distribution (7.18) comporte deux paramètres ajustables $m \geq -1$ et $a_0 > 0$ qui peuvent être liés à la polydispersité $g = (\langle a^2\rangle - \langle a\rangle^2)^{1/2}/\langle a\rangle$ et au rayon moyen de l'ensemble des gouttes

$$g \approx (2m+2)^{-1/2}, \tag{7.19}$$

$$\langle a\rangle \approx a_0[(m+0.5)/2]^{1/2}. \tag{7.20}$$

Ces approximations ont une précision meilleure que 1% quand $m > 4$, ce qui est notre cas. L'approche scalaire de la diffraction résulte [14] en une dépendance de l'intensité I_0 avec la taille moyenne des gouttes, présentée sur la fig. 7.5a. Les positions des extrêmes des courbes $I_0(\langle a\rangle)$ ne varient que très légèrement avec g et ε^2 et peuvent donc servir d'indicateur de rayon des gouttes et d'angle de contact (fig. 7.5b). Ce rayon peut être donc obtenu si on connaît l'angle

de contact. Puisque d'après les résultats théoriques et expérimentaux [9], la polydispersité ne varie pas fortement pendant la croissance de la buée, elle peut être supposée constante et les évolutions temporelles de ε^2 et $\langle a \rangle$ peuvent être récupérées à partir des données expérimentales pour $I_0(t)$ (fig. 7.4b).

7.7 Conclusion

Ce chapitre est consacré à l'étude de la cinétique de la condensation atmosphérique. Les applications pratiques, notamment pour la récupération de l'eau à partir de l'air sont très importantes pour les régions arides (cf. le site Web de l'Association OPUR[1]). L'expérience accumulée pendant ces études nous a permis de participer à de projets industriels (avec AREVA-La Hague) pour tenter d'élucider le rôle de la condensation sur les parois de locaux contaminés par des polluants radioactifs.

7.8 Bibliographie

[1] Opur, association loi 1901, voir www.opur.u-bordeaux.fr.

[2] voir http://www.cham.co.uk/.

[3] Beysens, D., Gioda, A., Katiushin, E., Milimouk, I., Morel, J.-P., & Nikolayev, V. S. Les puits aériens. *La Recherche*(287) 30 – 33 (Mai 1996).

[4] Beysens, D., Marcos-Martin, M., Nikolayev, V., & Sibille, P. Procédé et dispositif de caractérisation d'une modification au cours du temps de l'etat de condensation de gouttelettes sur une cible. Brevet français #96 11310 du 17/09/1996 au nom du CEA (Réf. DD 1511).

[5] Beysens, D., Milimouk, I., Nikolayev, V., Berkowicz, S., Muselli, M., Heusinkveld, B., & Jacobs, A. F. G. Comment on "The moisture from the air as water resource in arid region : hopes, doubts and facts" by Kogan & Trahtman. Accepté, 2005.

[6] Beysens, D., Milimouk, I., Nikolayev, V., Muselli, M., & Marcillat, J. Using radiative cooling to condense atmospheric vapor : a study to improve water yield. *J. Hydrology* **276** 1 – 11 (2003).

[7] Beysens, D., Muselli, M., Nikolayev, V., Narhe, R., & Milimouk, I. Measurement and modelling of dew in island, coastal and alpine areas. *Atmospheric Research* **73**(1-2) 1 – 22 (2005).

[8] Campbell, G. S. *An introduction to environmental biophysics*. Springer, New-York, 1977.

[9] Fritter, D., Knobler, C. M., & Beysens, D. A. Experiments and simulation of the growth of droplets on a surface (breath figures). *Phys. Rev. A* **43**(6) 2858 – 2869 (1991).

[10] Jumikis, A. R. Aerial wells : secondary sources of water. *Soil Science* **100**(2) 83 – 95 (1965).

[11] Kogan, B., & Trahtman, A. The moisture from the air as water resource in arid region : hopes, doubts and facts. *J. Arid Environments* **53**(2) 231 – 240 (2003).

[12] Mylymuk, I., & Beysens, D. *A la Poursuite des Fontaines Aériennes ou Les Incroyables Aventures des Français en Ukraine*. Book-e-book, Nice, 2005.

[13] Nikolayev, V. S., Beysens, D., Gioda, A., Milimouk, I., Katiushin, E., & Morel, J.-P. Water recovery from dew. *J. Hydrology* **182** 19 – 35 (1996). (voir page 117 de cette thèse).

[14] Nikolayev, V. S., Sibille, P., & Beysens, D. Coherent light transmission by a dew pattern. *Optics Communications* **150** 263 – 269 (1998). (voir page 146 de cette thèse).

[15] Pedro, M. J., & Gillespie, T. J. Estimating dew duration. I. Utilizing micrometeorological data. *Agricultural Meteorology* **25** 283 – 296 (1982).

8 Conclusion générale et projets

Au cours de ces années passées au sein de différents organismes de recherche et d'enseignement supérieur, j'ai pu acquérir une certaine expérience. J'ai travaillé dans plusieurs domaines de la physique, tous liés aux transitions de phase et/ou aux interfaces libres. Dans cette thèse, j'ai décrit l'essentiel de mes travaux. En commençant par un aperçu bref de mes études des instabilités d'une couche fluide dans le champ électrique lors de ma thèse de doctorat, je passe à un problème de transition de phase structurelle dans le solide considéré lors de mon travail à l'institut de Physique Théorique de Kiev. Les propriétés de la structure périodique ferroélastique dans des composées céramiques supraconducteurs à haute température critique sont particulièrement intéressantes en raison de leur non-stœchiométrie d'oxygène. Au CEA et à l'université de la Nouvelle-Orléans, j'ai travaillé sur des problèmes de cinétique des transitions de phase dans les fluides. J'ai appris à utiliser les moyens de la physique théorique (hydrodynamique, physique de la transition de phase, thermique, optique...) ainsi que des méthodes numériques (parmi elles, celle des éléments finis de frontière) pour traiter ces problèmes.

Parmi ceux-ci, je distingue des problèmes qui sont les plus intéressants pour les études futures, en l'occurrence ceux sur les singularités thermique (chapitre 5) et hydrodynamique (chapitre 6) à la ligne de contact solide-liquide-gaz. Ce sont eux ainsi que la séparation de phase sous vibrations qui constitueront probablement les vecteurs de mon futur travail.

En ce qui concerne la singularité thermique, notre approche est basée sur l'effet de recul de la vapeur, l'effet qui devient important au voisinage de la ligne triple en raison de cette singularité et conduit à l'étalement de la vapeur sur la paroi chauffante ce qui mène à la crise d'ébullition. Sa compréhension, qui n'est pas encore acquise complètement, est très importante pour des applications industrielles, notamment spatiales. Il s'agit de poursuivre le programme de recherche intégrant des volets expérimentaux (sur un banc de lévitation magnétique au Service des Basses Températures du CEA Grenoble et dans l'installation DECLIC à bord de la Station Spatiale Internationale) et de simulation. En dehors des parties grenobloise (CEA/SBT), bordelaise (ICMCB) et parisienne (ESPCI) de notre laboratoire (ESEME), plusieurs équipes de chercheurs sont associées à ces études dans le cadre des projets nationaux et internationaux que j'ai montés au cours des dernières années (projet EGIDE en cours avec une équipe ukrainienne de Dnipropetrovsk, projets ESA et CNES avec des chercheurs des universités de Paris, Nouvelle-Orléans et Limoges).

Les études de la singularité hydrodynamique sont liées au mouvement de la ligne triple le long d'un substrat solide partiellement mouillé par le liquide. Nous nous concentrons sur le cas encore mal étudié où la ligne triple est déformée. Il s'agit soit de la relaxation de sa déformation initiale, soit des hétérogénéités de substrat qui servent de centres d'accrochage et donc déforment la ligne triple en mouvement. Une théorie phénoménologique quasistatique a été proposée. Elle est basée sur l'hypothèse que toute la dissipation dans un fluide comportant la ligne triple peut être réduite à la dissipation localisée sur la ligne triple. Nous avons démontré que cette hypothèse simple conduit au même résultat que plusieurs autres modèles de mouvement de la ligne triple antérieurs bien plus compliqués. Nous collaborons avec des chercheurs de l'ESPCI (M. Fermigier, G. Delon) afin de valider ce modèle. Les premiers résultats sont encourageants. Il sera intéressant

de comprendre l'effet collectif de défauts microscopiques du substrat sur la dynamique moyenne de la ligne triple près du seuil d'accrochage via l'analyse numérique.

Notre approche permet d'étudier un effet de l'inertie du fluide sur le mouvement d'une ligne triple de forme arbitraire. Une théorie a été proposée en collaboration avec une équipe de Marseille. Nous voulons pouvoir décrire des oscillations de gouttes sessiles d'une faible viscosité et le mouvement de la ligne triple lors d'une coalescence de deux gouttes sessiles pour expliquer des résultats expérimentaux existants.

Nous étudions la condensation naturelle sur un substrat (chapitre 7) afin de pouvoir récolter de l'eau atmosphérique. Bien que la quantité d'eau récoltée par m^2 de substrat est limitée en général, elle peut constituer un complément précieux dans des régions arides de la planète. Je co-encadre un étudiant en thèse sur le sujet d'optimisation des condenseurs (géométrie, matériau de surface,...).

Durant ma carrière scientifique, j'ai été amené à changer souvent de lieu du travail, ce qui empêchait l'encadrement prolongé des étudiants. J'en ai néanmoins encadré plusieurs pendant leurs stages post-doctoraux, de DEA ou de maîtrise.

Remerciements

Je voudrais exprimer ma gratitude envers mes collaborateurs, surtout à D. Beysens pour son soutien permanent et ses encouragements. Je remercie mes amis et collègues S. Gaultier, D. Beysens, H. Gouin et D. Chatain pour la lecture critique et les corrections du français de cette thèse (je l'avoue, très nombreuses). Je suis très reconnaissant aux membres du jury d'avoir pris le soin d'examiner ma thèse.

9 Quelques articles représentatifs

La liste complète de publications se trouve p. 8.

УДК 532.594

М. К. Новоселец, В. С. Николаев

ЭЛЕКТРИЧЕСКАЯ НЕУСТОЙЧИВОСТЬ КАПИЛЛЯРНЫХ ВОЛН ДЛЯ НЬЮТОНОВСКОЙ ЖИДКОСТИ КОНЕЧНОЙ ГЛУБИНЫ

Введение

Электрическая неустойчивость капиллярных волн для идеальной проводящей жидкости бесконечной глубины была предсказана в [1]. Ее механизм очень прост: если давление электрического поля на возмущенной поверхности F_n превышает лапласовское $p_л$, то возмущение развивается по экспоненциальному закону [2]. Впоследствии такая неустойчивость была детально изучена в связи с ее использованием в жидкометаллических эмиттерах [3]. Подобный тип неустойчивости характерен и для жидких диэлектриков; он хорошо изучен в случае заряженной поверхности жидкого He [4] и вязких полимерных слоев, использующихся для термопластической записи информации [5—7].

Для заряженной диэлектрической поверхности неустойчивость определяется не только нормальным давлением F_n, но и тангенциальным натяжением F_τ на возмущенной поверхности; вследствие этого движение жидкости не прекращается не только при $F_n = p_л$, но и ни при каких соотношениях F_n, F_τ, $p_л$. Это приводит к различиям условий существования неустойчивости, изученных в приближении ползучего течения (справедливого при очень больших вязкостях) в работах одного из авторов [6]. Таким образом, электрическая неустойчивость диэлектрических слоев исследована либо в случае идеальной жидкости бесконечной глубины (где отсутствует затухание волн) [4], либо в приближении ползучего течения, исключающего волновые решения.

Цель данной работы — анализ электрической неустойчивости слоев конечной глубины d и произвольной вязкости μ.

1. Постановка задачи

Для описания электрической неустойчивости слоя несжимаемой ньютоновской жидкости произвольной μ и конечной d использовалась система линеаризованных уравнений Навье — Стокса, которая дополнялась уравнением Лапласа для потенциала электрического поля φ:

$$\rho \frac{\partial \vec{v}}{\partial t} = -\vec{\nabla} p + \mu \Delta \vec{v}, \quad \operatorname{div} \vec{v} = 0, \quad \Delta \varphi = 0. \tag{1}$$

Здесь $\vec{v}$ — скорость, p — давление, ρ — плотность жидкости.

Считалось, что жидкость покоится на жесткой проводящей подложке, а на ее свободной поверхности распределен заряд плотностью σ, который наряду с внешним электрическим полем напряженностью E_0, перпендикулярным подложке, создает электрические натяжения. Система координат $0X_1X_2X_3$ выбрана так, что ось $0X_3$ перпендикулярна подложке, совпадающей с плоскостью $x_3 = 0$ (рис. 1, *а*).

Граничные условия для гидродинамической и электрической задач аналогичны используемым в [6] и отличаются наличием E_0 в выражении для составляющей электрического поля E_3, которая входит в тензор электрических натяжений $M_{ik} = \varepsilon\varepsilon_0 (E_i E_k - E^2 \delta_{ik}/2)$:

$$\vec{v} = 0, \quad \varphi = 0 \text{ при } x_3 = 0,$$

$$(P_{ik} + M_{ik}) n_i + M'_{ik} n'_i + R_{ik} n_i = 0, \quad \varphi = \varphi', \quad \varepsilon \frac{\partial \varphi}{\partial n} + \varepsilon' \frac{\partial \varphi'}{\partial n'} = \frac{\sigma}{\varepsilon_0} \text{ при} \tag{2}$$

$$x_3 = d + h(x_1, x_2).$$

Здесь $P_{ik} = -p\delta_{ik} + \mu(\partial v_i/\partial x_k + \partial v_k/\partial x_i)$ — гидродинамический тензор натяжений; тензор $R_{ik} = (\partial^2 h/\partial x_1^2 + \partial^2 h/\partial x_2^2)\gamma\delta_{i3}\delta_{k3}$ описывает капиллярное давление, γ — коэффициент поверхностного натяжения, h — возмущение свободной поверхности, ε — диэлектрическая проницаемость; величины без штрихов относятся к области внутри деформируемого слоя, а со штрихами — к области $x_3 \geqslant d + h(x_1, x_2)$; $\vec{n}$ — внешняя нормаль соответствующей области. Возмущение электрического поля убывает при удалении от поверхности, т. е. $\partial\varphi/\partial x_1$, $\partial\varphi/dx_2 \to 0$, $\partial\varphi/dx_3 \to -E_0$ при $x_3 \to \infty$. Величины $\vec{v}$ и h связаны соотношением

$$\partial h/\partial t = v_3(x_1, x_2, d). \tag{3}$$

Перераспределение заряда учитывалось в приближении, согласно которому он сосредоточен в узком приповерхностном

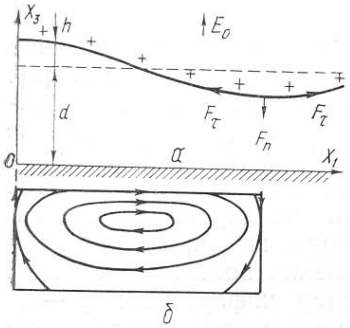

б

Рис. 1. *а* — геометрия задачи; *б* — линии тока в жидкости, рассчитанные при $\xi = 2{,}5$, $\varepsilon/\varepsilon' = 3$, $\mu \to \infty$

слое и перераспределяется за счет дрейфа, обусловленного омической поверхностной проводимостью конвективного типа:

$$\frac{\partial\sigma}{\partial t} + (\vec{v}\cdot\vec{\nabla}_2)\sigma + \vec{\nabla}_2\cdot(\varkappa_s E_\tau) = 0. \tag{4}$$

Здесь $\varkappa_s$ — удельная поверхностная проводимость, E_τ — тангенциальная составляющая напряженности поля, $\vec{\nabla}_2 = (\partial/\partial x_1, \partial/\partial x_2)$.

Для получения дисперсионного соотношения производилась линеаризация по h. В линейном приближении трехмерная задача заменяется двумерной и краевые условия на свободной поверхности $y \equiv x_3 = d$ приобретают вид

$$-p + 2\mu\frac{\partial v_y}{\partial y} + \gamma\frac{\partial^2 h}{\partial x^2} + F_n = 0, \quad \mu\left(\frac{\partial v_x}{\partial y} + \frac{\partial v_y}{\partial x}\right) + F_\tau = 0,$$

$$\varphi - E_y^{(0)}h = \varphi' - E_y^{(0)\prime}h, \quad \varepsilon\frac{\partial\varphi}{\partial y} - \varepsilon'\frac{\partial\varphi'}{\partial y} = \frac{\sigma}{\varepsilon_0}. \tag{5}$$

Здесь $E_y^{(0)}$ — среднее по x значение $E_y(d)$, $x \equiv x_1$, $y = d$.

Данная задача отличается от известной задачи поиска дисперсионного соотношения для капиллярных волн на свободной поверхности [8] только наличием F_n и F_τ в краевых условиях.

2. Дисперсионное уравнение

Для получения дисперсионного уравнения воспользуемся преобразованиями Фурье по координате x и Лапласа по времени t, что эквивалентно поиску волновых решений для h в виде $h(x, t) = \tilde{h}(k, s)e^{(ikx+st)}$, где k — волновое число, знак $\sim$ соответствует фурье-лапласовскому образу соответствующей величины.

Решение краевой электростатической задачи с заряженной деформированной поверхностью приводит к следующему результату для распределения потенциала:

$$\tilde{\varphi} = \left(\frac{\sigma_0}{\varepsilon\varepsilon_0} - \frac{\varepsilon'}{\varepsilon}E_0\right)\frac{y\delta(k)}{s} + \frac{\operatorname{sh}(ky)}{(\varepsilon'/\varepsilon)\operatorname{th}\xi + 1}\left\{-\frac{\varepsilon'\tilde{h}}{\varepsilon\operatorname{ch}\xi}\left[\frac{\sigma_0}{\varepsilon\varepsilon_0} + \left(1 - \frac{\varepsilon'}{\varepsilon}\right)E_0\right] + \right.$$

$$\left. + \frac{\tilde{\sigma}}{k\varepsilon\varepsilon_0\operatorname{ch}\xi}\right\}, \tag{6}$$

$$\tilde{\varphi}' = \left\{\left[\frac{\sigma_0}{\varepsilon\varepsilon_0} + \left(1 - \frac{\varepsilon'}{\varepsilon}\right)E_0\right]d - E_0 y\right\}\frac{\delta(k)}{s} + \frac{\exp(\xi - ky)}{(\varepsilon'/\varepsilon)\operatorname{th}\xi + 1} \times$$
$$\times \left\{\frac{\tilde{\sigma}\operatorname{th}\xi}{k\varepsilon\varepsilon_0} + \tilde{h}\left[\frac{\tilde{\sigma}_0}{\varepsilon\varepsilon_0} + \left(1 - \frac{\varepsilon'}{\varepsilon}\right)E_0\right]\right\}.$$

Здесь σ_0 — усредненная по свободной поверхности плотность заряда, $\xi \equiv kd$.

Распределение $\tilde{\sigma}(k, s)$ исключается из уравнений (6), так как оно связано с $\tilde{h}$ посредством уравнения переноса заряда

$$s\tilde{\sigma} + ik\varkappa_s \tilde{E}_\tau(\tilde{h}) = 0, \quad E_\tau = -ik\tilde{\varphi}|_{y=d} + ik\tilde{h}\left(\frac{\varepsilon'}{\varepsilon}E_0 - \frac{\sigma_0}{\varepsilon\varepsilon_0}\right), \tag{7}$$

полученного линеаризацией уравнения (4).

В результате подстановки $\tilde{\varphi}$ и $\tilde{\varphi}'$ в $\tilde{M}_{ik}$ и процедуры линеаризации получаем выражение, связывающее деформирующие нагрузки $\tilde{F}_n = \tilde{M}_{xy}$ и $\tilde{F}_\tau = \tilde{M}_{yx} + 2ikM_{yy}^{(0)}\tilde{h}$ с возмущением поверхности:

$$\tilde{F}_n = k^2 A_n(k, s)\,\tilde{h}, \quad F_\tau = ik^2 A_\tau(k, s)\,\tilde{h}.$$

Коэффициенты A_n, A_τ имеют ту же размерность, что и γ:

$$A_n = \frac{\gamma}{[(\varepsilon'/\varepsilon)\operatorname{th}\xi + 1]\,\xi\varphi_0^2}\left\{\frac{\operatorname{cth}\xi}{1 + s\tau_s}[\varphi_2 - \varphi_1(1 + \operatorname{th}\xi)]^2 + \right.$$
$$\left. + \frac{\varepsilon}{\varepsilon'}\left[\frac{\varepsilon'}{\varepsilon}\varphi_2 + \varphi_1\left(1 - \frac{\varepsilon'}{\varepsilon}\right)\right]^2\right\}, \tag{8}$$

$$A_\tau = -\frac{\gamma}{[(\varepsilon'/\varepsilon)\operatorname{th}\xi + 1]\,\xi\varphi_0^2}\{\varphi_2^2 - \varphi_1\varphi_2(1 + \operatorname{th}\xi)\}\frac{s\tau_s}{1 + s\tau_s}.$$

Здесь $\tau_s = \tau_\pi(\varepsilon' + \varepsilon\operatorname{cth}\xi)/(\varepsilon' + \varepsilon)\xi$, $\tau_\pi = d\varepsilon_0(\varepsilon + \varepsilon')/\varkappa_s$ — время поверхностного растекания заряда, $\varphi_1 = E_0 d\varepsilon'/\varepsilon$ и $\varphi_2 = \sigma_0 d/\varepsilon\varepsilon_0$ — составляющие потенциала невозмущенной поверхности, созданные зарядом и внешним полем соответственно, $\varphi_0 = \sqrt{\gamma d/\varepsilon\varepsilon_0}$ — константа, имеющая размерность потенциала. Для определения вида дисперсионного уравнения $D(s, k) = 0$ воспользуемся, как и в [8], анализом гидродинамической краевой задачи со следующими условиями на движущейся границе:

$$-\tilde{p} + 2\mu\frac{\partial\tilde{v}_y}{\partial y} + (A_n - \gamma)k^2\tilde{h} = 0, \quad \mu\left(\frac{\partial\tilde{v}_x}{\partial y} + ik\tilde{v}_y\right) - A_\tau k^2\tilde{h} = 0. \tag{9}$$

В результате таких же, как и в [8], преобразований получено следующее дисперсионное уравнение:

$$\mu k\{\alpha\operatorname{ch}\xi\operatorname{ch}\alpha[4 + (1 + l^2)^2] - \xi\operatorname{sh}\xi\operatorname{sh}\alpha[4l + (1 + l^2)^2] - 4\alpha(1 + l^2)\} +$$
$$+ \rho(\gamma - A_n)(\alpha\operatorname{ch}\alpha\operatorname{sh}\xi - \xi\operatorname{ch}\xi\operatorname{sh}\alpha) - \rho A_\tau(l^2 - 1)^{-1}[\alpha(\operatorname{ch}\xi\operatorname{ch}\alpha - 1) \times$$
$$\times (3 + l^2) - \xi\operatorname{sh}\alpha\operatorname{sh}\xi(1 + 3l^2)] = 0, \tag{10}$$
$$\alpha = l\xi, \quad l = \sqrt{1 + Y}, \quad Y = \rho s/\mu k^2.$$

Оно существенно упрощается для коротких волн ($\xi > 1$), что эквивалентно приближению глубокой жидкости

$$(l + 1)\left\{[(l^2 + 1)^2 - 4l]\frac{\mu k^2}{\rho} + \gamma - A_n\right\} - A_\tau(l - 1) = 0. \tag{11}$$

3. Исследование неустойчивости

Проанализируем сначала наиболее простое приближение коротких волн для непроводящей свободной поверхности. В этом случае удается получить рациональное относительно Y уравнение, содержащее все корни дисперсионного уравнения (11) ($E_0=0$):

$$Y^5+8Y^4+4Y^3(X+6)+16Y^2[1+X(1+N/2)]+4YX(X+4)+ \\ +16X^2N(1-N)=0, \tag{12}$$

где

$$X=\frac{\rho\gamma}{2\mu^2k^2}(k+k_0),\quad N=\frac{k_0}{k+k_0}\frac{\varepsilon}{\varepsilon-\varepsilon'},\quad k_0=\frac{\sigma_0^2}{\varepsilon\varepsilon_0\gamma}\frac{\varepsilon-\varepsilon'}{\varepsilon+\varepsilon'}.$$

Для поиска и анализа зон неустойчивости воспользуемся методом Вышеградского — Найквиста [9, с. 298—307]. Выделим на координат-

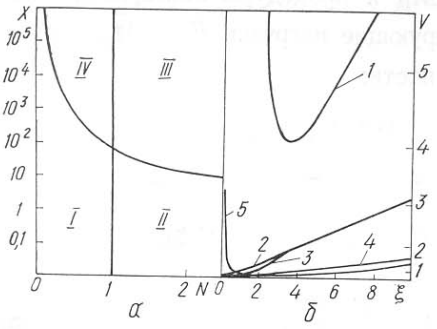

Рис 2. *а* — области неустойчивости для уравнения (12) с числом корней при $\mathrm{Re}\,Y>0$, равным 0, 1, 3, 2 соответственно в областях *I*, *II*, *III*, *IV*; *б*—границы зон неустойчивости в координатах V, ξ для различных комбинаций параметров: *1* — $V=\varphi_2/\varphi_0$, $\varphi_1=0$, $\varkappa_s=0$; *2* — $V=\varphi_1/\varphi_0$, $\varphi_2=0$, $\varkappa_s=0$; *3* — $V=\varphi_2/\varphi_0$, $\varphi_1=0$, $\varkappa_s\neq0$; *4* — $V=\varphi_1/\varphi_0$, $\varphi_2=0$, $\varkappa_s\neq0$; *5* — $V=\varphi_1/\varphi_0$, $\varphi_2=3\varphi_0$, $\varkappa_s=0$. Зоны неустойчивости находятся выше соответствующих границ, $\varepsilon/\varepsilon'=3$

ной плоскости NX области, в которых количество корней, удовлетворяющих условию $\mathrm{Re}\,Y>0$, постоянно. Границы этих областей (разделительные кривые) приведены на рис. 2, *а*. Из анализа корней Y_j, удовлетворяющих уравнению (11) для каждой из областей, следует, что условие $\mathrm{Re}\,Y_j>0$ выполняется только при $N>1$ для единственного корня, это соответствует, как и для проводящей жидкости [1], абсолютной неустойчивости.

Для проводящей поверхности из (11) следует рациональное уравнение шестой степени, аналогичное (12), содержащее все корни дисперсионного уравнения.

Границы области неустойчивости определяются из уравнения (10) при $s\to0$ и не зависят от μ. Непроводящая поверхность ($\varkappa_s=0$) неустойчива, если

$$\frac{\varepsilon}{\varepsilon'}\left[\varphi_1\left(1-\frac{\varepsilon'}{\varepsilon}\right)+\frac{\varepsilon'}{\varepsilon}\varphi_2\right]^2+\xi^2\left[\frac{\mathrm{sh}\,2\xi}{2}-\xi\right]^{-1}[\varphi_1\varphi_2(1+\mathrm{th}\,\xi)-\varphi_2^2]> \\ >\xi\left(1+\frac{\varepsilon'}{\varepsilon}\mathrm{th}\,\xi\right)\varphi_0^2. \tag{13}$$

В случае $\varkappa_s\neq0$

$$(\varphi_1-\varphi_2)^2+\frac{\varepsilon}{\varepsilon'}\varphi_1^2\,\mathrm{th}\,\xi>\varphi_0^2\xi\,\mathrm{th}\,\xi. \tag{14}$$

Для жидких металлов $\varepsilon\to\infty$, поэтому выражение (14) можно заменить на соотношение, полученное в [1]:

$$\varepsilon'\varepsilon_0E_0^2>\gamma k. \tag{15}$$

Для примера на рис. 2, *б* приведены зоны неустойчивости в координатах ξ, $V=\varphi_j/\varphi_0$. При заданном φ_2/φ_0 для проводящей поверхности неустойчивость, как и в [1], наблюдается для значений k, ограничен-

ных сверху ($k_в$), и обусловлена нормальными силами (рис. 1). Эти силы создают поток жидкости, способствующий развитию возмущения h, тангенциальные же силы на возмущенной поверхности, напротив, формируют поток, сглаживающий возмущения и препятствующий развитию неустойчивости. Поэтому в диэлектрических слоях тангенциальные силы, роль которых возрастает по мере уменьшения k, приводят к

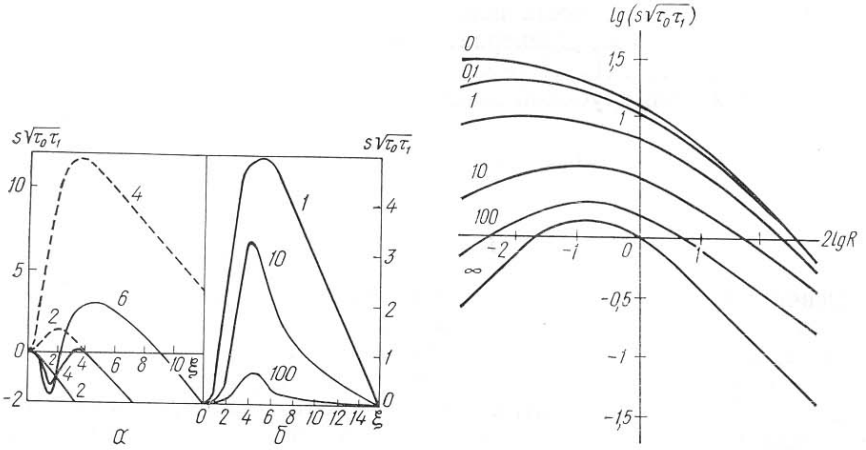

Рис. 3. a — $\varkappa_s = 0$, цифры у кривых — значения V, сплошные кривые — $\varphi_1 = 0$, $V = \varphi_2/\varphi_0$, штриховые — $\varphi_2 = 0$, $V = \varphi_1/\varphi_0$; $б$ — $\varkappa_s \neq 0$, $\varphi_1 = 0$, $\varphi_2 = 5\varphi_0$, цифры у кривых — значения $\tau_п/\sqrt{\tau_0\tau_1}$

Рис. 4. Зависимости $s(R)$ при $\xi = 5$, $\varphi_2/\varphi_0 = 5$, $\varphi_1 = 0$, цифры у кривых — значения $\tau_п/\sqrt{\tau_0\tau_1}$

ограничению области неустойчивости снизу ($k \in [k_н, k_в]$), а также к появлению критического потенциала $\varphi_{2кр}$, ниже которого неустойчивость не наблюдается ни при каких k, что впервые отмечено в [6].

Если заряженная поверхность помещена во внешнее поле, увеличивающее вклад тангенциальных сил при $\varphi_1\varphi_2 > 0$ и уменьшающее его при $\varphi_1\varphi_2 < 0$, то, как следует из анализа соотношения (13) при постоянном φ_2, в первом случае $k_н$ будет уменьшаться, а во втором — расти и, начиная с некоторого значения $\varphi_1' = \varphi_1'(\varepsilon/\varepsilon')$, неустойчивость исчезнет и восстановится затем при $\varphi_1'' = \varphi_1''(\varepsilon/\varepsilon')$. Значения φ_1' и φ_1'' находятся численно из (13). В случае $\varkappa_s \neq 0$ при достаточно больших временах $t/\tau_п > 1$ происходит выравнивание потенциала поверхности: тангенциальные силы и связанное с ними ограничение $k > k_н$ исчезают.

Зависимости $s(\xi)$, вычисленные для неустойчивой ветви дисперсионного соотношения, приведены на рис. 3. Нормировочный множитель $\sqrt{\tau_0\tau_1}$, введенный для инкремента s, не зависит от μ; здесь $\tau_0 = 2\mu d/\gamma$ и $\tau_1 = d^2\rho/\mu$ — характерные времена релаксации возмущения поверхности и установления ползучего течения. Роль вязкости можно проследить по зависимости s от безразмерного параметра $R = \sqrt{\tau_0/\tau_1} \sim \mu$, приведенной на рис. 4 для $kd > 1$. В приближении ползучего течения ($R > 1$) трение между движущимися слоями (линии тока показаны на рис. 1) приводит к уменьшению s.

Такой же эффект при уменьшении μ ($R < 1$) объясняется возрастанием роли инерционных эффектов, препятствующих увеличению скорости жидкости и описывающихся членом $\rho\partial\vec{v}/\partial t$ в уравнении (1). Причем эти эффекты проявляются прежде всего для потоков, созданных нормальными силами, так как они замыкаются на большей глубине и приводят в движение бóльшие массы жидкости, чем потоки, обуслов-

ленные тангенциальными натяжениями. Следовательно, с уменьшением μ относительный вклад тангенциальных сил (а они, как было указано выше, препятствуют развитию неустойчивости) растет, что приводит к уменьшению s.

Таким образом, существование оптимальной вязкости μ_{opt} связано с наличием тангенциальных сил, поэтому при $\varkappa_s \to \infty$ $\mu_{opt} \to 0$. Инерционные эффекты при развитии неустойчивости проявляются также в зависимости s от φ_1 и φ_2. Вместо неограниченного роста имеет место насыщение при $(\varphi_1, \varphi_2) \to \infty$. Дисперсионное уравнение в этом случае можно получить из (10) при $A_n, A_\tau \to \infty$.

В приближении глубокой жидкости оно имеет простое решение

$$s(k) = 4 \frac{\varepsilon\varepsilon'}{(\varepsilon - \varepsilon')^2} \frac{\mu k^2}{\rho}.$$

Заключение

Основные особенности электрической неустойчивости капиллярных волн для слоев непроводящей жидкости произвольной вязкости обусловлены, как показал анализ, тангенциальными натяжениями на свободной поверхности. Именно эти натяжения обусловливают ограничение пространственного спектра неустойчивости снизу для слоев конечной толщины, существование оптимальной вязкости, обеспечивающей наибольшие значения инкремента неустойчивости. В связи с этим большое значение должны иметь явления на поверхности жидкости, способные изменить соотношение между нормальными и тангенциальными силами. К ним относятся, в частности, перераспределение заряда, простейшая модель которого рассмотрена в настоящей работе, и перераспределение поверхностно-активных веществ, вызывающее пространственную модуляцию коэффициента поверхностного натяжения. Все эти эффекты можно учесть в рамках данной модели, изменив функции $A_n(k)$ и $A_\tau(k)$ в уравнении (10).

Авторы благодарны Н. Г. Находкину за руководство работой.

SUMMARY. The appearance of the instability on the surface of the viscous liquid layer in the electric field is theoretically analyzed. The instability is demonstrated to be absolute. The conditions under which instability takes place are obtained. The existence of the optimal viscosity — viscosity of the maximum instability increment — is shown.

1. *Френкель Я. И.* К теории Тонкса о разрыве поверхности жидкости постоянным электрическим полем в вакууме // ЖЭТФ.— 1936.—**6**, вып. 4.— С. 347—350.
2. *Tonks L.* Theory of liquid surface rapture by a uniform elektric field // Phys. Rev.— 1935.—**48**, N 1.— P. 562—570.
3. *Габович М. Д.* Жидкометаллические эмиттеры ионов // УФН.— 1983.—**140**, вып. 1.— С. 137—153.
4. *Шикин В. Б., Лейдерер П.* О колебаниях и устойчивости заряженной поверхности гелия // ЖЭТФ.— 1981.—**81**, вып. 1.— С. 184—201.
5. *Budd H. F.* Dynamical theory of thermoplastic deformation // J. Appl. Phys.— 1965.— **36**, N 5.— P. 5169—5172.
6. *Бутенко А. Д., Новоселец М. К.* Особенности развития «морозной» деформации // Способы записи информ. на бессеребрян. носителях.— 1977.— Вып. 8.— С. 109—119.
7. *Выборонов В. И., Панасюк Л. М., Русанов М. М.* Механизм образования видимого изображения при фототермопластическом способе записи информации // ЖТФ.— 1984.—**54**, вып. 5.— С. 929—933.
8. *Шуляк Б. А.* Физика волн на поверхности сыпучей среды и жидкости.— М. : Наука, 1971.—278 с.
9. *Фукс Б. А., Левин В. И.* Функции комплексного переменного и их приложения.— М. ; Л. : Гостехиздат, 1951.— 307 с.

Киев. ун-т им. Т. Г. Шевченко

Получено 18.11.85,
в окончательном варианте — 28.01.86

4. *Зайцев А. К., Зайцев Н. К., Кузьмин М. Г.* // Вестн. МГУ. Сер. 2.. Химия. 1987. Т. 28. № 2. С. 144.
5. *Байер М., Зайцев А. К., Кузьмин М. Г.* // Хим. физика. 1988. Т. 7. № 2. С. 172.
6. *Зайцев Н. К., Демяшкевич А. Б., Кузьмин М. Г.* // Докл. АН СССР. 1980. Т. 255. № 3. С. 622.
7. *Демяшкевич А. Б., Зайцев Н. К., Кузьмин М. Г.* // Химия высоких энергий. 1982. Т. 16. № 1. С. 60.
8. *Зайцев Н. К., Зайцев А. К., Кузьмин М. Г.* // Химия высоких энергий. 1986. Т. 20. № 4. С. 326.
9. *Frahm J., Diekman S., Haase A.* // Ber. bunsenges. phys. Chem. 1980. B. 84. № 6. S. 566.

Московский государственный
университет им. М. В. Ломоносова
Химический факультет

Поступила в редакцию
16.VII.1987

УДК 532.529.5.097

АНИЗОТРОПНЫЙ СПИНОДАЛЬНЫЙ РАСПАД БИНАРНОЙ СМЕСИ ПОЛИМЕРОВ В ЭЛЕКТРИЧЕСКОМ ПОЛЕ

Новоселец М. К., Николаев В. С.

Спинодальный распад бинарной смеси наблюдается, если при быстром изменении внешних параметров смесь удается перевести в термодинамически неустойчивое состояние. В этом случае релаксация системы сопровождается усилением случайных неоднородностей объемных концентраций компонент $n_{1,2}$ и приводит к появлению пространственных структур, которые изменяют механические, электрические, оптические свойства вещества [1–3]. Хорошо изучены и описаны в литературе [4, 5] особенности распада, вызванного переходом температуры через точку спинодали T_s.

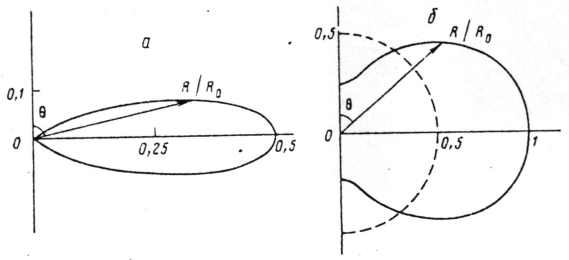

Индикатриса инкремента неустойчивости R для: $а - T<T_s$, $E_0=(\delta\varepsilon)^{-1}(3A\bar{e}/\varepsilon_0)^{1/2}$; $б - T>T_s$. Сплошная кривая соответствует $E_0=\frac{1}{2\delta\varepsilon}(3|A|\bar{e}/\varepsilon_0)^{1/2}$, пунктир – $E_0=0$; $K=|A|/(2k^2)$, $R_0=M|A|k^2$

(она соответствует условию $(\partial^2 f/\partial c^2)_{T_s}=0$, где f – плотность свободной энергии смеси, $c=n_1/(n_1+n_2)$).

Как показано в [6], начальная стадия распада, описывающаяся линейным приближением, для полимеров в отличие от других веществ длится достаточно долго. Уравнения, описывающие распад, в этом случае имеют вид [5]

$$\frac{\partial c(\mathbf{r}, t)}{\partial t} + \nabla \mathbf{j}(\mathbf{r}, t) = 0, \quad \mathbf{j} = -M\nabla\mu, \tag{1}$$

$$\mu = \left(\frac{\partial^2 f}{\partial c^2}\right)_{T,\delta c=0} c - K\nabla^2 c. \tag{2}$$

Здесь δc – отклонение c от среднего значения, $\mathbf{j}$ – диффузионный поток, M – подвижность молекул первой компоненты во второй, μ – локальный химический потенциал смеси, градиентный член в котором описывает дополнительную энергию неоднородностей. При переходе через T_s величина $A=(\partial^2 f/\partial c^2)_{T,\delta c=0}$ становится отрицательной, что приводит к экспоненциальному нарастанию δc.

Цель данной работы – исследование особенностей спинодального распада бинарной полимерной смеси, помещенной в электрическое поле. Изменение температуры спинодали в этом случае было обнаружено экспериментально в [7] и объяснено как следствие изменения μ в однородном поле. Однако такое объяснение не является последовательным, так как разделение компонент неизбежно приводит к пространственной неоднородности поля, которая служит причиной качественно иного характера распада. Его исследование актуально в связи с проблемой электрической стойкости полимеров и их применимости в электрографии и фототермопластической записи информации [8].

Для описания распада смеси двух компонент с мало отличающимися (на $\delta\varepsilon$) диэлектрическими проницаемостями в электрическом поле напряженности E в выражение (2) для μ введем добавку $\Delta\mu = -{}^1/_2\varepsilon_0 E^2\, \partial\varepsilon/\partial c$. При этом и ε, и E зависят от r и удовлетворяют уравнению $\operatorname{div}(\varepsilon E)=0$, в котором выражение для диэлектрической проницаемости смеси $\varepsilon(c)$ взято из [9]. После линеаризации по δc всех приведенных выражений из (1) получаем уравнение эволюции пространственного фурье-спектра неоднородности концентрации $\widetilde{\delta c}(\mathbf{k})$

$$\frac{\partial(\widetilde{\delta c})}{\partial t} = -k^2 M \widetilde{\delta c}\left\{A + Kk^2 + \frac{(\delta\varepsilon)^2\varepsilon_0}{\bar{\varepsilon}}\left[\frac{(\mathbf{E}_0\mathbf{k})^2}{k^2} - \frac{E_0^2}{3}\right]\right\}, \qquad (3)$$

где k – волновой вектор, $\bar{\varepsilon}$ и $\mathbf{E}_0$ – средние по объему значения ε и E.

Из (3) следует, что спинодальный распад может происходить и при температурах $T<T_*$ при наложении поля

$$E_0 > E_{crit}(T) = \frac{1}{\delta\varepsilon}\left(\frac{3\bar{\varepsilon}A(T)}{2\varepsilon_0}\right)^{1/2}.$$

Распад должен иметь ярко выраженную анизотропию, так как потеря устойчивости имеет место для k, составляющих угол $\theta > \arccos[{}^2/_3(1-E_{crit}^2/E_0^2)]^{1/2}$ с $\mathbf{E}_0$. Пример индикатриссы инкремента неустойчивости $R(\mathbf{k}) = t^{-1}\ln(\widetilde{\delta c}(t)/\widetilde{\delta c}(0))$ для этого случая приведен на рисунке *а*. Анизотропия распада должна сохраняться и при $T>T_*$: распад в этом случае, как видно из рисунка *б*, происходит по всем направлениям, но поле любой напряженности уменьшает R вдоль и увеличивает его поперек $\mathbf{E}_0$.

В результате анизотропного спинодального распада образуются неоднородности, сжатые в направлении внешнего поля. Это должно привести к анизотропии механических, оптических и электрических свойств полимеров.

ЛИТЕРАТУРА

1. *Биндер К.* // Синергетика. М.: Мир, 1984. С. 64.
2. *Де Жен П.* Идеи скейлинга в физике полимеров. М.: Мир, 1982.
3. *Маневич Л. И., Митлин В. С., Шагинян Ш. А.* // Хим. физика. 1984. Т. 3. С. 283.
4. *Скрипов В. П., Скрипов А. В.* // Успехи физ. наук. 1979. Т. 128. С. 193.
5. *De Gennes P. G.* // J. Chem. Phys. 1980. V. 72. P. 4756.
6. *Izumitani T., Hashimoto T.* // J. Chem. Phys. 1985. V. 83. P. 3694.
7. *Reich S., Gordon J. M.* // J. Polym. Sci.: Polym. Phys. Ed. 1979. V. 17. P. 371.
8. *Черкасов Ю. А.* // Несеребряные фотографические процессы. Л.: Химия, 1984. С. 23.
9. *Ландау Л. Д., Лифшиц Е. М.* Электродинамика сплошных сред. М.: Наука, 1982. С. 67.

Киевский государственный университет

Поступила в редакцию 4.IX.1987

Технический редактор *В. П. Наботова*

Сдано в набор 05.07.88 Подписано к печати 1.09.88 Т-12807 Формат бумаги 70×108 1/16
Высокая печать Усл. печ. л. 11,2 Усл. кр.-отт. 7,3 тыс. Уч.-изд. л. 12,0 Бум. л. 4,0
Тираж 739 экз. Зак. 1793

Ордена Трудового Красного Знамени издательство «Наука»,
103717 ГСП, Москва, К-62, Подсосенский пер., 21
2-я типография издательства «Наука», 121099, Москва, Г-99, Шубинский пер., 6

1292

PHYSICAL REVIEW B VOLUME 50, NUMBER 6 1 AUGUST 1994-II

Twin spacing and the structural phase transitions in $R\mathrm{Ba_2Cu_3O_{7-\delta}}$ high-T_c superconductors

Vadim S. Nikolayev*
Bogolyubov Institute for Theoretical Physics, Ukrainian Academy of Science, 252143, Kiev, Ukraine
(Received 17 February 1994)

The properties of the structural twins in $R\mathrm{Ba_2Cu_3O_{7-\delta}}$ compounds are investigated in a wide range of temperatures in the framework of the suggested model. The dependence of the size of the twins versus temperature is considered. The temperature interval of the sharp increase of twin size with increase of the temperature is found.

I. INTRODUCTION

The high-T_c superconductors of the class $R\mathrm{Ba_2Cu_3O_{7-\delta}}$ (1:2:3 below for the sake of brevity; R is a rare earth) are well known to form a developed twin structure in its orthorhombic phase. According to optical experiments the twins are similar to the ones in well-investigated ferroelastic crystals (see, e.g., Ref. 1 and references therein). But there exists an essential difference. In the case of ferroelastic crystals the martensitic phase transformation which leads to the twins' formation is of displacement type; i.e., it is controlled by elastic stresses. The functionally analogous tetragonal-to-orthorhombic (T-O) transition in 1:2:3 compounds is the order-disorder one. In other words, it is controlled by the rearrangement of the nonstoichiometric (chain) oxygen and the orthorhombic deformation of the lattice plays a secondary part. This difference vanishes when the composition is close to the stoichiometric one ($\delta = 0$), since there are no chances for oxygen ions to be distributed stochastically. (As was shown in Refs. 2 and 3, in this case the usual twin boundaries convert to antiphase ones.) It was shown in Ref. 4 that this difference manifests itself in deviation of $L(D)$ (L is the period of the twins; D is the size of the crystal) dependence from the classical square root law.[5] The second consequence is a spatial dependence of the local oxygen concentration. It turns out to be larger in the bulk of the twins and lower inside the boundaries.

In fact the authors of Ref. 6 discovered that the twin boundaries have the short-time memory of their positions. They were not able to explain their experiment without using the idea of the accumulation of the oxygen vacancies in the close vicinity of the boundaries. The second experiment, which can be considered as evidence (though indirect) of the oxygen depletion of the boundaries, is high-resolution electron microscopy (HREM) testing of 1:2:3 performed in Ref. 2. The intensity of the oxygen spots decreases near the boundary line and the spots themselves become diffuse.

The probability approach to twinning in 1:2:3 compounds suggested in Ref. 4 allows one to analyze the twin structure in the whole temperature range and the whole oxygen concentration range although the model should not be adequate outside the interval

$$\alpha < \delta \lesssim 0.5 ,$$

where α is a small quantity. The limitation $\delta > \alpha$ is due to the formation of antiphase boundaries mentioned above. The second limitation arises since we consider only two oxygen atoms per unit cell (i.e., only one order parameter) thus eliminating the formation of so-called "ortho-II" structure which is more advantageous for $\delta \gtrsim 0.5$. Besides the model is mean-field like. And, certainly, it contains all the faults of the approximation. For instance it should give wrong results when the temperature is close to zero. Moreover, this approach leads to the wrong phase diagram (see below) because of the elimination of the ortho-II structure. Really, numerical modeling[7] shows that the phase diagram does not contain a $T + O$ (see below) part. Meanwhile the absence of oxygen (i.e., appearance of the T phase in our terms) in the neighborhood of the twin boundary is clearly visible in the figures of Ref. 7. Thus while a strict mean-field limit of the present model gives an incorrect phase diagram, the method is applicable for materials with a second phase at the boundary (tetragonal for the case of 1:2:3). It should be noted here that the dependences of the twins' size on the different parameters so far cannot be obtained in the framework of the lattice-gas models.[7,12] And it is quite interesting to investigate the equilibrium twin structure of the monocrystal with a fixed size when its temperature is falling from the point of the T-O transition to the low temperatures. Such an experiment was performed by Smith and Wohlleben.[8] It has shown some unusual properties, in particular jumps of twin period during the thermocycling. The aim of the present paper is to make an attempt to explain those experiments and to investigate the twin structure in the whole temperature range for the practically interesting values of δ in the interval $\alpha < \delta \lesssim 0.2$.

II. MODEL

Let us consider briefly the main points of the model.[4] The basic variables of the model are the probabilities of filling of the oxygen sites in the basis plane of the 1:2:3 compound ($\mathrm{CuO_{1-\delta}}$ plane). To describe the referred structure one can introduce two variables, the scale of variation of which is more than several lattice constants. They correspond to two inequivalent positions in the two-

dimensional unit cell. According to the mean-field character of the model they are assumed to be averaged in statistical meaning. The probabilities of occupation of these sites will be called p_i, $0 \leq p_i \leq 1$. The index denotes the crystallographic direction: 1 corresponds to [100] and 2 to [010] directions. For convenience I shall operate with an equivalent set of variables $c = p_1 + p_2$ (the concentration of oxygen in a unit cell) and $\eta = p_1 - p_2$ (the order parameter, which differs in sign in the neighboring twins).

The surfacial density of the free energy can be divided into four parts:

$$F = F_O + F_e + F_i - TS. \tag{1}$$

The first part is the Coulomb energy of the oxygen ion interaction

$$F_O = V_1(c^2 - \eta^2) + (V - V_1)c^2 + r(\nabla\eta)^2, \tag{2}$$

where V_1 is an interaction with the nearest-neighboring O ions and $V - V_1$ is an interaction with the other O ions. The second term in (1) is the elastic energy,

$$F_e = c_{ijkl}u_{ij}u_{kl}/2, \tag{3}$$

where u_{ij} are the deformation tensor components, and c_{ijkl} are the elastic tensor ones.

The next term in Eq. (1) is the energy of the interaction between the oxygen and elastic subsystems:

$$F_i = -c_{ijkl}(A^1_{kl}p_1 + A^2_{kl}p_2)u_{ij}, \tag{4}$$

where

$$A^1 = \begin{pmatrix} b_1 & 0 \\ 0 & b_2 \end{pmatrix}, \quad A^2 = \begin{pmatrix} b_2 & 0 \\ 0 & b_1 \end{pmatrix},$$

and b_i are the material constants. The last term introduces the temperature T into the model, and

$$S = -[p_i \ln p_i + (1 - p_i)\ln(1 - p_i)] \tag{5}$$

is the configurational entropy.

It is easy to show that the condition which defines the orthorhombic deformation

$$(u_{11} - u_{22})/\sqrt{2} = \eta(b_2 - b_1)/\sqrt{2} \tag{6}$$

is necessary to provide the minimum of the free energy. Then the expression for F takes the form

$$F = c^2 - \gamma\eta^2 + g^2(d\eta/dz)^2 - \tau S, \tag{7}$$

after division by V. Here $\tau = T/V$, $g^2 = 2r/V$,

$$\gamma = [(b_1 - b_2)^2(c_{1111} - c_{1122})/4 + V_1]/V > 1, \tag{8}$$

c and η are the functions of the space variable $z = (x_1 + x_2)/\sqrt{2}$, and the problem appears to be one dimensional. Thus the free energy of a periodical twin structure per unit volume could be written as

$$E = \frac{NV}{L}\int_{-L/2}^{L/2} F dz, \tag{9}$$

where N is the number of unit cells per unit volume.

III. TREATMENT OF THE MODEL

The phase diagram has been suggested for the strict mean-field limit (i.e., for $g \to \infty$) of the functional (7) by Khachaturyan *et al.*[9] It is presented in Fig. 1, where T and O mark the regions of stability of the tetragonal and orthorhombic phases and the decomposition to tetragonal and orthorhombic domains is energetically advantageous in the $T + O$ region. In the case of finite g the phase diagram conserves its shape but the regions O, $T + O$, etc., accept another meaning.

The formation of the twin structure is energetically advantageous in the whole (T-c) plane except for the region of stability of the tetragonal phase (T), the phase, for which the condition $p_1 = p_2$ is fulfilled. Since the twin boundary is virtually a kink it is important to know its shape in the different parts of the phase diagram. As has been shown in Ref. 4, the kink solution which conserves the mean level of c [i.e., with $c(\pm\infty) = \bar{c}$; $\bar{c}$ is a mean oxygen concentration] exists only in the O region in Fig. 1. The numerical calculations show that near the O-($T + O$) transition (coexistence) curve the width of the kink increases and just on the curve tends to infinity. Such a behavior is usual for the vicinity of a first-order phase transition.[10] There are kinks in the $T + O$ region which do not conserve the mean level of c. They could be characterized by the function $\eta(z)$ with $\eta(-\infty) = 0$ and $\eta(\infty) = \pm\eta_d$. Antikink solutions exist also. Thus one needs a more complicated broken line than the one used in Ref. 4 for the O region to approximate the shape of the long-periodic solutions with the same accuracy. These model broken lines are presented in Fig. 2. It is easy to see that they reduce to the model[4] when $w \to 0$.

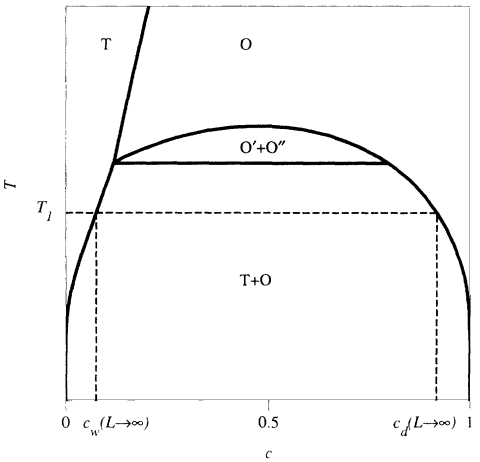

FIG. 1. Shape of the phase diagram $T(\bar{c})$ for the strict mean-field limit of the model for $\gamma > 1$; $\bar{c} = 1 - \delta$. The $O' + O''$ region exists for $\gamma < 4$ only (Ref. 9).

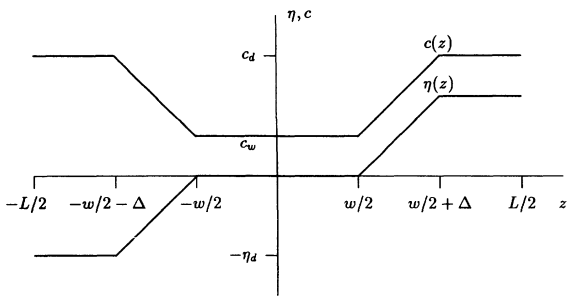

FIG. 2. The schematical coordinate dependences of the order parameter η and local oxygen concentration c. c_d and η_d denote the values of c and η inside the twin domain. c_w is the value of c inside the twin boundary, where $\eta = 0$.

Therefore it is possible to use the present model both for O and $T + O$ regions.

The dependences of equilibrium twins' period on the size of the monocrystal are shown in Fig. 3. The points of break correspond to the transition from the phase with $w = 0$ (at lower values of L, with O-O walls) to the phase with $w > 0$ (at larger values of L, with O-T-O walls). Let us try to understand this result. When the temperature is higher than that for the O-$(T+O)$ transition the walls are of O-O type for all values of L. The value of c inside the twin domain (c_d) tends to $\bar{c}$ when $L \to \infty$. The limiting values of η_d and c_w are close to $\bar{c}$ (see Fig. 2 for notation). Both c_w and c_d are decreasing functions of L.

The O-T-O walls can exist in the $T + O$ region of the phase diagram. The period dependences are different for this case. The limiting ($L \to \infty$) values of c_d and c_w differ strongly and correspond to two points of the coexistence curve for the given value of $T = T_1$ (see Fig. 1). In fact, those limiting values do not depend on $\bar{c}$. The difference between c_d and c_w can be interpreted as a decomposition into T and O phases. $c_d(L)$ is an increasing function for the case of T-O-T walls.

The procedure of the free energy minimization for the case of O-T-O walls is completely analogous to the one used in Ref. 4 for the case of O-O walls. The only difference is one more parameter of the minimization Δ (see Fig. 2). Since the dependence of the free energy on Δ turns out to be very simple, the analytical minimization with respect to Δ is possible. After such a procedure the expression for the energy (9) takes the form (it is assumed here that $w > 0$)

$$E = G(\eta_d, c_d) + \frac{c_d - \bar{c}}{c_d - c_w}[G(0, c_w) - G(\eta_d, c_d)] + \frac{4g}{L}\{A - [G(0, c_w) + G(\eta_d, c_d)]/2\}^{1/2},$$

where $G(\eta, c) = F(\eta, c)|_{g=0}$,

$$A = -\frac{\tau}{4[(c_d - c_w)^2 - \eta_d^2]}\left\{2(c_d - c_w)\left[c_w^2 \ln\frac{c_w}{2} - (2 - c_w)^2 \ln\frac{2 - c_w}{2}\right]\right.$$
$$+(c_d - c_w + \eta_d)\left[(2 - c_d + \eta_d)^2 \ln\frac{2 - c_d + \eta_d}{2} - (c_d - \eta_d)^2 \ln\frac{c_d - \eta_d}{2}\right]$$
$$\left.+(c_d - c_w - \eta_d)\left[(2 - c_d - \eta_d)^2 \ln\frac{2 - c_d - \eta_d}{2} - (c_d + \eta_d)^2 \ln\frac{c_d + \eta_d}{2}\right]\right\} - \tau + (c_d^2 + c_d c_w + c_w^2 - \eta_d^2\gamma)/3.$$

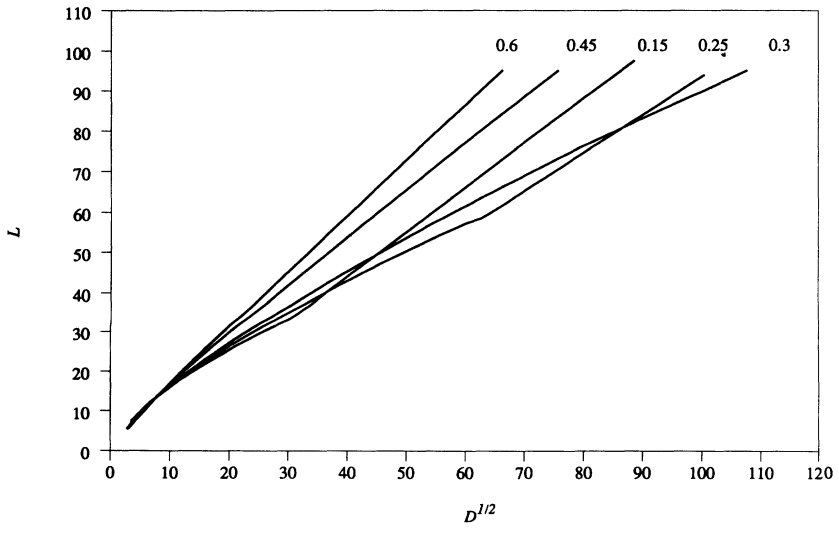

FIG. 3. Twin spacing vs crystal size, both expressed in arbitrary units. The parameter of the curves is T/V. $\bar{c} = 0.9$.

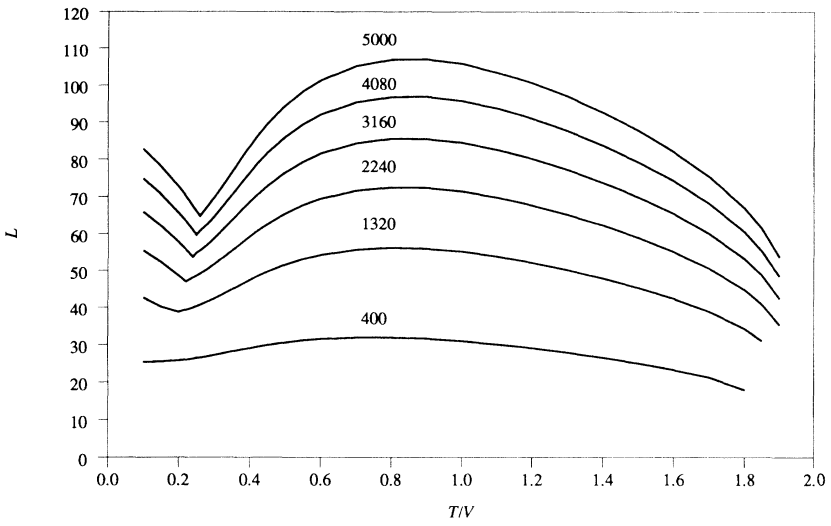

FIG. 4. Twin spacing in arbitrary units vs temperature. The parameter of the curves is D in arbitrary units. $\bar{c} = 0.9$.

Since c_w, c_d, and η_d tend to constants when $L \to \infty$, the L-dependent part of E is proportional to L^{-1}. It means [see Eq. (18) of Ref. 4] that the $L(D)$ dependence is very close to square root one. Figure 3 shows that it is really so. Hereafter I mean under L the optimal value of the twins' period, the result of minimization of energy (9) with respect to η_d, c_d, c_w, w, Δ.

Despite the drastic difference in the properties of two wall types there is no jump from one mechanism to another. Indeed, for the constant temperature when $\bar{c}$ approaches the point of the O-$(T+O)$ transition (c_{cc}, coexistence curve) from inside the miscibility gap, i.e., from the left, $c_d(\infty) \equiv c_{cc}$. When approaching the value of c_{cc} from the right side $c_d(\infty) \to c_{cc}$ also.

IV. $L(T)$ DEPENDENCE

The $L(T)$ dependence is shown in Fig. 4 for different values of D. The decrease at the large values of T near the point of the T-O phase transition ($T/V = 1.98$ for the case of Fig. 4) is easy to predict even without the complicated calculations. There are several articles in which this decrease and subsequent formation of a tweed structure are investigated both experimentally and theoretically (see Refs. 11 and 12, and references therein). At the same time the sharp decrease of L at the low temperatures was observed by Smith and Wohlleben[8] only. The observed abruptness of the changes can be the purely kinetic effect due to the pinning of the walls by the defects of the lattice. The finite length of the monocrystal in the direction perpendicular to the boundary plane can be another reason for the discontinuity because this length can contain only an integer number of periods.

The point of the local minimum corresponds to the transition from O-O walls to O-T-O ones, i.e., to the O-$(T + O)$ transition or decomposition as I shall call it below. It is easy to see that the temperature of the transition depends slightly on the size of the crystal and tends to the strict mean-field limit (≈ 0.37 for the case of Fig. 4) when $D \to \infty$. So the sharp coexistence curve in Fig. 1 must be replaced by the transition zone, the width of which is about $\Delta\bar{c} \approx 0.15$ according to Fig. 4. As a matter of fact the sharpness of the singularities in Fig. 3 and as a consequence in Fig. 4 is connected with the approximation (see Fig. 2) of the solutions of the variational equations for the Lagrangian (7).

V. CONCLUSIONS

(1) A model of the decomposition of the 1:2:3 compounds to the mixture of tetragonal and orthorhombic phases valid for $0 < \delta \lesssim 0.2$ is suggested. According to it a tetragonal phase exists inside the twin boundaries when the parameters correspond to the miscibility gap; the regions of the orthorhombic phase turn out to be the twin domains.

(2) The dependence of the equilibrium twin size on the temperature is investigated. The interval of the temperatures where the period is an increasing function of the temperature is discovered. This provides the explanation for the experiment of Smith and Wohlleben[8] and probably for the singularities in different physical properties of the 1:2:3 compounds observed near $T = 200$ K.[13]

(3) The coexistence curve in the T-$\bar{c}$ phase diagram should be replaced by a transition zone with a finite width. The exact point of the decomposition depends on the size of the monocrystal grains.

ACKNOWLEDGMENT

This work was supported in part by a Soros Foundation Grant awarded by the American Physical Society.

* Present address: Service de Physique de l'Etat Condensé, CE Saclay, 91191 Gif-sur-Yvette Cedex, France.
[1] Y. Yamada, Phys. Rev. B **46**, 5906 (1992).
[2] Y. Zhu, M. Suenaga, J. Tafto, and D. O. Welch, Phys. Rev. B **44**, 2871 (1991).
[3] S. C. Cheng *et al.*, Physica C **184**, 385 (1991).
[4] V. S. Nikolayev, Phys. Lett. A **180**, 157 (1993).
[5] A. G. Khachaturyan, *Theory of Structural Transformations in Solids* (Wiley, New York, 1983).
[6] V. I. Voronkova and V. K. Yanovskii (unpublished).
[7] S. Semenovskaya and A. G. Khachaturyan, Phys. Rev. B **64**, 6511 (1992).
[8] J. F. Smith and D. Wohlleben, Z. Phys. B **72**, 323 (1988); F. M. Mueller *et al.*, Phys. Rev. B **37**, 5837 (1988).
[9] A. G. Khachaturyan, S. V. Semenovskaya, and J. W. Morris, Jr., Phys. Rev. B **37**, 2243 (1988).
[10] A. E. Jacobs, Phys. Rev. B **31**, 5984 (1985).
[11] Y. Zhu, M. Suenaga, and J. Tafto, Philos. Mag. A **66**, 457 (1992).
[12] S. Semenovskaya and A. G. Khachaturyan, Phys. Rev. Lett. **67**, 2223 (1991).
[13] G. Canelli *et al.*, Supercond. Sci. Technol. **5**, 247 (1992).

ELSEVIER

Journal of Hydrology 182 (1996) 19–35

Journal of Hydrology

Water recovery from dew

V.S. Nikolayev[a,1], D. Beysens[a,*], A. Gioda[b], I. Milimouk[a], E. Katiushin[c], J.-P. Morel[d]

[a]*Service de Physique de l'Etat Condensé du Commissariat à l'Energie Atomique, Centre d'Etudes de Saclay, F-91191 Gif-sur-Yvette Cedex, France*

[b]*ORSTOM – BP 5045, F-34032 Montpellier Cedex, France*

[c]*Museum for Regional Study of Feodosia, 11, Lenin Avenue, 334800, Feodosia, Ukraine*

[d]*Centre National de la Recherche Scientifique, URA 284, Université de Provence, F-13621 Aix-en-Provence, France*

Received 28 October 1994; revision accepted 23 September 1995

Abstract

The recovery of clean water from dew has remained a longstanding challenge in many places all around the world. It is currently believed that the ancient Greeks succeeded in recovering atmospheric water vapour on a scale large enough to supply water to the city of Theodosia (presently Feodosia, Crimea, Ukraine). Several attempts were made in the early 20th century to build artificial dew-catching constructions which were subsequently abandoned because of their low yield. The idea of dew collection is revised in the light of recent investigations of the basic physical phenomena involved in the formation of dew. A model for calculating condensation rates on real dew condensers is proposed. Some suggestions for the 'ideal' condenser are formulated.

1. Introduction

Atmospheric humidity can in principle be an alternative source of potable water in the arid and semi-arid zones. Condensation of the atmospheric vapour into water occurs in nature near the ground surface in two different forms: fog and dew. Fog is a cloud of already condensed water droplets. A high relative humidity (in practice 100%) is necessary for the formation of fog. Water collection from fog is a resource in the arid zones where dense fog is frequent. Fog water collection by trees (Gioda

[1] Present address: Bogolyubov Institute for Theoretical Physics, National Ukrainian Academy of Sciences, 252143 Kiev, Ukraine.

* Corresponding author at: DRFMC, CENG, 17 rue des Martyrs, 38054 Grenoble Cedex, France.

SSDI 0022-1694(95)02939-7

Fig. 1. Present state of a tumulus which was thought to be an Early Greek condenser. It is situated on the hills of Tepe-Oba near the old Jewish Cemetery.

et al., 1992) or by synthetic nets is very useful in the low mountain regions close to the ocean. Nowadays, it represents a non-negligible resource especially in Chile and Peru (Schemenauer and Cereceda, 1991; Bouloc, 1993; Gioda et al., 1993a,b).

The formation of dew requires a cold surface, but 100% humidity is not necessary. Thus, dew is common even in the dryer zones of the world. In contrast, fog is rare except in very particular locations like mountainous and coastal areas. This is why the idea of the recovery of dew water by collecting the water condensing on walls of special devices is so attractive.

2. Historical sketch

The history of the devices mentioned began in Feodosia, city of the Crimean peninsula in Ukraine. There is an old myth in science that the Early Greeks who founded Theodosia (Greek name for the present Feodosia) about 6th century BC used dew condensers to fulfil their water needs (Hitier, 1925; Jumikis, 1965; Gioda and Acosta Baladón, 1991). This belief comes from the Russian forester F.I. Zibold who was in charge of some countryside around Feodosia. To prove his theory he built an experimental condenser following what he considered to be an Early Greek condenser (Zibold, 1905, 1907; Hitier, 1925). Because of the importance of this pioneer's research we have investigated carefully the original manuscripts and other related documents as well as the remains of Zibold's construction.

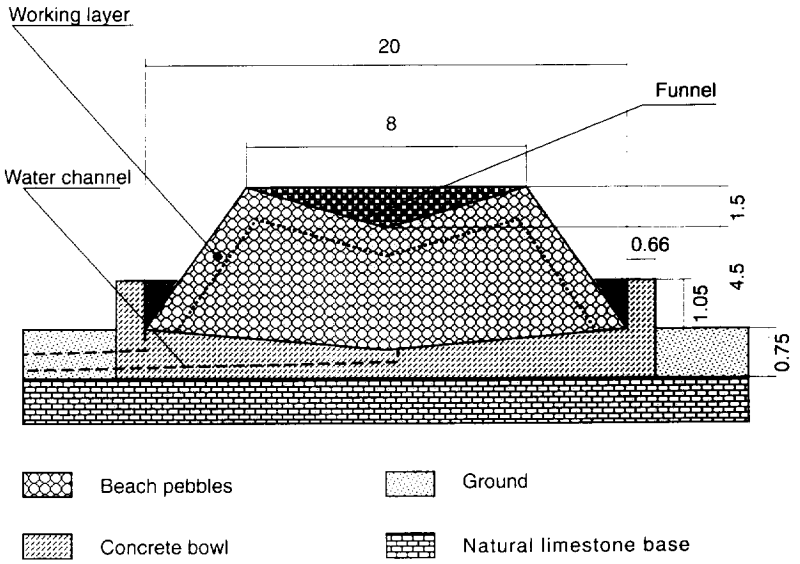

Fig. 2. Section of the condenser of F.I. Zibold (initial state). The slope of the bowl is enlarged for illustrative purposes. All the dimensions are given in m. We have shown the working layer of the condenser by the dotted line.

Zibold (1905) mentioned that "the climate in Feodosia is quite dry, the rains are rare and the droughts during several months are usual". From the Feodosia weather station data, the average annual rainfall is 366 mm and the average number of days with fog during a year is 25. At the same time the conditions suitable for dew formation exist there as masses of humid air, which move from the sea in the evening, rise over the surrounding hills, the so-called Mount Tepe-Oba (c. 300 m a.s.l.) (Totchilov, 1938). While uprising, this humid air cools down and condensation can occur. Zibold mentioned a large quantity of dew but was unable to find any natural water sources in Feodosian forest. The existence of the ancient water supply which is functioning even now (Beysens, 1994; Beysens et al., 1996) whose source remains unknown (Anonymous, 1935) led him to query the purpose of the numerous mounds on Tepe-Oba (Fig. 1). Zibold (1907) excavated around some of them and reported the remains of the ancient pipes and water channels. Finally, he concluded that the mounds were condensers of dew made by Early Greeks. However, at least several of the piles are actually tumuli without any signs of hydraulic purpose including a water supply system (Anonymous, 1935).

Based on the results of the archaeological excavations (Katiushin, 1979), one of us (E.K.) suggested that the chain of mounds described by Zibold is a part of the necropolis of antic Theodosia. Since the 1850s more than 80 mounds in the surroundings of Feodosia have been excavated (Beysens, 1994; Beysens et al., 1996); they turned out to be the tombs either of ancient Greeks or Scythes and then dated to 4th–3rd century BC. These excavations revealed neither tubes nor water channels under the mounds.

Fig. 3. The present state of the remnants of the Zibold condenser.

While the mounds belong to 4th–3rd century BC, most of the water supply tubes which were found on Tepe-Oba and in Feodosia were laid out during the Middle-Ages when Feodosia became a Genoa city called Caffa. Hence, it is unlikely that the mounds and these tubes could function in the same water supply system. Meanwhile, it is possible that Italian inhabitants from Genoa replaced the tubes of the Early Greeks.

To prove that dew can be a source of water, Zibold built a model condenser, a huge truncated cone of sea-beach pebbles with a funnel on the top. It was mounted on a concrete bowl (Fig. 2) with a channel to let condensed water out. The structure was ready by the beginning of 1912 and was said by one Jacob Mironovitch Nikitas, a meteorologist of Zibold's forestry to yield up to 300–360 l of water day^{-1} (Zhukov, 1931; Anonymous, 1935). Unexpectedly, the condenser stopped functioning. A leakage of the bowl was suspected (Anonymous, 1915) and then the cone of pebbles was demolished. However, the bowl is still visible (Fig. 3). Topological measurements (Beysens, 1993) show that the slope between the perimeter and the centre of the bowl is now half that reported in the 1912 documents. Thus, settling of the condenser base has occurred. It is hard to say if the leakage was the principal reason of low yield. Unfortunately, no documents concerning the functioning of the condenser are available.

Zibold's attempt inspired the experiments performed in the South of France from 1928 to 1957 by French hydrologists L. Chaptal and M. Goddard and the Belgian engineer A. Knapen (Chaptal, 1932; Jumikis, 1965 and references therein). Their

installations, which they called "aerial wells", were very massive. The best of them yielded several litres of condensed water a day. After 1957, there was no reported attempts to recover water from vapour despite the attractiveness of this idea.

The main reason for the failures of these constructions may be found in the idea on which their creation was based. F.I. Zibold's ideas on the hydrological cycle were close to Aristotle's conception which was far from the conception of Perrault, Mariotte, and Halley (17th–18th century), i.e. the modern theory (L'Hôte, 1987). He believed that water forms continuously in the soil, as atmospheric air penetrates the pores and fissures in the ground; cooling condenses water which then accumulates and finally rises to the surface in the form of springs and rivers (Galbrecht, 1987). Hence, the tumuli which are located at the top of the hills may have been mistaken for springs.

3. Model for condensation in Zibold-type condensers

Since the 1950s the formation of dew has been investigated both by physicists and by hydrologists. The objects of the physical investigation are 'breath figures', i.e. the condensation of water on a surface, e.g. on a piece of glass (Beysens et al., 1991). Agrometeorologists are interested in dew formation in nature (Monteith, 1957; Pedro and Gillespie, 1982a, b); in particular, Lhomme and Jimenez (1992) were interested in dew on banana plantations because there is a close link between dew and cryptogamic development on the leaves. Environmental scientists study the dew as a source of acid pollution (Pierson et al., 1986; Janssen et al., 1991).

Dew formation on a surface requires cooling of the latter, generally by thermal irradiation during the night. Alternatively, cooling can occur due to the thermal contact with the ground if the ground is cooler. But at depth the temperature of the soil corresponds to the average daily temperature and remains constant. Thus, this ground level functions like a furnace which heats the ground surface during the night due to the thermal conductivity. An object which is thermally isolated from the ground lacks such a source of heating and thus its temperature can be lower. Hence, engineers of condensers should avoid good thermal contact with the ground. This statement is the first (though not the main) reason for the failure of the condensers in Southern France which had the concrete shells with massive foundations (Jumikis, 1965). Zibold's installation consisted of rather large (15–40 cm in diameter) pebbles of rounded form. The pebbles thus had weak physical and thermal contact with each other and with the bowl. Thus we can neglect this kind of thermal loss in our rough approximation. Moreover, due to the small thermal conductivity we can assume that temperature varies with time only on a small part of the condenser. Indeed, only two or three surface-layers of pebbles can perform the irradiation heat exchange with an environment. Also, the fresh humid air cannot penetrate deep into the pile of stones. Therefore we shall consider the working layer to be of the depth 0.3 m (see Fig. 2). This depth corresponds to three layers of 0.15 m diameter pebbles out of which the outer layers of Zibold's condenser were made. All this working part as well as the condensed water will be supposed to have a uniform temperature T_c. We assume also that the pebbles themselves take only

a half of the volume of this layer when estimating its mass. The heat balance equation for the condenser is

$$\frac{dT_c}{dt}(Mc_c + mc_w) = R_i + R_{he} + R_{cond}, \tag{1}$$

where the left-hand side represents the rate at which the amount of heat of the condenser changes, M and m are the masses of the working part of the condenser and condensed water respectively, c_c and c_w are the specific heats of the material of the condenser and water; t is time. Hereafter, SI units are supposed for all the values except temperature which is expressed in Celsius degrees. The variables in the right-hand side represent the different physical processes due to which the heat energy comes to or leaves the condenser surface: R_i (W) is the irradiation, R_{he} (W) is the heat exchange with the surrounding air, R_{cond} (W) is the energy gain due to the latent heat of the condensation (L per unit mass). Thus

$$R_{cond} = L\frac{dm}{dt}. \tag{2}$$

The heat exchange term can be expressed in the usual form as

$$R_{he} = S_c a(T_a - T_c), \tag{3}$$

where a is a heat transfer coefficient, T_a is the air temperature. S_c is the surface area which takes part in heat exchange with the air. Due to the porous structure of the condenser the fresh air penetrates into it and goes out constantly. That is why the value of S_c is larger than the external surface of the condenser S_i and depends on the wind speed u: the increase of u causes deeper penetration and thus a larger value of S_c. a relates to the width of the aerodynamical boundary air layer and thus depends on u too (see Beysens et al., 1991). The formula (Pedro and Gillespie, 1982a)

$$a = f\sqrt{u/D}, \tag{4}$$

in which the numerical factor $f = 4$ (W K^{-1} m^{-2} s$^{1/2}$) is empirical for the flow parallel to a plane sheet of size D. As a rough estimate $D \approx \sqrt{S_i/2}$.

The total irradiation term from Eq. (1) can be divided into several parts:

$$R_i = R_b + R_l + R_s - R_c. \tag{5}$$

R_b is the direct beam irradiation, R_l and R_s are the long-wave and short-wave parts of the diffuse incoming irradiation and R_c is the outgoing irradiation of the condenser which is so important. It can be represented by

$$R_c = S_i \epsilon_c \sigma (T_c + 273)^4, \tag{6}$$

where σ is the Stephan–Boltzmann constant and ϵ_c is the emissivity of the condenser. The long-wave and short-wave radiation terms are given by Pedro and Gillespie (1982a) (below, it is assumed that clouds are absent):

$$R_l = S_i \epsilon_s \epsilon_c \sigma (T_a + 273)^4, \tag{7}$$

$$R_s = S_i R_{sol} \frac{d}{2}(1 - A^q)\sin\alpha, \tag{8}$$

where ϵ_s is the emissivity of the sky, R_{sol} is the solar constant (1350 W m^{-2}), d is the short-wave absorptivity of the condenser, A is the atmospheric transmission constant, $q = 1/\sin\alpha$, where α is defined as the angle of elevation of the Sun over the horizon. The coefficient ϵ_s in (7) depends on the vapour pressure, but the dependence is very weak. For average conditions, $\epsilon_s \approx 0.82$.

It is supposed that night comes when α becomes equal to zero (though it is not exactly so; due to the atmospheric refraction, night comes when $\alpha = -36'36''$). α can be estimated by the classical expression (Campbell, 1977)

$$\sin\alpha = \sin\phi\sin\delta + \cos\phi\cos\delta\cos[\pi(t-12)/12], \tag{9}$$

where t is the time of day in h, ϕ is the latitude of the place (for Feodosia $\phi = 45°01'45''$) and δ is a solar declination.

The estimation of the direct beam irradiation is a slightly more difficult problem. It can be represented by the expression

$$R_b = S_p R_{sol} d A^q, \tag{10}$$

where S_p is a surface of a geometrical projection of the condenser on the plane perpendicular to the direction of the beams. Since this direction is defined by α, S_p is a function of α. For example for the horizontal plane

$$S_p = S\sin\alpha, \tag{11}$$

for the vertical plane

$$S_p = S\cos\alpha, \tag{12}$$

where S is the surface of the plane. For the plane which has an angle

$$\alpha_{max} = \pi/2 - \phi + \delta \tag{13}$$

with the horizon $S_p = 0$, since such a plane will be parallel to the solar beams all day long. In all the cases, the planes are supposed to be parallel to the direction East–West. For the truncated cone (see Appendix)

$$\begin{aligned} S_p &= (R^2 - r^2)\sin\alpha[(\tan^2\beta\cot^2\alpha - 1)^{1/2} - \arccos(\tan\alpha\cot\beta)] \\ &\quad + \pi R^2\sin\alpha, \qquad \text{if } 0 < \alpha < \beta \\ S_p &= \pi R^2\sin\alpha, \qquad \text{if } \beta < \alpha < \pi/2 \end{aligned} \tag{14}$$

where R and r are the radii of the base and the top of the cone, $\tan\beta = h/(R-r)$ and h is the height of the cone.

The equation for m represents the condensation rate:

$$\frac{dm}{dt} = \begin{cases} S_c b(p_v - p_c(T_c)), & \text{if} \quad p_v > p_c(T_c) \\ 0, & \text{otherwise.} \end{cases} \tag{15}$$

Here p_v is the partial pressure of the water vapour in the atmosphere which is considered constant during the night. $p_c(T_c)$ is the vapour pressure over the condenser at which condensation on its surface begins. b is proportional to a in Eq. (4):

$$b = 0.656a/(pc_a), \tag{16}$$

where p is the atmospheric pressure and c_a is the specific heat of air. This expression

Table 1
Values of physical parameters which are used for the calculations

Parameter	Notation	Value
Sky emissivity	ϵ_s	0.8
Emissivity of condenser	ϵ_c	0.9
Short-wave absorptivity of the condenser	d	0.5[a]
Atmospheric transmission constant	A	0.84
Specific heat of water	c_w	$4.18 \cdot 10^3$ (J kg^{-1} K)
Specific heat of stones	c_c	$1.09 \cdot 10^3$ (J kg^{-1} K)
Specific heat of air	c_a	$1.01 \cdot 10^3$ (J kg^{-1} K)
Density of stones	–	$2.5 \cdot 10^3$ (kg m^{-3})
Latent heat of condensation	L	$2.26 \cdot 10^6$ (J kg^{-1})

[a] For white beach pebbles.

as well as the numerical factor comes from the calculations of the vapour transfer coefficient (Pedro and Gillespie, 1982a).

Generally speaking, $p_c(T)$ does not coincide with the saturation pressure of the water vapour $p_s(T)$ and depends on the degree of wetting of the surface by the water which can be characterized by the contact angle (Zhao and Beysens, 1995). For the surface which is incompletely wetted by water (such as for ordinary surfaces which are inevitably coated by some oil or grease) (Beysens et al., 1991), $p_c(T) \leqslant p_s(T)$. We consider for the sake of simplicity the case

$$p_c(T) = p_s(T), \tag{17}$$

although in reality $p_c(T) < p_s(T)$.

Evaporation is neglected (cf. the second option in Eq. (15)) and it is assumed that all condensed water flows immediately into a container inside the condenser. The water is removed from the container as soon as condensation stops.

The day of 8 April 1992 has been chosen for the calculation as it is typical of the spring and fall seasons during which the condensation is the largest (Totchilov, 1938). For this day $\delta \approx 7°$ (Campbell, 1977); the maximum and minimum air temperatures for that sunny day were 15.2°C and 9.5°C, respectively, the atmospheric pressure was 750 mm Hg and the maximal relative humidity for the Tepe-Oba mountain at night was 97%. This corresponds to the dew point temperature $T_d = 9$°C. We suggest also that the variation of T_a is assumed sinusoidal with the period of 24 h and the maximum at 13 h 30 min. This delay with respect to the maximum of sun irradiation (12 h) is usual. The other physical constants for the simulation are given in Table 1.

4. Numerical simulation of Zibold's condenser

Now that all the parameters of the set of Eqs. (1)–(15) have been defined, the set

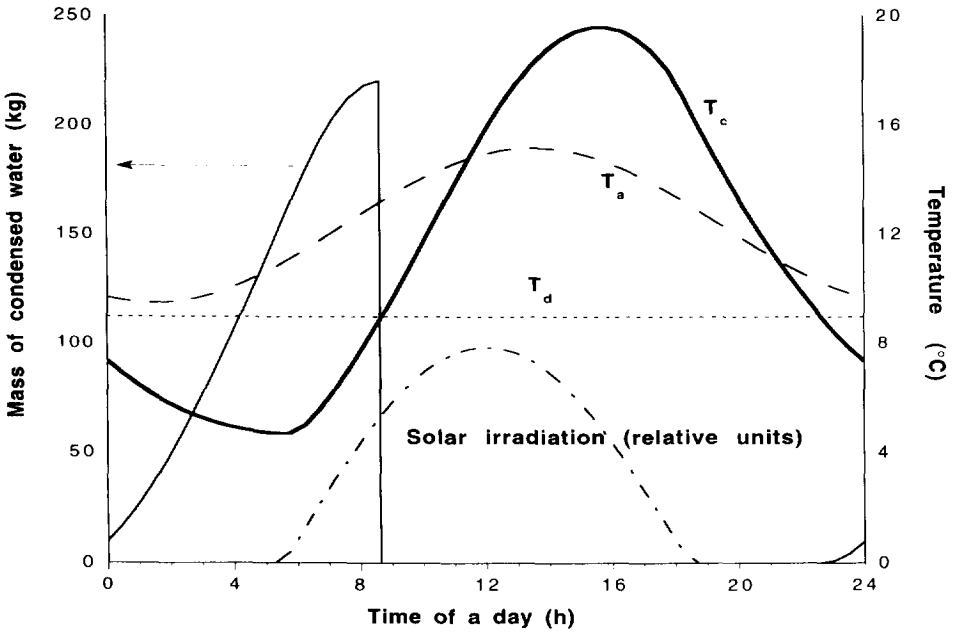

Fig. 4. Day evolution of the temperatures of the Zibold condenser (T_c) and the surrounding air (T_a) as well as the mass of condensed water inside the condenser. The evolution of the solar irradiation intensity and dew point temperature (T_d) is shown also. $u = 10$ m s^{-1}.

can be solved numerically. The conditions

$$T_c(0\text{ h}) = T_c(24\text{ h}),$$

$$m(0\text{ h}) = m(24\text{ h})$$

have to be specified to provide a periodical (with the period of 24 h) change of all the physical values.

The simulation shows that during the day of 09/04/1992 Zibold's condenser would yield 221 l of water. This result is in good agreement with the reported data — 300–360 l. The evolution of all the important parameters is shown in Fig. 4. Condensation stops at about 09:00. The dash–dotted line represents the intensity of the direct beam irradiation of the horizontal plane during the day. The condensation starts 4 h after the sunset when T_c approaches T_d. Unfortunately there are no other available data concerning the functioning of the condenser and so a more detailed comparison is impossible.

The ratio S_c/S_i has been assumed to be equal to 2 due to the penetration of the fresh air into the condenser for a rather strong wind ($u = 10$ m s^{-1}). When the wind is weaker, the fresh humid air penetrates to a smaller depth into the pebble pile and this ratio is smaller. The results for different velocities are presented in Table 2. For the case of Zibold's condenser the water yield is an increasing function of the wind velocity.

Table 2
Water yield of Zibold's condenser depending on the wind speed

Wind speed (m s^{-1})	S_c/S_i	Water yield (l)
10	2	221
5	1.5	155
1	1.1	61

5. Simulation of Zibold-type condensers

One can distinguish two limiting types of condensers. The first are massive, with $S_c > S_i$, 'Zibold-type condensers'. For these it is assumed that $S_c/S_i = 2$ in the following. The representative of the second type is a 'grass-like' condenser which is simply a sheet of some light material with both sides working as a condenser. Hence, for these $S_c = S_i$. The water yield of the first type depends strongly on direct solar irradiation which is determined by the value $S_p < S_i$, Eq. (10). S_p, in turn, depends on the shape of the condenser. To generalize the model the shape factor has been excluded from the consideration by defining an effective surface of irradiation S_{eff}, $S_p < S_{eff} < S_i$. S_{eff} is the area of a horizontal plane whose total irradiation balance during the day is very close to that of the real condenser. Hence S_{eff} should be

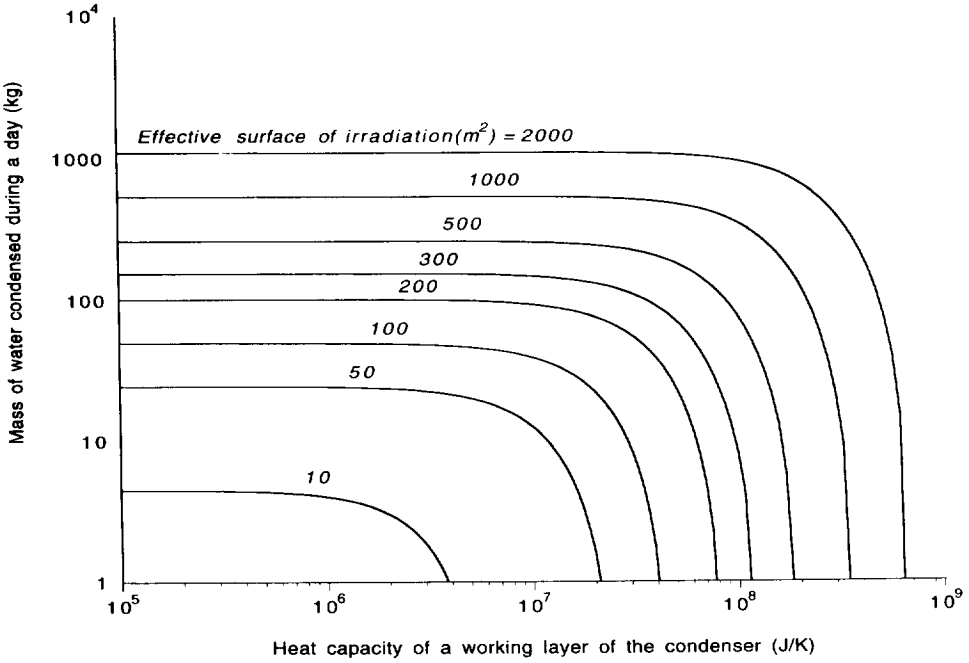

Fig. 5. Mass of water condensed during the day versus heat capacity of the working layer of the Zibold-type condenser. $u = 10$ m s^{-1}.

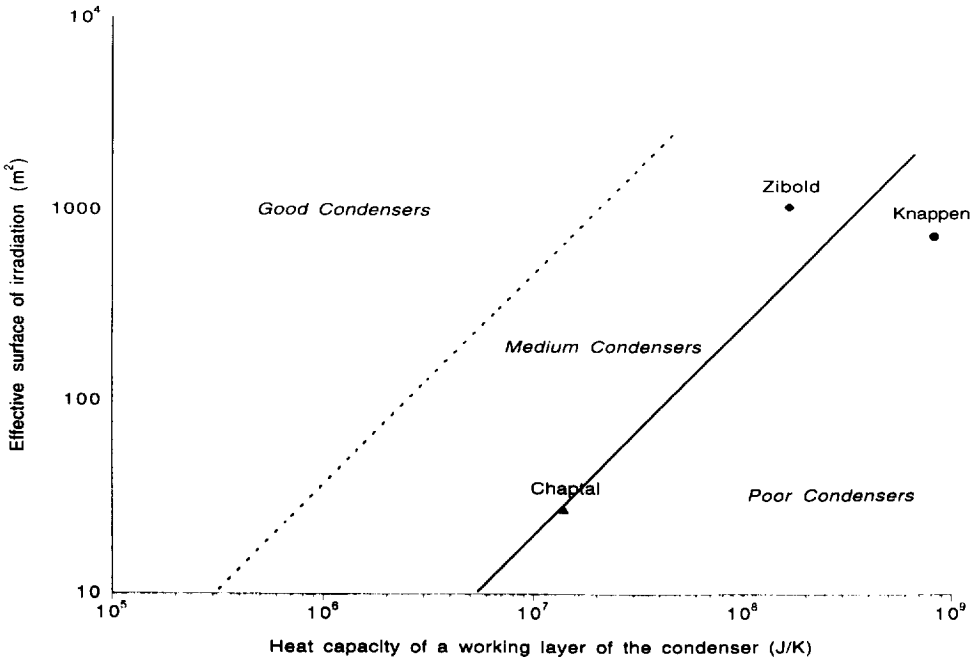

Fig. 6. Diagram of the Zibold-type condensers. For explanations see the text.

substituted for S_i in Eqs. (6)–(8). Then in (10) we mean under S_p the value from (11) where we should substitute S_{eff} for S also.

For the sake of comparison the same meteorological data and the same values of material constants (Table 1) will be applied as for the case of Zibold's condenser.

The dependence of water yield on the heat capacity Mc_c of the working layer is shown in Fig. 5. The condenser will work ($m > 0$) if Mc_c is less than some limiting value which depends on S_{eff} (this dependence is presented in Fig. 6 as a solid line); the large thermal inertia of the massive working layer may not permit cooling below the dew point temperature during the night (see Fig. 4). The water yield grows very quickly as Mc_c decreases and soon reaches saturation. The dependence of this value of Mc_c where saturation is reached (the point where m is less by 5% than the saturation value) on S_{eff} is depicted in Fig. 6 as a dashed line. The lower the working mass of the condenser, the higher the water yield.

Saturation takes place due to the interplay of two effects: thermal inertia and irradiation. When Mc_c is small the temperature evolution will not depend on its value. Then the kinetics is defined by other terms in Eq. (1), mostly by the irradiation term. In this case the heat capacity of the condenser can be neglected as occurred in the studies of dew on leaves (Pedro and Gillespie, 1982a, b; Lhomme and Jimenez, 1992).

Two lines in Fig. 6 divide the $S_{eff}-Mc_c$ plane into three regions of good, medium and poor condensers. This diagram is not universal; its exact shape will depend slightly on the meteorological conditions and the constants of the materials of real

Table 3
Estimated physical parameters of the different devices

Inventor	M, 10^3 kg	S_i, m^2	S_{eff}, m^2
Zibold	152	854	1075
Chaptal	12.8	22	27.7
Knappen	759	601	757

structures. Nevertheless, it suffices to compare the quality of the condensers since the parameters S_{eff} and Mc_c are the most important. We compare here the quality of Zibold's condenser to the quality of two experimental devices, detailed data on which are available from the literature — Chaptal's first captor in Montpellier and Knappen's aerial well in Trans-en-Provence. The estimated parameters of them are summarized in Table 3.

The corresponding points are depicted in Fig. 6. The positions of the points are in good agreement with the experimental results of the inventors. In fact, both devices were not good condensers giving only several litres of water on the best days. But Chaptal's structure was the more efficient taking into account its smaller size.

It appears that the main fault of the condensers was their large mass.

6. Simulation of 'grass-like' condensers

The leaves of plants represent nearly ideal dew condensers although their surface is hydrophobic. A good wetting by water is essential to facilitate the condensation with the lower partial vapour pressure p_v (Zhao and Beysens, 1995). In addition, the separate drops do not flow quickly from the surface of the leaves so that evaporation of those drops may occur when the sun shines in the morning. A sheet of some polymer material is more suitable for these studies. For a polyethylene sheet with a thickness 0.5 mm, density $0.95 \cdot 10^3$ kg m^{-3} and specific heat $c_c = 1.9 \cdot 10^3$ J kg^{-1} K, the water yield m versus the surface area S of one side of the sheet is presented in Fig. 7. The inertial term in Eq. (1) is small for this case and the temperature follows mainly the change in irradiation.

Three angles of the sheets with the horizon were simulated: α_{max} defined by (13), 0° and 90°. In all the cases the sheets are supposed to be parallel to the direction East–West. Due to the small thermal inertia, the difference in yield of water depends only slightly on the angle. But the difference is drastic in the maximal temperature of the sheets: for the horizontal or vertical sheets it is about 60°C, for the inclined one is about 15°C. The dependence on the wind speed u for this case seems to be unusual — the water yield decreases with the increase of u. This is because an increase in air velocity has two consequences: it increases the condensation rate (b, Eq. (16)) and it increases the heat exchange with outer air (a, Eq. (4)). Because during most of the day $T_c < T_a$ (see Eq. (3)), the second effect leads to a heating of the sheet while

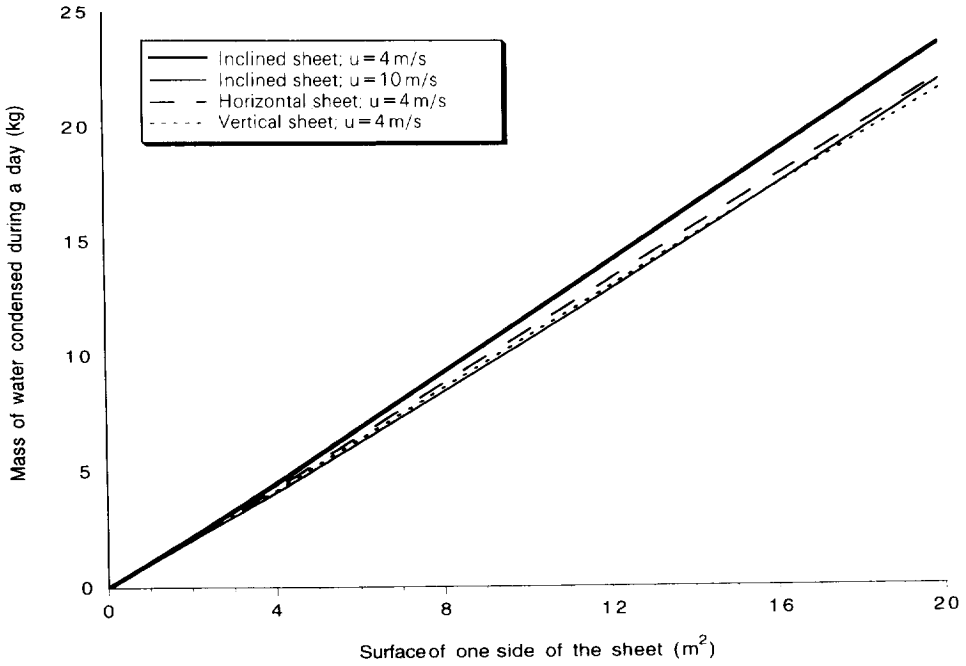

Fig. 7. Mass of water condensed during the day versus surface of one side of the polyethylene sheet with the thickness 0.5 mm.

the first leads to a cooling. For a thin sheet (in contrast to the Zibold-type condenser) the heating appears to be stronger with an increase in u.

The small curvature of $m(S)$ lines in Fig. 7 is due to the velocity dependence of the heat transfer coefficient.

7. Conclusions

This paper investigated the history and functioning of dew condensers. It is difficult to strictly refute Zibold's hypothesis concerning the Early Greek condensers. This would need extensive excavation work. The Tepe-Oba mountain is fissured by the remains of a sophisticated system of ancient water supply and tubes can be found within hundreds of metres of every mound. But excavations of more than 80 mounds did not reveal any signs of a hydraulic system. On the contrary, tombs were found in each of them. Where water still comes out of the broken water supply, it contains dissolved minerals and thus does not come out of condensers, because condensed water is almost distilled. Moreover, the dry remains of the ancient water tubes are covered (inside) by a thick layer of mineral deposits. Hence, it is thought that there were no ancient dew condensers in the surroundings of Feodosia.

We describe the main physical principles of the functioning of dew condensers and suggest a model to simulate them. It turns out that Zibold's condenser might

have been the most successful experimental device among those that ever existed; its yield was of the order of 100–200 l of water day^{-1}.

We suggest a simple diagram (Fig. 6), which can be used to estimate the quality of the massive ('Zibold-type') condenser and compare it with the other constructions.

The huge mass of the devices was their main fault. It caused the large thermal inertia which did not allow them to cool during the night and thus the conditions for the dew formation were poor. The creators of the massive condensers were not aware that the cooling is, in fact, due to irradiation, and they tried to increase the condensation surface, not the irradiation surface. It is their second fault. Their third fault was a too high thermal contact with the ground. The temperature of a good condenser is lower than ground temperature during most of the day. Thus, the ground heats the condenser. The decrease of its quality is a consequence.

Hence the 'ideal' condenser should be 'grass-like', i.e. a light sheet thermally isolated from the massive parts and the ground. It is very important that its surfaces should be open to let them irradiate the energy into space. It means that nothing that can reflect the infrared irradiation of the condenser should be placed near its surface and vice-versa, the condenser itself should be placed far enough from such surfaces, e.g. the ground to avoid the 'greenhouse' effect. In practice, a sheet of some (polymer) film would be suitable. The material of the sheet should be well (ideally completely) wetted by the water to decrease the nucleation barrier. The place of the condenser should be chosen on an open area but where the winds are not strong and dew is frequent (i.e. where humidity is high enough).

A sheet of polyethylene, assuming that there is no evaporation and that all the condensed water flows into a vessel, should yield approximately 1 l m^{-2} under the meteorological conditions defined above.

Hence, practical utilization of dew water contained in the air seems possible. Using the present study, engineers of future dew condensers will be able to obtain a volume of very clean water.

Acknowledgements

The authors thank Mr Dmitri Novitski, Mayor of Feodosia in Crimea, and Mr Jean-Pierre Porthelet, Mayor of Trans-en-Provence in France, for their warm welcome. Valuable scientific information was obtained from Dr Alexander Zibold (F.I. Zibold's grandson), his wife Katerina (Donetsk) and Prof. V.N. Dublyansky (Simferopol State University). Mrs A. Wasowicz (Warsaw, Poland) provided precious help because of her Early Greek archaeological knowledge of the Crimea. The French Embassy in Kiev is thanked for funding expeditions to Feodosia (in 1993 and 1994). The contribution of the European Center for Advanced Studies in Thermodynamics to the 1994 mission is also acknowledged. J.-P. Lhomme is thanked for the critical reading of this article. One of the authors (V.N.) would like to thank the collaborators of SPEC Saclay for their kind hospitality.

Appendix

To obtain Eq. (14), i.e. to find S_p for the truncated cone, first find it for a full cone with base radius R and height H such that

$$H/R = h/(R - r) = \tan\beta. \tag{A1}$$

Then the truncated cone is a part of the full cone. Assume that $\alpha \leqslant \pi/2$ — if not, one should substitute $\pi - \alpha$ for α in the final expression.

To calculate S_p for the cone, substitute for the cone the regular pyramid with the same top and with all the base vertices lying on the circle — the base of the cone. Obviously, all the characteristics of the pyramid will tend to those of a cone as the number of vertices tends to infinity. Choose the reference point O of the Cartesian coordinates at the centre of the base, the axis OZ as the vertical one and axis OX so that the Sun will be in the XOZ plane. Then the plane defined by the equation

$$z + x\cot\alpha = 0 \tag{A2}$$

is perpendicular to the direction of solar beams — it is the projection plane. The sides of the pyramid differ by the polar angle γ (in the plane XOY with respect to the point O and axis OX) of one of the bottom summits. The other one has the angle $\gamma + d\gamma$ where $d\gamma$ tends to zero as the number of summits tends to infinity. Then the equation of the geometrical plane, which contains the side as its part, is

$$x\cos\left(\gamma + \frac{d\gamma}{2}\right) + y\sin\left(\gamma + \frac{d\gamma}{2}\right) + (z - H)\frac{R}{H}\cos\left(\frac{d\gamma}{2}\right) = 0. \tag{A3}$$

The surface of this side is $dS = \sqrt{H^2 + R^2}Rd\gamma/2$. Now S_p is defined as a sum which is transformed into the integral when $d\gamma \to 0$:

$$S_p = \int \cos\xi dS$$

$$= \sqrt{H^2 + R^2}\frac{R}{2}\int \cos\xi d\gamma. \tag{A4}$$

ξ is an angle between two inscribed planes, which can be found out of Eqs (A2) and (A3) by the straightforward application of the known formula of analytical geometry and is given by

$$\cos\xi = \sin\beta\cos\alpha\cos\gamma + \cos\beta\sin\alpha. \tag{A5}$$

It follows from Eq. (A5) that when $\alpha > \beta$, i.e. when all the surface of the cone is exposed to the solar irradiation, ξ is always less then $\pi/2$. Thus the integration in (A4) should be performed from 0 to 2π yielding

$$S_p = \pi R^2 \sin\alpha. \tag{A6}$$

When $\alpha < \beta$, the sides which have $\xi > \pi/2$ are not exposed to the solar irradiation. Taking into account that $\xi < \pi/2$ if $\gamma_1 < \gamma < 2\pi - \gamma_1$, where $\gamma_1 = \arccos(-\tan\alpha\cot\beta)$,

as it follows from Eq. (A5), S_p should be computed as a sum of two integrals (A4): the first from 0 to γ_1 and the second from $2\pi - \gamma_1$ to 2π. Hence,

$$S_p = R^2 \sin\alpha[(\tan^2\beta\cot^2\alpha - 1)^{1/2} + \pi - \arccos(\tan\alpha\cot\beta)] \quad \text{(A7)}$$

is valid when $\alpha < \beta$ for the full cone.

Now the cone can be truncated 'cutting' its topmost part. Evidently, Eq. (A6) is valid for this case when $\alpha > \beta$, since the square of the projection will not depend on inner details (this is also the reason why S_p does not depend on the presence of the funnel). To obtain the first part of Eq. (14) (for $\alpha < \beta$), the value of S_p for the cone with the base radius r and the same angle β (topmost part) has to be subtracted and the square of the projection of the upper base $\pi r^2 \sin\alpha$ added.

References

Anonymous, 1915. Proceedings of the inspection of the condenser, which was built in the Feodosian forest. 19.06.1915 (in Russian, manuscript kept in the Feodosian Museum). French Translation: Rapport CEA-Saclay, 1995, DIST, No. 95002495.

Anonymous, 1935. Stenograph of the proceedings of the 1st Conf. on the condensation of the atmospherical water vapour (Aerial well). Moscow, Leningrad (in Russian, manuscript kept in the Feodosian Museum). French Translation: Rapport CEA-Saclay, 1995, DIST, No. 95002495.

Beysens, D., 1993. Rapport de la mission franco-ukranienne effectuée à Féodosia (Crimée, Ukraine) en Septembre–Octobre 1993 (unpublished).

Beysens, D., 1994. Rapport de la mission franco-ukranienne effectuée à Féodosia (Crimée, Ukraine) en Août 1994 (unpublished).

Beysens, D., Steyer, A., Guenoun, P., Fritter, D. and Knobler, C.M., 1991. How does dew form? Phase Transitions, 31: 219–246.

Beysens, D., Gioda, A., Katioushine, E., Milimouk, I., Morel, J.-P. and Nikolayev, V., 1996. Les puits aériens. La Recherche, in press.

Bouloc, J., 1993. De la toile d'araignée ... au piège à brouillard. La Houille Blanche, 5: 337–344.

Campbell, G.S., 1977. An Introduction to Environmental Biophysics. Springer Verlag, New York.

Chaptal, L., 1932. La captation de la vapeur d'eau atmosphérique. La Nature, 60(2893): 449–454.

Galbrecht, G., 1987. Hydraulic engineering, hydrology and hydraulics in Antiquity. ICID Bull., 36: 1–10.

Gioda, A. and Acosta Baladón, A.N., 1991. Les puits aériens de Théodosia, de Montpellier et de Trans. Sécheresse, 2: 215–219.

Gioda, A., Acosta Baladón, A., Fontanel, P., Hernández Martin, Z. and Santos, A., 1992. L'arbre fontaine. La Recherche, 23: 1400–1408.

Gioda, A., Beysens, D. and Acosta Baladón, A., 1993a. Dew and atmospheric wells in mediterranean climates. In: A. Becker, B. Sevruk and M. Lapin (Editors), Proc. Symp. on Precipitation and Evaporation, 20–24 September 1993, Bratislava, Slovakia, Swiss Federal Institute of Technology, Zurich, Switzerland, 3: 279–284.

Gioda, A., Espejo Guasp, R. and Acosta Baladón, A., 1993b. Fog collectors in the tropics. In: A. Becker, B. Sevruk and M. Lapin (Editors), Proc. Symp. on Precipitation and Evaporation, 20–24 September 1993, Bratislava, Slovakia, Swiss Federal Institute of Technology, Zurich, Switzerland, 3: 273–278.

Hitier, H., 1925. Condensateurs des Vapeurs Atmosphériques dans l'Antiquité. Comptes-Rendus Académie d'Agriculture, Paris, pp. 679–683.

Janssen, L.H.J.M., Römer, F.G. and Kema, N.V., 1991. The frequency and duration of dew occurrence over a year. Model results compared with measurements. Tellus, 43B: 408–419.

Jumikis, A.R., 1965. Aerial wells: secondary sources of water. Soil Sci. 100: 83–95.

Katiushin, E.A., 1979. Excavations in the Surroundings of Feodosia. Arheologitcheskie otkrytija 1978 goda, Nauka, Moscow, pp. 334–339 (in Russian).

L'Hôte, Y., 1987. Rappel de l'historique du concept du cycle de l'eau dans la culture occidentale. IAHS Publ., 164: 37–45.

Lhomme, J.-P. and Jimenez, O.F., 1992. Estimating dew duration on banana and plantain leaves from standard meteorological observations. Agric. For. Meteorol., 62: 263–274.

Monteith, J.L., 1957. Dew. Q. J. Royal Meteorol. Soc., 83: 322–341.

Pedro, M.J. and Gillespie, T.J., 1982a. Estimating dew duration. I. Utilizing micrometeorological data. Agric. Meteorol., 25: 283–296.

Pedro, M.J. and Gillespie, T.J., 1982b. Estimating dew duration. II. Utilizing standard weather station data. Agric. Meteorol., 25: 297–310.

Pierson, W.R., Brachaczek, W.W., Gorse, R.A., Japar, S.M. and Norbeck, J.M., 1986. On the acidity of dew. J. Geophys. Res., 91: 4083–4096.

Schemenauer, R.S. and Cereceda, P., 1991. Fog-water collection in arid coastal locations. Ambio, 20: 303–308.

Totchilov, V.I., 1938. Condensers of Feodosia and the conditions of condensation in the surroundings. Soviet Water Works Sanitary Eng., 1: 61–67 (in Russian). French Translation: Rapport CEA-Saclay, 1995, DIST, No. 95002495.

Zhao, H. and Beysens, D., 1995. From droplet growth to film growth on a heterogeneous surface: condensation associated with a wettability gradient. Langmuir, 11: 627–634.

Zhukov, N.N., 1931. About the ancient hydrotechnical constructions in the surrounds of Feodosia. In: Feodosian Section of the Society of Crimea Study and the Museum of Archeology (Editors), Collection of the articles on economy, mode of life and history of Feodosian region, No. 1, Feodosia (in Russian). French Translation: Rapport CEA-Saclay, 1995, DIST, No. 95002495.

Zibold, F.I., 1905. The role of underground dew in water supply of Feodosia. Trudy opytnyh lesnitchestv, No. III (in Russian, manuscript kept in the Feodosian Museum). French Translation: Rapport CEA-Saclay, 1995, DIST, No. 95002495.

Zibold, F.I., 1907. The experiment of the ancient-Theodosian way of potable water extraction. Lecture given in Feodosia (in Russian, manuscript kept in the Feodosian Museum). French Translation: Rapport CEA-Saclay, 1995, DIST, No. 95002495.

VOLUME 76, NUMBER 17 PHYSICAL REVIEW LETTERS 22 APRIL 1996

New Hydrodynamic Mechanism for Drop Coarsening

Vadim S. Nikolayev,* Daniel Beysens, and Patrick Guenoun
Service de Physique de l'Etat Condensé, CE Saclay, F-91191 Gif-sur-Yvette Cedex, France
(Received 9 March 1995)

We discuss a new mechanism of drop coarsening due to coalescence only, which describes the late stages of phase separation in fluids. Depending on the volume fraction of the minority phase, we identify two different regimes of growth, where the drops are interconnected and their characteristic size grows linearly with time, and where the spherical drops are disconnected and the growth follows $(\text{time})^{1/3}$. The transition between the two regimes is sharp and occurs at a well defined volume fraction of order 30%. [S0031-9007(96)00006-3]

PACS numbers: 64.60.–i, 47.55.Dz, 83.70.Hq

In this Letter we concentrate on the kinetics of the late stages of the phase separation. This subject has received considerable attention recently [1–4]. Most of the experiments on growth kinetics have been performed near the critical point of binary liquid mixtures (or simple fluids) because there the critical slowing down allows the phenomenon to be observed during a reasonable time. After a thermal quench from the one-phase region to the two-phase region of the phase diagram (Fig. 1), the domains of the new phases nucleate and grow. It turns out that two alternative regimes of coarsening are possible. The first can be observed when the volume fraction ϕ of the minority phase is lower than some threshold [5], and the domains of the characteristic size R grow according to the law $R \propto t^{1/3}$ (t is the time elapsed after the quench) as spherical drops. The second regime manifests itself when the quench is performed at high volume fraction, the coarsening law is $R \propto t^1$, and the domains grow as a complicated interconnected structure. Recent experiments [2] show that when $0.1 < \phi < 0.3$ the $t^{1/3}$ growth can be explained by a mechanism of Brownian drop motion and coalescence rather than the Lifshitz-Slyozov mechanism [6] which holds for $\phi \to 0$ and which we will not discuss here. We are interested in the late stages of growth when phase boundaries are already well developed and the concentrations of the phases are very close to the equilibrium values at given temperature T as defined by the coexistence curve (Fig. 1). Then the drops grow just because the system tends to minimize the total surface separating the phases (i.e., due to coalescence) and ϕ no longer depends on time.

Brownian coalescence.—The Brownian mechanism was considered first by Smoluchowski [7] for coagulation of colloids and was then applied to phase separation by Binder and Stauffer [8] and Siggia [9]. According to this mechanism, the rate of collisions per unit volume due to the Brownian motion of spherical drops in the liquid of shear viscosity η is

$$N_B = 16\pi D R n^2 f(\phi), \tag{1}$$

where n is an average number of drops per volume, R is the average radius of the drops, and D is the diffusion coefficient of the drops of the same viscosity

$$D = k_B T / 5\pi\eta R. \tag{2}$$

The factor f represents the correction which takes into account the hydrodynamic interaction between the drops. It depends on the ratio of the viscosities of the liquid inside and outside the drops and the average distance between the drops and, therefore, on the volume fraction ϕ. This correction has been calculated in the dilute limit ($\phi \to 0$) by Zhang and Davis [10]. In the proximity of the critical point we can assume the viscosities of the phases are equal and

$$f(0) = 0.56. \tag{3}$$

According to the model, the drops coalesce immediately after the collision. Coalescence is the only reason for the decrease of the total number of the drops with the rate

$$dn/dt = -N_B. \tag{4}$$

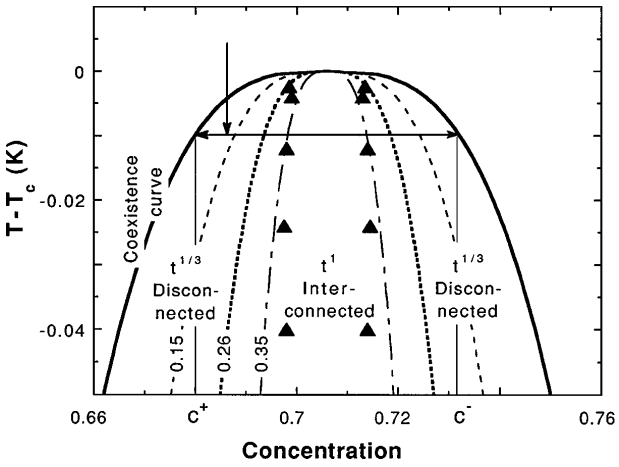

FIG. 1. Coexistence curve for a model two-phase system (density-matched cyclohexane-methanol) from Ref. [1]. The dotted curve is the calculated boundary (see text) between the $t^{1/3}$ and t^1 growth regions which corresponds to $\phi = 0.26$. The triangles are the experimental data from Ref. [1]. The curves corresponding to $\phi = 0.15$ (random percolation limit) and $\phi = 0.35$ (the value which gives the best fit to the experimental data from Ref. [1]) are also presented for comparison. The volume fraction of the minority phase at the point (c, T) can be calculated as $\phi = 1/2 - |c - c_c|/(c^- - c^+)$, where c_c (= 0.707 for this case) is the critical concentration.

 0031-9007/96/76(17)/3144(4)$10.00

With the relation

$$\phi = \tfrac{4}{3}\pi R^3 n = \text{const}, \quad (5)$$

Eq. (4) yields a $R \propto t^{1/3}$ law. The further improvements (see [11] and references therein) of this model influence mainly the numerical factor in (1) which is not important for the present considerations.

Hydrodynamic approaches.—The origin of the $R \propto t^1$ growth law, observed at high volume fraction where domains are interconnected, is much less clear. By means of a dimensional analysis, Siggia [9] has shown that hydrodynamics is needed to explain the kinetics. It assumed the growth to be ruled by the Taylor instability of the long tube of fluid, which breaks into separate drops, and associated the growth rate with the rate of the evolution of the unstable fluctuations. This idea has been developed by San Miguel, Grant, and Gunton in [12]. However, it was not clear how this process was related to the growth.

Another approach has been considered by Kawasaki and Ohta [3] who used a model of coupled equations of hydrodynamics and diffusion. It was assumed that the growth is controlled by diffusion, and the hydrodynamic correction to this process was calculated. However, the translational movement of the drops due to the pressure gradient was not taken into account. The motion of the liquid was supposed to be induced by the concentration gradient only. At the same time, it is well known that the concentration variation does not enter the equations of hydrodynamics of the liquid mixture in a first approximation [13]. Moreover, it is evident that at high volume fraction the coalescence process induced by the translational motion of the drops becomes very important.

Recently, several groups [14–18] performed large scale direct numerical simulations by using different approaches to solve coupled equations of diffusion and hydrodynamics. Some recovered the linear growth law [15,17], while others were not able to reach the late stages of separation and measured the transient values of the growth exponent (between 1/3 and 1). In spite of these efforts, the physical mechanism for the linear growth has not been clarified. To our knowledge, the simulations never showed two asymptotical laws depending on the volume fraction: The exponent is either larger than 1/3 when accounting for hydrodynamics or 1/3 for pure diffusion. Thus the precise threshold in ϕ separating the t^1 and $t^{1/3}$ regimes is not predicted either by any theory or by simulation.

Simulation of coalescence.—We show here that a t^1 growth can originate from a coalescence mechanism whose limiting process between two coalescences is not Brownian diffusion but rather flows induced by previous coalescence. We use the concept of "coalescence-induced coalescence" as introduced by Tanaka [4] who, however, thought that induction by the hydrodynamic flow was not relevant, having stated that coalescence takes place after the decay of the flow. We consider here a coalescence process between two drops and study numerically the generated flow and its influence on the third neighboring drop. The fully deterministic hydrodynamic problem within the creeping flow approximation (which is well justified near the critical point [9]) was solved. The free boundary conditions were applied on all drop interfaces whose motion is driven by surface tension. At each time step the velocity of each mesh point on the interface contours was computed using a boundary integral approach [19]. When the new positions of the interfaces were calculated, the procedure was continued iteratively. The details of the solution will be presented elsewhere [20]. We begin the simulation when coalescence starts between two drops of size R (Fig. 2), i.e., when the drops of the minority phase approach to within a distance of coalescence ψ which corresponds to the interface thickness of the drop [9]. We choose for the simulation $R = 10\psi$. We then place another drop at the distance d_0 from the composite drop (defined as the aggregate of two coalescing drops) and envelope these two drops by a spherical shell to mimic the surrounding pattern of tightly packed drops. Thus the distance between the drops and the shell has been chosen to be d_0 also. The surface tension σ is supposed to be the same for all the interfaces. Unfortunately, due to the prohibitively long computing times, we could not simulate the process of coalescence of two *spherical* drops. Instead, we had to use a configuration with cylindrical symmetry with respect to the axis $X' - X$ (see Fig. 2) which is expected to retain the main features associated with the spherical shape. In the beginning of the simulation the composite drop looks more like a torus. The spherical shell approximation can be justified by the fact that the main effect of the assembly of surrounding drops (as well as of the spherical shell) is to confine the motion of the neighboring drops—see [20]

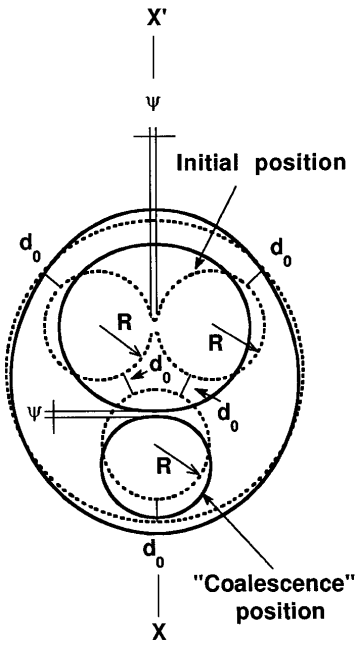

FIG. 2. The positions of the drop surfaces at the beginning (dotted line) and at the end (solid line) of the simulation. ψ is the coalescence distance, d_0 is the initial distance between the drops, and $X' - X$ is the axis of cylindrical symmetry.

for an advanced discussion. A setup with only three drops without either a shell or surrounding drops would not permit coalescence to occur even for the smallest interdrop distances. Though we cannot control quantitatively this approximation, it is the simplest one which captures the main features of the process.

A first important result from the simulation is that the flow generated by the first coalescence is able to generate *a second coalescence* between the composite drop and the neighboring drop (Fig. 2). This means that the lubrication interaction with the surrounding drops (with the shell in our model) make the composite and the neighboring drops attract (note that the second coalescence *does not* take place between this neighboring drop and the shell). This leads to the formation of a new elongated droplet. When the drops are close enough to each other the composite drop will have no time to relax to a spherical shape since a new coalescence takes place before relaxation. An interconnected pattern naturally follows. In contrast, when the drops are far from each other ($d_0/R \gg 1$), the second coalescence will never take place. The droplets take a spherical shape and the liquid motion stops. It is also clear that if $d_0/R < l_G$, which we call "geometric coalescence limit," coalescence necessarily occurs due to geometrical constraint. We find $l_G \approx 0.484$ [20,21].

The second important result is that the coalescence also takes place for $l_G < d_0/R < l_H$, where l_H is a value which we call "hydrodynamic coalescence limit." It is defined as a reduced initial distance where the time between two coalescences (t_c) becomes infinite. Since there is only one length scale (R) in the problem, t_c can be written in the scaled form

$$t_c = \alpha \eta R/\sigma\,, \tag{6}$$

where α is a reduced coalescence time which depends on d_0/R only (Fig. 3).

The quantity d_0/R is related to the volume fraction of the drops (minority phase) ϕ:

$$\phi = b[1 + d_0/2R]^{-3}. \tag{7}$$

The constant b depends on the space arrangement of the drops. The hydrodynamic interaction between them is always repulsive due to the lubrication force. Thus they tend to be as far from each other as possible. Moreover, experiment shows a liquidlike order for the drop positions. Such a correlation explains why the drops do not percolate [1] when the volume fraction ϕ reaches the *random* percolation limit ($\phi \approx 0.15$).

Since no quantitative information is available to determine b, we calculate its upper and lower bounds. Ideally, we can assume that the drops are arranged into a regular lattice, with the vertices as far from each other as possible. This is the face centered cubic lattice, where $b = \pi/3\sqrt{2} \approx 0.74$ and which corresponds to the fully ordered structure. We can also consider as a lower bound the random close packing arrangement for spheres of radius $R + d_0/2$. This corresponds to the absence of a short-range order [22] and implies $b \approx 0.64$. We note that the value of b is not very sensitive to the particular space arrangement. In the following, we adopt the median value $b = 0.69$.

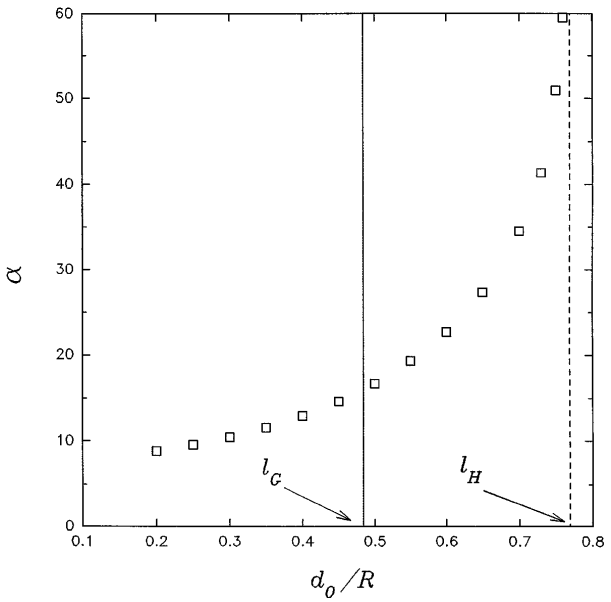

FIG. 3. The simulation data on the dependence of the reduced coalescence time α on d_0/R. The vertical lines show the geometric and hydrodynamic coalescence limits.

Generalization of the hydrodynamic model.—Now we can generalize the above hydrodynamic mechanism for an arbitrary shape of the drops. The self-similarity of the growth implies the following relation for the characteristic sizes of the drops between ith and $(i + 1)$th coalescences: $R^{(i+1)} = \beta R^{(i)}$, where β is a universal shape factor, which depends on ϕ only. We can also rewrite Eq. (6) for the time between the coalescences in the form $t_c^{(i)} = \alpha(\phi)\eta R^{(i)}/\sigma$, where $\alpha(\phi)$ is also the universal function. The last expression conforms to the scaling assumption which implies the independence of $t_c^{(i)}$ on the second length scale ψ. Then, after n coalescences,

$$R = \beta^n R^{(0)}, \qquad t = \sum_{i=0}^{n-1} t_c^{(i)},$$

and

$$R = R^{(0)} + [(\beta - 1)/\alpha](\sigma/\eta)t\,, \tag{8}$$

where $R^{(0)}$ is the initial size of the drop. Noting that $\beta = 2^{1/3}$ for the spheres and $\beta \gtrsim 1$ for the long tubes, we can take $\beta \sim 1.1$ for the estimate. Since $\alpha \sim 10$ for $\phi = 0.5$, as it follows from Fig. 3 and Eq. (7), we obtain $R \sim 0.01\sigma/\eta$, which compares well with the experiment [23], which gives 0.03 for the numerical factor.

Competition between two mechanisms.—Now using Eq. (7) we can relate l_H to a volume fraction ϕ_H. It is clear that the described hydrodynamic mechanism works only when $\phi > \phi_H$, while the Brownian coalescence takes place in the whole range of ϕ. Below we shall consider the regime for which $\phi > \phi_H$ in order to obtain the position of the boundary between $t^{1/3}$ and t^1 regions on the phase diagram.

Taking into account the competition between the two mechanisms, we consider the relation

$$dn/dt = -(N_B + N_H), \tag{9}$$

instead of (4), where N_H is the rate of the coalescences due to the hydrodynamics which can be calculated by using Eq. (8) and the relation between n and R [Eq. (5)]. The latter, however, depends on the shape of the drop. We assume that in the early stages the drops are spherical and we use Eq. (5). It should be noted that Eq. (9), rewritten for the scaled wave number, coincides exactly with the semiempirical equation suggested by Furukawa [24].

The Brownian mechanism dominates when $N_B > N_H$. In the vicinity of the critical point one can use the two-scale-factor universality [25] expression $\sigma = k_B T/\gamma\xi^2$, where ξ is the correlation length in the two-phase region and $\gamma \approx 0.39$ is a universal constant. Then we reduce the last inequality to

$$R^2/\xi^2 < G(\phi), \tag{10}$$

where

$$G(\phi) = C\phi f(\phi)\alpha(\phi) \quad \text{and} \quad C = \gamma/5\pi(\beta - 1).$$

We do not know much about the function $f(0)$ which has been discussed in Eq. (1). However, it is unphysical to assume that it exhibits singularities or a steep behavior. We shall use the constant value (3) in the following. We recall that all our considerations are valid only when the drop interfaces have already formed (late stages of growth), which means that the initial radius of a drop cannot be less than the interface thickness, i.e., $\approx 4\xi$ [26]. It follows readily from the inequality (10) that growth would obey the law $R \propto t^{1/3}$ when

$$G(\phi) > 16. \tag{11}$$

Now we aim to estimate the function $G(\phi)$ by using for $\alpha(\phi)$ the calculated function in Fig. 3 along with Eq. (7). It turns out that the function $G(\phi)$ fits the power law

$$G(\phi) \propto (\phi - \phi_H)^{-\delta} \tag{12}$$

for $\phi > \phi_H$ well where $\phi_H \approx 0.26$, $\delta \approx 0.33$, and the divergency comes from $\alpha(\phi)$. From (12), it is easy to deduce that (11) is valid when $0 < \phi - \phi_H \lesssim 10^{-6}$. In practice, this means that for all $\phi > \phi_H$, *only* the hydrodynamic mechanism will determine the growth from the very beginning of the drop coarsening. Alternatively, for $\phi < \phi_H$, the drops will grow according to the Brownian mechanism only. This explains the sharp transition in the kinetics ($t^1 \rightarrow t^{1/3}$) which is controlled by the volume fraction of the minority phase as observed in [1] and [2]. The curve which corresponds to the threshold value $\phi = 0.26$ is plotted in Fig. 1. It shows a reasonable agreement with the experimental data in spite of our very particular choice of the form and arrangement of the drops.

It should be mentioned that our model can be applied to any system where the growth is due to the coalescence of liquid drops inside another fluid (phase separation, coagulation, etc.).

One of the authors (V. N.) would like to thank the collaborators of SPEC Saclay for their kind hospitality and Ministère de l'Enseignement Supérieur et de la Recherche of France for financial support.

*On leave from Bogolyubov Institute for Theoretical Physics, National Ukrainian Academy of Sciences, 252143, Kiev, Ukraine. Electronic address: vnikol@amoco.saclay.cea.fr

[1] Y. Jayalakshmi, B. Khalil, and D. Beysens, Phys. Rev. Lett. **69**, 3088 (1992).
[2] F. Perrot, P. Guenoun, T. Baumberger, D. Beysens, Y. Garrabos, and B. Le Neindre, Phys. Rev. Lett. **73**, 688 (1994).
[3] K. Kawasaki and T. Ohta, Physica (Amsterdam) **118A**, 175 (1983); T. Koga, K. Kawasaki, M. Takenaka, and T. Hashimoto, Physica (Amsterdam) **198A**, 473 (1993).
[4] H. Tanaka, Phys. Rev. Lett. **72**, 1702 (1994).
[5] J. D. Gunton, M. San Miguel, and P. S. Sahni, in *Phase Transitions and Critical Phenomena*, edited by C. Domb and J. L. Lebowitz (Academic Press, New York, 1983), Vol. 8, p. 267.
[6] I. M. Lifshitz and V. V. Slyozov, J. Phys. Chem. Solids **19**, 35 (1961).
[7] M. von Smoluchowski, Z. Phys. Chem. **92**, 129 (1917).
[8] K. Binder and D. Stauffer, Phys. Rev. Lett. **33**, 1006 (1974).
[9] E. D. Siggia, Phys. Rev. A **20**, 595 (1979).
[10] X. Zhang and R. H. Davis, J. Fluid Mech. **230**, 479 (1991).
[11] H. Hayakawa, Physica (Amsterdam) **175A**, 383 (1991).
[12] M. San Miguel, M. Grant, and J. D. Gunton, Phys. Rev. A **31**, 1001 (1985).
[13] L. D. Landau and E. M. Lifshitz, *Fluid Mechanics* (Pergamon, London, 1959).
[14] S. Puri and B. Dünweg, Phys. Rev. A **45**, R6977 (1992).
[15] F. J. Alexander, S. Chen, and D. W. Grunau, Phys. Rev. B **48**, 634 (1993).
[16] O. T. Valls and J. E. Farrell, Phys. Rev. E **47**, R36 (1993).
[17] A. Shinozaki and Y. Oono, Phys. Rev. E **48**, 2622 (1993).
[18] C. Appert, J. F. Olson, D. H. Rothman, and S. Zaleski, "Spinodal Decomposition in a Three-Dimensional, Two-Phase, Hydrodynamic Lattice Gas" (to be published).
[19] C. Pozrikidis, *Boundary Integral and Singularity Method for Linearized Viscous Flow* (Cambridge University, Cambridge, England, 1991).
[20] V. S. Nikolayev and D. Beysens, "Coalescence-Induced Coalescence by Hydrodynamic Flow" (to be published).
[21] The shell diameter D_s at the initial moment can be defined according to Fig. 2 as a function of R, ψ, and d_0. If there is no coalescence, the toruslike composite drop eventually becomes a sphere with a diameter D_c deduced from its initial volume, the latter being conserved during the evolution. The l_G value is determined by the condition $D_s = D_c + 2R + 3\psi$ which means that two drops of final spherical shape must fit inside the spherical shell with the gaps of thickness ψ.
[22] J. H. Berryman, Phys. Rev. A **27**, 1053 (1983).
[23] P. Guenoun, R. Gastaud, F. Perrot, and D. Beysens, Phys. Rev. A **38**, 4876 (1987).
[24] H. Furukawa, Adv. Phys. **34**, 703 (1985).
[25] M. R. Moldover, Phys. Rev. A **31**, 1022 (1985).
[26] D. Beysens and M. Robert, J. Chem. Phys. **87**, 3056 (1987); **93**, 6911 (1990).

Coalescence limited by hydrodynamics

Vadim S. Nikolayev[a)]
SI3M, Département de Recherche Fondamentale sur la Matière Condensée, CEA Grenoble, 17, rue des Martyrs, 38054, Grenoble Cedex 9, France

Daniel A. Beysens
Département de Recherche Fondamentale sur la Matière Condensée, CEA Grenoble, 17, rue des Martyrs, 38054, Grenoble Cedex 9, France

(Received 20 May 1997; accepted 16 July 1997)

We consider an assembly of liquid drops imbedded in another immiscible liquid of similar viscosity. It is shown that a coalescence between two drops induces another coalescence when the average distance between the drops is less than a threshold value, resulting in a ''chain reaction'' of coalescences. The threshold value is calculated using a ''shell'' model that is based on the boundary integral approach. Another ''many-drop'' model is developed to test the shell approximation. We show that, although the shell model is adequate, its results can be improved by lowering the shell surface tension. © *1997 American Institute of Physics.* [S1070-6631(97)03511-3]

I. GROWTH BY COALESCENCE

A system formed of small droplets imbedded in a liquid is not stable. It tends to lower its total surface energy by drop coalescence, which occurs while the drops collide during their stochastic Brownian motion. The average radius of the drops grow. This model corresponds to a ''diffusion-limited'' growth because the time between two coalescence events is limited by diffusion of the drops. This model was first evoked in the pioneering article of Smoluchowski[1] on coagulation of colloids (see also Ref. 2 and refs. therein). The average characteristic drop size R obeys the asymptotic growth law

$$R \propto t^{1/3}, \tag{1}$$

where t is time.

In contrast to this model, a purely deterministic coalescence model is discussed here. Our consideration is based on the following idea. Let us first imagine all the drops to be in vacuum rather than inside another liquid, so as to be able to neglect any interactions between them. All the drops are quiescent except two coalescing drops which form a ''composite drop.'' If the average distance between the drops d_0 is less than a threshold value (''coalescence limit''), the composite drop will touch a neighboring drop (''drop D'', Fig. 1). A second coalescence follows. The threshold value depends only on the shape of the drops and can be calculated from mere geometrical arguments.

When the drops are imbedded in another liquid, the scenario changes because of hydrodynamic interactions. The relaxing composite drop induces a flow, the direction of which is shown by the arrows in Fig. 1. This flow pushes the drop D away and hinders the second coalescence. The hydrodynamic coalescence limit should thus be less than the vacuum coalescence limit.

Subsequent coalescences follow each other and the average radius of the drop pattern grows. This chain of coalescences never stops if the drop pattern is self-similar; the growth law is linear:[3]

$$R \propto t. \tag{2}$$

It is much faster than that (1) for the Brownian mechanism. We call this model ''growth limited by hydrodynamics,'' because the rate of coalescence is determined by hydrodynamics. The purpose of this work is to demonstrate that a coalescence, induced by another coalescence, is indeed possible and to analyze the process in detail.

The lubrication forces which prevent two interfaces from approaching are very strong. This is why the interfaces of the composite drop and the drop D would never approach without the effect of surrounding drops. In the presence of the surrounding drops, the same lubrication forces act between the drop D and the surrounding drops. Then the drop D cannot be displaced strongly by the flow generated by the relaxing composite drop and the interfaces of the two drops' approach with time. We assume that when the surfaces of two drops approach each other to a distance ψ, which we call the ''distance of coalescence,'' a bridge between them forms immediately, i.e., coalescence begins.[4]

This retardation of the motion of the drops is due to the lubrication force which is proportional to the relative velocity of the drops. The relative velocity of the drops distant from the composite drop is proportional in turn to the velocity gradient of the fluid. The considered effect should thus be stronger inside a finite container than in an infinite system because the velocity reaches a zero value (boundary condition on the walls) at a finite distance from the composite drop and the velocity gradient is larger. Hence, if we show that a coalescence induces another coalescence in the absence of walls, it will be all the more true for the case of a finite system. The case of an infinite number of liquid drops in another liquid of infinite extent is thus considered below. The volume fraction ϕ of the droplets (ϕ=volume of drops/total volume) is, however, finite and can be related to d_0. The liquids of similar large viscosities are supposed to be

[a)]On leave from Bogolyubov Institute for Theoretical Physics, National Academy of Sciences of Ukraine, 252143, Kiev, Ukraine. Electronic mail: vnikol@drfmc.ceng.cea.fr

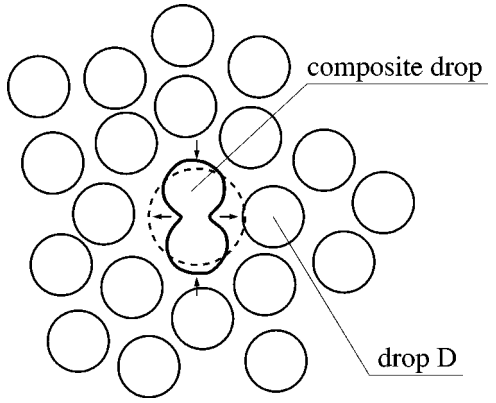

FIG. 1. Sketch of the drop pattern undergoing coalescence.

immiscible, and diffusion is neglected. A good example of this situation can be found in the late stages of phase separation of complex fluids and that of simple liquids (see Ref. 5 and refs. therein). Another example is the coagulation process of colloids.

A mathematical formulation for the problem is given in Sec. II. A ''shell'' model for coalescences is developed in Secs. III and IV to calculate the hydrodynamic coalescence limit. The model is solved numerically and its results are discussed in Sec. V. We show how one coalescence induces another coalescence. In Sec. VI another simple ''many-drop'' model is developed. It cannot describe the second coalescence, nevertheless the validity of the shell model can be tested by comparing the results from the two models. Conclusions are given in Sec. VII.

II. HYDRODYNAMIC FORMULATION

We consider drops of a liquid phase M^+ separated from another liquid phase M^- by the interfaces ∂M, with surface tension σ. Both fluids are supposed to be incompressible and Newtonian and to have the same large shear viscosity η. These assumptions are well justified in the vicinity of a critical point of a liquid mixture. Then the problem can be treated in the creeping flow approximation. The hydrodynamic equations can be written for every point $\vec{x}$ inside M^+ or M^- as

$$\nabla \cdot \overleftrightarrow{T} = 0, \tag{3}$$

$$\nabla \cdot \vec{v} = 0, \tag{4}$$

where $\vec{v}$ is a fluid velocity and $\overleftrightarrow{T}$ is a hydrodynamic stress tensor:

$$\overleftrightarrow{T} = -p\overleftrightarrow{I} + 2\eta[\nabla \vec{v}]^s,$$

where the superscript s denotes symmetrization and $\overleftrightarrow{I}$ is the unit tensor. The free boundary conditions should be specified for $\vec{x} \in \partial M$:

$$\Delta \vec{v} = 0, \tag{5}$$

$$\Delta(\overleftrightarrow{T} \cdot \vec{n}) = \vec{f}, \tag{6}$$

where Δ denotes a difference across the surface (outer minus inner), $\vec{n}$ is an outward normal to ∂M, and $\vec{f}$ is the force density that the fluid exerts on the interface. The force direction is opposite to Laplace's force,

$$\vec{f} = \sigma \vec{n}(\nabla \cdot \vec{n}). \tag{7}$$

The position of the interface as defined by the vector $\vec{y}$ can be derived by the kinematic condition

$$\frac{d\vec{y}}{dt} = \vec{v}(\vec{y}), \quad \vec{y} \in \partial M. \tag{8}$$

The motion of the fluid is assumed to be due only to the surface tension of the interface ∂M. It is then quiescent far from the interface:

$$\vec{v} \to 0 \quad \text{as} \quad |\vec{x}| \to \infty. \tag{9}$$

The hydrodynamic problem (3)–(7) and (9) can be solved explicitly[6,7] in the integral form

$$\vec{v}(\vec{x}) = -\frac{1}{8\pi\eta} \int_{(\partial M)} \overleftrightarrow{J}(\vec{x}-\vec{y}) \cdot \vec{f}(\vec{y})\, dS_y, \tag{10}$$

where

$$\overleftrightarrow{J}(\vec{x}) = \frac{\overleftrightarrow{I}}{|\vec{x}|} + \frac{\vec{x}\vec{x}}{|\vec{x}|^3} \tag{11}$$

is the Oseen tensor. In the case of the cylindrical symmetry of the interface ∂M one can perform an angular integration in (10):

$$\begin{aligned} v_r(r,z) &= \frac{1}{8\pi\eta} \int_{(L)} dl_y\, [B_{rr}(r,z,r_y,z_y) f_r(r_y,z_y) \\ &\quad + B_{rz}(r,z,r_y,z_y) f_z(r_y,z_y)], \\ v_z(r,z) &= \frac{1}{8\pi\eta} \int_{(L)} dl_y\, [B_{zr}(r,z,r_y,z_y) f_r(r_y,z_y) \\ &\quad + B_{zz}(r,z,r_y,z_y) f_z(r_y,z_y)]. \end{aligned} \tag{12}$$

Here L is the curve whose rotation around the z axis generates the drop interfaces ∂M. The expressions for the nondimensional quantities B_{ij}, $i,j = r,z$, are presented[8–11] in Appendix A. Each point of L can be specified in the r-z coordinate system ($r \geqslant 0$), whose axes are shown in Fig. 2. The quantities f_r and f_z are the projections of the vector f (7) on the axes. As one can see, the surface integral in (10) is now replaced by a line integral.

The set of equations (8) and (12) allows the time evolution of the interface positions to be calculated for the given initial conditions for liquid velocity and interface positions. They are defined in the next section.

III. SHELL MODEL

We aim to analyze the retardation of the motion of the drop D by the surrounding drops. As was explained in Sec. I, the retardation is effective when one can find a drop (far from the composite drop) with *zero* velocity at any moment of time. Since the hydrodynamic forces decay very slowly [cf. Eq. (11)] and the interdrop distance should be small to observe the effect, we need to simulate a very large number

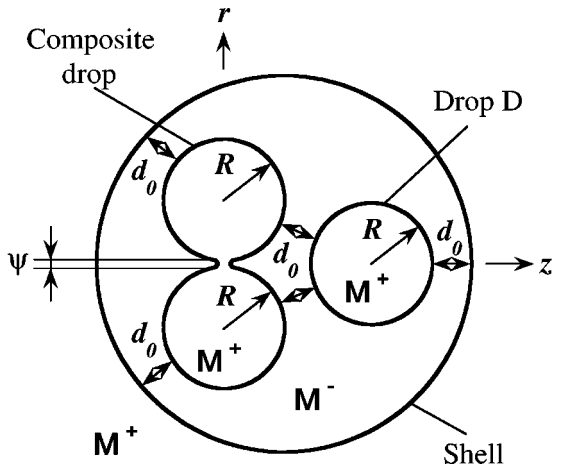

FIG. 2. Positions of the drop surfaces at the beginning of the simulation. Here ψ is the coalescence distance and d_0 is the initial distance between the drops.

of drops, which is impossible because of prohibitively long computer times. An alternative way to demonstrate the effect with a small number of drops is to surround them by a *closed* shell which is a mean-field-like imitation of the influence of all other drops.

The chosen initial arrangement of the interfaces is shown in Fig. 2. The composite drop is an aggregate of drops that have just approached within the distance ψ. We consider another drop of radius R (drop D) at the distance d_0 from the composite drop. These two drops are enveloped by the spherical shell with the same surface tension σ as the drops (the validity of this approximation is discussed in Sec. VI B). We suppose that just before coalescence takes place, the motion of the fluid is much weaker than after the coalescence (the justification of this assumption is given *a posteriori* in Sec. V). Thus the initial fluid velocity can then be taken to be zero everywhere. A flow in our model system is created by the composite drop which relaxes due to its surface tension and we are interested in obtaining the time t_c between two coalescences as a function of d_0.

We have arbitrarily chosen $\psi = R/10$ in the simulation. We think that the precise definition of this distance is not relevant to the present hydrodynamic problem provided that ψ/R remains small. The value for ψ can influence the time t_c between two coalescences in two ways. On one hand, a smaller value for ψ increases the curvature of the composite drop, which then relaxes faster, thus decreasing t_c. On the other hand, the surfaces will spend more time approaching to within a smaller distance ψ, which increases t_c. One sees, at least qualitatively, that t_c can be independent of ψ. In addition, if one considers the particular case of phase separation near a critical point, scaling implies that there is only one lengthscale (R) on which all the variables depend, including t_c. Hence, the latter must be independent[3] of ψ.

The setup of three spherical droplets which are arranged as shown in Fig. 2 has a low (mirror) symmetry and this arrangement requires a fairly long simulation time. This is why we chose instead, for the actual simulation, the setup of Fig. 2, but with a cylindrical symmetry with respect to the z axis. Then the composite drop is more like ''a torus without the hole'' than a dumbbell of two spheres. Such a configuration is expected to retain the main features of the real physical system since the real pattern is a complicated figure of interconnected interfaces where the drops do not resemble spherical objects at all.[5] At the very least our model system should serve to demonstrate the physical ideas presented here.

Hence, we can use (12) with the integration contour L which consists of three unconnected parts that correspond to the half contours of the drops in Fig. 2.

IV. NUMERICAL SCHEME

Even the simplified axisymmetric version of the problem remains nonlinear due to the free boundaries. Hence, a numerical method of solution is needed. The algorithm[10] with the following minor changes is used. It is possible to avoid the rather artificial correction of the normal component of the interface velocity[10] by increasing the number of divisions of the integration contour. We checked that 400 mesh points on the contour of the composite drop (700 for all three parts of the contour) are enough to ensure that the increase of the drop volumes during the whole evolution does not exceed a few percent. The parametric integration with the trapezoidal rule is used in (12). When $|dr/dz|$ is smaller than 5, the variable z is chosen as an integration parameter, it is r otherwise. The algorithm is not very stable, and it is necessary to maintain the distances between the mesh points approximately equal during the evolution. For this purpose a new point is added between two points (by using the three-point interpolation rule) if the distance between two points exceeds twice the average distance. Similarly, if the distance between two points becomes less than half the average distance, one point is eliminated.

V. SIMULATION RESULTS

A priori, there are two different asymptotic regimes depending on the choice of d_0. The first corresponds to large values of d_0 when the drops relax to their spherical equilibrium shape without further coalescence. This regime takes place when reduced initial interdrop distance d_0/R exceeds a hydrodynamic coalescence limit L_H. As discussed in Sec. I, L_H is smaller than the coalescence limit in vacuum L_V. For the chosen geometry of the two drops (see Appendix B) $L_V = 0.99$.

The second regime appears when d_0/R is less than a ''geometric coalescence limit'' L_G. When d_0 is very small, further coalescence becomes mandatory simply because the initial shell radius R_s (which depends on d_0, see Fig. 2) is so small that there is not enough room to contain two drops of spherical shape. It is shown in Appendix B by purely geometrical argument that in our case $L_G = 0.48$.

A question arises whether the actual value of L_H is larger than L_G. It is also interesting to know whether the new coalescence takes place between two neighboring drops or between a drop and the shell. The simulation gives answers to these questions.

We present the time evolution of the system of drops in Fig. 3. Independently of d_0, the new coalescence takes place

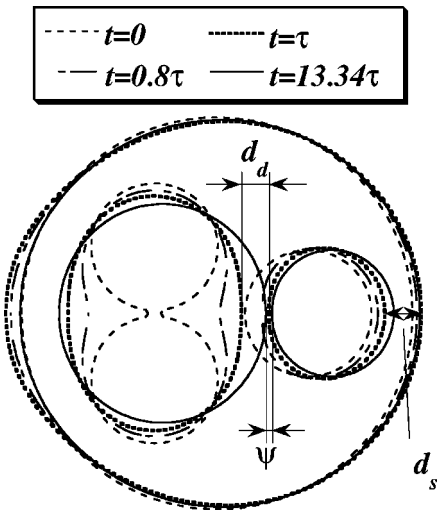

FIG. 3. Time evolution of the positions of the drop surfaces for $d_0/R=0.65$. The second coalescence takes place at $t=t_c=13.34\tau$, $\tau=\eta R/\sigma$. The distances between two drops d_d and between the drop D and the shell d_s are shown for the case $t=\tau$.

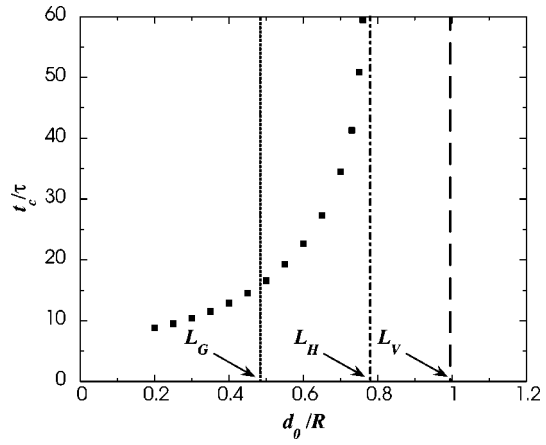

FIG. 5. Dependence of the time lag between two subsequent coalescences t_c on d_0/R, $\tau=\eta R/\sigma$. The vertical lines show the geometric and hydrodynamic coalescence limits and the coalescence limit in vacuum.

between the composite drop and the neighboring drop D and not between drop D and the shell. This is shown clearly in Fig. 4 where the distance between the composite and D drops (d_d) and the distance between drop D and the shell (d_s) are depicted versus time.

The result of several coalescences will therefore produce a large drop of a complicated shape. This explains the ''tube-like'' interconnected morphology of the growing phases which is currently observed in the experiments.[5] The most important result of the simulation is the dependence of the time lag between two subsequent coalescences (t_c) on d_0/R (Fig. 5). t_c goes to infinity for a value $d_0/R=L_H=0.769$ which is larger than L_G. This means that the lubrication interaction with the shell (surrounding drops) slows down the drop D sufficiently to produce the second coalescence and the geometrical constraint of L_G (which is an artifact of the shell model) is irrelevant.

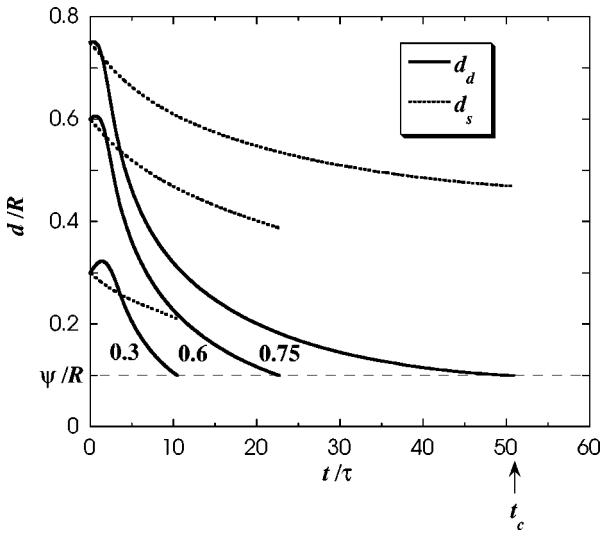

FIG. 4. Time evolution of the distances d_s and d_d for the different values of d_0/R. The distance at which the second coalescence occurs is shown as a horizontal dashed line. Coalescence time t_c is shown for $d_0/R=0.75$. Here d_d grows in the beginning slightly because it is defined as a *minimum* distance between the drop surfaces. There is no growth in the dependence of the distance between the closest points of the two drops on the axis of revolution.

The time evolution of the slope of the curves in Fig. 4 reflects the time evolution of the fluid velocity in the whole space. Being initially zero (see Sec. III), it rapidly achieves its maximum value and then slowly decreases to the value $v_c(\vec{x})$ at the moment of the new coalescence at $t=t_c$. Since a chain of subsequent coalescences is considered, $v_c(\vec{x})$ should be adopted as the initial condition for the fluid velocity at the beginning of the next coalescence. We consider it to be zero. This assumption is justified when d_0/R is close to L_H, which is the most interesting case. Indeed, from the definition of L_H, $v_c(\vec{x})\to 0$ when $d_0/R\to L_H$ (Fig. 4).

It should be noted that the symmetric position of drop D in the chosen geometry can be unstable, and any fluctuation may lead to its sidewise shift. However, Fig. 3 shows that the change in d_d will depend only slightly on this shift. Thus the specific geometry of our simulation should not influence t_c strongly.

Experiments[12] have shown that, under the conditions of an interconnected droplet pattern, coalescence proceeds through the formation of a rim, or dimple. However, in the simulation, no dimple can be observed. Only a flattening (see Fig. 3) can be seen. This discrepancy can be understood if one considers the theoretical results.[13] They show that a dimple does not form during the coalescence of two drops when the Reynolds number is less than 1, as it is in our case.

VI. VALIDITY OF THE SHELL APPROXIMATION

It is important to know whether the influence a large number of surrounding drops can be modeled by the shell approximation as introduced in Sec. III. In this section we introduce another model and compare its results with that of the shell model.

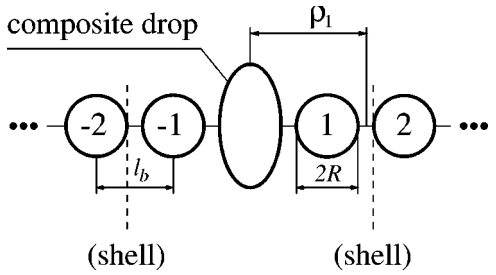

FIG. 6. Initial (equidistant) positions of the drops in the many-drop model. The distance ρ_n is shown for $n=1$.

A. Many-drop model

Since it is impossible to solve explicitly the problem of the relaxation of a composite drop surrounded by infinite number of drops, several simplifications are made which we think retain the essence of the problem:

(1) The composite drop remains an oblate spheroid during most of the relaxation time. Its eccentricity is allowed to change.
(2) The environment does not influence the relaxation of the composite drop, i.e., the latter moves as if it were alone.
(3) All the drops, except the composite drop and drop D, remain spherical during the evolution. Figure 3 shows that even drop D deforms just slightly during the evolution, which suggests that more distant drops should not deform.
(4) The spherical drops move because of the flow imposed by the relaxing composite drop. The distance between two neighboring drops changes because of the spatial gradient of this flow. We suppose that each pair of spherical drops moves as if it were alone in a flow with a constant velocity gradient. The value of this gradient at the point where the pair is situated is calculated from the solution for the creeping flow created by the composite drop. At the same time we keep in mind that in reality, the velocity gradient vanishes at infinity.
(5) Since the gradient is strongest along the axis of revolution of the composite drop, we consider *only* those drops whose centers are on this axis. At the beginning of the relaxation the distance l_b between their centers is supposed to be equal to the average interdrop distance which is related to the drop volume fraction ϕ.

The drops are numbered consecutively, the drop 1 (or -1 because of symmetry) corresponds to the drop D (see Fig. 6). The position of the right edge of the shell in Figs. 2 and 3 corresponds to the position of the left edge of drop 2 in Fig. 6. The aim of this subsection is to find the velocity $v^{(2)}$ of drop 2, in order to compare it with the velocity of the right edge of the shell.

The velocity field created by the relaxation of the composite drop is calculated in Appendix C for the case

$$\rho > R, \tag{13}$$

where ρ is the distance from the center of the composite drop. The results[14] are used (see Appendix D) to determine the relative velocity of the spherical drops in each pair imbedded in the gradient flow. For the relaxing oblate spheroid the maximum gradient is induced in the direction of its rotation axis (z axis, $r=0$) and one can substitute into (D1) a value for g derived from the expression (C1)

$$g=\left.\frac{\partial v_z}{\partial z}\right|_{r=0}=-\frac{\sigma}{\eta}\frac{G(\varepsilon)R^2}{2\rho^3}, \tag{14}$$

where G is given in (C2) as function of the eccentricity ε of the drop (see Appendix C). Since $g<0$, the drops approach each other.

The simplification (4) above can be justified if

$$|\Delta g/g|<1, \tag{15}$$

where $|\Delta g|$ is a variation of g on the lengthscale.[15] R and $\Delta g = R\, dg/d\rho$. Thus (15) yields the condition $\rho > 3R$ which is compatible with the condition (13) for the validity of the flow calculations in Appendix C. The surrounding drops move due to the flow gradient g, which tends to zero as $\rho\to\infty$. Hence, we can find a drop (numbered N) whose absolute velocity $v^{(N)}$ is zero. Then

$$v^{(N-1)}=V^{(N-1)}, \quad v^{(N-2)}=V^{(N-2)}+V^{(N-1)}, \ \ldots,$$

$$v^{(2)}=\sum_{n=2}^{N-1} V^{(n)}, \tag{16}$$

where $V^{(n)}$ is the relative velocity of the drop n with respect to the drop $(n+1)$ [cf. Eqs. (D1) and (14)]:

$$V^{(n)}=\frac{\sigma}{\eta}\frac{G(\varepsilon)R^2}{2\rho_n^3}\, l(n)F[R/l(n)]. \tag{17}$$

Here the function F is given by the expressions (D2) and (D3), ρ_n is a coordinate of the nth pair of the drops

$$\rho_n=\frac{1}{2}\, l(n)+\sum_{i=0}^{n-1} l(i), \tag{18}$$

and $l(n)$ is the distance between the nth and $(n+1)$th drops. At the beginning of the relaxation $l(n)=l_b$ (see Fig. 6).

Although the function $l(n)$ is not known *a priori*, some useful information can be obtained, which turns out to be sufficient to calculate the upper and lower bounds for $v^{(2)}$. The distribution $l(n)$ changes with time. Since the flow is stronger near the composite drop, l is an increasing function of n during the relaxation:

$$l(1)\leqslant l(n)\leqslant l(\infty)\equiv\lim_{i\to\infty} l(i). \tag{19}$$

Because the flow gradient is always zero at infinity, $l(\infty)$ does not change with time:

$$l(\infty)=l_b. \tag{20}$$

Since $(R/l)^2F(R/l)$ is a decreasing function of l for the most important interval $l>2.2R$ (cf. Appendix D), (19) and (20) imply the inequality

$$v_l^{(2)}\leqslant v^{(2)}(t)<v_u^{(2)}, \tag{21}$$

where

$$v_l^{(2)}=0.0591\,\frac{\sigma}{\eta}\,\frac{G(\varepsilon)R^2}{l_b^2}\,F\left(\frac{R}{l_b}\right), \tag{22}$$

$$v_u^{(2)}=0.0591\,\frac{\sigma}{\eta}\,\frac{G(\varepsilon)R^2}{l^2(1)}\,F\left[\frac{R}{l(1)}\right]. \tag{23}$$

These expressions can be obtained[16] by using (16) with $N\to\infty$, (17) and (18), and the standard formula

$$\sum_{n=0}^{\infty}(2n+1)^{-3}=1.05\,180.$$

It appears that $v_l^{(2)}$ and $v_u^{(2)}$ are functions of time because ε and $l(1)$ also depend on time.

B. Comparison between the shell and the many-drop models

The shell model gives a number of very interesting results. However, a justification of the shell approximation is needed. We cannot compare directly the values of L_H in the shell model with that in the many-drop model because the latter cannot give a dynamic picture of coalescence, from which L_H is obtained. However, it is possible to make an indirect check of the shell model correctness by comparing the velocity of drop 2 and that of the right edge of the shell (cf. Figs. 2 and 6). These velocities should correspond to each other in the two models. We shall demonstrate here that the shell approximation yields a reasonable result and how the shell model can be improved.

First, one needs to associate the variables of both models. It is easy to establish the relations (see Figs. 2, 3, and 6)

$$l(1)=d_s+2R \quad \text{and} \quad l_b=d_0+2R. \tag{24}$$

The upper (23) and lower (22) bounds calculated with the substitution (24) from the simulation results appear to be very close to each other (within several percent) and thus their average can be used hereafter for $v^{(2)}(t)$.

We aim to compare $v^{(2)}$ with the velocity of the right edge of the shell in Figs. 2 and 3. Because of the symmetry of the setup in Fig. 6, the velocity of the composite drop center is equal to zero in contrast to the shell model. Hence, $v^{(2)}$ should be compared to the *relative* velocity v_s of the right edge of the shell with respect to the composite drop center.

The simulation shows that the composite drop becomes convex shortly after the beginning of its evolution (see Fig. 3). Then the drop has a degree of asymmetry two orders smaller than its oblate deformation, as can be calculated easily from the simulation data. This justifies the simplification (1) above in the many-drop model and allows the center of the composite drop and its eccentricity ε to be determined from the shell model simulation.

The dependence of $v^{(2)}$ and v_s on ε is shown in Fig. 7. Smaller values of ε correspond to the later stages of evolution. The start of the relaxation of the composite drop, when it is not convex and cannot be approximated by a spheroid, is not shown in Fig. 7.

The comparison of $v^{(2)}$ and v_s evolutions shows that the two independent models give similar values at $\varepsilon>0.6$. However, at small ε (late stages of evolution) the sign of v_s changes to negative, i.e., the shell begins to move backwards. This is unphysical from the point of view of a many-drop system. This artifact is due to the nature of the shell: in the beginning of the evolution the shell first undergoes a prolate deformation and then relaxes because of its finite surface tension (see Fig. 3). The negative value of v_s corresponds to the relaxation.

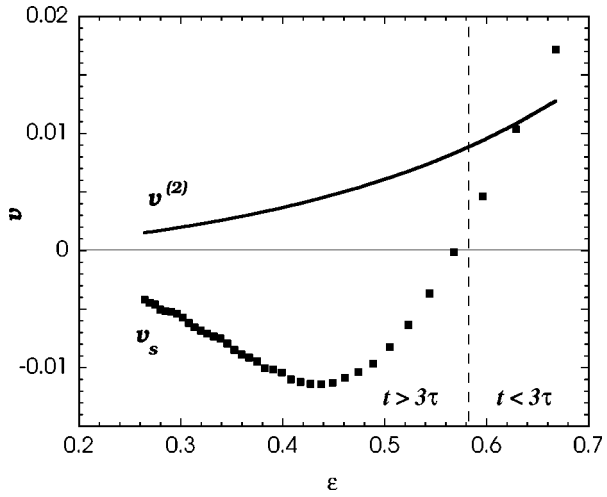

FIG. 7. Comparison of the dependencies of v_s and $v^{(2)}$ on composite drop eccentricity ε for $d_0=0.7R$ which implies $\tau_s\approx 3\tau$. A region in which the shell model gives the correct values for the drop velocities is shaded. In the shell model simulation, the composite drop reaches at $t=3\tau$ the value of eccentricity which corresponds to the boundary between two regions. The velocities are in the units σ/η.

This artifact can be suppressed by imposing to the shell a larger relaxation time, e.g., by lowering its surface tension σ_s. Since the relaxation time of the shell is given by the formula $\tau_s=\eta R_s/\sigma_s$, where R_s is the shell radius, the inequality

$$t<\tau_s \tag{25}$$

should yield the time interval where the shell behaves correctly. Figure 7 shows that it is really so. The inequality (25) can be rewritten to give the value of σ_s which insures the correct behavior of the shell:

$$\frac{\sigma_s}{\sigma}<\frac{R_s}{R}\,\frac{\tau}{t}, \tag{26}$$

where $\tau=\eta R/\sigma$ is the characteristic time of the drop relaxation. The minimum value of R_s [defined by (B1)] and the maximum evolution time t under consideration should be substituted into (26). For the given geometry one can choose $\sigma_s=\sigma/10$ in future simulations. This increases only slightly the coalescence time t_c; the correction is small, as in the present simulation the shell deforms only slightly (see Fig. 3). As a matter of fact, the new value for σ_s will make L_H somewhat smaller. In other words, the corresponding value of drop volume fraction ϕ_c will be larger than that obtained from the present simulation[3] (≈ 0.26). It will thus be closer to the experimental value[5] (≈ 0.3).

It should be noted that the drawing together of the composite drop and drop D is not an artifact due to the backward motion of the shell. The comparison between the Figs. 4 and

7 shows that the drops approach each other even before the beginning of the backward motion of the shell.

The considerations of Sec. VI A can be repeated for every direction of space: only the value of g will vary. For instance, it is easy to check that the drop closest to the composite drop in the r direction (see Fig. 2) will approach it slightly, akin to the shell during the first stage of the shell deformation (while $v_s>0$) (see Fig. 3). The motion of the other nearest neighbors will also conform to the motion of the corresponding parts of the shell.

We note here that the shell velocity does not influence directly the value of L_H. Thus the poor agreement of the specific values of the velocities in Fig. 7 at small ε cannot change L_H by any significant amount.

VII. CONCLUSIONS

Two approaches to the hydrodynamically controlled coalescence have been developed. The first (the shell model) allows a detailed hydrodynamic description of a coalescence induced by a previous coalescence. This induction is possible when the average distance between the drops exceeds a critical value. This value has been calculated for a chosen geometry. A physical analysis[3] shows that the model can explain some unusual experimental facts, e.g., a linear growth law of the average size of drops (2) and an interconnected morphology of the drop pattern. At the same time, the model requires making serious simplifications: the influence of the surrounding drops is accounted for by the introduction of a spherical surface (shell) which encloses the coalescing drops. The second model, the many-drop model, is developed to examine the validity of this approximation. Although it does not give information on the motion of the coalescing drops themselves, it describes the motion of the surrounding drops. The detailed comparison of the two models shows that the shell approximation is appropriate for the description of the process of chain coalescences, both models giving similar results in the beginning of the evolution. A shell interface tension smaller than that for the drops can be chosen to improve the shell model description at the later stages of the evolution.

ACKNOWLEDGMENTS

VN would like to thank the direction of DRFMC, CEA/Grenoble, for their kind hospitality and the Ministère de l'Enseignement Supérieur et de la Recherche of France for financially supporting this work.

APPENDIX A: THE EXPLICIT FORM OF THE COMPONENTS OF *B*

The arguments of B_{ij} are omitted for simplicity:

$$B_{rr}=kr^{-3/2}r_y^{-1/2}\{-[r^2+r_y^2+2(z-z_y)^2]F+[2(z-z_y)^4+3(z-z_y)^2(r^2+r_y^2)+(r^2-r_y^2)^2]E/r_{xy}^2\},$$

$$B_{rz}=kr^{-3/2}r_y^{1/2}(z_y-z)\{F+[r^2-r_y^2-(z-z_y)^2]E/r_{xy}^2\},$$

$$B_{zr}=kr^{-1/2}r_y^{-1/2}(z-z_y)\{F-[r^2-r_y^2+(z-z_y)^2]E/r_{xy}^2\},$$

$$B_{zz}=-2kr^{-1/2}r_y^{1/2}\{F+(z-z_y)^2]E/r_{xy}^2\},$$

where $k=2(rr_y)^{1/2}[(r+r_y)^2+(z-z_y)^2]^{-1/2}$ and $r_{xy}^2=(r-r_y)^2+(z-z_y)^2$. Here F and E are the complete elliptical integrals of the first and second kind with modulus k.

APPENDIX B: GEOMETRIC COALESCENCE LIMIT AND COALESCENCE LIMIT IN VACUUM

For the case of the shell model, there is a geometrical criterion for the second coalescence: $d_0/R<L_G$, where L_G is calculated below. For the real case of the many-drop system there is no geometrical constraint of L_G because the closed shell is absent.

The shell radius R_s is defined by

$$R_s=R+d_0+2(R+d_0/2)^2/[4(R+d_0/2)^2-(R+\psi/2)^2]^{1/2} \tag{B1}$$

according to Fig. 2. If there is enough room inside the shell, the composite drop eventually becomes spherical with the radius R_c. Here R_c can be determined from the value of the total volume of the composite drop V_c which is conserved during the evolution:

$$R_c=(3V_c/4\pi)^{1/3}. \tag{B2}$$

In turn, V_c can be calculated with sufficient accuracy as the sum of the volume of the torus and the small cylinder at its center of diameter ψ:

$$V_c=2\pi^2R^2(R+\psi/2)+\pi\psi^3/2. \tag{B3}$$

The geometric coalescence limit can be determined from the following condition. If R_s is smaller than

$$R_s^{\mathrm{cr}}=R_c+R+3\psi/2, \tag{B4}$$

the drops cannot avoid a point contact either between themselves or with the shell in their evolution to the equilibrium spherical shape. The value of R_s^{cr}/R can be determined explicitly from Eqs. (B2)–(B4) for given ψ/R. Then one can find the corresponding value of d_0/R (i.e., the geometric coalescence limit L_G itself) by solving (B1). For $R/\psi=10$ one finds $L_G\approx0.48$.

The coalescence limit in vacuum L_V defined in Sec. I can be found using the criterium (see Figs. 1 and 2)

$$(R_c+R+\psi)^2+(R+\psi/2)^2=(2R+L_VR)^2. \tag{B5}$$

For the chosen value of ψ it gives $L_V\approx0.99$.

APPENDIX C: VELOCITY FIELD FAR FROM THE SPHEROIDAL DROP

First, it is necessary to reduce the expressions for B_{ij} (see Appendix A) for the case $\rho\gg\rho_y=(r_y^2+z_y^2)^{1/2}$,

$$B_{rr}=\pi rr_y^2\rho^{-5}(2z^2-r^2),$$

$$B_{rz}=2\pi rr_y\rho^{-5}[-z\rho^2-z_y(2z^2-r^2)],$$

$$B_{zr}=\pi zr_y^2\rho^{-5}(2z^2-r^2),$$

$$B_{zz}=2\pi r_y\rho^{-5}[-\rho^2(z^2+\rho^2)-zz_y(2z^2-r^2)],$$

where $\rho=(r^2+z^2)^{1/2}$ is the distance from the reference point (center of the spheroid). One needs to calculate B_{ij} within the accuracy $O[(\rho_y/\rho)^2]$, because the first approximation gives zero for velocities when the integration path in (12) is symmetric (f_z and thus the integrands are odd with respect to z_y). In this case

$$v_r=\frac{Pr}{8\eta\rho^5}(2z^2-r^2), \quad v_z=\frac{Pz}{8\eta\rho^5}(2z^2-r^2), \tag{C1}$$

where

$$P=\int_{(L)} dl_y\,(r_y^2 f_r-2r_y z_y f_z).$$

For the spheroid $r^2/a^2+z^2/b^2=1$ and $\vec{f}$ from Eq. (7) the integration yields

$$P=\frac{b^2\sigma}{\varepsilon^2}\left[\frac{3+\varepsilon^2}{2\varepsilon}\ln\left(\frac{1-\varepsilon}{1+\varepsilon}\right)+\frac{3-\varepsilon^2}{1-\varepsilon^2}\right],$$

where $\varepsilon=(a^2-b^2)^{1/2}/a$ is the eccentricity of the spheroid. The oblate spheroid can be identified with the composite drop from Fig. 2 by equalizing their volumes [cf. Eq. (B3)]:

$$\frac{4}{3}\pi a^2 b=2\pi^2 R^3.$$

After elimination of b, P takes the form

$$P=R^2\sigma G(\varepsilon),$$
$$G(\varepsilon)=\frac{1}{\varepsilon^2}\left[\frac{3\pi}{2}(1-\varepsilon^2)\right]^{2/3}\left[\frac{3+\varepsilon^2}{2\varepsilon}\ln\left(\frac{1-\varepsilon}{1+\varepsilon}\right)+\frac{3-\varepsilon^2}{1-\varepsilon^2}\right]. \tag{C2}$$

APPENDIX D: RELATIVE VELOCITY OF SPHERICAL DROPS IN A GRADIENT FLOW

Because Ref. 14 is written in Russian, we present here some of its main results. Zinchenko considers the relative motion of two liquid drops of the same radius R embedded in another fluid with the velocity field

$$\vec{v}_\infty=\overleftrightarrow{E}\cdot(\vec{x}-\vec{x}_0)$$

at infinity where $\overleftrightarrow{E}$ and $\vec{x}_0$ are arbitrary and constant. We are interested in the particular choice of an axisymmetric flow for which the tensor $\overleftrightarrow{E}$ has the form

$$\overleftrightarrow{E}=\mathrm{diag}\,(-g/2,-g/2,g),$$

and the centers of the drops lie on the z axis. In this case the relative velocity of the drops is directed along the same axis,

$$V_z=glF, \tag{D1}$$

where l is the distance between the drop centers and F is a function of $\alpha=R/l$. For equal fluid viscosities inside and outside the drops, the asymptotic form for F in the limit of large distance is

$$F(\alpha)=1-\frac{7}{2}\alpha^3+\frac{18}{5}\alpha^5-\frac{49}{4}\alpha^6+O(\alpha^7). \tag{D2}$$

For large α the asymptotic limit is

$$\frac{1}{F(\alpha)}=0.690\left(\frac{\pi^2}{16}\delta^{-1/2}-\frac{2}{9}\ln\delta+0.559\right)+o(1), \tag{D3}$$

where $\delta=1/\alpha-2$. These expressions well describe the function F, (D2) being applied for $l/R>2.2$ and (D3) applied otherwise.

A positive value of V_z in (D1) corresponds to separating drops whereas a negative value corresponds to approaching drops.

[1] M. von Smoluchowski, ''Versuch einer matematishen Theorie dar koagulationskinetik kollider Lösungen,'' Z. Phys. Chem. (Munich) **92**, 129 (1917).

[2] H. Hayakawa, ''Fluctuation effects in coagulation processes,'' Physica A **175**, 383 (1991).

[3] V. S. Nikolayev, D. Beysens, and P. Guenoun, ''New hydrodynamic mechanism for drop coarsening,'' Phys. Rev. Lett. **76**, 3144 (1996).

[4] ψ can be defined as an effective range for attractive forces (e.g., van der Waals) which overcome the lubrication forces and, hence, make coalescence possible.

[5] Y. Jayalakshmi, B. Khalil, and D. Beysens, ''Phase separation under a weak concentration gradient,'' Phys. Rev. Lett. **69**, 3088 (1992).

[6] D. A. Ladyzhenskaya, *The Mathematical Theory of Viscous Incompressible Flow*, 2nd ed. (Gordon and Breach, New York, 1969).

[7] J. M. Rallison and A. Acrivos, ''A numerical study of the deformation and burst of a viscous drop in an extensional flow,'' J. Fluid Mech. **89**, 191 (1978).

[8] These expressions were used in Ref. 9 and 10, but there were misprints in both articles. The correct formulas are presented in Ref. 11.

[9] G. K. Youngren and A. Acrivos, ''Stokes flow past a particle of arbitrary shape: a numerical method of solution,'' J. Fluid Mech. **69**, 377 (1975).

[10] D. Ziemanas and A. Nir, ''On the viscous deformation of biological cells under anisotropic surface tension,'' J. Fluid Mech. **193**, 217 (1988).

[11] C. Pozrikidis, *Boundary Integral and Singularity Methods for Linearized Viscous Flow* (Cambridge U.P., Cambridge, 1992).

[12] D. Beysens, P. Guenoun, P. Sibille, and A. Kumar, ''Dimple and nose coalescences in phase-separation processes,'' Phys. Rev. E **50**, 1299 (1994).

[13] A. K. Chesters and G. Hofman, ''Bubble coalescence in pure liquids,'' Appl. Sci. Res. **38**, 353 (1982).

[14] A. Z. Zinchenko, ''Hydrodynamic interaction of two equal fluid spheres in linear flow field,'' Prikl. Mat. Mekh. **47**, 56 (1983).

[15] It is supposed that $R\sim l_b$, i.e., the volume fraction ϕ of the drops is large.

[16] There is a small error in the estimation of $v_u^{(2)}$ stemming from the difference between $l(0)$ and $l(1)$, but the accuracy is largely sufficient for the present consideration.

ELSEVIER

1 May 1998

OPTICS COMMUNICATIONS

Optics Communications 150 (1998) 263–269

Full length article

Coherent light transmission by a dew pattern

Vadim S. Nikolayev [a,1], Patrick Sibille [b], Daniel A. Beysens [a]

[a] *Département de Recherche Fondamentale sur la Matière Condensée, CEA Grenoble, 17, rue des Martyrs, 38054 Grenoble Cedex 9, France*

[b] *Service de Physique de l'Etat Condensé, CEA Saclay, 91191 Gif-sur-Yvette Cedex, France*

Abstract

We study both theoretically and experimentally the transmission of coherent light by a drop pattern (dew). The theory is based on the Kirchhoff scalar approach to diffraction. The polarization of the diffracted wave in the zero diffraction order is analyzed separately. The intensity in the zero diffraction order in the far zone is an oscillatory function of the drop size. These oscillations are observed with a pattern of water drops growing on glass. The model allows for the evolution of the important parameters of the drop pattern (average radius and surface coverage) to be obtained from the light intensity in the zero diffraction order.

1. Introduction

Depending on the wettability of the surface on which vapor condenses, dew forms a transparent film or a diffuse assembly of droplets. The knowledge of the properties of dew, ''breath figures'' or, generally speaking, dropwise condensation, opens a vast field of applications ranging from high-technology processes of film growth [1] to soil desinfection in agronomy [2], sterilization in pharmacology [3] and water recovery in dew condensers [4]. The optical properties of dew have received considerable attention from the scientists who studied the natural physical effects (see, e.g. Refs. [5,6]) and from those who are interested in industrial applications [7,8].

The morphology and kinetics of dew formation were investigated extensively both theoretically and experimentally (see e.g. Refs. [9,10] and references therein). Its growth can be characterized by several physical values, the most important of which are the mean radius $\langle a \rangle$ of the drops and the surface coverage ε^2, which is the fraction of surface area covered by the projections of the drops on the surface.

Two regimes of growth can be identified. At the beginning of the condensation process the drops grow independently, $\langle a \rangle$ follows a power law $\langle a \rangle \sim t^{\mu_0}$, where t is the elapsed time, and the surface coverage increases. When the temperature of the substrate is kept constant, $\mu_0 = \frac{1}{3}$. When the drop radius becomes large enough, coalescences between drops occur and the exponent changes to another value $\mu = 3\mu_0$. The growth is then self-similar and the surface coverage reaches a saturation value ε_∞^2 as well as all the statistical characteristics of the drop pattern, except $\langle a \rangle$. When the surface is ideally smooth and clean $\varepsilon_\infty^2 \approx 0.55$ independently of the wetting properties (characterized by the contact angle ϕ, see Fig. 1). For a nonideal surface, the pinning of the contact lines by the surface heterogeneities leads to a hysteresis of the contact angle, i.e. to a significant difference between the advancing and receding contact angles. The shape of the drop is no more a spherical cap. In this case ε_∞^2 becomes dependent on the hysteresis, and since the hysteresis effects are stronger for small contact angles [11], ε_∞^2 becomes higher as ϕ is smaller. This dependence will be used in Section 3 to determine the contact angle. In the analysis below, the drops are considered to be spherical caps and the influence of gravity, which is important only when the drop reaches

[1] Present address: Department of Physics, University of New Orleans, New Orleans, LA 70148, USA. E-mail: vnikol@uno.edu

0030-4018/98/$19.00
PII S0030-4018(98)00051-0

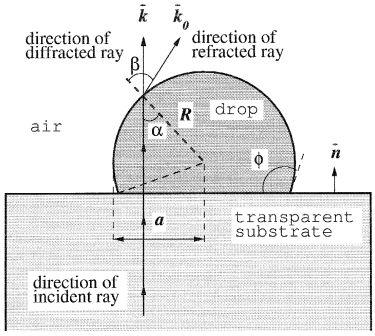

Fig. 1. Geometry of a drop. See text for explanation.

a size of ≈ 2 mm (the water capillary length), is neglected.

2. Theoretical description

Despite its importance, the optical properties of a dew pattern have up to now been investigated to our knowledge by geometrical optics only [2,6]. Indeed, the light scattering by a random set of nearly hemispherical drops with different size is quite difficult to describe. Here we give a solution in a particular, but important, case: we calculate the intensity of the zero order of the far zone diffraction, i.e. the transmission of a coherent light through the dew pattern.

2.1. Optical properties of a single drop

Let a monochromatic linearly polarized plane wave with amplitude $\boldsymbol{E}^s$ travel through a transparent substrate and then fall normally on the interface between the transparent substrate and a water drop (see Fig. 1). The wave is partially reflected, and the amplitude of the wave just after the plane substrate–water interface is [12] $2n_w\boldsymbol{E}^s/(n_w+n_s)$, where n_s and n_w are the refractive indices of the substrate and water respectively. Passing through water, the wave gains a phase shift. Thus the complex amplitude of the wave just before the water–air interface is

$$\boldsymbol{E}^i = 2n_w/(n_w+n_s)\boldsymbol{E}^s\exp(ik_0 n_w l), \tag{1}$$

where $k_0 = 2\pi/\lambda$, λ being the wavelength in vacuum, and

$$l = \sqrt{R^2 - r^2} - R\cos\phi, \tag{2}$$

is the geometrical path of the ray inside the water drop. Here r is the distance of the ray from the center of the drop (Fig. 1), R is the radius of curvature of the drop and ϕ is the contact angle. Then the ray is refracted and its polarization changes according to the Fresnel formulae [12]. While the component of the field which lies in the plane of incidence is transformed according to

$$E^t_{\parallel} = E^i_{\parallel} t_{\parallel} \quad \text{with } t_{\parallel} = \frac{2\sin\beta\cos\alpha}{\sin(\alpha+\beta)\cos(\alpha-\beta)}, \tag{3}$$

the component which lies in the perpendicular plane is

$$E^t_{\perp} = E^i_{\perp} t_{\perp}, \quad \text{with } t_{\perp} = \frac{2\sin\beta\cos\alpha}{\sin(\alpha+\beta)}, \tag{4}$$

where α and β are the angles of incidence and refraction respectively (see Fig. 1). These angles are related through the Descartes-Snellius law

$$n_w\sin\alpha = n_a\sin\beta, \tag{5}$$

where n_a is the refractive index of air and α is defined directly by r:

$$\sin\alpha = r/R. \tag{6}$$

We consider a polar coordinate system in a plane parallel to the substrate, see Fig. 2. It is chosen in such a way that its reference point coincides with the drop center O and the reference direction (called the ξ-axis below) is the direction of polarization of the incident wave. Then for an arbitrary point with coordinates (r,ψ)

$$E^i_{\parallel} = E^i\cos\psi, \quad E^i_{\perp} = E^i\sin\psi. \tag{7}$$

Using the $\xi O\eta$ Cartesian coordinate system (Fig. 2), it is easy to check with the help of Eqs. (3), (4) and (7) that

$$E^t_{\xi} = E^i\left(t_{\parallel}\cos^2\psi + t_{\perp}\sin^2\psi\right), \tag{8}$$

$$E^t_{\eta} = E^i\left(t_{\perp} - t_{\parallel}\right)\sin\psi\cos\psi. \tag{9}$$

Waves of different polarization do not interfere and can be analyzed separately. The η-components of the waves, emitted by two mirror symmetrical points (r,ψ) and $(r,-\psi)$ of the drop surface satisfy the following relation

$$E^t_{\eta}(r,\psi) + E^t_{\eta}(r,-\psi) = 0. \tag{10}$$

Because the drop is a spherical cap and the incidence is normal, the angles α and β as defined by Eqs. (5) and (6) are independent of the ψ-coordinate of the incident ray (Fig. 2). Thus $t_{\parallel}$ and $t_{\perp}$ as defined in (3) and (4) are

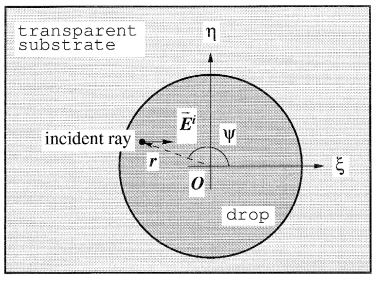

Fig. 2. Top view of the drop in Fig. 1 with $\xi O\eta$ Cartesian and $rO\psi$ polar coordinate systems.

independent of ψ too. Then (10) follows from (9). Therefore, as far as only the zero order of diffraction is concerned, the η-polarized components of the waves which come from two these points annihilate each other. Since this argument is applicable to every two symmetrical points, the η-polarized components of the waves yield no contribution. Therefore, the wave in the zero order of diffraction (unlike any other point in the image plane) is polarized in the ξ-direction, i.e. in the direction of polarization of the incident wave. This allows the index ξ to be omitted hereafter and the scalar wave theory for the ξ-component to be applied. The key parameter of this theory [12] is the complex transparency of the drop which we introduce now.

The visible radius of the drop a can be related to its curvature radius R through the contact angle ϕ (see Fig. 1):

$$\zeta \equiv \frac{a}{R} = \begin{cases} \sin\phi, & \text{if } \phi < \pi/2, \\ 1, & \text{otherwise.} \end{cases} \tag{11}$$

We neglect the contribution of the rays which are multiply reflected or refracted before leaving the drop. Each reflection or refraction decreases strongly the amplitude of the corresponding fields according to the Fresnel formulae, the angles of reflection or refraction being there large. An additional attenuation is due to the light absorption by water. Another reason for amplitude decrease is the angle factor K, which is small for the large angles of refraction (see below).

When the angle of incidence at the surface of the drop α (see Fig. 1) is larger than α_{cr}, which is defined by the relation

$$\sin\alpha_{\mathrm{cr}} = \gamma \equiv n_a/n_w,$$

full internal reflection occurs. Therefore, two regions can be defined in a drop: an inner transparent region of radius $a' < a$ and an outer annular ''black'' region. The ratio $\chi = a'/R$ is easy to determine by using Fig. 1 after straightforward geometrical arguments:

$$\chi = \begin{cases} \gamma, & \text{if } \alpha_{\mathrm{cr}} < \phi < \pi - \alpha_{\mathrm{cr}}, \\ \sin\phi, & \text{otherwise.} \end{cases} \tag{12}$$

The contribution of the rays which have to cross an air layer before entering the drop when $\phi > \pi/2$ is neglected in accordance with our ''single-refraction'' assumption.

The complex transparency of the drop with visible radius a can be written as

$$\tau_a(\boldsymbol{r}) = \begin{cases} \dfrac{n_w(n_a+n_s)}{n_a(n_w+n_s)} C(\psi) \mathrm{e}^{ik_0(n_w-n_a)l-\mu l} & \text{if } 0 \le r \le a', \\ 0, & \text{if } a' < r < a, \\ 1, & \text{if } r \ge a, \end{cases} \tag{13}$$

where μ is the coefficient of light absorption. It is negligible for visible light and we put $\mu = 0$ in the following. The function $C(\psi)$ is given by

$$C(\psi) = t_{\|}\cos^2\psi + t_{\perp}\sin^2\psi. \tag{14}$$

Eq. (13) follows from (8) after substitution of (1) and division by the amplitude of the wave unperturbed by the presence of the drop.

2.2. Diffraction by a single drop.

Kirchhoff's formula [12], reduced for the diffraction in the far zone, gives the following expression for the amplitude depending on the direction to the point of observation $\boldsymbol{k}$:

$$E(\boldsymbol{k}) = \int\int \tau_a(\boldsymbol{r}) K \exp\left[-in_a \boldsymbol{r}\cdot(\boldsymbol{k}_0+\boldsymbol{k})\right] \mathrm{d}\boldsymbol{r}, \tag{15}$$

where τ_a is the complex transparency of the object and K is the angle factor given by

$$K = \frac{1}{2k_0}(\boldsymbol{k}_0+\boldsymbol{k})\cdot\boldsymbol{n}. \tag{16}$$

The integration in (15) is performed over the reference plane parallel to the substrate, $\boldsymbol{n}$ is a unit normal to it (Fig. 1), $\boldsymbol{k}_0$ is a normal vector to the wave front which falls on the reference plane, $|\boldsymbol{k}_0| = |\boldsymbol{k}| = k_0$. Expression (15) holds just for the small scattering angles, i.e. for $\boldsymbol{k}$ close to $k_0\boldsymbol{n}$ (in the case considered here $\boldsymbol{k} = k_0\boldsymbol{n}$ exactly). Thus (16) reads

$$K = \tfrac{1}{2}\left(\frac{\boldsymbol{k}_0}{k_0}\cdot\boldsymbol{n} + 1\right).$$

For the diffraction by the drop (see Fig. 1) this expression reduces to

$$K = \tfrac{1}{2}\left[\cos(\beta-\alpha)+1\right]. \tag{17}$$

In the familiar case of the Fraunhofer diffraction by a hole or by a quasi-flat phase object, $\boldsymbol{k}_0$ does not depend on $\boldsymbol{r}$, $\boldsymbol{k}_0 = k_0\boldsymbol{n}$, and $E(\boldsymbol{k})$ is just the Fourier-transform of $\tau_a(\boldsymbol{r})$. In the case of a drop, the direction of $\boldsymbol{k}_0$ is a function of $\boldsymbol{r}$, and $E(\boldsymbol{k})$ is the Fourier transform of the function

$$\tilde{\tau}_a(\boldsymbol{r}) = \tau_a(\boldsymbol{r}) K \exp(-in_a \boldsymbol{r}\cdot\boldsymbol{k}_0). \tag{18}$$

Note that $\tilde{\tau}_a(\boldsymbol{r}) = \tau_a(\boldsymbol{r}) = 1$ outside the drop.

2.3. Zero-order diffraction by a dew pattern

The theory of diffraction by an assembly of objects is presented in Ref. [13] under the assumption of applicability of the conditions of Fraunhofer diffraction when the amplitude in the image plane is the Fourier transform of the object transparency. It is shown in Ref. [13] that the intensity in the zero diffraction order is defined by the

so-called ''Debye volume scattering term'' which can be written within a constant as

$$I_0 \equiv |E(\boldsymbol{k}=0)|^2 = |\langle\tau\rangle|^2, \tag{19}$$

where

$$\langle\tau\rangle = \frac{1}{s_1}\left\langle \int_{(s_1)} \tau_a(\boldsymbol{r})\,\mathrm{d}\boldsymbol{r}\right\rangle. \tag{20}$$

Here s_1 is the total illuminated area of the substrate divided by the total number of the drops and the angle brackets mean an average over the size distribution. Although the theory was developed for a real transparency $\tau_a(\boldsymbol{r})$ (called ''density'' in Ref. [13]), it can be easily generalized for the complex case. The invariance with respect to the spatial distribution of the drops is an interesting feature of expression (19).

As already discussed, the function $\tilde{\tau}_a(\boldsymbol{r})$ should be used in (20) instead of $\tau_a(\boldsymbol{r})$. It is easy to check that this function is radially symmetric which is a necessary condition of the applicability of the results [13]. Thus

$$\tau = 1 - \frac{\pi a^2}{s_1} + \frac{1}{s_1}\,\frac{n_a+n_s}{n_w+n_s}\,\frac{n_w}{n_a} \times \int_0^{a'} JKr \exp\{ ik_0[(n_w-n_a)l + n_a r\sin(\beta-\alpha)]\}\,\mathrm{d}r, \tag{21}$$

where

$$J = \int_0^{2\pi} C(\psi)\,\mathrm{d}\psi = \pi(t_\parallel + t_\perp).$$

In order to find an average of (21), one needs to introduce the distribution $H(a)$, which defines the probability to find a drop with the visible radius a. Since the two important physical values are the average size $\langle a\rangle$ and the polydispersity $g = (\langle a^2\rangle - \langle a\rangle^2)^{1/2}/\langle a\rangle$, a distribution with only two free parameters can be considered. We choose for this purpose the Maxwellian distribution as described in Ref. [13]:

$$H(a) = \frac{B(m)}{a_0}\left(\frac{a}{a_0}\right)^m \mathrm{e}^{-(a/a_0)^2}, \tag{22}$$

where $B(m)$ is a normalization constant. The free parameters $m \geq -1$ and a_0 can be related to g and $\langle a\rangle$ [13] through

$$g \approx (2m+2)^{-1/2}, \tag{23}$$

$$\langle a\rangle \approx a_0[(m+0.5)/2]^{1/2}. \tag{24}$$

These approximations become accurate within less than 1% when $m > 4$.

The mean surface coverage ε^2 is related to s_1 by $\varepsilon^2 = \pi\langle a^2\rangle/s_1$. Note that it is defined here by the *projected* area covered by the drops, not by the actual area in contact with water. The set of Eqs. (21)–(24) allows one to calculate $\langle\tau\rangle$ as a function of the parameters $\langle a\rangle$, g (or a_0, m) and ε^2:

$$\langle\tau\rangle = 1 - \varepsilon^2 + \frac{\varepsilon^2}{\zeta^2\gamma^2}\,\frac{n_a+n_s}{n_w+n_s}B(m+2) \times \int_{\sqrt{1-\chi^2}}^1 \mathrm{d}x\,\frac{x^2(1+\gamma+\upsilon x-x^2)^2}{(\upsilon+x)(\upsilon x+1-x^2)} \times \int_0^\infty \mathrm{d}y\, y^{m+2}\exp\left\{ iyn_w\frac{2\pi a_0}{\zeta\lambda}[(1-\gamma)(x-\cos\phi) - (1-x^2)(x-\upsilon)] - y^2\right\}, \tag{25}$$

where $\upsilon = \sqrt{x^2+\gamma^2-1}$. The intensity of the zero diffraction order I_0 can now be calculated by using (19).

Let us analyze now the function $I_0(\langle a\rangle)$ with g and ε^2 as parameters. This choice reflects the growth kinetics of the self-similar regime (see Section 1) when the only growing parameter is $\langle a\rangle$. Oscillations of the function $I_0(\langle a\rangle)$ can occur due to the exponential dependence of ia_0, the latter being related to $\langle a\rangle$ by (24).

The asymptotic values of the function $I_0(\langle a\rangle)$ can be calculated explicitly:

$$I_0(\langle a\rangle \to 0) = \left[1 - \varepsilon^2 + \frac{\varepsilon^2}{\zeta^2\gamma^2}\,\frac{n_a+n_s}{n_w+n_s} \times \int_{\sqrt{1-\chi^2}}^1 \frac{x^2(1+\gamma+\upsilon x-x^2)^2}{(\upsilon+x)(\upsilon x+1-x^2)}\,\mathrm{d}x\right]^2, \tag{26}$$

$$I_0(\langle a\rangle \to \infty) = (1-\varepsilon^2)^2. \tag{27}$$

The interesting feature of these expressions is that they do not depend on the polydispersity and, therefore, on the form of the function $H(a)$. While (26) is not particularly useful for practical purposes (since $\varepsilon^2 = 0$ always when $\langle a\rangle = 0$, giving $I_0 = 1$), Eq. (27) is more interesting because it relates $I_0(t\to\infty)$ to ε_∞^2. It is easy to see that the value (27) gives the geometrical optics limit and corresponds to the transparency of an assembly of black spots. In this case $\langle\tau\rangle = 1-\varepsilon^2$ and I_0 depends either on the shape or on the size of the spots through ε^2 only. One can therefore conclude that the presence of the oscillations is connected to the phase shift of the transmitted wave by the drops.

The results of the calculations of the function $I_0(\langle a\rangle)$ for different constant values of the other parameters are presented in Figs. 3 and 4. We recall here that in a real condensation experiment g and ε^2 are not constant in the beginning of the growth (see Section 1). Thus the curves presented in Figs. 3 and 4 cannot be observed experimentally. For example, it is generally impossible to obtain $\varepsilon^2 = 0.6$ for small values of $\langle a\rangle$, while the curve which

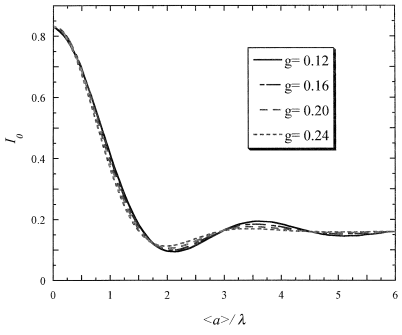

Fig. 3. The function $I_0(\langle a\rangle)$ for $\varepsilon^2 = 0.6$, $\phi = 90°$ and for different values of g.

corresponds to this surface coverage is plotted for all values of $\langle a\rangle$ in Fig. 4.

Figs. 3 and 4 show that the amplitude of the oscillations of the function $I_0(\langle a\rangle)$ is controlled mainly by the polydispersity, while the ''mean'' level, around which the intensity oscillates, depends strongly on ε^2. A large polydispersity suppresses the oscillations. The positions of the extrema of $I_0(\langle a\rangle)$ are practically independent of ε^2 and g over a wide range of the parameters. However, the dependence of the positions of the extrema on the contact angle ϕ is stronger. It is presented in Fig. 5. These features allow the values of the parameters $\langle a\rangle$ and ε^2 to be determined experimentally as will be demonstrated below.

3. Experimental: determination of the characteristics of a dew pattern

The sketch of the experimental setup is shown in Fig. 6. It is derived from the setup in Ref. [14]. It permits simultaneous observation of the scattered light and measurement of the intensity on the optical axis. No direct visualization of the droplets was sought. Dew is produced

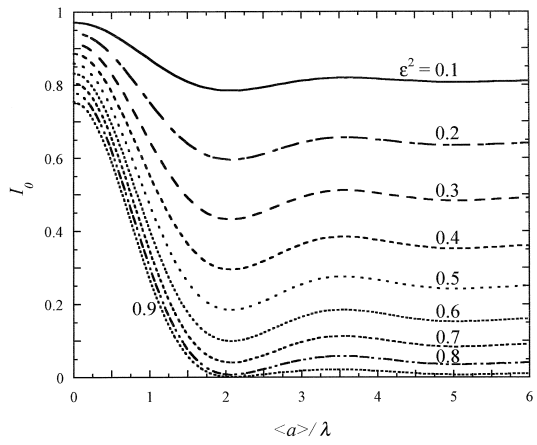

Fig. 4. The function $I_0(\langle a\rangle)$ for $g = 0.16$, $\phi = 90°$ and for different values of ε^2.

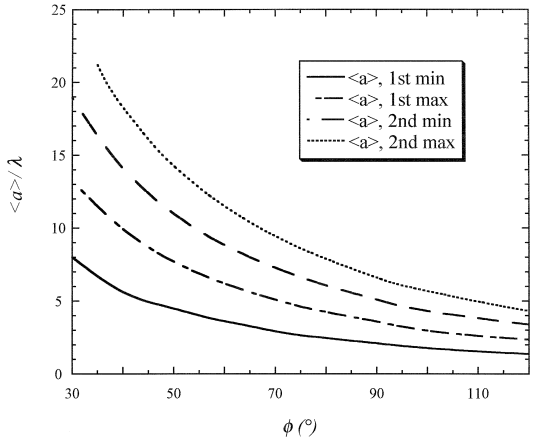

Fig. 5. The positions of the four first extrema of the function $I_0(\langle a\rangle)$ versus the contact angle ϕ for $g = 0.16$ and $\varepsilon^2 = 0.6$.

by blowing air saturated with water vapor on a cooled glass slide coated with a hydrophobic layer of silane, which plays the role of the substrate from the optical point of view. The process of glass coating is described in Ref. [10]. The coherent light beam generated by a 5 mW He-Ne laser ($\lambda = 0.6328$ μm) passes through the glass plate and the dew pattern. The diffracted light is collected by a large lens (10cm diameter) placed at its focal length. The diffraction pattern is visualized through a translucid screen. The pictures are recorded by a CCD video camera and digitized for further analysis. A mirror placed at the center of the lens deviates the transmitted light perpendicularly towards a photodiode. The distance between the photodiode and the mirror is chosen so as to provide the conditions of Fraunhofer diffraction [12] in the photodiode plane. The size of the mirror and the pin-hole in front of the photodiode correspond to the width of the laser beam. This allows all the light to be collected in the absence of scattering by dew. When condensation starts, the photodiode measures the intensity of the zero diffraction order. The temperature of the glass slide is stabilized by an attached large copper block connected to the Peltier ele-

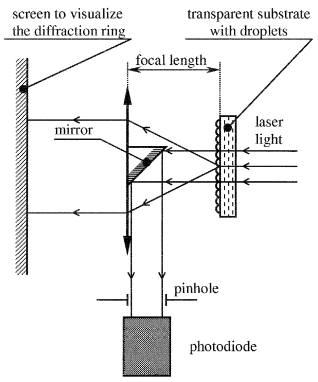

Fig. 6. Schematic diagram of the experimental setup.

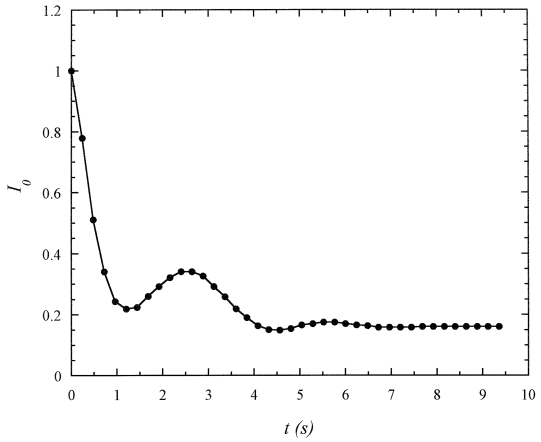

Fig. 7. Experimental time evolution of I_0. The data are normalized by the value I_0 at $t = 0$.

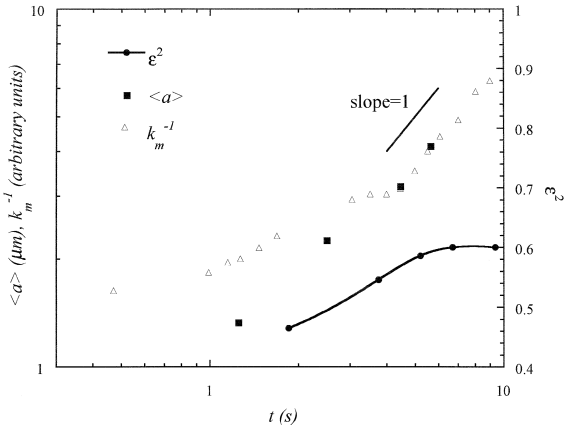

Fig. 8. Time evolution of the wave vector modulus k_m, the drop surface coverage ε^2 and the mean radius of the droplets $\langle a \rangle$.

ment and a power supply. The temperature is controlled during the experiment. The video image and the photodiode signal are simultaneously recorded when vapor is blown onto the glass slide.

A typical I_0 recording is shown in Fig. 7. The time evolution of I_0 can be understood on the basis of the model considered in the previous section. The sharp decrease of the ''mean'' value with respect to the oscillations reflects the evolution of the surface coverage ε^2. The latter increases until it reaches the value ε_∞^2. Several oscillations appear, in agreement with the above theoretical prediction. Moreover, the model gives an opportunity to determine the parameters of the dew pattern by using the time dependence of I_0 (Fig. 7). The algorithm for the determination of ε^2 and $\langle a \rangle$ as functions of time t can be described as follows.

1. The value of I_0 at large time corresponds to the saturation value (27). Here we obtain $I_0 = 0.16$, thus $\varepsilon_\infty^2 = 0.6$.

2. The data [11] where ε_∞^2 is plotted versus contact angle shows that this value corresponds to an average contact angle $\phi \simeq 90°$. We thus use the data calculated for this particular value of ϕ.

3. Because the positions of the extrema of the function $I_0(\langle a \rangle)$ are nearly independent of ε^2 and g, we can determine with high accuracy the values of $\langle a \rangle$ at the times which correspond to the extrema of the function $I_0(t)$. They are plotted versus t in Fig. 8.

Fig. 3 shows that the value of I_0 is independent of the polydispersity g in the inflection points [2] of the function $I_0(\langle a \rangle)$. By making use of this property, we can obtain the values of ε^2 by the following steps.

4. The time values at the inflection points and the corresponding values of the intensity are extracted from Fig. 7.

5. The values of $\langle a \rangle$ at these values of time are determined by the interpolation of the dependence $\langle a \rangle(t)$ obtained in step 3.

6. Eq. (25) can be rewritten in the form

$$\langle \tau \rangle = 1 - \varepsilon^2 + \varepsilon^2 (A + iD), \tag{28}$$

where the quantities A and D are independent of ε^2. Then (19) with the substitution of (28) can be easily solved for ε^2:

$$\varepsilon^2 = \left\{ 1 - A - \left\{ I_0 \left[D^2 + (1-A)^2 \right] - D^2 \right\}^{1/2} \right\} / 2 / \left[D^2 + (1-A)^2 \right]. \tag{29}$$

Since A and D can be calculated for an arbitrary value of g (we took $g = 0.16$) and values of $\langle a \rangle$, obtained in the step 5, the corresponding values of ε^2 can be determined from (29) by using the values of I_0 from step 4. These data for $\varepsilon^2(t)$ are plotted in Fig. 8 with the saturation value from the step 1.

One can see that the curve $\varepsilon^2(t)$ is similar to the curve obtained by numerical simulation [10]. The time evolution of $\langle a \rangle$ can be compared with that of k_m^{-1}. The value of k_m is defined as the wavevector corresponding to the maximum intensity in the diffraction pattern (ring). It is obtained by the image analysis of the diffraction picture as recorded by the video camera. One can see that for large times the growth laws of k_m^{-1} and $\langle a \rangle$ are the same. They correspond to the growth exponent $\mu \simeq 1$.

4. Conclusions

The theoretical model developed here deals with the intensity of the coherent light transmitted by a time dependent dew pattern. The theory explains the oscillations of the intensity observed in the zero diffraction order in the

[2] The only exception is the first inflection point, not used in the following.

far zone. In addition, the model allows the evolution of the two most important parameters of the drop pattern to be assessed: the average drop radius and the drop surface coverage.

Acknowledgements

V.N. would like to thank the direction of DRFMC, CEA/Grenoble for its kind hospitality and the Ministère de l'Enseignement Supérieur et de la Recherche of France for financially supporting this work.

References

[1] D. Beysens, C.M. Knobler, H. Schaffar, Phys. Rev. B 41 (1990) 9814.
[2] A. Jaffrin, S. Makhlouf, C. Scotto La Massese, A. Bettachini, R. Voisin, Agronomie 9 (1989) 729.
[3] M. Marcos-Martin, A. Bardat, R. Schmitthaeusler, D. Beysens, Pharm. Techn. Eur. 8 (1996) 24.
[4] V.S. Nikolayev, D. Beysens, A. Gioda, I. Milimouk, E. Katiushin, J.P. Morel, J. Hydrology 182 (1996) 19.
[5] A.B. Fraser, Appl. Optics 33 (1994) 4539.
[6] B.J. Briscoe, K.P. Galvin, Solar Energy 46 (1991) 191.
[7] J.G. Pieters, J.M. Deltour, M.J. Debruyckere, J. Phys. III (France) 6 (1996) 975.
[8] S. Matsumoto, S. Toyooka, Optics Comm. 91 (1992) 5.
[9] B.J. Briscoe, K.P. Galvin, Phys. Rev. A 43 (1991) 1906.
[10] D. Fritter, C.M. Knobler, D.A. Beysens, Phys. Rev. A 43 (1991) 2858.
[11] H. Zhao, D. Beysens, Langmuir 11 (1995) 627.
[12] M. Born, E. Wolf, Principles of Optics, Pergamon Press, Oxford, 1980.
[13] R. Hosemann, S.N. Bagchi, Direct Analysis of Diffraction by Matter, North-Holland, Amsterdam, 1962.
[14] F. Perrot, D. Beysens, Rev. Sci. Instrum. 58 (1987) 183.

EUROPHYSICS LETTERS 1 August 1999

Europhys. Lett., **47** (3), pp. 345-351 (1999)

Boiling crisis and non-equilibrium drying transition

V. S. Nikolayev and D. A. Beysens

Département de Recherche Fondamentale sur la Matière Condensée, CEA Grenoble 17, rue des Martyrs, 38054, Grenoble Cedex 9, France

(received 22 December 1998; accepted in final form 31 May 1999)

PACS. 68.45Gd – Wetting.
PACS. 68.45Da – Adsorption and desorption kinetics; evaporation and condensation.

Abstract. – Boiling crisis is the rapid formation of the quasi-continuous vapor film between the heater and the liquid when the heat supply exceeds a critical value. We propose a mechanism for the boiling crisis that is based on the spreading of the dry spot under a vapor bubble. The spreading is initiated by the vapor recoil force, a force coming from the liquid evaporation into the bubble. Since the evaporation intensity increases sharply near the triple contact line, the influence of the vapor recoil can be described as a change of the apparent contact angle. Therefore, for the most usual case of complete wetting of the heating surface by the liquid, the boiling crisis can be understood as a drying transition from complete to partial wetting.

The state of nucleate boiling, which is boiling in its usual sense, is characterized by a very large rate of heat transfer from the heating surface to the bulk because the superheated liquid is carried away from the heating surface by the departing vapor bubbles. If the heating power is increased, the temperature of the heating surface increases with the heat flux. When the heat flux from the heater reaches a threshold value q_{CHF} (the critical heat flux, CHF), the vapor bubbles suddenly form a film which covers the heating surface and insulates the latter from the bulk of the liquid. The temperature of the heating surface grows so rapidly that the heater can fuse unless its power is controlled. This phenomenon is known under the names of "boiling crisis", "burnout", or "Departure from Nucleate Boiling" (DNB) [1]. The final state of this transition is called film boiling.

This problem has become very important since the 1940s, with the beginning of the industrial exploitation of heat exchangers with large heat fluxes (as with nuclear power stations). Since then a huge amount of research has been done for the various conditions of pool boiling (boiling without imposed external flow) and flow boiling (boiling of the flowing water) [2]. Numerous empirical correlations have been proposed, each describing the dependence of the CHF on the physical parameters of the liquid and of the heater more or less correctly for a particular geometry and particular conditions of boiling [2]. A strong dependence of the threshold on the details of the experimental setup coupled with difficulties in separating the consequences of DNB from its causes is at the origin of a large number of frequently controversial hypotheses [2]. The violence of boiling makes observations quite difficult. Good-quality

photographic experiments are presented in only a few articles (see, *e.g.*, [3-6]). Despite an increasing interest in the physical aspect of the problem during recent years [7,8] and numerous empirical approaches, the underlying physics still remains obscure. In this letter, we propose a model based on a non-equilibrium drying transition.

DNB is a really universal phenomenon which occurs inevitably for pool as well as for flow boiling and for different flow structures, flow velocities, liquid temperatures and pressures. Apparently, the occurrence of the crisis does not induce any change in the flow. The phenomenon is local [9]: it depends strongly only on the local values of the parameters in a very thin layer of liquid adjacent to the heating surface. This layer is nearly quiescent because of the no-slip boundary condition for the fluid velocity at the heating surface. It is thus unreasonable to assume different physical causes for DNB according to the different conditions of pool or flow boiling, and we think that the crisis should be induced by the *same physical phenomenon*. The occurrence of DNB is influenced by the local values of only a few parameters, the most important being the distribution of the local temperature. As a consequence of the local origin of DNB, the threshold depends strongly on the wetting properties of the heating surface. *A priori*, it is quite difficult to extract the dependence of the CHF on the parameters of the heating surface because even a minor modification of its chemical composition can cause a large change in its thermal resistance which controls the temperature distribution and, hence, DNB itself. However, numerous experiments [2,10] show the general tendency: a poor wetting of the heating surface by the liquid favors the DNB and *vice versa*.

The experiments [4,6] in visualization of dry spots under the vapor bubbles on the heating surface show that at the CHF a *single* dry spot suddenly begins to spread. However, its size at the CHF remains finite. These experiments show that the bubble coalescence on the heating surface is not the leading process. In [7,11,12] the vapor recoil instability [13] is proposed as a reason for DNB. Although it is not clear how an instability can induce the spreading of the dry spots, the authors show that the vapor recoil force can be important at large evaporation rates. The force originates in the uncompensated momentum of vapor which is generated on the liquid-vapor interface during the evaporation. In the reference frame of the bulk liquid, the momentum conservation implies

$$\vec{P}_{\mathrm{r}} + \eta(\vec{v}_{\mathrm{V}} + \vec{v}_{\mathrm{i}}) = 0, \tag{1}$$

where $\vec{P}_{\mathrm{r}}$ is the vapor recoil force per unit interface area, η is the evaporated mass per unit time and unit interface area, $\vec{v}_{\mathrm{i}}$ is the interface velocity, and $\vec{v}_{\mathrm{V}}$ is the vapor velocity with respect to the interface. It is easy to establish that $\vec{v}_{\mathrm{i}} = -\eta/\rho_{\mathrm{L}}\ \vec{n}$, where $\vec{n}$ is a unit vector normal to the interface directed inside the vapor bubble (fig. 1). The mass conservation on the interface yields $\vec{v}_{\mathrm{V}} = -\rho_{\mathrm{L}}/\rho_{\mathrm{V}}\ \vec{v}_{\mathrm{i}}$, where ρ_{L} and ρ_{V} are the mass densities of the liquid and the vapor. Therefore, (1) implies [13]

$$\vec{P}_{\mathrm{r}} = -\eta^2(\rho_{\mathrm{V}}^{-1} - \rho_{\mathrm{L}}^{-1})\vec{n}. \tag{2}$$

The surface deformation caused by this force is important whenever the evaporation is strong, *e.g.*, during high-power welding [14] or for evaporation at low pressures [13].

The rate of evaporation η can be related to the local heat flux across the interface q_{L} by the equality

$$q_{\mathrm{L}} = H\eta, \tag{3}$$

where H is the latent-heat of evaporation. Hereafter, we neglect heat conduction in the vapor with respect to the latent heat effect.

Below, we treat only the case of a system at high pressure, comparable to the critical pressure for the sake of simplicity. Then the growth of the bubble is slow enough to let the surface

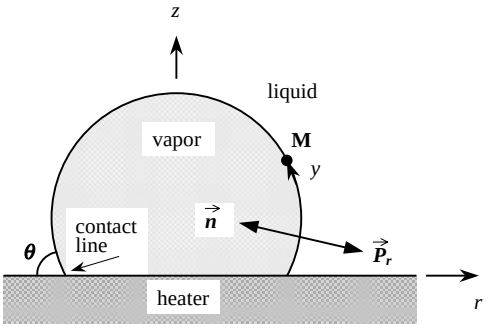

Fig. 1. – Vapor bubble on the heating surface surrounded by liquid. The directions of the vectors $\vec{P}_{\rm r}$ and $\vec{n}$ are shown as well as the axes for the cylindrical coordinate system.

tension equilibrate its shape, and the forces of hydrodynamic origin can be neglected [1]. This allows the problem to be considered in the quasi-static approximation. However, the vapor recoil remains the leading effect for any pressure.

The spreading of the dry spot looks similar to the spreading of a liquid that wets a solid. But in the case of DNB, it is *vapor* which seems to "wet" the solid. This never happens for a non-metal liquid under equilibrium conditions (zero heat flux) on a perfectly clean and smooth metal surface [15], the finite contact angle being possible due to the surface defects only. We show below that a kind of drying transition occurs due to the vapor recoil force at some heat flux that we associate with the CHF.

Using the quasi-static approximation, the variational approach [16] can be applied to analyze the shape of a vapor bubble just before the boiling crisis. The free energy of the system consists of two parts. The first part is conventional [16],

$$U_1 = \sigma A + \sigma_{\rm VS} A_{\rm VS} + \sigma_{\rm LS} A_{\rm LS} - \lambda V, \tag{4}$$

where σ, $\sigma_{\rm VS}$, and $\sigma_{\rm LS}$ are the surface tensions for vapor-liquid, vapor-solid and liquid-solid interfaces, respectively; $A_{\rm VS}$ and $A_{\rm LS}$ are the corresponding interface areas; and A is the area of the vapor-liquid interface (fig. 1). The last term in (4) reflects the fact that the shape of the bubble should be found for its given volume V, λ being the Lagrange multiplier. The equation $\delta U_1 = 0$, where δU_1 is the energy change due to an infinitesimal displacement $\delta\vec{r}$ of A [16] yields the classical conditions of the bubble equilibrium in the absence of the external forces.

The second part U_2 of the free energy accounts for the virtual work of the external forces:

$$\delta U_2 = -\int_{(A)} \vec{P}_{\rm r} \cdot \delta\vec{r}\, {\rm d}A. \tag{5}$$

The minimization $\delta U_1 + \delta U_2 = 0$ of the total energy leads [16] to two equations. The first is the condition for local equilibrium of the interface

$$K\sigma = \lambda + P_{\rm r}, \tag{6}$$

where K is the local curvature of the bubble and $P_{\rm r} = |\vec{P}_{\rm r}|$. The second equation is $\cos\theta = c$, where $c = (\sigma_{\rm VS} - \sigma_{\rm LS})/\sigma$ and θ is the contact angle (fig. 1). For the case $c > 1$ (as for the case of water on metal surface) the second equation should be substituted by the condition $\theta = 0$.

Let us denote by y the distance along the bubble contour measured from the triple line to a given point M as shown in fig. 1. To find the bubble shape by solving eq. (6) we need to know

the vapor recoil as a function of y. In the following, we introduce a rough approximation to solve the very complicated problem of the heat exchange around the growing bubble. The case of saturated boiling is assumed. Thus the vapor-liquid interface is maintained at temperature T_s, the saturation temperature at the system pressure. We also assume for simplicity that the thermal effect of convection can be taken into account by renormalizing the liquid thermal conductivity. To estimate how P_r varies near the contact line (*i.e.* when $y \to 0$) we suppose the bubble to be two-dimensional with the contact angle $\theta = \pi/2$. Since we describe the heat exchange in a thin layer adjacent to the heating surface, we can imagine the bubble contour A to be a line Oy perpendicular to the Ox heater line. Then q_L can be obtained from the solution of a simple two-dimensional problem of unsteady heat conduction in a quarter plane $x, y > 0$, the point $O(x = 0, y = 0)$ corresponding to the contact line. The boundary and the initial conditions for this problem can be written in the form

$$T_\mathrm{L}|_{x=0} = T_\mathrm{s}, \qquad -k_\mathrm{L} \left.\frac{\partial T_\mathrm{L}}{\partial y}\right|_{y=0} = q_\mathrm{S}, \qquad T_\mathrm{L}|_{t=0} = T_\mathrm{s},$$

where $T_\mathrm{L}(x, y, t)$ is the liquid temperature, k_L is the liquid thermal conductivity, and q_S is the heat flux from the heating surface which is assumed to be uniform for the case of the thin heating wall. The solution for this problem of heat conduction reads

$$T_\mathrm{L} = T_\mathrm{s} + \frac{q_\mathrm{S}}{k_\mathrm{L}} \sqrt{\frac{\alpha_\mathrm{L}}{\pi}} \int_0^t \frac{\mathrm{d}t}{\sqrt{t}} \operatorname{erf}\left(\frac{x}{2\sqrt{\alpha_\mathrm{L} t}}\right) \exp\left[-\frac{y^2}{4\alpha_\mathrm{L} t}\right], \tag{7}$$

where α_L is the liquid thermal diffusivity. This solution implies the following expression for $q_\mathrm{L}(y)$:

$$q_\mathrm{L} = -k_\mathrm{L} \left.\frac{\partial T_\mathrm{L}}{\partial x}\right|_{x=0} = -\frac{q_\mathrm{S}}{\pi} E_1\left(\frac{y^2}{4\alpha_\mathrm{L} t}\right). \tag{8}$$

The exponential integral $E_1(y)$ [17] decreases as $\exp[-y]/y$ as $y \to \infty$. Therefore P_r (related to q_L via (2) and (3)) is a rapidly decreasing function of y. Note that $E_1(y)$ diverges logarithmically at the point $y = 0$. The divergence demonstrates that the evaporation is strongest in the vicinity of the contact line. Since this singularity is integrable, the heat flux through any finite part of the interface is finite.

In the following we will use for illustration the dependence $P_\mathrm{r}(y)$ in the form that retains the main physical features:

$$P_\mathrm{r} = -C \log(y/L) \exp[-(y/y_\mathrm{r})^2], \tag{9}$$

where L is the length of the half-contour of the 3D axially symmetrical bubble. The coordinate y is measured along the contour from the triple line as shown in fig. 1. The characteristic length of the vapor recoil decay y_r changes in time and is proportional to $\sqrt{\alpha_\mathrm{L} t}$ (cf. (8)). Meanwhile, the bubble grows and its radius is proportional to the same factor [1] during the late stages of its growth. Therefore, y_r is proportional to the bubble size; this fact is taken care of by the expression $y_\mathrm{r} = aL$, where a is the non-dimensional fraction of the bubble surface on which the vapor recoil is important. From the physical point of view, y_r characterizes the width of the superheated layer of liquid, which is always less than the bubble size [1], thus $a \ll 1$. This allows the upper limit of integration to be put to infinity in the following expression for the non-dimensional strength of the vapor recoil:

$$N_\mathrm{r} = \frac{1}{\sigma} \int_0^\infty P_\mathrm{r}\, \mathrm{d}y. \tag{10}$$

The integration can be performed analytically yielding the relation between C and N_r: $N_\mathrm{r} = CaL/(4\sigma)\sqrt{\pi}[\gamma + \log(4/a^2)]$, where $\gamma = 0.577\ldots$ is Euler's number [17].

To estimate N_r at CHF when the radius of the dry spot is of the order of the radius of the drop R, we assume that heat is transferred to the fluid only through the belt of the width y_r at the foot of bubbles. Then $q_\mathrm{S} \sim 2\pi R y_\mathrm{r} n_\mathrm{b} q_\mathrm{L}$, where n_b is a number of the bubbles per unit interface area of the heater. At CHF a large part of the heater is covered by the bubbles, we assume it to be 50% for the estimation: $n_\mathrm{b}\pi R^2 \sim 0.5$. Then we obtain $q_\mathrm{L} \sim q_\mathrm{S}/a$ using $y_\mathrm{r} \sim aR$. Since $N_\mathrm{r} \sim q_\mathrm{L}^2 y_\mathrm{r}/(H^2\rho_\mathrm{V}\sigma) \sim q_\mathrm{S}^2 R/(aH^2\rho_\mathrm{V}\sigma)$, the estimate gives $N_\mathrm{r} \sim 1$ for $a \sim 0.01$ (usual for large bubbles, see [18]) and for the parameters characteristic for water at high pressures: $R \sim 1$ mm, $q_\mathrm{S} = q_\mathrm{CHF} \sim 1$ MW/m^2, $H \sim 1$ MJ/kg, $\rho_\mathrm{V} \sim 10$ kg/m^3, and $\sigma \sim 10^{-2}$ N/m.

Using the cylindrical r-z system of coordinates (see fig. 1), (6) can be written in parametric form as a system of three ordinary differential equations

$$\mathrm{d}r/\mathrm{d}y = \cos u, \tag{11}$$

$$\mathrm{d}z/\mathrm{d}y = \sin u, \tag{12}$$

$$\mathrm{d}u/\mathrm{d}y = -(\sin u)/r + \lambda + P_\mathrm{r}(y) \tag{13}$$

with the boundary conditions

$$z = 0, \quad u = \theta \quad \text{at} \quad y = 0; \qquad r = 0, \quad u = \pi \quad \text{at} \quad y = L. \tag{14}$$

The 4th condition is necessary to determine the unknown L. The mathematical problem is completed by the equation, which allows the Lagrange multiplier λ to be determined:

$$V = \pi \int_0^L r^2 \sin u \, \mathrm{d}y, \tag{15}$$

where V is the given bubble volume. In the following, the case of the water on metal heater is considered, $\theta = 0$.

The solution of the problem (9)-(15) is presented in fig. 2. Note that, although the actual contact angle is zero for all of the curves (see the insert), the apparent contact angle grows with $N_\mathrm{r} \propto q_\mathrm{S}^2$. At small values of q_S the dry spot under the bubble corresponds to the size of the vapor bubble nucleation spot (assumed to be zero for the calculations of fig. 2). The bubble grows with its contact line pinned at the defects on the surface of the heater until bubble departure under action of gravity or external hydrodynamic forces. The departure size of the bubble is small because the adhesion (which is proportional to the contact line length [19]) is small. At some value of q_S the contact line can depin under the action of the vapor recoil before the bubble detaches from the heating surface. Figure 2 shows that the dry spot reaches the size equal to the bubble diameter at $N_\mathrm{r} \sim 1$, the value that compares well with our estimation. The adhesion force increases with the increase of the dry spot thus hindering the bubble departure. The departure time (the time interval during which the bubble is attached to the heating surface) grows sharply. We think that this feedback is at the origin of the DNB, with this value of q_S to be associated with q_CHF.

There are two additional mechanisms of the dry spot growth. Each of them starts to act when the size of the dry spot attains some critical value. First, when the dry spot becomes larger than the characteristic heat diffusion length of the solid, the temperature of the dry spot increases faster than the temperature of the wetted surface. Second, as the apparent contact angle reaches 90°, the coalescence of bubbles on the heating surface increases rapidly, which causes further spreading of the dry spot. As soon as the critical size of the dry spot is reached due to vapor recoil, these two effects increase the temperature in the vicinity of the bubble thus enhancing vapor recoil and providing a feedback.

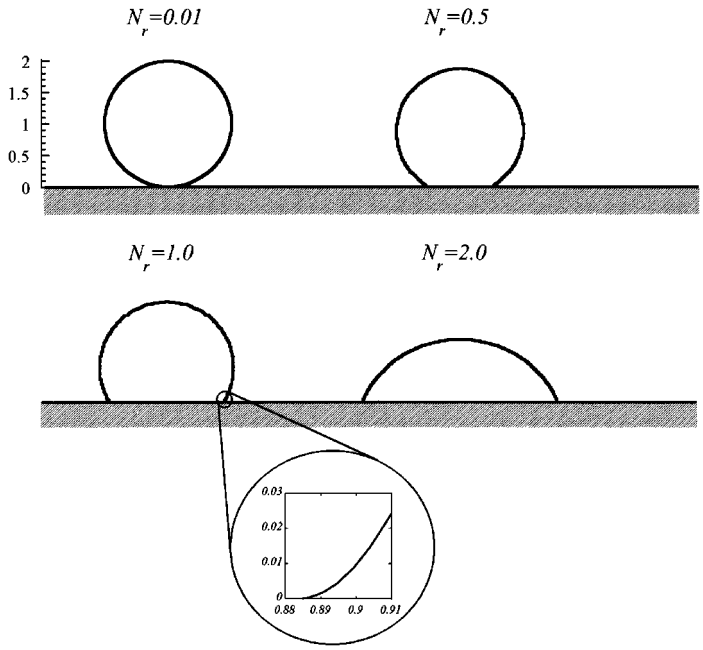

Fig. 2. – Shape of the 3D axisymmetrical vapor bubble on the heating surface under action of the vapor recoil force calculated for $a = 0.01$ (see text). The volume V is the same for all bubbles. The actual contact angle is zero as demonstrated in the insert. The coordinates are scaled by $(3V/4\pi)^{1/3}$.

For poor wetting conditions a smaller value of the vapor recoil (and q_{CHF}) is needed to create a large dry spot. This explains the decrease of q_{CHF} with the increase of the contact angle and surface roughness [10].

In this letter we have proposed a mechanism for the boiling crisis based on a transition from complete to partial wetting of the heating surface as due to a vapor recoil force. Unfortunately, it is quite difficult to obtain the analytical form of the DNB criterion only from the above considerations. They can be helpful, however, for future numerical simulations that take into account more realistic temperature distributions, the balance between adhesion and lift-off forces, and the changing bubble shape. This model makes the departure time be the crucial parameter that should increase rapidly near the crisis. Unfortunately, such experimental studies are not available.

It is clear now why vapor recoil can be the triggering phenomenon for the boiling crisis under various conditions of boiling. Providing that the vapor recoil force operates in a very thin belt at the base of the bubble, the change in the bubble shape can be accounted for by a change in an apparent contact angle controlled by the vapor recoil force. Another interesting result is the possibility to change the size of the dry spot under the bubble while the actual contact angle remains zero.

***

One of the authors (VN) would like to thank the Direction of DRFMC, CEA/Grenoble for its kind hospitality, and CEA and EDF for financial support. The authors are grateful to E. Brière, S. Pujet, J.-M. Delhaye and D. Grand for fruitful discussions and exhaustive information on the boiling crisis.

REFERENCES

[1] Tong L. S., *Boiling Heat Transfer and Two-Phase Flow*, 2nd edition (Taylor & Francis, New York) 1997.

[2] Katto Y., *Int. J. Multiphase Flow Suppl.*, **20** (1994) 53.

[3] Galloway J. E. and I. Mudawar, *Int. J. Heat Mass Transfer*, **36** (1993) 2511.

[4] van Ouwerkerk H. J., *Int. J. Heat Mass Transfer*, **15** (1972) 25.

[5] Kenning D. B. R., *Int. J. Heat Mass Transfer*, **35** (1992) 73.

[6] Torikai K., Suzuki K. and Yamaguchi M., *JSME Int. J. Ser. II*, **34** (1991) 195.

[7] Sefiane K., Benielli D. and Steinchen A., *Colloid. Surf.*, **142** (1998) 361.

[8] Pomeau Y., *Physica D*, **97** (1996) 223.

[9] Bricard P., Péturaud P. and Delhaye J.-M., *Multiphase Sci. Tech.*, **9** No. 4 (1997) 329.

[10] Diesselhorst T., Grigull U. and Hahne E., in *Heat Transfer in Boiling*, edited by E. Hahne and U. Grigull (Hemisphere Publ.) 1977, p. 99.

[11] Pavlov P. A. and Liptchak A. I., in *Metastable Phase States and Kinetics of Relaxation* (Russian Academy of Sciences, Ural Division, Sverdlovsk) 1992, p. 119 (in Russian).

[12] Avksentyuk B. P. and Ovchinnikov V. V., in *Two-Phase Flow Modelling and Experimentation*, edited by G. P. Celata and R. K. Shah (Edizioni ETS) 1995, p. 1205.

[13] Palmer H. J., *J. Fluid Mech.*, **75**, part 3, (1976) 487.

[14] DebRoy T. and David S. A., *Rev. Mod. Phys.*, **67** (1995) 85.

[15] de Gennes P. G., *Rev. Mod. Phys.*, **57** (1985) 827.

[16] Finn R., *Equilibrium Capillary Surfaces* (Springer, New-York) 1986.

[17] Abramovitz M. and Stegun I. A. (Editors), *Handbook of Mathematical Functions* (Dover, New York) 1972.

[18] Cooper M. G., *Int. J. Heat Mass Transfer*, **12** (1969) 915.

[19] van Helden W. G. J., van der Geld C. W. M. and Boot P. G. M., *Int. J. Heat Mass Transfer*, **38** (1995) 2075.

PERGAMON International Journal of Heat and Mass Transfer 44 (2001) 3499–3511

International Journal of HEAT and MASS TRANSFER

www.elsevier.com/locate/ijhmt

Growth of a dry spot under a vapor bubble at high heat flux and high pressure

V.S. Nikolayev [a,*], D.A. Beysens [a], G.-L. Lagier [b], J. Hegseth [c]

[a] *ESEME, Service des Basses Temperatures, CEA Grenoble, 17, rue des Martyrs, 38054 Grenoble Cedex 9, France*
[b] *Laboratoire de Thermohydraulique Avancée, SMTH, CEA Grenoble, 17, rue des Martyrs, 38054 Grenoble Cedex 9, France*
[c] *Department of Physics, University of New Orleans, New Orleans, LA 70148, USA*

Received 28 March 2000; received in revised form 22 October 2000

Abstract

We report a 2D modeling of the thermal diffusion-controlled growth of a vapor bubble attached to a heating surface during saturated boiling. The heat conduction problem is solved in a liquid that surrounds a bubble with a free boundary and in a semi-infinite solid heater by the boundary element method. At high system pressure the bubble is assumed to grow slowly, its shape being defined by the surface tension and the vapor recoil force, a force coming from the liquid evaporating into the bubble. It is shown that at some typical time the dry spot under the bubble begins to grow rapidly under the action of the vapor recoil. Such a bubble can eventually spread into a vapor film that can separate the liquid from the heater thus triggering the boiling crisis (critical heat flux).

Keywords: Boiling; Bubble growth; CHF; Contact angle; Vapor recoil

1. Introduction

In nucleate boiling, a very large rate of heat transfer from the heating surface to the bulk is due to both the phase change (latent heat of vaporization) and the fact that the superheated liquid is carried away from the heating surface by the departing vapor bubbles. Therefore, the knowledge of the nucleation and growth of the bubbles on the heating surface is very important for calculations of the heat transfer rate. Many works were focused on the bubble growth kinetics, see e.g. [1–6]. However, as it was recently recognized [7], the behavior of the fluid in contact with the solid heater remains poorly studied. We think that this situation is due to the success of the microlayer model [2] that proved to be self-sufficient for the description of the bubble growth kinetics and the heat transfer rate. The microlayer model postulates the existence of a thin liquid film between the heater and the foot of the vapor bubble. This model is based on observations of the bubbles at low system pressures with respect to the critical pressure for the given fluid. At low pressures, the fast bubble growth creates a hydrodynamic resistance that makes the bubble almost hemispherical [8]. As proved by direct observations [9–12] through the transparent heating surface, the dry spot (i.e. the spot of the direct contact between the liquid and the vapor) does exist around the nucleation site while the bubble stays near the heating surface. The origin of the dry spot can be explained as follows. First, it is necessary that the vapor-solid adhesion exists to avert the immediate removal of the bubble from the heater by the lift-off forces. This adhesion only appears when the vapor contacts the solid directly. Second, the strong generation of vapor at the triple contact line around the nucleation site prevents covering of the nucleation site by the liquid. As a consequence, the existence of the dry spot under the bubble is necessary during most of the time of the bubble growth, until the bubble departure from the heater.

* Corresponding author. Address: CEA-ESEME Institut de Chimie de la Matiere Condensée de Bordeaux, 87, Avenue du Dr. Schweitzer, 33608 Pessac Cedex, France. Tel.: +33-5-56-84-26-88; fax: +33-5-56-84-27-61.

0017-9310/01/$ - see front matter
PII: S0017-9310(01)00024-2

Nomenclature

$\vec{a}$	arbitrary vector
b	exponent for boundary meshing
C	arbitrary constant
c_p	specific heat, J/(kg K)
$d_{\min}$	smallest element length, m
$\vec{e}_x, \vec{e}_y$	unit vectors directed along the axes
F, f	non-dimensional time
Fo	Fourier number
G	Green function, BEM coefficient
H	latent heat, J/kg, BEM coefficient
Hi	Hickman number
Ja	Jakob number
j	volume heat supply, W/m^3
K	curvature, m^{-1}
k	thermal conductivity, W/(m K)
L	half-length of the bubble contour, m
M	molar weight of water, kg/mol
N	total boundary elements number
$\vec{n}$	internal unit normal vector
P_r	vapor recoil pressure, N/m^2
q	heat flux, W/m^2
q_{CHF}	critical heat flux, MW/m^2
q_0	control value of heat flux, MW/m^2
R	bubble radius, m
R_0	initial bubble radius, m
R_g	molar gas constant, J/(mol K)
$\vec{r}$	radius-vector
T	temperature, K
t	time, s
t_c	transition time, s
t_{dep}	bubble residence time, s
u	auxiliary angle
V	2D-bubble volume, m^2
v^n	interface velocity, m/s
x	abscissa
y	ordinate

Greek symbols

α	thermal diffusivity, m^2/s
β	exponent
Δt	time step, s
ζ	reduced heat flux
η	rate of evaporation, kg/(s m^2)
θ	liquid contact angle
λ	vapor/liquid pressure difference, N/m^2
ξ	non-dimensional curvilinear coordinate
ρ	mass density, kg/m^3
σ	surface tension, N/m
τ	dummy
ψ	reduced temperature
Ω	2D-domain
$\partial\Omega$	contour of the 2D-domain

Subscripts

d	dry spot
e	external to the bubble
F, f	value at time F or f
i	vapor–liquid interface
i, j	value at the node i or j
inf	at $x \to \infty$ (also as a superscript)
L	liquid
max	maximum
S	solid (heater)
sat	saturation
V	vapor
w	wetted part of the heater

Superscripts

x	x-component of the vector
y	y-component of the vector
$^-$	reference value

Owing to the hemispheric bubble shape, the apparent bubble foot is much larger than the dry spot. That is why the microlayer model works so well at low pressures. For high system pressure, comparable to the critical pressure (see [13,14] for the discussion of the threshold between these two regimes), the picture is different. The bubble growth is much slower so that the hydrodynamic forces are small with respect to the surface tension. Consequently, the bubble resembles a sphere much more than a hemisphere [8]. It is very hard to identify the microlayer as a thin film in this case. In this article, we will limit ourselves to this particular case.

One of the most important phenomena in boiling at the large heat fluxes used in industrial heat exchangers is the boiling crisis called alternately 'burnout', 'departure from nucleate boiling', or 'critical heat flux' (CHF) [1,8]. When the heat flux from the heater exceeds a critical value (the CHF), the vapor bubbles abruptly form a film that thermally insulates the heater surface from the liquid. Consequently, the temperature of the heater rapidly grows. The dry spot is recognized as playing a key role in the boiling crisis [15]. A new physical approach [16] was recently suggested by some of us to describe this phenomenon. It is based on the experimental results [9–12] that show that the boiling crisis can begin with the fast growth of a dry spot under a *single* bubble, although several simultaneously spreading bubbles can coalesce later on. The model associates the onset of the boiling crisis with the beginning of the spreading of the dry spot below a vapor bubble attached to the heater surface. The purpose of the present article is to rigorously calculate in

2D the temporal evolution of the dry spot under a single bubble.

Two main difficulties arise while solving this problem. The first of them is the necessity to solve the full free-boundary problem for the bubble. Unfortunately, we cannot assume a simple shape for the bubble foot as has been done in all previous simulations of the vapor bubble growth that we are aware of, see e.g., [3,4,6]. The reason is that these models do not rigorously determine the size of the dry spot. Instead, they use an empirical correlation for the microlayer parameters chosen to satisfy the experimentally observed growth rate of the bubble. In the present formulation, the dry spot size is determined in a self-consistent manner from the position of the triple contact line. Such a free-boundary problem is difficult because of its non-linearity and can be solved by only a few numerical methods, e.g., boundary element method (BEM) [17] or front tracking method. The latter was recently used [18] to simulate the film boiling in 2D.

The second difficulty of the dry spot problem is associated with the calculation of the heat transfer in the most important region – the vicinity of the triple contact line (i.e., the microlayer). It is analyzed analytically in the subsection 3.1 for two fixed values of the contact angle. Although these results are not used in the numerical simulation, we need them to check the accuracy of the heat transfer calculation in this important region.

Our calculations are valid in the simplified situation where the hydrodynamic effects in liquid are neglected. This simplification is justified by the slow growth assumption valid for high system pressures. This approximation is common [5] for the thermal diffusion-controlled bubble growth. The only dynamic condition that cannot be neglected [16] is the dynamic balance of mechanical momentum at the bubble interface that results in the vapor recoil pressure. This approach allows us to apply the quasi-static approximation for the bubble shape determination in Section 2 and neglect the convection terms in the heat transfer problem that is discussed in Section 3. The numerical algorithm is described in Section 4. The results of the simulation and the conclusions are presented in Sections 5 and 6.

2. Bubble shape determination

When the heat flux q_S from the heater is small, the vapor bubble grows with its triple vapor–liquid–solid contact line pinned by the surface defect on which the vapor nucleation has started. The size of the dry spot is thus very small with respect to the bubble size. According to the model [16] (that should be valid for any system pressure), at some value of q_S the contact line de-pins and moves under the influence of the vapor recoil pressure P_r,

$$P_r = \eta^2(\rho_V^{-1} - \rho_L^{-1}), \tag{1}$$

where η is the mass of the evaporated liquid per unit time per unit area of the vapor–liquid interface. P_r may vary along the interface and is directed normally to this interface towards the liquid [20]. By neglecting heat conduction in the vapor with respect to the latent heat effect, η can be related to the local heat flux across the interface q_L by the equation

$$q_L = H\eta, \tag{2}$$

where H is the latent heat of vaporization. Because of the strong temperature gradient in the vicinity of the heating surface, q_L increases sharply near the contact line, and consequently η and P_r also increase. In other words, the recoil pressure increases near the contact line and causes it to recede. Therefore, the dry spot under the bubble should grow with time.

The bubble shape is determined using a quasi-static approximation. We neglect all but two forces that define the bubble shape: the surface tension and the vapor recoil pressure P_r defined by Eq. (1). The bubble shape is then defined by the pressure balance (see [16])

$$K\sigma = \lambda + P_r, \tag{3}$$

where K is the local curvature of the bubble, σ is the vapor–liquid interface tension and λ is a constant difference of pressures between the vapor and the liquid. λ should be determined using the known volume V of the 2D bubble. At any time, the volume V of the 2D bubble (see Appendix A) can be written as:

$$V = \frac{1}{2}\int_{(\partial\Omega_i)} (xn_e^x + yn_e^y)\,\mathrm{d}\,\partial\Omega, \tag{4}$$

where $\partial\Omega_i$ is the vapor–liquid interface, and the external unit normal vector $\vec{n}_e = (n_e^x, n_e^y)$ to the bubble is defined in a Cartesian (x, y) coordinate system. An axisymmetric bubble shape is assumed as follows, see Fig. 1.

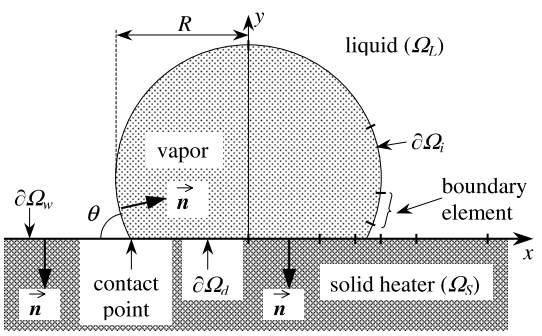

Fig. 1. Vapor bubble on the heating surface surrounded by liquid. The chosen direction of the unit normal vector $\vec{n}$ is shown for each of the subcontours $\partial\Omega_w$, $\partial\Omega_d$ and $\partial\Omega_i$. The discretization is illustrated for the right half of the subcontours.

It is convenient to describe the bubble shape in parametric form while choosing a non-dimensional length ξ measured along the bubble contour as an independent variable. Then the coordinates (x, y) for a given point on the bubble interface are functions of ξ that varies along the bubble half-contour (its right half in Fig. 1) from 0 to 1, $\xi = 0$ and $\xi = 1$ corresponding to the topmost point of the bubble and to the contact point, respectively. Eq. (3) for the 2D case is equivalent to the following parametric system of ordinary differential equations:

$$\mathrm{d}x/\mathrm{d}\xi = L\cos u, \tag{5}$$

$$\mathrm{d}y/\mathrm{d}\xi = -L\sin u, \tag{6}$$

$$\mathrm{d}u/\mathrm{d}\xi = L(\lambda + P_\mathrm{r}(\xi))/\sigma, \tag{7}$$

were $u = u(\xi)$ is the angle between the tangent to $\partial\Omega_i$ at the point ξ and the vector directed opposite to the x-axis; L is the half-length of $\partial\Omega_i$.

The boundary conditions for Eqs. (5)–(7) are then given by

$$x(0) = 0, \quad u(0) = 0, \quad y(1) = 0. \tag{8}$$

A 4th condition $u(1) = \pi - \theta$ that fixes the liquid contact angle θ is necessary to determine the unknown L using (7):

$$L = (\pi - \theta)\sigma\left[\int_0^1 P_\mathrm{r}(\xi)\mathrm{d}\xi + \lambda\right]^{-1}. \tag{9}$$

In the following, we consider the usual case of complete wetting of the heating surface by the liquid, $\theta = 0$. The solution of the problem (Eqs. (1)–(9)) allows the bubble shape to be determined provided the heat flux through the vapor–liquid interface is known.

3. Heat transfer problem

The calculation of the heat transfer around a growing vapor bubble is a free-boundary problem. To our knowledge, only two other groups have solved the full free-boundary boiling problem [18,19]. In both works the singular effects, which appear in the region adjacent to the triple contact line (microlayer), are not discussed. However, we know that almost all the heat flux supplied to the vapor bubble goes through this particular region, a region on which we concentrate in this work. As a first step, we neglect the heat transfer due to the liquid motion. Thermal conduction and the latent heat effects are taken into account to describe the time evolution of the 2D vapor bubble. The vapor is assumed to be non-conducting. The case of saturated boiling is considered. This means that the temperature in the liquid far from the heater is equal to T_sat, the saturation temperature for the given system pressure. Thus only evaporation is allowed on the bubble interface. Since we consider a slow process with no liquid motion, the pressures are assumed to be uniform both in the vapor and in the liquid. However, they are different according to Eq. (3) where λ is the difference between the pressures inside and outside the vapor bubble. The saturation temperature T'_sat for the vapor inside the bubble depends on the vapor pressure according to the Clausius–Clapeyron equation (see, e.g., [4])

$$T'_\mathrm{sat} = T_\mathrm{sat}\left[1 + \frac{\lambda}{H}(\rho_\mathrm{V}^{-1} - \rho_\mathrm{L}^{-1})\right].$$

Since σ/λ is the bubble radius at the top of the bubble (where P_r is negligible), it is easy to estimate that the correction to T_sat is less than $10^{-3}\%$ even for the smallest bubble size considered. Therefore, in the following, the bubble surface is supposed to be at constant temperature T_sat.

3.1. Model for the vicinity of the contact line

First of all, we need to understand how q_L behaves in the vicinity of the contact line where the contour of the bubble $\partial\Omega_i$ can be approximated by a straight line that forms an angle θ with the Ox heater line, see Fig. 2. Then q_L can be obtained from the solution of a simple two-dimensional problem of unsteady heat conduction in this wedge of liquid, the point $O(x = 0, y = 0)$ corresponding to the contact line. In our previous article [16], the model problem was solved to show that when $\theta = \pi/2$ and a constant heat flux from the heater is imposed, the heat flux through the liquid–vapor interface q_L diverges weakly (logarithmically) near the contact line. In the present work, we treat two cases $\theta = \pi/4$ and $\theta = \pi/8$ which also allow an analytical treatment.

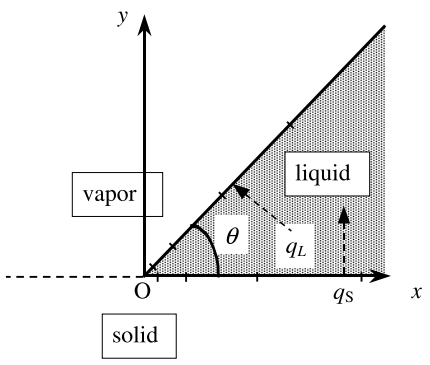

Fig. 2. Geometry for the analytical calculation of the heat conduction in the wedge. The BEM discretization of the wedge is also illustrated.

The heat conduction equation for the temperature $T_L(x,y,t)$ in the liquid

$$\frac{\partial T_L}{\partial t} = \alpha_L \nabla^2 T_L, \tag{10}$$

has the initial and boundary conditions

$$T_L|_{t=0} = T_{sat}, \tag{11}$$

$$T_L|_{\partial\Omega_i} = T_{sat}, \tag{12}$$

$$-k_L \frac{\partial T_L}{\partial y}|_{y=0} = q_0, \tag{13}$$

where k_L and α_L are the thermal conductivity and the thermal diffusivity of the liquid, and the heat flux q_S from the heating surface is assumed to be constant ($= q_0$) for the case of the thin heating wall. The solution of this 2D problem for the angles $\theta = \pi/2^m$, where m is an integer, can be obtained using the method of images [21] for the Green function. For $\theta = \pi/4$ it reads

$$T_L = T_{sat} + T_{inf}(y,t) - T_{inf}(x,t), \tag{14}$$

where the function $T_{inf}(y,t)$ is a solution for this problem at $x \to \infty$

$$T_{inf}(y,t) = \frac{q_0}{k_L}\left[\sqrt{\frac{4\alpha_L t}{\pi}}\exp\left(-\frac{y^2}{4\alpha_L t}\right) - y\,\mathrm{erfc}\left(\frac{y}{2\sqrt{\alpha_L t}}\right)\right], \tag{15}$$

erfc(z) being the complementary error function [22]. Then the heat flux q_L

$$q_L = -k_L(\vec{n}\cdot\nabla)T_L|_{\partial\Omega_i} \tag{16}$$

can be calculated as a function of x using the expression for the unit normal vector $\vec{n} = (-\sin\theta, \cos\theta)$:

$$q_L = q_0\sqrt{2}\ \mathrm{erfc}\left(\frac{x}{2\sqrt{\alpha_L t}}\right). \tag{17}$$

It is easy to see that, unlike the problem [16] for $\theta = \pi/2$, the heat flux remains finite at the contact line ($x = 0$). This is also true for the case $\theta = \pi/8$, for which

$$T_L = T_{sat} + T_{inf}(y,t) + T_{inf}(x,t) - T_{inf}\left(\frac{x+y}{\sqrt{2}}, t\right) - T_{inf}\left(\frac{x-y}{\sqrt{2}}, t\right), \tag{18}$$

and

$$q_L = q_0\sqrt{\sqrt{2}+2}\left[\mathrm{erfc}\left(\frac{(\sqrt{2}-1)x}{2\sqrt{\alpha_L t}}\right) - (\sqrt{2}-1)\ \mathrm{erfc}\left(\frac{x}{2\sqrt{\alpha_L t}}\right)\right]. \tag{19}$$

Although these solutions present important benchmarks for the numerical calculations of the heat transfer near the contact line, they cannot be used in the simulation itself for two reasons. The first is the impossibility to employ the uniform heat flux boundary condition Eq. (13) because in reality the heat flux varies strongly between the dry and wetted parts of the solid surface. In particular, the heat flux through the dry spot under a bubble is very small (we assume it to be zero in the following). The second reason is the impossibility to approximate the bubble contour by a straight line for the case $\theta = 0$, most important for industrial applications.

3.2. Mathematical formulation

We consider the growth of a vapor bubble on the semi-infinite ($y < 0$) solid heater Ω_S in the semi-infinite ($y > 0$) liquid Ω_L, see Fig. 1. We assume that no superheat is needed for the bubble nucleation so that the circular bubble of radius R_0 and volume V_0 has already nucleated at the heater surface at $t = 0$. The validity of this assumption is discussed in Section 5. The known heat supply $j(t)$ is generated homogeneously inside the heater with the heat conductivity k_S and the heat diffusivity α_S so that heat conduction equation for the domain Ω_S

$$\frac{\partial T_S}{\partial t} = \alpha_S \nabla^2 T_S + \frac{\alpha_S}{k_S} j(t), \quad y < 0 \tag{20}$$

should be solved with the boundary and initial conditions

$$q_S = -k_S \frac{\partial T_S}{\partial y}|_{y=0} = \begin{cases} -k_L \frac{\partial T_L}{\partial y} & \text{at } \partial\Omega_w \\ 0 & \text{at } \partial\Omega_d \end{cases}, \tag{21}$$

$$T_S|_{\partial\Omega_w} = T_L|_{y=0}, \tag{22}$$

$$T_S|_{t=0} = T_{sat}, \tag{23}$$

where $\partial\Omega_d$ is the vapor–solid interface (i.e., the dry spot) and $\partial\Omega_w$ is the liquid–solid interface (wetted surface), see Fig. 1. The problem for the domain Ω_L is completed by Eqs. (10)–(12).

The bubble volume V increases due to evaporation [1]:

$$H\rho_V \frac{dV}{dt} = \int_{(\partial\Omega_i)} q_L\, d\partial\Omega, \tag{24}$$

where q_L is calculated using Eq. (16) in which $\vec{n}$ is the *inner* normal vector to $\partial\Omega_i$, $\vec{n} = -\vec{n}^e$.

The formulated mathematical problem can be solved by the BEM generalized for moving boundary problems [23]. Before its direct application, we consider the integration contours for the domains Ω_L and Ω_S. Obviously,

they should contain $\partial\Omega_i$, $\partial\Omega_d$ and $\partial\Omega_w$ and a circle that closes the contours at infinity. The non-zero values of the temperature and flux at infinity complicate the solution. Therefore, we calculate these values T_S^{inf} and T_L^{inf} at $x \to \infty$ and then subtract them from T_S and T_L. The resulting modified variables are zero at infinity. This transformation allows the integration contour to be reduced to $\partial\Omega_i \cup \partial\Omega_d \cup \partial\Omega_w$.

3.3. Solution at infinity

The solution at infinity satisfies the same problem as T_S and T_L but with the eliminated dependence on x and $\partial\Omega_d = \emptyset$. The separate solutions for $y \geqslant 0$ and $y \leqslant 0$ can be easily found using the known Green function for the semi-infinite space [21]:

$$T_L^{inf} = T_{sat} + \frac{\sqrt{\alpha_L}}{k_L\sqrt{\pi}} \int_0^t \frac{q_0(t-\tau)}{\sqrt{\tau}} \exp\left(-\frac{y^2}{4\alpha_L t}\right) d\tau, \quad y \geqslant 0 \tag{25}$$

$$T_S^{inf} = T_{sat} + \frac{\alpha_S}{k_S}\int_0^t j(\tau)d\tau - \frac{\sqrt{\alpha_S}}{k_S\sqrt{\pi}} \int_0^t \frac{q_0(t-\tau)}{\sqrt{\tau}} \times \exp\left(-\frac{y^2}{4\alpha_S t}\right) d\tau, \quad y \leqslant 0 \tag{26}$$

The unknown heat flux from the heater, $q_0(t)$, can be found for arbitrary $j(t)$ out of the integral equation that results from equality of Eqs. (25) and (26) at $y = 0$. It is worth mentioning that if $j \propto t^{-1/2}$, a constant q_0 satisfies this integral equation. This means that in the bubble growth problem with this choice of $j(t)$ the heat flux from the heater would remain constant at least far from the growing bubble. This choice will allow us to avoid the influence of the varying heat flux on the bubble growth and thus will be used in the following. The solution in analytical form is

$$j(t) = C/\sqrt{t},$$

$$q_0 = C\sqrt{\pi}\alpha_S k_L/(k_S\sqrt{\alpha_L} + k_L\sqrt{\alpha_S}),$$

$$T_S^{inf} = T_{sat} + \frac{2\alpha_S}{k_S} C\sqrt{t} - \frac{q_0}{k_S}\left[\sqrt{\frac{4\alpha_S t}{\pi}}\exp\left(-\frac{y^2}{4\alpha_S t}\right) + y\,\mathrm{erfc}\left(-\frac{y}{2\sqrt{\alpha_S t}}\right)\right], \quad y \leqslant 0, \tag{27}$$

$$T_L^{inf} = T_{sat} + T_{inf}(y,t), \quad y \geqslant 0, \tag{28}$$

where C and q_0 are constant and the function $T_{inf}(y,t)$ is defined in Eq. (15). It is easy to see that besides the advantage of the zero values at infinity for the modified variables $T_{L,S} - T_{L,S}^{inf}$, the equation for both of them has the form Eq. (10) with no source term.

3.4. Non-dimensional formulation

By introducing the characteristic scales for time (Δt, the time step), length (R_0, the initial bubble radius), heat flux ($\bar{q}$), and thermal conductivity ($\bar{k}$), all other variables can be made non-dimensional. In particular, the characteristic temperature scale in the system is $\bar{q}R_0/\bar{k}$. The following four non-dimensional groups define completely the behavior of the system

$$Fo_{L,S} = \alpha_{L,S}\Delta t/R_0^2 \text{ – Fourier numbers,}$$

$$Ja = \frac{\rho_L c_{pL}}{\rho_V H}\frac{\bar{q}R_0}{\bar{k}} \text{ – Jakob number [1],}$$

$$Hi = \frac{R_0\bar{q}^2}{\sigma H^2}(\rho_V^{-1} - \rho_L^{-1}) \text{ – Hickman number,}$$

provided that non-dimensionalized values of q_0 and $k_{L,S}$ are fixed. The following is the complete non-dimensional heat transfer problem formulated in terms of $\psi_{L,S} = (T_{L,S} - T_{L,S}^{inf})/(\bar{q}R_0/\bar{k})$:

$$\frac{\partial\psi_{L,S}}{\partial t} = Fo_{L,S}\nabla^2\psi_{L,S} \tag{29}$$

$$\psi_{L,S}|_{t=0} = 0, \tag{30}$$

$$\psi_L|_{\partial\Omega_i} = -T_{inf}(y,t), \tag{31}$$

$$\zeta_L|_{\partial\Omega_w} = \zeta_S|_{\partial\Omega_w}, \quad \zeta_{L,S} = k_{L,S}\frac{\partial\psi_{L,S}}{\partial\vec{n}}, \tag{32}$$

$$\zeta_L|_{\partial\Omega_d} = -q_0, \tag{33}$$

$$\frac{dV}{dt} = Fo_L \cdot Ja \int_{(\partial\Omega_i)} (\zeta_{inf} - \zeta_L)\, d\partial\Omega, \quad \zeta_{inf} = q_0 n^y \,\mathrm{erfc}\left(\frac{y}{2\sqrt{Fo_L t}}\right), \tag{34}$$

where n^y is the ordinate of the vector $\vec{n}$ and all quantities are non-dimensionalized. The whole problem is completed using the non-dimensionalized set of equations for the bubble shape (Eqs. (5)–(9)) where the non-dimensional expression for the vapor recoil pressure is used

$$P_r = Hi(\zeta_{inf} - \zeta_L)^2. \tag{35}$$

3.5. Boundary element techniques applied to bubble growth

As it is shown in [23], the heat conduction problem (Eqs. (29) and (30)) is equivalent to the set of two integral equations, written for each of the domains Ω_L and Ω_S:

$$\int_0^{t_F} \mathrm{d}t \int_{(\partial\Omega_{\mathrm{L,S}})} \left[G^{\mathrm{L,S}}(\vec{r}', t_F; \vec{r}, t) \left(Fo_{\mathrm{L,S}} \frac{\zeta(\vec{r}, t)}{k_{\mathrm{L,S}}} + \psi(\vec{r}, t) v^n(\vec{r}, t) \right) - Fo_{\mathrm{L,S}} \psi(\vec{r}, t) \frac{\partial_r G^{\mathrm{L,S}}(\vec{r}', t_F; \vec{r}, t)}{\partial \vec{n}} \right] \mathrm{d}_r \partial\Omega = \frac{1}{2} \psi(\vec{r}', t_F), \tag{36}$$

where $\vec{r}'$ is the evaluation point and t_F is the evaluation time. The integration is performed over the closed contours $\partial\Omega_{\mathrm{L}}$ and $\partial\Omega_{\mathrm{S}}$ that surround the domains Ω_{L} and Ω_{S}, vector $\vec{n}$ being external to them. v^n is the projection of the local velocity of the possibly moving integration contour on the vector $\vec{n}$. Since the points $\vec{r}'$ and $\vec{r}$ belong to these contours, the BEM formulation does not require the values of ψ and ζ to be calculated in the internal points of the domains, which is a great advantage of this method. The functions $G^{\mathrm{L,S}}$ are the Green functions for the equations [17], adjoint to Eq. (29):

$$G^{\mathrm{L,S}}(\vec{r}', t_F; \vec{r}, t) = \frac{1}{4\pi Fo_{\mathrm{L,S}}(t_F - t)} \exp\left[-\frac{|\vec{r}' - \vec{r}|^2}{4 Fo_{\mathrm{L,S}}(t_F - t)} \right]. \tag{37}$$

The indices L and S will be dropped for the sake of clarity until the end of this section.

The constant element BEM [17] was used, i.e., ζ and ψ were assumed to be constant during any time step and on any element, their values on the element being associated with the values on the node at the center of the element. The time steps are equal, i.e., $t_f = f$. Therefore, the values of ζ and ψ on the element j at time f can be denoted by ζ_{fj} and ψ_{fj}. Each of the integral equations Eq. (36) reduces to the system of linear equations

$$\sum_{f=1}^{F} \sum_{j=1}^{2N_f} \left[(\zeta_{fj}/k + \psi_{fj} v^n_{fj}/Fo) G^{Ff}_{ij} - \psi_{fj} H^{Ff}_{ij} \right] = \psi_{Fi}/2, \tag{38}$$

where N_f is the number of elements on one half of the integration contour at time step f, $F_{\max}$ is the maximum number of time steps for the problem; $i = 1 \ldots 2N_F$ and $F = 1 \ldots F_{\max}$. It is important that the algorithm for the calculation of the coefficients H_{ij} and G_{ij} [17] be fast. We used the analytical expressions calculated [24] for the case $i = j$. For all other cases the coefficient H_{ij} can be expressed analytically [24] through G_{ij}. G_{ij} was calculated numerically. The system (38) can be simplified due to axial symmetry of the problem ($\psi_{fj} = \psi_{f(2N_f - j)}$, etc.):

$$\sum_{f=1}^{F} \sum_{j=1}^{N_f} \left[(\zeta_{fj}/k + \psi_{fj} v^n_{fj}/Fo) \tilde{G}^{Ff}_{ij} - \psi_{fj} \tilde{H}^{Ff}_{ij} \right] = \psi_{Fi}/2, \tag{39}$$

where $i = 1 \ldots N_F$, $F = 1 \ldots F_{\max}$, $\tilde{G}^{Ff}_{ij} = G^{Ff}_{ij} + G^{Ff}_{i(2N-j)}$ and $\tilde{H}^{Ff}_{ij} = H^{Ff}_{ij} + H^{Ff}_{i(2N-j)}$. This equation can be rewritten in the form that reveals explicitly the unknown variables on each time step F:

$$\sum_{j=1}^{N_F} \left[(\zeta_{Fj}/k + \psi_{Fj} v^n_{Fj}/Fo) \tilde{G}^{FF}_{ij} - \psi_{Fj} (\tilde{H}^{FF}_{ij} + 1/2) \right] = -\sum_{f=1}^{F-1} \sum_{j=1}^{N_f} \left[(\zeta_{fj}/k + \psi_{fj} v^n_{fj}/Fo) \tilde{G}^{Ff}_{ij} - \psi_{fj} \tilde{H}^{Ff}_{ij} \right]. \tag{40}$$

Unfortunately, no effective time marching scheme [17] can be applied because of the free boundaries. Since the terms in the sum over f decrease with the decrease of f, this sum can be truncated as suggested in [25]. However, in our case, the magnitude of these terms can be controlled directly because the coefficients H and G must be recalculated for each f. It should be noted that, because of moving boundaries, the positions of the ith point at times f and F can be different. Therefore, it is very important that $\tilde{G}^{Ff}_{ij}$ be calculated using the coordinates of the ith point at time moment F and those of jth point at time moment f.

3.6. Validation of the algorithm for BEM

The BEM algorithm was tested for the wedge problem solved analytically in Section 3.1. The adaptive discretization of the integration contour is organized as follows. Since ζ decreases to zero far from the bubble, the two ending points (most distant from the contact point $(0, 0)$) can be found for the given t from the condition that $\zeta(x, y, t)$ be sufficiently small. In practice, $x_{\max} \sim 10\sqrt{Fo\, t}$. The element lengths grow exponentially ($d_{\min}, d_{\min} e^b, d_{\min} e^{2b}, \ldots$) from the contact point into each of the sides of the wedge (see Fig. 2), where b is fixed at 0.2. Being an input parameter, $d_{\min}$ is adjusted slightly on each time step to provide the exponential growth law for the elements on the interval with the fixed boundaries $(0, x_{\max})$. Since $x_{\max}$ increases, the total number of the elements also increases during the evolution of the bubble. Remeshing on each time step was performed to comply with the free-boundary nature of the main problem where the remeshing is mandatory.

The results for $\theta = \pi/4$ and $\pi/2$ are shown in Fig. 3 to be compared with the solid curves calculated using (17) and its analog for $\theta = \pi/2$ (Eq. (8) from [16]). It is easy to see that the method produces excellent results even for coarse discretization, except for the element closest to the contact point. The algorithm overestimates the value of q_{L} at this element. The error is larger for the $\pi/2$ wedge, for which $q_{\mathrm{L}} \to \infty$ at the contact point. Fig. 3 demonstrates that the increase of the numerical error with the increase of time and space steps is very weak.

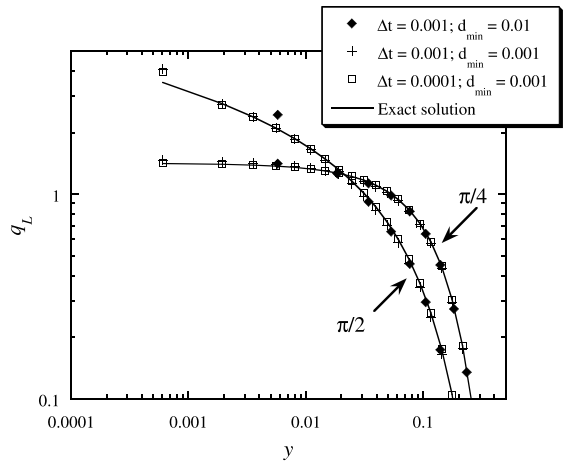

Fig. 3. The $q_{\mathrm{L}}(y)$ curves calculated for the $\pi/2$ and $\pi/4$ wedges and for the values of the parameters $q_0 = 1, \alpha_{\mathrm{L}} = 1$ and $t = 0.01$. The results of the numerical solution by BEM (to be compared with the exact analytical solution) are presented for the different time and space discretization parameters.

4. Numerical implementation

Since we chose ψ and ζ to be zero at infinity, (36) is satisfied trivially on the semicircles of the infinite radius that close the contours $\partial\Omega_L$ and $\partial\Omega_{\mathrm{S}}$. Thus these circles can be excluded. Then $\partial\Omega_{\mathrm{L}} = \partial\Omega_i \cup \partial\Omega_{\mathrm{w}}$ and $\partial\Omega_{\mathrm{S}} = \partial\Omega_d \cup \partial\Omega_{\mathrm{w}}$. The direction of the unit normal vector $\vec{n}$ is chosen to be external to Ω_{L} in the following, see Fig. 1. Then it is internal to Ω_{S}, which requires the sign of the integral over $\partial\Omega_{\mathrm{S}}$ to be changed. Making use of the boundary conditions (31)–(33), the system of Eq. (36) reduces to

$$\int_0^{t_F} \mathrm{d}t \left\{ \int_{(\partial\Omega_i)} \left[G^{\mathrm{L}} \left(Fo_{\mathrm{L}} \frac{\zeta_{\mathrm{L}}}{k_{\mathrm{L}}} - T_{\mathrm{inf}} v^n \right) + Fo_{\mathrm{L}} T_{\mathrm{inf}} \frac{\partial G^{\mathrm{L}}}{\partial \vec{n}} \right] \mathrm{d}\partial\Omega + Fo_{\mathrm{L}} \int_{(\partial\Omega_{\mathrm{w}})} \left(G^{\mathrm{L}} \frac{\zeta_S}{k_{\mathrm{L}}} - \psi_{\mathrm{S}} \frac{\partial G^{\mathrm{L}}}{\partial \vec{n}} \right) \mathrm{d}\partial\Omega \right\} = \frac{1}{2} \begin{cases} \psi_S, & \vec{r}_F \in \partial\Omega_{\mathrm{w}}, \\ -T_{\mathrm{inf}}, & \vec{r}_F \in \partial\Omega_i, \end{cases} \tag{41}$$

$$Fo_{\mathrm{S}} \int_0^{t_F} \mathrm{d}t \left[\int_{(\partial\Omega_{\mathrm{w}})} \left(- G^{\mathrm{S}} \frac{\zeta_{\mathrm{S}}}{k_{\mathrm{S}}} + \psi_{\mathrm{S}} \frac{\partial G^{\mathrm{S}}}{\partial \vec{n}} \right) \mathrm{d}\partial\Omega + \int_{(\partial\Omega_d)} \left(G^S \frac{q_0}{k_S} + \psi_S \frac{\partial G^S}{\partial \vec{n}} \right) \mathrm{d}\partial\Omega \right] = \frac{1}{2} \psi_S, \quad \vec{r}_F \in \partial\Omega_d \cup \partial\Omega_w, \tag{42}$$

where the arguments of all functions are supposed to be exactly as in Eq. (36). These equations should be solved using the BEM described in the previous section for unknown functions $\zeta_{\mathrm{L}}(\vec{r}, t)$ for $\vec{r} \in \partial\Omega_i$, $\psi_{\mathrm{S}}(\vec{r}, t)$ for $\vec{r} \in \partial\Omega_{\mathrm{d}} \cup \partial\Omega_{\mathrm{w}}$, and $\zeta_{\mathrm{S}}(\vec{r}, t)$ for $\vec{r} \in \partial\Omega_{\mathrm{w}}$.

The discretization of the integration subcontours $\partial\Omega_{\mathrm{w}}$, $\partial\Omega_{\mathrm{d}}$ and $\partial\Omega_i$ follows the same exponential scheme (see Fig. 1) that was used for the discretization of the wedge sides in the test example above. The only difference is the axial symmetry of the mesh that corresponds to the symmetry of the bubble. Since the free boundary introduces a non-linearity into the problem, the following iteration algorithm is needed to determine the bubble shape on each time step [23]:

1. Shape of the bubble is guessed to be the same as in the previous time step;
2. The variations of v^n and P_{r} along the bubble interface are guessed to be the same as in the previous time step;
3. Discretization of the contours $\partial\Omega_{\mathrm{w}}$, $\partial\Omega_{\mathrm{d}}$ and $\partial\Omega_i$ is performed;
4. Temperatures and fluxes on the contours $\partial\Omega_{\mathrm{w}}$, $\partial\Omega_{\mathrm{d}}$ and $\partial\Omega_i$ are found using the above-described BEM techniques;
5. Volume V and vapor recoil P_{r} are calculated using (34) and (35);
6. Bubble shape is determined (see Section 2) for the calculated values of V and P_{r};
7. If the calculated shape differs too much from that of the previous iteration, the velocity of interface v^n is calculated, and steps 3–7 are repeated until the required accuracy is attained.

As a rule, three iterations give the 0.1% accuracy which is sufficient for our purposes.

The normal velocity of interface v^n_{Fi} at the time F and at node i is calculated using the expression

$$v^n_{Fi} = (x_{Fi} - x_{(F-1)j}) n^x_{(F-1)j} + (y_{Fi} - y_{(F-1)j}) n^y_{(F-1)j}, \tag{43}$$

where x_{Fi} is the coordinate of the node i at time F, and j is the number of the node (at time $F-1$) geometrically closest to (x_{Fi}, y_{Fi}).

The system of Eqs. (5)–(7) is solved by direct integration. The integration of the right-hand side of (7) is performed using the simple mid-point rule, because the values of P_{r} are calculated at the mid-points (nodes) only. The subsequent integration of the right-hand sides of Eqs. (5) and (6) is performed using the Simpson rule (to gain accuracy) for the non-equal intervals. The trapezoidal rule turns out to be accurate enough for the calculation of volume in (4). For the simulation we used the parameters for water at 10 MPa pressure on the heater made of stainless steel (Table 1).

The above-described algorithm should give good results when $\int_0^1 P_{\mathrm{r}}(\xi)\mathrm{d}\xi$ exists (cf. Eq. (9)). In our case $P_{\mathrm{r}}(\xi)$ can be approximated by the power function $(1-\xi)^{-2\beta}$ when $\xi \to 1$. The exponent β, which comes from the approximation for $q_{\mathrm{L}}(\xi)$, turns out to be larger than one half (see discussion in the next section). Thus if

Table 1
Values of parameters used in the simulation

Description	Notation	Value	Units
Saturation temperature	T_{sat}	311	°C
Thermal conductivity of liquid	k_L	0.55	W/(m K)
Specific heat of liquid	c_{pL}	6.12	J/(g K)
Mass density of liquid	ρ_L	688.63	kg/m^3
Mass density of vapor	ρ_V	55.48	kg/m^3
Latent heat of vaporization	H	1.3	MJ/kg
Surface tension	σ	12.04	mN/m
Thermal conductivity of steel	k_S	15	W/(m K)
Specific heat of steel	–	0.5	J/(g K)
Mass density of steel	–	8000	kg/m^3
Initial bubble radius	R_0	0.05	mm
Reference heat flux	$\bar{q}$	1	MW/m^2
Reference thermal conductivity	$\bar{k}$	1	W/(m K)
Minimal discretization step	d_{min}	0.001	R_0
Time step	Δt	1	ms

the data were extrapolated to the contact point $\xi = 1$, this integral would diverge. It is well known, however, that the evaporation heat flux is intrinsically limited [8] by a flux q_{max}. As calculated in the kinetic theory of gases

$$q_{max} = 0.74\rho_V H\sqrt{R_g T_{sat}/(2\pi M)} \approx 10^4 \text{ MW/m}^2. \quad (44)$$

In our model the above divergence appears because of the assumption that the temperature remains constant along the vapor–liquid interface. In reality, this assumption is violated in the very close vicinity of the contact point where the heat flux q_L is comparable to q_{max}. Thus we accept the following approximation for the function $q_L(\xi)$, $\xi < 1$. It is extrapolated using the power law $q_L(\xi) \propto (1-\xi)^{-\beta}$ until it reaches the value of q_{max} and remains constant while ξ increases to unity. This extrapolation is used to calculate the integrals in Eqs. (34) and (35). There is no need to modify the constant-temperature boundary condition for the heat transfer calculations because the calculated heat flux q_L always remains less than q_{max}.

The calculations show that the function $q_L(\xi)$ (see Fig. 4) can be described well by the above power law where $\beta \sim 1$ grows slightly with time. We note that for the growing bubble the divergence is stronger than for the 90° wedge analyzed in [16]. The difference between these two cases is the behavior of the heat flux q_S in the vicinity of the contact point. While it was supposed to be uniform for the 90° wedge, the function $q_S(x)$ increases strongly near the contact point for the growing bubble case, see the discussion associated with Fig. 9.

Sometimes, an occasional 'bump' on the $q_L(\xi)$ curve appears during the iteration of the steps 3–7 of the algorithm because of inaccurate calculation of the bubble shape when the automatically chosen number of boundary elements in the vicinity of the contact line is too small. This bump disappears during at most three time steps. This disappearance indicates a good numer-

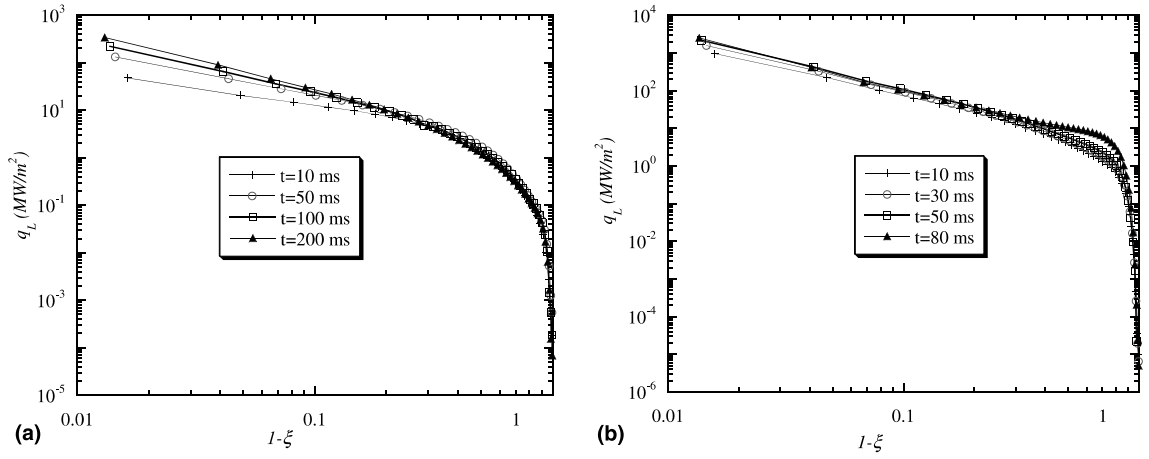

Fig. 4. Variation of the heat flux q_L (defined in (16)) along the bubble contour for different moments of time. The curvilinear coordinate ξ varies along the bubble contour; $\xi = 1$ at the contact point: (a) $q_0 = 0.05$ MW/m^2, (b) $q_0 = 0.5$ MW/m^2.

ical stability of the algorithm. When the bubble evolution is exceedingly slow, it may be necessary to increase the time step several times. While not influencing accuracy strongly (this is an intrinsic property of the BEM [24]), such a change decreases the temporal resolution.

5. Results and discussion

There are a number of new results that we have obtained from this simulation. The most important is the time evolution of the dry spot under the vapor bubble. At low heat flux, the shape of the bubble stays nearly spherical Fig. 5(a) until it leaves the heating surface under the action of gravity or hydrodynamic drag forces. Fig. 5(b) shows that at large heat flux the radius of the dry spot can approach the bubble radius during its evolution, thus confirming previous theoretical predictions [16] where the apparent contact angle grows with time. It should be emphasized that the *actual* contact angle remains zero during the evolution, see Section 2. The large *apparent* contact angle is due to the strong change in slope of the bubble contour near the contact line where the vapor recoil force is very large (see [16] for the advanced discussion). The temporal evolution of the radius R_d of the dry spot is illustrated in Fig. 6, where the time evolution of R_d/R is shown. R is the visible bubble radius defined as the maximum abscissa for the points of the bubble contour as shown in Fig. 1. Note that $R_d/R \leqslant 1$ by definition. At low heat fluxes $q_0 < 100$ kW/m^2 R_d stays very small during a long time interval (see Fig. 5(a)). In this regime the bubble should leave the heater quickly because of the small adhesion that is proportional to the contact line length. After a transition time t_c which depends on q_0, the growth of the dry spot accelerates steeply (see Fig. 6). This time t_c corresponds to the moment where the growing vapor recoil force becomes comparable to the surface tension. This force balance was analyzed in detail in [16], where numerical estimates were given. The dependence $t_c(q_0)$ is presented in Fig. 7. Clearly, t_c is a decreasing function of q_0. This means that, at a sufficiently large q_0, the dry spot becomes very large in a short time and the departure of the bubble is prevented because of the large adhesion to the heater. During further growth this bubble can either create alone a nucleus for the film boiling or coalesce with another similarly spreading neighboring bubble. Therefore, we can associate this value of q_0 with the q_{CHF}. Without a careful analysis of the time of departure, it is not possible to determine a precise value for q_{CHF}. This will be the subject of future studies.

We neglected the initial superheating for the sake of simplicity. The initial superheating would accelerate the bubble growth slightly in the initial stages that are not important for the dry spot spreading that becomes significant later on.

Slight oscillations in the dry spot growth are clearly visible in Fig. 6, especially in the fast growth regime. We varied the numerical discretization parameters in order to check whether these oscillations appear due to a numerical instability. Neither the amplitude nor frequency of the oscillations depends on numerical discretization parameters. We conclude that the oscillations reflect a physical effect (see below) rather than a numerical artifact.

The kinetics of the bubble growth is illustrated in Fig. 8, where the temporal evolution of the bubble radius R is presented. At $t < t_c$ we recover a general tendency of the bubble growth curves (see, e.g., [2,3]), where $R \propto t^{1/2}$. At $t > t_c$ the growth exponent is larger. The curve $R(t)$ exhibits oscillations with their amplitude increasing with time. We suspect that this effect appears when the temperature distribution in the heater responds too slowly to maintain the fast growth rate in the bubble.

Our simulation enables the heat transfer under the bubble to be rigorously calculated. The variation of the heat flux q_S along the heating surface is shown in Fig. 9(a) and (b) for the different values of the heat flux q_0. The value of q_S on the liquid side in the vicinity of the contact line turns out to be very close to q_L, the heat flux that produces evaporation on the vapor–liquid interface

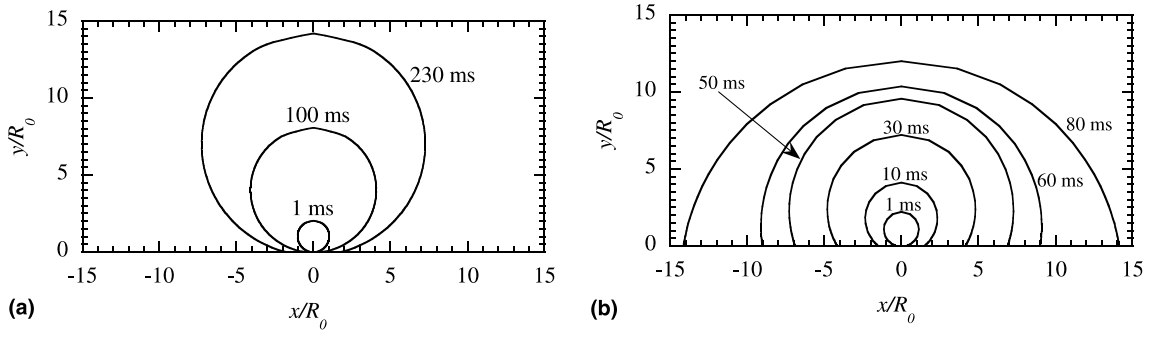

Fig. 5. The bubble shape shown for the different growth times. (a) $q_0 = 0.05$ MW/m^2; (b) $q_0 = 0.5$ MW/m^2.

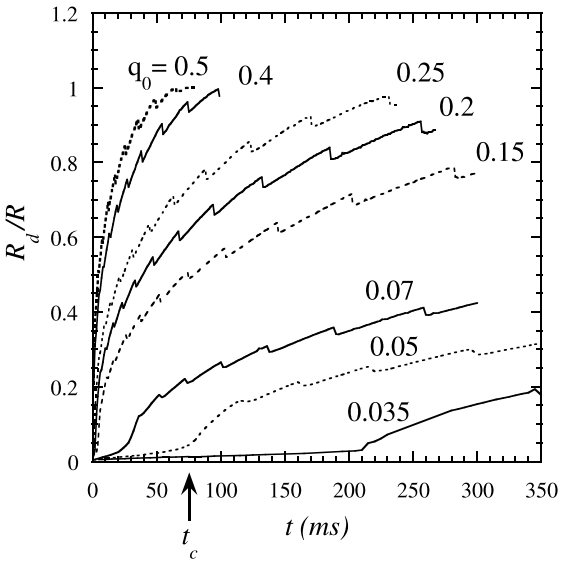

Fig. 6. The temporal evolution of the quotient of the dry spot radius R_d and the bubble radius R for different values of q_0 expressed in MW/m^2. R is measured as shown in Fig. 1. The transition time t_c is shown for $q_0 = 0.05$ MW/m^2.

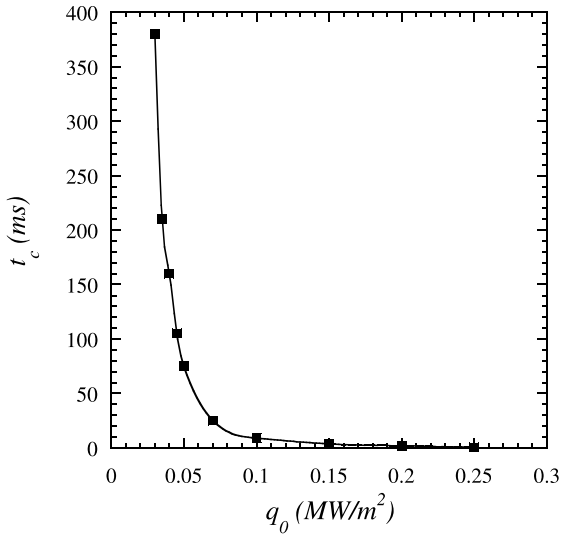

Fig. 7. The transition time t_c as a function of the heat flux q_0.

and that diverges on the contact line (see Fig. 4). This correspondence was expected, because all the heat flux supplied by the heater to the foot of the bubble is consummated to evaporate the liquid, in agreement with the 'liquid microlayer' models. Since q_S is zero (cf. (21)) if the contact line is approached from the dry spot side, the function $q_S(x)$ is discontinuous in the vicinity of the contact point. Far from the bubble $q_S = q_0$ as it should be.

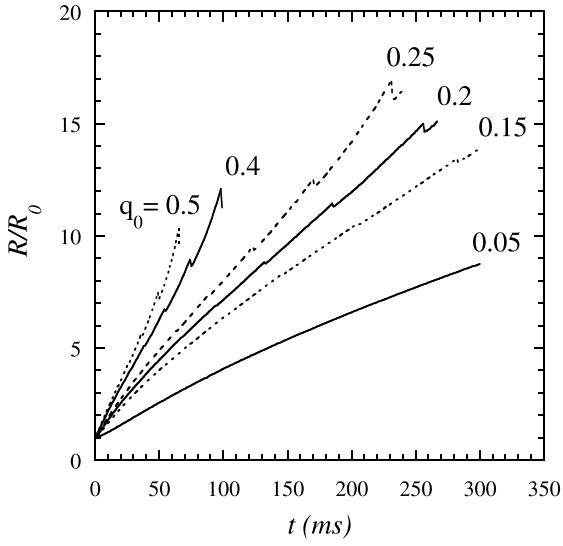

Fig. 8. Temporal evolution of the bubble radius R for different values of q_0 expressed in MW/m^2. R is measured as shown in Fig. 1.

The variation of the temperature along the heating surface $T_S(x)$ is also shown in Fig. 9. Far from the bubble, T_S has to increase with time independently of x and follows a square root law according to (27). It decreases to T_{sat} near the contact point because the temperature should be equal to T_{sat} on the whole vapor–liquid interface, according to the imposed boundary condition. Fig. 9 demonstrate that there is a zone of lowered temperature around the bubble, in agreement with the experimental observations [2]. Inside the dry spot, T_S increases with time sharply because the heat transfer through the dry spot is blocked. Fig. 9(b) shows that at high heat flux and $t > t_c$ the temperature inside the dry spot becomes larger than the temperature far from the bubble. This temperature increase leads to an eventual burnout of the heater observed during the boiling crisis. The presence of singularities in the functions $T_S(x)$ and $q_S(x)$ is the reason for our choice of the boundary conditions on the heating surface in the form (21) and (22). As a matter of fact, an application of the conditions of the uniform heat flux or uniform temperature would lead to the physically inconsistent results such as non-integrable divergency of q_L at the contact line. We note that an error in the calculation of q_L should strongly influence the results for the dry spot dynamics.

6. Conclusions

The 2D free-boundary simulation allows us to calculate the actual bubble shape and the variation of the

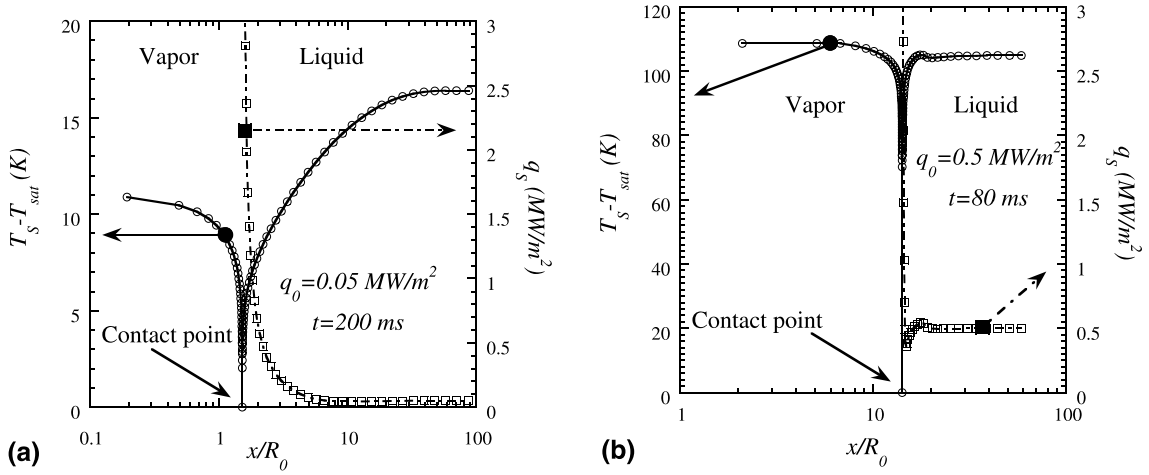

Fig. 9. Variation of the heat flux q_S and the temperature T_S along the surface of the heater for (a) $q_0 = 0.05$ MW/m^2, $t = 200$ ms; (b) $q_0 = 0.5$ MW/m^2, $t = 80$ ms. The point $x = 0$ corresponds to the center of the bubble. $T_S - T_{sat} = 0$ at the contact point, $q_S = 0$ to the left of it, i.e., inside the dry spot.

temperatures and fluxes along the vapor–liquid, vapor–solid, and liquid–solid interfaces. The description of the heat transfer in the vicinity of the triple contact line presents the most difficult part of the problem. Our variation of the boundary element method is capable of adequately describing it.

Our main result is the evidence for the growth of the dry spot under the vapor bubble. While this increase is very slow in the beginning of the bubble growth, it accelerates steeply after a growth time t_c that depends on the external heat supply. At low heat supply, t_c is very large so that the bubble can grow large enough to satisfy the conditions for departure from the heating surface *before* the dry spot becomes significant. In contrast, at high heat supply, t_c is small so that the dry spot grows very rapidly which means that the bubble spreads over the heating surface. Although our analysis is limited to the case of high system pressures, we note that at low pressures this effect can also be important because the forces of dynamical origin 'press' the bubble against the heater, thus favoring its spreading. The results of this simulation thus confirm the validity of the 'drying transition' model suggested in [16] to describe the boiling crisis.

Unfortunately, observations of the bubble shape and the dry spot growth during boiling at high pressures and high heat fluxes are unknown to us, preventing a direct comparison of our results with the experimental data. We note, however, that the growth of the dry spot immediately before the boiling crisis was observed in [9–12], where observations have been carried out through a transparent heating surface. The authors of [10–12] state that 'When the heat flux is sufficiently large, suddenly at some point on the heating surface a dry area is not wetted and starts growing, leading to burnout'. This observation confirms directly the validity of our model.

Acknowledgements

The authors would like to acknowledge the financial support of EDF (V.N. and D.B.) and NASA (V.N. and J.H.). This work has been done when one of the authors (V.N.) stayed at the Department of Physics of the UNO, which he would like to thank for its kind hospitality. V. N. thanks Dr. Hervé Lemonnier for the introduction into the BEM for the heat diffusion. The authors are grateful to Jean-Marc Delhaye for fruitful discussions.

Appendix A. Volume determination

The volume V of an object Ω can be calculated as

$$V = \int_{(\Omega)} \mathrm{d}\Omega = \frac{1}{2} \int_{(\Omega)} \mathrm{div}(x\vec{e}_x + y\vec{e}_y)\,\mathrm{d}\Omega, \tag{A.1}$$

using the obvious equality

$$\mathrm{div}(x\vec{e}_x + y\vec{e}_y) = 2,$$

where $\vec{e}_x = (1,0)$ and $\vec{e}_y = (0,1)$ are the unit vectors directed along the axes. The Gauss integral theorem is valid for any $\vec{a}$ and Ω:

$$\int_{(\Omega)} \mathrm{div}\,\vec{a}\,\mathrm{d}\Omega = \int_{(\partial\Omega)} \vec{a}\cdot\vec{n}_e\,\mathrm{d}\partial\Omega, \tag{A.2}$$

where $\partial\Omega$ denotes the surface of Ω, and $\vec{n}_e$ is the external unit normal vector to this surface. In our case $\partial\Omega = \partial\Omega_i \cup \partial\Omega_d$, where $\partial\Omega_d$ is the surface of the vapor–solid contact, i.e., the dry spot. The application of the equality (A.2) to the last integral in (A.1) yields the expression

$$V = \frac{1}{2}\int_{(\partial\Omega_i \cup \partial\Omega_d)} (xn_e^x + yn_e^y)\,\mathrm{d}\partial\Omega. \qquad (A.3)$$

Since $y = n_e^x = 0$ on $\partial\Omega_d$ (see Fig. 1), the integral over it is equal to zero. Thus (A.3) reduces to (4).

References

[1] L.S. Tong, in: Boiling Heat Transfer and Two-Phase Flow, second ed., Taylor & Francis, New York, 1997.

[2] M.G. Cooper, A.J.P. Lloyd, The microlayer in nucleate pool boiling, Int.J. Heat Mass Transfer 12 (1969) 895–913.

[3] P. Stephan, J. Hammer, A new model for nucleate boiling heat transfer, Wärme- und Stoffübertrangung 30 (1985) 119–125.

[4] R.C. Lee, J.E. Nydahl, Numerical calculation of bubble growth in nucleate boiling from inception through departure, J. Heat Transfer/Trans. ASME 111 (1989) 474–478.

[5] R. Mei, W. Chen, J.F. Klausner, Vapor bubbles growth in heterogeneous boiling, Int. J. Heat Mass Transfer 38 (1995) 909–919.

[6] V.K. Dhir, D.M. Qiu, N. Ramanujapu, M.M. Hasan, Investigation of nucleate boiling mechanisms under microgravity conditions, in: Proc. IVth Microgravity Fluid Physics & Transport Phenomena Conf. Cleveland, (NASA Publication in the form of Compact Disk, available also from http://www.ncmr.org/events/fluids1998/papers/459.pdf), 1998, pp. 435–440.

[7] Yu.A. Buyevich, Towards a unified theory of pool boiling – the case of ideally smooth heated wall, Int. J. Fluid Mech. Res. 26 (2) (1999) 189–223.

[8] van P. Carey, in: Liquid–Vapor Phase Change Phenomena, Hemisphere, Washington, DC, 1992.

[9] H.J. van Ouwerkerk, Burnout in pool boiling: the stability of boiling mechanisms, Int. J. Heat Mass Transfer 15 (1972) 25–34.

[10] K. Torikai, M. Hori, M. Akiyama, T. Kobori, H. Adachi, Boiling transfer and burn-out mechanism in boiling-water cooled reactors, in: Proc. Third UN Int. Conf. Peaceful Uses of Atomic Energy. (Geneva, Aug. 31–Sept. 9, 1964) United Nations, New York, 8, 1964, pp. 146–155.

[11] K. Torikai, K. Suzuki, M. Yamaguchi, Study on contact area of pool boiling bubbles on a heating surface (observation of bubbles in transition boiling), JSME Int. J. Series II 34 (1991) 195–199.

[12] K. Torikai, K. Suzuki, T. Inoue, T. Shirakawa, Effects of microlayer and behavior of coalesced bubbles in transition boiling for heat transfer, in: Heat Transfer: Proc. 3rd UK National Conf. Inc. First Eur. Conf. Therm. Sci., Birmingham, 1992, pp. 599–605.

[13] A.K. Chesters, Modes of bubble growth in the slow-formation regime of nucleate pool boiling, Int. J. Multiphase Flow 4 (1978) 279–302.

[14] M.A. Johnston, J. de la Pena, R.B. Mesler, Bubble shapes in nucleate boiling, AIChE J. 12 (1966) 344.

[15] P. Bricard, P. Péturaud, J.-M. Delhaye, Understanding and modeling DNB in forced convective boiling: modeling of a mechanism based on nucleation site dryout, Multiphase Sci. Techn. 9 (4) (1997) 329–379.

[16] V.S. Nikolayev, D.A. Beysens, Boiling crisis and non-equilibrium drying transition, Europhysics Letters 47 (1999) 345–351.

[17] H.L.G. Pina, J.L.M. Fernandes, Applications in transient heat conduction, in: C.A. Brebbia, (Ed.), Topics in Boundary Element Research, vol. 1, Basic Principles and Applications, Springer, Berlin, 1984, pp. 41–58.

[18] D. Juric, G. Tryggvason, Computations of boiling flows, Int. J. Multiphase Flow 24 (1998) 387–410.

[19] A. Mazouzi, Etude thermique et hydrodynamique de la croissance des bulles de vapeur en ébullition nucléée. Thèse de l'Université P. et M. Curie, Paris, 1995.

[20] A. Prosperetti, M.S. Plesset, The stability of an evaporating liquid surface, Phys. Fluids 27 (1984) 1590–1601.

[21] H.S. Carslaw, J.C. Jaeger, in: Conduction of Heat in Solids, II ed., University Press, Oxford, 1959.

[22] M. Abramovitz, I.A. Stegun, (Eds.), Handbook of Mathematical Functions, Dover, New York, 1972.

[23] W. DeLima-Silva, L.C. Wrobel, A front-tracking BEM formulation for one-phase solidification/melting problems, Engineering Analysis with Boundary Elements 16 (1995) 171–182.

[24] G.-L. Lagier, Application de la méthode des élements de frontière à la résolution de problémes de thermique inverse multidimensionnels (Application of the boundary element method to multidimensional inverse heat conduction problems), Thése de l'Institut National Polytechnique de Grenoble, Grenoble, 1999.

[25] V. Demirel, S. Wang, An efficient boundary element method for two-dimensional transient wave-propagation problems, Appl. Math. Modeling 11 (1987) 411–416.

PHYSICAL REVIEW E, VOLUME 64, 051602

Gas spreading on a heated wall wetted by liquid

Y. Garrabos and C. Lecoutre-Chabot
CNRS-ESEME, Institut de Chimie de la Matière Condensée de Bordeaux, Université de Bordeaux I, Avenue du Dr. Schweitzer, F-33608 Pessac Cedex, France

J. Hegseth
Department of Physics, University of New Orleans, New Orleans, Louisiana 70148

V. S. Nikolayev*,† and D. Beysens†
ESEME, Service des Basses Températures, CEA-Grenoble, Grenoble, France

J.-P. Delville
Centre de Physique Moléculaire, Optique et Hertzienne, CNRS, Université de Bordeaux I, Cours de la Libération, F-33608 Talence Cedex, France

(Received 22 May 2001; published 17 October 2001)

This study deals with a simple pure fluid whose temperature is slightly below its critical temperature and whose density is nearly critical, so that the gas and liquid phases coexist. Under equilibrium conditions, such a liquid completely wets the container wall and the gas phase is always separated from the solid by a wetting film. We report a striking change in the shape of the gas-liquid interface influenced by heating under weightlessness where the gas phase spreads over a hot solid surface showing an apparent contact angle *larger* than 90°. We show that the two-phase fluid is very sensitive to the differential vapor recoil force and give an explanation that uses this nonequilibrium effect. We also show how these experiments help to understand the boiling crisis, an important technological problem in high-power boiling heat exchange.

DOI: 10.1103/PhysRevE.64.051602 PACS number(s): 68.03.Cd, 05.70.Jk, 44.35.+c, 64.60.Fr

I. INTRODUCTION

Singular properties of a simple fluid [1,2] appear when it is near its critical temperature T_c and its critical density ρ_c. When the fluid's temperature T is slightly lower than T_c and the average fluid density ρ is close to ρ_c the fluid exhibits perfect wetting (i.e., zero contact angle) of almost any solid by the liquid phase in equilibrium. In this article we study a system that is slightly out of equilibrium. Our experiments, performed in weightlessness [3–7] show that when the system's temperature T is being increased to T_c the *apparent* contact angle (see Fig. 7 below for definition) becomes very large (up to 110°), and the *gas* appears to spread over the solid surface. In Sec. II we describe our experimental setup that allows the spreading gas to be observed. The gas-liquid interface shape at equilibrium, which is considered in Sec. III, plays a crucial role as an initial condition for the gas spreading phenomenon. Sections IV and V deal with the observations of the spreading gas. A theoretical model that allows this unusual phenomenon to be explained is proposed in Sec. VI. In Sec. VII, we discuss the boiling crisis, a phenomenon that plays an important role in industrial applications, and how it is relevant to the spreading gas.

*Email address: vnikolayev@cea.fr
†Mailing address: CEA-ESEME, Institut de Chimie de la Matière Condensée de Bordeaux, 87 Avenue du Dr. Schweitzer, 33608 Pessac Cedex, France.

II. EXPERIMENTAL SETUP

We report results that were obtained and repeated using several samples of SF_6 ($T_c = 318.717$ K, $\rho_c = 742$ kg/m^3). These samples were heated at various rates in cylindrical cells of various aspect ratios on several French-Russian and French-American missions on the Mir space station using the Alice-II instrument [8]. This instrument is specially designed to obtain high-precision temperature control (stability of $\approx 15\,\mu$K over 50 h, repeatability of $\approx 50\,\mu$K over 7 days). To place the samples near the critical point, constant mass cells are prepared with a high-precision density, to 0.02%, by observing the volume fraction change of the cells as a function of temperature on the ground [9].

A fluid layer was sandwiched between two parallel sapphire windows and surrounded by a copper alloy housing in the cylindrical optical cell, the axial section of which is shown in Fig. 1.

We consider here three cells of the same diameter $D = 12$ mm, the other parameters of which are shown in Table I. The liquid-gas interface was visualized through light transmission normal to the windows. Since the windows are glued to the copper alloy wall, some of the glue is squeezed inside the cell as shown in Fig. 1. This glue forms a ring that blocks the light transmission in a thin layer of the fluid adjacent to the copper wall, making it inaccessible for observations. Because of this glue layer, the windows may also be slightly tilted with respect to each other as discussed in Sec. III.

A 10 mm diam ring was engraved on one of the win-

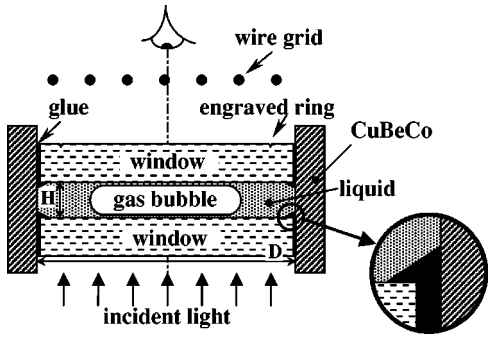

FIG. 1. Sketch of a cross section of the cylindrical sample cell (with parallel windows). The fluid volume is contained between two sapphire windows that are glued to a Cu-Be-Co alloy ring. The dimensions H (see Table I) and $D(=12$ mm) of the cell are indicated. Some glue is squeezed into the cell. The thickness of the glue layer is exaggerated for illustration purposes. In weightlessness, the gas bubble should be located in the middle of such an ''ideal'' cell; see Sec. III for discussion.

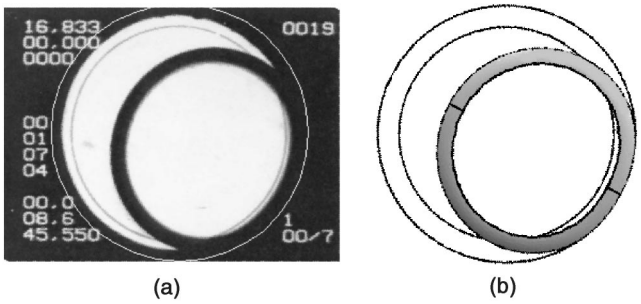

FIG. 2. The experimental image of cell 10 at room temperature (a) and the equilibrium bubble shape simulated for the tilt angle of 0.46° (b). When superposed, the images (a) and (b) give almost a perfect match. The outer white circle in (a) [black in (b)] shows the actual location of the cell wall. The inner black circles in (a) and (b) correspond to the engraved ring that allows the superposition to be made. The dark space between these two circles in the image (a) is made by the ring of glue as shown in Fig. 1. The image (b) is a frontal projection of the bubble shown in Fig. 4 below.

dows of each cell in order to calibrate the size of the visible area of the cell images as can be seen in each image. An out-of-focus wire grid, designed to visualize [10] fluid inhomogeneities and/or a fluid flow through light refraction, was also used. The grid was occasionally moved out of the light path, so that it is not always present in all images.

The sample cell was placed inside a copper sample cell unit (SCU) that, in turn, was placed inside a thermostat. Heat was pumped into and out of the SCU using Peltier elements and heaters. The temperature was sampled every second and is resolved to 1 μK.

Similar ground based experiments were done before these experiments using a copy of the same instrument. The gravity forces push the denser liquid phase to the bottom of the cell and completely different behavior is seen; see [11].

III. BUBBLE POSITION AT EQUILIBRIUM UNDER WEIGHTLESSNESS

The gas volume fraction ϕ (volume of the gas divided by the total cell volume) is defined by ρ and the densities of gas and liquid for the given temperature. In our experiments, $\phi \approx 0.5$ and the gas bubble is flattened between the windows (Fig. 1) due to the large aspect ratio D/H of the cell.

Let us first consider an ideally cylindrical cell as opposed to the real cell. At equilibrium, the windows and the copper wall are wetted by the liquid phase. Because the van der Waals forces from the walls act to make the wetting film as thick as possible, the weightless bubble should be located in the cell's center. Because the bubble is flattened and occupies one-half of the available volume, the distance of such a centered bubble to the copper wall is large (Fig. 1). The lateral centering forces are then much weaker than the centering forces in the direction of the cell axis. Any small external influences in the real cell can displace the bubble laterally from the cell's center. This displacement is illustrated in Fig. 2, which shows cell 10 at room temperature.

TABLE I. Physical parameters of the experimental cells. Cell 11 has a movable piston to change the cell volume. However, the volume was kept constant during these experiments.

Cell number	Cell thickness H (mm)	$(\rho-\rho_c)/\rho_c$ (%)
8	3.016	0.85
10	1.664	0.25
11	4.340	0.87

We note that there are two kinds of external influence that are easily identified: residual accelerations in the spacecraft and cell asymmetry.

Bubble images for cells 8 and 10 were recorded in four Mir missions between 1996 and 2000. Several images are reported in [3] (Cassiopeia mission, 1996) and in Fig. 6 below (GMSF2 mission, 1999) for cell 10. It is extremely likely that the space station changed its position with respect to the residual gravity vector between these runs. The bubble position with respect to the cell, however, always remained the same. The bubble location also varies from cell to cell without any dependence on the station's orientation. Therefore, we have no reason to attribute the off-center position of the bubble to the residual gravity.

Although the cells were manufactured with high precision, the cell windows could not be exactly parallel because of the glue layer as shown in Fig. 3. In the rest of this section we will discuss the influence of the windows' tilt on the position and shape of the bubble.

When the bubble's surface is curved, there is a constant excess pressure Δp inside the bubble defined by the Laplace formula

$$\Delta p = \sigma K, \tag{1}$$

where σ is a surface tension and K is the surface curvature. This excess pressure acts on all parts of the bubble interface. In particular, it acts on the part A_{sg} (where the index s stands for ''sapphire'' and g for ''gas'') of the flat window surface that contacts the gas directly (or, more accurately, through a wetting film that we assume to be of homogeneous thick-

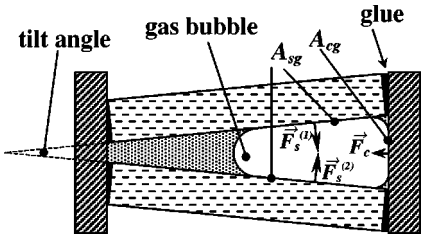

FIG. 3. Sketch of a cross section of the sample cell with tilted windows at equilibrium in weightlessness. The wetting film is not shown. The window tilt is possible due to the existence of a space between the window's edge and the copper wall, which is filled by glue. This space and the tilt are exaggerated for illustration purposes. Based on the manufacturing process a maximum tilt angle of $\approx 1°$ is possible. The glue squeezed into the cell is not shown. The reaction forces that act on the gas bubble are shown with arrows. The contact areas of the gas bubble with the solid are indicated.

ness). This pressure creates reactions forces $\vec{F}_s^{(1)}$ and $\vec{F}_s^{(2)}$ at each window that act on the bubble. Each of these forces is perpendicular to the corresponding window. The absolute values of $\vec{F}_s^{(1)}$ and $\vec{F}_s^{(2)}$ are equal to $A_{sg}\Delta p$. When the windows are exactly parallel, $\vec{F}_s^{(1)}+\vec{F}_s^{(2)}=0$ and the bubble remains at the cell's center. When the windows are tilted with respect to each other, the nonzero force $\vec{F}_s^{(1)}+\vec{F}_s^{(2)}$ pushes the bubble in the direction of the increasing cell thickness. This motion continues until the bubble touches (through a wetting film) the copper wall of the cell, thus forming a contact spot of the area A_{cg}, where the index c stands for ''copper.'' This direct contact with the solid results in another reaction force $\vec{F}_c$ with the absolute value $A_{cg}\Delta p$, such that

$$\vec{F}_s^{(1)}+\vec{F}_s^{(2)}+\vec{F}_c=0 \tag{2}$$

in equilibrium (see Fig. 3).

There are two equivalent ways to find the bubble shape at equilibrium. One can solve Eq. (1), which reduces to $K=\text{const}$, where the constant is obtained from the condition of the given bubble volume. The bubble volume is defined by the known gas volume fraction and the cell volume. One can also minimize the gas-liquid interface area with a bubble volume constraint. In both cases boundary conditions must be satisfied (zero contact angle in our case). The resulting bubble shape obviously depends on the cell geometry. It is also nearly independent of temperature as can be seen from Eq. (2), because all three terms of this equation are proportional to the surface tension σ, so that this force balance remains valid even near T_c, where σ disappears. There are, however, several sources of weak temperature dependence of the bubble shape. First, there is weak dependence of the gas volume fraction ϕ on temperature at constant average density ρ. This small deviation is smallest at the critical density ρ_c and slightly greater in these experiments due to the very small deviation (see Table I) of ρ from ρ_c. Second, the curvature K depends on the thickness of the wetting film

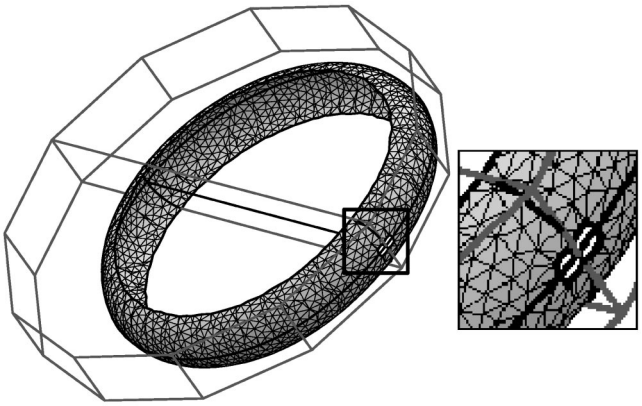

FIG. 4. The result of a 3D finite element calculation of the equilibrium gas-liquid interface for cell 10 with a window tilt angle of 0.46°. The vertices of the polygonal lines indicate the location of the cylindrical copper wall and they are shown to guide the eye. The shape of a circular cylinder was input to the simulation. The contact angle is zero. The part of the image marked by the square is enlarged to show the contact area A_{cg} of the gas with the copper wall (the small white rectangle crossed by two symmetry lines). The contact areas A_{sg} with the windows have an oval shape. The projection of this bubble shape onto the cell window is shown in Fig. 2(b).

which increases near T_c. The wetting film remains thin, however, in comparison with the cell thickness. Both of these effects are very weak.

The force $\vec{F}_c$, which is directed horizontally in Fig. 3, causes a distortion of the bubble. This distortion results in an oval image in Fig. 2 instead of a circle. The degree of distortion increases with increasing tilt angle because so does $\vec{F}_c$. This distortion can thus be used to estimate the tilt angle.

For these constant volume gas bubbles, the degree of distortion should decrease with increasing cell thickness H for the same window tilt. A larger value of H results in a less compressed (more spherelike) bubble shape with less area in contact with the wall. This smaller bubble curvature results in a smaller value for Δp according to Eq. (1). Consequently, the force $\vec{F}_c$, the area A_{cg} of the contact with the copper wall, and the bubble distortion are smaller. This window tilt hypothesis is consistent with observations: we were not able to detect any distortion of the gas bubble in cell 8 [see Fig. 10(a) below, which corresponds to the nearly equilibrium shape] which is approximately twice as thick (Table I) as cell 10 shown in Fig. 2. There is, however, some tilt in cell 8 because the bubble touches the wall. We expect that the tilt angles in all of the cells are of the same order of magnitude because they were all manufactured using the same method.

To verify the window tilt hypothesis, we performed a three-dimensional (3D) numerical simulation of the bubble surface by using the SURFACE EVOLVER finite element software [12]. The result of this calculation is shown in Fig. 4 for cell 10.

The experimentally observed bubble deformation matches the calculation performed for a tilt angle of 0.46° (see Fig. 2). The simulation resulted in the interface curvature $K=1.389\ \text{mm}^{-1}$ and in $A_{cg}=0.150\ \text{mm}^2$ calculated for the

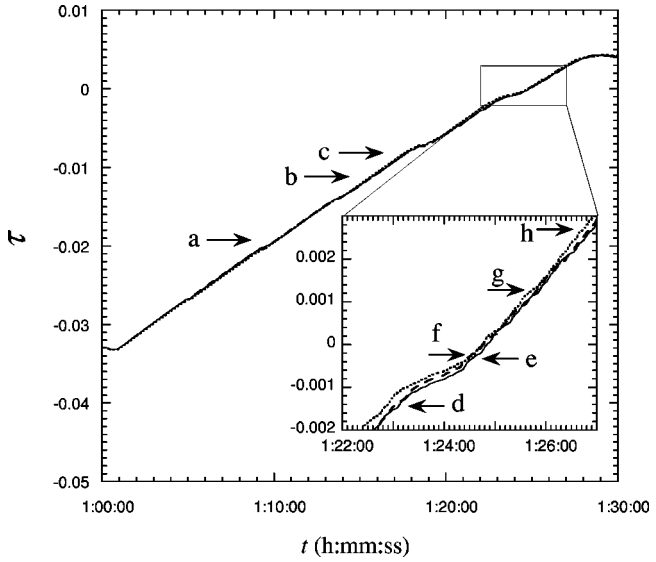

FIG. 5. Reduced temperature evolution for the image sequences shown in Fig. 6 (solid line), Fig. 8 (dotted line), and Fig. 9 (dashed line). The temperature values that correspond to each of the images (a)–(h) shown in these figures are indicated by arrows and the corresponding letters. The definition of τ is discussed in the text. The temperature is measured in the body of the SCU. The vicinity of the critical point is enlarged in the inset.

bubble volume $V\phi = 26.675$ mm^3. From these data, it is easy to calculate the effective acceleration g_{eff} that would create the equivalent buoyancy force $F_c = (\rho_L - \rho_V) V\phi\, g_{eff} = K\sigma A_{cg}$. It turns out that $g_{eff} = 1.55 \times 10^{-3} g$ for $T = 290$ K, where g is the gravity acceleration on Earth. This g_{eff} acceleration is much larger than the residual steady accelerations in the Mir space station ($\sim 10^{-6} g$) and this shows that the observed bubble deformation is not caused by residual accelerations. We conclude that the window tilt hypothesis about the origin of the bubble deformation and its off-center position is correct.

A similar off-center bubble position was observed under weightlessness in a cell similar to ours by Ikier *et al.* [13] and was attributed to a residual acceleration. However, they report only one run in a single cell, making the actual cause of the bubble off-centered position impossible to verify.

IV. CONTINUOUS HEATING EXPERIMENTS

In the continuous heating experiments, the cells 8, 10, and 11 were heated nearly linearly in time *t*. The evolution of the nondimensional temperature τ for each of these experiments is shown in Fig. 5.

The parameter τ is defined as $(T - T_{coex})/T_c$, where T_{coex} is the temperature of the coexistence curve that corresponds to the fluid's average density shown in Table I. Note that T_{coex} differs from T_c only by $1-50\,\mu$K because the density is very close to ρ_c for all cells. A 40 min temperature equilibration at $\tau \approx -0.033$ preceded the heating. The mean value of dT/dt at T_c was ≈ 7.2 mK/s.

Figure 6 shows the time sequence of the images of cell 10. The interface appears dark because the liquid-gas meniscus refracts the normally incident light away from the cell axis. After the temperature ramp was started but still far from the critical temperature, the bubble shape changed. The contact area A_{cg} of the gas with the copper wall appears to increase. In other systems the wetting film under a growing vapor bubble is observed to evaporate [14]. In near-critical fluids, however, the heat transfer processes are more complex [15]. In this system we believe that there may be a similar drying process, i.e., at some time the thin wetting film that separates the gas from the copper wall evaporates. In fact, we have observed low-contrast lines that appear within the A_{sg} area when the heating begins. An example of such a line is indicated in Fig. 6a by the white arrows. The out-of-focus grid shows that these lines correspond to a sharp change in the wetting film thickness. These lines are most likely triple contact lines and we have actually seen them pinned by an imperfection on the windows as they advance and retreat in other experiments. Since the heat conductivity of copper is larger than that of sapphire, the heat is supplied to the cell mainly through the hotter copper wall. Therefore the film should evaporate on the copper wall even earlier than on the sapphire. A more refined analysis of the contact line motion will be discussed elsewhere.

The increase of the area A_{cg} is accompanied by an evident increase in the apparent contact angle [see Figs. 6(d)–6(f) and the corresponding magnified images in Fig. 7]. Near the critical temperature the apparent contact angle becomes

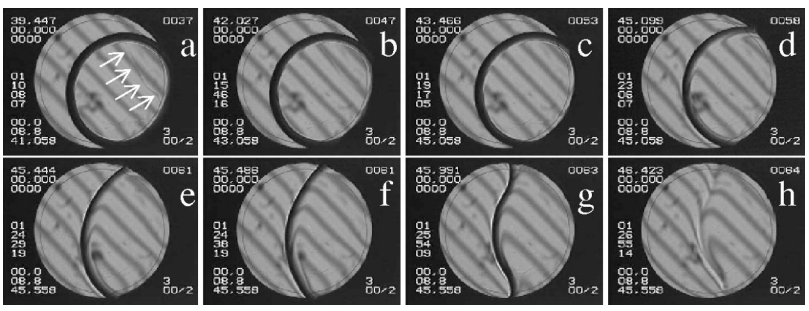

FIG. 6. Time sequence of images of cell 10 during the continuous heating through the critical point. The temperature values that correspond to each of the images (a)–(h) shown here are indicated in Fig. 5 by arrows and the corresponding letters. This run is a repeat of the run shown in Fig. 2 of [3]. The gradual increase of the apparent contact angle as the gas spreads with increasing temperature is clearly seen. The time corresponding to each image is shown to the left of the cell in the middle. The magnified upper regions close to the contact line from the images (e)–(g) are shown in Fig. 7.

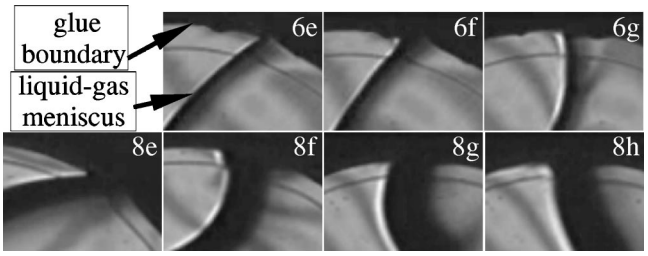

FIG. 7. The magnified upper regions close to the contact line from the images Figs. 6(e)–6(g) and from the images Figs. 8(e)–8(h). The apparent contact angle can be ''measured'' as the angle between the tangents to the black glue boundary and the liquid-gas meniscus. The latter corresponds to the boundary between the wide dark and narrow bright stripes on the images. The liquid domain is to the left of the meniscus. One can see that this apparent contact angle exceeds 90° in the images 6(g) and 8(f).

larger than 90°. We will analyze these effects theoretically in Sec. VI.

While crossing the critical point, the vapor bubble is rapidly evolving. At $T \approx T_c$, the surface tension vanishes, the bubble's relaxation from surface tension is negligible, so that the interface shape is defined by the variation of the local evaporation rate along the interface. The evaporation is stronger at the parts of the interface closest to the copper heating wall. This effect leads to the waved interface shape shown in Fig. 6(g). Diffusion causes the disappearance of the interface at $T > T_c$ as shown in Fig. 6(h).

Figure 8 shows the time sequence of the images of cell 8, which is approximately twice as thick as cell 10. The images in Fig. 8 were taken for exactly the same values of the nondimensional temperature τ (shown in Fig. 5) as the corresponding images in Fig. 6. The force $\vec{F}_c$ pushes the bubble against the cell wall as in the case of cell 10. As discussed above, this force is weaker than for cell 10 because the bubble appears almost circular at equilibrium [see Fig. 6(a) and Fig. 8(a)]. By comparing images (e) of both sequences, we can also see that the vapor spreads more slowly in cell 8. The increase of the apparent contact angle is also slower. The wave shaped interface appears earlier in Fig. 8(f), i.e., farther from T_c, than for cell 10. The interface is still quite sharp in Fig. 8(h), while it has already diffused in the case of the thinner cell [Fig. 6(h)]. This difference can be explained by the difference in the liquid-gas interface area, which is roughly proportional to the cell thickness. The surface tension force that tends to maintain the convex shape is not as strong for the thicker cell where a larger fluid volume has to be moved during the same time. The diffusion time is larger for cell 8 because the size of the inhomogeneity (i.e., interface) is larger.

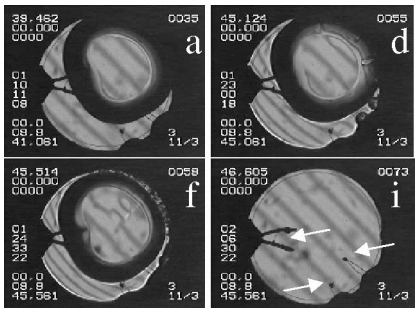

FIG. 9. Time sequence of images of cell 11 during continuous heating through the critical point. No bubble spreading is seen. The bubble does not touch the copper wall. The images (a), (d), and (f) were taken for exactly the same values of temperature (shown in Fig. 5) as corresponding images in Fig. 6 and Fig. 8. Cell 11 contains three thermistors shown in image (i) by arrows. This image was taken after temperature equilibration above T_c.

Figure 9 shows the time sequence of the images from cell 11, which is thicker than both cells 8 and 10. The images (a), (d), and (f) were taken for the same values of nondimensional temperature as corresponding images in Figs. 6 and 8. This cell contained three wetted thermistors [Fig. 9(i)] that constrain the bubble surface [Fig. 9(a)]. The bubble is only slightly squeezed by the windows so that the reaction forces that act on the bubble at equilibrium are weak. As a result, the bubble does not touch the copper heating wall at all. Although this is not clear in the image (a), because of the glue near the copper wall, it is clear in image (f) where small newly formed bubbles separate the initial bubble from the wall. These bubbles form from the local overheating of the fluid between the large bubble and the copper wall. There is enough fluid between the large bubble and the wall so that a small bubble may grow in it. These small bubbles push the large bubble away from the wall before any coalescence can take place.

The comparison of these three experiments clearly shows that, in order to obtain bubble spreading, the bubble needs to have direct contact with the heating wall, i.e., to be pushed to the heating wall by some force. Note that none of the images show any evidence of steady fluid motion which would be necessary to maintain the distorted bubble shapes in Figs. 6 and 8. We conclude that this distortion of the bubble equilibrium shape cannot be caused by fluid motion.

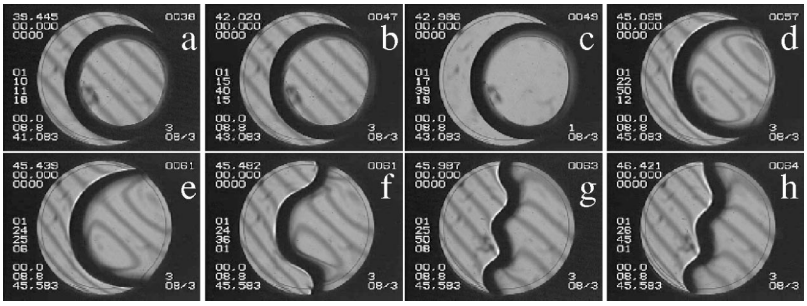

FIG. 8. Time sequence of the images from cell 8 during continuous heating through the critical point. Images (a)–(h) were taken for exactly the same values of temperature (shown in Fig. 5) as corresponding images in Fig. 6. The magnified upper regions close to the contact line from the images (e)–(h) are shown in Fig. 7.

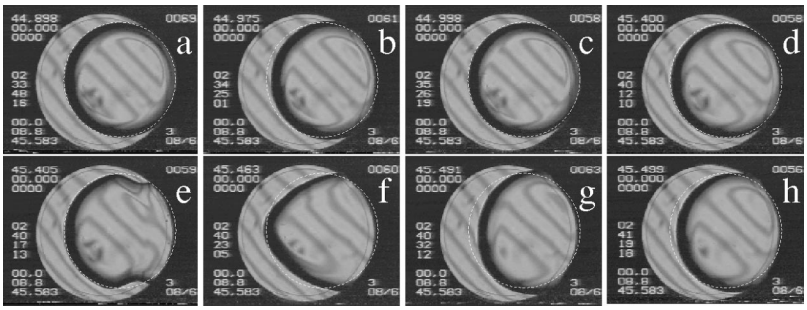

FIG. 10. Time sequence of images of cell 8 during two 100 mK quenches. The gas spreads during each quench, which lasts about 12 s. The equilibrium position of the vapor bubble with respect to the cell is shown by the white circle in each image for comparison.

Similar continuous heating experiments are reported by Ikier *et al.* in [13]. However, a smaller heating rate (1.7 mK/s) and erratic accelerations of the cell did not allow gas spreading to be observed.

V. QUENCHING EXPERIMENTS

Figure 10 shows the time sequence of the images of cell 8 when it was heated by 100 mK quenches as shown in Fig. 11.

While the heating rate is quite large during each quench, the time average of the heating rate 1.4 mK/s is smaller than that during the continuous heating due to the waiting time of ≈ 60 s after each quench. During this waiting time a partial equilibration takes place. The images (a)–(c) show a slight bubble spreading that appears during a quench that is farther from the critical point than the quench shown in images (d)–(h). After each quench as soon as the heating stops, the bubble interface begins to return to its initial form [Figs. 10(c,d)]. This shows that the spreading vapor is caused by a nonequilibrium effect. The second quench that precedes the crossing of the critical point [Figs. 10(d–h)] shows very rapid interface motion accompanied by fluid flows.

While the interface returns to its initial state during the waiting time of the first quench [Fig. 10(c)], it does not return in the second quench [Fig. 10(h)]. This occurs because the characteristic equilibration time grows dramatically near T_c.

The same phenomenon of spreading gas was also observed during the heating of CO_2 cells in other experiments (Pegasus BV4705, Post-Perseus F14) carried out by our group in the Mir station. However, these experiments were not designed to study the spreading gas and we do not discuss them here.

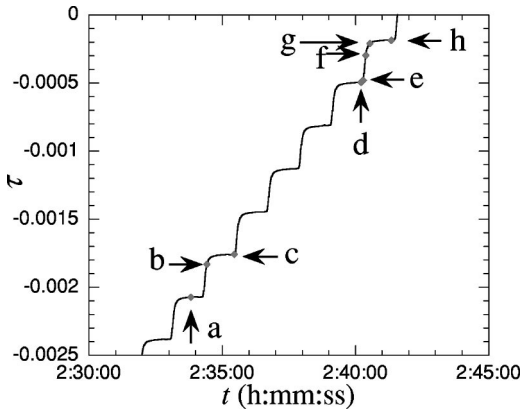

FIG. 11. Temperature evolution during the series of quenches. The points that correspond to each of the images in Figs. 10(a)–10(h) are indicated by arrows and corresponding letters. The temperature is measured in the body of the SCU.

VI. INTERFACE EVOLUTION DURING THE HEATING

The above experimental data showed that the spreading gas and the associated interface deformation are caused by an out-of-equilibrium phenomenon. This is especially demonstrated by the analysis of the interface shape at equilibrium (Sec. III) and by the return to the equilibrium shape after each quench in Sec. V. In this section we analyze possible causes of the spreading gas. Two causes are considered: Marangoni convection due to the temperature change δT_i along the gas-liquid interface, and the differential vapor recoil.

A. Marangoni convection

If a temperature change δT_i exists, it will create a surface tension change $\delta\sigma=(d\sigma/dT)\delta T_i$ that will drive a thermocapillary (Marangoni) flow in the bulk of both fluids [16–18]. The images obtained in our experiment are capable of visualizing convective flows from the shadow-graph effect. We have not seen any evidence of the steady convection that is required to create and maintain the observed bubble shape continuously during the heating. We conclude that Marangoni convection is absent.

This conclusion is an apparent contradiction with many works that study the Marangoni effect caused by evaporation (see, e.g., [19]). The main difference between these works and ours is in the conditions of evaporation. These works consider evaporation into an *open* space where the vapor pressure is very small. The interface temperature thus follows the temperature in the bulk of the liquid and a very large evaporation rate is possible, limited only by the average velocity of the fluid molecules. In our case, the gas phase is almost at saturation pressure. This means that the total evaporation (over the whole gas liquid interface) is small and limited by the amount of the supplied heat consumed by the latent heat. Therefore, any variation δT_i is rapidly dampened by the corresponding change in the evaporation rate, stabilizing the interface against Marangoni convection, see [15] for an extended discussion. This conclusion is confirmed by experiments [20] in which Marangoni convection was carefully studied in a *closed* cell with very clean water in contact with its vapor. *No* surface-tension-driven convection was

registered in spite of a large Marangoni number which was much greater than its critical value obtained in the classical Marangoni-Benard experiments with nonvolatile liquids [16]. It was argued in [16] that the convection was absent due to a hypothetical interface contamination present in spite of many careful preventive measures. According to our reasoning, a variation δT_i would have been strongly dampened in [16] because of the saturation conditions in the sealed cell. We also note that, even in evaporative driven Marangoni convection far from saturation, the convection cells may also tend to stabilize the interface resulting in intermittent cellular formation as was observed in [17]. It was also observed in [17] that the velocity of convection and frequency of intermittent cell formation decrease as the external gas becomes more saturated.

B. Differential vapor recoil

We now analyze another possible source of bubble deforming stress that does not require a temperature gradient along the interface. The bubble may be deformed by the normal stress exerted on the interface by the recoil from departing vapor [19]. Let $n(\vec{x})$ be the evaporating mass per unit time per unit interface area at the point $\vec{x}$ on the interface. The evaporating gas moves normally to the interface, and exerts a force per unit area (a ''thrust'') on the liquid of

$$P_r(\vec{x}) = n^2(\vec{x})(1/\rho_G - 1/\rho_L), \tag{3}$$

where ρ denotes mass density and the subscripts L and G refer to liquid and gas, respectively.

The interface shape can be obtained from a quasistatic argument when the experimentally observed interface velocity v_i is smaller than the characteristic hydrodynamic velocity σ/η, where η is the shear viscosity. A numerical estimate shows that the quasistatic approximation holds for the images (a)–(f) in Fig. 6 in which the spreading is observed. The quasistatic approximation does not appear to hold for the quench experiments (Fig. 10), where the interface moves rapidly.

According to the quasistatic argument [23], the interface shape can be determined from the modified Laplace equation

$$\sigma K = \Delta p + P_r(\vec{x}). \tag{4}$$

The 3D curvature K is equal to the sum of the 2D curvature c in the image plane and the 2D curvature in the perpendicular plane shown in Fig. 1. For the small cell thickness H, this last curvature can be accurately approximated by the constant value $2/H$. This is possible because the relatively small heat flow through the less conductive sapphire windows implies a small P_r near the contact line on the windows, as compared to the large value of Δp at this small H. The interface shape can thus be obtained from the 2D equation

$$\sigma c = \Delta p' + P_r(l), \tag{5}$$

where $\Delta p'$ is a constant to be determined from the known bubble volume and l is a coordinate that varies along the bubble contour in the image plane.

In order to find the distribution $n(\vec{x})$ at the interface it is necessary to solve the entire heat transfer problem. This problem is complicated by several important factors. First, we deal with a problem that contains a free boundary (gas-liquid interface) the position of which should be determined. Second, this interface contains lines of singularities (gas-liquid-solid contact lines) where various divergences are possible. Third, the adiabatic heat transfer [15,21,22] (''the piston effect'') should be taken into account for near-critical fluids. The first two complications were addressed in [23–25] for plane geometry, i.e., for a gas bubble growing on a plane. We showed that $n(\vec{x})$ can exhibit a divergence at the contact line and that it decreases exponentially far away from it. Because the bulk temperature varies sharply in the boundary layer adjacent to the walls of the cell [21] and the interface temperature is constant, the largest portion of mass transfer across the interface takes place near the triple contact line. Thus $n(\vec{x})$ is large in the vicinity of the contact line. In this work, we present first the scaling arguments and then an approximate calculation of the bubble shape to illustrate our explanation of the spreading gas in the cylindrical geometry.

We assume that $n(\vec{x})$ has the following form:

$$n(\vec{x}) = g(\vec{x})(T_c - T)^a \tag{6}$$

as $T \to T_c$, i.e., it has the same local behavior with respect to temperature as the critical temperature is approached. The integral rate of change of mass M of the gas bubble is defined as

$$dM/dt = \int n(\vec{x}) d\vec{x} \sim (T_c - T)^a, \tag{7}$$

where the integration is performed over the total gas-liquid interface area. On the other hand,

$$dM/dt = d/dt(V\phi\rho_G), \tag{8}$$

where V is the cell volume, and $\phi = 0.5$ is assumed. Near the critical point, the coexistence curve has the form $\rho_G = \rho_c - \Delta\rho/2$, where $\Delta\rho \sim (T_c - T)^\beta$ with the universal exponent $\beta = 0.325$, so that $dM/dt \sim (T_c - T)^{\beta-1} dT/dt$ as $T \to T_c$ according to Eq. (8). Thus Eq. (7) results in $a = \beta - 1$ and the curvature change due to the vapor recoil scales as

$$P_r/\sigma \sim (T_c - T)^{3\beta - 2 - 2\nu}, \tag{9}$$

where Eq. (3) and the scaling relationship $\sigma \sim (T_c - T)^{2\nu}$ ($\nu = 0.63$) were employed. Because this critical exponent ($3\beta - 2 - 2\nu \approx -2.3$) is very large, it should manifest itself even far from the critical point in agreement with the experiments. In summary, as $T \to T_c$, the vapor mass growth follows the growth of its density (the vapor volume remains constant), so that the diverging vapor production near the critical point drives a diverging recoil force.

This curvature change has a striking effect on the bubble shape because it is not homogeneously distributed along the bubble interface. Since the evaporation is strongest near the

copper heating wall where the strongest temperature gradients form, both P_r and c increase strongly near this wall, i.e., near the triple contact line. Note that c is proportional to the second derivative of the bubble shape function, i.e., to the first derivative of the bubble slope. If c is large, then the slope of the bubble contour changes sharply when moving along the bubble contour toward the contact line; see [5,23,24] for more details. Because the interface slope changes so abruptly near the contact line, the apparent contact angle should be much larger than its actual value.

Because c is proportional to the second derivative of the bubble shape function, Eq. (5) is a differential equation with the boundary condition given by the actual contact angle [23]. This actual contact angle defines the first derivative (the slope) of the bubble shape function at the solid wall. It is also specified by the interfacial tension balance and must be zero near the critical point. This condition of the zero contact angle gives a boundary condition for Eq. (5). In order to illustrate a possible solution of Eq. (5), we solved it using the same expression for $P_r(l)$ as in [23]:

$$P_r(l) \propto -N \ln(l/L) \exp\{-[l/(0.1\,L)]^2\}, \tag{10}$$

where $l \in [0,L]$, L being the length of the bubble half contour with $l=0$ at the solid wall. We use a nondimensional parameter N to measure the influence of the vapor recoil force relative to the surface tension. It is defined as

$$N = \frac{1}{\sigma}\int_0^L P_r(l)\,dl, \tag{11}$$

where the integration is performed over the drop contour in the image plane. The numerical coefficient (see [23]) in Eq. (10) can be determined from Eq. (11), where the upper integration limit can be replaced by infinity without any loss of accuracy. Although the expression Eq. (10) for the vapor recoil pressure is not rigorous, it contains the main physical features of the solution of the heat conduction problem: a weak divergence at the contact line and a rapid decay away from it. It is shown in [25] that the rigorous numerical solutions obtained far from the critical point follow this behavior.

The result of this calculation is shown in Fig. 12. Since Eq. (9) implies

$$N \sim (T_c - T)^{-2.3} \rightarrow \infty \tag{12}$$

as $T \rightarrow T_c$, the N increase mimics the approach to the critical point and qualitatively explains the observed shape of the vapor bubble (see Fig. 6). The increase of the apparent contact angle and of the gas-solid contact area A_{cg} can be seen in Fig. 12. Note that such a calculation is not able to predict wavy interface shapes like those in Fig. 6(g) or Figs. 8(f)–(h), because these images correspond either to $T > T_c$ [images (g) and (h) of both figures] or to the close vicinity of T_c where $\sigma < v_i \eta$ (see the discussion of the validity of the quasistatic approximation earlier in this section).

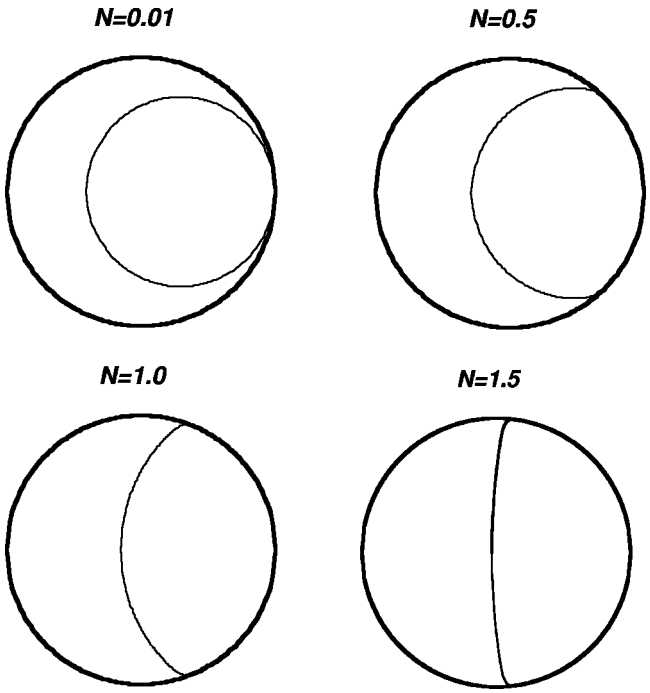

FIG. 12. Calculated bubble shape for different values of the nondimensional strength of vapor recoil N which goes to infinity at the critical point. Note that the actual contact angle is zero for all the curves.

VII. SPREADING GAS AND THE BOILING CRISIS

A very similar bubble spreading was observed far from T_c during boiling at large heat flux [26,27]. When the heating to a surface is increased past a critical heat flux (CHF) there is a sudden transition to ''film'' boiling, where the heater becomes covered with gas and may burn out [14]. This ''boiling crisis'' is an important practical problem in many industries where large heat fluxes are frequently used. We interpret [23,25] the boiling crisis to be similar to the gas spreading shown here. The main difference is that the large value of N is caused by large vapor production that can be achieved during strong overheating rather than by the critical effects.

It is well documented from experiments [14] that the CHF decreases rapidly when the fluid pressure p approaches the critical pressure p_c, i.e., when $T \rightarrow T_c$ in our constant volume system. Previously, this tendency has not been well understood. The divergence of the factor N, discussed above, helps to understand it. We first note that the evaporation rate n scales as the applied heat flux q and $N \sim q^2$, where Eqs. (3) and (11) are used. By assuming that the boiling crisis ($q = q_{CHF}$) begins when N attains its critical value $N_{CHF} \sim 1$ (see [23]), one finds that

$$q_{CHF} \sim (T_c - T)^{1+\nu-3\beta/2} \sim (T_c - T)^{1.1} \tag{13}$$

from Eq. (12). The same exponent is also valid for the pressure scaling,

$$q_{CHF} \sim (p_c - p)^{1.1}. \tag{14}$$

Equation (14) explains the observed tendency $q_{CHF} \rightarrow 0$ as $p \rightarrow p_c$.

Although the strict requirements on temperature stability and the necessity of weightlessness lead to experimental difficulties in studying the boiling crisis in the near-critical region, they also present some important advantages. Only a very small heating rate (heat flux) is needed to reach the boiling crisis because q_{CHF} is very small. At such low heat fluxes, the bubble growth is extremely slow due to the critical slowing down. In our experiments we were able to observe the spreading gas (i.e., the drying out that leads to the boiling crisis, see Fig. 6) during 45 min. Such experiments not only permit an excellent time resolution, but also allow the complicating effects of rapid fluid motion to be avoided.

VIII. CONCLUSIONS

In our experiments we observed a gas bubble spreading over a solid wall and a large value ($>90°$) of the apparent contact angle that appeared despite the zero actual contact angle with the solid. The spreading gas is a phenomenon that can occur in a sealed heated fluid cell only when the bubble is pressed against the heating wall. A 3D numerical calculation of the equilibrium bubble shape showed that the slightly tilted windows of the experimental cell pressed the bubble against the copper sidewall. Weightless conditions are needed in the near-critical region in order to observe this phenomenon when the surface tension is small and a bubble-like shape persists. The same phenomenon can be observed far from the critical point during boiling at high heat fluxes where it is known as the ''boiling crisis.'' While the gas spreads very quickly during the boiling crisis far from the critical point, the near-critical region allows a very slow spreading gas to be observed in great detail.

We explain this phenomenon as induced by the vapor recoil force that changes the shape of the vapor-liquid interface near the triple contact line. Our preliminary calculations of the gas-liquid interface shape are qualitatively consistent with the experimental images. The scaling analysis gives the critical exponent for the critical heat flux decrease near the critical point and explains the increase of the vapor recoil effect near the critical point. We believe that there is much to be learned about the boiling crisis in the near-critical region and hope that these experiments inspire more investigations.

ACKNOWLEDGMENTS

This work was supported by CNES and NASA Grant No. NAG3-1906. A part of this work was made during the stay of V.N. at the UNO and he would like to thank the Department of Physics of the UNO for their hospitality. We thank all of the Alice II team and everyone involved in the Mir missions. We especially thank J. F. Zwilling, and the French cosmonauts Claudie André-Deshays, Léopold Eyharts, and Jean-Pierre Haigneré. We thank Kenneth Brakke for creating the SURFACE EVOLVER software and for making it available for the scientific community.

[1] M. Schick, in *Liquids at Interfaces*, edited by J. Charvolin, J.-F. Joanny, and J. Zinn-Justin (Elsevier, Amsterdam, 1989), p. 415; D. Beysens, *ibid.*, p. 499.

[2] R.F. Kayser, J.W. Schmidt, and M.R. Moldover, Phys. Rev. Lett. **54**, 707 (1985).

[3] Y. Garrabos, C. Chabot, R. Wunenburger, J.-P. Delville, and D. Beysens, J. Chim. Phys. Phys.-Chim. Biol. **96**, 1066 (1999).

[4] J. Hegseth, Y. Garrabos, V.S. Nikolayev, C. Lecoutre-Chabot, R. Wunenburger, and D. Beysens, in Proceedings of the 14th Symposium on Thermophysical Properties, Boulder, CO, 2000 [Int. J. Thermophys. (to be published)], http://symp14.nist.gov/PDF/WET05HEG.PDF.

[5] V.S. Nikolayev, D.A. Beysens, and J. Hegseth, in Proceedings of the 14th Symposium on Thermophysical Properties, Boulder, CO, 2000 (Ref. [4]).

[6] Y. Garrabos, R. Wunenburger, C. Lecoutre, V. Nikolayev, D. Beysens, and J. Hegseth, in *Proceedings of the 1st International Symposium on Microgravity Research and Applications in Physical Sciences and Biotechnology, Sorrento, Italy, 2000*, ESA SP-454 (ESTEC, Noordwijk, 2000), p. 157.

[7] Y. Garrabos, R. Wunenburger, J. Hegseth, C. Lecoutre-Chabot, and D. Beysens, in *Space Technology and Applications International Forum—2000*, edited by M.S. El-Genk (AIP, Melville, NY, 2000), p. 737.

[8] R. Marcout, J.-F. Zwilling, J.M. Laherrere, Y. Garrabos, and D. Beysens, Microgravity Q. **5**, 162 (1995).

[9] C. Morteau, M. Salzman, Y. Garrabos, and D. Beysens, in *Fluids in Space, Proceedings of the 2nd European Symposium on Fluids in Space*, edited by A. Viviani (Jean-Gilder Congressi srl, Rome, 1997), p. 327.

[10] V. Gurfein, D. Beysens, Y. Garrabos, and B. Le Neindre, Opt. Commun. **85**, 147 (1991).

[11] J.P. Delville, M. Salzman, Y. Garrabos, and D. Beysens, in *Fluids in Space, Proceedings of the 2nd European Symposium on Fluids in Space* (Ref. [9]), p. 312.

[12] http://www.geom.umn.edu/software/evolver/

[13] C. Ikier, H. Klein, and D. Woermann, J. Colloid Interface Sci. **178**, 368 (1996).

[14] L.S. Tong, *Boiling Heat Transfer and Two-Phase Flow*, 2nd ed. (Taylor and Francis, New York, 1997).

[15] J. Straub, L. Eicher, and A. Haupt, Phys. Rev. E **51**, 5556 (1995).

[16] J.R.A. Pearson, J. Fluid Mech. **4**, 489 (1958).

[17] J.J. Hegseth, N. Rashidnia, and A. Chai, Phys. Rev. E **54**, 1640 (1996).

[18] S.H. Davis, Annu. Rev. Fluid Mech. **19**, 403 (1987).

[19] H.J. Palmer, J. Fluid Mech. **75**, 487 (1976).

[20] H.K. Cammenga, D. Schreiber, G.T. Barnes, and D.S. Hunter, J. Colloid Interface Sci. **98**, 585 (1984).

[21] Y. Garrabos, M. Bonetti, D. Beysens, F. Perrot, T. Fröhlich, P. Carlés, and B. Zappoli, Phys. Rev. E **57**, 5665 (1998), and references therein.

[22] R. Wunenburger, Y. Garrabos, C. Lecoutre-Chabot, D. Beys-

ens, and J. Hegseth, Phys. Rev. Lett. **84**, 4100 (2000).
[23] V.S. Nikolayev and D.A. Beysens, Europhys. Lett. **47**, 345 (1999).
[24] V.S. Nikolayev, D.A. Beysens, Y. Garrabos, and J. Hegseth, in Proceedings of the 4th International Conference on Multiphase Flow, New Orleans, 2001 [Int. J. Multiphase Flow (to be published)].
[25] V.S. Nikolayev, D.A. Beysens, G.-L. Lagier, and J. Hegseth, Int. J. Heat Mass Transf. **44**, 3499 (2001).
[26] H.J. van Ouwerkerk, Int. J. Heat Mass Transf. **15**, 25 (1972).
[27] K. Torikai, K. Suzuki, and M. Yamaguchi, JSME Int. J., Ser. II **34**, 195 (1991).

EUROPHYSICS LETTERS 15 July 2002

Europhys. Lett., **59** (2), pp. 245–251 (2002)

Liquid-vapor phase separation in a thermocapillary force field

D. Beysens[1](*), Y. Garrabos[2], V. S. Nikolayev[1], C. Lecoutre-Chabot[2], J.-P. Delville[3] and J. Hegseth[4]

[1] *ESEME, Service des Basses Températures, DSM/DRFMC, CEA-Grenoble Grenoble, France*(**)

[2] *CNRS-ESEME, Institut de Chimie de la Matière Condensée de Bordeaux 87, Avenue du Dr. Schweitzer, 33608 Pessac Cedex, France*

[3] *Centre de Physique Moléculaire, Optique et Hertzienne, CNRS Université de Bordeaux I - Cours de la Libération, 33405 Talence Cedex, France*

[4] *Department of Physics, University of New Orleans - New Orleans, LA 70148, USA*

(received 15 January 2002; accepted in final form 17 April 2002)

PACS. 68.35.Rh – Phase transitions and critical phenomena.
PACS. 44.35.+c – Heat flow in multiphase systems.
PACS. 68.03.Cd – Surface tension and related phenomena.

Abstract. – We study the growth of gas bubbles surrounded by liquid during the phase separation of a pure CO_2 sample quenched from one-phase to two-phase region of the phase diagram by rapid cooling in microgravity. The vicinity of the critical point ensures slowing-down of the growth process. The bubble growth by coalescence is modified by local laser heating. It induces a thermocapillary (Marangoni) effect that attracts the bubbles towards the center of the beam. At the beginning of the phase separation, a bubble is trapped there and "captures" the surrounding bubbles. The growth exponent for the central bubble radius is close to 0.5, while that for the other bubbles is 1/3. We present a theoretical model that explains the experimental data and justifies that the temperature can vary along the gas-liquid interface in a pure fluid during its phase separation.

Introduction. – On earth, phase separation processes in liquids are strongly affected by gravity. The density difference between the evolving phases leads to sedimentation and formation of layered structure. Under microgravity, Marangoni convection resulting from induced temperature gradients at the surface of the emerging drops can become predominant. These temperature gradients result in interfacial tension gradients that are known to cause linear motion of droplets (thermocapillary migration) [1]. The resulting flow generally increases the rate of collisions between the drops and thus the rate of coalescences. Such a phenomenon has already been observed in microgravity during sounding rocket flights [2]. However, due to

(*) E-mail: dbeysens@cea.fr
(**) Mailing address: CEA-ESEME, Institut de Chimie de la Matière Condensée de Bordeaux - 87 Avenue du Dr. Schweitzer, 33608 Pessac Cedex, France.

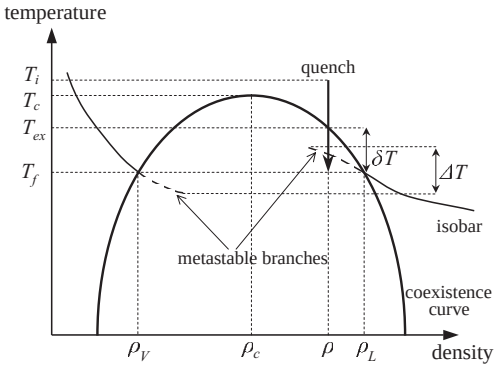

Fig. 1

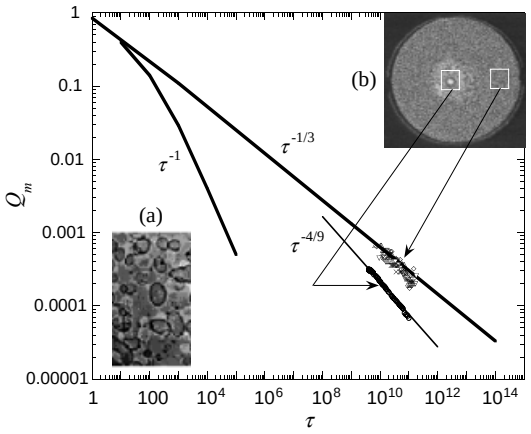

Fig. 2

Fig. 1 – Schematic phase diagram for simple fluids in the temperature-density coordinates. The isobar that corresponds to the final fluid state T_f is shown with its metastable branches.

Fig. 2 – Growth laws of phase-separating fluid close to the critical point in the reduced coordinates (inverse length Q_m, time τ). The experimental points illustrate the growth of the central single bubble for $\delta T = 85,\ 90,\ 100$ mK with the exponent close to -0.5 while the $Q_m(\tau) \sim \tau^{-1/3}$ behavior is recovered far from the illuminated area. The fit using the theoretical $-4/9 \approx -0.44$ exponent is also shown.

the short duration of the experiments, the expected thermocapillary-driven coarsening regime lasts roughly 15 s, which is not long enough. By performing experiments on board the Mir space station, we are able to observe the droplet coarsening during 13 hours which corresponds to almost two decades in reduced time. To avoid coupling with the temperature changes associated with the quenching procedure, Marangoni flows are here created in the sample with a He-Ne laser passing through the small central part of the sample.

A phase separation experiment consists of quenching a pure fluid (here CO_2) from the initial single-phase state (ρ, T_i) to another state (ρ, T_f) where homogeneous stability is lost and phase separation occurs (ρ is the mean density of the fluid sample cell, T_i is the initial temperature, and T_f is the final temperature). As illustrated in fig. 1, the evolution of the system is defined by the relationship between the critical temperature T_c, the coexistence temperature T_cx, and the quench depth $\delta T = T_\mathrm{cx} - T_\mathrm{f}$. Depending on the final (equilibrium) volume fraction ϕ of the minority phase, the phase transition may proceed either by the growth of isolated droplets when $\phi < 30\%$ (insert (b) in fig. 2) or by growth of interconnected domains when $\phi > 30\%$ (insert (a) in fig. 2).

The characteristic size of the evolving pattern L_m as a function of time t can be characterized [3] in terms of the reduced coordinates $Q_m = 2\pi\xi^-/L_m$ and $\tau = t/t_\xi$, where ξ^- and $t_\xi = 6\pi\eta_\mathrm{o}(\xi^-)^3/k_\mathrm{B}T_\mathrm{f}$ are, respectively, the correlation length of the density fluctuations inside the coexistence curve and the associated relaxation time scale, η_o being the fluid viscosity. In off-critical systems (isolated domains, fig. 2), a behavior $Q_m(\tau) = 0.95\,\tau^{-1/3}$ has been measured over more than seven decades in time [3] independently of the quench depth.

Experimental. – The CO_2 fluid (supplied by Air Liquide, with purity better than 99.998%) is enclosed between two transparent sapphire windows and a copper alloy cylindrical cell (11.6 mm internal diameter, thickness $L = 1.49$ mm). The cell is set in a high-precision

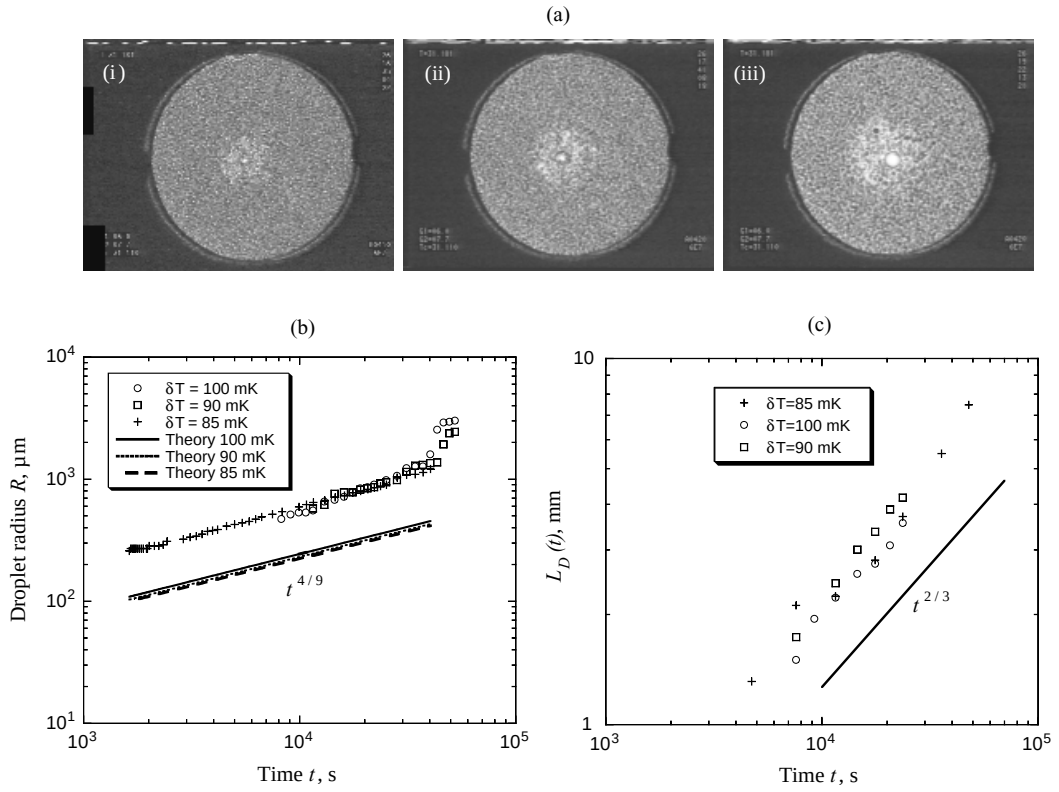

Fig. 3 – Growth of a single CO_2 gas bubble trapped by the beam for the quench depth $\delta T = 90$ mK. (a) Time evolution of the pattern: (i) $t = 7207$ s, (ii) $t = 11580$ s, and (iii) $t = 17640$ s. Note also the growth of the depletion zone centered around the growing bubble. (b) Experimental growth laws of the gas bubble trapped by the laser beam and (c) of the depletion zone for $\delta T = 85$, 90, and 100 mK. The growth curves calculated using (17) are also plotted in (b). The theoretically predicted slope 2/3 is shown in (c) for comparison.

thermostat (± 50 μK accuracy) which is located inside the ALICE instrument [4] onboard the Mir station. The experimental cell is filled at the density $\rho = 1.094\,\rho_c$, where ρ_c is the critical density. Initially, the fluid temperature is above the critical temperature, and the fluid is homogeneous. The sample is then thermally quenched below the coexistence curve, the total quench duration being about 10 s. The cell is illuminated by white light parallel to the cylindrical cell walls. A CCD video camera captures images of the entire volume, the depth of field being larger than the sample thickness. A He-Ne laser beam (power $P = 1$ mW, wavelength 632.8 nm in vacuum, beam diameter $2\omega = 300$ μm) propagates along the axis of the cell. Sapphire and CO_2 are transparent at this wavelength. However, a weak part $\gamma \approx 2 \cdot 10^{-6}$ [5] of the beam power is absorbed per window. As a consequence, the light beam induces a weak temperature gradient in the fluid.

Our phase separation experiments were carried out for the quench depths $\delta T = 85$, 90, and 100 mK. As illustrated in fig. 3a, a single drop emerges and grows rapidly in the beam center, while small bubbles grow everywhere in the sample. Growth continues when the central bubble becomes larger than the beam-illuminated area. The growth of the central bubble clearly generates in its vicinity a strong density depletion of small bubbles. In addition, this

central bubble grows faster than the small bubbles. From the three experiments shown in fig. 3b, we deduce that the evolution of the radius R of the single beam-trapped bubble is given by the power law $R(\tau) \sim t^x$, where $x = 0.47 \pm 0.01$ for $\delta T = 85$ mK, $x = 0.56 \pm 0.11$ for $\delta T = 90$ mK, and $x = 0.67 \pm 0.04$ for $\delta T = 100$ mK. When calculating these exponents, we do not consider the very late times data when the bubble diameter reaches the cell thickness and the bubble begins a lateral motion out of the beam center. This motion is due to a driving force that appears when the bubble is squeezed between the cell windows that are not strictly parallel. In microgravity, even a very small angle is sufficient to move a squeezed bubble, see the discussion in [6]. There is a crossover to a much faster growth when the opposite windows of the cell become joined by this gas "bridge", see fig. 3b. We will discuss this point later on.

The $Q_m(\tau)$ curve which corresponds to the central bubble growth (with $2R$ used for L_m) lies in between the two master curves in fig. 2. The average value for the exponent $x \sim -0.5$ does not coincide with the exponent observed [2] in a phase-separating binary mixture located in a thermal gradient induced by a Peltier element ($Q_m(\tau) \sim \tau^{-2}$ during 15 s). The comparison between both experiments is difficult as the heat flow configuration is different. We however stress that our experiment lasts almost two decades in the scaled time, which makes the determination of a power law exponent quite reliable.

For the same three experiments, we have also analyzed the growth of the diameter L_D of the depletion zone (fig. 3c). Results are, respectively, $L_\mathrm{D}(t) \sim t^{0.72\pm0.18}$, $L_\mathrm{D}(t) \sim t^{0.76\pm0.06}$, and $L_\mathrm{D}(t) \sim t^{0.68\pm0.10}$.

Theoretical model. – The observed beam trapping as well as the enhancement of the coarsening process can be explained by a Marangoni effect caused by a temperature variation at the bubble interface. A question arises whether such a variation can exist in a true single-component system. There is strong evidence [6] that when the liquid-gas interface is initially at saturation conditions, the interface is isothermal unless a contamination is present in the fluid [7]. However, in the present work, the system is already out of equilibrium at the initial moment of time (*i.e.* during the quench). A strong density variation forms at the beginning of the evolution. We consider the "late" stages during which the bubble interfaces are already well formed and the density variation in the bulk of the phases is smaller, but still exists. Since the pressure of the system is equilibrated quickly after the quench due to the piston effect [8], the system evolves along the metastable branches of the isobar shown in fig. 1 during most of the evolution time. The liquid phase is overheated and the gas is overcooled. Therefore, the interface temperature is not necessarily equal to the saturation temperature (*i.e.* T_f) that corresponds to the system pressure. It can thus vary along the bubble interface. One can estimate the upper limit for this variation as a difference ΔT between the maximum overheating and minimum undercooling temperatures, see fig. 1. Despite the presence of this (small) spatial density variation, the associated Lifshitz-Slyozov mechanism of bubble growth is not relevant. The kinetics turns out to be dominated by the droplet diffusion and coalescence (Binder-Stauffer mechanism), see [3].

For a small temperature inhomogeneity, the velocity $\vec{v}$ of thermocapillary migration of a bubble suspended in a fluid phase is proportional [9] to the externally imposed temperature gradient $\vec{\nabla} T$:

$$\vec{v} = -\frac{2}{2\eta_\mathrm{o} + 3\eta_\mathrm{i}} \frac{\mathrm{d}\sigma}{\mathrm{d}T} \frac{a}{2 + \lambda_\mathrm{i}/\lambda_\mathrm{o}} \vec{\nabla} T, \tag{1}$$

where η_o and λ_o (respectively, η_i and λ_i) are the viscosity and the thermal conductivity outside (respectively, inside) the bubble of radius a. Here the surface tension σ decreases with temperature so that $\mathrm{d}\sigma/\mathrm{d}T < 0$. According to (1), the bubble should migrate along the temperature gradient. Since in our case heating is localized inside the laser beam, the

bubbles should migrate towards its center, coalescing between each other. The formation of the centered single bubble provides a qualitative demonstration of the above theory.

In order to develop a quantitative approach, we need to determine the gradient $\vec{\nabla}T$ induced by the beam with the Gaussian radial intensity distribution

$$I(r) = \frac{2P}{\pi\omega^2} e^{-2r^2/\omega^2} \tag{2}$$

at the entrance of the cell. Here P is the beam power and r is the coordinate measured radially from the beam center.

The beam path in the cell consists of i) a thin absorbing layer on the sapphire-fluid boundary that absorbs the power γP, ii) a non-absorbing layer of CO_2, and iii) an absorbing layer equivalent to ii). There is only one trapped bubble on the entrance window because, during the quench, the bubbles that are forming in the bulk fluid scatter so much light that the laser beam is strongly attenuated before reaching the second window.

Due to the small thickness/radius ratio of the experimental cell, we will assume that the temperature distribution is of cylindrical symmetry with the axis along the beam as in [10]. In other words, we make the simplifying assumption that the power is dissipated homogeneously along the part of the beam that crosses the fluid, so that the heat power j generated per unit volume of the fluid is $j(r) = 2\gamma I(r)/L$.

For a long observation time we can also reasonably assume that the Piston effect is negligible and the temperature distribution is given by the stationary heat conduction equation

$$\lambda_{\mathrm{o}} \nabla^2 T + j = 0. \tag{3}$$

Note that this bubble trapping can be influenced by a dipolar ("optical trapping") effect [11] that appears because the refractive index of a gas bubble is smaller than that of the liquid phase. Then the dipolar forces act against the thermocapillary trapping by expulsing bubbles from the illuminated region. This effect is, however, negligibly small for the beam parameters used here. In addition, it is proportional to $|\mathrm{d}I/\mathrm{d}r|$ and thus follows the exponential decline of the beam intensity (2) at large r.

The solution of (3) results in the radial temperature gradient

$$|\vec{\nabla}T| = \frac{\partial T}{\partial r} = -\frac{\gamma P}{\pi r L \lambda_{\mathrm{o}}} \left(1 - e^{-2r^2/\omega^2}\right). \tag{4}$$

The velocity $\vec{v}$ as given by (1) behaves as

$$v = a\beta/r \tag{5}$$

outside the illuminated area and is directed towards the center of the beam (*i.e.* opposite to the r axis). The constant β is defined by

$$\beta = \frac{1}{2\eta_{\mathrm{o}} + 3\eta_{\mathrm{i}}} \left|\frac{\mathrm{d}\sigma}{\mathrm{d}T}\right| \frac{1}{2\lambda_{\mathrm{o}} + \lambda_{\mathrm{i}}} \frac{2\gamma P}{\pi L}. \tag{6}$$

For the temperature $T_{\mathrm{f}} = T_{\mathrm{c}} - 139.6$ mK that corresponds to the $\delta T = 90$ mK quench, $\beta = 0.173$ μm/s.

One can now obtain the growth law for the central bubble based on the expression (5). Let us denote by $c = c(r)$ the number of (small) gas bubbles in the unit volume. The total flux $\vec{f} = \vec{f}(r)$ of the bubbles (*i.e.* the average number of the bubbles that cross the unit area per unit time),

$$\vec{f}(r) = -D\vec{\nabla}c + c\vec{v}, \tag{7}$$

has two contributions. The first term corresponds to the diffusion of the bubbles with the diffusion constant D, while the second is responsible for the drift with the average velocity $\vec{v}$ in the external force field. In our case, the latter corresponds to the thermocapillary migration of the bubbles. Under the assumption of a nearly stationary distribution for $c(r)$, $\vec{f}(r)$ satisfies the equation

$$\mathrm{div}\vec{f} = 0. \tag{8}$$

Since the thickness L of the cell is much smaller than its diameter, the motion of the bubbles towards the beam center is almost 2D. Indeed, fig. 3c shows that the scale L_D of the $c(r)$ variation can be 3 times larger than L. Therefore, eqs. (7)-(8) should be solved in 2D, *i.e.* for a function $c(r)$ with a cylindrical symmetry. However, the central bubble is spherical because of the surface tension and cannot be assumed cylindrical. To solve this contradiction, we introduce a cylindrical bubble of radius R_2D which has the same volume V_R as the actual central bubble with the radius R,

$$V_R = \frac{4\pi}{3}R^3 = \pi R_\mathrm{2D}^2\, L. \tag{9}$$

In the cylindrical coordinates, (8) reduces to the 2nd-order ordinary differential equation

$$\frac{\mathrm{d}}{\mathrm{d}r}\left[r\left(-D\frac{\mathrm{d}c}{\mathrm{d}r} - \frac{ca\beta}{r}\right)\right] = 0. \tag{10}$$

Assuming that a is independent of r (*i.e.* that the rate of collisions is not influenced by the weak gradient of bubble concentration c), eq. (10) can be solved with two boundary conditions $c(R_\mathrm{2D}) = 0$ (which corresponds to the disappearance of the small bubbles when they touch the central bubble) and $c(\infty) = c_\infty$, the constant bubble concentration at infinity. The solution of (10) reads

$$c(r) = c_\infty[1 - (r/R_\mathrm{2D})^{-a\beta/D}] \tag{11}$$

and shows a depletion zone, that can be defined as the zone of $0 < r \leq L_\mathrm{D}/2$, where $c(r) \leq 0.9\, c_\infty$. According to (11), this condition results in

$$L_\mathrm{D} \sim R_\mathrm{2D} \sim t^{2/3}, \tag{12}$$

which fits the experimental data, see fig. 3c.

The central hemispherical bubble grows at the expense of the small bubbles that are absorbed by coalescence, so that

$$\mathrm{d}V_R/\mathrm{d}t = 2\pi R_\mathrm{2D} L f(R_\mathrm{2D}) V_a, \tag{13}$$

where $f(R_\mathrm{2D}) = c_\infty \beta a/R_\mathrm{2D}$ and V_a is the volume of a small bubble. The product $c_\infty V_a$ is the constant vapor volume fraction $\phi = (\rho_L - \rho)/(\rho_L - \rho_V)$, ρ_L and ρ_V being defined in fig. 1. Equation (13) then reduces to

$$R_\mathrm{2D}\, \mathrm{d}R_\mathrm{2D}/\mathrm{d}t = \beta\phi a. \tag{14}$$

The growth law for the small bubbles is

$$a = a_0\, t^{1/3} \tag{15}$$

with a_0 that follows from the equation $Q_m(\tau) = 0.95\tau^{-1/3}$ and the relationship [12] $\phi = 0.69\,(L_m/2a)^{-3}$,

$$a_0 = 1.91\,\phi\left(\frac{k_\mathrm{B}T_\mathrm{c}}{\eta_\mathrm{o}}\right)^{1/3}. \tag{16}$$

For the $\delta T = 90$ mK quench, $a_0 = 1.38 \cdot 10^{-6}$ ms$^{-1/3}$. Equations (9), (14), (15) result in the growth laws

$$R_{2D} = \sqrt{3\beta\phi a_0/2}\, t^{2/3}, \quad R = (9L\beta\phi a_0/8)^{1/3}\, t^{4/9}. \tag{17}$$

The $R(t)$ curve can now be plotted in fig. 3b. The theoretical curve fits the experimental data within a constant factor ≈ 2. In addition, its experimentally observed week dependence on δT is reproduced well by the model. Such a good agreement obtained in spite of several assumptions confirms the Marangoni origin of the fast growth of the cental bubble.

The crossover to the faster kinetics visible in fig. 3b can now be understood. It is observed when the central bubble joins the opposite cell windows. One can assume that this crossover has a geometrical origin. Indeed, if the bubble became exactly cylindrical, its growth exponent would be that of R_{2D}, *i.e.* the growth would accelerate. However, the actual growth law after crossover is difficult to obtain since the actual shape of this bubble squeezed between the windows is complicated, see [6].

Concluding remark. – This work shows that even a weak temperature gradient can strongly modify the kinetics of phase transitions and affect material processing. In addition, this work presents a clear evidence of the temperature gradient along the gas-liquid interface in a truly one-component fluid systems. While the Marangoni convection caused by such gradients is commonly observed in the presence of a second fluid, clear evidence of such an effect in a pure fluid is unknown to us.

REFERENCES

[1] Young N. O., Goldstein J. S. and Block M. J., *J. Fluid Mech.*, **6** (1959) 350.
[2] Braun B., Ikier C., Klein H. and Woermann D., *J. Colloid Interface Sci.*, **159** (1993) 515; Braun B., Ikier C., Klein H. and Woermann D., *Chem. Phys. Lett.*, **233** (1995) 565; Ikier C., Klein H. and Woermann D., *J. Colloid Interface Sci.*, **184** (1996) 693.
[3] Perrot F., Guenoun P., Baumberger T., Beysens D., Garrabos Y. and Le Neindre B., *Phys. Rev. Lett.*, **73** (1994) 688.
[4] Laherrère J.-M. and Koutsikides P., *Acta Astron.*, **29** (1993) 861.
[5] Highlights of the Zeno results from the USMP-2 Mission, Zeno homepage at `http://roissy.umd.edu/report/report.html`.
[6] Garrabos Y., Lecoutre-Chabot C., Hegseth J., Nikolayev V. S. and Beysens D., *Phys. Rev. E*, **64** (2001) 051602.
[7] Marek R. and Straub J., *Int. Heat J. Mass Transfer*, **44** (2001) 619.
[8] Garrabos Y., Bonetti M., Beysens D., Perrot F. and Fröhlich T., *Phys. Rev. E*, **57** (1998) 5665.
[9] Barton K. D. and Subramanian R. S., *J. Colloid Interface Sci.*, **133** (1989) 211.
[10] Marcano A. O. and Aranguren L., *Appl. Phys. B*, **56** (1993) 343.
[11] Delville J.-P., Lalaude C., Buil S. and Ducasse A., *Phys. Rev. E*, **59** (1999) 5804.
[12] Nikolayev V. S., Beysens D. and Guenoun P., *Phys. Rev. Lett.*, **76** (1996) 3144.

2D BEM modeling of a singular thermal diffusion free boundary problem with phase change

V. S. Nikolayev & D. A. Beysens
ESEME, Service des Basses Températures, DSM/DRFMC, CEA-Grenoble, France[*]

Abstract

We report a 2D BEM modeling of the thermal diffusion-controlled growth of a vapor bubble attached to a heating surface during saturated pool boiling. The transient heat conduction problem is solved in a liquid that surrounds a bubble with a free boundary and in a semi-infinite solid heater. The heat generated homogeneously in the heater causes evaporation, i. e. the bubble growth. A singularity exists at the point of the triple (liquid-vapor-solid) contact. At high system pressure the bubble is assumed to grow slowly, its shape being defined by the surface tension and the vapor recoil force, a force coming from the liquid evaporating into the bubble. It is shown that at some typical time the dry spot under the bubble begins to grow rapidly under the action of the vapor recoil. Such a bubble can eventually spread into a vapor film that can separate the liquid from the heater, thus triggering the boiling crisis (Critical Heat Flux phenomenon).

1 Introduction

Boiling is widely used to transfer heat from a solid heater to a liquid. The bubble growth in boiling attracted much of attention from many scientists and engineers. In spite of these efforts, some important aspects of growth of a vapor bubble attached to a solid heater remain misunderstood even on a phenomenological level. The most important aspect is the boiling crisis, a transition from nucleate boiling (where vapor bubbles nucleate on the heater) to film boiling (where the heater is

[*]Mailing address: CEA-ESEME, Institut de Chimie de la Matière Condensée de Bordeaux, 87, Avenue du Dr. Schweitzer, 33608 Pessac Cedex, France

covered by a continuous vapor film). The boiling crisis is observed when the heat flux q_S from the solid heater exceeds a threshold value which is called the "Critical Heat Flux" (CHF). The rapid formation of the vapor film on the heater surface decreases steeply the heat transfer efficiency and leads to a local heater overheating. In the industrial heat exchangers, the boiling crisis can lead to melting of the heater thus provoking a dangerous accident. Therefore, the knowledge of the CHF is extremely important. However, the CHF depends on many parameters. At this time, there are several semi-empirical correlations that predict the CHF more or less reliably for several particular regimes of boiling and heater configurations, see [1] for a recent review. However, a clear understanding of the triggering mechanism of the boiling crisis is still lacking.

The knowledge about what happens at the foot of the bubble which grows attached to the heater is crucial for the correct modeling of the boiling crisis. Unfortunately, the experimental observations at large heat fluxes close to the CHF are complicated by the violence of boiling and optical distortions caused by the strong temperature gradients. We proposed recently [2] to carry out boiling experiments in the proximity of the critical point where the CHF is very small and the bubble evolution is very slow. However, microgravity conditions are necessary in this case to obtain a convex bubble shape in order to observe a behavior similar to the terrestrial boiling.

The bubble foot contains the contact line of the bubble with the heater. This triple solid-liquid-gas contact line is a line of singularity points both for the hydrodynamic (see [3] and refs. therein) and for the heat conduction problems. In the present article we consider only the heat conduction part by assuming the slow growth and the quasi-static bubble shape which is common for the high pressure boiling. The results of such a calculation have already been described in [5]. The present article deals with the problem framework and some calculation details related to BEM.

2 Boundary conditions for the contact line problem

The choice of the boundary conditions adopted in the contact line is very important. Since the contact line is triple, boundary conditions should be specified at three surfaces that intersect there (Fig. 1). For the gas-liquid interface, we adopt the constant-temperature boundary condition with the temperature that corresponds to the saturation temperature T_{sat} for the given (constant) system pressure. The gas phase is assumed to be non-conductive, the heat flux through the solid-gas interface being zero. The boundary condition on the solid-liquid interface remains to be defined. It is the subject of the rest of this section.

There are three kinds of boundary conditions. Let us consider them on an example of the 2D wedge geometry as illustrated in Fig. 1 for which some important solutions can be obtained in analytical form.

Since the heater is a far better heat conductor than the liquid, the constant temperature boundary condition ($T = T_S$ =const along the solid-liquid interface) seems natural. In order to maintain boiling, $T_S > T_{sat}$ should be satisfied. The

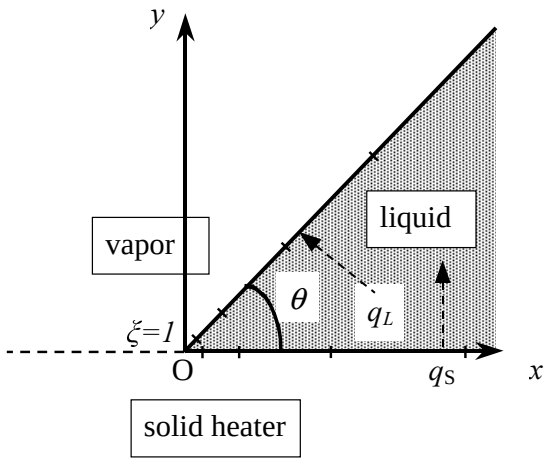

Figure 1: Geometry for the calculation of the heat conduction in the wedge geometry. The BEM discretization of the wedge is also illustrated.

resulting problem is ill posed because the temperature is discontinuous along the boundary of the liquid domain at the contact point O in Fig. 1. This discontinuity leads to a singular behavior of the heat flux q_L through the gas-liquid boundary, $q_L(y) \propto y^{-1}$ [4] and is not integrable. Note that the integral $\int q_L \mathrm{d}y$ is very important because it defines the amount of liquid evaporated into the bubble and thus the bubble growth rate, see Eq. (11) below. Since the result is infinite, the first kind boundary condition cannot be used.

Another choice is the constant heat flux q_S along the solid-liquid interface, which can be reasonable for a thin heater. The resulting transient problem can be solved analytically in the liquid domain by the reflections method [4]. Its solution can be obtained in the closed form for several contact angles θ, see Fig. 1. The solutions obtained in [5] for $\theta = \pi/4$ and $\theta = \pi/8$ result in a constant value for $q_l(y \to 0)$. Although the solution for $\theta = \pi/2$ diverges $q_L(y) \propto \log(-y)$ [6], it is integrable. In spite of these advantages, the constant heat flux boundary condition is not suitable for the bubble growth problem because it cannot be used in the dry spot (i. e. solid-gas contact) area where the heat flux should be zero. However, these analytical solutions can be used to test the BEM solver code (see Fig. 2).

A remaining option is the boundary conditions of a third kind, i.e. the coupling of the temperatures and the fluxes at the solid surface. The heat conduction problem is required to be solved in the solid domain in addition to the liquid domain. Unfortunately, we cannot solve the problem analytically in this case. Qualitatively, one can expect an integrable divergence of $q_L(y)$ which should appear because of the influence of the solid-gas contact area adjacent to the contact line. Since the heat flux that comes from the bulk of the solid heater is not able to pass through this area, it should be necessarily deviated towards the neighboring solid-liquid contact area thus increasing q_S at small x. Since $q_S \approx q_L$ near the contact line,

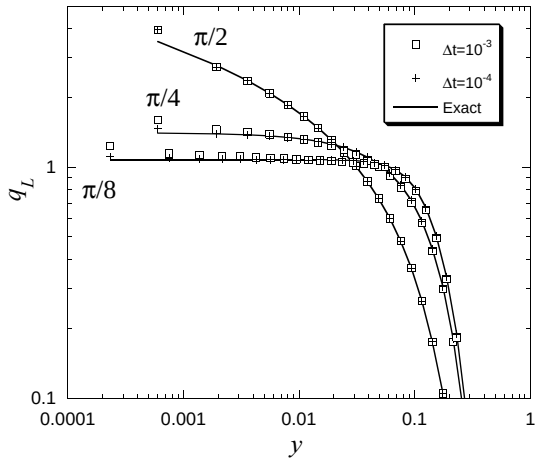

Figure 2: The $q_L(y)$ curves calculated for the $\pi/2$, $\pi/4$ and $\pi/8$ wedges for the values of the parameters $q_0 = 1$, $\alpha_L = 1$, $t = 0.01$ and $d_{min} = 0.001$ and two values of the time step Δt. The results of the numerical solution by BEM (data points) should be compared with the exact analytical solutions (lines).

$q_L(y)$ should vary steeper near the contact line than in the constant q_S case and is likely to diverge.

One can argue that the necessity of the calculation of the temperature field in the heater is a heavy complication that justifies the approximation of the simultaneous application of the boundary conditions of constant heat flux outside the dry spot and zero heat flux inside. However, the above considerations show that the behavior of $q_L(y)$ can deviate from its real behavior even qualitatively. Since such a large error cannot be admitted in the calculation of q_L that strongly influences the bubble dynamics, we need to calculate rigorously the conjugate heat conduction problem.

3 Mathematical problem statement

The 2D heat conduction problem in the domain $\Omega_L \cup \Omega_S$ (see Fig. 3) reads

$$\frac{\partial T_L}{\partial t} = \alpha_L \nabla^2 T_L, \quad \vec{r} \in \Omega_L \tag{1}$$

$$\frac{\partial T_S}{\partial t} = \alpha_S \nabla^2 T_S + \frac{\alpha_S}{k_S} j(t), \quad \vec{r} \in \Omega_S \tag{2}$$

where α and k is the thermal diffusivity and conductivity respectively, the indices L and S identify the liquid and the solid heater, and $\vec{r} = (x, y)$ denotes a point. The heat is assumed to be generated homogeneously in the heater with the power $j(t)$ per unit volume. We choose $j(t) = C/\sqrt{t}$, where C is constant. This condition

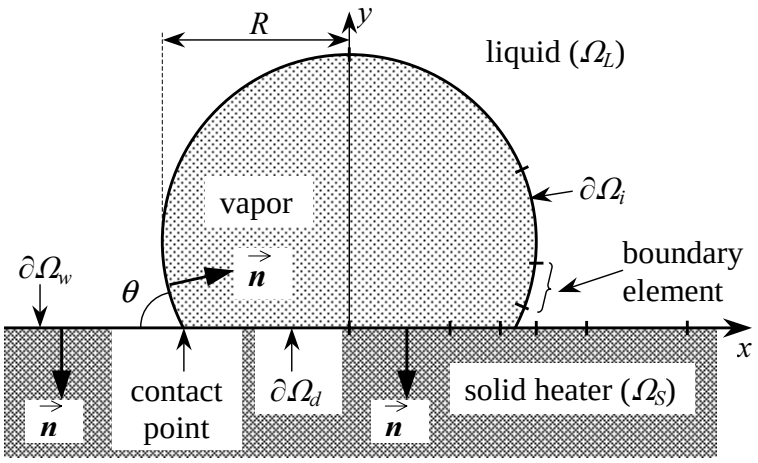

Figure 3: Vapor bubble on the heater (domain Ω_S) surrounded by the liquid (domain Ω_L). The chosen direction of the unit normal vector $\vec{n}$ is shown for each of the subcontours $\partial\Omega_w$, $\partial\Omega_d$ and $\partial\Omega_i$. The discretization is illustrated for the right half of the subcontours. (From [5] with permission from Elsevier Science)

results in a constant in time value of q_S far from the bubble, see (14) below. Initially $(t = 0)$ the temperature is homogeneous $T_L = T_S = T_{sat}$. The vapor bubble is assumed to be already nucleated. Since we assume the zero contact angle $\theta = 0$, the bubble shape is spherical with the radius R_0. The boundary conditions are formulated on the moving gas-liquid interface $\partial\Omega_i$ $(T_L|_{\partial\Omega_i} = T_{sat})$, on the solid-liquid interface $\partial\Omega_d$ $(\partial T_L/\partial y|_{\partial\Omega_d} = 0)$ and on the solid-liquid interface $\partial\Omega_w$:

$$\begin{aligned} q_S &= -k_S \left.\frac{\partial T_S}{\partial y}\right|_{\partial\Omega_w} = -k_L \left.\frac{\partial T_L}{\partial y}\right|_{y=0}, \\ T_S|_{\partial\Omega_w} &= T_L|_{y=0}. \end{aligned} \tag{3}$$

Because of the axial symmetry, this problem needs to be solved only for $x > 0$.

The shape of the gas bubble is calculated from the quasi-static equation [6]

$$K(\vec{r}_i)\sigma = \lambda + P_r(\vec{r}_i), \tag{4}$$

where K is the curvature of the bubble at the point on the surface $\vec{r}_i = (x_i, y_i)$, σ is the vapor-liquid interface tension and λ is a constant difference of pressures between the vapor and the liquid. The vapor recoil pressure

$$P_r(\vec{r}_i) = [q_L(\vec{r}_i)/H]^2(\rho_V^{-1} - \rho_L^{-1}), \tag{5}$$

where $q_L = -k_L(\vec{n}\cdot\nabla)\, T_L|_{\partial\Omega_i}$ appears due to the uncompensated momentum of vapor molecules that leave the interface. The latent heat of vaporization is denoted

by H, ρ_V and ρ_L being the vapor and liquid densities. Eq. (4) is convenient to solve when the bubble contour is described in parametric form $\vec{r}_i = \vec{r}_i(\xi)$ where ξ is the distance from the topmost point of the bubble to the point $\vec{r}_i$ measured along the bubble contour. When ξ is non-dimensionalized by the half-length of the bubble contour L, $\xi = 1$ corresponds to the contact point and (4) becomes equivalent to the following set of ODEs [5]:

$$\mathrm{d}x_i/\mathrm{d}\xi = L\cos u, \tag{6}$$

$$\mathrm{d}y_i/\mathrm{d}\xi = -L\sin u, \tag{7}$$

$$\mathrm{d}u/\mathrm{d}\xi = L(\lambda + P_r(\xi))/\sigma \tag{8}$$

were $u = u(\xi)$ is an auxiliary function. The boundary conditions for this set read $x_i(0) = 0$, $u(0) = 0$, $y_i(1) = 0$. By fixing the contact angle $u(1) = \pi - \theta$ one can determine the unknown L from (8),

$$L = (\pi - \theta)\sigma \left[\int_0^1 P_r(\xi)\mathrm{d}\xi + \lambda \right]^{-1}, \tag{9}$$

$\theta = 0$ is assumed in the rest of this article. The constant λ should be determined using the known volume V of the 2D bubble,

$$V = -\frac{1}{2} \int\limits_{(\partial\Omega_i)} (x_i n_x + y_i n_y)\, \mathrm{d}\, \partial\Omega, \tag{10}$$

where n_x and n_y are the components of $\vec{n}$, Fig. 3. The bubble volume increases in time due to evaporation at $\partial\Omega_i$

$$H\rho_V \frac{\mathrm{d}V}{\mathrm{d}t} = \int\limits_{(\partial\Omega_i)} q_L(\vec{r}_i)\, \mathrm{d}\, \partial\Omega, \tag{11}$$

This equation is used widely to describe the thermally controlled bubble growth. The initial condition is $V(t = 0) = 4/3\,\pi R_0^3$.

The problem (1-11) is now complete. It can be solved by BEM. However, it is not convenient to solve by BEM because the temperature and its gradient are both non-zero at infinity (more precisely, at $x \to \infty$), where the closing subcontours for the domains Ω_L and Ω_S are located. We solve this problem easily by subtracting the solutions at $x \to \infty$. These solutions for the both domains read [5]

$$T_L^{inf} = T_{sat} + \frac{q_0}{k_L} \left[\sqrt{\frac{4\alpha_L t}{\pi}} \exp\left(-\frac{y^2}{4\alpha_L t}\right) - y\,\mathrm{erfc}\left(\frac{y}{2\sqrt{\alpha_L t}}\right) \right], \tag{12}$$

$$T_S^{inf} = T_{sat} + \frac{2\alpha_S}{k_S} C\sqrt{t} -$$

$$\frac{q_0}{k_S}\left[\sqrt{\frac{4\alpha_S t}{\pi}}\exp\left(-\frac{y^2}{4\alpha_S t}\right)+y\,\mathrm{erfc}\left(-\frac{y}{2\sqrt{\alpha_S t}}\right)\right], \tag{13}$$

where $\mathrm{erfc}(\cdot)$ is the complementary error function [7]. As one can easily find, the flux from the heater q_0 far from the bubble

$$q_0 \equiv q_S(x\to\pm\infty) = C\sqrt{\pi}\alpha_S k_L/(k_S\sqrt{\alpha_L}+k_L\sqrt{\alpha_S}), \tag{14}$$

is constant in time. We use its value as a control parameter instead of C.

By introducing the characteristic scales for time (Δt, the time step), length (R_0, the initial bubble radius), heat flux ($\bar{q}$), and thermal conductivity ($\bar{k}$), all other variables can be made non-dimensional. In particular, the characteristic temperature scale in the system is $\bar{q}R_0/\bar{k}$. The following four non-dimensional groups define completely the behavior of the system

$$\mathrm{Fo}_{L,S} = \alpha_{L,S}\Delta t/R_0^2 \text{ — Fourier numbers,}$$

$$\mathrm{Ja} = \frac{k_L\bar{q}R_0}{\rho_V H\bar{k}\alpha_L} \text{ — Jakob number,}$$

$$\mathrm{Hi} = \frac{R_0\,\bar{q}^2}{\sigma H^2}(\rho_V^{-1}-\rho_L^{-1}) \text{ — Hickman number,}$$

together with the non-dimensionalized values of q_0 and $k_{L,S}$. The non-dimensional heat transfer problem can now be formulated in terms of temperatures $\psi_{L,S} = (T_{L,S}-T_{L,S}^{inf})/(\bar{q}R_0/\bar{k})$ and fluxes $\zeta_{L,S} = k_{L,S}\,\partial\psi_{L,S}/\partial\vec{n}$.

4 Numerical implementation

4.1 BEM formulation

Since $\psi_{L,S} = \zeta_{L,S} = 0$ at infinity, the heat conduction problem is equivalent to a set of two BEM equations [8] for the open integration contours $\partial\Omega_L = \partial\Omega_i \cup \partial\Omega_w$ and $\partial\Omega_S = \partial\Omega_d \cup \partial\Omega_w$. Using $t = 0$ as the initial time moment and taking into account that $\psi_{L,S}(t=0) = 0$ so that the volume integral disappears, these equations read

$$\int_0^{t_F}\mathrm{d}t\int_{(\partial\Omega_{L,S})}\left[G^{L,S}(\vec{r'},t_F;\vec{r},t)\left(\mathrm{Fo}_{L,S}\frac{\zeta_{L,S}(\vec{r},t)}{k_{L,S}}+\psi_{L,S}(\vec{r},t)v^n(\vec{r},t)\right)-\right.$$

$$\left.\mathrm{Fo}_{L,S}\,\psi_{L,S}(\vec{r},t)\frac{\partial_r G^{L,S}(\vec{r'},t_F;\vec{r},t)}{\partial\vec{n}_r}\right]\mathrm{d}_r\partial\Omega = \frac{1}{2}\psi_{L,S}(\vec{r'},t_F), \tag{15}$$

where the point $\vec{r'}$ belongs to $\partial\Omega_{L,S}$ respectively, v^n is the normal component of the contour velocity (nonzero only on $\partial\Omega_i$) and

$$G^{L,S}(\vec{r'},t_F;\vec{r},t) = \frac{1}{4\pi\mathrm{Fo}_{L,S}(t_F-t)}\exp\left[-\frac{|\vec{r'}-\vec{r}|^2}{4\,\mathrm{Fo}_{L,S}(t_F-t)}\right]. \tag{16}$$

In the following, the indices L and S for all variables in the equations will be dropped for the sake of clarity.

The constant element BEM [9] was used, i. e. both ζ and ψ were assumed to be constant during any time step and on any element $\partial\Omega_j$, their values on the element being associated with the values at the node B_j in the middle of the element approximated by a straight segment that joins its ends M_{j-1} and M_j. The time steps are equal, i.e. $t_f = f$. The values of ζ and ψ on the element j at time f are denoted by ζ_{fj} and ψ_{fj}. Each of the integral equations (15) reduces to the system of linear equations

$$\sum_{f=1}^{F}\sum_{j=1}^{2N_f}[(\zeta_{fj}/k + \psi_{fj}v_{fj}^n/\mathrm{Fo})G_{ij}^{Ff} - \psi_{fj}H_{ij}^{Ff}] = \psi_{Fi}/2, \tag{17}$$

where N_f is the number of elements on one half of the integration contour at time step f, F_{max} is the maximum calculation time; $i = 1 \ldots 2N_F$ and $F = 1 \ldots F_{max}$; H_{ij} and G_{ij} are the BEM coefficients:

$$\begin{aligned} G_{ij}^{Ff} &= \mathrm{Fo}\int_{f-1}^{f}\mathrm{d}t\int_{(\partial\Omega_j)} G(\vec{r}_i, F; \vec{r}, f)\mathrm{d}_r\partial\Omega, \\ H_{ij}^{Ff} &= \mathrm{Fo}\int_{f-1}^{f}\mathrm{d}t\int_{(\partial\Omega_j)} \frac{\partial G(\vec{r}_i, F; \vec{r}, f)}{\partial\vec{n}_r}\mathrm{d}_r\partial\Omega. \end{aligned} \tag{18}$$

Since the calculation of these coefficients takes the most of computation time, it should be made fast.

4.2 Algorithm for the BEM coefficients

The value of each particular BEM coefficient for the element $\partial\Omega_j = (M_{j-1}, M_j)$ of the length l is calculated using the coordinate transformation [11] to the Cartesian system where B_j is the reference point and the x axis is directed toward M_{j-1}. The direction of the normal vector $\vec{n}$ coincides with the y axis. The time integration [9] results in

$$G_{ij}^{Ff} = \int_{-l/2}^{l/2}\frac{1}{4\pi}\left[E_1\left(\frac{(x+u)^2+y^2}{4\,\mathrm{Fo}(F-f+1)}\right) - E_1\left(\frac{(x+u)^2+y^2}{4\,\mathrm{Fo}(F-f)}\right)\right]\mathrm{d}u, \tag{19}$$

$$H_{ij}^{Ff} = \int_{-l/2}^{l/2}\frac{y}{2\pi}\left[\frac{\exp\left(-\frac{(x+u)^2+y^2}{4\,\mathrm{Fo}(F-f+1)}\right)}{(x+u)^2+y^2} - \frac{\exp\left(-\frac{(x+u)^2+y^2}{4\,\mathrm{Fo}(F-f)}\right)}{(x+u)^2+y^2}\right]\mathrm{d}u, \tag{20}$$

where (x, y) denote the coordinates of the point $\vec{r}_i$ in the new reference system and $E_1(\cdot)$ is the exponential integral [7]. The situation $i = j$ (i.e. where $x = y = 0$) is particular, which is a quite general feature of BEM.

4.2.1 G coefficient

Note that the case $f = F$ for (19) is not singular, the second term of the integrand in (19) being zero. Therefore, we will deal only with this case. The integration of the second term that exists when $f < F$ is similar to the first.

The divergence of $E_1(z)$ at $z \to 0$ is logarithmic and thus integrable. Usually this means that the integration can be performed by the Gauss method. However, since our problem is singular due to the contact line effects, many Gauss points are needed to attain the required accuracy in the contact line region and a more sophisticated algorithm is necessary to get both accuracy and speed. The analytical integration [10] is used when $y = 0$ i.e. when the singularity occurs. Although there is no singularity when $y \neq 0$, the integrand varies sharply near the point $u = -x$ when $y \ll l$. For the case $|x| < l/2$, the integration interval can be split by the point $u = -x$ and changes of variables can be done in both integrals to produce

$$G_{ij}^{FF} = \frac{\sqrt{\mathrm{Fo}}}{4\pi} \left\{ \int_{y^2/4\mathrm{Fo}}^{[(x+l/2)^2+y^2]/4\mathrm{Fo}} \frac{E_1(z)}{\sqrt{z - y^2/4\mathrm{Fo}}}\,\mathrm{d}z + \int_{y^2/4\mathrm{Fo}}^{[(x+l/2)^2+y^2]/4\mathrm{Fo}} \frac{E_1(z)}{\sqrt{z - y^2/4\mathrm{Fo}}}\,\mathrm{d}z \right\}. \tag{21}$$

At first glance, no advantage is obtained because of the divergence. However, the approximation [7] of $E_1(z)$ for $z < 1$ allows the analytical integration to be performed term by term and results in

$$\begin{aligned} \int_b^a \frac{E_1(z)}{\sqrt{z-b}}\,\mathrm{d}z = -4\sqrt{b}\arctan\sqrt{\frac{a-b}{b}} + 2\sqrt{a-b}\,[1.422784 - \log(a) + \\ 0.333331\,(a+2b) - 0.0166607\,(3a^2+4ab+8b^2) + \\ 1.577134\cdot 10^{-3}\,(5a^3+6a^2b+8ab^2+16b^3) - \\ 3.09843\cdot 10^{-5}(35a^4+40a^3b+48a^2b^2+64ab^3+128b^4) + \\ 1.55638\cdot 10^{-6}(63a^5+70a^4b+80a^3b^2+96a^2b^3+128ab^4+256b^5)], \end{aligned} \tag{22}$$

where $b \leq a < 1$ are assumed. For the remaining part of the integration interval, the 8-point Gauss integration is performed and gives a sufficient accuracy.

The case $|x| > l/2$ should be solved similarly when the argument of E_1 in (19) can be less than unity somewhere in the integration interval.

4.2.2 H coefficient

The value of the coefficient (19) at $y = 0$ is zero. While no singularity exists when $f < F$ (this case can be integrated by Gauss method), the function

$$H_{ij}^{FF} = \frac{y}{2\pi} \exp\left(-\frac{y^2}{4\,\mathrm{Fo}}\right) \int\limits_{x-l/2}^{x+l/2} \frac{\exp\left(-\frac{u^2}{4\,\mathrm{Fo}}\right)}{u^2+y^2}\,\mathrm{d}u \tag{23}$$

is discontinuous at $y = 0$. The integration interval in (23) contains the point $u = 0$ when $|x| < l/2$. Since the integrand is an even function of u, this integral can be presented as

$$\int\limits_{x-l/2}^{x+l/2} \ldots = \int\limits_{0}^{x+l/2} \ldots + \int\limits_{0}^{l/2-x} \ldots$$

and the interval $(0, \varepsilon)$, where $0 < \varepsilon \ll l/2$, can be separated out of the both integrals. The contribution of this interval to (23) turns out to be

$$H_{ij}^{FF} = \frac{1}{\pi} \exp\left(-\frac{y^2+\varepsilon^2/4}{4\,\mathrm{Fo}}\right) \arctan\frac{\varepsilon}{y} + \ldots$$

The discontinuity is evident now: while $y \to +0$ limit is $1/2$, the value at $y = 0$ is zero and $y \to -0$ limit is $-1/2$.

After the integration over the interval $(-\varepsilon, \varepsilon)$ analytically, the Gauss method can be employed to integrate over the remaining parts of the interval in (23).

4.3 Calculation scheme

The system (17) can be simplified due to axial symmetry of the problem $\zeta, \psi_{fj} = \zeta\psi_{f(2N_f-j)}$:

$$\sum_{f=1}^{F} \sum_{j=1}^{N_f} [(\zeta_{fj}/k + \psi_{fj} v_{fj}^n/\mathrm{Fo})\tilde{G}_{ij}^{Ff} - \psi_{fj}\tilde{H}_{ij}^{Ff}] = \psi_{Fi}/2, \tag{24}$$

where $i = 1 \ldots N_F$, $F = 1 \ldots F_{max}$, $\tilde{G}_{ij}^{Ff} = G_{ij}^{Ff} + G_{i(2N_f-j)}^{Ff}$ and $\tilde{H}_{ij}^{Ff} = H_{ij}^{Ff} + H_{i(2N_f-j)}^{Ff}$. Unfortunately, no effective time marching scheme [9] can be applied because of the free boundaries. The position of each node depends on time. Therefore, it is very important that $\tilde{G}_{ij}^{Ff}$ be calculated using the coordinates of the i-th point at time moment F and those of j-th point at time moment f.

Our 2D BEM algorithm was tested for the fixed boundary wedge problem (for the Ω_L domain only) with the constant heat flux boundary condition described in section 2. Since ζ decreases to zero far from the contact point, integration contour can be closed at the distance $x_{max} \sim 10\sqrt{\mathrm{Fo}\,t}$ from the contact point O$(0, 0)$ where $\zeta(x, y, t)$ is sufficiently small. The element lengths grow exponentially ($d_{min}, d_{min}e^b, d_{min}e^{2b}, \ldots$) from the contact point into each of the sides of

the wedge (see Fig. 1), where b is fixed at 0.2. Since x_{max} increases with time, the total number of the elements also increases during the evolution of the bubble. Being an input parameter, d_{min} is adjusted slightly on each time step to provide the exponential growth law for the elements on the interval with the fixed boundaries $(0, x_{max})$. Remeshing on each time step was performed to comply with the free boundary nature of the main problem where the remeshing is mandatory.

The results for $\theta = \pi/8,\ \pi/4$ and $\pi/2$ are shown in Fig. 2 to be compared with the analytical solutions [5, 6]. It is easy to see that the method produces excellent results except for the element closest to the contact point. The algorithm overestimates the value of q_L at this element. The error is larger for the $\pi/2$ wedge, for which $q_L \to \infty$ at the contact point. We verified that the influence of the increase of the time and space steps on the numerical error is very weak.

The discretization of the integration subcontours of the bubble growth problem $\partial\Omega_w$, $\partial\Omega_d$ and $\partial\Omega_i$ follows the same exponential scheme (see Fig. 3) that was used for the discretization of the wedge sides in the test example above. Since the free boundary introduces a nonlinearity into the problem, the following iteration algorithm is needed to determine the bubble shape on each time step [8]:

1. Shape of the bubble is guessed to be the same as on the previous time step;
2. The variations of v^n and P_r along the bubble interface are guessed to be the same as on the previous time step;
3. Discretization of the contours $\partial\Omega_w$, $\partial\Omega_d$ and $\partial\Omega_i$ is performed;
4. Temperatures and fluxes on the contours $\partial\Omega_w$, $\partial\Omega_d$ and $\partial\Omega_i$ are found by solving (24) for $\psi, \zeta_{L,S}$ at the time moment F;
5. Volume V and vapor recoil P_r are calculated using (11) and (5);
6. Bubble shape is determined for the calculated values of V and P_r;
7. If the calculated shape differs too much from that on the previous iteration, the velocity of interface v^n is calculated, and steps 3 – 7 are repeated until the required accuracy is attained.

As a rule, three iterations give the 0.1% accuracy which is sufficient for our purposes.

The normal velocity of interface v^n_{Fi} at the time F and at node i is calculated using the expression

$$v^n_{Fi} = (x_{Fi} - x_{(F-1)j})n^x_{(F-1)j} + (y_{Fi} - y_{(F-1)j})n^y_{(F-1)j}, \qquad (25)$$

where x_{Fi} is the coordinate of the node i at time F, and j is the number of the node (at time $F-1$) geometrically closest to (x_{Fi}, y_{Fi}).

The system of Eqs. 6 – 8 is solved by direct integration. The integration of the right-hand side of (8) is performed using the simple mid-point rule, because the values of P_r are calculated at the mid-points (nodes) only. The subsequent integration of the right-hand sides of Eqs. 6 – 7 is performed using the Simpson rule (to gain accuracy) for the non-equal intervals. The trapezoidal rule turns out to be accurate enough for the calculation of volume in (10). For the simulation we used the parameters for water at 10 MPa pressure on the heater made of stainless steel listed in [5].

The above described algorithm should give good results when $\int_0^1 P_r(\xi)\mathrm{d}\xi$ exists (cf. Eq. 9). In our case $P_r(\xi)$ can be approximated by the power function $(1-\xi)^{-2\beta}$ when $\xi \to 1$. The exponent β, which comes from the approximation for $q_L(\xi)$, turns out to be larger than one half (see discussion in the next section). Thus if the data were extrapolated to the contact point $\xi = 1$, this integral would diverge. We note, however, that the evaporation heat flux is limited [12] by a flux q_{max} which is about 10^4 MW/m^2 for the chosen parameters.

The q_L divergence is originated from the assumption that the temperature remains constant along the vapor-liquid interface. In reality, this assumption is violated in the very close vicinity of the contact point where the heat flux q_L is comparable to q_{max}. Thus we accept the following approximation for the function $q_L(\xi)$, $\xi < 1$. It is extrapolated using the power law $q_L(\xi) \propto (1-\xi)^{-\beta}$ until it reaches the value of q_{max} and remains constant while ξ increases to unity. This extrapolation is used to calculate the integrals in (11) and (9). There is no need to modify the constant-temperature boundary condition for the heat transfer calculations because the calculated heat flux q_L remains always less than q_{max}.

5 Results of the numerical calculation

The calculations show that the function $q_L(\xi)$ (see Fig. 4) can be described well by

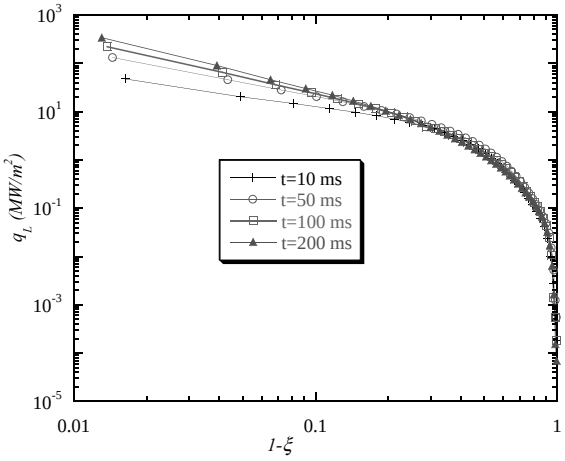

Figure 4: Variation of the heat flux q_L calculated for $q_0 = 0.05$ MW/m^2 along the bubble contour for different moments of time. The curvilinear coordinate ξ varies along the bubble contour; $\xi = 1$ at the contact point. (Reprinted from [5] with permission from Elsevier Science)

the above power law where $\beta \sim 1$ grows slightly with time. As expected, for this conjugate heat conduction problem the divergence is stronger than for the wedge model, Fig. 2. The difference between these two cases is caused by the behavior

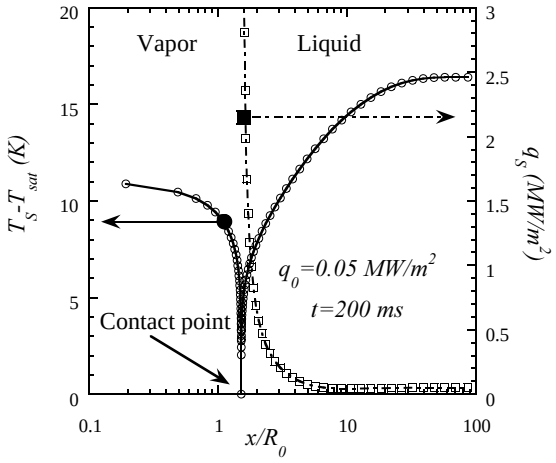

Figure 5: Variation of the heat flux q_S and the temperature T_S along the surface of the heater for $q_0 = 0.05$ MW/m^2, $t = 200$ ms. The point $x = 0$ corresponds to the center of the bubble. (Reprinted from [5] with permission from Elsevier Science)

of the heat flux q_S in the vicinity of the contact point. While it was imposed to be uniform for the wedge, the function $q_S(x)$ increases strongly near the contact point for the conjugate heat conduction, see Fig. 5. As expected, the value of q_S on the liquid side in the vicinity of the contact line is very close to q_L, the heat flux that produces evaporation on the vapor-liquid interface and that diverges on the contact line (see Fig. 4). At some distance from the bubble center q_S reaches the value of q_0, the flux at infinity. Note that the Fig. 5 corresponds to the quasi-spherical bubble shape (see Fig. 6a) and the visible bubble radius (see Fig. 3 for the definition) $R \sim 7R_0$, so that the heat flux q_S is virtually homogeneous outside the bubble.

The variation of the temperature along the heating surface $T_S(x)$ is also shown in Fig. 5. Far from the bubble, $T_S = T_S^{inf}$ has to increase with time independently of x according to (13). It decreases to T_{sat} near the contact point because the temperature should be equal to T_{sat} on the whole vapor-liquid interface, according to the imposed boundary condition. Inside the dry spot, T_S increases with time because the heat transfer through the dry spot is blocked. It is smaller than T_S^{inf} while the dry spot under the bubble remains much smaller than R. Since q_L grows with time, at some time moment the vapor recoil pressure $P_r \propto q_L^2$ overcomes the surface tension (cf. Eq. 4) and the dry spot begins to grow, see Fig. 6b. This bubble spreading was observed experimentally in several works, e. g. [2]. The spreading bubble serves as a nucleus for the formation of a continuous vapor film that separates the solid from the liquid, i. e. triggers the boiling crisis. The heat transfer becomes blocked at a larger portion of the solid surface (i.e. dry spot) and its temperature grows faster than T_S^{inf}. This temperature increase leads to the

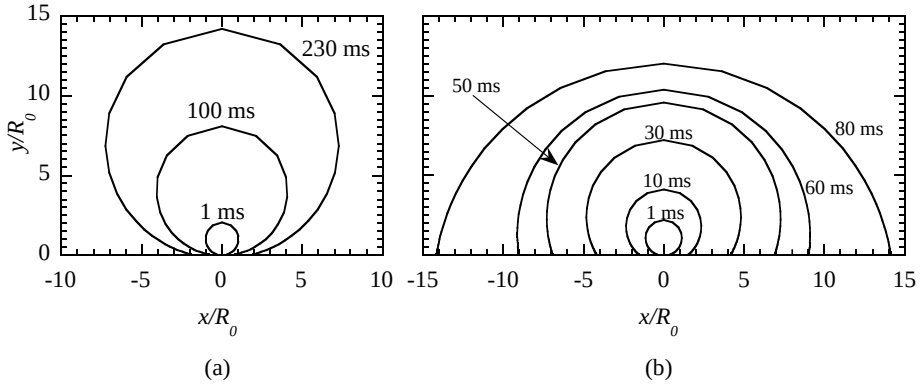

Figure 6: The bubble shape shown for the different growth times.
a) $q_0 = 0.05$ MW/m^2; b) $q_0 = 0.5$ MW/m^2.
(Reprinted from [5] with permission from Elsevier Science)

burnout of the heater observed during the boiling crisis.

6 Conclusions

Several conclusions can be made. Our analysis of the bubble growth dynamics shows the strong coupling of the heat conduction in the liquid and in the solid heater. Therefore, only a conjugate heat transfer calculation of the bubble growth can properly simulate the boiling crisis. We show that BEM suits well for such a simulation. We carried out a 2D BEM calculation. It shows that the vapor recoil can be at the origin of the boiling crisis. We demonstrated how a vapor bubble spreads over the heating surface thus initiating the boiling crisis.

Acknowledgements

We gratefully acknowledge a permission of Elsevier Science B. V. to reproduce some figures from [5]. We thank our colleagues H. Lemonnier, J. Hegseth and G.-L. Lagier for the fruitful discussions.

References

[1] Dhir, V.K., Boiling Heat Transfer, *Annu. Rev. Fluid. Mech.*, **30**, pp. 365–401, 1998.
[2] Garrabos, Y., Lecoutre-Chabot, C., Hegseth, J., Nikolayev, V.S., Beysens, D., Gas spreads on a heated wall wetted by liquid, *Phys. Rev. E*, **64**, pp. 051602-1–10, 2001.
[3] Andrieu, C., Beysens, D., Nikolayev, V.S., Pomeau, Y., Coalescence of sessile

drops, *J. Fluid. Mech.*, **453**, pp. 427–438, 2002.

[4] Carslaw, H.S. & Jaeger, J.C., *Conduction of Heat in Solids* (2nd Edn), University Press: Oxford, 1959.

[5] Nikolayev V.S., Beysens D. A., Lagier G.-L., Hegseth J., Growth of a dry spot under a vapor bubble at high heat flux and high pressure, *Int. J. Heat Mass Transfer* **44**, pp. 3499–3511, 2001.

[6] Nikolayev, V.S., Beysens, D.A., Boiling crisis and non-equilibrium drying transition, *Europhys. Lett.*, **47**, pp. 345–351, 1999.

[7] *Handbook of Mathematical Functions*, eds. M. Abramovitz & I. A. Stegun, Natl. Bureau of Standartds, Dover, New York (1972).

[8] DeLima-Silva, W. & Wrobel, L. C., A front-tracking BEM formulation for one-phase solidification/melting problems, *Engineering Analysis with Boundary Elements*, **16**, pp. 171–182, 1995.

[9] Pina, H.L.G. & Fernandes, J.L.M., Applications in Transient Heat Conduction. *Topics in Boundary Element Research, Vol.1, Basic Principles and Applications* ed. C.A. Brebbia, Springer-Verlag, Berlin, pp. 41–58, 1984.

[10] Lagier, G.-L., Application de la méthode des élements de frontière à la résolution de problèmes de thermique inverse multidimensionnels (Application of the BEM to multidimensional inverse heat conduction problems), Ph. D. Thesis, l'Institut National Polytechnique de Grenoble, Grenoble, 1999.

[11] Hess, J.L. & Smith, A.M.O., Calculation of potential flow about arbitrary bodies, *Progress in Aeronautical Sciences, Vol.8* ed. D. Küchemann, Pergamon, 1967.

[12] Carey, van P., *Liquid-Vapor Phase Change Phenomena*, Hemisphere: Washington D.C., 1992.

J. Fluid Mech. (2002), *vol.* 453, *pp.* 427–438.
DOI: 10.1017/S0022112001007121 Printed in the United Kingdom

Coalescence of sessile drops

By C. ANDRIEU[1], D. A. BEYSENS[1], V. S. NIKOLAYEV[1] AND Y. POMEAU[2]

[1]CEA-ESEME, Institut de Chimie de la Matière Condensée de Bordeaux, 87, Avenue du Dr. Schweitzer, 33608 Pessac Cedex, France
email: dbeysens@cea.fr

[2]Laboratoire ASCI, Bat. 506, 91405 Orsay Cedex, France

(Received 20 September 2000 and in revised form 29 July 2001)

We present an experimental and theoretical description of the kinetics of coalescence of two water drops on a plane solid surface. The case of partial wetting is considered. The drops are in an atmosphere of nitrogen saturated with water where they grow by condensation and eventually touch each other and coalesce. A new convex composite drop is rapidly formed that then exponentially and slowly relaxes to an equilibrium hemispherical cap. The characteristic relaxation time is proportional to the drop radius R^* at final equilibrium. This relaxation time appears to be nearly 10^7 times larger than the bulk capillary relaxation time $t_b = R^*\eta/\sigma$, where σ is the gas–liquid surface tension and η is the liquid shear viscosity.

In order to explain this extremely large relaxation time, we consider a model that involves an Arrhenius kinetic factor resulting from a liquid–vapour phase change in the vicinity of the contact line. The model results in a large relaxation time of order $t_b \exp(L/\mathscr{R}T)$ where L is the molar latent heat of vaporization, $\mathscr{R}$ is the gas constant and T is the temperature. We model the late time relaxation for a near spherical cap and find an exponential relaxation whose typical time scale agrees reasonably well with the experiment.

1. Introduction

Fusion or coalescence between drops is a key process in a wide range of phenomena: phase transition in fluids and liquid mixtures or polymers, stability of foams and emulsions, and sintering in metallurgy (Eggers 1998), which is why the problem of coalescence has already received considerable attention. Most of the studies of this process so far have been devoted to the coalescence of two spherical drops floating in a medium. The kinetics of the process before and after the drops have touched each other is governed by the hydrodynamics inside and outside the drops and by the van der Waals forces when the drops are within mesoscopic distance from each other (Yiantsios & Davis 1991). The composite drop that results from the coalescence of two drops relaxes to a spherical shape within a time which is dominated by the relaxation of the flow inside and outside (Nikolayev, Beysens & Guenoun 1996; Nikolayev & Beysens 1997). There are no studies, to our knowledge, of the coalescence of two sessile drops after they touch each other. In this paper, we report a preliminary study of the dynamics and morphology of this process, in the case of hemispherical water droplets which grow slowly on a plane surface at the expense of the surrounding atmosphere, forming what is called 'dew' or 'breath figures' (Beysens *et al.* 1991; Beysens 1995). The drops eventually touch each other and coalesce to form an elongated composite

drop, which then relaxes to a spherical cap or to a less elongated drop. We study the composite drop relaxation, which depends on the droplet size and morphology (contact angle θ). When the contact angle is large ($70^\circ < \theta < 90^\circ$), the composite drop relaxes very rapidly (within a time frame of a video camera) to a hemispherical cap (Zhao & Beysens 1995). The relaxation process also appears fast if the contact angle is small ($\theta < 20^\circ$). However, in this case the drop never relaxes to a hemispherical cap: its shape remains complicated. We study here the intermediate range of contact angles where the composite drop relaxes to a near-hemispherical drop, and report on two experiments where the contact angles are 30° and 53°. We find that the relaxation process can be described by an exponential function, with a typical time scale proportional to the radius of the drop.

Such a relaxation process cannot be accounted for by the bulk dissipation of the flow inside the drops. Available information in the literature shows that there are no widely accepted theories because of the complicated interplay between macroscopic and molecular scale phenomena (Blake & Haynes 1969; de Gennes 1985; Dussan V. & Davis 1986; Hocking 1994). We propose a simple approach here based on an Arrhenius factor arising from the gas–liquid transition that occurs in the vicinity of the contact line and that limits the contact line mobility.

2. Experimental

When water vapour condenses on a cold substrate under partial-wetting conditions, one observes an assembly of droplets (dew) that continuously grow and merge. We use this process to study the coalescence of sessile drops. The surface properties of the substrate play a crucial role in this process through the contact angle. The experiments consist in observing with a microscope drops that grow at a low rate in a condensation chamber. The images before and after drop coalescence are studied by means of an image analysis system. The condensation chamber is a Plexiglas box filled with N_2 gas saturated with water at room temperature (22 °C). To avoid dust and to saturate the gas, N_2 is bubbled in pure water. The gas flow is controlled with a flow meter and all the experiments presented here are performed at the flow rate of 13.5 $cm^3\,s^{-1}$. The substrate on which condensation takes place involves a Peltier-element thermostat to lower the substrate temperature and is set on a 5 mm thick block made of electrolytic copper. This block ensures a homogeneous temperature diffusion from the Peltier element to the substrate. The thermal contact is ensured by a silicon free heat sink compound (Tech Spray). The temperature is monitored with a thermocouple of type K placed on the copper block near the substrate. The experimental procedure consists in rapidly cooling the substrate from room temperature down to 15 °C. The growth of dew is observed with an optical microscope and recorded with a CCD camera. The video data are analysed by a digital processing system.

The surface for condensation is made of 0.7 mm thick glass wafers with 37 mm diameter. The surfaces are first cleaned with diluted fluorhydric acid, then with optical soap and finally rinsed with pure water and ethanol. The cleaned substrates are baked at 120 °C, dipped in a fluorochlorosilane (FClSi) solution and then put back in the oven at 120 °C for an hour. At this temperature the FClSi molecules are chemically grafted on the glass surface and do not react with water. Several wafers were used for the experiments reported here.

The treated surface is hydrophobic. Water condenses on it as droplets with a finite contact angle θ. To measure θ, a small drop of water (2 mm diameter) is deposited with a syringe on the substrate and observed with a CCD camera through a macrolens. We

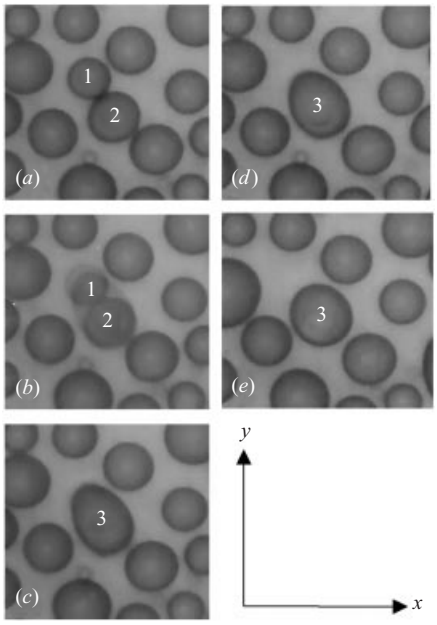

FIGURE 1. Photos of the coalescence process. The side of each photo corresponds to 276 μm. (*a*) $t = 5.59$ s; (*b*) $t = 5.63$ s, the coalescence time; (*c*): 5.65 s; (*d*): 6.65 s; (*e*): 42.76 s.

report two sets of experiments, for $\theta = 30^\circ$ and 53°. (The contact angle was modified by changing the experimental conditions.) The hysteresis of the contact angle was of order 15° in both cases.

The morphology of the coalescence-induced composite drop is analysed as follows. After calibration, we measure the contact area, the major and minor axes (the latter is taken perpendicularly to the former) for several composite drops as a function of time. In figure 1 we report a typical evolution of two hemispherical drops ('parents') that coalesce to form an elongated, composite drop ('child'), which eventually returns to a spherical cap shape (within 3–4%). The return to a spherical cap indicates that the surface roughness is small enough that the contact line is not pinned in a metastable state. Note figure 1(*b*) where, within a time-frame (40 ms), one can observe the two parents and the child at the same time. This is because the video image is made of two interlaced frames with 20 ms scanning time.

3. Observation and preliminary analysis

From the data obtained, we can analyse the behaviour of several quantities of interest.

3.1. *Position of the centre of mass*

We report in figure 2 the details of a typical coalescence event, similar to the one shown in figure 1. Here the parent drops are labelled 1 and 2. Drop 3 is the child drop. The coordinates (x_i, y_i) of the centre of mass of the drops $i = 1, 2$ and 3 are calculated from their contact area on the substrate. Drops 1 and 2 and at late times drop 3, are nearly hemispherical and this approximation is fully justified. A difficulty comes when dealing with the early times of drop 3 where only one symmetry axis is seen and whose three-dimensional shape cannot be determined from the pictures.

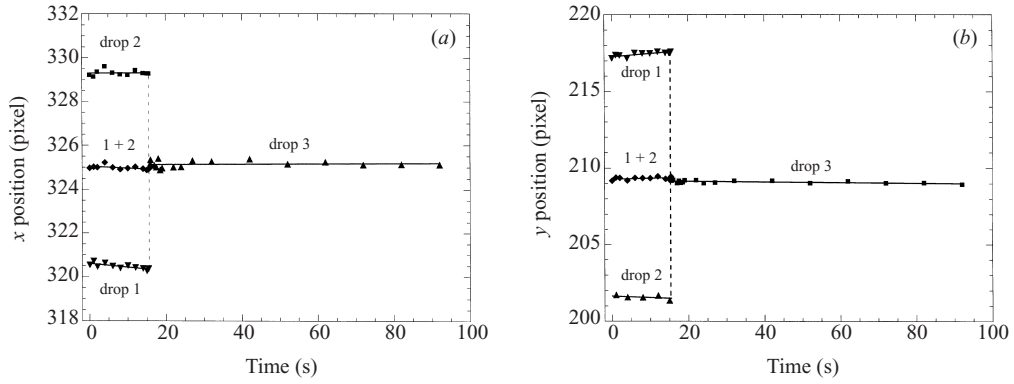

FIGURE 2. Evolution of the coordinates of the centres of mass of the parent drops (1, 2) and of the composite drop 3 after coalescence: (*a*) abscissas (*b*) ordinates.

However, its asymmetry with respect to the axis perpendicular to the symmetry axis is small. Therefore, we assume that the position of the centre of mass can be calculated from the two-dimensional formulas as if the drop were of homogeneous thickness. The centre of mass of the system drop 1 + drop 2 can be calculated according to the well-known formulas (here the contact angle does not enter in the equation, because it is assumed to be the same for both drops)

$$x_3 = \frac{x_1 R_1^3 + x_2 R_2^3}{R_1^3 + R_2^3}, \tag{3.1}$$

$$y_3 = \frac{y_1 R_1^3 + y_2 R_2^3}{R_1^3 + R_2^3}, \tag{3.2}$$

where x_i, y_i, R_i are the coordinates and radius of drop i, with $i = 1, 2, 3$.

Before coalescence, during growth, the coordinates of the centre of mass of the parents are reported in figure 2 with respect to the axes shown in figure 1. Also shown is the evolution of the centre of mass of the ensemble drop 1 + drop 2, calculated from (3.1) and (3.2). A small variation is observed, which we attribute to the interference of the neighbouring drops, which distorts the gradient of vapour concentration around them. (Note that the mass transfer is maximum at the triple line, where the temperature gradient is maximum (Steyer, Guenoun & Beysens 1992).)

As already noted, the centre of mass of drop 3 does not move during its relaxation towards a spherical cap. However, there is a small systematic difference between the coordinates of the drop 3 centre of mass and the centre calculated from the ensemble drop 1 + drop 2. This can be related to external forces, such as those that pin the contact line. The centre of mass after coalescence moves towards to the largest drop (drop 2), that is, the drop with the longest contact line.

3.2. *Relaxation of the composite drop*

Figure 3 shows a schematic view of the coalescence process. In a simplified manner, the contact line of the child, or composite, drop can be assumed to be an ellipse of width R_x (resp. R_y) along the small (resp. long) axes. The most obvious dynamical quantity to analyse is the evolution of R_x and R_y. A typical curve is shown in figure 4(*a*), showing as well that the parent drops are circular within $\pm 3\%$ accuracy. The coalescence process is characterized by three time regions:

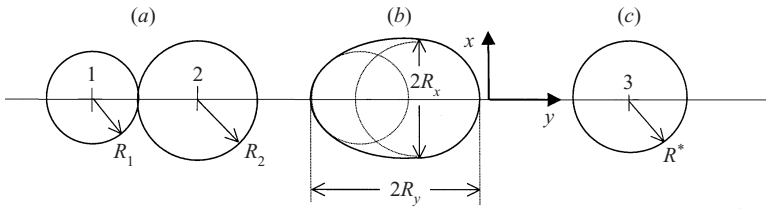

FIGURE 3. Sketch of the coalescence event as in figure 1. (*a–c*) is the time sequence.

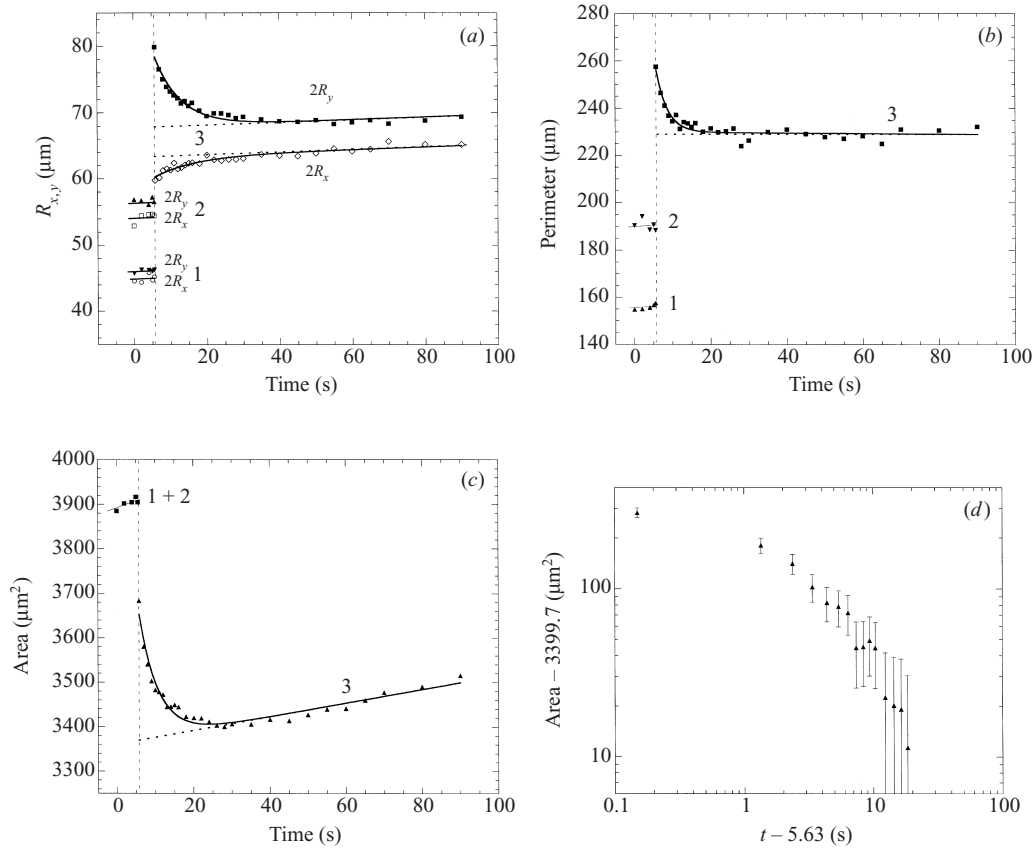

FIGURE 4. Evolution of (*a*) the large and small axes, (*b*) perimeter, and (*c*) area of the drops 1 and 2 ('parents', see figure 1), and drop 3 (composite drop). The curves are fits to (3.3). The relaxation times for these three fits are equal within the experimental error. The (dotted) asymptotic lines correspond to the condensation-induced slow growth. In (*d*) the data from (*c*) are shown in a log-log plot.

(i) Nucleation of a liquid bridge between the two parent drops and subsequent formation of a convex composite drop occurs in a time period smaller than half the video scanning time, i.e. 20 ms (figure 1*b*). In the theoretical explanation sketched below, the corresponding dynamics is fast because, during the growth of this bridge, the contact line moves locally by vapour condensation, a process not slowed down by an *a priori* Arrhenius factor.

(ii) Decrease of the large axis R_y with time, small increase of the small axis R_x, such that the ratio R_y/R_x eventually reaches a value about unity.

(iii) Slow growth of the drop due to condensation.

Regime (ii) takes up most of the time in the coalescence process. Once the slow growth observed in (iii) is subtracted from the evolution of R_x and R_y, the evolution of the small axis R_x is usually negligible and the evolution of the drop can be characterized by R_y only.

Parameters other than R_y, such as the liquid–solid contact area A_{LS} (figure 4*c*) or its perimeter P (figure 4*b*), can give useful information. Their behaviour is quite similar to that of R_y. In the following, we will discuss only the evolution of the contact area A_{LS}, the quantity which can be measured with the best accuracy. As shown in figure 4(*c*), the evolution of $A_{LS}(t)$ cannot be described by a power law. It can, however, be successfully fitted to the following function:

$$A_{LS}(t) = A_0 \exp[-(t - t_0)/t_c] + A_1(t - t_0) + A_2. \tag{3.3}$$

The first term corresponds to the relaxation of the composite drop, which dominates in regime (ii) and the second and third terms to the growth by condensation detected during period (iii) (figure 4*d*). Since the stage (i) is very rapid, the time t_0 can be considered as the time of the beginning of the coalescence. The free parameters in the fit are t_c, A_0, A_1, and A_2. The area A_2 is related to the drop radius R^* at equilibrium (when the drop becomes a spherical cap) by $A_2 = \pi R^{*2}$.

There are three time scales that correspond to regimes (i), (ii) and (iii). The first regime is controlled by a time scale < 20 ms. The second regime corresponds to $t_c \sim 5$ s. Before the beginning of the third stage, the relaxation to the final shape is almost complete. In this third stage, the total liquid mass grows due to condensation, which is necessary to make the drops grow and coalesce. This third time scale is of the order of 150 s and can be characterized by the coefficient A_1. Since these three time scales differ substantially, the corresponding regimes can be considered independently from each other. In the following, we discuss only the time t_c that fully characterizes the relaxation of the convex drop. Its value should be independent of the externally imposed small condensation rate.

In figure 5, we report how t_c varies with R^* for two contact angles ($\theta = 53°$ and 30°). The data show that t_c varies linearly with R^* and can be fitted to

$$t_c = \frac{1}{u} R^*, \tag{3.4}$$

where u is a characteristic velocity. This fit gives $u = (6.5 \pm 0.4)\, 10^{-6}\, \mathrm{m\, s^{-1}}$ for $\theta = 53°$ and $u = (12 \pm 1)\, 10^{-6}\, \mathrm{m\, s^{-1}}$ for $\theta = 30°$. The statistical error corresponds to the values of the linear correlation coefficient 0.93 ($\theta = 53°$) and 0.87 ($\theta = 30°$).

Note that t_c should depend on the difference between the sizes of the two parent drops. However, this dependence is weak when the difference is small because the composite drop is nearly symmetrical, see figure 1.

The relaxation time appears to be larger for $\theta = 53°$ than for $\theta = 30°$. This seems paradoxical since the relaxation driving force (see (4.5) below) should be larger for larger angles thus causing a smaller relaxation time. (In fact, for large angles $\theta > 70°$ the relaxation becomes too fast to be measured within a video scanning time, which fits well with this argument.) The small relaxation time at small angles can be explained by the pinning of the contact line on surface defects, leading to a metastable equilibrium in a shorter time, so that the total relaxation time becomes smaller. The pinning is likely to occur for a smaller contact angle where the relaxation driving

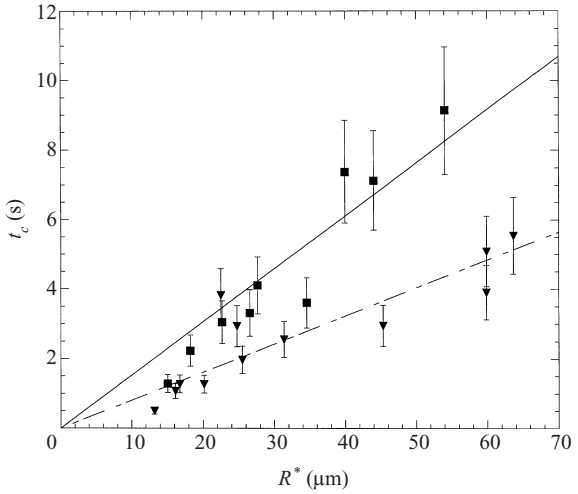

FIGURE 5. Variation of the relaxation time t_c with the composite drop radius R^* measured at the end of relaxation, see figure 3. Data corresponding to $\theta = 30^\circ$ (triangles) and $\theta = 53^\circ$ (squares) are shown. The lines are the best fits.

force is smaller. For $\theta \leqslant 20^\circ$ the shape of the drops becomes quite complex and thus unsuitable for analysis because of the contact line pinning (Zhao & Beysens 1995).

The detailed study of the contact angle dependence of t_c is beyond the scope of this paper, which is focused on the unexpectedly long relaxation time found in these experiments.

4. Theoretical analysis

Let us consider first the relaxation of the drop to the spherical cap equilibrium shape as described by bulk hydrodynamics. The rate of relaxation of the slightly deformed drop is defined by three characteristic times. The first is the inviscid inertial time $t_e = (\rho R^{*3}\sigma)^{1/2}$, where ρ is the liquid density. It accounts for the slowing down of the relaxation by the inertia of the liquid. The second is the viscous inertial time $t_i = R^{*2}/\nu$, where ν is the kinematic viscosity, which accounts for dissipation at high Reynolds number in the boundary layer. The third characteristic time is t_b, the viscous relaxation driven by the surface tension σ. It is given by the expression $t_b = R^*\eta/\sigma$, where η is the shear viscosity.

Using data for water at 20 °C ($\eta = 10^{-3}$ Pa s, $\nu = 10^{-6}\,\mathrm{m^2\,s^{-1}}$, $\sigma = 73\,\mathrm{mN\,m^{-1}}$), it is easy to check that all of these times are many orders of magnitude less than the relaxation time reported in figure 5 (nearly seven orders for the viscous flow approximation). This section deals with the explanation of this large difference.

The relationship between the contact line motion and phase change has been studied previously in a number of works. The reaction of the liquid meniscus to the externally imposed contact angle change was analysed by Wayner (1993). He assumed implicitly that the vapour condenses homogeneously over the whole meniscus thus causing the contact line to advance along the prewetted solid surface. Subsequent studies (Anderson & Davis 1994; Nikolayev & Beysens 1999; Nikolayev *et al.* 2001) showed that the phase change rate varies along the meniscus, being much larger in the contact line vicinity than on the rest of the meniscus. This effect was taken into account by Anderson & Davis (1995) who studied the influence of the evaporation

on the value of the dynamic contact angle. The contact line was assumed to move due to the non-zero liquid–solid slip coefficient.

Previous studies of volatile liquids relied on the mechanisms of the contact line motion (de Gennes 1985) proposed for non-volatile liquids. These mechanisms cannot explain the very small factor 10^{-7} observed in our experiments.

The contact angle hysteresis that appears due to the surface defects is small and results in a small deviation of the final drop shape from a spherical cap, which would form in the absence of the hysteresis. This deviation can be estimated from figure 4(a) as $(R_y - R_x)/(R_y + R_x) \approx 3\%$, R_x and R_y being taken for $t \gg t_c$. The analysis of Nikolayev & Beysens (2001) shows that the weak defects are not likely to cause such a strong change in the relaxation rate. This large difference calls for a radical change in theory.

It is well known that such very small non-dimensional factors appear very often in the presence of an activation process that gives very small Arrhenius non-dimensional factors. For contact line motion, it has been proposed recently that such a factor could be present (Pomeau 2000) because of the following: the contact line, sticking on the solid, cannot move by hydrodynamic motion, since the fluid velocity is zero on the solid (no-slip condition). This condition can be satisfied during the contact line motion when evaporation (when the liquid is receding) or condensation (when the liquid is advancing) occurs in the vicinity of the contact line (Seppecher 1996). Although the rate of this phase change can be large (it is proportional to the contact line speed), it does not result in a large mass change of the drop because of the small part of the area where the phase change occurs. The rate of this process is therefore independent of the small global condensation rate present in our experiments.

Hereafter, we shall consider the receding process only, that is, evaporation. This evaporation is a thermally activated process because molecules in the liquid are in the bottom of a potential well, due to the attraction of the other molecules, an attraction necessary to maintain the cohesion of the liquid against spontaneous self-evaporation. Therefore, the rate of evaporation should be proportional to a very small Arrhenius factor

$$K = \exp\left(-\frac{W}{k_B T}\right), \tag{4.1}$$

where W is the difference of potential energy between the liquid and vapour side, taken as positive (in practice, this potential energy is zero in the dilute vapour, and $-W$ in the liquid). Supposing that the potential energy grows monotonically from a well in the liquid to its zero value in the vapour, one would obtain for W the latent heat per molecule. Using the molar latent heat $L \approx 44\,\mathrm{kJ\,mol^{-1}}$ (which is its value for 20 °C) one obtains $K = \exp(-L/\mathscr{R}T) \sim 10^{-8}$, where $\mathscr{R}$ is the ideal gas constant.

This physical phenomenon bears some similarity with the molecular kinetics theory (Blake & Haynes 1969), that also involves the Arrhenius factor. Note that, in contrast to the molecular kinetics theory, the Arrhenius factor K defined above is independent of the difference between the actual contact angle and its equilibrium value (and so is intrinsically very small and independent of the actual contact angle, as observed).

Now, it becomes simple to formulate the equations of motion for the relaxation of shape of the droplet: the pure hydrodynamic phenomena (inertial or viscous) are so fast that they can be taken as having reached equilibrium for a given droplet contour on the solid. In other terms, all the dynamics is enslaved to the slowest process, the receding motion of the contact line driven by evaporation. Therefore the dynamics is as follows: given a contour Γ for the droplet on the solid (a closed curve, i.e. a

triple contact line), and the volume of the droplet (its change of volume either by evaporation near the contact line or by condensation from the supersaturated vapour is a relatively small effect on the time scale of the shape relaxation), one computes the shape of the droplet by solving (numerically in general) Laplace's equation for the surface of the droplet $z = z(x, y)$:

$$\frac{\partial^2 z}{\partial x^2}\left[1+\left(\frac{\partial z}{\partial y}\right)^2\right]+\frac{\partial^2 z}{\partial y^2}\left[1+\left(\frac{\partial z}{\partial x}\right)^2\right]-2\frac{\partial^2 z}{\partial x \partial y}\frac{\partial z}{\partial x}\frac{\partial z}{\partial y}=p\left[1+\left(\frac{\partial z}{\partial x}\right)^2+\left(\frac{\partial z}{\partial y}\right)^2\right]^{3/2}, \tag{4.2}$$

where p is the Lagrange multiplier. It allows the volume of the droplet consistent with the Dirichlet boundary condition $z = 0$ on Γ to be imposed. This method of solution corresponds to the assumption that the process of the relaxation of the drop surface controlled by the very small hydrodynamic time scale t_e is much faster that the contact line motion controlled by the (large) time scale t_b/K. The solution of this (well posed) mathematical problem for $z(x, y)$ does not satisfy in general the Young–Dupré condition $\theta = \theta_{eq}$ for this contact angle. It gives *a priori* a non-constant value, $\theta(s)$, along Γ, a function of the curvilinear abscissa such that

$$\cos\theta(s) = \left[1+\left(\frac{\partial z}{\partial x}\right)^2+\left(\frac{\partial z}{\partial y}\right)^2\right]^{-1/2}\Bigg|_{z=0}. \tag{4.3}$$

The next step consists in using a mobility relation for the slow dynamics of the contact line, that in general takes the form

$$v_n = K\frac{\sigma}{\eta}F(\theta, \theta_{eq}), \tag{4.4}$$

where σ/η is the molecular velocity scale, of the order of the velocity obtained from the viscosity/capillarity balance, and K is the (small) Arrhenius factor introduced before. F is a non-dimensional function of the contact angle, of order 1 and equal to zero at equilibrium, when $\theta = \theta_{eq}$. In this framework, the driving force for the contact line motion is the difference between the actual value of the contact angle and its equilibrium value. The velocity v_n is the local speed of the contour, perpendicular to it along the solid plane, driven by evaporation, not by fluid motion. This kind of relationship is not new of course, and expressions like

$$F \propto (\cos\theta_{eq} - \cos\theta) \tag{4.5}$$

have been written before.

It is a major endeavour, far beyond the scope of the present work, to study in detail the specific problem of droplet merging in this theoretical (and well defined) framework. In particular, a complication arises because the droplet contour is receding in some places and advancing elsewhere. The advancing motion involves condensation at the drop foot instead of evaporation during receding. Since there is no potential barrier for the condensing molecules (unless there is a film barrier on the surface of the liquid), one expects advancing to happen at molecular speed, with $K \approx 1$. However, if there are receding parts on Γ, the slowest receding process still dominates the whole relaxation. Indeed, one expects that when two droplets merge, the major effect will be a receding motion of the contour, that is much larger at the beginning than at the end, when equilibrium is reached.

In what follows, we shall sketch the analysis of the simplest situation, and assume

that the droplet is circular and recedes from a large spherical cap to its equilibrium shape with a smaller contact circle. Indeed, there is no change of shape of the droplet in this very simple case, contrary to what happens in the experiments. (This question of the shape change is discussed in detail by Nikolayev & Beysens 2001.) For circular droplets, the solution of Laplace's equation is simple, and yields the following value (constant along Γ, a circle now) for θ:

$$\theta = \arcsin\left(\frac{r}{R}\right), \tag{4.6}$$

where we consider contact angles smaller than $\pi/2$, as in the experiments. The radius r is the radius of the contour Γ, and R is the radius of curvature of the droplet surface (a spherical cap in the present case). The radii r and R are related by the condition for the drop volume:

$$V = \frac{\pi}{3}\left(R - \sqrt{R^2 - r^2}\right)\left[r + R^2 - R\sqrt{R^2 - r^2}\right]. \tag{4.7}$$

Equation (4.4) yields an 'explicit' equation of motion for $r(t)$:

$$\frac{\mathrm{d}r}{\mathrm{d}t} = K\frac{\sigma}{\eta}F(\theta(r), \theta_{eq}). \tag{4.8}$$

This equation is explicit because $\theta(r)$ can in principle be obtained from the volume condition. We shall make another simplifying assumption, namely that the contact angle is small, so that R is much larger than r, an assumption that results in

$$V \approx \frac{\pi r^4}{4R}. \tag{4.9}$$

The contact angle becomes $\theta \approx r/R \approx 4V/(\pi r^3)$. The equation of motion for r then reads

$$\frac{\mathrm{d}r}{\mathrm{d}t} = K\frac{\sigma}{\eta}F\left(\theta(r) = \frac{4V}{\pi r^3}, \theta_{eq}\right). \tag{4.10}$$

Assuming now that the function F is linear in $\theta - \theta_{eq}$ when this difference is small, one obtains

$$\frac{\mathrm{d}r}{\mathrm{d}t} = K\frac{\sigma}{\eta}\left(\frac{4V}{\pi r^3} - \theta_{eq}\right). \tag{4.11}$$

Note that there is a positive sign in front of the right-hand side in the equation above: when the contact line is receding, θ is less than its equilibrium value, making $[4V/(\pi r^3) - \theta_{eq}]$ negative, so that r decreases. This equation can be integrated explicitly, yielding a cumbersome expression. To simplify the calculation, let us introduce the non-dimensional quantity $\omega = r/R^*$, which becomes equal to 1 when the contact angle reaches its equilibrium value. The equilibrium drop radius is $R^* = (4V/\pi\theta_{eq})^{1/3}$. The time dependence of ω follows from the implicit relation

$$\int \frac{\mathrm{d}\omega\omega^3}{1 - \omega^3} = -\frac{w}{\pi R^*}t, \tag{4.12}$$

where $w = K\sigma/\eta$ is the typical speed of the contact line that includes the Arrhenius factor K. The integration over ω can be performed. We shall detail only the asymptotic approach to equilibrium, corresponding to ω becoming close to 1 from above:

$$\omega \approx 1 + C\exp\left(-\frac{3wt}{\pi R^*}\right), \tag{4.13}$$

where C is a constant that depends on the initial condition. It is interesting to note that this simplified calculation allows the exponential decay observed in the experiments to be recovered. With $K \sim 10^{-8}$, the relaxation time

$$t_c = \frac{\pi}{3}\frac{R^*}{w} = \left(\frac{\pi}{3}\frac{\eta}{K\,\sigma}\right) R^* \tag{4.14}$$

is almost of the same order as in the experiments.

5. Concluding remarks

The surprising finding that the relaxation of coalescing drops on a substrate can occur with a typical time scale that is many order of magnitude larger than the bulk hydrodynamics is a spectacular demonstration of the strong dissipation that occurs in the motion of the triple (solid–liquid–gas) contact line. We have good reason to believe that this dissipation is due to a gas–liquid phase transition at the portion of the vapour–liquid interface adjacent to the triple line. This dissipation introduces a very small $K \sim 10^{-8}$ Arrhenius factor in the relation between the driving force and the contact line velocity. We believe that the dissipation appears when the contact line recedes so that local evaporation takes place. Further theoretical and experimental work seems necessary to fully describe the evolution of such a coalescence phenomenon.

We thank the CEA/DAM in Limeil for their help with the surface coating.

REFERENCES

Anderson, D. M. & Davis, S. H. 1994 Local heat flow near contact lines. *J. Fluid. Mech.* **268**, 231–265.

Anderson, D. M. & Davis, S. H. 1995 The spreading of volatile liquid droplets on heated surfaces. *Phys. Fluids* **7**, 248–264.

Beysens, D. 1995 The formation of dew. *Atmos. Res.* **39**, 215–237.

Beysens, D., Steyer, A., Guenoun, P., Fritter, D. & Knobler, C. M. 1991 How does dew form. *Phase Transitions* **31**, 219–246.

Blake, T. D. & Haynes, J. M. 1969 Kinetics of liquid/liquid Displacement. *J. Colloid Interface Sci.* **30**, 421–423.

Dussan V., E. B. & Davis, S. H. 1986 Stability in systems with moving contact lines. *J. Fluid Mech.* **173**, 115–130.

Eggers, J. 1998 Coalescence of spheres by surface diffusion. *Phys. Rev. Lett.* **80**, 2634–2637.

de Gennes, P.-G. 1985 Wetting: statics and dynamics. *Rev. Mod. Phys.* **57**, 827–863.

Hocking, L. M. 1994 The spreading of drops with intermolecular forces. *Phys. Fluids* **6**, 3224–3228.

Nikolayev, V. S. & Beysens, D. 1997 Hydrodynamically limited coalescence. *Phys. Fluids* **9**, 3227–3234.

Nikolayev, V. S. & Beysens, D. A. 1999 Boiling crisis and non-equilibrium drying transition. *Europhys. Lett.* **47**, 345–351.

Nikolayev, V. S. & Beysens, D. A. 2001 Relaxation of nonspherical sessile drops towards equilibrium. *Phys. Rev.* E in press.

Nikolayev, V. S., Beysens, D. & Guenoun, P. 1996 New hydrodynamic mechanism for drop coarsening. *Phys. Rev. Lett.* **76**, 3144–3148.

Nikolayev, V. S., Beysens, D. A., Lagier, G.-L. & Hegseth, J. 2001 Growth of a dry spot under a vapour bubble at high heat flux and high pressure. *Intl J. Heat Mass Transfer* **44**, 3499–3511.

Pomeau, Y. 2000 Representation of the moving contact line in the equations of fluid mechanics. *C. R. Acad. Sci.* IIb **238**, 411–416.

Seppecher, P. 1996 Moving contact lines in the Cahn-Hilliard theory. *Intl J. Engng Sci.* **34**, 977–992.

Steyer, A., Guenoun, P. & Beysens, D. 1992 Spontaneous jump of droplets. *Phys. Rev. Lett.* **68**, 64–66.

Wayner, P. C. 1993 Spreading of a liquid film with a finite contact angle by the evaporation/condensation process. *Langmuir* **9**, 294–299.

Yiantsios, S. G. & Davis, R. H. 1991 Close Approach and Deformation of Two Viscous Drops due to Gravity and van der Waals Forces. *J. Colloid Interface Sci.* **144**, 412–433.

Zhao, H. & Beysens, D. 1995 From droplet growth to film growth on a heterogeneous surface: condensation associated with a wettability gradient. *Langmuir* **11**, 627–634.

PHYSICAL REVIEW E, VOLUME 65, 046135

Relaxation of nonspherical sessile drops towards equilibrium

Vadim S. Nikolayev*,† and Daniel A. Beysens†
CEA-DSM-DRFMC-Service des Basses Températures/ESEME, CEA Grenoble, Grenoble, France
(Received 5 April 2001; revised manuscript received 25 October 2001; published 10 April 2002)

We present a theoretical study related to a recent experiment on the coalescence of sessile drops. The study deals with the kinetics of relaxation towards equilibrium, under the action of surface tension, of a spheroidal drop on a flat surface. For such a nonspherical drop under partial wetting conditions, the dynamic contact angle varies along the contact line. We propose a new nonlocal approach to the wetting dynamics, where the contact line velocity depends on the geometry of the whole drop. We compare our results to those of the conventional approach in which the contact line velocity depends only on the local value of the dynamic contact angle. The influence on drop dynamics of the pinning of the contact line by surface defects is also discussed.

DOI: 10.1103/PhysRevE.65.046135 PACS number(s): 05.90.+m, 68.08.Bc, 68.03.Cd

I. INTRODUCTION

At first glance, the motion of the gas-liquid interface along the solid surface is a purely hydrodynamic problem. However, it attracted significant attention from the physicists since the work [1], which showed an unphysical divergence that appears in the hydrodynamic treatment if a motion of a wedge-shaped liquid slides along the solid surface. The reason for this divergence lies in the no-slip condition (i.e., zero liquid velocity) at the solid surface. Being so common in hydrodynamics, this boundary condition is questionable in the vicinity of the contact line along which the gas-liquid interface joins the solid. In the absence of mass transfer between the gas and the liquid, the no-slip condition requires zero velocity for the contact line that is supposed to be formed of the liquid molecules in the contact with the solid. It means that, for example, an oil drop cannot move along the glass because of the no-slip condition. Of course, this contradicts the observations.

The experiment [2] demonstrated that the velocity on the liquid-gas interface is directed towards the contact line during the contact line advance. The authors interpreted this result by the rolling (caterpillar) motion of the drop [3]. However, later theoretical study [4] shows that such a motion is compatible with the no-slip condition on the nondeformable solid surface only for the contact angles close to 180°.

The justification of the no-slip condition is well known [5]: it is the excess of the attractive force between the solid and the liquid molecules over the force between two liquid molecules. This attraction has a tendency to prevent the motion of the liquid molecules adjacent to the solid. Obviously, the same forces resist when these molecules are forced to move. In other words, some relatively large (with respect to viscous dissipation) energy should be spent for this forcing.

Numerous microscopic theories (see, e.g., [5–12]) propose different phenomena as to be responsible for the contact line motion. However, no general theory has been agreed upon. This situation is partly due to the scarceness of the information that can be extracted from the experiments. Most of them deal with either drops with cylindrical symmetry (circular contact lines) or the climbing of the contact line over a solid immersed into a liquid (straight contact line). In these experiments, the contact line velocity v_n measured in the normal direction does not vary along the contact line on a macroscopic scale larger than the size of the surface defects. The experiments with nonspherical drops where such a variation exists can give additional information. This information can be used to test microscopic models of the contact line motion. To our knowledge, there are only two kinds of investigated situations that feature the nonspherical drops. The first one is the sliding of the drop along an inclined surface [13]. The second concerns the relaxation of the sessile drops of complicated shape towards the equilibrium shape of spherical cap. This latter case was studied experimentally in [6] for water drops on silanized silicon wafers at room temperature. The present paper deals with this second case.

The principal results of [6] can be summarized as follows.

(i) The relaxation of the drop from the elongated shape towards the spherical shape is exponential. The characteristic relaxation time τ is proportional to the drop size. The drop size can be characterized by the contact line radius R^* at equilibrium when the drop eventually relaxes towards a spherical cap.

(ii) The dependence of τ on the equilibrium contact angle θ is not monotonous, $\tau(30°)<\tau(53°)$ and $\tau(53°)>\tau(70°)$.

(iii) The relaxation is extremely slow. The capillary number $\mathrm{Ca}=R^*\eta/(\tau\sigma)$ is of the order of 10^{-7}, where σ is the surface tension and η is the shear viscosity.

Since the motion is not externally forced, a small Ca shows that the energy dissipated in the vicinity of the contact line is much larger than in the bulk of the drop.

The contact line motion is characterized by the normal component v_n of its velocity. Many existing theories result in the following relationship between v_n and the dynamic contact angle θ:

$$v_n = v_c F(\theta, \theta_s), \tag{1}$$

where θ_s is the static contact angle, v_c is a constant charac-

*Email address: vnikolayev@cea.fr
†Mailing address: CEA-ESEME, Institut de Chimie de la Matière Condensée de Bordeaux, 87, Avenue du Dr. Schweitzer, 33608 Pessac Cedex, France.

teristic velocity and F is a function of two arguments, the form of which depends on the model used. For all existing models, the following relation is satisfied:

$$F(\theta,\theta_s)=-F(\theta_s,\theta), \tag{2}$$

which implies the trivial condition $F(\theta_s,\theta_s)=0$. It means simply that the line is immobile when $\theta=\theta_s$.

The theories of Voinov [11] and Cox [10] correspond to

$$F=\theta^3-\theta_s^3. \tag{3}$$

There are many theories (see, e.g., [5,7]) which result in

$$F=\cos\theta_s-\cos\theta. \tag{4}$$

In a recent model by Pomeau and co-workers [6,9], it is proposed that

$$F=\theta-\theta_s \tag{5}$$

with the coefficient v_c that depends on the direction of motion (advancing or receding) but not on the amplitude of v_n.

Since the drop evolution is extremely slow, the drop shape can be calculated using the quasistatic argument according to which at each moment the drop surface can be calculated from the constant curvature condition and the known position of the contact line. The major problem is how to find this position. Independently of the particular contact line motion mechanism, at least two approaches are possible. The first of them is the ''local'' approach [6], which consists in the determination of the position of a given point of the contact line from Eq. (1) where θ is assumed to be the *local* value of the dynamic contact angle at this point. Another nonlocal approach is suggested in Sec. II. Both of these approaches should give the same result when v_n does not vary along the contact line. However, we show that the result is different in the opposite case.

The influence of surface defects on the contact line dynamics is considered in Sec. III.

II. NONLOCAL APPROACH TO THE CONTACT LINE DYNAMICS

In this section we generalize another approach, suggested in [14], for an arbitrary drop shape. This approach postulates neither Eq. (1) nor a particular line motion mechanism. It simply assumes that the energy dissipated during the contact line motion is proportional to its length and does not depend on the direction of motion (advancing or receding). Then, at low contact line velocity, the leading contribution to the energy dissipated per unit time (i.e., the dissipation function) can be written in the form

$$T=\oint\frac{\xi v_n^2}{2}dl, \tag{6}$$

where the integration is performed over the contact line and ξ is the constant dissipation coefficient. According to the earlier discussed experimental results [6], the dissipation in the bulk is assumed to be much smaller than that in the vicinity of the contact line.

Since we assume that most dissipation takes place in the region of the drop adjacent to the contact line, our discussion is limited to the case where the prewetting film (that is observed for zero or very low contact angles) is absent. This situation corresponds to the conditions of the experiment [6] where the dropwise (as opposed to filmwise) condensation shows the absence of the prewetting liquid film. The above assumption also limits the description to the partial wetting case. This assumption is also justified by the experimental conditions under which it is extremely difficult to obtain macroscopic convex drops for the contact angles less than 30° because of the contact line pinning [6]. The main reason is that the potential energy U of the drop from Eq. (A6) in Appendix A goes to zero as the contact angle goes to zero. At small contact angles U is not large enough to overcome the pinning forces that originate from the surface defects, see Sec. III. Therefore, the macroscopic convex drops under consideration cannot be observed at small contact angles.

Generally speaking, the behavior of the drop obeys the Lagrange equation [15]

$$\frac{d}{dt}\left(\frac{\partial\mathcal{L}}{\partial\dot{q}_j}\right)-\frac{\partial\mathcal{L}}{\partial q_j}=-\frac{\partial T}{\partial\dot{q}_j}, \tag{7}$$

where the Lagrangian $\mathcal{L}=K-U$ is the function of the generalized coordinates q_j and of their time derivatives, which are denoted by a dot. The current time is denoted by t, K is the kinetic energy, and $U=U(q_j)$ is the potential energy. Since there is no externally forced liquid motion in this problem and the drop shape change is slow, we can neglect the kinetic energy by putting $\mathcal{L}=-U$. Then Eq. (7) reduces to

$$\frac{\partial U}{\partial q_j}=-\frac{\partial T}{\partial\dot{q}_j}, \tag{8}$$

the expression applied first to the contact line motion in [5].

The potential energy of a sessile drop is [14]

$$U=\sigma(A_{VL}-A_{SL}\cos\theta_{eq}), \tag{9}$$

where σ is the liquid surface tension, A_{VL} and A_{LS} are the areas of the vapor-liquid and liquid-solid interfaces, respectively, and θ_{eq} is the equilibrium value of the contact angle. We neglect the contribution due to the van der Waals forces because we consider macroscopic drops and large contact angles $\geqslant 30°$. For such drops the van der Waals forces influence the interface shape only in the very close vicinity of the contact line and this influence can be neglected.

In general the static contact angle θ_s is not equal to θ_{eq} because of the presence of the defects, a problem that will be treated in the Sec. III. Meanwhile, we assume that $\theta_s=\theta_{eq}$. The gravitational contribution is neglected in Eq. (9) because the drops under consideration are supposed to be small, with the radius much smaller than the capillary length. The volume of a sessile drop is fixed. Its calculation provides

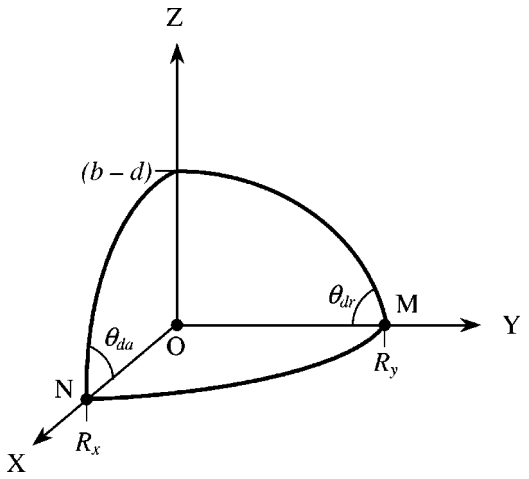

FIG. 1. Reference system to describe the 3D spheroidal cap. Only one quarter of it is shown. The surface is described by Eq. (11). The local contact angles at the points M and N are shown too.

us with another equation, which closes the problem provided that the shape of the drop surface is known. The drop shape is determined from the condition of the quasiequilibrium that results in the constant curvature of the drop surface.

Usually, the wetting dynamics are observed either for the spreading of droplets with the shape of the spherical cap, or for the motion of the liquid meniscus in a cylindrical capillary, or for the extraction of a solid plate from the liquid [5]. In all these cases, the contact line velocity v_n does not vary along the contact line and the dissipation function in the form of Eq. (6) results in the expression [14]

$$v_n=\frac{\sigma}{\xi}(\cos\theta_s-\cos\theta), \tag{10}$$

which is equivalent to Eq. (1), with the function F taking the usual form as in Eq. (4). One might think that this equivalence confirms the universal nature of this expression. In the following section we show that it is not exactly so because the nonlocal approach results in a different expression when v_n varies along the contact line.

Let us now apply the algorithm described above to the problem of drop relaxation. A shape for a nonspherical drop surface of constant curvature can be found only numerically. In order to treat the problem analytically, we approximate the drop shape by a spheroidal cap that is described in Cartesian (x,y,z) coordinate system by the equation

$$\frac{x^2}{a^2}+\frac{y^2+(z+d)^2}{b^2}=1, \tag{11}$$

at $z>0$, the plane X-Y corresponding to the solid surface. The symmetry of the problem allows only a quarter of the drop (see Fig. 1) to be considered. Since one of the parameters (a,b,d) is fixed by the condition of the conservation of the drop volume that can be calculated as

$$V=\frac{\pi}{3}\frac{a}{b}(2b^3-3b^2d+d^3), \tag{12}$$

there are only two free parameters left. The time-dependent parameters a and b can be taken as generalized coordinates. However, it is more convenient to use another set of parameters, R_x and R_y, which are the half axes of the ellipse that form the base of the drop (see Fig. 1), $R_y>R_x$. They are related to a and b by the equations

$$R_y^2+d^2=b^2 \quad \text{and} \quad R_xb=R_ya, \tag{13}$$

that follow from Eq. (11). At the end of the relaxation

$$R_x=R_y=R\sin\theta_s\equiv R^*, \tag{14}$$

where R is the final radius of curvature of the drop. Therefore, during the late stage

$$\begin{aligned} R_x&=R^*(1-r_x)\\ R_y&=R^*(1+r_y) \end{aligned} \tag{15}$$

with $|r_{x,y}|\ll 1$. Some points of the contact line advance, some points recede. The dynamic contact angle changes its value along the contact line. In particular, the point $N(R_x,0,0)$ in Fig. 1 advance and $M(0,R_y,0)$ recede. These points are extreme and their velocities have the maximum absolute values, positive for N and negative for M. The dynamic contact angles (θ_{da}: dynamic advancing contact angle in N and θ_{dr}: dynamic receding contact angle in M) also have the extreme values there. They can be found from the equations

$$\begin{aligned} \cos\theta_{dr}&=d/b,\\ \tan\theta_{da}&=R_y^2/(dR_x), \end{aligned} \tag{16}$$

that reduce for $r_x, r_y\ll 1$ to

$$\begin{aligned} \cos\theta_{dr}&=\cos\theta_s+\sin^2\theta_s(2+\cos\theta_s)(2r_y-r_x)/3,\\ \cos\theta_{da}&=\cos\theta_s-\sin^2\theta_s[(2+4\cos\theta_s)r_x-(4-\cos\theta_s)r_y]/3. \end{aligned} \tag{17}$$

Equation (8), written for the generalized coordinates r_x and r_y together with the expression for the dissipation function (see Appendix A), implies the set of equations

$$\begin{aligned} 3\dot{r}_x-\dot{r}_y&=\tau_0^{-1}(Br_y-Ar_x),\\ 3\dot{r}_y-\dot{r}_x&=\tau_0^{-1}(Br_x-Ar_y), \end{aligned} \tag{18}$$

where $\tau_0=\sigma R^*/\xi$ and the coefficients A and B are given by Eq. (A7) in Appendix A. The solutions of Eqs. (18) read

$$r_x(t)=[(r_x^{(i)}-r_y^{(i)})\exp(-t/\tau_s)+(r_x^{(i)}+r_y^{(i)})\exp(-t/\tau_n)]/2, \tag{19}$$

$$r_y(t)=[(r_y^{(i)}-r_x^{(i)})\exp(-t/\tau_s)+(r_x^{(i)}+r_y^{(i)})\exp(-t/\tau_n)]/2, \tag{20}$$

where $r_x^{(i)}$ and $r_y^{(i)}$ are the initial $(t=0)$ values for r_x and r_y, respectively, and the relaxation times

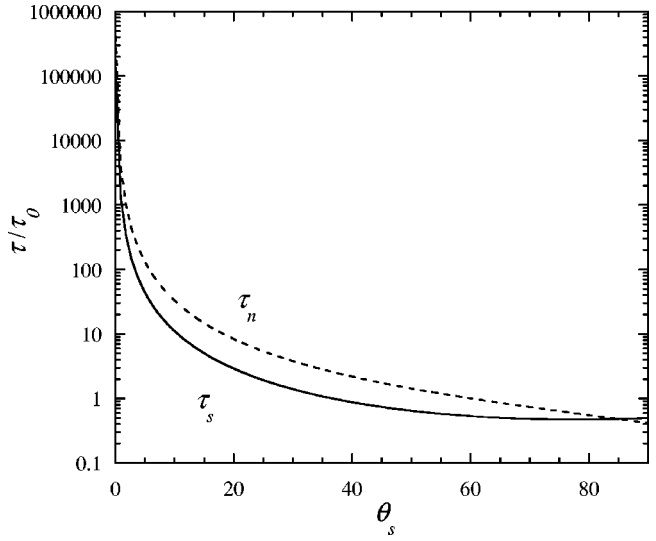

FIG. 2. The relaxation times $\tau_{s,n}$ versus the static contact angle θ_s.

$$\tau_s = \tau_0/[\sin^2\theta_s(2+\cos\theta_s)], \tag{21}$$

$$\tau_n = 45\tau_0(1+\cos\theta_s)/[(108+41\cos\theta_s+14\cos^2\theta_s + 17\cos^3\theta_s)(1-\cos\theta_s)]. \tag{22}$$

The variables r_x and r_y are defined in Eq. (15) in such a way that when $r_x^{(i)} = -r_y^{(i)}$ the drop surface remains spherical during its relaxation. One can see from Eqs. (19) and (20) that the evolution is defined entirely by the characteristic time τ_s (spherical) in this case. When $r_x^{(i)} = r_y^{(i)}$, only τ_n (nonspherical) defines the drop evolution. In the real experimental situation where $(r_x^{(i)} - r_y^{(i)}) \ll (r_x^{(i)} + r_y^{(i)})$, the relaxation time τ_n alone defines the relaxation of the drop as it follows from Eqs. (19) and (20). Therefore, τ_n should be associated with the experimentally observed relaxation time.

The functions $\tau_{s,n}(\theta_s)$ are plotted in Fig. 2 assuming that ξ is independent of θ_s. Clearly, both τ_s and τ_n increase monotonically with θ_s in agreement with the observed tendency for large contact angles. It is interesting to check whether or not by applying the local approach of Eq. (10) we recover the nonlocal result for v_n. This is easy to do for the case $r_x^{(i)} = r_y^{(i)}$, i.e., when $r_x = r_y$. In this case, the nonlocal model (18) implies $\dot{r}_x = -r_x/\tau_n$, and the contact line velocities at the points M and N are

$$v_n = -\frac{\sigma}{\xi}\frac{\tau_0}{\tau_n} r_x \quad \text{at the point } M, \tag{23}$$

$$v_n = \frac{\sigma}{\xi}\frac{\tau_0}{\tau_n} r_x \quad \text{at the point } N. \tag{24}$$

Since Eq. (17) results in

$$(\cos\theta_s - \cos\theta) = -\sin^2\theta_s(2+\cos\theta_s) r_x/3 \quad \text{at the point } M, \tag{25}$$

$$(\cos\theta_s - \cos\theta) = \sin^2\theta_s(5\cos\theta_s - 2) r_x/3 \quad \text{at the point } N, \tag{26}$$

the local approach (10) implies that

$$v_n = -\frac{\sigma}{\xi}\frac{1}{3}\sin^2\theta_s(2+\cos\theta_s) r_x \quad \text{at the point } M, \tag{27}$$

$$v_n = \frac{\sigma}{\xi}\frac{1}{3}\sin^2\theta_s(5\cos\theta_s - 2) r_x \quad \text{at the point } N. \tag{28}$$

The comparison of Eqs. (22)–(24) with Eqs. (27) and (28) show that the results of the local and the nonlocal approaches are different. However, one can verify that the results are the same in the limit of very small θ_s. For finite contact angles, the nonlocal approach is not equivalent to the local approach. The main difference can be summarized as follows. The v_n value that is obtained with our nonlocal approach can be presented in the form (1) common for the local approach. However, while the characteristic velocity v_c from Eq. (1) is constant in the local approach, it is *a function of the position on the contact line* in the nonlocal approach. Indeed, the comparison of Eqs. (23)–(26) with Eqs. (1) and (4) shows that

$$v_c = 3\frac{\sigma}{\xi}\frac{\tau_0}{\tau_n} \Big/ [\sin^2\theta_s(2+\cos\theta_s)] \quad \text{at the point } M, \tag{29}$$

$$v_c = 3\frac{\sigma}{\xi}\frac{\tau_0}{\tau_n} \Big/ [\sin^2\theta_s(5\cos\theta_s - 2)] \quad \text{at the point } N. \tag{30}$$

We do not expect our model to be a good description for the contact angles close to 90°. The reason is the limitation of the spheroid model for the drop shape. The spheroidal shape necessarily fixes $\theta_{dr} = 90°$ when $\theta_{da} = 90°$ independently of the contact line velocity, which is incorrect. In addition, the spheroid model does not work at all for $\theta_s > 90°$. One needs to find the real shape of the drop (which is defined by constant curvature condition) to overcome these difficulties.

In order to estimate the limiting value for θ_s for which the spheroid model works well we mention that the dynamic advancing and receding contact angles defined by Eq. (17) must satisfy the inequality $\theta_{dr} \leqslant \theta_s \leqslant \theta_{da}$. By putting $r_x^{(i)} = r_y^{(i)}$ in Eqs. (19) and (20) one finds that this inequality is satisfied when $\theta_s < 66°$. The last inequality provides us with the limit of the validity for the spheroidal model.

To conclude this section we note that our nonlocal approach to the dynamics of wetting is not equivalent to the traditional local approach. Both approaches allow the relaxation time to be calculated for a given contact angle provided that the contact angle dependence of the dissipation coefficient ξ is known. Additional experiments are needed to reveal which approach is the most suitable. Under the assumption that the $\xi(\theta_s)$ dependence (if any) is weak, we find that the relaxation time decreases with the contact angle.

This result explains the decrease of the relaxation time at large contact angles observed in [6]. We think that the opposite tendency observed for the small contact angles is related to the influence of the surface defects addressed in the following section.

III. INFLUENCE OF THE SURFACE DEFECTS ON THE RELAXATION TIME

The motion of the contact line in the presence of defects has been frequently studied (see [5] for a review). However, little is understood at the moment because the problem is very sophisticated. Most of its studies deal with the influence of the defects on the static contact line (see, e.g., [16]) when they are responsible for the contact angle hysteresis. The latter was studied in [17] and [18] for the wedge geometry that assumes the external forcing of the contact line. When the contact line moves under the action of a force f, it encounters pinning on the random potential created by surface defects. Thus, the motion shows the ''stick-slip'' behavior. It is characteristic for a wide range of physical systems where pinning takes place and is the basis of the theory of dynamical critical phenomena, in which the average contact line velocity is

$$v_n = v_c(f/f_c - 1)^{\beta}, \tag{31}$$

where the exponent β is universal and f_c is the pinning threshold. This expression is often applied (see [19], and references therein) to the contact line motion in the systems, where the geometry of the meniscus does not depend on the dragging force. However, the values of β vary widely depending on the experimental conditions and do not correspond to the theoretical predictions. The motion of the contact line during the coalescence of drops is even more complicated because the geometry of the meniscus is constantly changing. Therefore, application of the expression (31) is even more questionable in this situation.

In this section we employ the formalism developed in the preceding section in order to understand the influence of the surface defects on the relaxation time of the drop where the contact line is *not forced externally*. The surface defects are modeled by the spatial variation of the local density of the surface energy, which can be related to the local value of the equilibrium contact angle $\theta_{eq}(\vec{r})$ by the Young formula as was suggested in [17] to describe the static contact angles. The expression (9) can be rewritten for this case in the form

$$U = \sigma A_{VL} - \sigma \int_{(A_{LS})} \cos\theta_{eq}(\vec{r})\, d\vec{r}. \tag{32}$$

The contribution of the defects and, thus, the deformation δR_x of the contact line due to the defects is assumed to be small. Then, in the first approximation that corresponds to the ''horizontal averaging'' approximation from [17]

$$U = U^{(0)} + \Delta U. \tag{33}$$

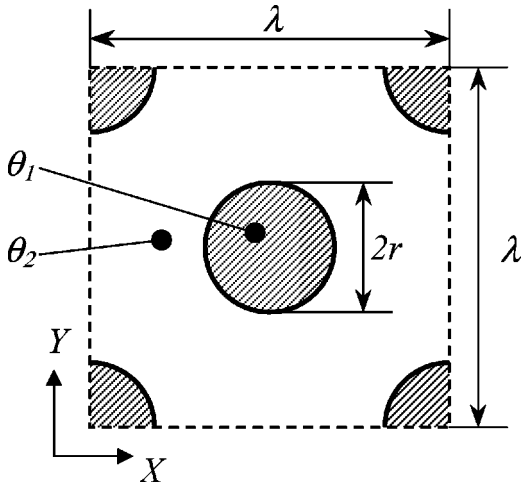

FIG. 3. Unit cell of the model defect pattern on the solid surface. The reference system and the values of the contact angle inside the round spots (θ_1) and outside them (θ_2) are also shown.

The superscript (0) means that the corresponding quantity is calculated for $\delta R_x = 0$ and for the constant value of the contact angle $\overline{\theta}_{eq}$ defined by the expression

$$\overline{\theta}_{eq} = \arccos\left[\frac{1}{A_{LS}^{(0)}}\int_{(A_{LS}^{(0)})} \cos\theta_{eq}(\vec{r})\, d\vec{r}\right]. \tag{34}$$

Then

$$U^{(0)} = \sigma A_{VL}^{(0)} - \sigma A_{LS}^{(0)} \cos\overline{\theta}_{eq}. \tag{35}$$

It can be shown that the first-order correction to this value, which appears due to the defects is

$$\Delta U = -\sigma \int_{(A_{LS}^{(0)})} [\cos\theta_{eq}(\vec{r}) - \cos\overline{\theta}_{eq}]\, d\vec{r}. \tag{36}$$

We accept the following model for defects because it is, on one hand, simple and, on the other hand, proven [17] to be a good description for the advancing and the receding contact angles in the approximation considered. The defects are supposed to be similar circular spots of radius r arranged in a *regular* spatially periodic pattern, λ being the spatial period, the same in both directions, see Fig. 3. The spots and the clean surface have the values of the equilibrium contact angle θ_1 and $\theta_2 < \theta_1$, respectively. For this pattern, Eq. (34) yields

$$\overline{\theta}_{eq} = \arccos[\varepsilon^2 \cos\theta_1 + (1-\varepsilon^2)\cos\theta_2], \tag{37}$$

the parameter ε^2 being the fraction of the surface covered by the defect spots. We consider the case $r < \lambda/4$ in the following. Then it is obvious from Fig. 3, that

$$\varepsilon^2 = 2\pi(r/\lambda)^2. \tag{38}$$

In the following, we will for simplicity treat a two-dimensional (2D) sessile drop, i.e., a liquid stripe of infinite

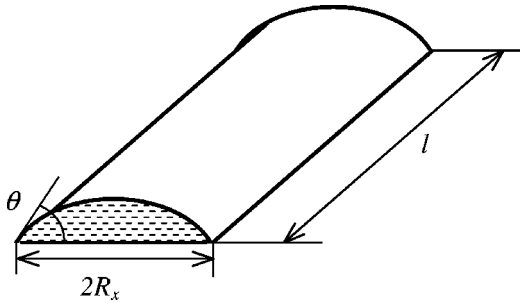

FIG. 4. Reference system to describe the 2D drop. The contact angle θ is shown too.

length, the cross section of which is the segment of a circle as shown in Fig. 4. The volume V of the stripe per its length l does not change with time,

$$V/l = \frac{R_x^2}{2\sin^2\theta}(\theta - \sin\theta\cos\theta), \tag{39}$$

where R_x is the half width of the stripe, see Fig. 4. The dynamic contact angle θ can be calculated from Eq. (39), provided that R_x is known. It can be shown by the direct calculation of $U^{(0)}$, Eq. (35) and the dissipation function T, Eq. (6) that Eq. (8) with the substitution $q_j \to R_x$ reduces to the equation

$$\dot{R}_x = \frac{\sigma}{\xi}(\cos\overline{\theta}_{eq} - \cos\theta) - \frac{1}{2\,\xi l}\frac{d\Delta U}{dR_x}. \tag{40}$$

The first-order correction to the drop energy ΔU can be calculated from Eq. (36) by following the guidelines of [17]. Its explicit expression for the chosen geometry is given in Appendix B. The kinetics of the relaxation is shown in Fig. 5. The relaxation kinetics for the drop on the ideal substrate with the equilibrium value of the contact angle equal to the value of $\overline{\theta}_{eq}$ is also shown for comparison. The half width of the drop on the ideal substrate relaxes to its equilibrium value R^* that is related to the volume of the drop through Eq. (39) written for $\theta = \overline{\theta}_{eq}$ and $R_x = R^*$. We chose $R^*/\lambda = 100$ for Fig. 5.

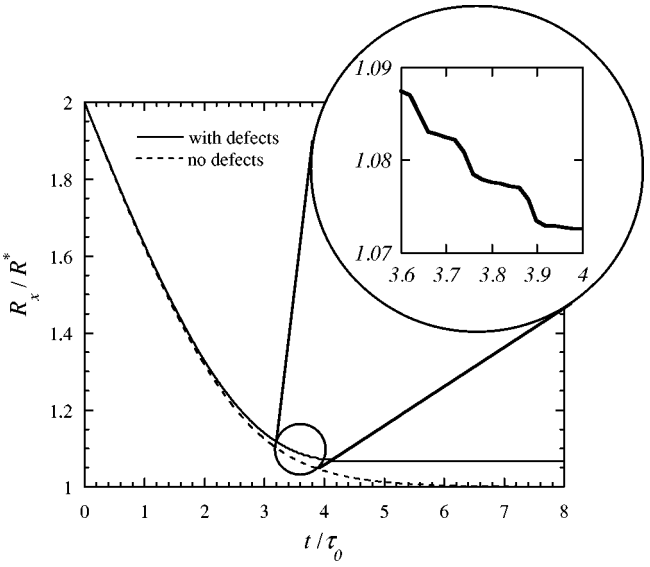

FIG. 5. Temporal evolution of the half width R_x of the drop with and with no defects with the same initial ($t=0$) value of $R_x = 2\,R^*$ and for $R^* = 100\lambda$ and $\overline{\theta} \approx 55°$. The latter value corresponds to the defect radius $r = 0.2\lambda$, $\theta_1 = 70°$, and $\theta_2 = 50°$.

The stick-slip motion is illustrated in the inset in Fig. 5. Note that the contact line in its final position for the nonideal case is pinned in a metastable state so that the final 2D radius of the drop is larger than R^*. The final contact angle (the equilibrium receding contact angle), thus, differs from that for an ideal surface. Because the contact line is being stuck on the defects, its motion is slowed down. However, the presence of defects does not change strongly the relaxation time. It remains of the order of $\tau_0 = R^*\xi/\sigma$ because this deceleration is compensated by the acceleration during the slip motion. Figure 5 shows the impact of the defects on the relaxation. The relaxation time appears to be *smaller* in the presence of defects than in the ideal case (no defects) because the contact line is pinned by defects whereas it would have continued to move on ideal surface.

It should be noted that this model is just a first step towards the description of contact line kinetics on a nonideal substrate. In reality, the different portions of the contact line slip at different moments in time (cascades of slips are observed, e.g., in [19]). This means that the liquid flows in the direction parallel to the contact line to the distances much larger than the defect size, i.e., the first-order approximation is not adequate. The direction of this flow reverses frequently. This effect can lead to the expression as Eq. (31) and to a large relaxation time.

IV. CONCLUSIONS

This paper deals with two important issues concerning contact line dynamics. First, it discusses the local versus nonlocal approaches to contact line motion. While the local approach consists in postulating a direct relationship between the normal contact line velocity and the dynamic contact angle *at a given point of the contact line*, the nonlocal approach starts from a more general hypothesis about the form of the dissipation function of the droplet. These approaches give the same results for very small contact angles or for the normal contact line velocity that does not vary along the contact line, which is the case of a drop that has the shape of a spherical cap. In other cases (large contact angle, nonspherical drops) the results of these two approaches differ. We carried out calculations assuming that the drop surface is a spheroid. In reality, its surface is not a spheroid and has a constant curvature. More work is needed to overcome this approximation.

The second issue treated in this article is the influence of surface defects on contact line dynamics. In the approximation of a 2D drop, it is assumed that the contact line remains straight during its motion. In this approximation, the stick-slip microscopic motion does not influence the average dynamics strongly. The defects manifest themselves by changing the final position of the contact line by pinning it in a metastable state. Therefore, the relaxation is more rapid than

that on an ideally clean surface simply because it is terminated earlier.

APPENDIX A: DERIVATION OF THE DYNAMIC EQUATIONS FOR r_x AND r_y

We used the *MATHEMATICA*™ system for the analytical computations. We find first the dissipation function T. The contact line can be described by the equation

$$F(x,y)=0 \quad \text{with} \quad F(x,y)=\frac{x^2}{R_x^2}+\frac{y^2}{R_y^2}-1, \tag{A1}$$

where R_x and R_y are time dependent. By using the well-known formula of differential geometry $v_n=-\dot{F}/|\nabla F|$, the integral (6) can be written in an explicit form. In order to obtain the first-order approximation for T, one can use the expansion (15). We need to keep only the second-order terms. Since the integrand is a quadratic form with respect to $\dot{r}_x,\dot{r}_y$, one can put $r_x,r_y=0$ in it. The resulting expression can be integrated to obtain the explicit expression for the dissipation function

$$T=\frac{\xi\pi R^3\sin^3\theta_s}{8}(3\dot{r}_x^2+3\dot{r}_y^2-2\dot{r}_x\dot{r}_y). \tag{A2}$$

It is easy to find out that $T\geqslant 0$ always holds as it should be.

It is more difficult to obtain the drop interface area

$$A_{VL}=\int_{A_{SL}}\sqrt{1+\left(\frac{\partial z}{\partial x}\right)^2+\left(\frac{\partial z}{\partial y}\right)^2}\,dA, \tag{A3}$$

where the function $z=z(x,y)$ is defined by Eq. (11). After the integration over y, Eq. (A3) reduces to

$$A_{VL}=4b\int_0^{R_x}\arctan\left(\frac{b}{d}\sqrt{1-\frac{d^2}{b^2}-\frac{x^2}{a^2}}\right)\sqrt{1-\frac{x^2}{a^2}\epsilon}\,dx, \tag{A4}$$

where $\varepsilon=1-R_y^2/R_x^2\sim(r_x-r_y)\ll 1$. The subsequent development of the integrand into the series over ϵ and its integration term-by-term results in

$$A_{VL}=a\pi\left[2(b-d)-\frac{\epsilon}{6\,b^2}(2b^3-3b^2d+d^3)-\frac{\epsilon^2}{160\,b^4}(8\,b^5-15b^4d+10b^2d^3-3d^5)\right]. \tag{A5}$$

This expression can be developed into a series with respect to r_x,r_y by using Eqs. (12) (13)–(15). Its substitution into Eq. (9) leads to the explicit expression for U,

$$U=\sigma\pi R^2\left\{2-3\cos\theta_s+\cos^3\theta_s+\frac{\sin^2\theta_s}{8}\times[A(r_x^2+r_y^2)-2Br_xr_y]\right\}, \tag{A6}$$

where

$$A=[(288+491\cos\theta_s+374\cos^2\theta_s+107\cos^3\theta_s)\times(1-\cos\theta_s)]/[45(1+\cos\theta_s)],$$

$$B=[(72+409\cos\theta_s+346\cos^2\theta_s+73\cos^3\theta_s)\times(1-\cos\theta_s)]/[45(1+\cos\theta_s)]. \tag{A7}$$

It is easy to show that the expression in the square brackets in Eq. (A6) is positive for an arbitrary θ_s. It means that the function $U(r_x,r_y)$ has its minimum at the point $(r_x=0,r_y=0)$, i.e., for the drop that has the shape of the spherical cap. This result was expected.

The substitution of Eqs. (A6) and (A2) into Eq. (8) written for $q_j=(r_x,r_y)$ results in the set of Eqs. (18) and, thus, concludes their derivation.

APPENDIX B: EXPRESSION FOR THE FIRST-ORDER CORRECTION TO THE DROP ENERGY CAUSED BY DEFECTS

The accepted assumptions facilitate calculation of the $\Delta U(R_x)$. The resulting function is periodical with the period $\lambda/2$, so that for $r<\lambda/4$ it can be presented in the form

$$\frac{\Delta U}{2\sigma\rho\Delta c}=-\begin{cases}\varepsilon^2\rho-[r^2\arcsin(\rho/r)+\rho(r^2-\rho^2)^{1/2}]/\lambda, & 0\leqslant\rho<r\\ \varepsilon^2(\rho-\lambda/4), & r\leqslant\rho<\dfrac{\lambda}{2}-r\\ \varepsilon^2(\rho-\lambda/2)+\{r^2\arcsin[(\lambda/2-\rho)/r]+(\lambda/2-\rho)[r^2-(\lambda/2-\rho)^2]^{1/2}\}/\lambda, & \dfrac{\lambda}{2}-r\leqslant\rho<\dfrac{\lambda}{2},\end{cases} \tag{B1}$$

where ρ is the fractional part of $2R_x/\lambda$, multiplied by $\lambda/2$, and $\Delta c=\cos\theta_2-\cos\theta_1$. Since $R_x\gg\lambda$, the presence of defects generates many local minima of the function $U(R_x)$ near its global minimum. These minima represent the metastable states. According to this model, the contact line is pinned in the minimum closest to its initial position.

[1] C. Huh and L.E. Scriven, J. Colloid Interface Sci. **35**, 85 (1971).
[2] E.B. Dussan V and S.H. Davis, J. Fluid Mech. **65**, 71 (1974).
[3] The hydrodynamic flow calculations (see, e.g., [1,7,8]), which use other contact line motion models show that they are all compatible with these experiments.
[4] L. Mahadevan and Y. Pomeau, Phys. Fluids **327**, 155 (1999).
[5] P.-G. de Gennes, Rev. Mod. Phys. **57**, 827 (1985).
[6] C. Andrieu, D. A. Beysens, V. S. Nikolayev, and Y. Pomeau, J. Fluid Mech. **453**, 427 (2002).
[7] Y.D. Shikhmurzaev, Phys. Fluids **9**, 266 (1997).
[8] P. Seppecher, Int. J. Eng. Sci. **34**, 977 (1996).
[9] Y. Pomeau, C. R. Acad. Sci., Ser. IIb: Mec., Phys., Chim., Astron. **328**, 411 (2000).
[10] R.G. Cox, J. Fluid Mech. **168**, 169 (1986).
[11] O.V. Voinov, Fluid Dyn. **11**, 714 (1976).
[12] T.D. Blake and J.M. Haynes, J. Colloid Interface Sci. **30**, 421 (1969).
[13] E.B. Dussan V, J. Fluid Mech. **174**, 381 (1987).
[14] M.J. de Ruijter, J. De Coninck, and G. Oshanin, Langmuir **15**, 2209 (1999).
[15] L. D. Landau and E. M. Lifschitz, *Mecanique*, 3rd ed. (Mir, Moscow, 1969).
[16] A. Hazareesing and M. Mézard, Phys. Rev. E **60**, 1269 (1999).
[17] L.W. Schwartz and S. Garoff, Langmuir **1**, 219 (1985).
[18] P. Collet, J. De Coninck, F. Dunlop, and A. Regnard, Phys. Rev. Lett. **79**, 3704 (1997).
[19] E. Schäffer and P.-Z. Wong, Phys. Rev. Lett. **80**, 3069 (1998).

EUROPHYSICS LETTERS 15 December 2003

Europhys. Lett., **64** (6), pp. 763–768 (2003)

Equation of motion of the triple contact line along an inhomogeneous surface

V. S. Nikolayev(*) and D. A. Beysens

ESEME, Service des Basses Températures, DSM/DRFMC, CEA - Grenoble, France(**)

(received 23 May 2003; accepted in final form 9 October 2003)

PACS. 68.08.Bc – Wetting.
PACS. 05.40.-a – Fluctuation phenomena, random processes, noise, and Brownian motion.

Abstract. – The wetting flows are controlled by the contact line motion. We derive an equation that describes the slow time evolution of the triple solid-liquid-fluid contact line for an arbitrary distribution of defects on a solid surface. The capillary rise along a partially wetted infinite vertical wall is considered. The contact line is assumed to be only slightly deformed by the defects. The derived equation is solved exactly for a simple example of a single defect.

Introduction. – The wetting flows (where the triple solid-liquid-fluid contact line is present) are important for many practical applications ranging from the metal coating to the medical treatment of the lung airways. The contact line statics and dynamics attracted a lot of attention from the scientific community during the last decades. It became clear that the hydrodynamics in the region of the liquid wedge close to the contact line (which we will call CLR, Contact Line Region) differs from the hydrodynamics in the bulk of the liquid. Because of the contact line singularity [1], the fluid motion in the presence of the contact line appears to be much slower than without it. This difference can be accounted for by the introduction of the anomalously large energy dissipation inside the CLR [1].

For practical purposes, one needs to know the dynamics of the liquid surface influenced by this dissipation. This influence is especially strong in the very common case of i) low-viscosity fluids that ii) wet partially the solid with iii) no precursor film on it. In this case, the bulk dissipation is particularly small with respect to the large CLR dissipation [2]. The contact line motion is very slow and the liquid surface can be described in the quasi-static approximation [3]. The dissipation in the liquid (energy per unit time) can then be approximated by the dissipation in the CLR as [4]

$$\int \frac{\xi v_{\mathrm{n}}^2}{2} \mathrm{d}l, \tag{1}$$

where v_{n} is the normal component of the contact line velocity and the integration is performed along the contact line. The generalized dissipation coefficient ξ is a constant that is assumed to

(*) E-mail: vnikolayev@cea.fr
(**) Mailing address: CEA-ESEME, Institut de Chimie de la Matière Condensée de Bordeaux - 87 Avenue du Dr. Schweitzer, 33608 Pessac Cedex, France.

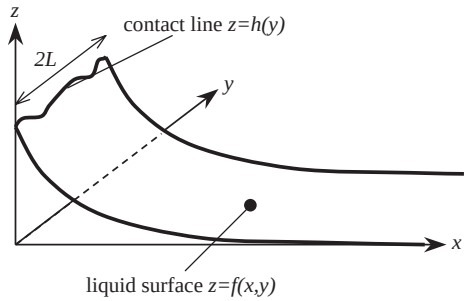

Fig. 1 – Reference system to describe the shape of the liquid surface.

be much larger than the liquid shear viscosity. Expression (1) assumes that the contribution of a piece of the CLR to the dissipation is proportional to the contact line length. Then the $v_{\rm n}^2$ term is leading for small $v_{\rm n}$. The dissipation coefficient ξ can be obtained, *e.g.*, from measurements of the kinetics of relaxation of an oval sessile drop toward its equilibrium shape (see [2], where it was found 10^7 times larger than the shear viscosity). It can also be obtained from the measurements of $v_{\rm n}$ and the dynamic contact angle θ by using the expression

$$v_{\rm n} = \frac{\sigma}{\xi}\big(\cos\theta_{\rm eq} - \cos\theta\big), \tag{2}$$

where $\theta_{\rm eq}$ is the equilibrium value of the contact angle and σ is the surface tension. Equation (2) is common for many contact line motion models. It can be shown [4] that eq. (2) follows from expression (1) for the cases where $v_{\rm n}$ does not vary along the contact line (*i.e.* for the contact line of constant curvature).

Usually, one is interested to know the displacement of the contact line (or its statistical properties in the case of the irregular solid) because its position serves as a boundary condition for the determination of the shape of the liquid surface. The recent articles on this subject show that no general approach to this problem is accepted. It is recognized generally [5–7] that the static contact line equation should be non-local because the contact line displacement at one point influences its position at other points through the surface tension. In dynamics, the local relations similar to eq. (2) were considered universal for a long time. In our previous work [8] we developed a non-local dynamic approach. We showed that if non-locality is taken into account, eq. (2) is not valid in the general case where $v_{\rm n}$ varies along the contact line. This variation can be due either to the initially inhomogeneous contact line curvature (like in [8]) or to a inhomogeneous substrate. In this letter we analyze this latter case. We use this non-local approach to derive an equation of motion for the very common case of the capillary rise of the liquid along a vertical solid wall with the account of the surface defects.

Derivation of the equation. – A Cartesian reference system xyz is chosen in such a way that the liquid surface far from the wall (defined by the yz plane) coincides with the xy plane, see fig. 1. The liquid surface described by the equation $z = f(x, y)$ is assumed to be weakly deformed so that

$$|\partial f/\partial x|,\ |\partial f/\partial y| \ll 1. \tag{3}$$

The contact line can be described by the equation $z = h(y) \equiv f(0, y)$. A piece of the liquid surface of length $2L$ in the y-direction (see fig. 1) is considered so that the final form for the equation of motion is found in the limit $L \to \infty$.

First, following the approach [5], we find the energy U of the liquid (per contact line length) as a functional of h. It is convenient to break U into two terms, $U = U_1 + U_2$. In approximation (3), the first term reads

$$U_1 = \frac{\sigma}{4L}\int_{-L}^{L} \mathrm{d}y \int_0^{\infty} \mathrm{d}x \left[\left(\frac{\partial f}{\partial x}\right)^2 + \left(\frac{\partial f}{\partial y}\right)^2 + \frac{f^2}{l_\mathrm{c}^2} \right], \tag{4}$$

where $l_\mathrm{c} = [\sigma/(\rho g)]^{1/2}$ is the capillary length, ρ is the liquid density and g is the gravity acceleration. The defects are accounted for in the second term [5,9]

$$U_2 = -\frac{\sigma}{4L}\int_{-L}^{L} \mathrm{d}y \int_0^{h(y)} c(y,z)\mathrm{d}z \tag{5}$$

by the fluctuations of the function $c(y,z)$ which is the difference of the surface energies (in σ units) of the gas-solid and liquid-solid interfaces at the point (y,z) of the solid surface. According to the Young expression, $c(y,z) = \cos[\theta_\mathrm{eq}(y,z)]$, where θ_eq is the local value of the equilibrium contact angle. When the surface defects exist, θ_eq is an arbitrary function of y, z.

In the quasi-equilibrium approximation, the surface shape f is found by minimization of the functional U resulting in the equation

$$\left(\partial^2 f/\partial x^2\right) + \left(\partial^2 f/\partial y^2\right) = f/l_\mathrm{c}^2, \tag{6}$$

which can be solved by separating the variables by using the boundary condition $f(x \to \infty) = 0$ and assuming that the function $f(x,y)$ is bounded at $y \to \pm\infty$. The solution reads

$$f = h_0 \exp[-x/l_\mathrm{c}] + \sum_{n=1}^{\infty} [a_n \cos(\pi n y/L) + b_n \sin(\pi n y/L)] \exp\left[-x\sqrt{l_\mathrm{c}^{-2} + \pi^2 n^2/L^2}\right], \tag{7}$$

where the coefficients h_0, a_n, b_n are the coefficients for the Fourier series

$$h(y) = f(x=0) = h_0 + \sum_{n=1}^{\infty} [a_n \cos(\pi n y/L) + b_n \sin(\pi n y/L)].$$

They can thus be related to $h(y)$ by the expressions

$$a_n = \frac{1}{L}\int_{-L}^{L} h(y) \cos\frac{\pi n y}{L}\mathrm{d}y, \qquad b_n = \frac{1}{L}\int_{-L}^{L} h(y) \sin\frac{\pi n y}{L}\mathrm{d}y, \qquad h_0 = \frac{1}{2L}\int_{-L}^{L} h(y)\mathrm{d}y. \tag{8}$$

One can notice that h_0 is simply the horizontally averaged displacement of the contact line. The back substitution of eq. (7) with h_0, a_n, b_n replaced by their values (8) into eq. (4) results in the functional

$$U_1 = \frac{\sigma}{4L^2}\int_{-L}^{L} \mathrm{d}y \int_{-L}^{L} \mathrm{d}y' h(y) h(y') \left[(2l_\mathrm{c})^{-1} + \sum_{n=1}^{\infty} \cos\frac{\pi n (y-y')}{L} \sqrt{\frac{1}{l_\mathrm{c}^2} + \frac{\pi^2 n^2}{L^2}} \right]. \tag{9}$$

Equation (5) together with eq. (9) define the functional $U[h(y)]$.

Now, one needs to calculate the dissipation function T (per unit length). In approximation (3), $v_n^2\,\mathrm{d}l \approx \dot{h}^2\,\mathrm{d}y$ in eq. (1) and

$$T = \frac{1}{2L}\int_{-L}^{L} \frac{\xi \dot{h}^2}{2}\mathrm{d}y, \tag{10}$$

where the dot means a time derivative. The equation of motion can be written in the quasi-static approximation as

$$\frac{\delta U[h]}{\delta h} = -\frac{\delta T[\dot{h}]}{\delta \dot{h}}\,, \tag{11}$$

where $\frac{\delta \dots}{\delta \dots}$ means variational derivative. By substituting eqs. (5), (9), (10) into eq. (11) and taking the variational derivatives, one obtains the dynamic equation of the contact line motion:

$$\dot{h}(y) = -\frac{\sigma}{\xi}\left[h_0/l_{\mathrm{c}} - c(y,h) + \frac{1}{L}\sum_{n=1}^{\infty}\int_{-L}^{L} \mathrm{d}y' h(y') \cos\frac{\pi n(y-y')}{L}\sqrt{l_{\mathrm{c}}^{-2} + \frac{\pi^2 n^2}{L^2}}\right], \tag{12}$$

where h and h_0 are assumed to be time dependent. The final form for the integral equation for the contact line motion can be obtained by taking the limit $L \to \infty$:

$$\dot{h}(y) = \frac{\sigma}{\xi}\left\{c(y,h(y)) - \frac{1}{\pi}\int_0^{\infty}\mathrm{d}p \int_{-\infty}^{\infty}\mathrm{d}y' h(y') \cos\left[p(y-y')\right]\sqrt{l_{\mathrm{c}}^{-2}+p^2}\right\}. \tag{13}$$

To treat the contact line equation, it is convenient to introduce the spatial fluctuation $h_1 = h - h_0$ and solve the equations for h_1 and h_0 separately. First, we derive the dynamic equation for h_0 by integrating eq. (12) over y from $-L$ to L, changing the integration order and dividing by $2L$. The integrals of all terms in the sum are zero and one obtains the following equation for h_0:

$$\dot{h}_0 = -\frac{\sigma}{\xi}(h_0/l_{\mathrm{c}} - c_0), \qquad c_0 = \frac{1}{2L}\int_{-L}^{L} c(y, h_1+h_0)\mathrm{d}y, \tag{14}$$

where c_0 is the (time-dependent) horizontal average of c. By subtracting eq. (14) from eq. (13) one obtains the equation for h_1 which has the same form as eq. (13), where c should be replaced by its fluctuation $c_1 = c(y, h_1 + h_0) - c_0$. Equation for h_1 simplifies in the Fourier space. By making use of the convolution theorem [10], one obtains

$$\dot{\tilde{h}}_1 = \frac{\sigma}{\xi}\left(\tilde{c}_1 - \tilde{h}_1\sqrt{l_{\mathrm{c}}^{-2}+k^2}\right), \tag{15}$$

where the tilde over a variable denotes its Fourier transform with the parameter k, *e.g.*,

$$\tilde{h}_1 = \tilde{h}_1(k,t) = \int_{-\infty}^{\infty} h_1(y,t)\exp[-iky]\mathrm{d}y. \tag{16}$$

This concludes the derivation of the equation of contact line motion. The stationary version of eq. (15) was derived first by Pomeau and Vannimenus [5].

The static contact line position is defined by the minimum of the energy $U[h(y)]$. However, it can exhibit multiple minima that correspond to the metastable states. In this case one needs to choose between them [9] to determine correctly the contact line position and corresponding local contact angle (which are both different in advancing and receding cases). In dynamics, eq. (13) provides us with a unique solution because the system "knows" the direction of the contact line motion and its history.

Simple example. – To show the relevance of this approach, we solve rigorously the contact line dynamics for a simple case of a single stripe-shaped defect at the wall,

$$c(y,z) = \begin{cases} c_d, & |y| \le \Delta, \\ c_s, & |y| > \Delta, \end{cases} \tag{17}$$

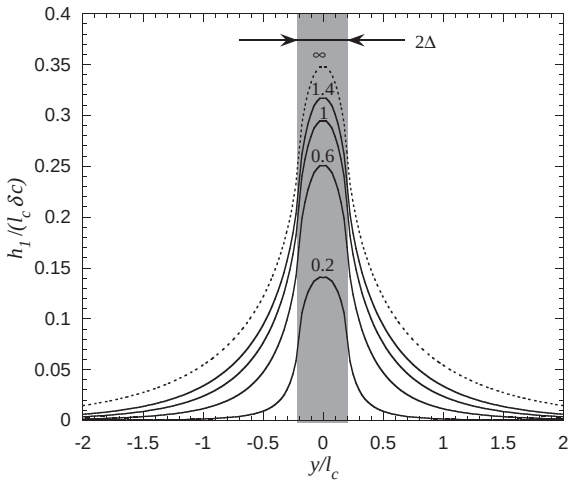

Fig. 2 – Time evolution of the deviation $h_1(y)$ of the contact line from its horizontally averaged value. The defect area (half-width of which is $\Delta = 0.2l_c$) is shadowed. The time values in the units $\xi l_c/\sigma$ are shown above the corresponding curve.

where $c_d, c_s \leq 1$ and Δ are constants. Consider first the contact line displacement at equilibrium described by the equations

$$h_0^{\rm eq} = c_0 l_c, \qquad \tilde{h}_1^{\rm eq} = \tilde{c}_1/\sqrt{l_c^{-2}+k^2}. \tag{18}$$

Notice that c_0 should be small enough so that f defined by eq. (7) satisfies conditions (3). Obviously, eq. (14) results in $c_0 = c_s$ and

$$\tilde{h}_1^{\rm eq} = \frac{2\delta c \sin k\Delta}{k\sqrt{l_c^{-2}+k^2}}\,, \tag{19}$$

where $\delta c = c_d - c_s$.

To show how this result relates to earlier approaches to the single-defect problem, we analyze first the limit $\Delta \to 0$. The inverse transform can easily be taken using the tables [11] and results in

$$h_1^{\rm eq}(y) = \frac{2\delta c\Delta}{\pi} K_0(y/l_c), \tag{20}$$

where $K_0(\cdot)$ is the modified Bessel function of zeroth order. One recognizes the result [12]. It leads to an unphysical divergence when $y \to 0$: $h_1^{\rm eq} \sim -\log(y)$ and a cut-off at small y is needed [1].

Using the present approach, one can understand the origin of this divergence. The limit $\Delta \to 0$ in the rigorous result (19) is equivalent to the limit $k \to 0$ since their product enters eq. (19). The asymptotics at $k \to 0$ in the Fourier transform corresponds [10] to the limit $y \to \infty$ in the original function, which means that eq. (20) is correct only at $y \to \infty$. However, it is not guaranteed that its asymptotics at $y \to 0$ is correct.

Let us return now to the rigorous expression (19). The Fourier transform (19) can be inverted analytically,

$$h_1^{\rm eq}(y) = \delta c[F(\Delta + y) + F(\Delta - y)]/\pi, \tag{21}$$

where $F(y) = \int_0^y K_0(y/l_c)\mathrm{d}y$. It is clear now that $h_1^{\mathrm{eq}}(y \to 0)$ remains finite, see the dotted curve in fig. 2.

The dynamic solution can be obtained the same way by using the initial condition $h(t = 0) = 0$:

$$\begin{aligned} h_0(t) &= c_s l_c\{1 - \exp[-t\sigma/(\xi l_c)]\}, \\ h_1(y,t) &= \delta c[F(\Delta + y) + F(\Delta - y) - G(\Delta + y, t) - G(\Delta - y, t)]/\pi, \end{aligned} \tag{22}$$

where

$$G(y,t) = \int_0^y K_0\Big(\sqrt{l_c^{-2}(y^2 + t^2\sigma^2\xi^{-2})}\Big)\mathrm{d}y.$$

The time evolution of $h_1(y)$ is shown in fig. 2. These curves can be compared to those obtained experimentally in [13–15], where the motion of the contact line over a single defect was studied. The comparison shows a good qualitative agreement. The results cannot be compared quantitatively since in each of these articles some parameters that enter eq. (22) (δc in particular) are missing.

Conclusion. – Equation (13) describes the spontaneous contact line motion for *arbitrary* distribution of surface energy given by the function $c(y, z)$ (provided $|c|$ is small enough so that the conditions (3) are satisfied). This function can be considered random and the equation becomes stochastic. It can be used to establish any statistical parameter of the contact line in dynamics. In particular, the collective effect of defects on the contact line motion can be studied.

In this work we solve a simple example where the defect properties do not vary along the average contact line velocity vector. In the general case, where the local value of the equilibrium contact angle (or of the function c) varies along this direction, the equation of the contact line motion becomes non-linear. More sophisticated methods are then needed to solve it.

* * *

We thank Y. Pomeau for the critical reading of this letter.

REFERENCES

[1] de Gennes P.-G., *Rev. Mod. Phys.*, **57** (1985) 827.
[2] Andrieu C., Beysens D. A., Nikolayev V. S. and Pomeau Y., *J. Fluid Mech.*, **453** (2002) 427.
[3] Pomeau Y., *C. R. Acad. Sci., Ser. IIb*, **328** (2000) 411.
[4] de Ruijter M. J., De Coninck J. and Oshanin G., *Langmuir*, **15** (1999) 2209.
[5] Pomeau Y. and Vannimenus J., *J. Colloid Interface Sci.*, **104** (1984) 477.
[6] Hazareesing A. and Mézard M., *Phys. Rev. E*, **60** (1999) 1269.
[7] Vannimenus J., *Physica A*, **314** (2002) 264.
[8] Nikolayev V. S. and Beysens D. A., *Phys. Rev. E*, **65** (2002) 046135.
[9] Schwartz L. W. and Garoff S., *Langmuir*, **1** (1985) 219.
[10] Korn G. and Korn T., *Mathematical Handbook for Scientists and Engineers* (Dover, New York) 2000.
[11] Bateman H. and Erdélyi A., *Tables of Integral Transforms*, Vol. **1** (McGrow-Hill, New York) 1954.
[12] Joanny J. F. and Robbins M. O., *J. Chem. Phys.*, **92** (1990) 3206.
[13] Nadkarni G. D. and Garoff S., *Europhys. Lett.*, **20** (1992) 523.
[14] Marsh J. M. and Cazabat A.-M., *Phys. Rev. Lett.*, **71** (1993) 2433; *Europhys. Lett.*, **23** (1993) 45.
[15] Paterson A., Fermigier M., Jenffer P. and Limat L., *Phys. Rev. E*, **51** (1995) 1291.

PHYSICAL REVIEW E **67**, 061202 (2003)

Fast heat transfer calculations in supercritical fluids versus hydrodynamic approach

V. S. Nikolayev,[1,*] A. Dejoan,[2,†] Y. Garrabos,[2] and D. Beysens[1]
[1]*DSM-DRFMC-Service des Basses Températures, CEA Grenoble, France, CEA-ESEME, Institut de Chimie de la Matière Condensée de Bordeaux, 87, Avenue du Dr. A. Schweitzer, 33608 Pessac Cedex, France*
[2]*CNRS-ESEME, Institut de Chimie de la Matière Condensée de Bordeaux, 87, Avenue du Dr. A. Schweitzer, 33608 Pessac Cedex, France*
(Received 29 October 2002; published 16 June 2003)

This study investigates the heat transfer in a simple pure fluid whose temperature is slightly above its critical temperature. We propose an efficient numerical method to predict the heat transfer in such fluids when the gravity can be neglected. The method, based on a simplified thermodynamic approach, is compared with direct numerical simulations of the Navier-Stokes and energy equations performed for CO_2 and SF_6. A realistic equation of state is used to describe both fluids. The proposed method agrees with the full hydrodynamic solution and provides a huge gain in computation time. The connection between the purely thermodynamic and hydrodynamic descriptions is also discussed.

DOI: 10.1103/PhysRevE.67.061202 PACS number(s): 44.35.+c, 05.70.Jk, 68.03.Cd, 64.60.Fr

I. INTRODUCTION

In fluids near their liquid-gas critical point, the characteristic size of the density fluctuations becomes larger than the characteristic size of the molecular structure. Consequently, the fluid behavior is ruled by fluctuations and not by its particular molecular structure. This implies that most fluids behave similarly near the critical point (like the 3D Ising model). This universality makes the study of near critical fluids very appealing. Due to their very low thermal diffusivity and to their very large thermal expansion and compressibility, the study of heat transfer in such fluids is particularly challenging. When such a fluid is confined in a heated cavity, a very thin hot boundary layer develops and induces a fast expansion that compresses the rest of the fluid. The resulting pressure waves spread at the sound velocity (i.e, very rapidly) and adiabatically compress the bulk of the fluid, which is therefore homogeneously heated. After several sound wave periods the pressure is already equilibrated and can be assumed to be nearly homogeneous along the cavity. During the initial stage of heating, this process of energy transfer, called "Piston effect" [1,2], is much more efficient than the usual diffusion scenario. Indeed, if the Piston effect were absent, the bulk of the fluid would remain at the initial temperature.

In the industrial domain, the Piston effect can be used to transfer heat much faster than by conduction. This feature can be readily applied to the development of heat exchangers under microgravity conditions [3,4] where heat transfer by natural convection is obviously not possible.

While the physical origin of the Piston effect is well understood, the calculations required to represent realistic experimental conditions are difficult because the inherent nonlinear dynamical behavior of such fluids is complicated by the highly nonlinear equations of state (EOS) used to describe real near-critical fluids. Two computational approaches have been suggested for confined fluids in absence of convection. In one of them, which we will refer as the "thermodynamic approach" [5], the Piston effect is taken into account by a supplementary term g, introduced in the heat conduction equation as follows:

$$\frac{\partial T}{\partial t} = \frac{1}{\rho c_p} \nabla \cdot (k \nabla \boldsymbol{T}) + g(T), \tag{1}$$

with

$$g(T) = \left(1 - \frac{c_v}{c_p}\right) \left(\frac{\partial T}{\partial p}\right)_\rho \frac{\partial p}{\partial t}, \tag{2}$$

where T is the local fluid temperature, c_v (c_p) the specific heat at constant volume (pressure) per unit mass, ρ the local density, and k the thermal conductivity of the fluid. One can note that the term $g(T)$ is only relevant near the critical point where $c_p \gg c_v$.

The fluid motions are neglected and the pressure p, assumed to be homogeneous, is only a function of time t. The pressure p is determined from the fluid mass conservation and computed via the nonlinear expression [5]

$$\frac{\partial p}{\partial t} = -\frac{\int_v (\partial \rho / \partial T)_p \partial T / \partial t \, dv}{\int_v \rho \chi_T \, dv}, \tag{3}$$

where $\chi_T = \rho^{-1}(\partial \rho / \partial p)_T$ is the isothermal compressibility and v the volume of the fluid sample. The resolution of Eq. (3) requires an iterative procedure for each time step. This consists in calculating the temperature *in the whole fluid volume* using Eqs. (1) and (2) for some trial value of p (and thus $\partial p / \partial t$) and determining the other thermodynamic parameters ($\rho, \chi_T, \ldots$) by an EOS

$$\Lambda(p, \rho, T) = 0. \tag{4}$$

*Email address: vnikolayev@cea.fr
†Present address: Aeronautics Department, Imperial College, Prince Consort Road, South Kensington, London, England, SW7 2BY, United Kingdom.

Subsequent computation of the *volume* integrals in Eq. (3) gives a value of $\partial p/\partial t$ from which the pressure p is corrected. The correction step is repeated until convergence. This approach has been extensively used by several groups [6,7] in one-dimensional (1D) calculation in conjunction with the restricted cubic EOS [8] and the finite difference numerical method. However, its extension to higher dimensions induces a large computational effort. First, it requires a sophisticated programming and, second, the computer resources rise steeply because the thermodynamic variables have to be evaluated at each grid point of the computational domain by means of the iterative procedure to solve Eq. (3).

Teams with expertise in theoretical hydrodynamics have developed a rigorous hydrodynamic approach [1] in which the Navier-Stokes and energy equations are coupled with the EOS. This set of equations has been solved analytically in 1D by asymptotic matching techniques [9] and also by direct numerical simulation (DNS) [10] via the finite volume method [11] both in 1D and 2D. For the sake of simplicity, the van der Waals EOS has been used in all these works. Although this simple EOS provides satisfactory qualitative results, accuracy can only be ensured by using a realistic EOS. However, as shown in the present study, inserting a realistic EOS into the hydrodynamic equations leads to a much more difficult computational task, which involves prohibitively large calculation times. For instance, to reach the final steady state in one of the 1D runs carried out for the cubic EOS in the present study, one requires about two months on a 800 MHz PC.

The purpose of this paper is twofold. We first formulate an approximate method, which is both simple and rapid (e.g., the same calculation cited above required only 20 s!), and then compare it with the DNS formalism. Second, since this work is the first one to use a realistic EOS for the DNS, we describe in detail the hydrodynamic approach for the near-critical fluids with a general EOS. We expect that this complete and unified description may be useful for the scientific community, as the hydrodynamic method is dispersed over many (some of them not easily accessible) publications.

The paper is organized as follows. In Sec. II we describe fast calculation method. Section III presents the hydrodynamic approach. Sec. IV deals with the comparison between both approaches. The conclusions are given in Sec. V.

II. FAST CALCULATION METHOD

The method is based on the thermodynamic approach, i.e., on the energy equation (1). However, a different pressure equation will be used instead of Eq. (3). While the latter equation integrates over the fluid *volume*, we are looking for a pressure equation that integrates only over the *boundaries* of the fluid domain. Such an equation would accelerate the iterative procedure. However, its advantage would not be decisive without an appropriate numerical method for Eq. (1) that should only require computation of the thermodynamic variables at the boundaries. Such a numerical method is called Boundary Element Method (BEM) and is broadly used in heat transfer problems. The BEM is expounded in Appendix A.

Several simplifications have to be introduced before presenting the formulation of the energy and pressure equations used in the present method. As stated in the Introduction, we are mainly interested in the description of the early stages of heating, i.e., on times of the order of the Piston effect time scale [12]. In this regime, the thermodynamic quantities $c_p, c_v, k, \ldots$ are constant in the bulk of the fluid and only vary in the very thin hot and cold boundary layers. Thus, the following assumptions can be made.

(1) The spatially varying parameters (c_p, c_v, k, etc.) in Eq. (1) can be replaced by the spatially homogeneous time-dependent values, which will be denoted hereafter by an overbar (e.g., $\overline{c_p}$). These values are calculated with the EOS using density $\langle\rho\rangle$ (where the brackets indicate the spatial average) and pressure $p=p(t)$. We note that density $\langle\rho\rangle$ is constant as the system is closed.

This assumption is equivalent to the statement that all these quantities should be calculated using the temperature value $\overline{T}=\overline{T}(t)$ obtained from the EOS for the pressure p and the density $\langle\rho\rangle$. The quantities calculated in such a way correspond to the overbar variables mentioned above. In general, for a thermodynamic quantity X, $\overline{X}\neq\langle X\rangle$.

(2) During the system evolution, the thermodynamic quantities are supposed not to vary sharply in time.

(3) The initial temperature T_0 is uniform.

Assumption (3) is made for simplicity and can be relaxed if necessary. However, the assumptions (1) and (2) are essential for this approach.

In the following section we formulate the energy and pressure equations that govern the kinetics of the supercritical fluid in a reduced gravity environment.

A. Energy equation

Using assumption (1) and the constancy of $\langle\rho\rangle$, one can write

$$dp=\overline{(\partial p/\partial T)_\rho}\,d\overline{T} \tag{5}$$

so that term (2) reduces to

$$\overline{g}(\overline{T})=\left(1-\frac{\overline{c_v}}{\overline{c_p}}\right)\frac{d\overline{T}}{dt}, \tag{6}$$

and Eq. (1) can be reduced to the equation

$$\frac{\partial\psi}{\partial t}=\overline{D}\nabla^2\psi. \tag{7}$$

The thermal diffusion coefficient $\overline{D}=\overline{k}/\langle\rho\rangle\overline{c_p}$ depends on $\overline{T}$, i.e., on time t only, and

$$\psi(\vec{x},t)=T(\vec{x},t)-T_0-E(\overline{T}) \tag{8}$$

with $\vec{x}$ the position vector and

$$E(\overline{T})=\int_{T_0}^{\overline{T}}\left(1-\frac{\overline{c_v}}{\overline{c_p}}\right)d\overline{T}. \tag{9}$$

The initial condition is $\psi|_{t=0}=0$ because according to assumption (3),

$$\overline{T}|_{t=0}=T_0. \tag{10}$$

Finally, a known dependence of $\overline{D}=D_d f(\overline{T})$, where D_d is a dimensional constant and f is a nondimensional function, allows time t to be replaced by an independent variable τ defined by the equation

$$\frac{d\tau}{dt}=f(\overline{T}), \tag{11}$$

whose initial condition can be imposed as $\tau|_{t=0}=0$. Since $\overline{T}$ is a function of t only, this initial-value problem is fully defined. The substitution of Eq. (11) into Eq. (7) results in the linear diffusion problem with the constant diffusion coefficient D_d

$$\frac{\partial\psi}{\partial\tau}=D_d\nabla^2\psi, \tag{12}$$

$$\psi|_{\tau=0}=0.$$

It can be solved with the BEM as shown in Appendix A.

Usually, the ''temperature step'' boundary condition has been applied for 1D problems. This heating process corresponds to a fluid cell, initially at a uniform temperature, which is submitted to a sudden increase of temperature at one of its boundaries, while the other is kept at the initial temperature (Dirichlet boundary conditions). This heating condition is physically unrealistic because the initial value for the heat flux at the heated boundary is infinite. Instead, in this work we use Neumann-Dirichlet boundary conditions: a heat flux q_{in} is imposed at one of the boundaries, while the initial temperature T_0 is maintained at the other boundary.

B. Boundary form of the pressure equation

Let us begin by writing the linearized relationship, valid under assumption (2):

$$\delta\rho=\left(\frac{\partial\rho}{\partial s}\right)_p\delta s+\left(\frac{\partial\rho}{\partial p}\right)_s\delta p, \tag{13}$$

where s is the fluid entropy per unit mass and δ stands for the variation of the thermodynamic quantity during the time interval δt. From the mass conservation it follows that $\langle\delta\rho\rangle=0$, and, from the pressure homogeneity that $\langle\delta p\rangle=\delta p$.

By averaging Eq. (13) one obtains

$$\left\langle\left(\frac{\partial\rho}{\partial s}\right)_p\delta s\right\rangle+\left\langle\left(\frac{\partial\rho}{\partial p}\right)_s\right\rangle\delta p=0. \tag{14}$$

The use of appropriate thermodynamic relationships leads to

$$\delta p=\frac{\left\langle\frac{\chi_T}{c_p}T\left(\frac{\partial p}{\partial T}\right)_\rho\rho\,\delta s\right\rangle}{\left\langle\frac{\chi_T}{c_p}\rho c_v\right\rangle}. \tag{15}$$

In order to use the second law of thermodynamics

$$\langle\rho\,\delta s\rangle=\frac{\delta Q}{v\overline{T}}, \tag{16}$$

where δQ is the total change of the amount of heat of the fluid, one needs to separate out the averages of the form $\langle YZ\rangle$ in Eq. (15). Under the assumption that Y (or Z) does not vary sharply over the fluid volume, the following approximation holds (see Appendix C):

$$\langle YZ\rangle\approx\langle Y\rangle\langle Z\rangle. \tag{17}$$

Among the quantities that appear in Eq. (15), only χ_T and c_p vary sharply near the critical point and could thus vary strongly across the fluid volume. However, only their ratio, which remains constant near the critical point, enters Eq. (15). Hence, the average of this ratio as well as the remainder averages of slowly varying quantities can be separated. By using the expression for the total heat change rate

$$\frac{\delta Q}{\delta t}=\int_A k\frac{\partial T}{\partial\vec{n}}dA, \tag{18}$$

where the right-hand side is simply the integrated heat flux supplied to the fluid through its boundary A (with $\vec{n}$ the external normal vector to it), one gets to the final expression

$$\frac{d\overline{T}}{dt}=\frac{1}{\langle\rho\rangle v c_v}\int_A k\frac{\partial T}{\partial\vec{n}}dA. \tag{19}$$

In the fast calculation method, Eq. (19) plays the role of the pressure equation (3). Equation (19) is both substituted directly into Eq. (6) and solved to get temperature $\overline{T}$, using initial condition (10). The obtained value for $\overline{T}$ is used to solve Eq. (11) and to calculate all the fluid properties. Note that $\overline{T}$ should not be confused with T from Eqs. (18) and (19). The spatially varying fluid temperature T has to be calculated with Eqs. (8) and (12).

Substituting $\overline{T}$ by $\langle T\rangle$, Eq. (19) coincides with the result of Onuki and Ferrell [2], which was derived by a different way. Equation (19), written in terms of $\langle T\rangle$, was employed recently [13,14] to simulate the gravitational convection in 2D by the finite difference method. However, the finite difference numerical method is not the most efficient for the computation of heat transfer problems.

III. HYDRODYNAMIC APPROACH

Analytical analysis as well as direct simulations were carried out in previous works. Bailly and Zappoli [15] have developed a complete hydrodynamic theory of density relax-

ation after a temperature step at the boundary of a cell filled with a nearly supercritical fluid in microgravity conditions. In Ref. [15] they describe the different stages of the fluid relaxation towards its complete thermodynamic equilibrium, covering the acoustic, Piston effect, and heat diffusion time scale. The analytical approach leans on the matched asymptotic expansions to solve the 1D Navier-Stokes equations for a viscous, low-heat-diffusing, near-critical van der Waals fluid (see Refs. [9] and [15]). The DNS of the Navier-Stokes equations were performed in 1D and 2D geometries. Some of them take into account gravity effects, as for example, the interaction of a near-critical thermal plume with a thermostated boundary [16]. Numerical results are also available on thermovibrational mechanisms [17].

To date the hydrodynamic approach has been solved for the classical, van der Waals, EOS. This EOS allows a considerable reduction in computational time when compared to the restricted cubic EOS. However, it does not provide a correct description of the real fluids. In particular, it fails to predict the critical exponents for the divergence laws of the thermodynamic properties. In the present work we use a more realistic cubic EOS to describe the fluid behavior in the near-critical region. Hereafter, we describe the methodology suitable for a general EOS.

A. Problem statement

The hydrodynamic description leads to the following set of equations:

$$\frac{d\rho}{dt}+\rho\vec{\nabla}\cdot\vec{u}=0, \tag{20}$$

$$\rho\frac{d\vec{u}}{dt}=-\vec{\nabla}p+\mu\nabla^2\vec{u}, \tag{21}$$

$$\rho\frac{de}{dt}=\vec{\nabla}\cdot(k\vec{\nabla}T)-p\vec{\nabla}\cdot\vec{u}+\Phi, \tag{22}$$

where e is internal energy per unit mass, $\vec{u}=(u_1,u_2,u_3)$ is the fluid velocity at the point $\vec{x}=(x_1,x_2,x_3)$,

$$\Phi=\mu\sum_{i,j}\left(\frac{\partial u_i}{\partial x_j}\frac{\partial u_j}{\partial x_i}+\frac{\partial u_i}{\partial x_j}\frac{\partial u_i}{\partial x_j}-\frac{2}{3}\frac{\partial u_i}{\partial x_i}\frac{\partial u_j}{\partial x_j}\right)$$

is the dissipation function due to the shear viscosity μ (the bulk viscosity is neglected). The operator d/dt is defined as

$$\frac{d}{dt}=\frac{\partial}{\partial t}+\vec{u}\cdot\vec{\nabla}. \tag{23}$$

The set of Eqs. (20)–(22) is closed by adding EOS (4).

B. c_v formulation

In the DNS, energy equation (22) is rewritten in terms of temperature T. This is achieved by expressing the internal energy as a function of density and temperature so that one can make use of the well-known relation

$$\frac{de}{dt}=\frac{1}{\rho^2}\left[p-T\left(\frac{\partial p}{\partial T}\right)_\rho\right]\frac{d\rho}{dt}+c_v\frac{dT}{dt}. \tag{24}$$

Then, by substituting Eqs. (20) and (22) into Eq. (24) one obtains

$$\rho c_v\frac{dT}{dt}=\vec{\nabla}\cdot(k\vec{\nabla}T)-T\left(\frac{\partial p}{\partial T}\right)_\rho\vec{\nabla}\cdot\vec{u}+\Phi. \tag{25}$$

Note that Eq. (25) involves c_v and not c_p as in thermodynamic equation (1). The "c_v formulation" is preferred to the "c_p formulation" because the much weaker near-critical divergence of c_v (in comparison with c_p) allows c_v assumed to be constant.

The boundary conditions for the Navier-Stokes equations are $\vec{u}=0$ at the walls. The initial conditions are given by $\vec{u}(t=0)=0$. For energy equation (25) the boundary and initial conditions are identical to those applied in energy equation (1) (cf. Sec. II). The values of the physical parameters used in the simulations are discussed in Appendix B.

C. Acoustic filtering

Heat transfer in supercritical fluid involves three characteristic time scales [12,18]: the acoustic time scale defined by $t_a=L/c_0$ (where c_0 is the sound velocity and L is the cell size), the diffusion time scale $t_D=L^2/D$ (D being the thermal diffusivity) and the Piston effect time scale defined by $t_{PE}=L^2/[D(c_p/c_v-1)^2]$, with $t_a\ll t_{PE}<t_D$. The present study is mainly concerned with time of the same order as the Piston effect time scale so that a fine description of the acoustic phenomena is not needed. This suggests that one can filter out the acoustic motions of the set of Eqs. (4), (20), (21), and (25) and retain only their integrated effects without altering the physics of our problem. The removal of the acoustic motions is achieved by applying the acoustic filtering method [19], which is broadly used in the computation of the low Mach number compressible Navier-Stokes equations because it avoids numerical instabilities when time steps, $\Delta t\gg t_a$, are used in the simulations. The following presents the main points of the acoustic filtering method.

The equation of momentum is first rewritten by choosing the sound velocity c_0 as the reference velocity scale and L/u_0 as the reference time scale (here u_0 is the characteristic velocity of large scale fluid motions, in our case $u_0=L/t_{PE}$). Using this time and velocity scale the Mach number $\mathrm{Ma}=u_0/c_0$ appears in the nondimensional momentum equation as follows:

$$\rho\left[\frac{\partial\vec{u}}{\partial t}+\mathrm{Ma}^{-1}(\vec{u}\cdot\vec{\nabla})\vec{u}\right]=-\frac{\mathrm{Ma}^{-1}p_c}{c_0^2\rho_c}\vec{\nabla}p+\frac{1}{\mathrm{Re}}\nabla^2\vec{u}, \tag{26}$$

where $\mathrm{Re}=\rho_c u_0 L/\mu$ is the Reynolds number, and the density and pressure are nondimensionalized by critical density ρ_c and critical pressure p_c taken as the reference values. For small Mach numbers, one can express the fluid variables as series of Ma,

$$\vec{u} = \mathrm{Ma}[\vec{u}^{(0)} + \mathrm{Ma}^2\vec{u}^{(1)} + o(\mathrm{Ma}^2)], \tag{27}$$

$$p = p^{(0)} + \mathrm{Ma}^2 p^{(1)} + o(\mathrm{Ma}^2). \tag{28}$$

While $\vec{u}$ in the left-hand side (lhs) of Eq. (27) is nondimensionalized with c_0, the term in the square brackets defines the velocity nondimensionalized with u_0. This explains the factor Ma in Eq. (27). The density and temperature are expanded like p in Eq. (28). By substituting series (27) and (28) into Eq. (26) and neglecting the terms of order $O(\mathrm{Ma})$, one obtains $\vec{\nabla} p^{(0)} = 0$, which means that $p^{(0)}$ depends on time only. By retaining $O(\mathrm{Ma})$ terms in Eqs. (20), (25), and (26) and $O(1)$ terms in EOS (4), one obtains the final (dimensional) form for the governing equations

$$\frac{d\rho^{(0)}}{dt} = -\rho^{(0)}\vec{\nabla}\cdot\vec{u}^{(0)}, \tag{29}$$

$$\rho^{(0)}\frac{d\vec{u}^{(0)}}{dt} = -\vec{\nabla}p^{(1)} + \mu\nabla^2\vec{u}^{(0)}, \tag{30}$$

$$\rho^{(0)}c_v^{(0)}\frac{dT^{(0)}}{dt} = -T^{(0)}\left(\frac{\partial p}{\partial T}\right)_\rho \vec{\nabla}\cdot\vec{u}^{(0)} + \vec{\nabla}\cdot(k\vec{\nabla}T^{(0)}), \tag{31}$$

$$\Lambda(p^{(0)}, \rho^{(0)}, T^{(0)}) = 0, \tag{32}$$

where $(p_c/c_0^2\rho_c)p^{(1)}$ is replaced by $p^{(1)}$ for the sake of compactness. The pressure term $p^{(1)}$ has to be interpreted as the dynamic pressure that makes the velocity field satisfy the continuity equation (29). This term reflects the contribution of the acoustic waves averaged over several wave periods to the total pressure field. One notes that the velocity scale c_0 is not present any more in Eqs. (29)–(32), which was the main purpose of the acoustic filtering.

The assessment of $p^{(0)}$ requires one more equation to close the set of Eqs. (29)–(32). This additional equation expresses the mass conservation:

$$\frac{1}{v}\int_v \rho^{(0)} dv = \langle\rho\rangle, \tag{33}$$

where $\langle\rho\rangle$ is a known constant.

In the following, the superscript (0) is dropped to conform to the notation of Sec. II.

D. Numerical procedure

For the time integration, the first-order Euler scheme is used. Equations (29)–(31) are solved by the iterative SIMPLER algorithm and by applying the finite volume method (FVM, see Appendix D) on each grid cell of the 1D cell. Near the walls the mesh is refined to properly resolve the very thin thermal boundary layers.

In the present work the thermodynamic variables are determined using the parametric EOS [8]. This uses two parameters r and θ, both depend on temperature T and density ρ. Therefore, one needs to solve two equations

$$\begin{aligned}\Lambda_1(r_i, \theta_i, T_i) &= 0,\\ \Lambda_2(r_i, \theta_i, p) &= 0\end{aligned} \tag{34}$$

instead of one Eq. (4) for each volume element i and time step.

The whole numerical procedure consists in solving by the Newton-Raphson method, at each time step, a set of equations that includes Eqs. (34), written for each volume element and Eq. (33). This makes a system of $2N+1$ equations to resolve, N being the total number of the volume elements. The local temperature T_i is given by the resolution of Eqs. (29)–(31) at each iteration of the SIMPLER algorithm for each time step, as described in Appendix D. For each value T_i the $2N+1$ (r_i, θ_i, p) variables are computed via system (34).

IV. RESULTS AND DISCUSSION

A brief analysis comparing the c_p and c_v formulations (1) and (31) of the energy equation allows us to gain more insight into the relation between the two approaches. Formally, Eqs. (1) and (31) become equivalent if the advection term

$$(\vec{u}\cdot\vec{\nabla})T \tag{35}$$

is added to lhs of Eq. (1). However, the equivalence of the two forms under which the pressure work appears [see second term of the lhs of Eqs. (1) and (31)] is not trivial and deserves to be detailed. At the early stage of the heating ($t < t_{PE}$) the velocity at the front of the cold boundary layer being very small, the velocity can be assumed to decrease linearly in the bulk cell as $\partial u/\partial x \simeq -u_{max}/L$, where u_{max} is the maximum velocity located at the front of the hot boundary layer and x the distance from the hot wall to the cold wall. The rate of temperature increase due to the pressure contribution in Eq. (31) can thus be written as follows:

$$-\frac{T}{\rho c_v}\left(\frac{\partial p}{\partial T}\right)_\rho \vec{\nabla}\cdot\vec{u} = \frac{T}{\rho c_v}\left(\frac{\partial p}{\partial T}\right)_\rho \frac{u_{max}}{L}. \tag{36}$$

By using the expression [12]

$$u_{max} = \frac{1}{T}\left(\frac{\partial T}{\partial p}\right)_\rho \frac{\delta Q}{A\,\delta t} \tag{37}$$

and Eqs. (18) and (19) one concludes that terms (36) and (6) are equivalent near the critical point, where $c_p \gg c_v$. One can note that in the hydrodynamic approach, the pressure work is directly related to the mass transfer from the hot boundary layer to the bulk fluid via the gradient velocity. It is then very important to asses properly the effect of the velocity field in order to compare the fast calculation and hydrodynamic methods. The above analysis has shown that the expressions of the pressure work is equivalent for both methods. Hence, the remaining potential interaction between the velocity and energy fields can manifest itself only through the advection term (35). This term is only relevant when, at the same spot of the fluid, both the fluid velocity and the temperature gradient are large. At the small times, $t < t_{PE}$,

the temperature gradients are confined very near the wall where the velocity remains small [18]. Later on, the velocity maximum shifts to the center of the cell where the temperature gradient is small. At very large times, $t>t_D$, the Piston effect is not efficient and the velocity tends to zero. We thus do not expect a strong influence of the advection effects on the temperature field. This will be confirmed by the results presented below. Note that the advection term cannot be neglected when the flux distribution over the heater surface is highly inhomogeneous. Hot jets [26] can be generated in this case.

The calculations have been performed for two fluids, CO_2 and SF_6, confined in a cell of length $L=5$ mm. The initial temperatures 1 K and 5 K above the critical point have been considered for CO_2. The computations related to SF_6 concern only the initial temperature 1 K above the critical point. The cell boundary situated at $x=0$ has been submitted to the constant heat flux $q_{in}=2$ W/m^2 (for $T_0=T_c+1$ K) and $q_{in}=9.5$ W/m^2 (for $T_0=T_c+5$ K) and the opposite boundary has been maintained at the constant temperature $T(x=L)=T_0$.

The time evolution of the temperature profiles and the temperature at the cell center $T_{center}=T(x=L/2)$ as well as the heat flux $q_{out}=-k[\partial T(x=L)/\partial x]$ are compared and analyzed. In the case of CO_2, the time evolution covers not only the Piston effect time scale t_{PE} but also the large diffusion time scale.

The set of Figs. 1–3 exhibit a very good qualitative agreement between the DNS and the fast calculation results. The thin boundary layers and the homogeneous enhancement of the temperature in the center cell are very well predicted. The quantitative comparison sets out two behaviors. On one hand, the flux q_{out} appears to fit very well with the DNS over the full time evolution, at the time scale t_{PE} as well as at the time scale t_D, see Figs. 2(b) and 3(b). On the other hand, the temperature at the cell center T_{center} tends to be lower than the DNS data. This discrepancy increases with time and is larger when the temperature is closer to the critical temperature [see Fig. 2(b) and Fig. 3(b)]. Both behaviors can be explained by considering how the thermal conductivity k is estimated in each method. In the hydrodynamic approach k is determined locally, whereas the fast calculation uses the spatial average value of k. Thus, keeping in mind that the thermal conductivity diverges when approaching the critical point, the increment in temperature near the heating surface tends to be smaller in the new method than in the DNS [see Fig. 2(a)]. At the opposite surface the temperature is fixed at the initial temperature and is closest to the bulk temperature so that the effect of averaging k is less influent in this region. One can note that the thermal diffusivity can be computed locally in the fast calculation method by applying the Kirchhoff substitution of the dependent variable ψ [defined by Eq. (8)] by $\phi=\int_0^{\psi}k(\psi)d\psi$.

A physical interpretation of the temperature $\overline{T}$, which was formally introduced in Sec. II, can now be given. Indeed, since in the fluid bulk (i.e., around the center of the cell) $\partial T/\partial x=0$ at $t<t_{PE}$, according to Eq. (1) we have $\partial T_{center}/\partial t=\overline{g}(\overline{T})$. As near the critical point $c_p \gg c_v$, Eq. (6) provides $\overline{g}(\overline{T})\approx\partial\overline{T}/\partial t$. Finally, one can conclude that $\overline{T}\approx T_{center}$. In other words, $\overline{T}$ can be considered as the bulk temperature.

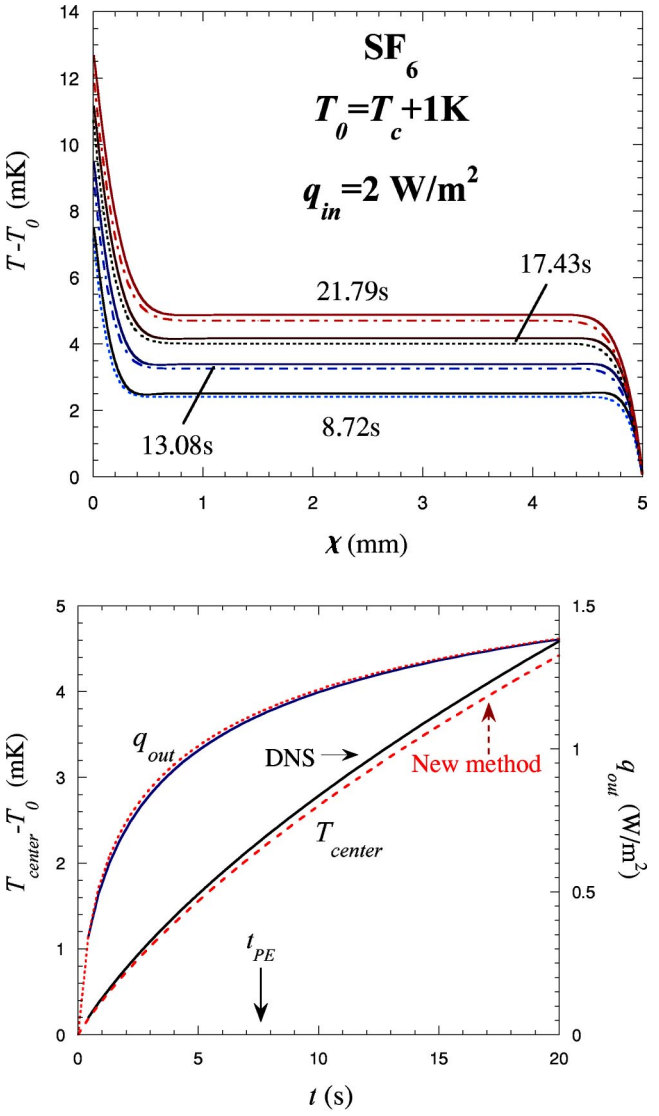

FIG. 1. (Color online) Comparison of two approaches for SF_6 at 1 K above T_c (reduced temperature 3.1×10^{-3}), $q_{in}=2$ W/m^2 and $\langle\rho\rangle=\rho_c$. Solid curves are the DNS results and the dotted curves are the new method results. (a) Spatial variation of the temperature at different times. (b) Time evolution of the temperature at the cell center and of the flux at the exit of the cell. The value of $t_{PE}=7.73$ s obtained with our EOS is shown by an arrow.

As a further remark, we note that for 1D Eq. (A1) could have been solved analytically by series expansion. Nevertheless, we prefer the use of the BEM for its generality and its possible extension to higher dimensions. We note that in 2D and 3D the BEM remains advantageous in resolving linearized problems when compared with other numerical methods. Its success is based on several factors. One of them is its numerical stability: the numerical solution of the integral equations is much more stable than that of the differential equations and allows the use of larger time steps. Another advantage consists in the possibility of determining analyti-

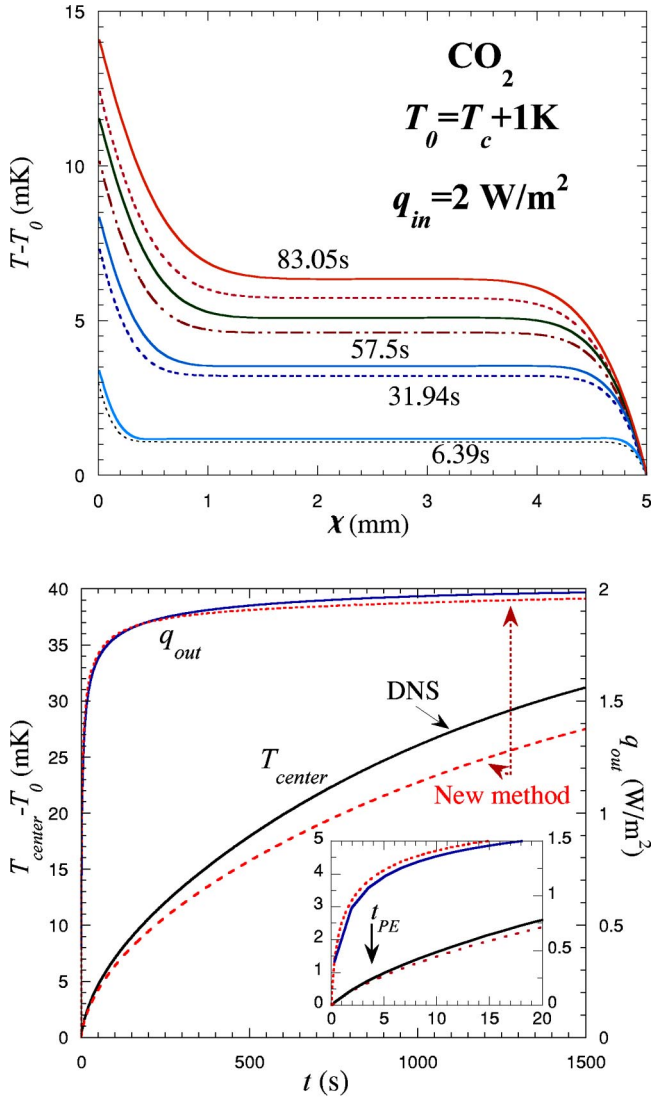

FIG. 2. (Color online) Comparison of the two approaches for CO_2 at 1 K above T_c (reduced temperature 3.3×10^{-3}), $q_{in}=2$ W/m^2 and $\langle\rho\rangle=\rho_c$. Solid curves are the DNS results and the dotted curves are the new method results. (a) Spatial variation of the temperature at different times. (b) Time evolution of the temperature at the cell center and of the flux at the exit of the cell. The value of $t_{PE}=3.45$ s obtained with our EOS is shown by an arrow in the inset that presents the short-time evolution.

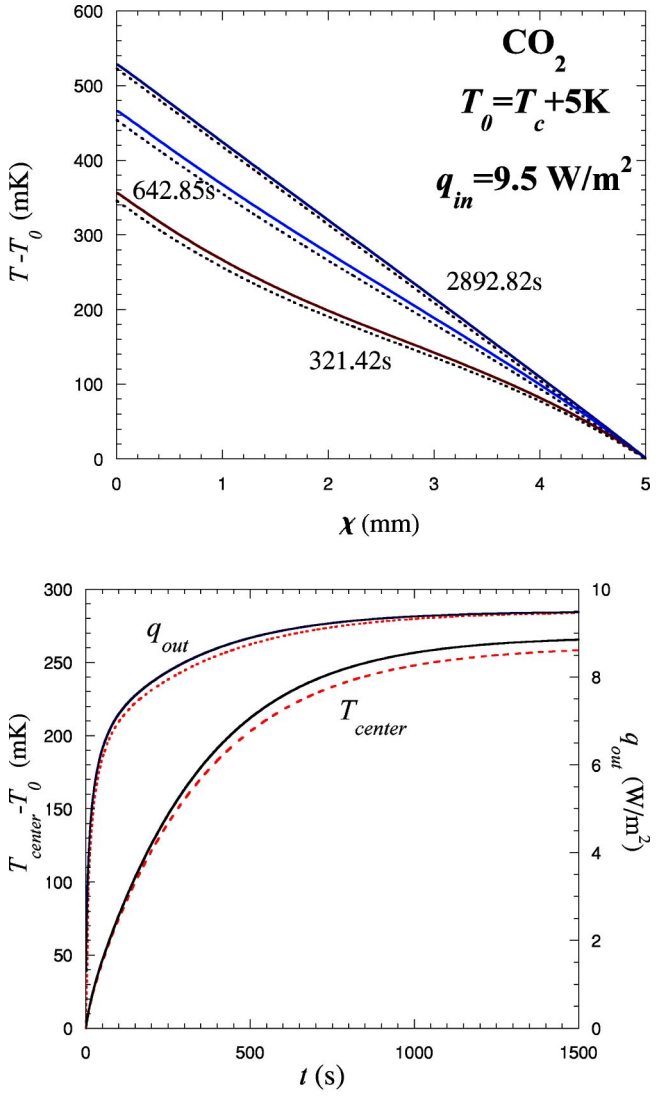

FIG. 3. (Color online) Comparison of two approaches for CO_2 at 5 K above the critical temperature (reduced temperature 1.6×10^{-2}), $q_{in}=9.5$ W/m^2 and $\langle\rho\rangle=\rho_c$. Solid curves are the DNS results and the dotted curves are the new method results. According to our EOS, $t_{PE}=25.67$ s. (a) Spatial variation of the temperature at different times. (b) Time evolution of the temperature at the cell center and of the flux at the exit of the cell.

cally the BEM coefficients, Eqs. (A6) and (A7). For 2D configurations, the diagonal coefficients G_{FF} and H_{FF} (which have the largest absolute value and thus are the most relevant) can be calculated analytically. The semianalytical integration can be used for the remaining coefficients [22,23].

V. CONCLUSIONS

In this work we propose a thermodynamic method for describing the heat transfer in supercritical fluids in absence of gravity effects. The method has been compared with the solution of the full hydrodynamic equations, showing an excellent agreement. In general, a thermodynamic approach leans on the possibility of expressing the pressure work independently of the velocity field. If so, the transfer of momentum does not need to be considered, allowing a large reduction in computational time. As an example, in calculations carried out for CO_2 and SF_6, the present thermodynamic method within minutes provided the complete evolution of the heat transfer process, while the direct numerical simulation of the full hydrodynamic equations required weeks of CPU time.

Compared to previous thermodynamic methods [5], the fast calculation method presented here does not require the evaluation of the variables at each cell of the computation domain. This fact ensures a much better performance. Moreover, the proposed method offers the possibility to explicitly include the thermal behavior of the material vessel containing the fluid by taking into account the heat conduction along the solid walls, see Ref. [4].

The direct numerical simulation of the flow has been used to analyze the validity of the method proposed here. The accuracy of the latter approach is explained by the fact that the advection of energy remains negligible.

For the sake of completeness, we have also presented a detailed description of the hydrodynamic approach. While it has been used for about a decade, some parts of its description for a general equation of state are either dispersed over many literature sources or not published at all in the accessible literature.

Concerning the future development of the present research, we plan to extend the fast calculation method to two- and three-dimensional problems. Finally, we intend to use this method to investigate the heat transfer in two-phase fluids.

ACKNOWLEDGMENTS

This work was partially supported by the CNES. We thank Carole Lecoutre for her help with the code launching. A.D. acknowledges Jalil Ouazzani for the helpful discussions on the numerical method used in the hydrodynamic approach.

APPENDIX A: BEM FOR THE DIFFUSION EQUATION

In this Appendix we use the traditional notation, so that D and t correspond to D_d and τ of Eq. (12). It can be shown [21] that the linear diffusion problem

$$\frac{\partial \psi}{\partial t} = D\nabla^2 \psi, \qquad \psi|_{t=0} = 0, \tag{A1}$$

with the constant thermal diffusion coefficient D is equivalent to the boundary integral equation

$$D\int_0^t dt' \int_A \left[G(\vec{x}-\vec{x}',t-t')\frac{\partial_{x'}\psi(\vec{x}',t')}{\partial \vec{n}} - \psi(\vec{x}',t')\frac{\partial_{x'}G(\vec{x}-\vec{x}',t-t')}{\partial \vec{n}} d_{x'}A = \frac{1}{2}\psi(\vec{x},t). \right. \tag{A2}$$

The integration is performed over the surface A of the fluid volume v, $\vec{x}\in A$. The outward unit normal to A is $\vec{n}$. Green's function G for the infinite space for the equation adjoint to Eq. (A1) reads

$$G(\vec{x},t) = (4\pi Dt)^{-d/2}\exp\left(-\frac{|\vec{x}|^2}{4Dt}\right), \tag{A3}$$

where d is the spatial dimensionality of the problem (A1).

Only the 1D case with the space variable $x\in(0,L)$ is considered below, the 2D counterpart being described elsewhere [22,23]. For $d=1$, A degenerates into two points, and Eq. (A2) reduces to two equations

$$2D\int_0^t dt' \left[G(x-x',t-t')\frac{\partial \psi}{\partial x'} - \psi(x',t')\frac{\partial G(x-x',t-t')}{\partial x'} \right]\Bigg|_{x'=0}^{x'=L} = \psi(x,t) \tag{A4}$$

written for $x=0,L$. A variety of numerical methods can be applied to solve Eqs. (A4). The simplest way is to present the integral over $(0,t)$ as a sum of the integrals over (t_{f-1},t_f), $f=1,\ldots,F$ with $t_0=0$ and $t_F=t$ and assume a constant value $\psi_f=\psi(t_f)$ and $\psi_f'=\partial\psi(t_f)/\partial x$ over each of these intervals. Equations (A4) will reduce then to the set of $2F_m$ (t_{F_m} is the maximum desired calculation time) linear equations

$$\sum_{f=1}^{F}\left[\psi_f(0)H_{Ff}(x)-\psi_f(L)H_{Ff}(x-L)-\psi_f'(0)G_{Ff}(x)+\psi_f'(L)G_{Ff}(x-L)\right]=\psi_{Fi}/2, \qquad x=0,L;F=1,\ldots,F_m \tag{A5}$$

for $4F_m$ variables ψ_f, $\psi_f'(0,L)$, $2F_m$ of them being defined by the boundary conditions. The coefficients in these equations can be calculated analytically:

$$G_{Ff}(x) = D\int_{t_{f-1}}^{t_f} G(x,t_F-t')dt' = \frac{|x|}{2} \times \left[\mathrm{erfc}(\sqrt{u}) - \frac{\exp(-u)}{\sqrt{u\pi}}\right]_{x^2/4D(t_F-t_f)}^{x^2/4D(t_F-t_{f-1})} \tag{A6}$$

and

$$H_{Ff}(x) = -D\int_{t_{f-1}}^{t_f}\frac{\partial G(x,t_F-t')}{\partial x}dt' = -\frac{\mathrm{sign}(x)}{2}\,\mathrm{erfc}(\sqrt{u})\Big|_{x^2/4D(t_F-t_f)}^{x^2/4D(t_F-t_{f-1})}, \tag{A7}$$

where

$$\mathrm{erfc}(x) = \int_x^\infty \exp(-u^2)du,$$

is the complementary error function and

$$\mathrm{sign}(x) = \begin{cases} 1, & x>0, \\ -1, & x<0. \end{cases}$$

One needs to mention that the case $x=0$ is special: $H_{Ff}(0)=0$ for all f and F and

$$G_{Ff}(0) = \sqrt{D_0/\pi}\left(\sqrt{t_F-t_{f-1}}-\sqrt{t_F-t_f}\right).$$

The set of linear equations (A5) can be solved by any appropriate method, e.g., by the Gauss elimination.

APPENDIX B: THE FLUID PROPERTIES

The thermal conductivity k is deduced from the thermal diffusivity

$$D=D_1\left(\frac{T-T_c}{T_c}\right)^{\varphi_1}+D_2\left(\frac{T-T_c}{T_c}\right)^{\varphi_2} \tag{B1}$$

and the constant pressure specific heat at critical density ρ_c, $k=D\rho_c c_p|_{\rho_c}$. The values of the coefficients for CO_2 are $D_1=5.891\,84\times10^{-8}$ m^2/s, $D_2=7.98068\times10^{-7}$ m^2/s, $\varphi_1=0.67$, and $\varphi_2=1.24$. The coefficients of the values for SF_6 are $D_1=6.457\times10^{-7}$ m^2/s, $D_2=0$, $\varphi_1=0.877$, and $\varphi_2=0$. The specific heat at constant pressure is calculated by using the thermodynamic relationship

$$c_p=c_v+T\left(\frac{\partial p}{\partial T}\right)_\rho^2\chi_T. \tag{B2}$$

The isothermal compressibility coefficient χ_T and the specific heat at constant volume are given by the restricted cubic model [8]. For the reference hydrodynamic DNS we used a constant c_v value calculated for the initial value of temperature and density. We used a constant value for the viscosity μ: 3.74×10^{-5} Pa s for SF_6 and 3.45×10^{-5} Pa s for CO_2.

APPENDIX C

According to the integral theorem about the mean value [24], there is always a point $\vec{x}_m\in v$ so that

$$\int_v Y(\vec{x})Z(\vec{x})d\vec{x}=Y(\vec{x}_m)\int_v Z(\vec{x})d\vec{x} \tag{C1}$$

if the functions Y and Z are continuous. When the spatial variation of Y in v is small, $\langle Y\rangle\approx Y(\vec{x}_m)$, and Eq. (17) stems from Eq. (C1).

APPENDIX D: APPLICATION OF THE FINITE VOLUME METHOD (FVM) AND SIMPLER ALGORITHM

According to the FVM, the calculation domain is divided into a number of nonoverlapping control volumes so that there is one control volume surrounding each grid point. The differential equations are integrated over each control volume. The attractive feature of this method is that the integral balance of mass, momentum, and energy is exactly satisfied over any control volume (called below the cell for the sake of brevity), and thus over the whole calculation domain. The integral formulation is also more robust than the finite difference method for problems that present strong variations of properties observed in a near-critical fluid [10,20]. The equations are resolved on a staggered grid. This means that the velocity is computed at the points that lie on the faces of the cell while the scalar variables (pressure, density, and temperature) are computed at the center of the cell. This choice is made to avoid pressure oscillations in the computations [11]. For the time discretization, the first-order Euler scheme is used. For the sake of simplicity and clarity we present the finite volume method for the 1D generalized transport equation for a variable Y (where Y can be substituted by either u or T)

$$\frac{\partial\rho Y}{\partial t}+\frac{\partial\rho uY}{\partial x}=\frac{\partial}{\partial x}\left(\Gamma\frac{\partial Y}{\partial x}\right)+S, \tag{D1}$$

where Γ denotes the generalized diffusion coefficient and S the generalized source term (volume forces). Integrated over the ith cell of the length δx, Eq. (D1) takes the form

$$\frac{\rho_P Y_P-\rho_P^p Y_P^p}{\Delta t}\Delta x+J_e-J_w=S_P\Delta x, \tag{D2}$$

where the superscript p denotes the value on the previous time step, the subscript P represents the center of the cell, and the subscripts e and w represent its ''east'' and ''west'' faces respectively. The calculation of the flux

$$J=\rho uY-\Gamma\frac{\partial Y}{\partial x} \tag{D3}$$

on the faces requires the knowledge of Y and ρ at the *centers* of two neighboring ''East'' and ''West'' cells denoted by the *capital* letters E and W. Their values at the faces can be found by linear interpolation between their values at the centers, e.g., $Y_e=0.5(Y_P+Y_E)$ if the nodes are equidistant.

The continuity equation integrated on the control volume is given by

$$\frac{\rho_P-\rho_P^p}{\Delta t}\Delta x+F_e-F_w=0 \tag{D4}$$

with $F=\rho u$. When multiplying Eq. (D4) by Y_P and subtracting the result from Eq. (D2), one obtains the equation

$$\frac{\rho_P^p\Delta x}{\Delta t}(Y_P-Y_P^p)+(J_e-Y_PF_e)-(J_w-Y_PF_w)=S_P\Delta x, \tag{D5}$$

which can be rewritten in the following form:

$$a_PY_P=a_WY_W+a_EY_E+b. \tag{D6}$$

The tridiagonal set of linear equations (D6) with respect to Y_P is solved by the Thomas algorithm [25]. The stencil coefficients a_P, a_W, and a_E depend on the discretization scheme. Their general expression is

$$\begin{aligned} a_W&=B_wA_w+\max(-F_w,0),\\ a_E&=B_eA_e+\max(F_e,0),\\ a_P&=a_W+a_E+\rho_P^p\Delta x/\Delta t,\\ b&=S_P\Delta x+\rho_P^pY_P^p\Delta x/\Delta t, \end{aligned} \tag{D7}$$

where $B=\Gamma/\Delta x$. We use the "power law scheme" [11] that requires

$$A_i=\max\left[0,\left(1-\frac{0.1|F_i|}{B_i}\right)^5\right], \quad i=e,w.$$

Set (D6) should be written and solved both for the velocity and the temperature. While the above scheme can be directly applied for the temperature case, the coupling of the velocity and the pressure $p^{(1)}$ (which is defined implicitly by the continuity equation) requires a special treatment for the velocity equation as described below.

The nondimensionalized and discretized Navier-Stokes equation (30),

$$a_e u_e=\sum a_{nb}u_{nb}+(p_P^{(1)}-p_E^{(1)})+b, \tag{D8}$$

where the subscript nb denotes the neighbors of point e, can be solved only when the pressure field is given. Unless the correct pressure field is employed, the resulting velocity field will not satisfy the continuity equation. We use the iterative SIMPLER algorithm [11] to couple the velocity and the pressure fields. This algorithm is based on successive corrections of the velocity field and pressure field at a given time step. The velocity and pressure variables are decomposed as follows:

$$\begin{aligned} u&=u^*+u', \\ p^{(1)}&=p^{(1)*}+p^{(1)'}, \end{aligned} \tag{D9}$$

where the asterisk denotes the guesses and the prime denotes the corrections. The steps of the SIMPLER algorithm are the following

(1) Start with a guessed velocity field.

(2) A pseudovelocity $\hat{u}$ (without taking into account the pressure gradient) is first computed and is defined as

$$\hat{u}_e=\frac{\sum a_{nb}u_{nb}+b}{a_e}, \tag{D10}$$

where u_{nb} represents the neighbor velocities. $\hat{u}$ satisfies

$$u_e=\hat{u}_e+\frac{p_P^{(1)*}-p_E^{(1)*}}{a_e}. \tag{D11}$$

(3) Compute the pressure $p^{(1)*}$ whose equation is deduced by applying the divergence operator to Eq. (D11) and using the continuity equation (D4):

$$\left(\frac{\rho_w}{a_w}+\frac{\rho_e}{a_e}\right)p_P^{(1)*}=\frac{\rho_w}{a_w}p_W^{(1)*}+\frac{\rho_e}{a_e}p_E^{(1)*}+\frac{\rho_P^p-\rho_P}{\Delta t}\Delta x-\rho_e\hat{u}_e+\rho_w\hat{u}_w. \tag{D12}$$

(4) Solve Eq. (D8) with $p^{(1)*}$ used for $p^{(1)}$, and thus obtaining u^*.

(5) Compute $p^{(1)'}$ whose equation is obtained analogously to Eq. (D12) from

$$u_e=u_e^*+\frac{(p_P^{(1)'}-p_E^{(1)'})}{a_e}. \tag{D13}$$

It takes the form

$$\left(\frac{\rho_w}{a_w}+\frac{\rho_e}{a_e}\right)p_P^{(1)'}=\frac{\rho_w}{a_w}p_W^{(1)'}+\frac{\rho_e}{a_e}p_E^{(1)'}+\frac{\rho_P^p-\rho_P}{\Delta t}\Delta x-\rho_e u_e^*+\rho_w u_w^*. \tag{D14}$$

(6) Calculate the velocity u using Eq. (D13). Do not correct the pressure $p^{(1)}$, $p^{(1)'}$ is used to correct only the velocity field, the pressure being computed by Eq. (D14).

(7) Solve the energy equation for T using the obtained u values.

(8) Calculate the density distribution and $p^{(0)}$ via Eqs. (33) and (34).

(9) Return to step 2 and repeat until the converged solution is obtained.

It has to be noted that whereas the fractional step PISO algorithm [10] is successful in resolving Eqs. (29)–(32) on the acoustic time scale, it is not the case when the acoustic filtering method is used. Due to the different meanings of pressure (see Sec. III C) in the momentum equation (involving $p^{(1)}$) and in the energy equation (involving $p^{(0)}$), it appears that only an iterative algorithm can correctly couple the thermodynamic field and the velocity field, the PISO algorithm leading to unstable solutions.

[1] B. Zappoli, D. Bailly, Y. Garrabos, B. Le Neindre, P. Guenoun, and D. Beysens, Phys. Rev. A **41**, 2264 (1990).

[2] A. Onuki and R.A. Ferrell, Physica A **164**, 245 (1990).

[3] D. Beysens, D. Chatain, V. S. Nikolayev, and Y. Garrabos, in *Proceedings of Fourth International Conference on Launcher Technology*, Liege, Belgium (CNES, Toulouse, 2002), Paper 148, CDROM.

[4] D. Beysens, D. Chatain, V. S. Nikolayev, Y. Garrabos, and A. Dejoan (unpublished).

[5] H. Boukari, J.N. Shaumeyer, M.E. Briggs, and R.W. Gammon, Phys. Rev. A **41**, 2260 (1990).

[6] J. Straub, L. Eicher, and A. Haupt, Phys. Rev. E **51**, 5556 (1995).

[7] F. Zhong and H. Meyer, Phys. Rev. E **51**, 3223 (1995).

[8] M.R. Moldover, J.V. Sengers, R.W. Gammon, and R.J. Hocken, Rev. Mod. Phys. **51**, 79 (1979); note that χ_T is defined differently.

[9] B. Zappoli and P. Carlès, Eur. J. Mech. B/Fluids **14**, 41 (1995).

[10] S. Amiroudine, J. Ouazzani, P. Carlès, and B. Zappoli, Eur. J. Mech. B/Fluids **16**, 665 (1997).

[11] S. V. Patankar *Numerical Heat Transfer and Fluid Flow* (Hemisphere, Washington, DC, 1980).

[12] Y. Garrabos, M. Bonetti, D. Beysens, F. Perrot, T. Fröhlich, P. Carlès, and B. Zappoli, Phys. Rev. E **57**, 5665 (1998).
[13] Y. Chiwata and A. Onuki, Phys. Rev. Lett. **87**, 144301 (2001).
[14] A. Furukawa and A. Onuki, Phys. Rev. E **66**, 016302 (2002).
[15] D. Bailly and B. Zappoli, Phys. Rev. E **62**, 2353 (2000).
[16] B. Zappoli, S. Amiroudine, P. Carlès, and J. Ouzzani, J. Fluid Mech. **316**, 53 (1996).
[17] A. Jounet, Phys. Rev. E **65**, 037301 (2002).
[18] Y. Garrabos, A. Dejoan, C. Lecoutre, D. Beysens, V. Nikolayev, and R. Wunenburger, J. Phys. (France) **11**, Pr6-23 (2001).
[19] S. Paolucci, Sandia National Laboratories Report No. SAND 82-8257, 1982.
[20] B. Zappoli and A. Durant-Daubin, Phys. Fluids **6**, 1929 (1994).
[21] C. A. Brebbia, J. C. F. Telles, and L. C. Wrobel, *Boundary Element Techniques* (Springer, Berlin, 1984).
[22] V.S. Nikolayev, D.A. Beysens, G.-L. Lagier, and J. Hegseth, Int. J. Heat Mass Transfer **44**, 3499 (2001).
[23] V. S. Nikolayev and D. A. Beysens, in *Boundary Elements XXIV*, edited by C. A. Brebbia, A. Tadeu, and V. Popov, Int. Ser. Adv. Boundary Elements Vol. 13 (WIT Press, Southhampton, 2002), p. 511.
[24] G. Korn and T. Korn, *Mathematical Handbook for Scientists and Engineers* (Dover, New York, 2000).
[25] D. A. Anderson, J. C. Tannehill, and R. H. Pletcher, *Computational Fluid Mechanics* (Hemisphere Publishing Corporation, New York, 1984).
[26] D. Beysens, T. Fröhlich, V. S. Nikolayev, and Y. Garrabos (unpublished).

Mécanique & Industries 5, 553–558 (2004)

DOI: 10.1051/meca:2004056

Mécanique & Industries

Crise d'ébullition : inhibition du détachement de la bulle de vapeur par la force de recul

Vadim S. Nikolayev[1,a], Daniel Beysens[1] et Yves Garrabos[2]

[1] ESEME, Service des Basses Températures, CEA Grenoble, France[b]
[2] CNRS-ESEME, Institut de Chimie de la Matière Condensée de Bordeaux, 87 Av. du Dr. Schweitzer, 33608 Pessac Cedex, France

Reçu le 8 octobre 2003, accepté le 30 janvier 2004

Résumé – La crise d'ébullition est une transition entre deux régimes d'ébullition : ébullition nucléée (la bulle se forme sur la surface chauffante) et ébullition en film (la surface chauffante est couverte par un film continu de vapeur séparant la surface chauffante du liquide). Dans cette communication, nous présentons un modèle physique de la crise d'ébullition basé sur le concept de recul de vapeur. Nos simulations numériques de croissance thermiquement contrôlée montrent comment une bulle attachée à la surface chauffante commence soudainement à s'y étaler, formant le germe d'un film de vapeur. La force de recul de vapeur ne provoque pas seulement l'étalement de la bulle, elle crée également une force additionnelle d'adhérence qui empêche le départ de la bulle de la surface chauffante lors de sa croissance. Près du point critique liquide-vapeur, la croissance de la bulle est très lente. Si, de plus, des conditions de microgravité sont remplies, la bulle garde la forme convexe et il est possible d'observer expérimentalement une augmentation de l'angle apparent de contact ainsi que la croissance de la tache sèche. Ces observations confirment l'explication proposée.

Mots clés : Crise d'ébullition / flux critique / point critique / microgravité

Abstract – Boiling crisis as inhibition of bubble detachment by the vapor recoil force. Boiling crisis is a transition between nucleate and film boiling. In this communication we present a physical model of the boiling crisis based on the vapor recoil effect. Our numerical simulations of the thermally controlled bubble growth at high heat fluxes show how the bubble begins to spread over the heater thus forming a germ for the vapor film. The vapor recoil force not only causes the vapor spreading, it also creates a strong adhesion to the heater that prevents the bubble departure, thus favoring the further bubble spreading. Near the liquid-gas critical point, the bubble growth is very slow and allows the kinetics of the bubble spreading to be observed. Since the surface tension is very small in this regime, only microgravity conditions can preserve a convex bubble shape. Under such conditions, we observed an increase of the apparent contact angle and spreading of the dry spot under the bubble, thus confirming our model of the boiling crisis.

Key words: Boiling crisis / CHF / critical point / microgravity

1 Introduction

Quand le flux de chaleur provenant d'une paroi chauffante dépasse une valeur critique pendant l'ébullition (le flux critique, le CHF en anglais), la vapeur forme brutalement un film sur la paroi chauffante, qui l'isole thermiquement du liquide. En d'autres termes, la paroi chauffante se dessèche. Le transfert thermique est inhibé et la température de la paroi croît rapidement. Ce phénomène s'appelle la crise d'ébullition par caléfaction [1]. L'évaluation correcte du CHF exige une compréhension claire du phénomène physique qui déclenche la crise. De nombreux modèles sont proposés, cf. [2] pour une revue. Pourtant, chacun d'eux ne s'applique qu'à des régimes et des configurations d'expériences très particuliers. Pour des raisons d'importance industrielle, les expériences d'ébullition les plus communes sont effectuées sous pesanteur terrestre à des pressions basses par rapport à la pression critique du fluide donné. La valeur du CHF est alors grande,

[a] Auteur correspondant : vnikolayev@cea.fr
[b] Adresse postale : CEA-ESEME, PMMH-ESPCI, 10 rue Vauquelin, 75231 Paris Cedex 05, France

ce qui rend l'ébullition violente et les observations difficiles. Même les dispositifs les plus avancés [3] ne peuvent aider à valider un modèle avec certitude. Cependant, de nombreuses observations montrent que la crise commence par la croissance d'une tache sèche sous les bulles de vapeur attachées à la paroi.

En diminuant la force d'Archimède, la microgravité permet d'améliorer la qualité des observations grâce au temps de résidence plus long de la bulle sur la paroi chauffante [4]. Cependant, la croissance reste aussi rapide que sur Terre. Sous de grandes pressions, la croissance est plus lente, l'influence des flux hydrodynamiques sur cette croissance est moins importante, ce qui permet d'identifier les mécanismes thermiques, notamment l'influence de la force de recul de vapeur sur la croissance de la tache sèche. Du point de vue de la modélisation, cela permet une grande simplification en négligeant (en première approximation) le couplage thermique-hydrodynamique et en supposant une forme quasi-statique de la bulle. Dans la section 2 ci-dessous, nous développons l'approche [5] qui montre que la force de recul peut être à l'origine de la crise d'ébullition.

Si les pressions sont si grandes que le fluide se trouve près de son point critique, la croissance de la bulle devient exceptionnellement lente et permet des observations très claires de l'assèchement de la paroi [6], cf. section 3 ci-dessous.

2 Force de recul de vapeur et croissance de la tache sèche sous une bulle

La force de recul de vapeur vient de l'impulsion mécanique non compensée des molécules qui quittent l'interface liquide-gaz lors de l'évaporation. Sa valeur par unité de surface (=pression) s'écrit [7] $P_\mathrm{r} = \eta^2(\rho_\mathrm{V}^{-1} - \rho_\mathrm{L}^{-1})$ où η est le taux massique d'évaporation, c'est-à-dire la masse de fluide évaporée par unité de surface pendant l'unité du temps, et $\rho_\mathrm{L}(\rho_\mathrm{V})$ signifie la densité du liquide (vapeur). La force de recul est normale à l'interface et est toujours dirigée vers le liquide. En négligeant la conductivité thermique dans la vapeur par rapport à celle dans le liquide, on écrit $q_\mathrm{L} = H\eta$ où H est la chaleur latente de vaporisation et q_L et le flux thermique qui arrive à l'interface du côté liquide.

Considérons maintenant une bulle de vapeur attachée à la surface de la paroi chauffante (Fig. 1). Lors de l'ébullition, le liquide est surchauffé dans une couche pariétale d'épaisseur l_r. Cependant, la température de l'interface vapeur-liquide est constante (c'est en fait la température de saturation pour la pression donnée du système). Cela signifie que le flux q_L reste élevé dans une « ceinture » sur la surface au pied de la bulle. De fait, la majeure partie de l'évaporation dans la bulle de vapeur est produite dans cette ceinture, dont l'épaisseur est habituellement beaucoup plus petite que le rayon de la bulle [8]. Le recul de la vapeur près de la ligne de contact est alors beaucoup plus grand que sur l'autre partie de la surface de la bulle. En conséquence, sa surface se déforme

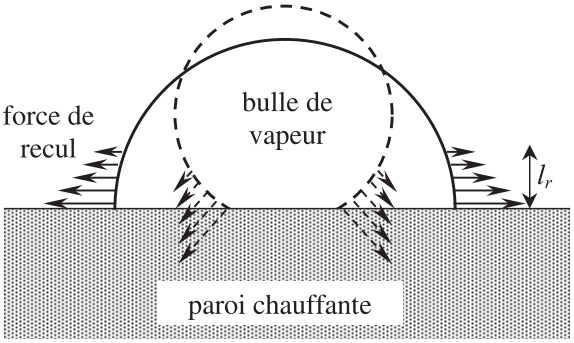

Fig. 1. Étalement d'une bulle de vapeur sous l'action de la force de recul de la vapeur.

comme si la ligne triple de contact liquide-vapeur-solide était tirée de côté, comme montré dans la figure 1. Ceci signifie que, sous l'action du recul de la vapeur, la tache sèche sous la bulle de vapeur s'étale et peut couvrir la surface de la paroi chauffante.

Dans ce qui suit, nous montrons par un exemple simple que l'influence du recul de vapeur peut être interprétée en terme de changement d'angle apparent de contact.

2.1 Recul de vapeur et angle de contact apparent : une approche simplifiée

Considérons une coordonnée curviligne l mesurée le long du contour de la bulle, comme dans la figure 2. Deux forces définissent la forme de la bulle dans l'approximation quasi-statique : la force de recul et la tension superficielle σ,

$$K\sigma = \lambda + P_\mathrm{r}(l) \tag{1}$$

où K est la courbure locale de la bulle et λ est la différence de pression entre l'intérieur et l'extérieur de la bulle, indépendante de l. Cette équation est difficile à résoudre analytiquement et le calcul numérique [5, 9] (onéreux au niveau du temps) s'impose. Cependant, l'approche simplifiée ci-dessous permet d'estimer et de mieux comprendre l'effet de la force du recul sur la forme de la bulle.

Par angle de contact apparent θ_ap, nous sous-entendons celui mesuré à la distance l_r (=épaisseur de la couche limite) de la ligne triple comme marqué dans la figure 2. Cette définition est valable quand $l_\mathrm{r} \ll R$, le rayon de la bulle. Dans ce cas-là, la fonction $P_\mathrm{r}(l)$ peut être approximée par la fonction δ de Dirac :

$$P_\mathrm{r}(l) = 2\sigma_\mathrm{r}\delta(l) \tag{2}$$

La fonction $\delta(l)$ est définie de telle manière, que $\delta(l) = 0$ si $l \neq 0$, $\delta(0) = \infty$ et $\int_{-\infty}^{\infty} \delta(l)\mathrm{d}l = 1$. D'après (1), ceci signifie que le recul de vapeur est localisé à la ligne de contact, et la tension superficielle donne au reste de la surface de la bulle la forme d'une calotte sphérique. La supposition (2) se justifie par le calcul plus rigoureux [5] qui montre que $P_\mathrm{r}(l)$ diverge quand $l \to 0$, $\int_0^\infty P_\mathrm{r}(l)\mathrm{d}l$ restant fini.

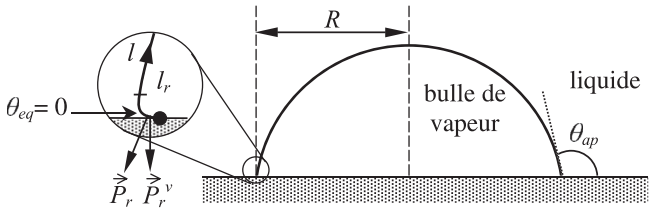

Fig. 2. Les angles de contact apparent $\theta_{\rm ap}$ et réel $\theta_{\rm eq}$. Le point noir indique la ligne de contact, c'est-à-dire zéro pour la coordonnée curviligne l.

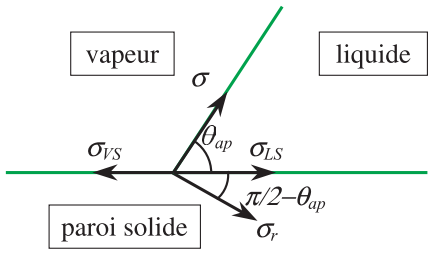

Fig. 3. Équilibre des forces qui agissent sur la ligne triple de contact, où $\sigma_{\rm vs}$ et $\sigma_{\rm ls}$ sont les tensions superficielles pour les interfaces respectivement vapeur-solide et liquide-solide.

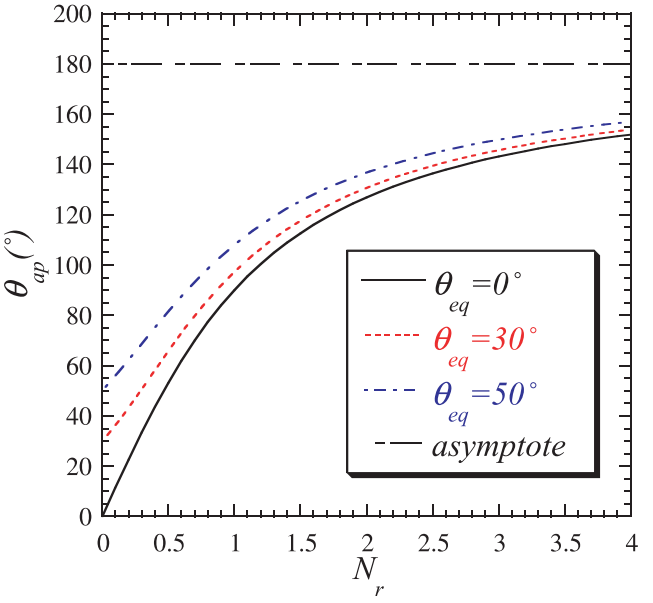

Fig. 4. Angle apparent de contact par rapport en coefficient de recul $N_{\rm r}$ pour différentes valeurs de l'angle de contact d'équilibre.

L'amplitude $\sigma_{\rm r}$ du recul de vapeur a la dimension d'une tension superficielle et doit être incluse[1] dans le bilan de (quasi-)équilibre des tensions agissant sur la ligne de contact montrées dans la figure 3. La ligne de contact est stationnaire quand la composante horizontale de la somme des vecteurs de toutes les forces est égal à zéro, ce qui se résume en

$$\cos\theta_{\rm ap} = \cos\theta_{\rm eq} - N_{\rm r}\sin\theta_{\rm ap} \qquad (3)$$

où l'angle de contact d'équilibre est donné par l'expression classique $\cos\theta_{\rm eq} = (\sigma_{\rm vs} - \sigma_{\rm ls})/\sigma$. Le « coefficient de recul »

$$N_{\rm r} = \frac{\sigma_{\rm r}}{\sigma} = \frac{1}{\sigma}\int_0^{l_{\rm r}} P_{\rm r}(l)\,{\rm d}l \qquad (4)$$

caractérise la force de recul de la vapeur relativement à la tension superficielle.

La dépendance de $\theta_{\rm ap}$ par rapport à $N_{\rm r}$, calculée à partir de (3), est présentée sur la figure 4. On peut voir que la force de recul augmente l'angle de contact apparent. Quand la puissance de la paroi chauffante reste constante, le flux de la chaleur $q_{\rm L}$ augmente avec le temps en augmentant $N_{\rm r}$. Par conséquent, l'angle de contact apparent croît dans le temps. Comme la bulle est une calotte sphérique (ce qui est définie par l'Éq. (1) avec $P_{\rm r}(l) = 0, l \neq 0$), l'augmentation de l'angle de contact se traduit par l'étalement de la tache sèche, son rayon $R_{\rm dry}$ étant lié au rayon de la bulle R (cf. Fig. 2) par l'expression

$$R_{\rm dry} = R\sin\theta_{\rm ap} \qquad (5)$$

qui provient de la géométrie de la calotte sphérique.

[1] En se basant sur l'approche variationelle [5], on peut montrer cela rigoureusement.

La force d'adhésion de la bulle à la paroi $F_{\rm ad}$ s'avère très importante pour estimer la valeur du CHF (voir ci-dessous). Elle peut être obtenue à partir du bilan vertical des tensions dans la figure 3. La force $F_{\rm ad}$ est le produit de la longueur ($= 2\pi R_{\rm dry}$) de la ligne triple et de la tension non-compensée :

$$F_{\rm ad} = 2\pi R\sigma(\sin\theta_{\rm ap} - N_{\rm r}\cos\theta_{\rm ap})\sin\theta_{\rm ap} \qquad (6)$$

Les dépendances de $R_{\rm dry}$ et $F_{\rm ad}$ de $N_{\rm r}$ sont montrées dans la figure 5. Le comportement de la force d'adhésion est correcte : elle augmente avec $N_{\rm r}$. En contrepartie, la décroissance de $R_{\rm dry}$ donnée par (5) à partir d'une certaine valeur de $N_{\rm r}$ est paradoxale. Cette décroissance apparaît quand $\theta_{\rm ap}$ dépasse 90°. La composante verticale $\vec{P}_{\rm r}^{\rm v}$ de $\vec{P}_{\rm r}$ change alors de direction. Cette incohérence est due au fait que la forme exacte de la bulle dans la proximité de la ligne triple (cf. l'inséré dans Fig. 2) n'est pas prise en compte. En réalité, la surface est fortement courbée et $\vec{P}_{\rm r}^{\rm v}$ est dirigée vers le bas. Un autre défaut de la théorie simplifiée réside dans l'impossibilité de calculer le temps de départ (puisque avant le départ, la forme de la bulle dévie fortement de celle d'une calotte sphérique) C'est pourquoi il est nécessaire d'abandonner la notion d'angle apparent qui est fondée sur l'expression (2) pour la force de recul. Cette dernière doit être obtenue plus rigoureusement pour calculer la forme de la bulle, ce qui sous-entend une approche numérique ou des expériences.

Cependant, l'approche de l'angle apparent ci-dessus illustre bien l'idée principale de l'étalement sous l'action du recul. Elle permet, en principe, de calculer le champ thermique autour de la bulle en tenant compte de l'effet de recul sans traiter l'équation (1) pour déterminer la forme de la bulle. On peut en effet effectuer le calcul thermique

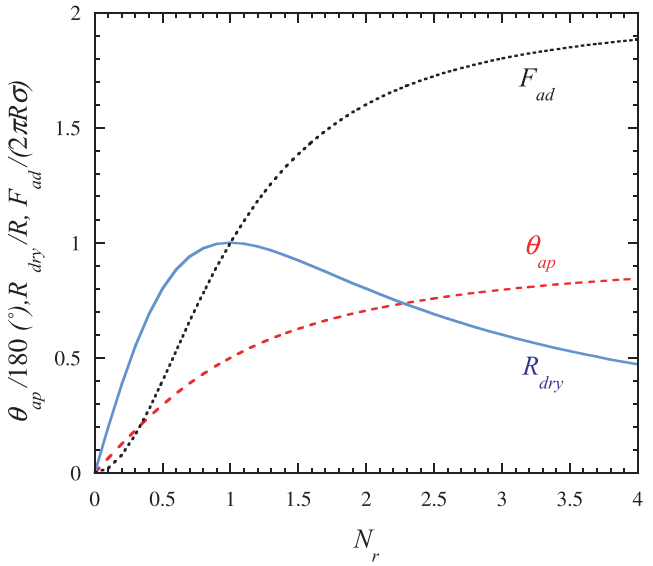

Fig. 5. Dépendance du rayon de la tache sèche et de la force d'adhésion du coefficient du recul N_r calculés pour $\theta_\mathrm{eq} = 0$. θ_ap est aussi représenté pour comparaison.

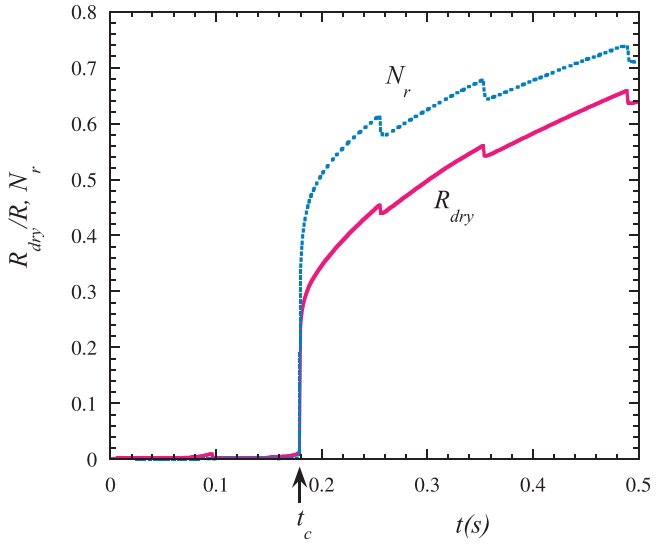

Fig. 6. Évolutions temporelles du rayon R_dry de la tache sèche et du coefficient du recul N_r issus du calcul réalisé d'après l'article [9] pour $q_0 = 0.1$ MW.m^{-2}.

pour une calotte sphérique et ajuster son angle de contact en utilisant l'équation (3).

2.2 Résultats d'une approche numérique

Les simulations numériques [9], qui sont basées sur l'équation (1) avec $P_\mathrm{r}(l)$ calculée à partir de la distribution de température dans le liquide et la paroi chauffante, mettent en évidence la croissance de la tache sèche. La précision des calculs est améliorée par rapport à l'article cité en utilisant un nouvel algorithme [10]. La tache sèche reste petite jusqu'au temps de transition t_c (cf. Fig. 6) où elle s'agrandit brusquement. Nous associons cette transition avec la crise d'ébullition. La croissance de la tache sèche juste avant la crise est confirmée par nombre de travaux expérimentaux, voir par exemple [3]. Étant très petite jusqu'à l'instant t_c, la force de recul caractérisée par le paramètre N_r devient alors de l'ordre de l'unité (cf. Fig. 6) ce qui se compare bien avec l'estimation pour le CHF donnée dans l'article [5]. Abordons maintenant la question de la valeur du CHF.

2.3 Comment estimer le CHF : inhibition du détachement de la bulle par la force de recul

Comme les « forces de départ » (force d'Archimède, poussée du flux hydrodynamique, ...) qui tendent à arracher la bulle de la paroi sont absentes de l'équation (1), la bulle reste toujours accrochée sur la paroi dans la simulation de type [9]. Dans la situation réelle, la bulle quitte la paroi au moment t_dep. Si t_dep est plus petit que le temps t_c issu de la simulation [9], la bulle quitte la paroi avant que la tache sèche puisse s'étaler et la crise d'ébullition ne se produit pas. L'analyse de départ de la bulle s'avère alors cruciale pour trouver la valeur du CHF.

Le temps t_c est une fonction décroissante du flux thermique q_0 de paroi [9]. Cependant, t_dep dépends aussi de q_0. Pour trouver la fonction $t_\mathrm{dep}(q_0)$, on doit analyser la force d'adhésion F_ad d'une bulle à la paroi. Cette force se divise en deux parties $F_\mathrm{ad} = F^\sigma_\mathrm{ad} + F^\mathrm{r}_\mathrm{ad}$. La première partie s'écrit $F^\sigma_\mathrm{ad} = 2\pi R_\mathrm{dry}\sigma \sin\theta_\mathrm{eq}$. F^σ_ad est très importante au début de la croissance, lorsque la ligne triple est attachée au défaut de la paroi qui a servi de centre de nucléation (et qui donne à θ_eq une grande valeur), elle devient négligeable par la suite. Comme on ne peut pas connaître la valeur locale de θ_eq, F^σ_ad est difficile à estimer. On suppose ensuite que $\theta_\mathrm{eq} = 0$ sur le reste de la paroi où la ligne triple se déplace. La deuxième partie

$$F^\mathrm{r}_\mathrm{ad} = \int P^\mathrm{v}_\mathrm{r}\,\mathrm{d}A \qquad (7)$$

est due à la force de recul dont la composante verticale P^v_r (dirigée vers la paroi) est intégrée sur toute la surface A de la bulle. Bien que le calcul [9] est bidimensionnel, on peut raisonnablement supposer que la valeur de la P_r obtenue s'applique aussi pour le cas 3D axi-symétrique (comme si la bulle avait une symétrie axiale en 3D).

Le calcul montre que F^r_ad reste très petite au début de l'évolution (ce qui correspond au cas $t_\mathrm{dep} < t_\mathrm{c}$), par rapport aux forces de départ, notamment la force d'Archimède. Si la bulle reste attachée à la paroi pendant ce régime, c'est grâce à la force F^σ_ad. À partir de l'instant $t = t_\mathrm{c}$, la croissance de F^r_ad s'accélère brutalement et c'est elle qui domine. Autrement dit, quand la tache sèche commence à croître, la bulle reste attachée à la paroi en coalescant avec les bulles voisines. C'est ainsi que la crise d'ébullition devrait se dérouler.

On voit (Fig. 7) que la croissance de la bulle est une superposition d'un processus monotone et d'oscillations

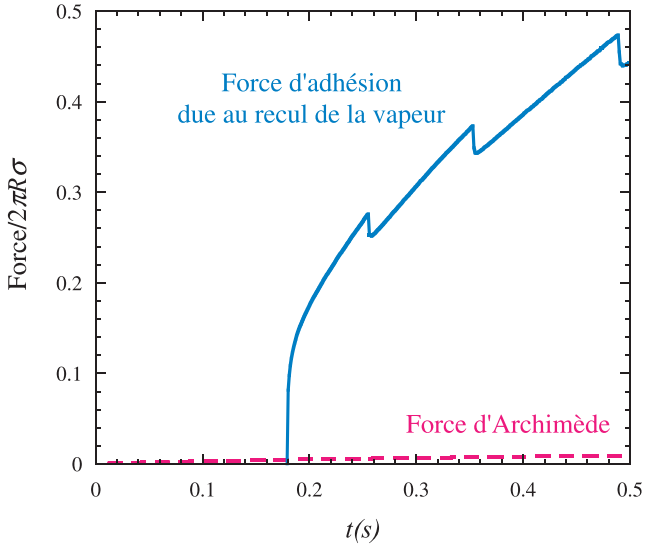

Fig. 7. Évolutions temporelles de la force d'Archimède et de la force d'adhésion $F_{\rm ad}^{\rm r}$, issues du calcul réalisé d'après l'article [9] pour un flux $q_0 = 0.1$ MW.m^{-2}. Les forces sont exprimées dans les unités $2\pi R\sigma$ pour pouvoir comparer avec les résultats de l'approche simplifiée (Fig. 5).

d'amplitudes croissantes. Ces oscillations apparaissent probablement à cause de l'instabilité de recul [7,11]. Une de ces oscillations initie la croissance brutale de la tache sèche.

Le comparaison des résultats numériques avec ceux du modèle simplifié montre que la force d'adhésion est surestimée par ce dernier d'à peu près 50 %. Ce fait confirme la nécessite de poursuivre des études numériques qui permettront d'obtenir la valeur du CHF compte tenu des forces de départ. Le CHF apparaît ainsi comme la valeur du flux thermique de transition entre deux régimes qui ne peuvent pas coexister : le régime de départ et le régime d'étalement de la bulle.

3 Évidence expérimentale de l'étalement d'une bulle en microgravité

Les expériences [6] confirment que notre modèle d'étalement d'une bulle est valide dans la région critique, c'est-à-dire pour des pression et température proches de la pression et de la température critiques pour le fluide donné. Le point critique présente beaucoup de propriétés singulières. En particulier, le coefficient de diffusion thermique s'évanouit, ce qui ralentit la croissance des bulles et permet d'observer les détails de la croissance sans une agitation gênante du liquide provoquée par des mouvements rapides. Par exemple, la croissance d'une seule bulle a pu être observée [6] pendant environ quinze minutes.

Puisque la longueur capillaire $[\sigma/(\rho_{\rm L} - \rho_{\rm V})g]^{1/2}$ (où g est la gravité terrestre) disparaît également au point critique et les bulles sont écrasées contres des parois. Les bulles de vapeur de forme habituelle convexe ne sont donc

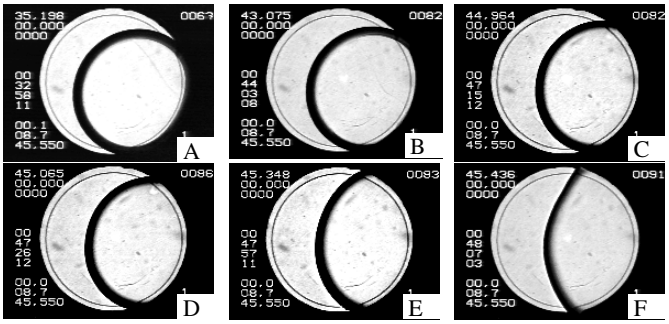

Fig. 8. Évolution d'une bulle de vapeur dans une cellule cylindrique remplie de SF_6 proche de son point critique. Les images ont été obtenues pendant un chauffage continu de la cellule. La dernière image (F) correspond à la température juste en dessous de la température critique. L'augmentation de l'angle de contact apparent est évidente.

pas observables en pesanteur terrestre. Pour cette raison, notre expérience a été exécutée à bord de la station spatiale MIR. La valeur du CHF disparaît au point critique [1], par conséquent, on s'attend à ce qu'un taux de chauffage très lent produise l'étalement de la bulle. En raison de cette évolution lente, les effets hydrodynamiques sont très faibles et la forme de la bulle n'est pas distordue. Une cellule expérimentale de forme cylindrique a été remplie par du SF_6 à densité presque critique. On a observé l'évolution de la bulle à travers les bases transparentes du cylindre (fenêtres). La figure 8 montre comment la bulle, initialement circulaire ($\theta_{\rm eq} = 0$) s'étale sur la paroi chauffante cylindrique. L'angle de contact apparent augmente clairement avec le temps. Bien que le volume de la bulle soit constant, la masse de vapeur augmente suite à la densité croissante. À la différence du régime de basse pression, la densité dépend fortement de la température dans la région proche du point critique.

4 Conclusions

Nous proposons une explication physique pour la crise d'ébullition : l'étalement de la tache sèche sous une bulle de vapeur est provoquée par la force de recul de la vapeur. Une fois l'étalement commencé, la bulle reste attachée à la paroi par le même effet de recul et l'étalement (accompagné des coalescences possibles avec des bulles voisines) peut se prolonger jusqu'à la formation du film continu de vapeur. L'approche théorique est soutenue par la simulation numérique de la croissance de la bulle sous un grand flux de chaleur, ainsi que par des données expérimentales sur la croissance de la bulle dans des conditions proches du point critique. Des simulations numériques basées sur cette approche devraient permettre de déterminer le CHF comme étant le flux thermique de transition entre deux régimes : le régime de départ et le régime d'étalement de la bulle.

Références

[1] L.S. Tong, Boiling Heat Transfer and Two-Phase Flow, (2nd Ed.), Taylor & Francis, New York, 1997

[2] Yu.A. Buyevich, Towards a Unified Theory of Pool Boiling – the Case of Ideally Smooth Heated Wall, Int. J. Fluid Mech. Res. 26 (1999) 189–223

[3] T.G. Theophanous, T.H. Dinh, J.P. Tu, A.P. Dinh, The boiling crisis phenomenon, Part II : dryout dynamics and burnout, Exp. Thermal Fluid Sci. 26 (2002) 793–810

[4] J. Straub, Boiling Heat Transfer and Bubble Dynamics in Mirogravity, Adv. Heat Transfer 35 (2001) 57–172

[5] V.S. Nikolayev, D.A. Beysens, Boiling crisis and non-equilibrium drying transition, Europhys. Lett. 47 (1999) 345–351

[6] Y. Garrabos, C. Lecoutre-Chabot, J. Hegseth, V.S. Nikolayev, D. Beysens, J.-P. Delville, Gas spreading on a heated wall wetted by liquid, Phys. Rev. E 64 (2001) 051602

[7] H.J. Palmer, The hydrodynamic stability of rapidly evaporating liquids at reduced pressure, J. Fluid. Mech. 75(3) (1976) 487–511

[8] P. van Carey, Liquid-Vapor Phase Change Phenomena, Hemisphere, Washington D.C., 1992

[9] V.S. Nikolayev, D.A. Beysens, G.-L. Lagier, J. Hegseth, Growth of a dry spot under a vapor bubble at high heat flux and high pressure, Int. J. Heat Mass Transfer 44 (2001) 3499–3511

[10] V.S. Nikolayev, D.A. Beysens, 2D BEM modeling of a singular thermal diffusion free boundary problem with phase change, Boundary elements XXIV (Incorporating meshless solutions), C.A. Brebbia, A. Tadeu, V. Popov (ed.), Int. Series on Advances in Boundary Elements, v.13 WIT Press, Southhampton (2002) 501–525

[11] K. Sefiane, D. Benielli, A. Steinchen, A new model for pool boiling crisis, recoil instability and contact angle influence, Colloids and Surfaces 142 (1998) 361–373

Langmuir **2004,** *20,* 1213−1221

Contact Line Dynamics in Drop Coalescence and Spreading

R. Narhe, D. Beysens,* and V. S. Nikolayev

Equipe du Supercritique pour l'Environnement, les Matériaux et l'Espace, Service des Basses Températures, CEA-Grenoble, Grenoble, France

Received June 5, 2003. In Final Form: December 1, 2003

The dynamics of coalescence of two water sessile drops is investigated and compared with the spreading dynamics of a single drop in partially wetting regime. The composite drop formed due to coalescence relaxes exponentially toward equilibrium with a typical relaxation time that decreases with contact angle. The relaxation time can reach a few tenths of seconds and depends also on the drop size, initial conditions, and surface properties (contact angle, roughness). The relaxation dynamics is larger by 5 to 6 orders of magnitude than the bulk hydrodynamics predicts, due to the high dissipation in the contact line vicinity. The coalescence is initiated at a contact of the drops growing in a condensation chamber or by depositing a small drop at the top of neighboring drops with a syringe, a method also used for the studies of the spreading. The dynamics is systematically faster by an order of magnitude when comparing the syringe deposition with condensation. We explain this faster dynamics by the influence of the unavoidable drop oscillations observed with fast camera filming. Right after the syringe deposition, the drop is vigorously excited by deformation modes, favoring the contact line motion. This excitation is also observed in spreading experiments while it is absent during the condensation-induced coalescence.

1. Introduction

The phenomenon of the coalescence of sessile drops is of critical importance for a number of technological processes. It is also a key phenomenon in the growth of droplets on a surface (dew, breath figures, etc.).[1−3] However, little is known about its dynamics. While knowledge of the liquid viscosity and surface tension is sufficient to describe the kinetics of coalescence of freely suspended drops, the contact line motion influences strongly the coalescence kinetics of sessile drops. The study of this kinetics is then a tool to study the contact line motion itself.

The contact line motion, i.e., the motion of gas−liquid interface along the solid surface for the case of partial wetting, remains a very active field of study despite numerous works that were published on this subject during the past decades. It was found theoretically that the contact line motion was incompatible with the no-slip boundary condition (zero fluid velocity) on the solid surface[4] that causes the diverging dissipation in the near contact line region of the liquid wedge. In reality, the dissipation is high but finite. Consequently, the response of the contact line to external influence is much slower in comparison to that of the bulk fluid. There is still no certainty on the exact microscopic mechanism of the contact line motion. Some results are described satisfactory by one mechanism and some by others. The contact line motion is sensitive to many factors and is an excellent example of the influence of the microscopic phenomena on the macroscopic motion. Among these factors one can list surface defects (geometric and chemical), presence of a liquid film on the solid, the wetting properties, etc. It is extremely difficult to characterize these factors in practice. The wetting properties are characterized by the contact angle. It appears that the experimental error in the contact angle is often so large that its measurements are not certain, as shown by Lander et al. and de Ruijter et al.[5,6] who obtained quite different values depending on the measurement setup (Wilhelmy balance or sessile drop). Therefore, in the dynamic measurements we prefer to consider a well-defined contact line position rather than the contact angle.

The capillary spreading of a sessile drop due to heterogeneties in solid surface was studied by Shanahan.[7] De Gennes[8] described the spreading of liquid in the presence of a precursor film. The precursor film facilitates the spreading and allows the hydrodynamics of spreading to be explained. However, the ellipsometric studies of Voué et al.[9] showed that while the precursor film plays an important role during the spreading in the complete wetting regime, it is absent for the partial wetting regime. These studies were confirmed indirectly by de Ruijter et al.[6,10] and Rieutord et al.[11] They found that the spreading for the partial wetting regime was much slower than that in the complete wetting case meaning that the application of de Gennes precursor film theory led to unphysical values for the parameters of the theory. We conclude from these studies that in a quite common situation of partial wetting, the precursor film is absent and another model of contact line motion should be applied. Several microscopic models by Blake and Haynes,[12] Shikhmurzaev,[13] and Pomeau[14] have been proposed, some accounting for a phase transition

* To whom correspondence should be addressed. E-mail: dbeysens@cea.fr. Mailing address: CEA-ESEME, ICMCB, 87, Av. Dr. A. Schweitzer, 33608 Pessac Cedex, France.

(1) Beysens, D.; Knobler, C. M. *Phys. Rev. Lett.* **1986**, *57*, 1433.
(2) Beysens, D. *Atmos. Res.* **1995**, *39*, 215.
(3) Briscoe, B. J.; Galvin, K. P. *J. Phys. D*: *Appl. Phys.* **1990**, *23*, 422.
(4) Huh, C.; Scriven, L. E. *J. Colloid Interface Sci.* **1971**, *35*, 85.
(5) Lander, L. M.; Siewierski, L. M.; Brittain, W. J.; Vogler, E. A. *Langmuir* **1993**, *9*, 2237.
(6) de Ruijter, M. J.; De Coninck, J.; Blake, T. D.; Clarke, A.; Rainkin, A. *Langmuir* **1997**, *13*, 7293.
(7) Shanahan, M. E. R. *J. Phys. D*: *Appl. Phys.* **1990**, *23*, 321.
(8) De Gennes, P. G. *Rev. Mod. Phys.* **1985**, *57*, 827.
(9) Voué, M.; Valignat, M.P.; Oshanin, G.; Cazabat, A. M.; de Coninck, J. *Langmuir* **1998**, *14*, 5951.
(10) de Ruijter, M. J.; De Coninck, J.; Oshanin, G. *Langmuir* **1999**, *15*, 2209.
(11) Rieutord, F.; Rayssac, O.; Moriceau, H. *Phys. Rev. E* **2000**, *62*, 6861.
(12) Blake, T. D.; Haynes *J. Colloid Interface Sci.* **1969**, *30*, 421.
(13) Shikhmurzaev, Y. D. *Phys. Fluids* **1997**, *9*, 266.
(14) Pomeau, Y. *C. R. Acad. Sci., Ser. IIb* **2000**, *238*, 411.

10.1021/la034991g CCC: $27.50
Published on Web 01/23/2004

in the immediate vicinity of the contact line. Their discussion is out of the scope of this article. We only note that most of them result in the following expression of the contact line velocity v_n in the direction normal to the contact line as a function of the dynamic contact angle θ

$$v_n = \frac{\sigma}{\xi}(\cos\theta_{eq} - \cos\theta) \quad (1)$$

Here θ_{eq} is the equilibrium value of the contact angle, σ is the surface tension, and ξ is a model-dependent parameter that we will call the "dissipation coefficient". Another common feature of these theories is that they predict a large ξ value so that the ratio

$$K = \eta/\xi \quad (2)$$

where η is the shear viscosity, is smaller than unity. A small K value means that the dissipation in the contact line region is large with respect to the dissipation in the bulk of the liquid. The study of Andrieu et al.[15] on the coalescence of sessile drops imposed by condensation growth showed extremely small values $K \approx 10^{-6}$–10^{-7}.

It is recognized generally that the static contact line equation should be nonlocal because the contact line displacement at one point influences its position at other points through the surface tension. In dynamics, the local relations similar to eq 1 (where v_n depends only on the *local* value of θ) were considered universal for a long time. Nikolayev and Beysens[16] have developed a nonlocal dynamic approach and applied it to the analysis of the relaxation of the composite drop formed by the coalescence of two drops. If nonlocality is taken into account, eq 1 is not valid in the general case where θ varies along the contact line.

The purpose of this article is 2-fold. First, we study the coalescence of water drops on various kinds of substrates under the conditions of partial wetting. Second, we investigate two different ways to initiate the coalescence of the drops, namely, condensation growth and syringe deposition on a substrate. One of the common ways to study the contact line dynamics is the observation of the spreading of a deposited drop. During the syringe deposition, an additional energy is necessarily transferred to the drop due to its collision with the substrate. This additional *kinetic* energy accelerates the contact line motion and has to lead to an additional term in (1) because its right-hand part is simply a variation of the *potential* energy[6] of the drop. The contribution of this kinetic energy can be checked by comparing the two above-mentioned ways to initiate coalescence. If the contribution of the kinetic energy is important, the expression of the type 1 is invalid and cannot be used for the interpretation of all the existing data obtained by syringe deposition of low viscosity drops.

2. Experimental Section

For this study silicon wafers (untreated and treated) and a polyethylene sheet (≈50 μm thick) were used as substrates with different average contact angle and hysteresis. The coalescence of two drops is studied either in (i) a condensation chamber, where droplets grow by condensation and coalesce when they touch each other, or (ii) by adding a small drop on top of one of two neighboring drops by a microsyringe. Method ii also enables (iii) spreading of a single drop to be studied.

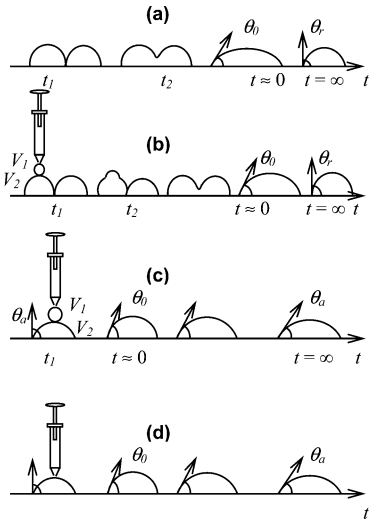

Figure 1. Sketch of (a) coalescence process in condensation experiment, (b) coalescence process in syringe deposition experiment, and (c, d) spreading of drop in syringe deposition experiment.

We will use the water parameters at 20 °C: surface tension $\sigma = 73$ mN/m, shear dynamic viscosity $\eta = 10^{-3}$ Pa·s, density $\rho = 1.0$ g cm^{-3}.

2.1. Chamber Experiments. In condensation experiments a small piece of cleaned substrate of 1 cm^2 is fixed on a thick electrolytic copper plate by a thin film of water in order to have good thermal contact with the copper plate. The condensation chamber consists of a Peltier-element thermostat enclosed in a Plexiglas box. The surface temperature can be adjusted above, equal, or below the dew temperature (T_D). The substrate was cooled from room temperature ($T_R \approx 23$ °C) to the desired temperature T_s that was kept in this series of experiments to $T_s \approx T_R - 5$ K. The substrate temperature was measured by a K-type thermocouple placed close to the substrate. The chamber was filled with pure N_2 gas saturated with water at room temperature. To avoid dust and to saturate the gas, N_2 is bubbled in pure water. The gas flow rate was controlled with a flow meter and kept fixed at 0.60 L/min. The growth and subsequent coalescence of drops (Figure 1a) were observed with high-resolution black and white CCD camera (COHU, 4910 series, 50 frames/s) attached to an optical microscope (Leica, DMRXE) and recorded on a video recorder. The video images were then analyzed by image analysis software (ImageTool).

2.2. Syringe Experiments. We used 0.2 μm filtered distilled water for all experiments. To induce coalescence in the syringe experiments, two water drops of known volume, V_2, were deposited very close to each other on a substrate. A small drop of known volume, V_1, was deposited on the top of one of the drops; see Figure 1b. The process of coalescence and relaxation was filmed with a CCD camera equipped with a macrozoom lens and recorded on a video recorder. The initial process of fusion of two drops for both condensation and syringe experiments was observed with a high-speed CCD camera (HCC1000 strobe, 1000 frames/s). For the spreading study, a small water drop of known volume, V_2, was deposited on the substrate (Figure 1d). The spreading was also observed after equilibration of a drop on the substrate and subsequent deposition of a small drop (volume V_1) on the top of the first (Figure 1c). The syringe experiments were all performed at open room atmosphere (room temperature and humidity).

2.3. Surface Properties. The following substrates were used: (i) 50 μm thick polyethylene sheet; (ii) silicon wafers with different surface treatment. The surface properties, which determine the contact angle, are changed on the silicon surface using the following silanization procedure.[17] The silicon substrates, 1 cm × 1 cm, are cut from a fresh silicon wafer. The wafer is cleaned in (i) acetone for 5 min, (ii) ethanol for 5 min, and (iii)

(15) Andrieu, C.; Beysens, D. A.; Nikolayev, V. S.; Pomeau, Y. *J. Fluid. Mech.* **2002**, *453*, 427.

(16) Nikolayev, V. S.; Beysens, D. A. *Phys. Rev. E* **2002**, *65*, 46135.

(17) Zhao, H.; Beysens, D. *Langmuir* **1995**, *11*, 627.

Table 1. The Contact Angles and Relaxation Rates of a Composite Water Drop on Silicon with Various Treatments, Glass, and Polyethylene Substrates[a]

				U^* (m/s)		
				coalescence		spreading
substrate	θ_r (deg)	θ_a (deg)	θ_{eq} (deg)	condensation	syringe	syringe
glass + silane from ref 15	46 23	60 37	53 30	$(6.5 \pm 0.4) \times 10^{-6}$ $(1.2 \pm 0.1) \times 10^{-5}$		
silicon I	22 ± 2	25 ± 2	23.5	$(2.5 \pm 0.12) \times 10^{-5}$	$(1.89 \pm 0.12) \times 10^{-3}$	$(1.19 \pm 0.04) \times 10^{-2}$
silicon I + silane	55 ± 2	79 ± 2	67	$(1.47 \pm 0.19) \times 10^{-4}$	$(3.42 \pm 0.65) \times 10^{-3}$	$(9.3 \pm 1.6) \times 10^{-3}$
silicon II	47 ± 2	57 ± 2	52	$(9.74 \pm 0.12) \times 10^{-4}$	$(9.54 \pm 0.7) \times 10^{-3}$	$(9.3 \pm 1.6) \times 10^{-3}$
silicon III from ref 11	10	12	11			3.65×10^{-3}
polyethylene	80 ± 2	90 ± 2	85	$(7.24 \pm 0.7) \times 10^{-4}$	$(6.15 \pm 0.6) \times 10^{-3}$	$(4.1 \pm 0.9) \times 10^{-3}$

[a] The U^* value for silicon III was obtained by fitting the data (ref 11) to an exponential relaxation (see Figure 10).

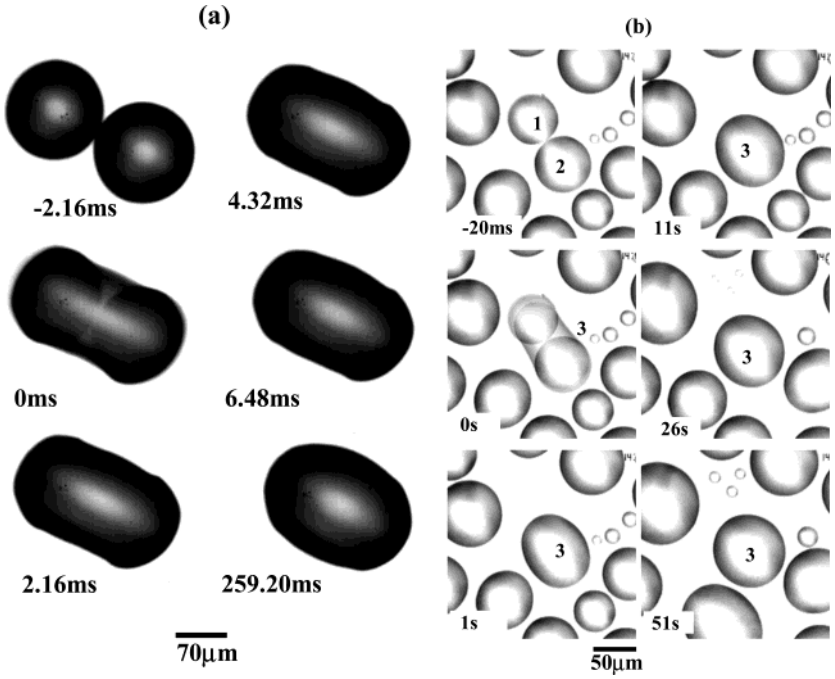

Figure 2. (a) Fast camera picture of coalescence process on silicon II substrate. The bar corresponds to 70 μm. (b) Photo of the coalescence process on silicon I in a condensation chamber. The bar corresponds to 50 μm.

fresh solution of H_2O_2 and H_2SO_4 (1:4) for 30 min. Steps i and ii are performed in an ultrasonic bath.

At the end of each step, the wafer is dried by blowing pure dry nitrogen. A small drop of 50 μL of decyltrichlorosilane is put in a cavity of 1.5 cm radius and 0.5 cm height made (preliminarily) in a Teflon block. The cleaned silicon wafer is placed at distance of 0.5 cm from the top of the block on a height adjustable stand. Since decyltrichlorosilane is volatile, the vapor diffuses and reacts with the wafer's surface. The whole assembly is covered with small glass beaker to prevent the silane vapor from being disturbed. The silanization process time is 1 min. After silanization the substrate is rinsed with distilled water and dried by blowing dry nitrogen. One can vary the contact angle by changing the stand height (i.e., the distance between the wafer and the decyltrichlorosilane) while keeping the silanization time constant.

The contact angle of water on a substrate is measured by a sessile drop method. A small drop of 1 μL is deposited on the substrate by means of a microliter syringe and visualized using a CCD camera with a macro lens. The *static* receding contact angle (θ_r) and advancing contact angle (θ_a) are measured by adding/removing small amounts of water to/from the drop with a microsyringe. The values of θ_a and θ_r for silicon and polyethylene substrates that we used are given in Table 1. We introduce the "equilibrium" value of the contact angle $\theta_{eq} = (\theta_a + \theta_r)/2$ to characterize a substrate by a single quantity.

3. Results and Discussion

3.1. Coalescence in a Condensation Chamber. As sketched in Figure 1a, the coalescence process is characterized by three time stages.

1. Formation of liquid bridge between two drops of radii R_1 and R_2 and subsequent formation of a convex composite drop (between the time moments t_1 and $t = 0$ in Figure 1a) takes less than 2 ms as shown by Figure 2a, a fast camera microscopic picture (silicon II substrate, see Table 1 for its properties). The drop shape can be characterized by the large axis $2R_y$ measured in the direction of maximum elongation and the small axis $2R_x$ measured in the perpendicular direction, where R_y and R_x are large and small drop radii, respectively; see Figure 3. The contact line dynamics is characterized by quick increase of R_x due to its advancing motion in the "bottleneck" region of the composite drop due to the strong negative drop surface curvature in this region. R_y remains practically unchanged, i.e., no contact line receding occur. We note that the composite drop relaxes toward equilibrium without visible oscillations.

2. Decrease of large radius R_y with time and increase of small radius R_x such that the drop approaches the shape of spherical cap (Figures 2b and 3).

3. Slow growth of the composite drop by condensation.

We confirm and extend the data of stage 2 obtained by Andrieu et al.[15] The composite drop finally becomes hemispherical with equilibrium radius R. The dynamics is very slow, and the complete relaxation takes long time. The relaxation velocity is proportional to the restoring

1216 *Langmuir, Vol. 20, No. 4, 2004* *Narhe et al.*

Table 2. The Calculated Initial Contact Angle θ_0 and the Capillary Force f per Unit Length of the Contact Line in the Cases of Coalescence and Spreading

		condensation or deposition coalescence				spreading				
				f, mN/m					f, mN/m (eq 16)	
substrate	θ_{eq} (deg)	θ_0 (deg) calcd	θ_r (deg)	f_1, from eq 4	f_2, from eq 6	θ_0 (deg) calcd $V_1/V_2 = 1/4$	θ_0 (deg) calcd $V_1/V_2 = 1$	θ_a (deg)	$V_1/V_2 = 1/4$	$V_1/V_2 = 1$
glass + silane from ref 15	53	34.53	46	9.43	23.64					
	30	19.51	23	1.61	10.51					
silicon I	23.5	12.81	22	3.50	5.02	30.7	46.05	25	3.4	15.5
silicon I + silane	67	50.42	55	4.64	32.58	88.0	104.7	79	11.3	32.5
silicon II	52	32.35	47	11.88	21.91	66.3	85.68	57	10.4	34.3
silicon III from ref 11	11									
polyethylene	85	61.59	80	22.06	34.73	98.1	113.1	90	10.3	28.6

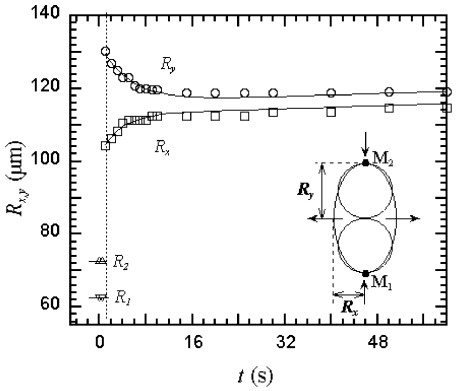

Figure 3. Evolution of large radius R_y and small radius R_x of the composite drop in a condensation chamber experiment. R_1 and R_2 are the radii of two drops before coalescence.

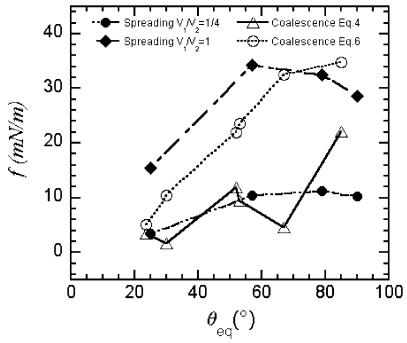

Figure 4. Contact angle dependence of the restoring capillary force f in mN/m as calculated from the experimental data; see Table 2.

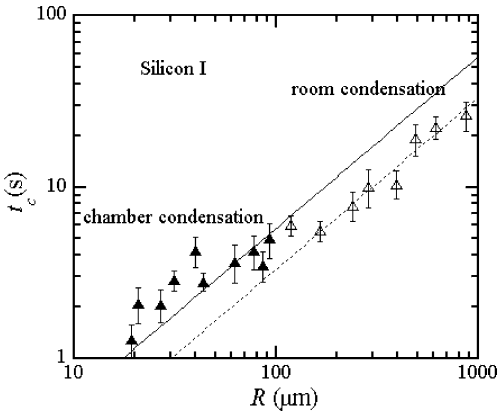

Figure 5. Relaxation time on silicon I by condensation in chamber and in open room atmosphere (at T_R = 23 °C, T_D = 18 °C, $T_s = T_D - 5$ °C) with respect to the equilibrium drop radius R (log−log plot). Lines: best fit to eq 8.

force F, which is defined by the variation of the drop surface energy; see Nikolayev and Beysens.[16]

On stage 2 the restoring force f per unit length of the contact line can be approximated by the expression

$$f = \sigma(\cos\theta - \cos\theta_r) \tag{3}$$

where $\theta = \theta(t)$ is the time-dependent dynamic receding contact angle at the points M_1 and M_2 that lie on the long axis (see Figure 3). A rough evaluation of the initial value of this force

$$f_1 = \sigma(\cos\theta_0 - \cos\theta_r) \tag{4}$$

can be obtained by estimating the initial contact angle $\theta_0 = \theta$ ($t = 0$) at the beginning of stage 2. To estimate this θ_0 angle, we assume that during stage 1, R_y does not change so that the contact line stays pinned at the points M_1 and M_2. For estimation purposes, it can be assumed that the composite drop at $t = 0$ takes the spheroid shape which has been described analytically by Nikolayev and Beysens.[16] As can be seen on Figure 2b, the image for $t = 0$ s shows that the small axis is equal to the radius of each of the coalescing drops. One thus postulates $R_y = 2R_x$, and obtains a relationship between the composite drop volume V_c, R_y, and cos θ_0 (see Appendix). The volume V_c can be found by adding the volumes of two identical spherical cap-shaped drops 1 and 2 of volume $V_1 = V_2$, $V_c = 2V_1$. These drops are assumed to be at equilibrium (i.e., that the contact angle is θ_a after stage 3 where the contact line advances very slowly due to condensation) just before coalescence begins. Their base radius R_1 can then be obtained from the expression[10]

$$R_1^3 = \frac{3V_1}{\pi}\frac{(1+\cos\theta_a)\sin\theta_a}{(1-\cos\theta_a)(2+\cos\theta_a)} \tag{5}$$

Since the points M_1 and M_2 are assumed to be immobile during the first stage, $R_y = 2R_1$. For estimation of θ_0, we use eq A5, as given in the Appendix. These equations allow θ_0 and f to be calculated provided θ_a is given. Its values are reported in Table 2. Note that θ_0 is independent of V_1.

The roughness influence can be estimated by comparing the force calculated in eq 4 with

$$f_2 = \sigma(\cos\theta_0 - \cos\theta_{eq}) \tag{6}$$

where the surface roughness influence is neglected. In Figure 4 we have plotted the forces $f_{1,2}$ given by eqs 4 and 6 with respect to θ_{eq}. As expected, eq 6 gives a larger value for the force.

In Figures 5 and 6, the relaxation time t_c versus equilibrium radius R is plotted for silicon I and polyethylene substrates (see Table 1 for their properties). The relaxation time t_c is obtained by fitting the relaxation data

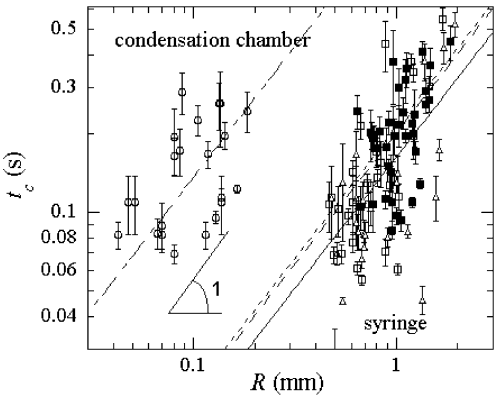

Figure 6. The relaxation time t_c variations with equilibrium drop radius R for condensation and syringe experiments on polyethylene (log−log plot) with different temperatures of substrate around the room dew temperature ($T_D = 13$ °C): open circles, condensation; open triangles, syringe, $T_s = T_D + 5$ °C; open square, syringe, $T_s = T_D$; full squares, syringe, $T_s = T_D - 5$ °C; full line, best fit of the data at $T_s = T_D + 5$ °C to eq 8; broken line, best fit of the data at $T_s = T_D - 5$ °C to eq 8; dotted line, best fit of the data at $T_s = T_D$ to eq 8.

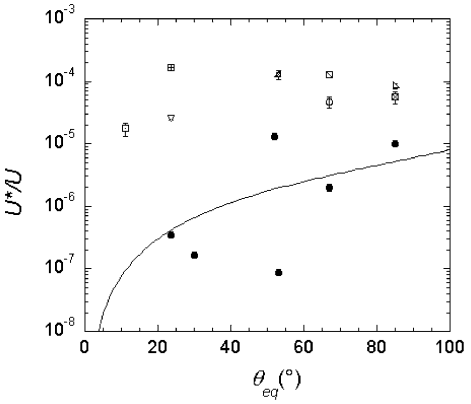

Figure 7. Experimental ratio U^*/U from Table 1 with respect to θ_{eq} for different substrates and coalescence methods (semilog plot): full dots, results of chamber condensation; full curves, best fit of full dots to $K/\Phi(\theta)$, with $K = 2.5 \times 10^{-6}$; open symbols, syringe experiments. Coalescence: inverted triangle, silicon I; dot in open circle, silicon I−silane; right triangle (bottom left), silicon II; right triangle (bottom right), polyethylene. Spreading: plus sign, in box, silicon I; back slash, in box, silicon I−silane; open circle, silicon II; dot in open box, silicon III (ref 11); times sign in box, polyethylene. ($U = \sigma/\eta = 73$ m/s.)

by an equation of the form

$$R_{x,y}(t) = R_0 \exp\left[\frac{-(t - t_0)}{t_c}\right] + R + A(t - t_0) \quad (7)$$

The first term corresponds to the relaxation of the composite drop, which is dominating in regime 2, the second and third terms are an expansion that approximately describes the slow growth due to condensation in regime 3. The time where coalescence begins is t_0. Its experimental value is imposed in the fit. R_0, R, A, and t_c are the fitting parameters. From Figures 5 and 6 one can deduce that the relaxation time t_c follows a linear variation with the final equilibrium radius R of the drop

$$t_c = (1/U^*)R \quad (8)$$

where the parameter U^* characterizes the contact line relaxation rate.

U^* should not be confused with the contact line speed, which obviously varies with time during the relaxation process. The U^* values obtained for silicon and polyethylene substrate are given in Table 1 together with data available from literature. It shows that U^* for a silicon surface is 1 order smaller than that for polyethylene. The relaxation dynamics is faster for larger contact angle as the restoring force f that moves the contact line is larger (see Table 2). This result is in agreement with the predictions of Nikolayev and Beysens.[16] According to them, t_c should vary with $\theta = \theta_{eq}$ as

$$t_c = \frac{1}{K}\frac{\eta}{\sigma}\Phi(\theta)\, R \quad (9)$$

This defines U^* as

$$U^* = K\frac{U}{\Phi(\theta)} \quad (10)$$

with

$$\Phi(\theta) = 45\frac{1 + \cos\theta}{(108 + 41\cos\theta + 14\cos^2\theta + 17\cos^3\theta)(1 - \cos\theta)} \quad (11)$$

and

$$U = \sigma/\eta \quad (12)$$

In Figure 7 the values of U^*/U are plotted with respect to θ_{eq}. Both condensation and syringe experiments were done many times, and each data point was obtained by averaging over 15−20 measurements. Although the data exhibit a large scatter, they can be reasonably fitted by the $K/\Phi(\theta)$ variation (Figure 7, continuous curve), resulting in the value $K \approx 2.5 \times 10^{-6}$. The reasons for such a scatter cannot be found in the difference of restoring force due to different θ_r. Indeed, in the framework of a linear approach (see, e.g., refs 15 and 16) the magnitude of the restoring force cannot influence the relaxation time. The above scatter probably could be explained by the influence of defects. The effect of successive pinning and depinning of the contact line (cf. Figure 9a below) can result either in an increase of the relaxation time (the contact line stays longer on the defects) or in a decrease (the contact line jumps quickly between the defects). Two-dimensional simulation[16] shows that these two antagonist effects nearly cancel. A nonlinear approach (e.g., that of ref 18) should be applied to elucidate the collective effect of the defects on the contact line motion.

The size of the drops in the chamber condensation experiments is limited by the minimum microscope magnification (the drops grow out of the field of view). To analyze the growth kinetics on longer time scale, we performed the condensation experiments with the same substrate in the open room atmosphere using the observation device used for the syringe deposition. The substrate (of temperature T_s) was cooled below the dew temperature, T_D, to achieve the condensation. The results of these

(18) Nikolayev, V. S.; Beysens, D. A. *Europhys. Lett.* **2003**, *64*, 763.

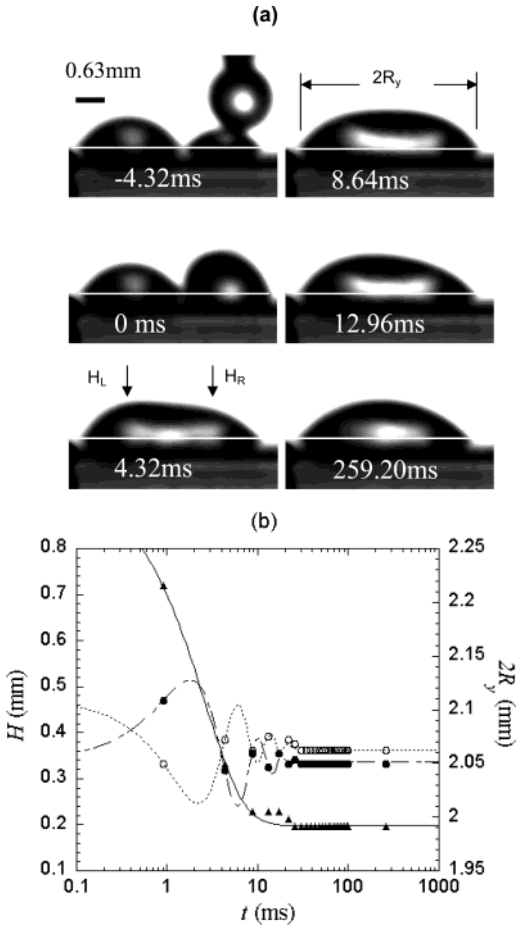

Figure 8. (a) Coalescence of two water drops in a syringe experiment at short time scale. Photos are taken with a fast camera on silicon I substrate. The volumes of three drops in the $t = -4.32$ ms image are 0.7, 0.25, and 0.23 μL. The white horizontal line indicates the substrate surface. The reflection is visible below this line. $H_L(H_R)$ represents the height of the composite drop on the left (right) side as indicated by the arrows. (b) Evolution of H_L (open circles, H_R (full circles), and $2R_y$ (full triangles) in a semilog plot. The broken lines are the fits to eq 13 and the full line to eq 7, with $A = 0$.

observations are plotted in Figure 5. They can also be described by (8). However, the U^* value is slightly different.

While the chamber condensation results in $U^* = (3.0 \pm 0.15) \times 10^{-5}$ m/s (see solid line in Figure 5), the coalescence at room atmosphere conditions results in $U^* = (1.7 \pm 0.16) \times 10^{-5}$ m/s (broken line in Figure 5). This difference can be attributed to the substrate and water contamination impossible to avoid in the open atmosphere.

3.2. Coalescence Initiated by Syringe Deposition. After deposition of the third drop at the top of one of the neighboring drops (see Figure 1b), the relaxation takes place. Since the drop was filmed sidewise in the syringe experiments, the evolution of the smaller drop radius R_x could not be analyzed. The R_y data are fitted to the exponential relaxation (7) where the condensation rate $A = 0$. While the restoring force is expected to be similar to that in the condensation experiments (see Table 2 and Figure 4), the receding is 1 to 2 orders of magnitude faster than that in the condensation-induced coalescence; see Figure 6 and Table 1. However, the kinetics remains much slower than that predicted by bulk hydrodynamics. The value of K is of the order 10^{-4}; cf. Figure 7.

3.3. Short Time Coalescence Kinetics. In the syringe deposition coalescence experiments (see Figure 1b), strong oscillation of the liquid−vapor interface of the composite drop occurs due to the impact with a newly added drop. The drop evolution on silicon I substrate (see Table 1) is filmed with the fast camera (Figure 8a) and reveals a quick surface motion. Such oscillations are observed commonly when drops are intentionally projected against a substrate.[19] However, to our knowledge such oscillations were never observed during syringe deposition where the drops are deposited very gently. In Figure 8b are plotted the time evolution of the heights of the drop profile H_L and H_R measured at distances $0.5R_y$ and $1.5R_y$, respectively, from the left contact point (see Figure 8a). The evolution of $H_{L,R}$ can be decomposed into exponential relaxation, due to the evolution of R_y and periodic oscillations whose amplitudes decrease exponentially. The following function

$$H_{L,R} = H_0 + H_1 \exp(-t/\tau_1) + H_2 \exp(-t/\tau_2) \times \cos\left(2\pi \frac{t}{\tau} + \varphi\right) \quad (13)$$

fits correctly the data of Figure 8a. The important parameter of the fits is here the oscillation period $\tau = 7.7$ ms (H_L) and 8.3 ms (H_R), with uncertainty ± 0.2 ms. The relaxation times are $\tau_1 \approx 16$ ms and $\tau_2 \approx 7$ ms. The value of the oscillation period compares well with the period of oscillations of a freely suspended drop of density ρ

$$\tau = (2\pi\rho R^3/3\sigma)^{1/2} \quad (14)$$

which gives $\tau \approx 10$ ms for $R = 1$ mm. The latter expression can be obtained easily from the balance of the pressure gradient (σ/R^2) induced by the surface tension and the inertial term ($\rho\partial v/\partial t$) $\sim \rho R/\tau^2$ in the Navier−Stokes equation, with ρ the density and v the typical interface velocity. A similar value for τ was measured by von Bahr et al.[19]

Similarly to the long-time R_y data, the short-time data can also be successfully fitted to the exponential relaxation (7) with $A = 0$. However, the relaxation time $t_c = 2.6 \pm 0.13$ ms turns out to be much smaller than that calculated from the long time relaxation data from Table I, resulting in $t_c = R/U^* \approx 100$ ms (syringe experiments) or $t_c \approx 1$ s (condensation chamber).

This difference can be explained by the influence of the oscillations on the contact line motion. During the oscillations, the contact line is pulled by the drop surface. In Figure 8, one can see a strong correlation between the end of the oscillations and the end of the drop relaxation. It means basically that in the case of the syringe deposition, the moving force of the contact line motion is related to the kinetic energy of the drop surface motion instead of the potential surface energy. This potential energy is used as a basis to derive the expression (6) for the restoring force and (1) for the contact line velocity,[6] which means that both (1) and (6) are not valid descriptions of the spreading by syringe deposition of low viscosity drops.

The total duration of this "oscillation stage" of a freely suspended drop would be of the order of the bulk viscous damping time $R^2\rho/\eta \sim 1$ s. In the case of the sessile drop, the oscillation damping is faster due to the additional dissipation in the contact line region.

The faster oscillation-induced relaxation on the short time scale should result in a faster relaxation to the spherical cap shape when comparing to the case with no oscillations. In fact, we were not able to detect such oscillations in the condensation experiments and the

(19) von Bahr, M.; Tiberg, F.; Zhmud, B. *Langmuir* **2003**, *19*, 10109.

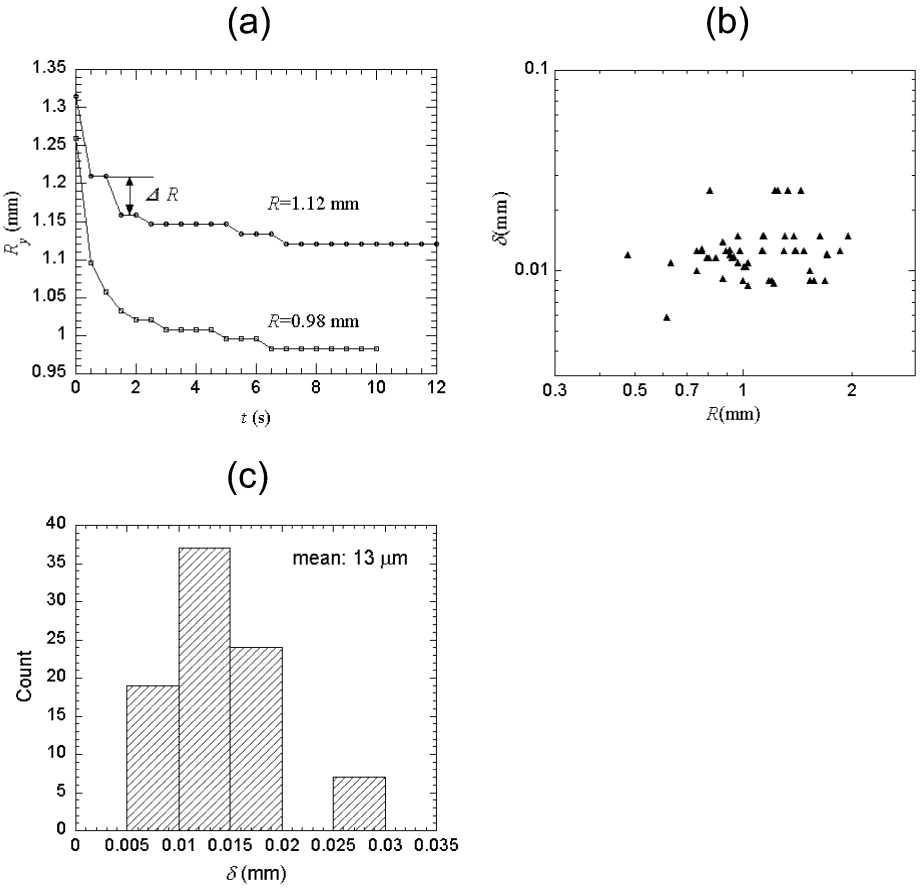

Figure 9. Pinning of the contact line (syringe deposition, silicon I + silane, $V_1/V_2 = 1/4$) during the coalescence. (a) Effects on relaxation. The slips ΔR are due to pinning on defects. (b) Amplitude (15) of the last slips obtained in multiple experiments on the same substrate as a function of R, in a semilog plot. (c) Histogram of the amplitude (15) of the last slips from part b.

relaxation time is indeed 1 to 2 orders of magnitude larger in the latter case.

3.4. Estimation of the Characteristic Scale for Surface Roughness. From the long time relaxation data, it is possible to study the statistics of the surface roughness. In Figure 9a, the relaxation of coalescence is shown for drops of about 1.3 mm radius on silicon I + silane substrate (see Table 1).

Pinning of the contact line on the defects leads to the "stick−slip" motion clearly seen in Figure 9a. as "slips" or jumps with amplitude ΔR. For small times, where the moving force is stronger, the line can jump several defects at a time and ΔR is large. Near the end of the relaxation, ΔR is small and can be a measure of the average distance between the defects

$$\delta = \min(\Delta R) \qquad (15)$$

In Figure 9b the δ values are plotted for various R. There is no visible R dependence. The statistics of these δ are shown in Figure 9c, which gives as mean size $\delta = 13\ \mu$m.

3.5. Influence of the Supersaturation. To test a possible influence of mass transfer on the contact line motion predicted by Shanahan,[20] the syringe experiments were carried out at different temperatures of the substrate T_s such that $T_s > T_D$, $T_s = T_D$, $T_s < T_D$, where T_D denotes the dew temperature. Changing the substrate temperature modifies the supersaturation at the substrate level and then the intensity of the condensation or evaporation. In our experiment, $T_s > T_D$ means HR <100%, and drop evaporation occurs, and $T_s < T_D$ corresponds to supersaturation, and condensation starts on the drop surface and the substrate. The results of these experiments are presented in Figure 6. We conclude from it that within the accuracy of our experiments, the change in the condensation/evaporation rate does not affect the contact line motion.

Note that when $T_s < T_D$, tiny condensing drops are visible on the substrate, some of them coalesce with the composite drop formed during the coalescence of two deposited drops. The volume change of the composite drop due to these multiple coalescences is negligible, and the kinetics of the triple line motion is not affected by the presence of these tiny drops.

3.6. Spreading Initiated by Syringe Deposition. The schemes of the spreading experiments are shown in parts c and d of Figure 1. We noticed that for both cases the results are comparable. The fast camera filming of the spreading also shows fast drop surface oscillation analogous to that observed during the coalescence initiated by syringe deposition. Figure 10 reports $R_y = R_x$ data plotted with respect to t for spreading of a water drop on the silicon I surface in the syringe experiment. The relaxation time is obtained by fitting the data by the exponential function (7) with $A = 0$.

We can compare the spreading relaxation with that observed by Rieutord et al.[11] when they are fitted to the same exponential relaxation. Both sets of data clearly fit well an exponential relaxation, with values of U^* in the same range magnitude (Figure 10). The Rieutord et al. data show the larger values and the larger data scatter. This is because in Rieutord et al. experiments the contact

(20) Shanahan, M. E. R. *C. R. Acad. Sci., Sér. 2* **2001**, *IV*, 157.

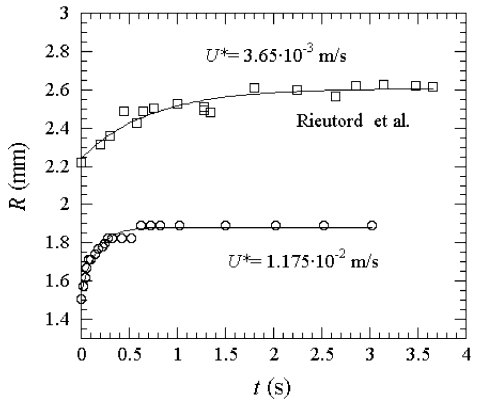

Figure 10. R with respect to t for spreading of a water drop on silicon I surface in the syringe experiment (circles) and the data of Rieutord et al.[11] (squares). The fits to the exponential relaxation and the resulting U^* values are shown too. For syringe experiment (circle), $V_1/V_2 = 1/4$.

angle was half of the smallest of ours; see Table 1. The defect influence is stronger at small contact angles as shown by the analysis of the restoring force performed below.

The initial restoring force in the advancing-controlled spreading case can be calculated using the expression

$$f = \sigma(\cos\theta_0 - \cos\theta_a) \qquad (16)$$

where the initial contact angle θ_0 is related to R_y through the expression (5) in which θ_a is replaced by θ_0. The volume ratio V_1/V_2 of the added drop (V_1) at the top of the other (V_2) was varied from 1/4 to 1 to show the influence of this ratio on the restoring force. When V_1/V_2 is larger, the difference between θ_a and θ_0 should be larger, which provides a larger f value and thus a quicker relaxation.

To estimate the initial contact angle θ_0 for the spreading of a single drop of volume V_2 by adding new drop of volume V_1, we assumed that at $t = 0$ (Figure 1c), the contact line of drop of volume V_2 stays pinned at the three-phase contact line, and its volume increases due to the additional volume of the newly added drop, so that the total volume of the new drop is $V_1 + V_2$. By using a spherical cap approximation and by knowing volume V_2, V_1, and the base radius R of initial drop of volume V_2, we can calculate the initial contact angle θ_0. The f data are shown in Table 2 and in Figure 4 for the sake of comparison.

One can notice that the larger V_1/V_2 results in the stronger restoring force value. Figure 4 shows that the restoring force is small for the small contact angles. Therefore, the defects with the same pinning strength influence the relaxation at the small contact angle stronger than that for the large contact angles. As shown in ref 16, the defect influence leads to the paradoxical decrease of the total relaxation duration, which manifests itself in U^* increase.

The relaxation rate U^* is similar to that for the receding syringe experiments with coalescence (Table 1 and Figure 7). The relaxation rate in both experiments is 10−100 times larger than that for the condensation experiments. We attribute this difference to the additional energy brought to the system due to the impact of the drop during the syringe deposition process. This impact induces the oscillations of the composite drop surface, which create the additional (to f) pulling force acting on the contact line.

4. Conclusion

These experiments show that the dynamics of low viscous sessile drops during spreading and coalescence can be markedly affected by initial conditions. In particular, the relaxation rate depends also on the initial kinetic energy given to the drop at the beginning of its relaxation. The syringe deposition induces strong oscillations of the drop. At each oscillation, the drop surface "pulls" the contact line which thus accelerates its motion. In contrast, drop oscillations are not detected for the case of coalescence observed during the condensation and the relaxation turns out to be 10−100 times slower. This means that the contact line motion studies carried out with the traditional drop deposition method are not accurate enough because of uncontrollable oscillations, important especially for low viscosity fluids. The condensation-induced coalescence presents a more reliable way to study the contact line motion because the oscillations do not occur.

On the other hand, within the accuracy of the experiment, there is no visible influence of the condensation/evaporation kinetics on the contact line motion.

It is very difficult to assign a precise value for the ratio $K = \eta/\xi$, which is found to be of the order 10^{-4} for the syringe deposition and 2.5×10^{-6} in the condensation coalescence. Such small K values clearly show that the dynamics of low viscous sessile drops (spreading, coalescence) in the regime of partial wetting is limited by the dissipation at the region of the drop close to the contact line. This dissipation leads to relaxation 5 to 6 orders of magnitude slower than that expected from bulk dissipation, a value which cannot be compared easily from the current theories, except the Pomeau expectation that K is a thermally activated Arrhenius factor;[14] however, in this theory, spreading is expected to be much faster than receding as the Arrhenius factor is no longer present. We were unable to put in evidence such a difference in our experiments since spreading studies can be performed only with syringe deposition, which is unreliable because of the drop oscillations.

The relaxation rate was seen to increase with the contact angle, leading to an angle variation in reasonable agreement with the theory of sessile drop relaxation by two of us (V.N. and D.B.[16]).

Acknowledgment. We thank F. Rieutord for giving us his experiment data files and provided us with CEA-LETI silicon wafers and are grateful to Y. Pomeau for exciting discussions. We are indebted to F. Palencia for helping us with the video acquisition apparatus.

Appendix: Estimation of the Initial Receding Contact Angle

Following Nikolayev and Beysens,[16] we approximate the composite drop shape by that of the spheroidal cap defined by the equation

$$x^2/a^2 + [y^2 + (z + d)^2]/b^2 = 1, \qquad z > 0 \qquad (A1)$$

in the Cartesian coordinates (x,y,z). The parameters a, b, and d can be found from the following equations (see ref 16 for more details on them). The first of them fixes the drop volume V_c:

$$V_c = \frac{\pi}{3}\frac{a}{b}(2b^3 - 3b^2d + d^3) \qquad (A2)$$

The next two equations connect a, b, and d to the parameters R_x and R_y:

$$R_y^2 + d^2 = b^2$$

$$R_x b = R_y a \tag{A3}$$

The initial receding angle is then defined by the expression

$$\cos \theta_0 = d/b \tag{A4}$$

By using the assertion $2R_x = R_y$ (meaning that the small axis is equal to the diameter of each of the coalescing drops, which verifies experimentally, see Figure 2b, the image for $t = 0$ s), one finds out easily the equation

$$V_c = \frac{\pi}{6} R_y^3 \frac{(1 - \cos \theta_0)^{1/2}(2 + \cos \theta_0)}{(1 + \cos \theta_0)^{3/2}} \tag{A5}$$

that should be solved numerically for $\cos \theta_0$ while R_y and V_c are known.

LA034991G

INSTITUTE OF PHYSICS PUBLISHING JOURNAL OF PHYSICS: CONDENSED MATTER

J. Phys.: Condens. Matter **17** (2005) 2111–2119 doi:10.1088/0953-8984/17/13/009

Dynamics and depinning of the triple contact line in the presence of periodic surface defects

Vadim S Nikolayev[1]

ESEME, Service des Basses Températures, DRFMC/DSM, CEA-Grenoble, France

E-mail: vnikolayev@cea.fr

Received 12 October 2004, in final form 3 December 2004
Published 18 March 2005
Online at stacks.iop.org/JPhysCM/17/2111

Abstract

We propose an equation that describes the shape of the driven contact line in dynamics in the presence of an arbitrary (possibly random) distribution of the surface defects. It is shown that the *triple* contact line depinning differs from the depinning of interfaces separating *two* phases; the equations describing these phenomena have an essential difference. The force–velocity dependence is considered for a periodical defect pattern. It appears to be strongly nonlinear both near the depinning threshold and for large contact line speeds. This nonlinearity is comparable to experimental results on the contact line depinning from random defects.

1. Introduction

Motion of interphase boundaries in a random environment remains an open problem of general interest. Much attention has been paid to the depinning transition in systems where collective pinning creates nontrivial critical behaviour of the interface separating two different phases: fluid invasion in porous media, magnetic domain wall motion, flux vortex motion in type II superconductors, charge density wave conduction, dynamics of cracks, solid friction [1, 2]. The theory of the depinning transition is based on the analysis of the following equation for the interface position h:

$$\frac{\partial h}{\partial t} = F + \eta(h) + G[h], \tag{1}$$

where F is the externally imposed force, η is the noise due to the randomness of the media, t is time, and $G[\cdot]$ is some operator. When F is close to the depinning threshold F_c (where the interface begins to move), this approach generally results in the power law for the average interface velocity v

$$v \sim (F - F_c)^{\beta}, \tag{2}$$

[1] Corresponding address: CEA-ESEME, PMMH, ESPCI, 10, rue Vauquelin, 75231 Paris Cedex 5, France.

where the exponent β is universal. The origin of this dependence lies in the peculiar interface dynamics near the pinning threshold, namely a random succession of avalanches of depinning events. When $F \gg F_c$, a conventional mobility law

$$v \sim F \tag{3}$$

becomes valid.

Depinning of the triple gas–liquid–solid contact line on a solid surface with defects is another example of the depinning transition. The general approach to the interface depinning phenomena outlined above is frequently applied to the contact line depinning [3–6]. However, the discrepancy between the theory and the experimental data on contact line motion is notable. First, $\beta < 1$ according to the theoretical studies (see [3, 6]), while $\beta \geqslant 1$ was found experimentally [4, 7]. Second, the linear regime (3) has never been obtained [7].

In this paper we propose a framework suitable for explaining these results.

2. Modelling of the contact line motion

The major problem in this field is related to the failure of the conventional hydrodynamic approach based on the 'no-slip' boundary condition (zero liquid velocity) at the solid surface in the vicinity of the contact line. Such an approach [8] would result in a mathematical singularity at the contact line: the diverging viscous dissipation. In reality the dissipation in the vicinity of the contact line is large but finite [9]. The mechanism of the singularity removal for the partial wetting case is still under debate. Multiple singularity removal mechanisms were proposed [10, 11]. Most of these models (those which are not limited to the small values of the dynamic contact angle θ) result in the following expression for the contact line velocity v_n:

$$v_n = \frac{\sigma}{\xi}(\cos\theta_{\mathrm{eq}} - \cos\theta) \tag{4}$$

where θ_{eq} is the equilibrium (Young) value of the contact angle, σ is the surface tension, and ξ is a mechanism-dependent coefficient that has the same dimension as the shear viscosity μ.

Since the contact line is not straight due to the presence of the defects, the theoretical analysis of pinning requires 3D modelling. Such a modelling can be extremely difficult when using the hydrodynamic contact line motion models where the flow pattern depends on the contact line curvature. Recent papers [12, 13] have introduced a simpler approach. It is valid if most of the dissipation that occurs in the fluid with the moving contact line takes place in the near contact line region. The latter is defined as a fluid 'thread' adjacent to the contact line. Its diameter is assumed to be much smaller than the radius of curvature of the fluid surface. In other words, the viscous dissipation in the bulk of the fluid is neglected with respect to the dissipation that occurs close to the contact line. This assumption is verified by numerous experiments (see for example [14, 15]).

A single constant dissipation coefficient ξ is introduced to account for the anomalous dissipation in the vicinity of the contact line without detailing its origin. By further assuming that this dissipation is the same both for advancing and receding contact line motion, the energy dissipation rate can be written in the lowest order in v_n as [16]

$$T = \int \frac{\xi v_n^2}{2}\,\mathrm{d}l, \tag{5}$$

where the integration is performed along the contact line. The equation for the contact line motion can be obtained from the force balance between the induced and friction forces [9]

$$-\frac{\delta U}{\delta h} = \frac{\delta T}{\delta \dot{h}}, \tag{6}$$

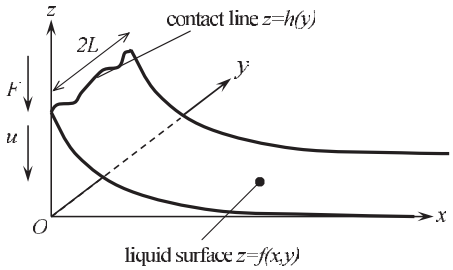

Figure 1. Reference system to describe the Wilhelmy balance experiment. The Wilhelmy plate is positioned in the yOz plane. The positive directions for u and F are shown too.

where $\frac{\delta \dots}{\delta \dots}$ means the functional derivative, the dot means the time derivative, and h defines the contact line position. The potential energy U of the system needs to be calculated assuming that each time moment the fluid surface takes its equilibrium shape. It was shown recently [17] that such a quasistatic scheme leads to equation (4) for an arbitrary contact line geometry. The dynamic approach (where the fluid surface shape is determined from hydrodynamics) is considered elsewhere [18]. It appears to lead to the same equation (4).

The quasistatic approach is of course not new. It was applied by many researchers, in particular by Golestanian and Raphaël in the approximation of small contact angles [19]. The advantage of our approach is the account of the gravity or/and fluid volume conservation which allow us to obtain the contact line shapes rigorously. In particular, for the Wilhelmy geometry considered below, we take into account the gravity influence [13] which permits us to avoid divergences [9] and thus obtain the contact line profile. When the gravity is irrelevant (as for small drops), the fluid volume conservation plays this stabilizing role [12, 18].

3. Contact line equation for the forced motion

The equation for spontaneous motion has been derived in [13]. In this paper we deal with the Wilhelmy geometry (figure 1), where the vertical plate with surface defects can be moved up and down with a constant velocity u ($u > 0$ for the advancing contact line is assumed). The average value of the force F exerted on this plate due to the presence of the moving contact line can be measured with a high precision [7]. The liquid–gas interface is assumed to be described by the function $z = f(x, y, t)$ where t is time and

$$|\nabla f| \ll 1 \tag{7}$$

is assumed. The position of the contact line is then given by its height $h = h(y, t)$ such that $h(y) = f(x = 0, y)$. From now on, we omit the argument t.

Under the assumption (7), the minimization of the potential energy U of the liquid with respect to f results [13] in the following expression:

$$f = \frac{1}{2L} \sum_{n=-\infty}^{\infty} \exp\left(-x\sqrt{l_c^{-2} + \pi^2 n^2/L^2}\right) \int_{-L}^{L} \mathrm{d}y'\, h(y') \cos\frac{\pi n(y - y')}{L}, \tag{8}$$

where $l_c = \sqrt{\sigma/\rho g}$ is the capillary length, ρ is the liquid density and g is the gravity acceleration. We assume that f is periodic (period $2L$) in the y-direction perpendicular to the direction of u. Following [20, 21], the surface defects are modelled by the spatial variation of the equilibrium value of the contact angle $\theta_{eq}(y, z)$ along the plate.

The contact line velocity with respect to the solid reads $v_n = \dot{h} + u$. Taking into account the expression for the dynamic contact angle θ obtained under the condition (7),

$$\cos\theta = -\partial f/\partial x|_{x=0}, \tag{9}$$

one obtains from equation (4) the following governing equation for h

$$\dot{h}(y) + u = \frac{\sigma}{\xi}\left\{c[y, h(y)+ut] - \frac{1}{2L}\sum_{n=-\infty}^{\infty}\sqrt{l_c^{-2}+\pi^2 n^2/L^2}\int_{-L}^{L} \mathrm{d}y'\, h(y')\cos\frac{\pi n(y-y')}{L}\right\}, \tag{10}$$

where $c(y, z) = \cos[\theta_{eq}(y, z)]$ is introduced for brevity.

Consider the contact line motion equation for an arbitrary defect pattern. It can be obtained from equation (10) when taking the limit $L \to \infty$:

$$\dot{h}(y) + u = \frac{\sigma}{\xi}\left\{c[y, h(y)+ut] - \frac{1}{\pi}\int_0^{\infty} \mathrm{d}p\,\sqrt{l_c^{-2}+p^2}\int_{-\infty}^{\infty} \mathrm{d}y'\, h(y')\cos[p(y-y')]\right\}. \tag{11}$$

An equation in a very similar form has already been written [23]. However, the integration order was inverted which resulted in a mathematically intractable expression. Equations (10) and (11) reduce to those obtained in [13] when $u = 0$.

One can easily derive a simpler 'long-wave limit' version of equation (11) by expanding $h(y')$ around $h(y)$ in the Taylor series:

$$\dot{h} + u = \frac{\sigma}{\xi}\left[c(y, h+ut) - \frac{h}{l_c} + \frac{l_c}{2}\frac{\partial^2 h}{\partial y^2}\right]. \tag{12}$$

Notice that this further simplification is fully consistent with the initial assumption (7). This form of the governing equation clearly shows why one needs to account for the gravity while considering the deformation of the initially straight contact line. When the gravity influence tends to zero, l_c increases and the gravity induced (second derivative) term that describes the contact line deformation becomes dominating. In other words, the gravity influence on the contact line deformation is important even in the large capillary length limit.

Consider now equations (11) and (12) from the point of view of the theory of the interface depinning [1, 2, 6]. They have the form (1), where the random term η is replaced by the random term c. In equation (12), one recognises the well-studied (see [5] and references therein) quenched Edwards-Wilkinson equation. However, the external force F is missing in both equations.

4. External force

Generally, one cannot apply a force directly to the contact line to make it move. Probably the only exception is a motion of a sessile drop on a solid with a wettability gradient. This special case will not be considered here. In the more common situation of homogeneous average wettability, the contact line can be moved by either exerting a force at the fluid mass as a whole or moving the solid with respect to the fluid similarly to the Wilhelmy balance experiments, using which this force can be measured.

The additional force F that acts on the Wilhelmy plate due to the presence of the contact line (per unit plate width in the y-direction) consists of two parts [23]: the contribution of the interface tensions at the contact line and the 'friction' force due to the energy dissipation:

$$F = \frac{1}{2L}\int_{-L}^{L} \mathrm{d}y\left\{\sigma_{LS} - \sigma_{GS} + \xi\left[\dot{h}(y) + u\right]\right\}. \tag{13}$$

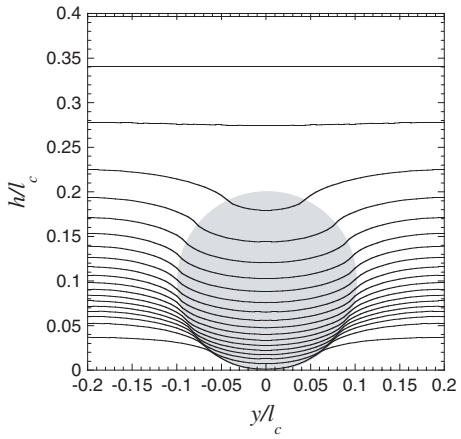

Figure 2. A unit cell for the periodic defect pattern (the area of a defect is shadowed) and periodic (both in *time* and space) solution of equation (10). 20 snapshots of the contact line with equal time intervals $0.2\xi l_c/\sigma$ are shown for $v = 0.1\sigma/\xi$. The chosen parameters of the defect pattern are $2L = 0.4l_c$, $r = 0.1l_c$, $\theta_s = 70°$, and $\theta_d = 110°$. The full picture of the contact line motion can be obtained by periodic continuation of this image in both vertical and horizontal directions.

where the surface tensions of the gas–solid (σ_{GS}) and liquid–solid (σ_{LS}) interfaces are introduced. According to the Young formula, $c(y, z) = (\sigma_{GS} - \sigma_{LS})/\sigma$. By using equation (4), one obtains the final expression

$$F = -\frac{\sigma}{2L}\int_{-L}^{L} \cos\theta(y)\,\mathrm{d}y, \tag{14}$$

which means that the force in σ units at each time moment can be obtained by averaging the cosine of the dynamic contact angle along the contact line. The expression (14) has already been used by several authors (see for example [7, 22]). This force can be measured directly by separating it out from viscous drag using special experimental techniques [7] and is presented as a counterpart of the external force F in equation (1) for the case of contact line depinning.

One can now clearly see the difference between interface depinning and contact line depinning. For interface depinning, the force F enters directly into the governing equation (1). It can be controlled, imposed, and may take an arbitrary value. For contact line depinning, the external force does not directly enter the governing equations (11) and (12). It is hardly possible to be controlled. However, it can be measured when the velocity u is imposed. It can be calculated using equation (14). According to the latter, the force (per unit plate width) is bounded by the surface tension value. This fact can explain the nonlinearity of the $F(v)$ dependence observed in [7] at large velocities. However, the model based on equations (11) and (12) cannot exhibit this saturation. Because of the conditions (7) and (9), $|F| \ll \sigma$ was implicitly assumed during the derivation of equations (11) and (12).

5. Application to a periodic defect pattern

We consider below a periodical (both in the directions y and z) pattern of round spots of radius r shown in figure 2. Inside the spots, $\theta_{eq} = \theta_d$, the rest of the plate having $\theta_{eq} = \theta_s$.

Because of the nonlinearity in the c term, equation (10) seems to be complicated and difficult to solve numerically. However, the following considerations allow a quite efficient numerical algorithm for its resolution to be proposed.

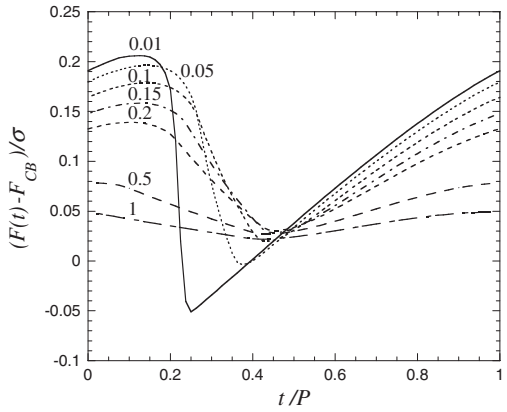

Figure 3. Periodic (with period P) variations of the force that acts at the Wilhelmy plate during its downward motion. The parameter of the curves is v in σ/ξ units. We used the same parameters of the defect pattern as for figure 2.

The function $c(y, z)$ can be made even with respect to y by choosing properly the position of the point $y = 0$ with respect to the defect pattern. The function $h(y)$ is then even too and $\cos[\pi n(y - y')/L]$ in equation (10) factorizes into $\cos(\pi ny/L)\cos(\pi y'/L)$. Both the integration and the n-summation can be performed numerically with a highly efficient fast Fourier transform (FFT) algorithm [24]. The fourth-order Runge–Kutta method [24] is applied to solve the differential (with respect to time) equation (10). We are interested in its solutions periodic both in y and t. The time periodicity is sought to obtain time averaged values independent of the initial position of the liquid surface. The time averages are denoted by the angle brackets; for example, the average force is

$$\langle F\rangle = \frac{1}{P}\int_0^P F(t)\,\mathrm{d}t, \tag{15}$$

where $P = 2L/|u|$ is the time period. The average contact line speed $v \equiv \langle v_n\rangle = u$. The time-periodic behaviour appears after the contact line goes through several first rows of the defects.

An example for such a double periodic solution is shown in figure 2. The snapshots of the contact line are 'taken' with the equal time intervals; the contact line speed can be evaluated from the density of the snapshots. One can see that when the contact line meets a line of defects, its central portion remains stuck until the whole contact line slows down to let the liquid surface accumulate its energy. During this stage, the difference between the dynamic and equilibrium contact angles increases ('stick' stage). The slip stage follows, during which the contact line accelerates. The difference between the average velocities in the stick and slip phases can be very large near the pinning threshold; see the curve for $v = 0.01\sigma/\xi$ in figure 3 where the steepest portion corresponds to the slip. This sequence of accelerations and decelerations of the whole contact line is a collective effect which characterizes the contact line motion in the presence of defects.

The force (14) can be calculated using equation (9) for each of the $h(y)$ curves like those in figure 2. The $F(t)$ curves are presented in figure 3, where F is counted from the value

$$F_{\mathrm{CB}} = \sigma\cos\theta_{\mathrm{CB}} - \xi v, \tag{16}$$

where $\cos\theta_{\mathrm{CB}} = \varepsilon^2\cos\theta_{\mathrm{d}} + (1-\varepsilon^2)\cos\theta_{\mathrm{s}}$ is the Cassie–Baxter value of the static contact angle, and $\varepsilon^2 = \pi(r/2L)^2$ is the defect density. F_{CB} corresponds to a force that would be induced by a homogeneous solid with the equilibrium contact value equal to θ_{CB}, which is simply a

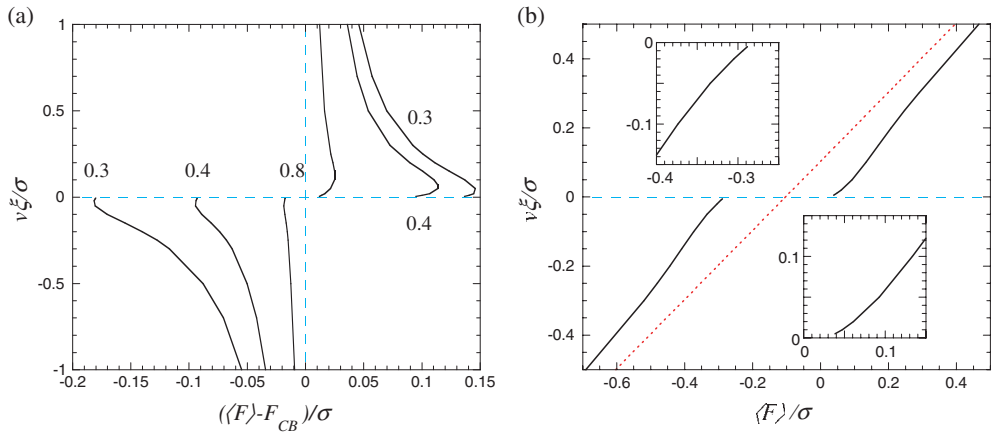

Figure 4. (a) $v(\langle F\rangle - F_{\mathrm{CB}})$ curves calculated for different distances between defect centres $2L$ (shown as a curve parameter in l_{c} units). Both advancing ($v > 0$) and receding ($v < 0$) branches are presented. (b) $v(\langle F\rangle)$ curve for $2L = 0.3l_{\mathrm{c}}$. The $v(F_{\mathrm{CB}})$ dependence is shown as a dotted line. The portions of the curves near $v = 0$ are zoomed in the inserts. Note that the abscissa is the averaged value of $\cos\theta$. Same parameters of the defect pattern as for figure 2 are used.

(This figure is in colour only in the electronic version)

spatially averaged value of the contact angle. It does not take into account the pinning on the defects. The difference $F - F_{\mathrm{CB}}$ characterizes the influence of the spatial fluctuations of θ_{eq} on the contact line motion, i.e. the pinning strength.

The dependence of $\langle F\rangle - F_{\mathrm{CB}}$ on v (inverted for compatibility with figure 4(b)) is shown in figure 4(a) for different defect densities ε^2 that correspond to different L values. Both advancing ($v > 0$) and receding ($v < 0$) branches are presented. The deviation of $\langle F\rangle$ from F_{CB} increases with the increasing defect density (decreasing distance between the defects) which is explained by the increasingly strong pinning. By recalling that the average cosine of the contact angle is $\langle F\rangle/\sigma$, one finds out that the cosines of the static advancing and receding contact angles (the values of $\langle F\rangle/\sigma$ at $v \to \pm 0$) also drift away from the Cassie–Baxter value with the increasing pinning.

One can notice some asymmetry of the force with respect to the direction of motion (advancing or receding), which is visible in figure 4(a). In other words, $\cos\theta_{\mathrm{CB}} \neq [\cos\theta(v) + \cos\theta(-v)]/2$ in spite of the perfect symmetry of the pattern. This is explained by the asymmetry of the problem geometry (figure 1) with respect to the motion direction.

One notices that the surface defects manifest themselves much more strongly at smaller velocities. This is quite a general feature: at $|v| \geqslant \sigma/\xi$ the contact line does not 'feel' the θ_{eq} fluctuations any more and the average cosine of the dynamic contact angle is defined by $\cos\theta_{\mathrm{CB}} - \xi v/\sigma$ for any defect pattern (until it attains the saturation regime at $\cos\theta \approx \pm 1$, see section 4).

While we study the pinning on the periodic patterns and the exponents proper to the random behaviour cannot be recovered, it is however interesting to study the dependence of $\langle F\rangle$ on v and compare it to the behaviour defined by equations (2) and (3). The inverse functions $v(\langle F\rangle)$ are presented in figure 4(b). The $v(F_{\mathrm{CB}})$ linear dependence (inverted equation (16)) is drawn for the sake of comparison.

Figure 4(b) can be compared to the experimental results [7] obtained for the random defect pattern (studies with the ordered patterns in this geometry are unknown to us). At small $|v|$, the

sign of the curvature is the same as in the experiment and corresponds to $\beta > 1$ in equation (2). This comparison suggests that $\beta > 1$ behaviour appears due to the collective pinning rather than due to the randomness. Figure 4(a) shows that the calculations for the other defect densities exhibit the same curvature sign both for the advancing and for the receding directions. The value of F_c is defined by the static contact angle (advancing or receding depending on the direction of motion). However, the linear increase of $\langle F \rangle(v)$ at large $|v|$ similar to equation (3) is simply a consequence of the approximation (7) discussed in the previous section. In reality, the $v(\langle F \rangle)$ dependence is strongly nonlinear at large $|v|$ and should have vertical asymptotes at $\langle F \rangle = \pm\sigma$.

The decreasing slope of the $v(F)$ curve at $F \to F_c$ (that appears due to the influence of defects when $\beta > 1$) can explain the extremely slow relaxation observed during the coalescence of sessile drops [14, 15]. In this case a very small force F was imposed by surface tension. Since the effective dissipation coefficient was inferred from the $v(F)$ slope value (inversely proportional to it), it appeared to be very large while the actual ξ value could be much smaller.

Previously, the $F(v)$ behaviour has been studied by Joanny and Robbins [23] for the 1D case (they introduced an averaging along the y axis) where c was a function of z (see figure 1) only. The contact line resulting from such a calculation was thus always straight. They considered several shapes for the $c(z)$ distribution and found that the $F(v)$ curvature sign was different depending on the shape and periodicity of the $c(z)$ curve. For the square well shape that would correspond to one studied here, they found linear $F(v)$ dependence. In the present study, c varies also in the y direction, $c = c(y, z)$.

In this work we study an ordered defect pattern. Further studies will show if the universality in the $v(F)$ law (2) exists for random defect patterns; it does not seem reasonable to us to estimate the β value at this stage.

6. Conclusions

It was demonstrated in this paper that the descriptions of the depinning of interface separating two phases (e.g. for fluid invasion of porous media) and of the triple contact line, while similar in many respects, have essential differences. The main one is related to the external force that can be controlled directly for the case of interface depinning and enters its equation of motion as an additive term. An external force can hardly be imposed directly to the triple contact line and thus does not enter its equation of motion. The experimentally measured force associated with the contact line motion can be calculated and it turns out to be essentially nonlinear in the contact line velocity. At small velocities, the nonlinearity is due to the collective pinning at the surface defects, while at large velocities the force per unit contact line length is bounded by the value of the surface tension. Our theoretical results obtained for a periodical defect pattern suggest that the experimentally observed [7] nonlinearity of the force–velocity curve is a result of the collective pinning on the defects rather than a consequence of their randomness.

This nonlinearity was obtained from the model with a constant dissipation coefficient ξ. Therefore, by basing on the nonlinearity of this curve it is hardly possible to make a judgement about the nonlinearity of the microscopic mobility expression (i.e. dependence of the friction force that enters equation (13) on velocity) or, equivalently, on the dependence of ξ on the contact line speed. Our results suggest that when an external force is imposed (as for the elongated sessile drop returning to its final shape), the contact line motion should be slowed down near the pinning and depinning thresholds.

The obtained profiles of the contact lines compare well with the recent experimental profiles obtained with periodic defect patterns for the sessile drop geometry [25].

The equations of the contact line motion are derived. They can be applied to analyse the collective effect of surface defects on the contact line motion for random defect patterns.

Acknowledgments

The author would like to thank E Rolley and S Moulinet for useful discussions and D Beysens for numerous fruitful discussions and friendly support.

References

[1] See e. g. Barabási A-L and Stanley H E 1995 *Fractal Concepts in Surface Growth* (Cambridge: Cambridge University Press)
[2] Fisher D S 1998 *Phys. Rep.* **301** 113
[3] Ertaş D and Kardar M 1994 *Phys. Rev.* E **49** R2532
[4] Schäffer E and Wong P-Z 2000 *Phys. Rev.* E **61** 5257
[5] Rosso A and Krauth W 2001 *Phys. Rev. Lett.* **87** 187002
[6] Chauve P, Le Doussal P and Wiese K 2001 *Phys. Rev. Lett.* **86** 1785
[7] Moulinet S 2003 Rugosité et dynamique d'une ligne de contact sur un substrat désordonné *PhD Thesis* University Paris 7-Denis Diderot
Moulinet S, Guthmann C and Rolley E 2004 *Eur. Phys. J.* B **37** 127
[8] Huh C and Scriven L E 1971 *J. Colloid Interface Sci.* **35** 85
[9] de Gennes P-G 1985 *Rev. Mod. Phys.* **57** 827
[10] Ramé E 2002 *Encyclopedia of Surface and Colloid Science* ed A T Hubbard (New York: Dekker)
[11] Pomeau Y 2000 *C. R. Acad. Sci.* IIb **328** 411
[12] Nikolayev V S and Beysens D A 2002 *Phys. Rev.* E **65** 046135
[13] Nikolayev V S and Beysens D A 2003 *Europhys. Lett.* **64** 763
[14] Andrieu C, Beysens D A, Nikolayev V S and Pomeau Y 2002 *J. Fluid Mech.* **453** 427
[15] Narhe R, Beysens D and Nikolayev V S 2004 *Langmuir* **20** 1213
[16] de Ruijter M J, De Coninck J and Oshanin G 1999 *Langmuir* **15** 2209
[17] Nikolayev V S, Gavrilyuk S L and Gouin H 2005 submitted
[18] Iliev S, Pesheva N and Nikolayev V S 2005 *Preprint*
[19] Golestanian R and Raphaël E 2003 *Phys. Rev.* E **67** 031603
[20] Pomeau Y and Vannimenus J 1984 *J. Colloid Interface Sci.* **104** 477
[21] Schwartz L W and Garoff S 1985 *Langmuir* **1** 219
[22] Jin W, Koplik J and Banavar J R 1997 *Phys. Rev. Lett.* **78** 1520
[23] Joanny J F and Robbins M O 1990 *J. Chem. Phys.* **92** 3206
[24] Press W H, Teukolsky S A, Vetterling W T and Flannery B P 1997 *Numerical Recipies in C* 2nd edn (Cambridge: Cambridge University Press)
[25] Cubaud T and Fermigier M 2004 *J. Colloid Interface Sci.* **269** 171

PHYSICAL REVIEW E **72**, 011606 (2005)

Quasistatic relaxation of arbitrarily shaped sessile drops

Stanimir Iliev* and Nina Pesheva
Institute of Mechanics, Bulgarian Academy of Sciences, G. Bonchev Street 4, 1113 Sofia, Bulgaria

Vadim S. Nikolayev†
ESEME, Service des Basses Températures, CEA-Grenoble, France
(Received 15 February 2005; published 19 July 2005)

We study a spontaneous relaxation dynamics of arbitrarily shaped liquid drops on solid surfaces in the partial wetting regime. It is assumed that the energy dissipated near the contact line is much larger than that in the bulk of the fluid. We have shown rigorously in the case of quasi-static relaxation using the standard mechanical description of dissipative system dynamics that the introduction of a dissipation term proportional to the contact line length leads to the well-known local relation between the contact line velocity and the dynamic contact angle at every point of an arbitrary contact line shape. A numerical code is developed for three-dimensional drops to study the dependence of the relaxation dynamics on the initial drop shape. The available asymptotic solutions are tested against the obtained numerical data. We show how the relaxation at a given point of the contact line is influenced by the dynamics of the whole drop which is a manifestation of the nonlocal character of the contact line relaxation.

DOI: 10.1103/PhysRevE.72.011606 PACS number(s): 68.03.Cd, 05.90.+m, 68.08.Bc

I. INTRODUCTION

The spreading of a liquid drop deposited on a solid substrate has many technological applications stimulating active research on acquiring accurate knowledge on its relaxation that follows the deposition. More specifically, one is interested to know how the relaxation rate depends on the initial drop shape and the properties of the contacting media. It is a complex theoretical problem and there are numerous studies devoted to drop relaxation using different approaches and techniques: e.g., macroscopic [1–7] and more recent microscopic approaches using molecular dynamic simulations, [8,9] and Monte Carlo simulations of three-dimensional (3D) lattice gas [10] and 2D [11] and 3D Ising models [12], etc., to mention just a few.

In the case of partial wetting this problem turns out to be very difficult because of the presence of the triple gas-liquid-solid contact line. Since the work [1], it has become obvious that the contact line motion cannot be described with the classical viscous hydrodynamics approach that uses the no-slip boundary condition at the solid surface. The velocity ambiguity at the moving contact line leads to the unphysical divergences of the hydrodynamic pressure and viscous dissipation. Multiple approaches were suggested to overcome this problem. Among the most popular solutions one can name a geometrical cutoff [5] or the local introduction of the slip near the contact line [6]. One finds experimentally [13,14] that while the dissipation is finite, it is very large with respect to the bulk viscous dissipation. Several physical mechanisms are suggested to describe the contact line motion [15,16].

Following a suggestion in Ref. [5], a combined approach was proposed in Ref. [17] considering both the bulk viscous dissipation and the dissipation occurring at the moving contact line, to study the drop relaxation in the partial wetting regime. A phenomenological dissipation per unit contact line length was introduced. It was taken to be proportional to the square of the contact line velocity v_n (the first term symmetric in v_n) in the direction normal to the contact line. There the standard mechanical description of dissipative system dynamics was applied to describe the time evolution of the drop contact line in the case of a spherical cap approximation for the drop shape in the quasistatic regime. Considering the drop as a purely mechanical system, the driving force for the drop spreading was balanced by the rate of total dissipation. No assumption was made for a particular line motion mechanism.

This approach was further generalized to any contact line shape in Ref. [18] by writing the energy dissipated in the system per unit time as

$$T = \oint \frac{\xi v_n^2}{2} dl, \tag{1}$$

where the integration is over the contact line of the drop and ξ is the dissipation coefficient.

In the present work we employ this approach to study the quasistatic relaxation of arbitrarily shaped drops in the partial wetting regime. It is assumed here that the energy dissipated near the contact line is much larger than that in the bulk of the fluid. In Sec. II we show that this approach actually leads to the local relation (first obtained in the molecular-kinetic model of contact line motion of Blake and Haynes [15]) between the contact line velocity and the dynamic contact angle at every point of an arbitrarily shaped contact line. In Sec. III we describe a numerical 3D code for studying the relaxation of an arbitrarily shaped drops starting directly from the variational principle of Hamilton, taking into account the friction dissipation during the contact line

*email: stani@imbm.bas.bg
†Mailing address: CEA-ESEME, PMMH, ESPCI, 10, rue Vauquelin, 75231 Paris Cedex 5, France.

motion. In Sec. IV we obtain numerically and discuss the quasistatic relaxation of a drop with different initial shapes. Section V deals with our conclusions.

II. THE MODEL

We consider a model system consisting of a 3D liquid drop placed on a horizontal, flat, and chemically homogeneous solid substrate. Both the drop and the substrate are surrounded by an ambient gas and it is assumed that the liquid and the gas are mutually immiscible. Initially the drop deposited on the substrate is out of equilibrium. Under the action of the surface tension, the incompressible liquid drop relaxes towards spherical cap shape. The drop is assumed to be small enough so that the influence of the gravitation on its shape can be neglected. According to the capillary theory [19,20], the potential energy of the system is

$$U = A_{lg}\sigma_{lg} + A_{ls}\sigma_{ls} + A_{sg}\sigma_{sg}, \tag{2}$$

where the surfaces A_{lg}, A_{ls}, and A_{sg} (with corresponding surface tensions σ_{lg}, σ_{ls}, and σ_{sg}) separate the liquid/gas, liquid/solid, and solid/gas phases respectively. In accordance with the approach described in Refs. [15,17,18], we assume that with the moving contact line a dissipation function T is related, given by Eq. (1).

According to the variational principle of Hamilton one writes

$$\int_{t_0}^{t_1} (\delta K + \delta W)dt = 0, \tag{3}$$

where δW is the virtual work of the active forces and δK is the variation of the kinetic energy of the system. The virtual work is $\delta W = -\delta U + \delta W_1$, where δW_1 is the virtual work related to the friction dissipation (1). A class of virtual displacements is considered in Eq. (3) satisfying the conditions of immiscibility, of conservation of the area of the solid surface, and the condition of constant volume V. Since the Lagrangian is $\mathcal{L} = K - U$, the variational condition given by Eq. (3) can be put in the following form:

$$\int_{t_0}^{t_1} (\delta \mathcal{L} + \delta W_1)dt = 0. \tag{4}$$

The contribution of the kinetic energy of the fluid motion is assumed to be negligible because we consider a quasistatic relaxation here, so that $\mathcal{L} = -U$.

The radius vectors $\vec{R}$ of the points of the liquid/gas interface A_{lg} are taken as generalized coordinates. These coordinates are not independent, their displacements have to satisfy the condition of constant drop volume. Taking into account this condition by introducing a Lagrange multiplier λ and adding the term λV into Eq. (4) one obtains

$$\int_{t_0}^{t_1} (-\delta U + \delta W_1 + \lambda \delta V)dt = 0. \tag{5}$$

The Lagrange multiplier λ (its physical meaning is the pressure jump across the drop surface A_{lg}) varies in time. So in the quasistatic regime one has the following equation:

$$-\delta U + \delta W_1 + \lambda \delta V = 0, \tag{6}$$

where δW_1 is given by (see, e.g., Ref. [21])

$$\delta W_1 = -\xi \oint_L v_n \delta \vec{R} dl. \tag{7}$$

The variation of the potential energy under the constant volume constraint reads [19]

$$\delta(-U + \lambda V) = \int_{A_{lg}} (2\sigma_{lg}k - \lambda)\delta \vec{R} dA_{lg} + \sigma_{lg} \oint_L (\cos\theta_{eq} - \cos\theta)\delta \vec{R} dl, \tag{8}$$

where k is the mean curvature of the liquid/gas interface A_{lg}, $\delta \vec{R}$ is the virtual displacement of the points normal to the drop surface A_{lg} in the first and to the contact line L in the second integrals, respectively, θ is the dynamic contact angle, and θ_{eq} is the equilibrium contact angle defined by the well-known Young equation

$$\cos\theta_{\mathrm{eq}} = (\sigma_{gs} - \sigma_{ls})/\sigma_{lg}. \tag{9}$$

Substituting Eqs. (7) and (8) in Eq. (6) and taking into account the independence of the virtual displacements of the points of the interface A_{lg} and of the contact line L (due to which each of the integrands must be equated to zero separately), one obtains the Laplace equation

$$-2\sigma_{lg}k + \lambda = 0, \tag{10}$$

from which the surface shape can be obtained at any time moment and the equation

$$[\cos\theta_{\mathrm{eq}} - \cos\theta(\vec{R})] = \frac{\xi}{\sigma_{lg}} \vec{v}_n(\vec{R}), \quad \vec{R} \in L \tag{11}$$

valid at the contact line. Equation (11) serves as a boundary condition for Eq. (10). For a given volume V and arbitrary initial contact line position L_0, Eqs. (10) and (11) define the evolution of the drop shape and of the drop contact line. However, in our calculations we will not use Eqs. (10) and (11) directly, we will use Eqs. (6) and (7) instead.

The final drop shape is that of a spherical cap. The radius R^* of its contact line serves as a characteristic length scale. The time

$$\tau_0 = R^* \xi / \sigma_{lg} \tag{12}$$

defines a characteristic time scale.

When the spherical cap approximation can be used for the drop shape then at any moment of time only one parameter is needed to specify the instantaneous configuration of the drop: either the time-dependent base radius $R(t)$ or the dynamic contact angle $\theta(t)$. The drop volume conservation condition implies a relationship between $R(t)$ and $\theta(t)$:

$$R^3(t) = \frac{3V}{\pi} \frac{[1 + \cos\theta(t)]\sin\theta(t)}{[1 - \cos\theta(t)][2 + \cos\theta(t)]}. \tag{13}$$

Thus Eq. (11) leads to the following ordinary differential equation for the dynamic contact angle $\theta(t)$ [22]:

$$\frac{d\theta}{dt} = \left(\frac{\pi}{3V}\right)^{1/3} \{[1-\cos\theta(t)][2+\cos\theta(t)]^2\}^{2/3} \times[\cos\theta(t) - \cos\theta_{\mathrm{eq}}]. \quad (14)$$

Note, that the well known dependencies $\theta(t) \sim t^{-3/7}$ and $R(t) \sim t^{1/7}$ (see, e.g., Refs. [17,22,23]) are asymptotic solutions of Eqs. (13) and (14) for small contact angles.

Nikolayev and Beysens [18] considered the relaxation of an elongated drop by assuming its surface to be a part of a spheroid at any time moment. The contact line is then ellipse with half axes $R^*(1-r_x)$ and $R^*(1+r_y)$ where the relative deviations r_x and r_y were assumed to be small $0 < r_x, r_y \ll 1$. Such an approximation can be adequate at the end of the relaxation. However, it allowed only the case $\theta_{\mathrm{eq}} < \pi/2$ to be considered. Nikolayev and Beysens obtained exponential asymptotic solutions for $r_x(t)$ and $r_y(t)$. Two relaxation times were identified. One of them appears when the drop surface is a spherical cap, i.e., when $r_x(0) = -r_y(0)$:

$$\tau_s = \tau_0/[\sin^2\theta_{\mathrm{eq}}(2+\cos\theta_{\mathrm{eq}})]. \quad (15)$$

When the initial contact line is an ellipse with $r_x(0) = r_y(0)$, the relaxation time obtained using spheroidal approximation reads

$$\tau_n = 45\tau_0(1+\cos\theta_{\mathrm{eq}})/[(108+41\cos\theta_{\mathrm{eq}}+14\cos^2\theta_{\mathrm{eq}} + 17\cos^3\theta_{\mathrm{eq}})(1-\cos\theta_{\mathrm{eq}})]. \quad (16)$$

III. DESCRIPTION OF THE NUMERICAL ALGORITHM

The following numerical algorithm was implemented. First, for a given position of the contact line and fixed volume V the equilibrium drop shape is determined. Then the normal projection of the velocity at every point of the contact line is obtained by the help of Eqs. (6) and (7). Next, from the kinematics condition

$$\frac{d\vec{R}}{dt} = \vec{v}_n, \quad (17)$$

the contact line position at the next instant of time is found explicitly. The above algorithm is repeated for the successive time steps.

The main ingredients of this algorithm are the determination of the equilibrium drop shape with given volume and given contact line, and the calculation of the velocity of the contact line. The drop shape algorithm is essentially an iterative minimization procedure based on the local variations method [24]. Here, only a very concise description will be given; more details can be found in Ref. [25]. The drop shape is approximated by a set of flat triangles with total of $N=12781$ vertex points, $N_L=360$ of these are located at the contact line (see Fig. 4). For a given contact line, the area of the drop surface is expressed in terms of the coordinates of the N points. The change of the drop shape is achieved by approximation of the virtual displacements. In the $3N-3N_L$ coordinate space, the set of all possible displacements of $N-N_L$ points is considered while keeping the volume and the contact line constant. We use the Monte Carlo scheme for choosing the points which we will try to move. At every iteration step the drop shape is changed in such a way that the free energy decreases while the drop volume is kept constant. Thus eventually the minimal drop surface is found.

The approximation of the normal projection of the velocity of the contact line at each of the $N_L=360$ vertex points of the contact line is obtained by solving the finite approximation of Eq. (6). The method takes into account that the finite approximation of Eq. (6) is described by energy and volume variations under displacements of these points. The correctness of the obtained solution at every time step is checked by keeping track of the accuracy with which the coordinates of the points from the surface satisfy the Laplace condition and Eq. (11). For given contact line and volume, the initial approximation of the drop shape is found in the following way. First, for the given volume we find the spherical cap approximation. Then we perform an iterative procedure which transforms the contact line gradually while the volume is kept fixed until the desired contact line is obtained.

In order to ensure better work of the minimization procedure, we perform regular check of the surface mesh and readjust the mesh to keep the approximation of the liquid/gas interface uniform. This allows us to maintain high accuracy in determining the contact angle with an error of the order of 0.01°. At a given contact line node point the contact angle is defined as the angle between the plane of the substrate and the plane of the triangle whose corner coincides with that point.

IV. RESULTS AND DISCUSSION

A. Spherical cap relaxation

To test the described above 3D code, we check it against the numerical solution of Eqs. (13) and (14) obtained for a broad interval of values of the equilibrium contact angle θ_{eq}. The initial contact line radius differs from its equilibrium (final) value R^*, the deviation being $\Delta R_0 = R(0) - R^*$. As follows from Eq. (12), we can set $R^*=1$ and $\tau_0=1$ without a loss of generality.

A comparison of the numerical data, obtained by both methods and displayed in Fig. 1, shows a very high (less than 1%) accuracy of the 3D code. It can be seen from Fig. 1 that for the same values of θ_{eq} and $|\Delta R_0|$ the solutions for receding contact line $R(0) > R^*$ and advancing contact line $R(0) < R^*$ differ. This follows directly from Eqs. (11) and (13) since the following inequality holds:

$$|\cos\theta(R^*) - \cos[\theta(R^*) + \delta\theta]| \neq |\cos\theta(R^*) - \cos[\theta(R^*) - \delta\theta]|. \quad (18)$$

By substituting this inequality in Eq. (11) it follows that for the same absolute value of the deviation $|\Delta R_0|$ there is a difference in the initial velocities for advancing and receding contact lines.

We studied the possibility to fit the obtained numerical solutions for $R(t)$ by power and exponential functions. We

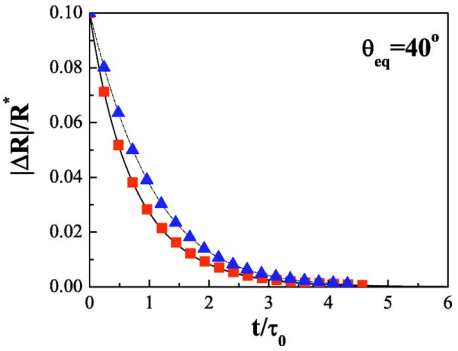

FIG. 1. (Color online.) Time dependence in τ_0 units of the absolute value of the deviation of the contact line radius from the equilibrium value $|\Delta R(t)|$ in R^* units for $\theta_{eq}=40°$ calculated for a drop with a spherical cap shape. Solid and dashed lines: solutions of Eqs. (14) and (13) for $R(0)<R^*$ and $R(0)>R^*$, respectively. Squares and triangles: numerical 3D calculations for $R(0)<R^*$ and $R(0)>R^*$, respectively (for convenience, every 20th data point is displayed).

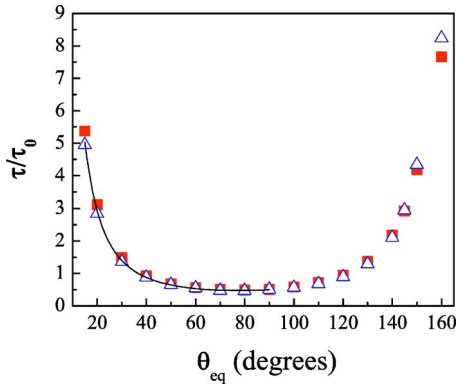

FIG. 2. (Color online.) The spherical cap relaxation time τ in τ_0 units as function of the equilibrium contact angle θ_{eq} for initial deviation $|\Delta R_0|=0.03$ in R^* units: the solid squares are the results for $\Delta R_0=0.03$; the empty triangles are the results for $\Delta R_0=-0.03$ and the solid line is τ_s [Eq. (15)] for $\theta_{eq}<90°$.

use the following definition of the relative error of the fit $\overline{R(t)}$ with respect to $R(t)$:

$$\Delta = \max_{t=0}^{t^*}\left(\frac{|R(t)-\overline{R(t)}|}{|R(t)-R^*|}\right). \tag{19}$$

For small initial deviations $|\Delta R_0|$, it turns out that the exponential fit with

$$\overline{R(t)} = R^* + |\Delta R_0|\exp(-t/\tau), \tag{20}$$

where τ is the only fitting parameter, describes very well the data for all studied values of θ_{eq}. The relaxation time τ depends on the initial deviation ΔR_0 and when $|\Delta R_0|\to 0, \tau$ tends to the spherical relaxation time τ_s [Eq. (15)].

We first obtained the solutions for $|\Delta R(t)|$ by the 3D numerical simulation for initial deviation $|\Delta R_0|=0.03$ and for contact angles $15°\leqslant\theta_{eq}\leqslant 165°$. By fitting the obtained solutions with exponential decay function we determined the corresponding relaxation time τ as function of the equilibrium contact angle θ_{eq} in the above interval of values. This dependence is shown in Fig. 2: the squares are the results for $\Delta R_0=-0.03$ and the open triangles are for $\Delta R_0=0.03$. The thin solid line in the figure is the spherical relaxation time τ_s [see Eq. (15)] in the interval $\theta_{eq}<90°$. The exponential approximations of the solutions are obtained in the time interval $[0,t_{end}^{100}]$ determined so that $|R(t_{end}^{100})-R^*|=0.01|R(0)-R^*|$, that is the amplitude of the initial deviation has decreased hundred times. The exponential approximation is obtained under the condition that it coincides with the numerical solution at the initial and final points $\{0,t_{end}^{100}\}$. The maximal relative deviation of the obtained exponential approximations from the numerical solutions does not exceed $\Delta<3\%$. When $|\Delta R_0|$ decreases the precision of the exponential approximation increases. When $|\Delta R_0|$ increases, e.g., $|\Delta R_0|=0.1$, 0.2 the precision of the exponential approximation to the numerical solution of Eqs. (13) and (14) in the time interval $[0,t_{end}^{100}]$ decreases.

When the equilibrium contact angle θ_{eq} increases the relative deviation Δ decreases. The cases of advancing and receding contact lines differ with less than 1–2 % for $\theta_{eq}\geqslant 40°$. Also when $|\Delta R_0|$ increases, so does the deviation of the relaxation exponent τ [Eq. (20)] from the spherical relaxation time τ_s. When the exponential approximation in the interval $[0,t_{end}^{100}]$ becomes unacceptable, e.g., when Δ more than 3%, or $-\frac{1}{3}R^*\leqslant\Delta R\leqslant 3R^*$ then a good approximation could be obtained either by splitting the interval $[0,t_{end}^{100}]$ into several subintervals and approximating the numerical solution on every such subinterval with an exponential function with a specific relaxation time τ or by fitting the numerical solution with a second or higher order exponential decay function. For example, for the considered cases $|\Delta R_0|=0.1,0.2$ the fit with an exponential decay function of the second order

$$\overline{R(t)} = R^* + a_1\exp(-t/\tau_1) + a_2\exp(-t/\tau_2); |a_1|\geqslant|a_2|, \tag{21}$$

where a_1,τ_1,a_2,τ_2 are the fitting parameters, on the interval $[0,t_{end}^{100}]$ becomes much better than with the first order exponential decay function [Eq. (20)] especially for $\theta_{eq}<40°$. For

TABLE I. Relative deviation Δ of the exponential approximation of second order

	τ_s/τ_0	a_1	τ_1/τ_0	a_2	τ_2/τ_0	Δ
$\theta_{eq}=10°$	11.1	−0.08	10.8	−0.02	3.9	2.7%
$\theta_{eq}=40°$	0.87	−0.084	0.866	−0.016	0.35	1%
$\theta_{eq}=70°$	0.48	−0.092	0.484	−0.008	0.248	0.08%

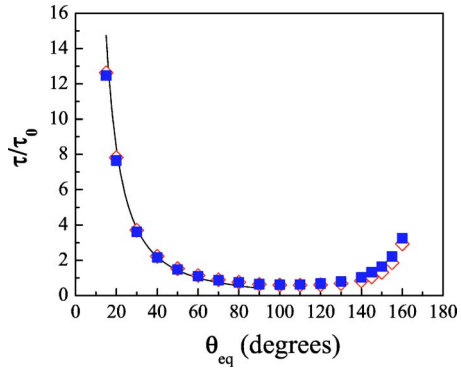

FIG. 3. (Color online.) The relaxation time for the elongated drop in τ_0 units as a function of the equilibrium contact angle θ_{eq} for $r_y(0)=r_x(0)=0.03$ in R^* units: the solid squares and empty diamonds are the results for the exponential fits of $r_x(t)$ and $r_y(t)$, respectively. The solid line is τ_n [Eq. (16)] for $\theta_{eq}<90°$.

example for $\theta_{eq}=40°$ and $\Delta R_0=-0.1$ the maximal deviation with Eq. (21) is less than 1% as compared to 10% with Eq. (20). As can be seen from Table I , τ_1 is close to τ_s and the amplitude a_2 is sufficiently large so that the influence of the second exponent should not be neglected. When the equilibrium contact angle $\theta_{eq}\to\pi/2$ the second amplitude a_2 decreases. For contact angles $\theta_{eq}\in(0,\pi/2)$ the amplitude a_2 in the case $\Delta R_0=0.1$ is smaller than in the case $\Delta R_0=-0.1$. For contact angles $\theta_{eq}>\pi/2$ the opposite is true.

For small contact angles, e.g., $\theta_{eq}=3°$, 5° we tried to fit our data also with a power function $f\sim t^{1/7}$. It appears that it is possible to find a time interval at the beginning where the numerical data is well described by the power function but the overall behavior is still better described by the exponential approximation.

B. Relaxation of elongated drops

Here we consider the relaxation of a liquid drop when the initially elliptical contact line [with initial deviations $r_x(0)=r_y(0)=|\Delta R_0|>0$] relaxes towards circular contact line. We study the time relaxation $r_x(t)$ and $r_y(t)$ of the two extreme

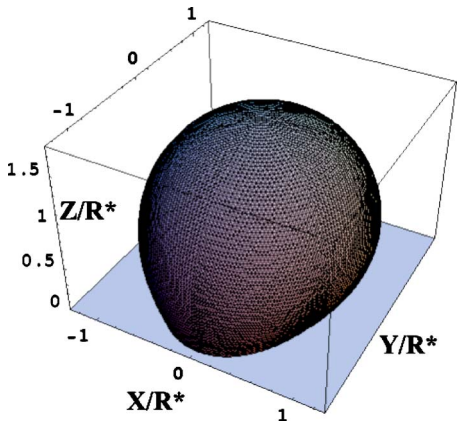

FIG. 4. (Color online.) The initial drop shape with elliptical contact line and minimal surface for $\theta_{eq}=120°$, $r_x(0)=0.2$ in R^* units and volume $V/R^{*3}=5.44$.

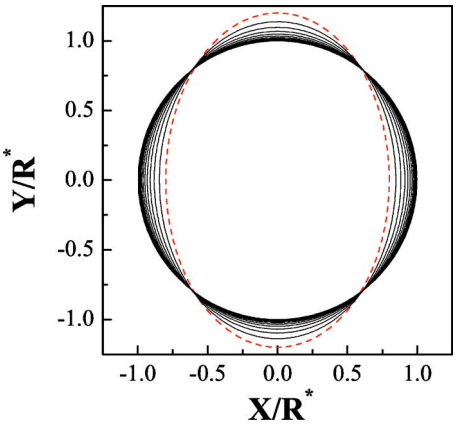

FIG. 5. (Color online.) The contact line positions obtained with time step $(0.2\tau_0)$ for $\theta_{eq}=120°$ and $r_x(0)=0.2$ in R^* units. The dashed line is the initial position.

points M and N of the ellipse, where $R^*(1-r_x)$ and $R^*(1+r_y)$ are the half axes of the contact line ellipse. The goal is to check the validity of the spheroidal approximation in Ref. [18] and extend the results to the domain $\theta>90°$. The analysis of the data obtained by the method described in Sec. III shows that the time relaxation for initial deviations up to $r_x(0)=0.2$ is again well described by an exponential decay function of the first or second order (i.e., by the sum of two exponential functions with different relaxation times) in the time interval $[0,t_{end}^{100}]$. The error of the fit is $\Delta<3\%$. The obtained values for the relaxation time τ [Eq. (20)] for contact angles in the interval $15°\leqslant\theta\leqslant165°$, $r_x(0)=0.03$, are shown in Fig. 3. For $15°\leqslant\theta_{eq}\leqslant50°$ the relative deviation from Eq. (16) is of the order of 2-4 %. Outside of this interval it increases fast and for $\theta_{eq}\sim90°$ it reaches ~60%. The increase of the deviation is due to the fact that the approximation of the spheroidal cap to the quasistationary drop shape is worsening with the increase of the contact angle θ_{eq}. Note that while the surface curvature k has to remain constant along the surface according to Eq. (10), it varies as much as 20% for the spheroid with $r_x(0)=0.1$. In the 3D simulation, the curvature variation along the surface is less than 0.5% which is a good accuracy.

The numerical results for $\theta_{eq}=120°$ and $r_x(0)=0.2$, are shown in Figs. 4–7. The results for other contact angles look

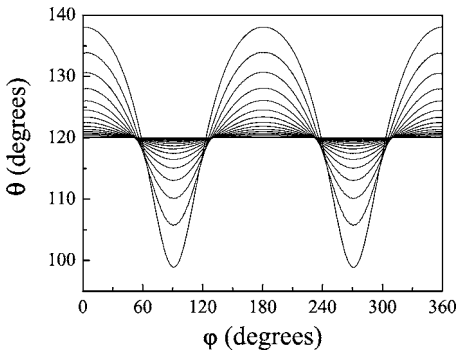

FIG. 6. The contact angle as a function of the polar angle φ at successive moments of time $\{0,0.2n,n=1,2,\ldots\}$ in τ_0 units for $\theta_{eq}=120°$ and $r_x(0)=0.2$.

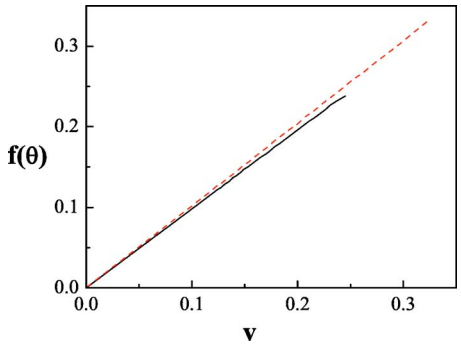

FIG. 7. (Color online.) The dependence of the function $f(\theta)=|\cos\theta(t)-\cos\theta_{eq}|$ on the contact line velocity at two contact line points (N and M) for $\theta_{eq}=120°$ and $r_x(0)=0.2$ in R^* units. The solid line corresponds to $v=dr_y/dt$, and dashed line to $v=dr_x/dt$ (in R^*/τ_0 units).

qualitatively the same way. The initial drop shape is shown in Fig. 4. The volume of the drop is chosen so that the final shape is the spherical cap with a radius of the contact line $R^*=1$ and a contact angle $\theta_{eq}=120°$. The contact line evolution is shown in Fig. 5. The time evolution of the contact angle along the contact line is shown in Fig. 6.

The algorithm efficiency can be checked against Eq. (11) which was not directly used. Figure 6 shows how good the algorithm precision is: the difference between the slopes of the two straight lines is less than 2%.

Note that for equal initial deviations $r_x(0)=r_y(0)$ at M and N the initial contact angles and the initial velocities at both points are different. From the fact that the relaxation times for both r_x and r_y are close [when exponential approximation Eq. (20) is used] it does not follow that the velocities of both points are close as it would seem if one simply differentiates Eq. (20) with respect to time t. This can be seen if one examines carefully Figs. 6 and 7. When the initial deviations are in the interval $\left(-\frac{1}{3}R^*, 3R^*\right)$ then a good approximation could be obtained either by splitting the time interval into several subintervals and approximating the numerical solution on every such subinterval with an exponential function with a specific relaxation time τ or by fitting the numerical solution with a sum of two or more exponential functions.

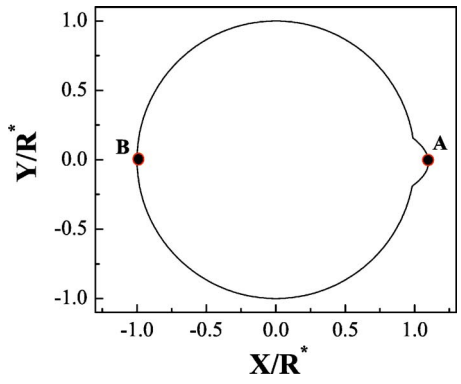

FIG. 8. (Color online.) The contact line of a drop which is almost a spherical cap with a small deformation around one point.

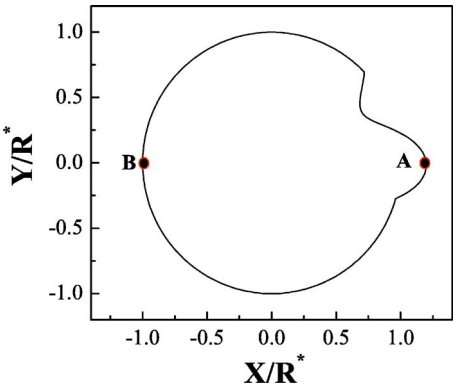

FIG. 9. (Color online.) The contact line of a drop which is almost a spherical cap with larger deformation around the point **A**.

C. Drops of complicated shapes

We study here the relaxation of drops with some example contact lines to demonstrate how the relaxation at one point of the contact line is influenced by the dynamics of the whole contact line. Consider the relaxation of a drop which is almost a spherical cap except for a local perturbation around one point of the contact line. More specifically, let us consider the relaxation of a drop with a final equilibrium contact angle $\theta_{eq}=50°$ and with the initial contact line shown in Fig. 8. We find that the time relaxation of the point **A**(1.1, 0) is well approximated by an exponential decay function (21) of the second order: $a_1=0.066, \tau_1=0.163, a_2=0.024, \tau_2=0.88$ and the relaxation of the point **B**$(-1,0)$ by the exponential decay function (20) of the first order with $\tau=1.05$. All the three relaxation times {0.163, 0.88, 1.05 differ from each other and from the relaxation times for spherical and elongated drops $\tau_s=0.65, \tau_n=1.43$ found for $\theta_{eq}=50°$ from Eqs. (15) and (16). It appears thus that the relaxation of the point **B** is influenced by the perturbation around the point **A**. Moreover even the type of the relaxation of the point **B**, whose neighborhood is a part of circle, is not universal and depends on the deformation around the point **A**. For example, when the contact line is of the type shown in Fig. 9 we obtain that the relaxation of the point **B** is as shown in Fig. 10. It is possible even to find a deformation around **A** such that the relaxation of the point **B** is practically linear in a broad time interval.

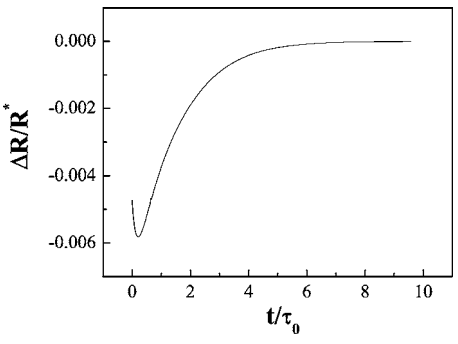

FIG. 10. Time dependence in τ_0 units of $\Delta R(t)$ in R^* units at the point **B** for a drop with initial contact line shown in Fig. 9.

V. CONCLUSIONS

We have described a method and applied it to simulate the quasistatic relaxation of drops with different initial 3D shapes starting directly from the variational principle of Hamilton, taking into account only the large dissipation in the vicinity of the contact line during the contact line motion.

We have shown rigorously for arbitrary contact line shape using the standard mechanical description of dissipative system dynamics that the introduction of a friction dissipation term proportional to the contact line length in the case of quasistatic relaxation leads to the well known local relation between the contact line velocity and the dynamic contact angle.

We find in the case of spherical cap approximation that the time relaxation of the contact line radius is very well described by an exponential decay function of the first or the second order depending on the magnitude of the initial deviation. The relaxation time τ depends on the initial deviation ΔR_0 and when $|\Delta R_0| \to 0, \tau$ tends to the spherical relaxation time τ_s defined in Ref. [18]. For higher values of $|\Delta R_0|$, e.g., $|\Delta R_0| = 0.1, 0.2$, the data is better described by the sum of two exponentials with different relaxation times. The power function fits do not describe well the data.

In the case of elongated drops, the relaxation is again very well described by an exponential decay function. The relaxation time is within 2–4 % from that obtained with the spheroid approximation for the drop shape [18] in the range $15° \leqslant \theta_{eq} \leqslant 50°$. For the larger angles, the relaxation time can only be obtained by the described 3D numerical simulation.

Previously exponential relaxation is found in some experimental studies, e.g., in Ref. [26] and more recently in Ref. [13]. Theoretically, exponential relaxation is found in Ref. [18] and asymptotically at long times in Ref. [17], as well as in the Monte Carlo simulations of the Ising model for drop spreading [12].

By simulating the relaxation of drops of complicated 3D shape, we showed that, although the local Eq. (11) is satisfied, the relaxation at a given point of the contact line is influenced by the relaxation dynamics of the whole drop surface. This is a manifestation of the nonlocal character of the contact line motion.

[1] C. Huh and L. E. Scriven, J. Colloid Interface Sci. **35**, 85 (1971).
[2] O. V. Voinov, Fluid Dyn. **11**, 714 (1976).
[3] E. B. V. Dussan, Annu. Rev. Fluid Mech. **11**, 371 (1979).
[4] L. H. Tanner, J. Phys. D **12**, 1473 (1979).
[5] P.-G. de Gennes, Rev. Mod. Phys. **57**, 827 (1985).
[6] C. Huh and S. G. Mason, J. Fluid Mech. **81**, 401 (1977).
[7] R. G. Cox, J. Fluid Mech. **168**, 169 (1986).
[8] T. D. Blake, A. Clarke, J. de Coninck, and M. J. de Ruijter, Langmuir **13**, 2164 (1997).
[9] M. J. de Ruijter, T. D. Blake, and J. de Coninck, Langmuir **15**, 7836 (1999).
[10] S. Tan, Colloids Surf., A **148**, 223 (1999).
[11] E. Cheng and C. Ebner, Phys. Rev. B **47**, 13 808 (1993).
[12] N. Pesheva and J. de Coninck, Phys. Rev. E **70**, 046102 (2004).
[13] C. Andrieu, D. A. Beysens, V. S. Nikolayev, and Y. Pomeau, J. Fluid Mech. **453**, 427 (2002).
[14] R. Narhe, D. Beysens, and V. Nikolayev, Langmuir **20**, 1213 (2004).
[15] T. D. Blake and J. M. Haynes, J. Colloid Interface Sci. **30**, 421 (1969).
[16] Y. D. Shikhmurzaev, Phys. Fluids **9**, 266 (1997).
[17] M. J. de Ruijter, J. de Coninck, and G. Oshanin, Langmuir **15**, 2209 (1999).
[18] V. S. Nikolayev and D. A. Beysens, Phys. Rev. E **65**, 046135 (2002).
[19] R. Finn, *Equilibrium Capillary Surfaces* (Springer, New York, 1986).
[20] L. D. Landau and E. M. Lifshitz, *Fluid Mechanics* (Pergamon Press, Oxford, 1987).
[21] L. D. Landau and E. M. Lifshitz, *Mechanics* (Elsevier Science, Burlington, 2003).
[22] M. de Ruijter, M. Charlot, M. Voué, and J. de Coninck, Langmuir **16**, 2363 (2000).
[23] F. Rieutord, O. Rayssac, and H. Moriceau, Phys. Rev. E **62**, 6861 (2002).
[24] F. L. Chernousko, J. Comput. Math. **4**, 749 (1965).
[25] S. Iliev, Comput. Methods Appl. Mech. Eng. **126**, 251 (1995).
[26] S. Newman, J. Colloid Interface Sci. **26**, 209 (1968).